Australian Centre for Advanced Photovoltaics

Annual Report 2020
Appendix

Change & Innovation

unsw.edu.au

COLLABORATION GRANTS

ACAP's competitively selected Collaboration Grants, are reported online at http://www.acap.net.au/annual-reports.

6.35 A CASE STUDY OF THE DEGRADATION OF FLEXIBLE PHOTOVOLTAIC MODULES

Lead Partner
CSIRO

CSIRO Team
Dr Hasitha Weerasinghe, Mrs Régine Chantler, Dr Doojin Vak, Ms Jyothi Ramamurthy, Mr Andrew Faulks, Mr Karl Weber, Ms Fiona Glenn, Dr Andrew Scully

Interns: Mr Rahul Banakar, Mr Oscar Elsasser

Academic Partner
Australian Academy of Technology and Engineering (ATSE): Mr Peter Pentland, Executive Manager ATSE Schools Program

Stanford University: Prof. Reinhold Dauskardt, Dept. of Materials Science and Engineering

Funding Support
ACAP, CSIRO

Overview

The features of printed solar films (PSFs) make it ideal for them to be integrated into a range of consumer products. In this context, future flexible solar modules are likely to be handled by consumers during the course of real application and the modules will be subjected to different stress conditions and thus cause degradation mechanisms that are not observed in the controlled laboratory environments (Weerasinghe et al. 2016a, b).

This project is a research study of the degradation of organic photovoltaic (OPV) modules exposed to end-user handling and testing, as well as an outreach initiative aiming to develop the awareness on the next generation solar technologies of students acting as the end-users during this study.

Over 100 schools in Australia, New Zealand, the Philippines and Indonesia are taking part in the program and over 25,000 students are involved.

Summary

The main objective of this project is to increase awareness of next generation solar technologies to school students while providing an insight into the degradation mechanisms involved in printed OPV modules under real-world environmental conditions.

The first year of the project was focused on:

- the fabrication and initial characterisation of over 500 OPV modules with varied parameters
- the design and mass-produced data acquisition systems
- the selection of the schools and preparation of training material.

In the second year, the OPV modules along with the measurement kit were deployed into a selected 102 schools from183 applications received. Students conducted experiments using the printed modules for approximately 12 months and returned the OPV modules along with the details about their experimentations and feedback about the program. OPV modules that were returned were subjected to post analysis.

Progress

Module fabrication

Over 100 m of printed solar film (PSF) were produced using roll-to-roll deposition methods in ambient conditions.

The architecture of this solar film is shown in Figure 6.35.1(a). Three layers of the PSF, that is, the electron transport layer (ETL), active polymer layer and hole transport layer (HTL) were coated onto the flexible ITO-PET substrate. The top electrode was printed using screen-printing. Modules were encapsulated in a nitrogen-filled glovebox following an intensive pre-conditioning step which removed the moisture and oxygen adsorbed on both the solar modules and encapsulation material.

Three parameters of the final PSF modules were varied: the ETL layer, the active polymer material and the encapsulation architecture.

Figure 6.35.1(b) illustrates the two different encapsulation architectures (full and partial) used during this study. Table 6.35.1 further illustrates the four types of modules (based on different ETL layer, active polymer material and encapsulation architecture) employed during this study.

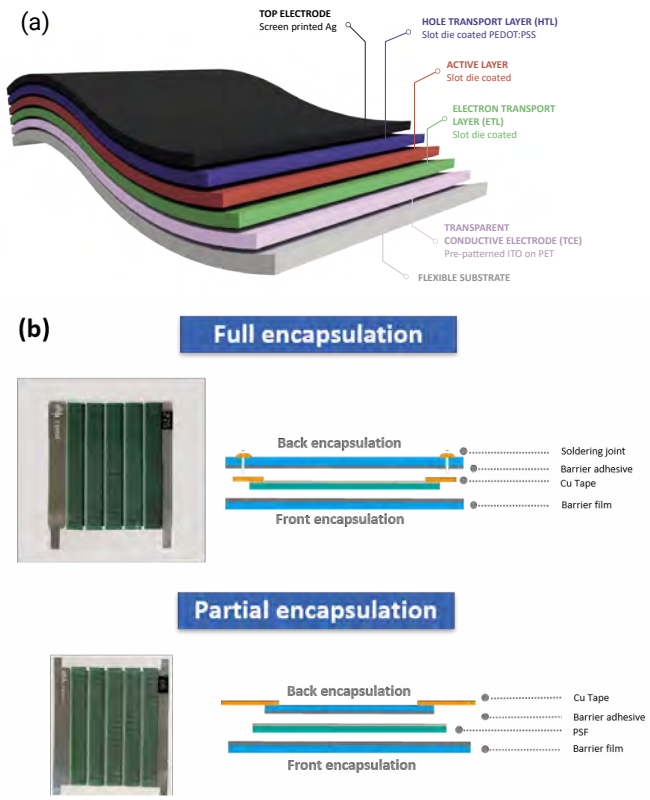

Figure 6.35.1: (a) Schematic of device architecture; and (b) photographic images and cross-section illustrations of full and partial encapsulation architectures.

Table 6.35.1: Overview of the four variants of the OPV modules fabricated with the following device structure: ITO/ETL/Active Layer/ PEDOT:PSS/Ag/Encapsulation.

	ETL	Active Layer	Encapsulation
# CONTROL	PEIE	Pi-4	Full
# P3HT:PCBM	PEIE	P3HT:PCBM	Full
# ZnO	ZnO	Pi-4	Full
# PARTIAL	PEIE	Pi-4	Partial

OPV module deployment

To accompany the modules, a measurement kit was developed.

The kit incorporated:

- four modules
- a load box
- testing leads
- an information booklet including instructions to produce a solar cell power output graph.

The aim of the data acquisition system is to permit students in Years 10–12 to acquire, calculate and plot IV (current-voltage) data from OPV modules. The final design of the acquisition system consists of a low-cost load box using sets of resistors customised for indoor and outdoor measurement. A current-voltage plot can be acquired using a multimeter as shown in Figure 6.35.2. The load box was designed by graduate mechatronics students and mass-produced by a local design house.

(a)

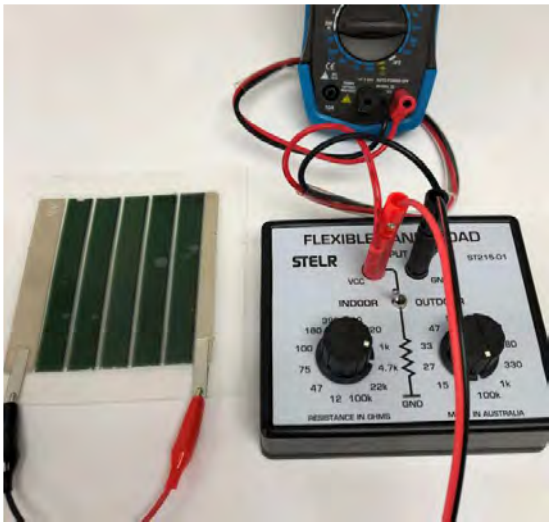

(b)

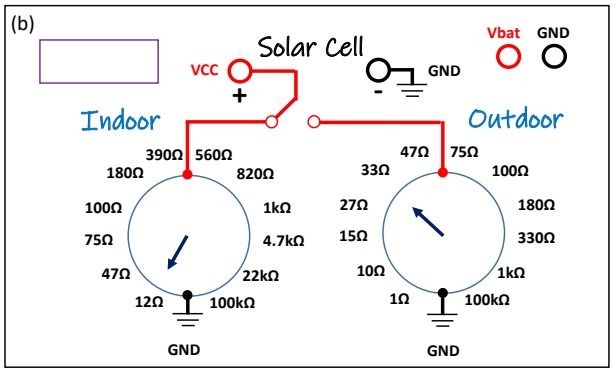

Figure 6.35.2: (a) Photo of the experimental setup used to measure OPV module performance; (b) electronic schematic of the load box used to calculate the module power output; and (c) example of data acquired by students using this setup.

(c)

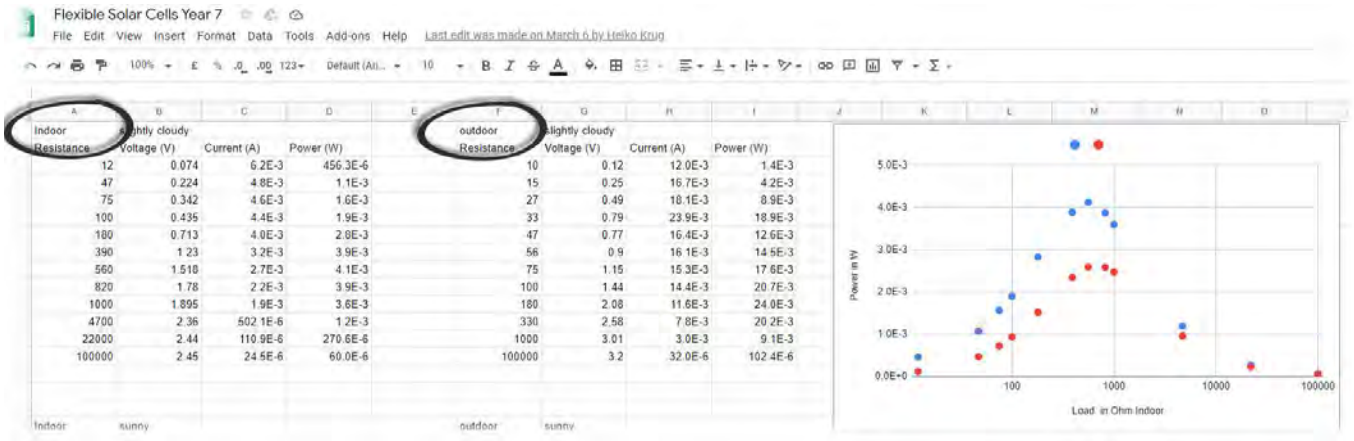

An expression of interest was sent out to over 600 schools and education centres linked to the STELR network.

The following parameters were considered during the selection of schools for this study:

- number of students expected to participate
- the geographical location of the school
- previous participation in the experiments with STELR kits or other STEM initiatives.

Out of the 183 applications received, 102 schools and education centres were selected. Locations of the selected schools are indicated on Figure 6.35.3. Modules were deployed for approximately 18 months between April 2019 and November 2020.

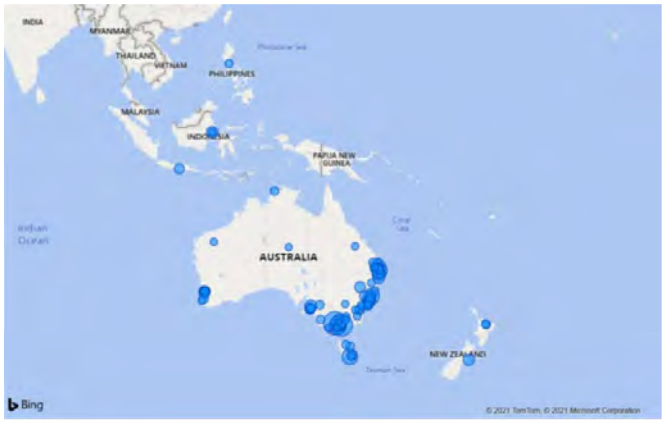

Figure 6.35.3: The map showing the locations of schools and education centres where modules were deployed in this study.

OPV module analysis

J-V curves were obtained using a CSIRO in-house solar simulator under one-sun illumination. Approximately 30% of the modules sent to the schools were returned to CSIRO for post-analysis. Figure 6.35.4 compares IV performance (V_{OC}, J_{SC}, FF and PCE) of the modules before and after returning from the school (after approximately 18 months with the initial measurement).

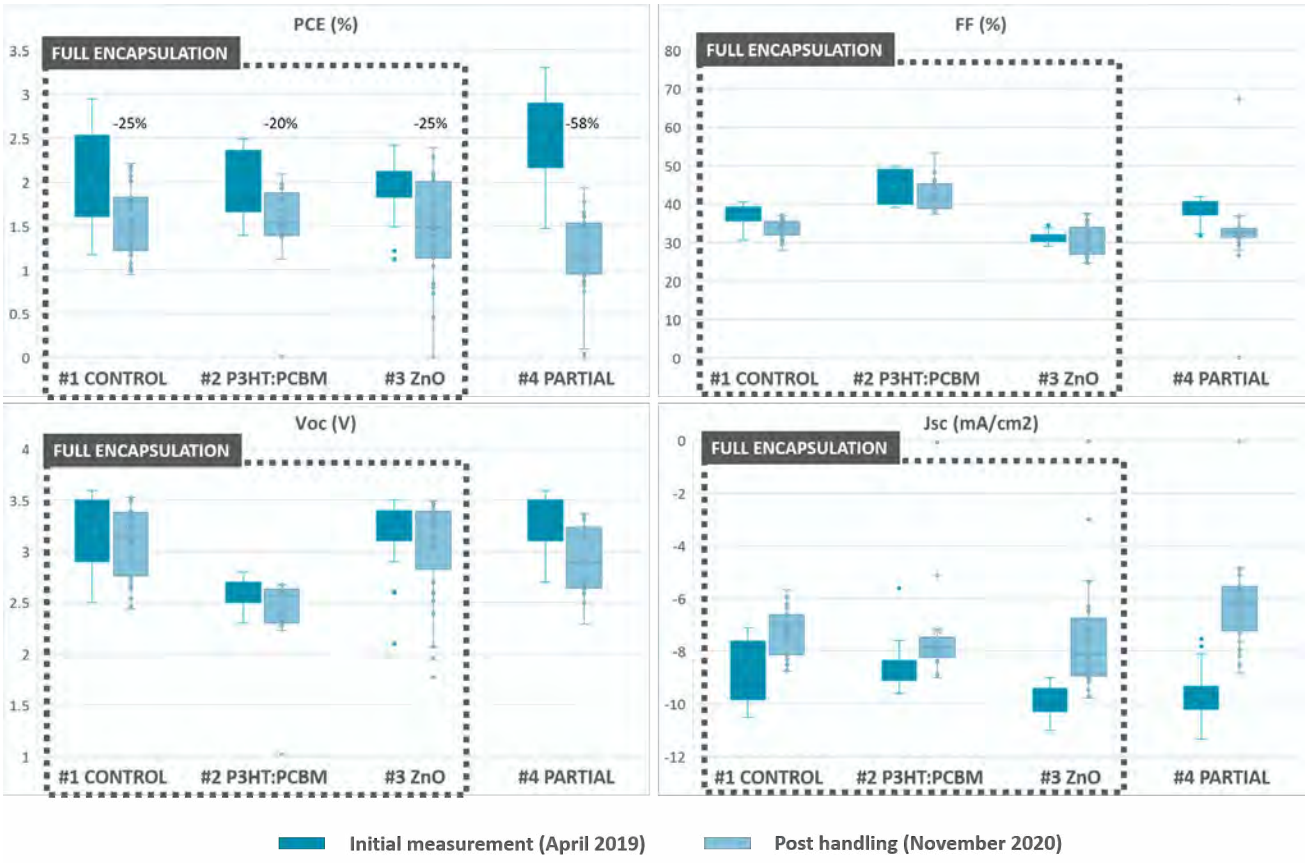

Figure 6.35.4: Distribution of OPV module IV performance measured before and after handling by the students during the study.

The modules were subjected to a wide range of experiments and handling conditions, resulting in various levels of wear and damage. Interpretation of the performance variation thus is complex. However, the PCE drop is significantly higher in partially encapsulated modules with an average of 58% compared with other variants looked at in this study (full encapsulation). Therefore, this preliminary analysis clearly indicates that encapsulation architecture without perimeter-seal is one of the main drivers of the degradation process. Perimeter-seal (new barrier pressure sensitive adhesive) used during this study has clearly prevented the moisture ingress from the sides demonstrating the improved durability compared to the partially encapsulated modules. These findings were confirmed using the photocurrent mapping techniques to determine potential degradation mechanisms. When the modules are encapsulated using the full-encapsulation architecture, no significant dependences of the durability on the two different ETLs (ZnO and PEIE) and the two different active layers (Pi4 and P3HT:PCBM) are observed.

Further analysis on degradation mechanisms

The photocurrent mapping technique is generally used to show the measured local variation in the photocurrent generation within the active area of a photovoltaic module. Our previous studies have demonstrated that modules without edge seal barrier are more susceptible to edge ingress of moisture from the sides and causing the module degradation (Weerasinghe et al. 2016b). The results of this study are in line with previous results. Figure 6.35.5(b) illustrates the degradation around the edge observed on the partially encapsulated modules compared with fully encapsulated modules (Figure 6.35.5(a)) when placed in similar environmental conditions. IV measurements of partially encapsulated modules also indicate that the degradation of the modules around the edge regions has caused a significant drop in the photocurrent of the modules due to the loss of the active area of the modules.

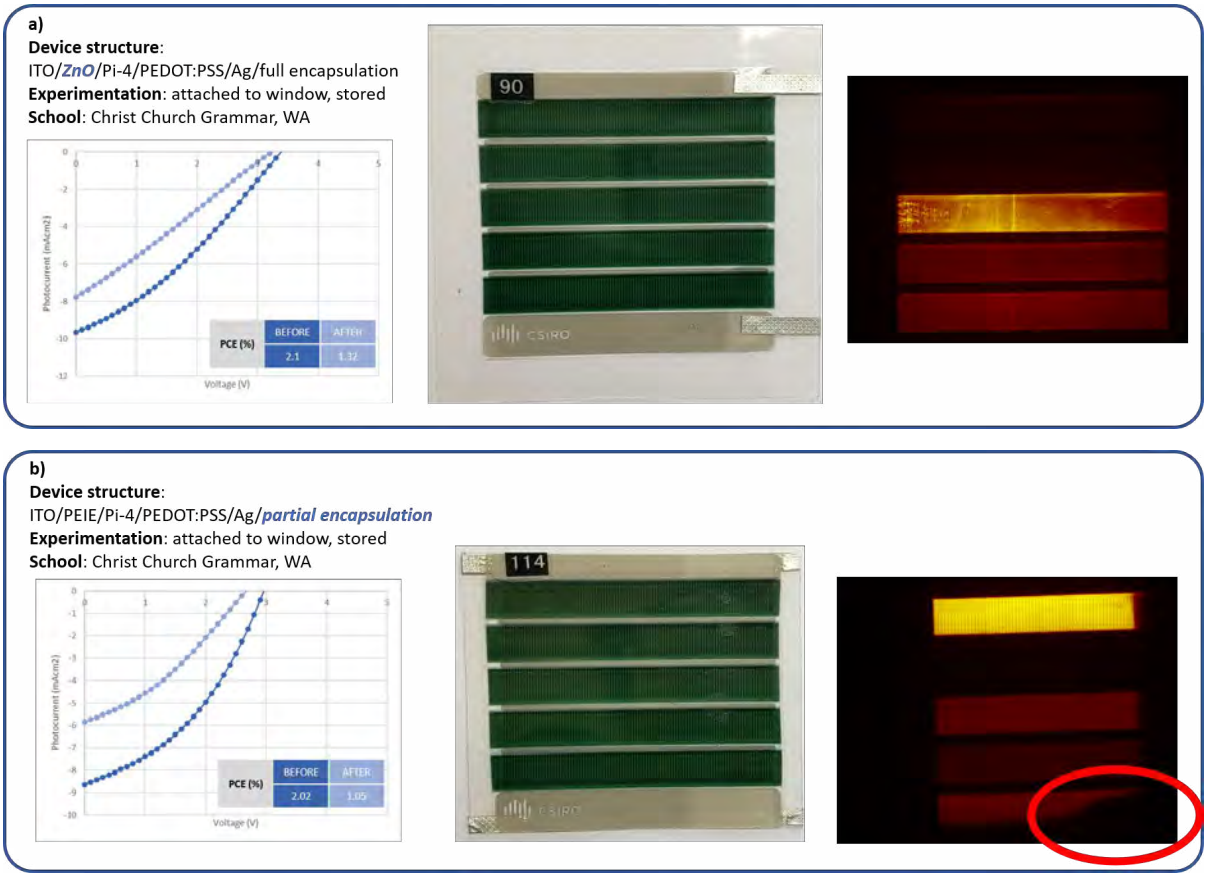

Figure 6.35.5: Image and associated I-V curve and photocurrent map of OPV modules pre and post handling. (b) Partially encapsulated module shows edge degradation (dark area with no current generated) with (a) fully encapsulated module deployed in the same environment.

During the study, some modules with the full encapsulation that had their perimeter edge seal compromised by trimming, sewing or other methods due to some of the experimentations conducted by the students also demonstrated similar edge degradation pattern around the edges of the modules. In addition, severe folding or complex mechanical handling resulted in damage to the barrier encapsulant and/or the delamination of the printed layers of the device. In this case, the degradation develops from the point of impact. These two different degradation patterns are illustrated in Figure 6.35.6.

Further analysis is currently underway to determine the exact failure mechanism in the case of impact degradation.

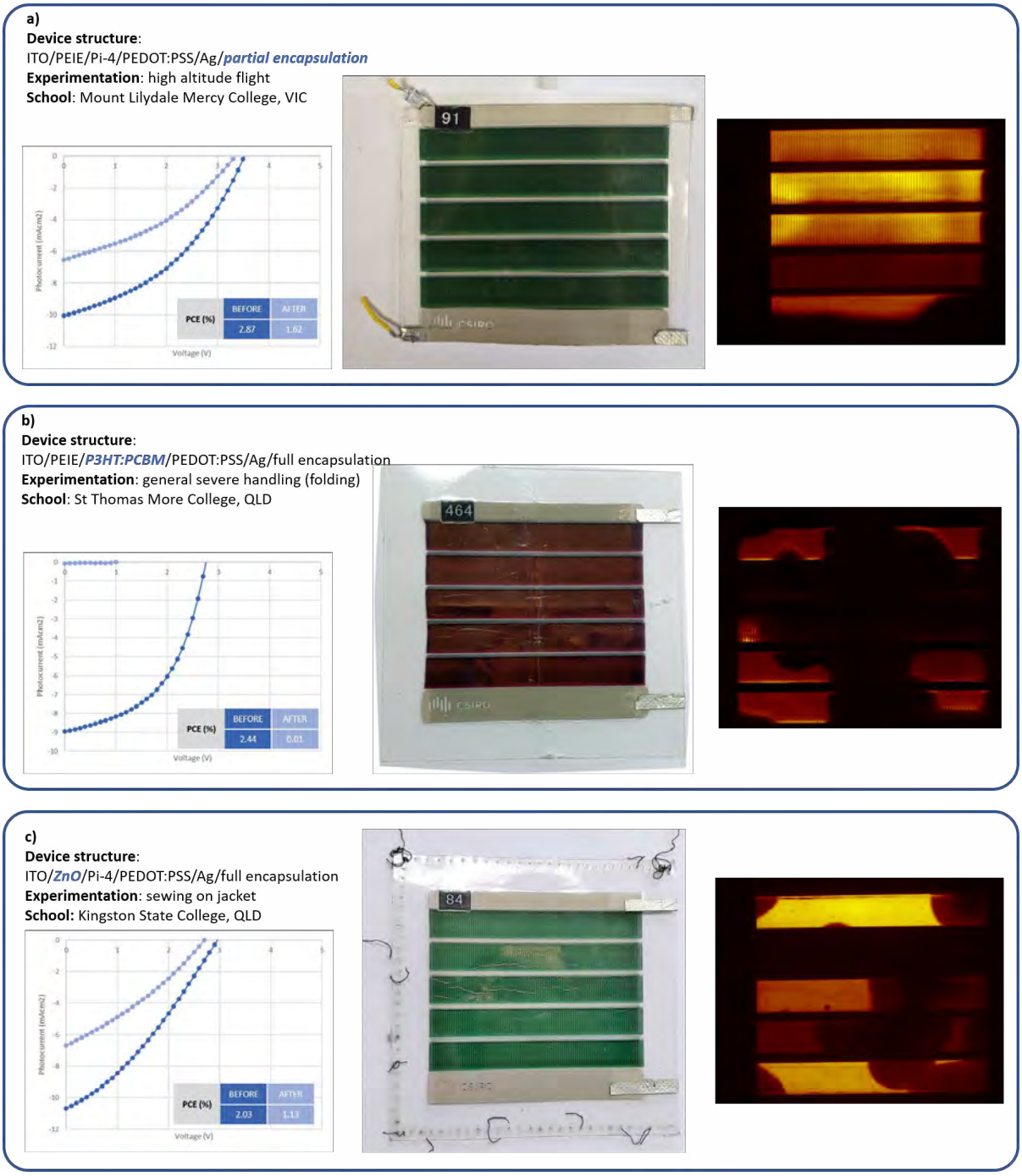

Figure 6.35.6: Photographic images and associated I-V curves (before and after) and photocurrent maps of OPV modules. Modules with compromised edge seal whether from (a) partial encapsulation or (c) sewing shows edge ingress degradation; (b) and (c) illustrate the modules with mechanical damage to the barrier film and/or the printed layers showing the impacted area.

Impact and Highlights

Thanks to this project, over 25,000 students have been introduced to this new printed solar technology. The program has been very well received among the participants.

Some students have developed elaborate experimentations as shown in Figure 6.35.7 and incorporated the OPV modules in various applications notably:

- wearable electronics
- urban design
- aerospace applications.

Students from Bontang High School in Indonesia appeared in the headline news with a short documentary about this new technology and this program (Figure 6.35.8).

Work accomplished in this study was awarded the ACAP Conference Staff prize in 2019. The success and impact of this project highlighted how research in new photovoltaic technologies can take part in the science curriculum in schools.

Figure 6.35.7: Images of some of the experimentations conducted by students. (a) OPV modules sewed onto a jacket at Kingston State College, QLD. (b) OPV modules incorporated into an urban design at Casey Tech School, VIC. (c) OPV modules adhered to the payload of a high-altitude balloon at Mount Lilydale Mercy College, VIC.

Figure 6.35.8: Images of students from Bontang High School, East Kalimantan, Indonesia running their experiments in a short documentary on Ekspos Kaltim, a local TV channel.

Future work

Despite the effect of the coronavirus pandemic, this program has demonstrated remarkable achievements and breakthroughs in 2020. Due to the pandemic situation, we have not been able to recover all the modules sent to the overseas partner but more importantly we have had a delay in conducting delamination and cohesion trials with our Stanford partner.

Preparation of another batch of encapsulated modules (~500 modules) is currently underway. These modules will be sent to the schools as replacements for the modules they have returned to us for the post-analysis.

over the next six months of the project, outdoor and indoor (accelerated) stability tests and decohesion analysis will be conducted to complete all project activities and complete the manuscript currently under preparation.

Given the impact the study has had with the outreach and education component, future work will focus on deepening the relationship with highly involved schools as well as broadening the program to more schools to increase students' awareness of the latest photovoltaic technologies.

References:

WEERASINGHE, H. C., ROLSTON, N., VAK, D., SCULLY, A. D. & DAUSKARDT, R. H. 2016a. A stability study of roll-to-roll processed organic photovoltaic modules containing a polymeric electron-selective layer. *Solar Energy Materials and Solar Cells*, 152, 133-140.

WEERASINGHE, H. C., VAK, D., ROBOTHAM, B., FELL, C. J., JONES, D. & SCULLY, A. D. 2016b. New barrier encapsulation and lifetime assessment of printed organic photovoltaic modules. *Solar Energy Materials and Solar Cells*, 155, 108-116.

6.37 IMPROVING UV STABILITY AND EFFICIENCY OF FOUR-TERMINAL PEROVSKITE/SILICON TANDEM SYSTEM WITH LUMINESCENT DOWNSHIFTING INCORPORATED ENCAPSULANT

Lead Partner

ANU

ANU Team

Dr The Duong, Prof. Kylie Catchpole, A/Prof. Thomas White

Academic Partners

Karlsruhe Institute of Technology (KIT): Prof. Bryce Richard, Dr Ulrich Paetzold
CSIRO Newcastle: Dr Benjamin Duck

Funding Support

ACAP

Aim

The objective of this project is to improve the efficiency and UV stability of perovskite/silicon tandem solar cells using a luminescent downshifting (LDS) material. In the tandem systems, the LDS material will be incorporated into the front encapsulant to convert short wavelength light in the UV range to longer wavelength light to which the perovskite cell responds more efficiently. This will also enhance the stability of the perovskite cell due to the presence of the TiO_2 electron transport layer.

Progress

The process of fabricating LDS-incorporated EVA sheets was again optimised at ANU, and the below procedure was found to be the optimal process to produce high quality sheets. It is worth noting that the EVA solution could be left drying on moulds in open air at room temperature instead of drying inside a vacuum chamber at 60°C as in the previously reported procedure. This significantly enhances the manufacturability of the LDS-incorporated EVA sheets since no vacuum system is required. The dye concentration of 0.13% or 1300 ppm (relative to EVA) was found to generate the highest

photoluminescence quantum yield (PLQY) signal while maintaining the dye uniformity in EVA and minimising the light scattering.

Step 1. Dissolve EVA pellets (DuPont PV1650) in dichloromethane with a concentration of 250 mg ml^{-1}, then stir for two hours on a hotplate at 90°C.

Step 2. Dissolve V570 dyes in dichloromethane with a concentration of 0.325 mg ml^{-1}, then stir for two hours at room temperature.

Step 3. Mix the two abovementioned solutions with a volume ratio of 1:1. This makes the dye concentration of 0.13% or 1300 ppm (relative to EVA). Stir the solution for two hours on a hotplate at 90°C.

Step 4. Take the solution off the hotplate and wait for it to cool down to room temperature. The solution is then poured on a mould and left to dry in open air at room temperature overnight.

As reported in the 2019 annual report, by simply using inverted pyramid textured silicon wafers as moulds, textured LDS-incorporated EVA sheets can be fabricated with PLQY close to 100% and absorption of light at the wavelength of 375 nm also close to 100%. When using at the front side of semi-transparent perovskite solar cells, the textured LDS-incorporated EVA sheets significantly reduce the reflectance between 400 nm and 700 nm and enhance the transparency of the device at the long wavelength region. As this would result in improvement in photocurrents of both semi-transparent perovskite top cells and silicon bottom cells in tandem configurations, J-V characteristics of the perovskite cells and silicon cells in the mechanically stacked tandem configuration (Figure 6.37.1(a)) was obtained and analysed. As shown in Figure 6.37.1(b), the J-V curves of a semi-transparent perovskite cell in both reverse and forward scans show a J_{SC} of 17.5 $mAcm^{-2}$. With the application of a textured LDS-incorporated EVA sheet at the front side of the semi-transparent perovskite cell, the J_{SC} is boosted up to 18.2 $mAcm^{-2}$. This translates to an enhancement in the photocurrent of 0.7 $mAcm^{-2}$ in the semi-transparent perovskite top cell. For comparison, the J_{SC} of the semi-transparent perovskite top cell when a textured EVA sheet without the incorporation of LDS dyes is applied on the front side is 18.0 $mAcm^{-2}$. That means the incorporation of LDS dyes slightly improves the photocurrent of the semi-transparent perovskite top cell by 0.2 $mAcm^{-2}$. The J-V curves of the silicon bottom cell are shown in Figure 6.37.1(c), showing an enhancement on the silicon bottom cell from 18.1 $mAcm^{-2}$ to 18.7 $mAcm^{-2}$ when a textured LDS-incorporated EVA sheet is used at the front side of the perovskite top cell. The same J_{SC} in the silicon bottom cell is observed when a textured EVA sheet without LDS dyes is used, which indicates that the use of the LDS dyes has no effect on the photocurrent of the bottom cell in case a textured foil is already used on the top cell. That is because the LDS dyes only convert UV light to visible light, which will be absorbed completely by the perovskite top cell. Due to the issue with the Quantum Yield (QE) equipment at ANU, it is not possible to obtain and analyse the external QE response of both devices. This could be done when the machine gets fixed in the middle of 2021.

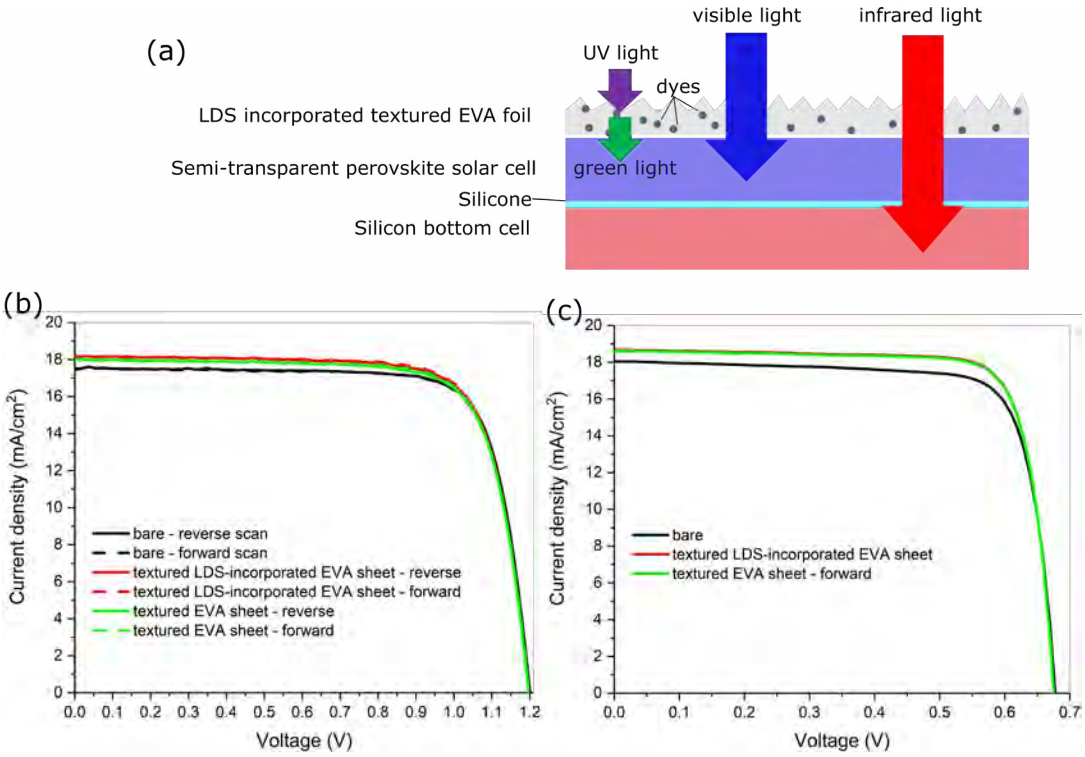

Figure 6.37.1: (a) Schematic of a perovskite/silicon tandem solar cell with an application of a textured LDS-incorporated EVA sheet. (b) J-V curves of a semi-transparent perovskite top solar cell with and without the use of a textured LDS-incorporated EVA sheet. (c) J-V curves of a silicon bottom solar cell with and without the use of a textured LDS-incorporated EVA sheet.

The use of LDS-incorporated EVA sheets at the front side of the perovskite cell is expected to enhance the UV stability of the device (Farooq et al., 2018). To test the UV stability of semi-transparent perovskite cells, high power LED (LZ4-04UV00-0000) was ordered and used as a light source. Figure 6.37.2(a) shows the relative spectral power distribution of the LED with the peak at 365 nm. When testing the semi-transparent perovskite solar cells under the UV LED light, the efficiency of the bare cell gradually degraded to ~93% of the initial efficiency while the cell with a textured LDS-incorporated EVA sheet retained ~98% of the initial efficiency after 24 hours of continuous light exposure. This shows that the LDS-incorporated EVA sheet improves the UV stability of the perovskite cells. UV stability testing with longer duration will be performed subsequently to better evaluate the benefit of the LDS-incorporated EVA sheet.

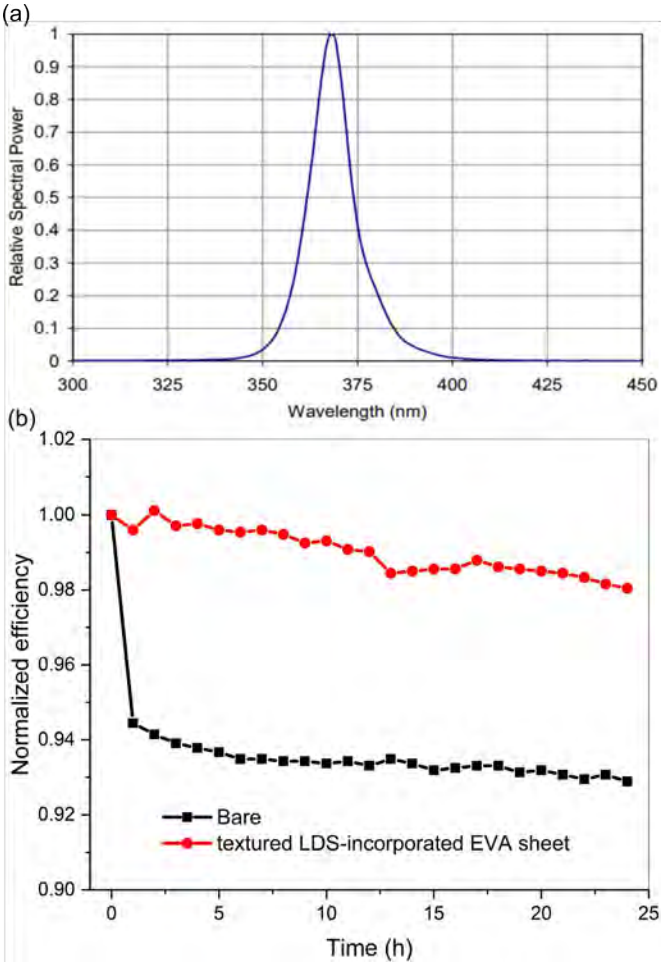

Figure 6.37.2: (a) Relative spectral power distribution of the UV LED. (b) UV stability of semi-transparent perovskite without and with the use of a textured LDS-incorporated EVA sheet.

Highlights

- Optimal procedure for fabricating textured LDS-incorporated EVA sheet was found.
- The use of textured LDS-incorporated EVA sheets improves the photocurrent of the semi-transparent perovskite top cell and silicon bottom cell in the mechanically stacked tandem configuration.
- The UV stability of semi-transparent perovskite is improved with the use of textured LDS-incorporated EVA sheets.

Future work

- Perform EQE measurements and analysis for perovskite/silicon tandem solar cells without and with the use of textured LDS-incorporated EVA sheets.
- Perform UV stability testing for semi-transparent perovskite solar cells without and with the use of textured LDS-incorporated EVA sheets for a duration up to 100 hours.
- Prepare a manuscript on the work to submit to conferences and/or scientific journals.

References

FAROOQ, A., HOSSAIN, I. M., MOGHADAMZADEH, S., SCHWENZER, J. A., ABZIEHER, T., RICHARDS, B. S., KLAMPAFTIS, E. & PAETZOLD, U. W. 2018. Spectral Dependence of Degradation under Ultraviolet Light in Perovskite Solar Cells. *ACS Applied Materials & Interfaces*, 10, 21985-21990.

6.38 NANOSCALE LOCALISATION OF DEFECTS IN SILICON AND CZTS VIA CATHODOLUMINESCENCE AND PHOTOLUMINESCENCE SPECTROSCOPY

Lead Partner

UNSW

UNSW Team

A/Prof. Ziv Hameiri, A/Prof. Xiaojing Hao, Dr Michael Pollard, Mr Robert Lee Chin

Academic Partner

AMOLF: Prof. Albert Polman

Funding Support

ACAP Collaboration Grant, UNSW, UNSW RIS, AMOLF

Aims

The main goals of this project are:

- development of cathodoluminescence- (CL) based measurement methods for silicon-based PV
- development of CL-based measurement methods for CZTS solar cells
- comparison between CL and micro-photoluminescence (μPL) measurements – identify the advantages and disadvantages of each method
- development of methods to extract injection-dependent lifetime using time-resolved PL and CL measurements
- establish a strong collaboration between UNSW and AMOLF.

Progress

In the last year, we have focused on development of a method to map the defect parameters from localised micro- photoluminescence (μPL) measurements. The sub-bandgap PL arising from dislocations in crystalline silicon (known as "D-lines") has been studied for over half a century. However, many properties of the D-lines such as the defect parameters and the underlying recombination mechanism are poorly understood. In this project, we perform both temperature-dependent and injection-dependent mapping and apply this to a cast-mono silicon sample held at room temperature and above. We parameterise the energy levels and defect densities of the D-lines in this sample. We also demonstrate for the first time that the D1 line in silicon wafers originates from the donor-acceptor pair (DAP) recombination mechanism.

Much research has been performed into understanding the nature of sub-bandgap PL (PL_{defect}) arising from the so-called radiative defects in silicon. Known radiative defects in silicon include dislocations, oxygen precipitates, thermal donors, carbon and irradiation-induced centres. In particular, dislocations produce four distinct PL_{defect} peaks known as the D-lines. In impurity-lean dislocated silicon, these are denoted D1, D2, D3 and D4 with peak emission energies of approximately 0.812, 0.875, 0.934 and 0.999 eV at 4.2 K, respectively. In practice, dislocations may be decorated with impurities, including oxygen precipitates or metals, which significantly modify the nature of the D-lines in terms of their peak emission energy and intensity. In multicrystalline (mc) and cast-mono silicon feedstock, dislocations are formed naturally during the growth process. They typically distribute non-uniformly as clusters of dark loops in the band-to-band PL (PL_{BB}) image due to higher recombination compared to the surrounding silicon.

Hence, spatially resolved measurements are useful to investigate D-lines. These measurements are commonly achieved through the use of infrared (IR) PL imaging (PLi) or hyperspectral mapping. IR PL imaging using indium-gallium arsenide (InGaAs) cameras has been used to study the D-lines in mc-silicon. This method requires the use of optical filters to separately image the PL_{BB} and PL_{defect}. In this approach, the entire region-of-interest (RoI) is illuminated and imaged simultaneously, resulting in rapid data acquisition. However, important spectral information, such as the peak emission energy and spectral shape, are not obtained as only the spectrally integrated PL is measured. Additionally, the PL_{defect} intensity itself may be underestimated if the emission occurs at energies outside of the range of the detector spectral sensitivity.

To the contrary, in hyperspectral mapping the spectral PL is measured point-by-point using a PL microscope coupled with a spectrometer. The trade-off relative to imaging approaches is a large increase in measurement time, in the order of seconds per pixel. However, spectral PL provides access to more information at each pixel relative to IR PLi.

A major gap of previous studies is extraction of the recombination parameters of the defects responsible for PL_{defect}. This requires first identifying the radiative recombination mechanism causing PL_{defect}. Such identification necessitates both temperature and excitation light intensity/excess carrier density (Δn) to be varied. However, most studies vary only the sample temperature. In 2019 we studied a mono-crystalline wafer using the above technique. We identified DAP recombination as the mechanism responsible for the observed PL_{defect} peaks. Subsequently, we applied physical models for DAP recombination from literature to determine the defect energies. In 2020 we investigated D-lines using both temperature- and injection-dependent hyperspectral mapping. These measurement methods are denoted as TDH-PL and IDH-PL, respectively.

Many previous studies were performed at temperatures down to as low as 4 K, as PL_{defect} is thermally quenched and therefore weak at room temperature. Only a few studies performed their measurements at room temperature. Here, we employ temperature in the range of 300–343 K. As sample cooling is not required, many measurement averages can be realised to improve signal-to-noise ratio (SNR). This largely compensates for the decreased PL_{defect} intensity with increased temperature. In addition, we perform advanced analysis of the hyperspectral maps including absolute PL calibration, optical and carrier corrections (to improve the spatial resolution) and pixel-by-pixel curve-fitting to extract the spatially resolved defect parameters.

Figure 6.38.1 shows the defect energies determined from TDH-PL and IDH-PL maps. The acceptor energy (E_a) and the donor energy (E_d) values vary within a wide range: 75–275 meV for both E_a and E_d. Remarkably, the sum of the defect energies E_a+E_d remains within the very narrow range of 310–375 meV. The variance is likely due to the standard errors associated with the defect energies, which are up to 20%.

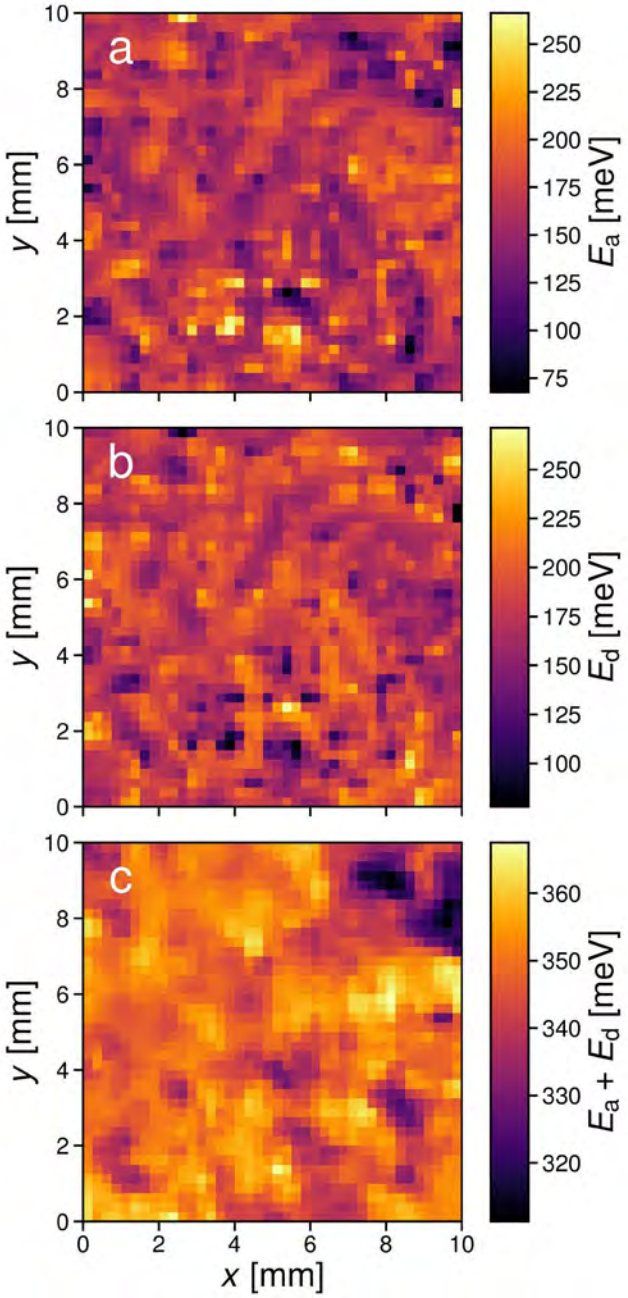

Figure 6.38.1: Defect energy maps (a) E_a (from TDH-PL and IDH-PL). (b) E_d (from TDH-PL) (c) $E_a + E_d$ (from IDH-PL).

Figure 6.38.2 presents the defect energies using a density plot and marginal histograms. The scatter plot gives the parameterisation E_a+E_d = 343:2 meV. For the histograms, both E_a and E_d form broad, symmetric distributions. These are fitted using the normal distribution with mean values (E_a and E_d) of E_a≈167 meV and E_d≈180 meV relative to their respective band edges and standard errors of 20 mV for both E_a and E_d.

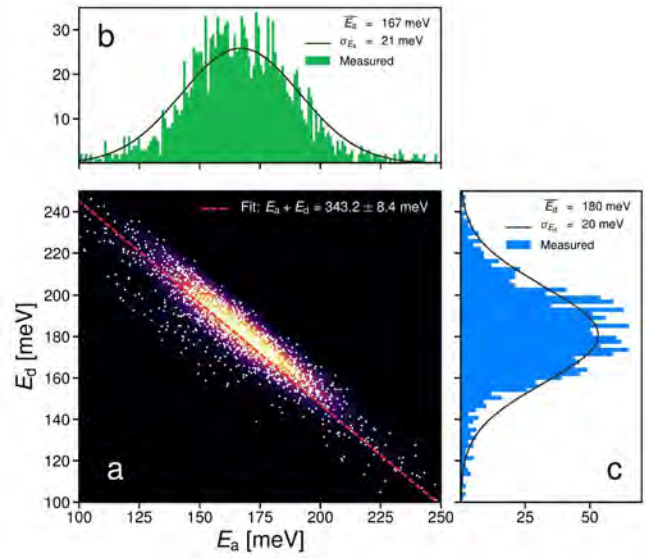

Figure 6.38.2: (a) Normalised density plot of E_d vs E_a. The white points are the measurement coordinates. The dashed, red line is a linear fit to the data. (b) Histogram of E_a. (c) Histogram of E_d.

Highlights

- A visit to UNSW by Professor Albert Polman (February 2020).
- One journal submission by Robert Lee Chin (under review for SOLMAT).
- Installation of a CL system at UNSW.

Summary (project)

In this project, novel hyperspectral-based analysis methods were developed to extract the spatially resolved defect parameters of dislocations in p-type cast-mono silicon. The recombination mechanism responsible for the D1 line was identified as DAP recombination, based on the blue-shift of the peak emission energy with increasing light intensity and the linear dependence of the recombination rate with light intensity. It is assumed the analysis method developed in this project can be extended to the investigation of other radiative bulk defects in silicon such as thermal donors, oxygen precipitates and dislocations in multicrystalline silicon. Bulk radiative defects in non-silicon semiconductor materials may also be probed, assuming a calibration procedure is established. It is noted that this analysis may be easily adapted for hyperspectral imaging. The advantage of such an approach would be the much faster measurement time of seconds/minutes with comparable spatial resolution.

Outcomes (project)

- Two journal papers.
- Development of cathodoluminescence (CL) measurement capabilities at UNSW.
- Development of methods to extract injection-dependent lifetime using time-resolved PL and CL measurements.

- Establish a strong collaboration between UNSW and AMOLF. Two visits of Professor Polman at UNSW and one visit of UNSW researcher (Robert Lee Chin) at AMOLF.

References

LEE-CHIN, R., POLLARD, M., ZHU, Y & HAMEIRI, Z. 2020. Detailed analysis of radiative transitions from defects in n-type monocrystalline silicon using temperature- and light intensity-dependent spectral photoluminescence. *Solar Energy Materials and Solar Cells*, 208, 110376.

LEE-CHIN, R., POLLARD, M. & HAMEIRI, Z. under review. Insights into the nature of the D1 dislocation luminescence in silicon via temperature- and injection-dependent hyperspectral micro-photoluminescence. *Solar Energy Materials and Solar Cells*. (under review)

6.39 OPTIMISATION OF SILICON SOLAR CELL FABRICATION PROCESSES USING MACHINE LEARNING ALGORITHM

Lead Partner

UNSW

UNSW Team

A/Prof. Ziv Hameiri, Dr Rhett Evans, Mr Yoann Buratti,
Mr Casper Eijkens (exchange student, Delft University of Technology)

Academic Partner

SERIS: Dr Shubham Duttagupta

Funding Support

ACAP Collaboration Grant, UNSW, SERIS

Aims

The main goals of this project are:

- development of manufacturing optimisation method of silicon solar cell using machine learning
- assess the capability of the developed method to optimise a non-silicon photovoltaic fabrication process
- strengthen the collaboration between UNSW and SERIS.

Progress

RE cently, the Intergovernmental Panel on Climate Change (IPCC) argued that a third of the global renewable energy should be supplied by photovoltaic (PV) energy to reduce emissions to acceptable levels. A key pathway to help accelerate solar growth – and to reach the IPCC's goal – is to increase the power conversion efficiency of PV systems, with even or reduced costs. One easy method to achieve these goals is by optimising the PV manufacturing processes. However, optimising a production line is neither easy nor cheap. For example, optimising a single process using a full factorial design with five key parameters and three levels per parameter requires $3^5 = 243$ experimental runs. Hence, to independently optimise ten consecutive processes, $10 \times 243 = 2{,}430$ experimental runs are needed. However, this procedure does not consider dependencies between processes, as processes are optimised individually. To measure the effect of these dependencies, the number of needed experimental runs increases to an unrealistic number ($3^{50} > 10^{23}$). Although this number can be reduced using design of experiment (DoE) approaches, they have severe limitations when more than 40 parameters are investigated.

In this project, we propose a machine learning (ML) framework for PV production line optimisation. ML has the capacity to learn a wide variety of non-linear patterns in high-dimensional data sets and can be used to build data-driven models of process intra- and inter-dependencies. The approach proposed in this project is a first-of-a-kind simultaneous optimisation of all the fabrication steps. Firstly, an ML model is built, associating process parameters with output cell efficiencies. Here, we use the natural variation of a production line to create an efficiency distribution. Next, a genetic algorithm (GA) optimiser is implemented to identify a set of process parameters that maximises the cell efficiency. At last, the new set of process parameters can be implemented in the production line, which generates a new distribution of cell efficiency. The optimisation method can then be repeated from the first step.

We demonstrate the capabilities of the proposed method using a simulated data set of an aluminum-back surface field (Al-BSF) production line. Using ML, we build an accurate data-driven model that predicts cell efficiencies from more than 40 input process parameters, with prediction errors less than 0.03% absolute efficiency. The proposed optimisation method increases the mean cell efficiency of the simulated production line from 18.07% to 19.45%. The method can be extended to other cell structures such as passivated emitted and rear cell (PERC) or heterojunction cells (HJT) and implemented in current solar production lines, taking PV manufacturing one step closer to industry 4.0.

Inspired by UNSW's Virtual Production Line and PV Lighthouse's PV Factory, a Python package has been developed to simulate the industrial manufacturing of monocrystalline Al-BSF silicon solar cells. The simulation features ten processing steps (such as saw damage etching, diffusion and passivation) and 47 different process parameter inputs (such as etching duration, diffusion temperature and deposition gas flow ratio). The outputs of the Python simulation (such as wafer thickness, diffusion profile and surface recombination velocity) are then fed to PC1D – a finite-element numerical solver for modelling semiconductor devices – to determine the cell efficiency. A combination of process input parameters (a "recipe"), achieving 18% cell efficiency, is chosen to be used as a baseline recipe for this study. A Monte-Carlo approach is used to randomly generate process input parameters following a Gaussian distribution, centred around the baseline recipe and allowing ±1% variation for each input parameter. This creates the "production" efficiency distribution spread typically

seen in Al-BSF solar cell manufacturing lines. It contains around 400,000 cells, with cell efficiencies ranging from 15% to 18.8% with a mean of 17.86% and a standard deviation of 0.32%.

Several commonly used ML models are trained and evaluated on the data set: support vector regression (SV), random forests (RF), adaptive boosting (AB) and neural networks (NN). A five-fold cross-validation (CV) is used to assess which ML model is best suited to learn the relationship between the inputted recipe and the resulting cell efficiency, while mitigating the risk of over-fitting.

Results

To compare the ML models, a five-fold cross-validation method is applied. The RMSE and R^2 as a function of the size of the used data set (from N=100 to N=400,000) is plotted in Figure 6.39.1. For each model, the average score ("symbol") on the validation block and its 95% confidence interval ("shaded area") are shown. The RMSE is shown on a semi-log plot to accentuate the differences between the ML models. For small data set size (N~100), the four ML models are comparable with RMSEs averaging 0.3% absolute efficiency error. As the data set size increases (N~1,000), the NN-based models significantly improve and outperform the other three ML models in both RMSE and R^2. This remains true for each fold of the CV, mitigating the risk of over-fitting. NN models have a higher variance than the other models, due to their sensitivity to the random initial weights and the random order in which the data is processed during training. With access to the entire data set (N~400,000), the NN models achieve an R^2=0.994±0.002 and predicts efficiency with an RMSE of 0.023±0.004% (absolute).

It is concluded that NN has the highest potential as a modelling algorithm for solar cell efficiency prediction. Hence, it is the model chosen for the GA optimiser. Focusing on the best NN model, trained on 80% of the full data set, the insert in Figure 6.39.1(b) compares the NN's prediction of cell efficiency to their true efficiency (simulated using Python/PC1D). On the validation set, the NN achieves an R^2 of 99.6% and RMSE of 0.019% absolute efficiency, corresponding to prediction with a relative error below 0.1%. This is a strong demonstration of the ability of NN to learn the complex relationship between a large number of input parameters (47) and the output cell efficiency solely using natural variation within the cell manufacturing processes. This level of accuracy and modelling of inter-process dependencies would be very costly and time-consuming to obtain through a DoE approach.

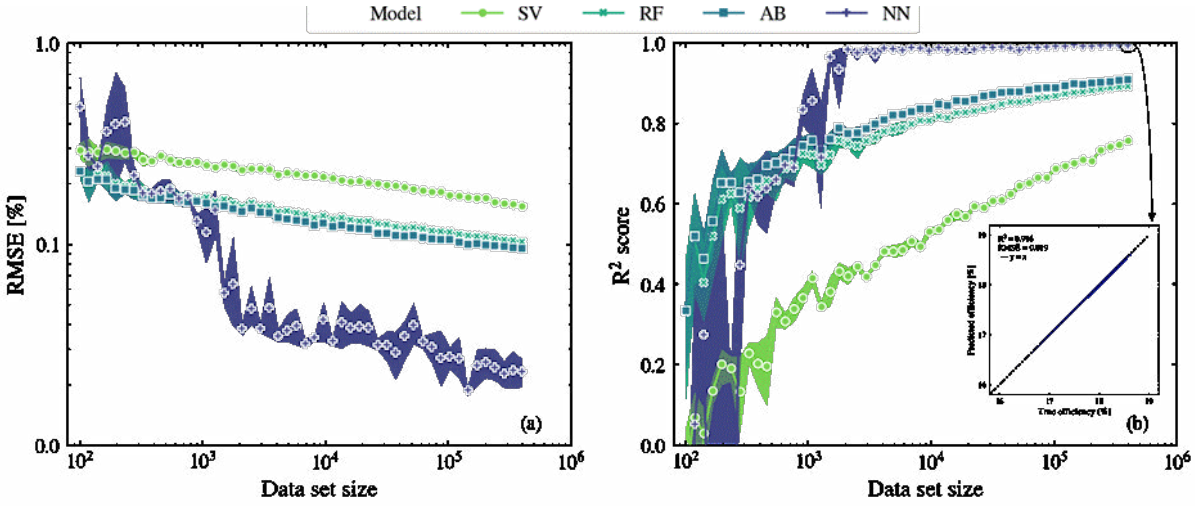

Figure 6.39.1: Machine learning algorithm comparison, each symbol represents the average score on the validation block, while the shaded area indicates the 95% confidence interval for both (a) RMSE scores and (b) R^2 scores of models as a function of data set size. The best performing neural network efficiency prediction selected by the cross-validation is shown as the true vs the predicted cell efficiency on the validation data set in the insert of (b).

In order to maximise the production line's efficiency, the NN model is passed to a GA optimiser as its objective function. The optimiser starts with a population of 100 random individuals, corresponding to 100 recipes (sets of input parameters) from the "production" data set. The optimisation process is inspired by Charles Darwin's natural selection theory of the survival of the fittest. In our study, a "fit individual" corresponds to a recipe producing high efficiency cells, according to the NN. A set of selection, breeding, cross-over and mutation operations transforms the first generation of recipes into a new population of 100 individuals (i.e. new recipes). With each new generation, the overall average fitness (in our study, efficiency) increases.

From the GA optimiser, a new recipe is generated from the average of the best ten recipes of the last generation. The new recipe is fed back to the Python/PC1D Monte-Carlo simulation to generate a new production-type data set, which is then used to iterate the process of training the NN model and optimising through the GA. The results of this process (coined as NEO-GA – NN efficiency optimiser using GA) are shown in Figure 6.39.2. Each iteration of NEO-GA consists of three steps: (1) train an NN to model the distribution, (2) perform GA optimisation and select a new recipe, and (3) generate a new "production" data set from the new recipe with the Python/PC1D simulation. For each new distribution, 10,000 cells are simulated, centred on the new recipe, allowing a ±1% variation for each input parameter. Step (2) is performed with 25 generations, as this amount is sufficient to reach a "plateau". A total of five iterations are performed.

For this part of the study, a new seed production data set is generated, with a mean efficiency of 18.07% and a maximum of 18.36%. After five iterations, the production line efficiencies reach a mean of 19.45% (7.6% relative increase) and a maximum of 19.72% (7.4% relative increase). For each GA optimisation step, the same behaviour is observed, as both NN-predicted (circle) and Python/PC1D-true (cross) average efficiencies match during the first few generations, before reaching a "plateau" from increased extrapolation and fitting errors. The final generation of each GA optimisation step is used to generate a new production data set, which will seed the next iteration of the NEO-GA process. That new data set's standard deviation is comparable with the original production data set (~0.3%) which indicates that the local maximum reached in the plateau phase is stable (less than ±0.5% efficiency variation from ±1% input variation). In iterations two and four, it is seen that the maximum efficiency is lower than the previous distribution. This can be explained by the random approach of the GA and is expected as a consequence of the large parameter space under investigation. However, in both cases the gap between the mean and the maximum efficiency is reduced allowing the NN to learn the relationship between the parameters and the cell efficiency as close as possible to the maximum reached efficiency which will minimise extrapolation error in the following iteration.

To put the significance of such an iterative improvement in perspective, in the International Technology Roadmap for Photovoltaics (ITRPV) reports of 2010, mono-Si production average cell efficiency was reported to be 18% and predicted to reach 19.5% in 2015, five years later. The proposed NEO-GA method has the potential to achieve rapid optimisation of solar cell manufacturing in only a few iterations, and could be implemented in a matter of days. Assuming that a ±1% input parameter variation is within statistical variation of a manufacturing line, by implementing rigorous statistical process control, monitoring processes' actual conditions and wafer tracking, which is the direction predicted by the last ITRPV report, it would be possible to build an initial data set from a standard industrial production line. By implementing the NEO-GA iteration method, running a new production batch with the newly found recipe in lieu of Step (3), it can be expected to significantly improve the average and maximum efficiency of the line, within an acceptable time frame. Note that we validate that the parameters outputted by the NEO-GA are >1% from the baseline recipe (as we assume changes below this threshold are too small to be practical) and stay within the expected process parameter window. On average, GA optimisation leads to input process parameters that differs by 10% from the baseline recipe (maximum change of 25%), which offers useful insights on the production line. Furthermore, by training the NN, an accurate model of the production line can be formed that can be used for R&D projects or further optimisation schemes.

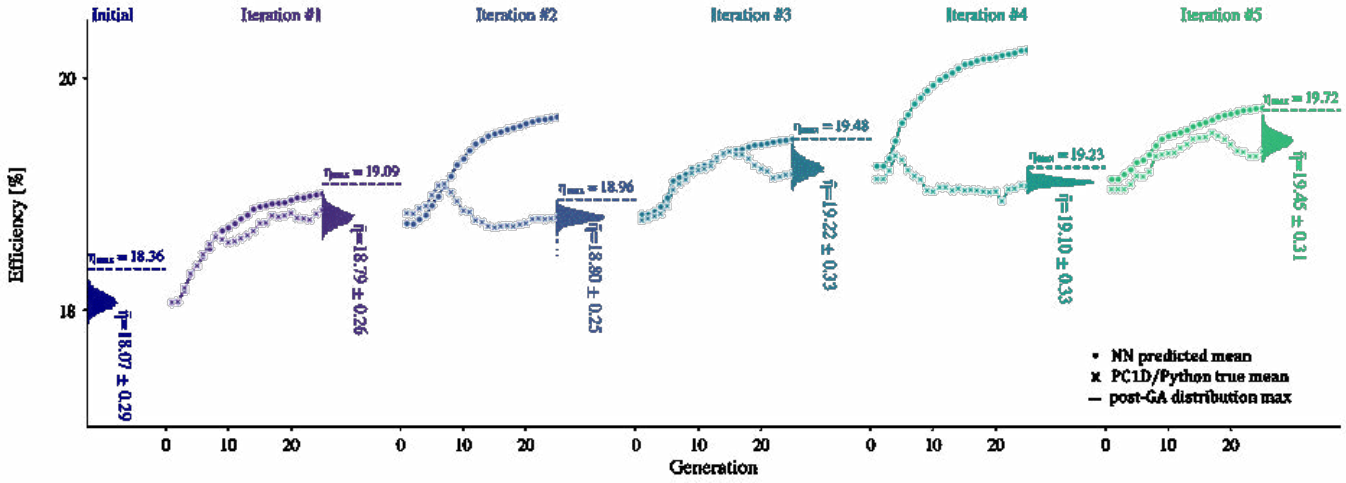

Figure 6.39.2: Successive iteration of the NEO-GA approach, showing the GA predicted (NN) and true (Python/PC1D) efficiency of the average of each generation followed by the efficiency distribution generated by the new recipe found (Python/PC1D); each dotted line reports the maximum efficiency of the distribution, generated from the previous GA step.

Highlights

- A journal publication.
- Initial discussion with PV companies to use the developed method in their production lines.

Project Summary

To keep improving the efficiency-to-cost ratio of photovoltaic solar cells, manufacturing lines need to be continuously improved. Efficiency optimisation is usually performed process-wise and can be slow and time-consuming. In this project, we propose a machine learning–based method to perform simultaneous multi-process optimisation. Using the natural variation of a production line, we train machine learning models to investigate the relationship between process parameters and cell efficiency. We employ genetic algorithms to identify new process parameters to maximise cell efficiency. The proposed method is demonstrated on a simulated production line of monocrystalline aluminium-back surface field solar cells. Using neural networks, an accurate model is built to predict cell efficiencies from input process parameters with errors less than 0.03% absolute efficiency. In five iterations, the mean cell efficiency increases from 18.07% to 19.45%. Provided strong process monitoring and accurate wafer tracking, the proposed method is directly applicable to production-type data sets, enabling the photovoltaic industry to build smart factories and join the fourth industrial revolution.

Project Outcomes

- Development of manufacturing optimisation method of silicon solar cell using machine learning.
- Two conference papers.
- One journal paper.
- Enhanced collaboration between UNSW and SERIS.

References

BURATTI, Y., EIJKENS, C. A. & HAMEIRI, Z. 2020. Optimization of solar cell production lines using neural networks and genetic algorithms. *ACS Applied Energy Materials*, 3, 10317-10322.

EIJKENS, C. A., BURATTI, Y. & HAMEIRI, Z. 2019. Multivariate process optimization of commercial solar cell manufacturing using machine learning, 29th International Photovoltaic Science and Engineering Conference, Xi'An, China, 4–8 November 2019.

EIJKENS, C. A., BURATTI, Y. & HAMEIRI, Z. 2019. Process optimization of commercial solar cell manufacturing using machine learning Asia-Pacific Solar Research Conference, Canberra, Australia, 2–5 December 2019.

6.40 ADVANCING THE PDS TECHNIQUE FOR ALL PHOTOVOLTAIC THIN FILMS

Lead Partner

UNSW

UNSW Team

Prof. Xiaojing Hao, Prof. Gavin Conibeer

UNSW Student

Xueyun Zhang

Academic Partners

University of Tokyo: Prof. Masakazu Sugiyama, Prof. Yoshitaka Okada

Macquarie University: Dr Binesh Puthen Veettil

Industry Partner

Open Instruments: Dr Henner Kampwerth, Dr Michael Pollard

Funding Support

AUSIAPV, UNSW, University of Tokyo

Aims

The system was initially developed at UNSW through an ARENA Fellowship during 2013–2015 and further developed towards commercialisation in stages with industrial collaborator Open Instruments and support from ACAP (ACAP Collaboration Grant Round 3) and ARENA (ARENA Commercialisation of R&D).

The relevant detail for this project is that the instrument measures the heat that is generated by the photo- absorption of the sample. The heat signature represents the number of absorbed photons by assuming that all absorbed energy will recombine thermally ("dark" recombination).

A typical PDS measurement does not extract charge carriers via electrical contacts and radiative emission (photoluminescence) can be calibrated out. However, if the measurement sample is a photovoltaic device with electrical contacts, the measured "dark" recombination can be altered; new measurement modes become possible.

For contacted devices, "dark" energy losses due to shunt resistance, series resistance and defect recombination and thermalisation are of interest. While shunt and series resistance losses can be measured electrically (I-V curve), losses due to defects and thermalization are extremely difficult to measure. It is here that the temperature-measuring PDS system comes into its own. With PDS, it is possible to measure all three of these components by modulating conditions that affect different loss mechanisms.

For this project, the latest laboratory PDS setup and first industrial setup, developed with ACAP support and in collaboration with Open Instruments, are used and shown in Figure 6.40.1. Both will be modified accordingly to allow electrical biasing.

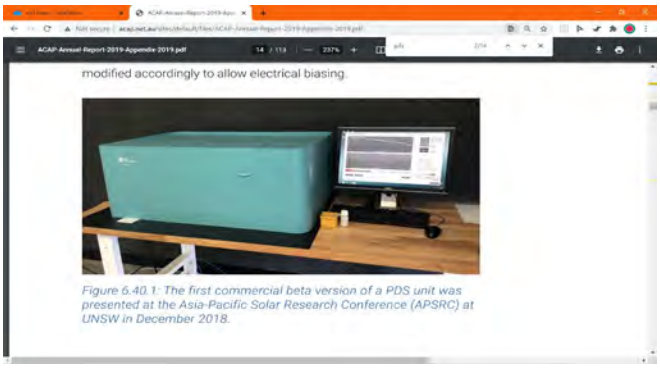

Figure 6.40.1: The first commercial beta version of a PDS unit was presented at the Asia-Pacific Solar Research Conference (APSRC) at UNSW in December 2018.

Progress

The collaboration grant application was prepared during Dr Kampwerth's private visit at Tokyo University, where he met Prof Sugiyama and his research group.

Once the grant became active, Prof Sugiyama visited UNSW for the Asia-Pacific Solar Research Conference (APSRC) at UNSW in December 2018. Subsequently various samples with thin-film quantum structures were send for measurements from Tokyo Uni to UNSW. The specifics of the project and samples required a modification of the measurement equipment at UNSW.

In the second half of 2019 PhD student Meita Asami was selected to come UNSW to facilitate most measurements and to allow a more personal collaboration. The travel was planned for the 1st quarter of 2020 but the outbreak of COVID shut down most of research activates and the planned visit of Mr Asami.

On 6th of March 2021, a six to eight months project extension was requested for the following reasons:

The standard device samples from our Japanese colleagues, turned out to be incompatible with our instruments. An alternative was suggested to adjust the project to focus on Photoreflectance Spectrometry instead, which was also build at SPREE. The measurement data are compatible with the overall aim of the project. The travel restrictions of COVID have been believed to be only of temporary nature, without the impact of the planned visit of a Japanese student.

Highlights

- An exciting new measurement capability of PDS, the measurement of dark carrier recombination, is being explored.

Future Work

With the ongoing COVID travel restrictions, we have cancelled all travel plans for this project. Instead we will extend the measurement work to techniques that are quite similar to PDS for comparison work. Remaining funds will be used for a laboratory assistant to help with measurements and for minor equipment modifications.

This project will conclude Nov 2021. Results will be summarised in the closing report.

References

ARENA - ASI-USASEC Strategic Research Initiative, Collaboration Grants Round 4. Advancing The PDS Technique For All Photovoltaic Thin-Films.

ACAP Collaboration Grant Round 3. Alignment-free PDS tool: From university to industry.

ARENA Commercialisation of R&D. "Launch of a Photothermal Absorption Spectrometer for Cost Reduction in PV Materials".

OPEN INSTRUMENTS. 2019. http://www.openinstruments.com.

6.41 PASSIVATING TUNNEL CONTACTS ON SI BY AI2O3-MONOLAYERS IN SIO2 AND SI-RICH/NANOCRYSTALLINE SIOX

Lead Partner

ANU

ANU Team

Dr Daniel Hiller

Academic Partner

Institute of Energy and Climate Research (IEK-5), Jülich Research Centre, Germany: Dr Kaining Ding, Dr Manuel Pomaska, Malte Köhler

Funding Support

ACAP

Aim

The objective of this project was to investigate combinations of ultra-thin films of SiO_2 or SiO_x and atomic layer deposited Al_2O_3 as passivating hole-selective tunnel contact materials on Si. The challenge was to achieve very good Si surface passivation with <2 nm SiO_2 or SiO_x layers and just (sub)-monolayers of Al_2O_3 so that the whole stack thickness still allows for direct quantum mechanical charge carrier tunnelling. Such layer stacks are optically fully transparent and the materials are firing-stable.

Progress

Initially, it was evaluated how low-temperature thermal tunnel oxides with <2 nm thickness can be grown on Si wafers. After RCA-cleaning including a final HF-dip an oxidation at 700°C for 1–5 minutes was found to provide SiO_2 thicknesses of 1.3 to 1.9 nm, according to variable angle spectroscopic ellipsometry (VASE) measurements. Tunnel oxide layers grown by wet-chemical oxidation or in situ in the ALD reactor were also investigated but were found to provide more inferior passivation qualities than thermal tunnel oxides.

The deposition of ALD ultra-thin films is generally not trivial and cannot be done by extrapolating the thicknesses of steady-state growth because the surface chemistry is different. In this case the tunnel-SiO_2 layer made by dry-thermal oxidation is terminated by Si-O bridge bonds, which leads to an initial growth inhibition in contrast to for example Si-OH terminated surfaces. Using reference-free grazing incidence X-ray fluorescence (GIXRF) measurements conducted at a beamline operated by the Physikalisch-Technische Bundesanstalt (PTB) at the BESSY II synchrotron, the Al-deposition of the initial ALD-cycles was studied. It turns out that the first ALD-Al_2O_3 cycle on thermal tunnel-SiO_2 results in just one-tenth of a steady-state ALD-Al_2O_3 monolayer (ML). Subsequently, it takes 4 ALD-cycles to complete this first ML and 10 ALD-cycles to approach steady-state deposition conditions.

The tunnel-SiO_2/Al_2O_3 (sub)-ML stacks require a thermal activation to form the Al-induced acceptor states in SiO_2 at the SiO_2/ Al_2O_3 interface. Interestingly, this activation also requires intense visible light as generally provided by lamp-heated rapid thermal annealing (RTA) furnaces. We argue that intense above-bandgap light generates a huge electron density in the wafer and provides thereby charge carriers to ionise the initially unoccupied Al-induced acceptor states. Control experiments with anneals in a resistively heated furnace or by sandwiching the sample between two clean dummy-wafers in the RTA (so-called "dark"-RTA) resulted in a 2- to 7-times higher surface saturation current density J_{0s} compared to conventional ("bright"-) RTA. The best RTA parameters found were 825°C for 30 seconds in N_2 atmosphere. These RTA-parameters resemble typical firing conditions of screen-printed silver pastes, rendering the passivating contact stack not only "firing-stable", but actually requiring a firing-like process.

All symmetrical lifetime samples fabricated on 5 Ω·cm n-type FZ-Si wafers with tunnel-SiO_2(1.6 nm)/Al_2O_3 (sub)-ML stacks and RTA exhibit high effective minority carrier lifetimes τ_{eff}. Even just 1 ALD-Al_2O_3 cycle (corresponding to only one-tenth of a steady-state monolayer) allows for J_{0s} values of 80 fA/cm², which drops to 40 fAcm^{-2} for 7 ALD-cycles. A further J_{0s} reduction down to 25 fA/cm² (corresponding to a surface recombination velocity S_{eff} of 2.7 cm s^{-1}) is achieved by an additional forming gas anneal (FGA) at 400°C. Hence, for a passivating contact very promising Si surface passivation qualities are achieved here.

In order to determine the contact resistivity ρ_c, current-voltage measurements were carried out using a Cox-and-Strack pattern with Pd-contacts on p-type Si (hole contact). For 1 ALD-cycle ~200 mΩ·cm² were measured, which increased for 2–4 ALD-cycles to ~540 mΩ·cm². For >5 ALD cycles ρ_c increased exponentially with the number of cycles towards ρ_c-values where a solar cell will experience significant resistivity losses. Hence, the contact resistivity clearly limits the number of ALD-cycles to ≤4 (here in combination with 1.6 nm tunnel-SiO_2), which, however, still provides for very good Si surface passivation.

When aiming for a back-side contact, the direct full-area metallisation of the hole-selective contact with a high work function metal is appropriate. For photoconductance measurements semi-transparent, 7–10 nm thin palladium (WF = 5.12 eV) and nickel (WF = 5.15 eV) layers were thermally evaporated. These experiments revealed however that both metals reduce τ_{eff} by 1–2 orders of magnitude. An uncompromised high level of surface passivation was only maintained by a silver contact. Yet, the Ag work function of 4.26 eV is not compatible with a hole-contact and ρ_c measurements revealed unreasonably high contact resistivities. Either other high work function metals can be found that maintain the Si surface passivation, or non-metal materials have to be taken into account such as transparent conductive oxides (TCO) or transition metal oxides like MoO_x (work function 6.4–6.9 eV). In addition, transparent hole-conducting polymers such as PEDOT:PSS are possible. Any of these non-metal contact materials also enable the use of the optically fully transparent passivating hole-selective contact stack based on tunnel-SiO_2 and Al_2O_3 (sub)-ML as front-side contact or in bifacial cells.

The results summarised here were published by Hiller et al. (2020).

References

HILLER, D., HÖNICKE, P. & KÖNIG, D. 2020. Material combination of Tun nel-SiO_2 with a (sub-)Monolayer of ALD-AlO_x on silicon offering a highly passivating hole selective contact. *Solar Energy Materials & Solar Cells*, 215, 110654.

6.42 OUTDOOR STABILITY/DURABILITY ASSESSMENT OF TWO-TERMINAL PEROVSKITE SILICON TANDEM CELLS

Lead Partner
UNSW

UNSW Team
A/Prof. Anita Ho-Baillie, Dr Jianghui Zheng, Dr Lei (Adrian) Shi

Academic Partner
CSIRO, Energy, Newcastle

Funding Support
ACAP

Aim

Monolithic integration of a perovskite/silicon tandem device in a two-terminal configuration, although an elegant approach, has inherent current matching limitations for such a series connected device. The aim of the project is to increase understanding of the effect of perovskite composition, varying spectrum, angle of incidence and temperature when two-terminal perovskite/silicon cells operate under real outdoor conditions.

Figure 6.42.1: Three types of Perovskite/Si tandem solar cell fabricated and encapsulated by UNSW undergoing outdoor testing at CSIRO, Energy, Newcastle field testing site.

Progress

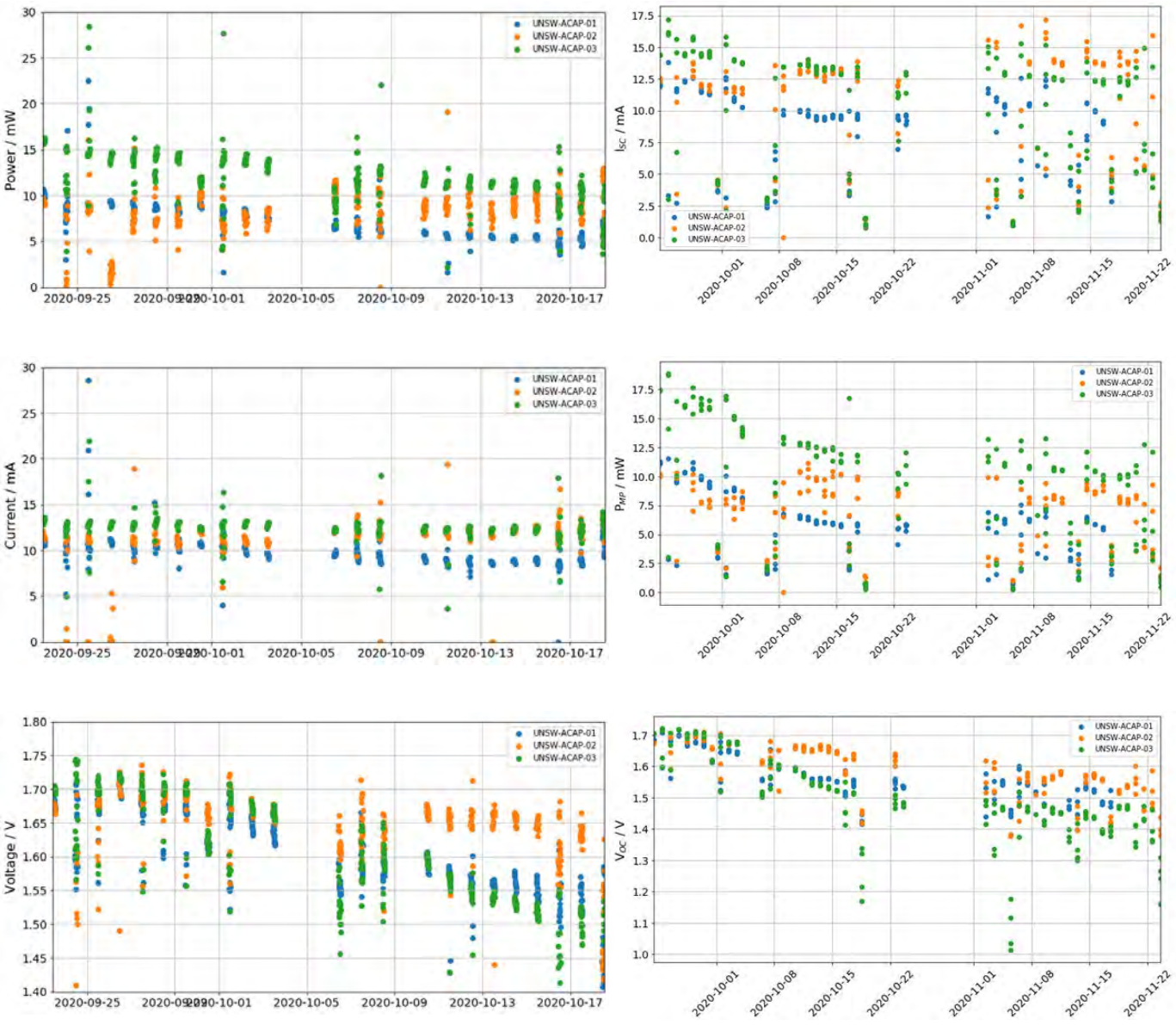

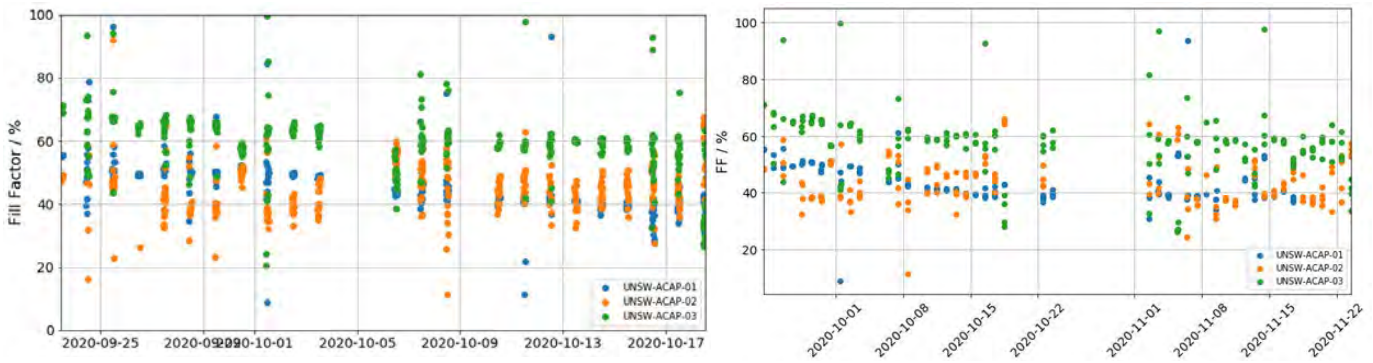

Fig. 6.42.2: Outdoor stability results (raw data on the left and filtered data on the right) showing (a) power; (b) current; (c) voltage; and (d) fill factor of three types of devices: FAMA based (#01); CsFAMA based (#02); CsFA based (#03).

Three types (FAMA, CsFAMA, and CsFA based) of two-terminal perovskite/Si tandems consisting of perovskite cells with a structure of SnO_2/perovskite/hole transport layer/MoOx/ITO/Ag on top of an n-type PERL cell with front p+ emitter has been fabricated (Zheng et al. 2018a, b) at UNSW.

A modified encapsulation method is developed by UNSW building on previous work (Shi et al. 2017, 2020) sealing the devices from moisture ingress.

Test jigs with monitoring equipment were set up by CSIRO Energy to collect current-voltage data of cells as well as device temperature, climate and irradiance data (Figure 6.42.1).

Results are shown in Figure 6.42.2. Data on the left-hand side shows rough performance data while data on the right has been treated for conditions near minimum solar zenith to eliminate the effect of spectrum and angle as much as possible (e.g. normalised to a plane of array (POA) irradiance of 1000 W/m2 followed by further filtering considering diffuse and global irradiance) for observing the rate of change of the device.

Results show that device 2 (CsFAMA) is the most stable with minimal average change in I_{SC} and P_{mp} and the slowest change in V_{OC}. Further work will be conducted to ascertain reasons for lower stability observed in the CsFA-based device despite the absence of MA cations.

Highlights

- Successful fabrication of two-terminal perovskite/Si tandem solar cells.
- Development of encapsulation method suitable for two-terminal perovskite/Si tandem solar cells for outdoor testing.
- Collection of useful electrical characteristic data of perovskite/Si tandem cells operating outdoor.
- Collection of useful climatic data for further cell analyses.
- Successful comparisons of outdoor stability perovskite cell with different perovskite compositions, CsFAMA being the most stable.

Future Work

- Indoor measurements under controlled conditions to determine the spectral response and temperature coefficients for the devices.
- A redesign of the packaging method to include a defined aperture size and plane and eliminate any possibility of light piping or lensing into the devices.
- Ideally temperature monitoring incorporated into the package at the back side of the cell.
- Analyse cell performance taking into account climatic data due to multiple variables introduced by real outdoor conditions.

References

SHI, L., BUCKNALL, M. P., YOUNG, T. L., ZHANG, M., HU, L., BING, J., LEE, D. S., KIM, J., WU, T., TAKAMURE, N., MCKENZIE, D. R., HUANG, S., GREEN, M. A. & HO-BAILLIE, A. W. Y. 2020. Gas chromatography–mass spectrometry analyses of encapsulated stable perovskite solar cells. Science, 368, eaba2412. DOI: 10.1126/science.aba2412.

SHI, L., YOUNG, T. L., KIM, J., SHENG, Y., WANG, L., CHEN, Y., FENG, Z., KEEVERS, M. J., HAO, X., VERLINDEN, P. J., GREEN, M. A. & HO-BAILLIE, A. W. Y. 2017. Accelerated Lifetime Testing of Organic–Inorganic Perovskite Solar Cells Encapsulated by Polyisobutylene. ACS Applied Materials & Interfaces, 9, 25073-25081. https://doi.org/10.1021/acsami.7b07625.

ZHENG, J., LAU, C. F. J., MEHRVARZ, H., MA, F.-J., JIANG, Y., DENG, X., SOERIYADI, A., åKIM, J., ZHANG, M., HU, L., CUI, X., LEE, D. S., BING, J., CHO, Y., CHEN, C., GREEN, M. A., HUANG, S. & HO-BAILLIE, A. W. Y. 2018a. Large area efficient interface layer free monolithic perovskite/homo-junction-silicon tandem solar cell with over 20% efficiency. Energy & Environmental Science, 11, 2432-2443. DOI: 10.1039/c8ee00689j.

ZHENG, J., MEHRVARZ, H., MA, F.-J., LAU, C. F. J., GREEN, M. A., HUANG, S. & HO-BAILLIE, A. W. Y. 2018b. 21.8% Efficient Monolithic Perovskite/Homo-Junction-Silicon Tandem Solar Cell on 16 cm2. ACS Energy Letters, 3, 2299-2300. https://doi.org/10.1021/acsenergylett.8b01382.

6.43 HIGH EFFICIENCY SPECTRUM SPLITTING CPV RECEIVER USING A TRIPLE-JUNCTION SOLAR CELL WITH INTERNAL BRAGG REFLECTOR

Lead Partner

UNSW

UNSW Team

Dr Yajie Jiang, Dr Mark Keevers, Scientia Prof. Martin Green

Industry Partners

AZUR SPACE Solar Power, RayGen Resources Pty Ltd

Funding Support

ACAP

Aim

UNSW has demonstrated a world record conversion efficiency of 40.6% with a spectrum splitting concentrator photovoltaic (CPV) submodule, using a 150-layer dielectric band-pass filter to divert the 900–1050 nm spectral band from a triple-junction solar cell (TJSC) to a Si cell. This project aims to develop a potentially lower cost and higher performance approach using a TJSC with an internal spectrum splitting Bragg reflector, which can be implemented with little additional cost during manufacture, in contrast to fabrication of discrete dielectric filters.

Progress

The centralised power tower technology is one of the most promising approaches to CPV, which is being developed by Australian company RayGen Resources, consisting of a field of heliostats concentrating the sunlight to a single flat 1 m² PV array atop a mast (Figure 6.43.1). The cells used in the receiver are high performance GaInP/GaInAs/Ge TJSCs. One disadvantage of these TJSCs is the bottom Ge cell having a much lower bandgap, generating much more current than the other two cells. The extra current is wasted as heat within the cell, increasing challenges in maintaining low operating temperatures where the cells are most efficient. Given this single large receiver, an efficient approach to solve this problem is using spectrum splitting by reflecting some of the excess photons reaching the Ge cell in the TJSC array onto a relatively inexpensive array of Si cells. This approach shows potential practical application to CPV power tower technology by replacing the TJ array with a V-shaped spectrum splitting receiver, which combines the TJ array with spectrum splitting DBR plus an additional Si array.

Figure 6.43.1: RayGen's Central Receiver CPV power tower. Inset shows original receiver and V-shaped spectrum splitting receiver design.

This project proposed a novel approach by integrating an intermediate distributed Bragg reflector (DBR) during TJSC fabrication, optimised to function as a suitable band-reflect filter (Jiang et al. 2019a). A single DBR was successfully integrated to a 10 x 10mm commercial CPV cell by our industrial partner AZUR SPACE previously, without major detriment to the cell performance compared with baseline cells (Jiang et al. 2019b). To explore further benefits of DBR spectrum splitting, both single DBR and double DBR were implemented to larger commercial CPV cells, with cell areas of 10 x 15mm2. The single DBR cell was fabricated as a baseline cell to compare with a previous iteration. Calculations suggest that there is still excess current of the Ge bottom cell with a single DBR design. Therefore, a double DBR cell was introduced to reflect more light to the external Si cell. Figure 6.43.2 shows the measured reflection of two TJSCs with single and double DBR. The single DBR design shows a broad reflection band between 950 and 1050 nm, consistent with previous iteration results. A broader reflection band between 930 and 1070 nm is achieved for the double DBR design.

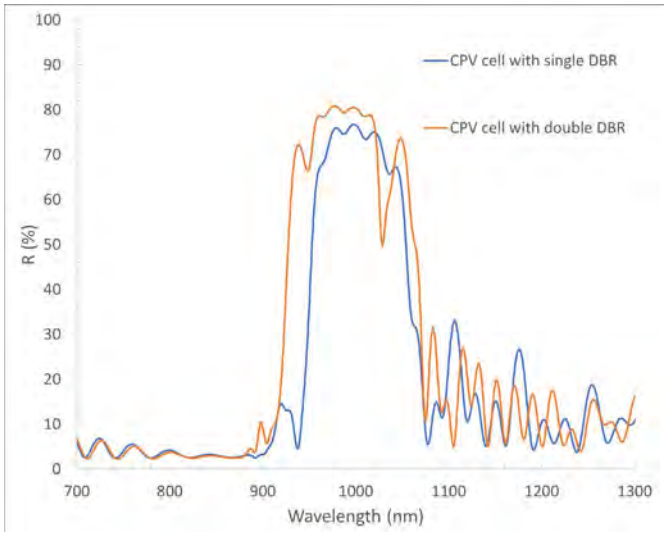

Figure 6.43.2: Reflectance measurements of two typical TJSCs with single and double DBR.

Another advantage of the DBR approach is the greatly reduced angular dependence. Using the Perkin-Elmer spectrophotometer with a universal reflectance accessory, we measured the specular reflectance of the TJSC with single and double spectrum splitting DBR for incident angles ranging from 8 to 60°. The reflection band is slightly blue shifted with the increase of incident angle, the reflection peaks have not been significantly affected.

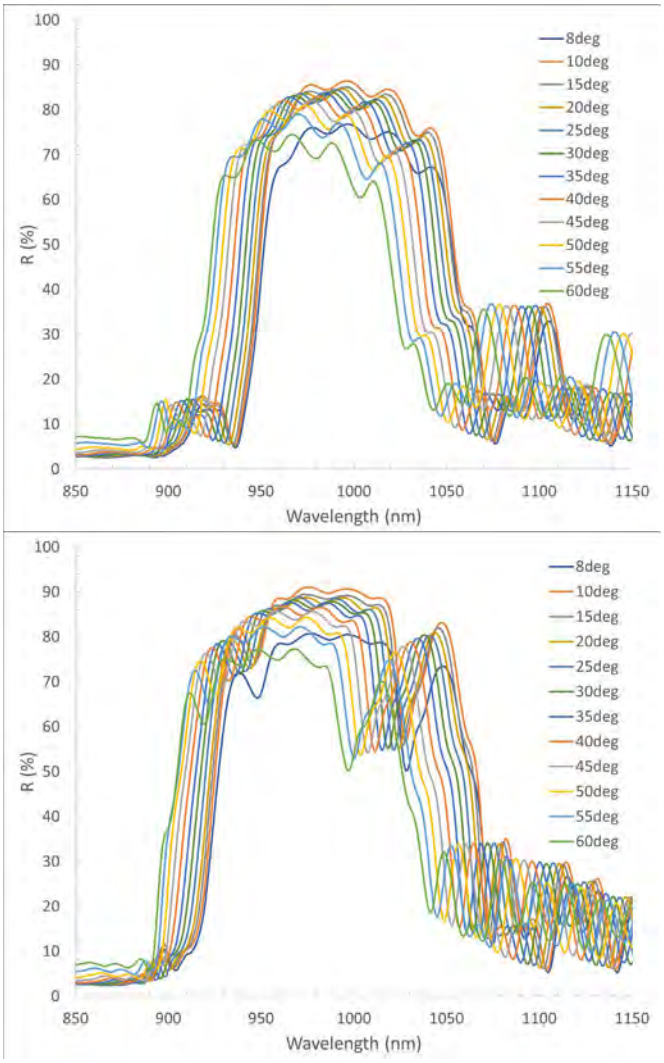

Figure 6.43.3: Angular dependent reflectance measurements of two typical TJSCs with (a) single and (b) double DBR.

The external quantum efficiency (EQE) of two typical TJSCs was measured as well. Figure 6.43.4 shows the EQE comparison of the two TJSCs with single and double DBR alongside the AM1.5D spectrum. The EQE of the top and middle sub-cells are almost identical, only the bottom sub-cell EQE is varied with different DBR designs.

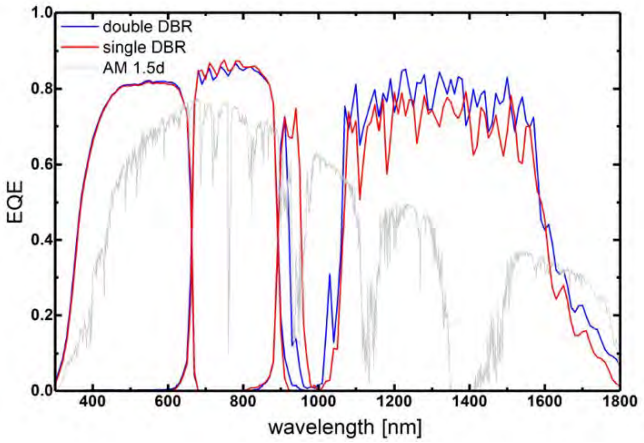

Figure 6.43.4: Relative external quantum efficiency (EQE) of TJSCs with single and double DBR.

Light current-voltage (LIV) measurements were conducted on all the cells under AM1.5D spectrum (350× concentration) at 25°C. Key parameters of the typical TJSCs from previous and current iterations are shown in Table 6.43.1. A and B are from the previous iteration with cell areas of 10 x 10 mm, while C and D are current iteration results with a 10 x 15 mm cell size. Within each iteration, different DBR designs show no major detriment to the cell performance. However, the single DBR design from the current iteration C shows a lower J_{SC} and FF compared with the previous iteration B. By investigating the metallisation shading effect under a microscope, the metallisation of B shows approximately 8% shading, while 11% is calculated for C. We could conclude that the J_{SC} reduction of the current iteration is mostly due to the larger metallisation area. In addition, the 10 x 10 mm cell is more standard CPV product, hence better engineering control can be expected from cells with this size.

Table 6.43.1: Measured LIV parameters of 10 x 10 mm TJSC and 10 x 15 mm TJSCs with various DBR designs.

	I_{SC} [A]	J_{SC}/Sun [mA.cm^{-2}]	V_{OC} [V]	I_{mp} [A]	V_{mp} [V]	P_{mp} [W]	FF	eta [%]
A. No DBR 10 x 10 mm	4.923	13.993	3.180	4.836	2.900	14.021	0.896	39.860
B. Single DBR 10 x 10 mm	4.970	14.128	3.163	4.885	2.856	13.945	0.887	39.650
Ratio B/A	1.010	1.010	0.995	1.010	0.985	0.995	0.990	0.995
C. Single DBR 10 x 15 mm	6.640	13.215	3.175	6.511	2.801	18.228	0.865	36.297
Ratio C/B	1.336	0.935	1.004	1.333	0.981	1.307	0.976	0.915
D. Double DBR 10 x 15 mm	6.639	13.214	3.169	6.482	2.764	17.909	0.851	35.650
Ratio D/C	1.000	1.000	0.998	0.996	0.987	0.983	0.984	0.982

The results suggest it is feasible to integrate double DBRs to a CPV cell while maintain high efficiency, however the standard cell size 10 x 10 mm should be used to guarantee good electrical performance.

Highlights

- Double distributed Bragg reflectors (DBRs) were successfully integrated in a 10 x 15 mm^2 triple-junction solar cell (TJSC).
- The DBR approach to spectrum splitting shows less dependence on incident angles.

Future Work

- Integrate a double DBR design to a standard 10 x 10 mm TJSC, to achieve closer to current matching conditions between three sub-cells in the GaInP/ GaInAs/Ge TJSC, while maintain high efficiency.
- Outdoor LIV measurements of the TJ(Bragg)/Si spectrum splitting CPV receiver, targeting over 40% efficiency.

References

JIANG, Y., KEEVERS, M. J., PEARCE, P., EKINS-DAUKES, N. & GREEN, M. A. 2019a. Bragg Reflector within Triple-Junction Solar Cells for Spectrum Splitting Application. 36th EU PVSEC, 9–19 September 2019, Marseille, France.

JIANG, Y., KEEVERS, M. J., PEARCE, P., EKINS-DAUKES, N. & GREEN, M. A. 2019b. Design of an intermediate Bragg reflector within triple-junction solar cells for spectrum splitting applications. *Solar Energy Materials and Solar Cells*, 193, 259-269.

6.44 LANDMARK 50% EFFICIENT PV RECEIVER

Lead Partner

UNSW

UNSW Team

Dr Mark Keevers, Dr Yajie Jiang, Dr Anastasia Soeriyadi, A/Prof. Ned Ekins-Daukes, Prof. Martin Green

Industry Partners

Tianjin Institute of Power Sources and 18th Research Institute of China Electronics Technology Group Corporation (CETC-18), Tianjin, China: Prof. Qiang Sun, He Wang
RayGen Resources Pty Ltd: Dr John Lasich
IQE (informal collaboration): Andrew Johnson

Funding Support

ACAP

Aim

Based on the UNSW spectrum splitting approach that was the first to achieve sunlight-to-electricity conversion efficiency above 40%, a more sophisticated concentrator photovoltaic (CPV) module capable of efficiency above 50% has been designed. This project provides seed funding to enable progress along the development path towards demonstrating this landmark efficiency, including establishing suitable collaborations, planning development paths, and applying for the required larger project funding.

Progress

Increasing efficiency is a key driver for PV cost reduction. In 2014, UNSW gained international attention by demonstrating the first PV receiver to achieve a sunlight-to-electricity conversion efficiency above 40% (independently confirmed by NREL). The prototype submodule uses a dielectric band-pass filter to divert otherwise wasted (900–1050 nm) photons away from a GaInP/GaInAs/Ge triple-junction (3J) solar cell to a Si cell to form a 4J receiver (Green et al. 2015) (Figure 6.44.1). In 2016, UNSW further improved this efficiency to 40.6%.

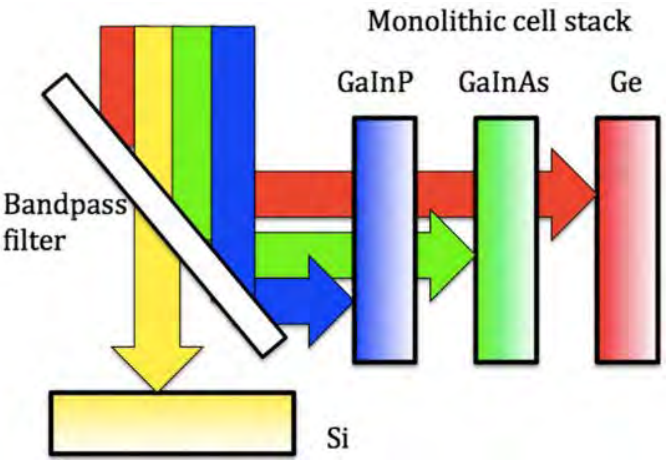

Figure 6.44.1: Schematic of the 3J + 1J spectrum splitting approach used to achieve 40% efficiency (Green et al. 2015).

A potential commercial application of this spectrum splitting approach is to upgrade the central receiver in Australian company RayGen's CPV power tower system, where sunlight is reflected from a field of sun-tracking heliostats to a dense-packed PV array receiver mounted on a central tower (Figure 6.44.2, also see section 6.1). In such systems, improved efficiency of the central receiver not only reduces costs by increasing energy output for a given investment in heliostats and towers but also reduces unwanted heat generation at the central tower. RayGen's technology is future-proofed due to the relative ease of

Figure 6.44.2: (left) RayGen's 750 kW_p PV power plant in Newbridge, Victoria. Each 250 kW_p unit uses a field of heliostats to concentrate sunlight onto a 1 m² high efficiency PV receiver. (right) Close-up of a receiver.

A more sophisticated PV receiver capable of increasing efficiency towards the historically significant value of 50% has been designed (Green 2017), which involves extending the spectrum splitting approach to a combination of two 3J solar cells for even better utilisation of the solar spectrum (Figure 6.44.3). The optimal design identified is predicted to have a practical efficiency of 51% at 300-suns concentration and 51.7% at 500 suns. The higher energy ($1.4 < E_{ph} < 2.3$ eV) photons are converted using a 3J solar cell (based on lattice-matched solid solutions of GaAs, GaP, InP, AlP and AlAs) on a GaAs wafer, while the lower energy ($0.73 < E_{ph} < 1.4$ eV) photons are converted using a 3J cell (based on lattice-matched solid solutions of GaAs, InAs, InP, AlAs and GaSb) on an InP wafer. A long-pass filter performs the required spectrum splitting.

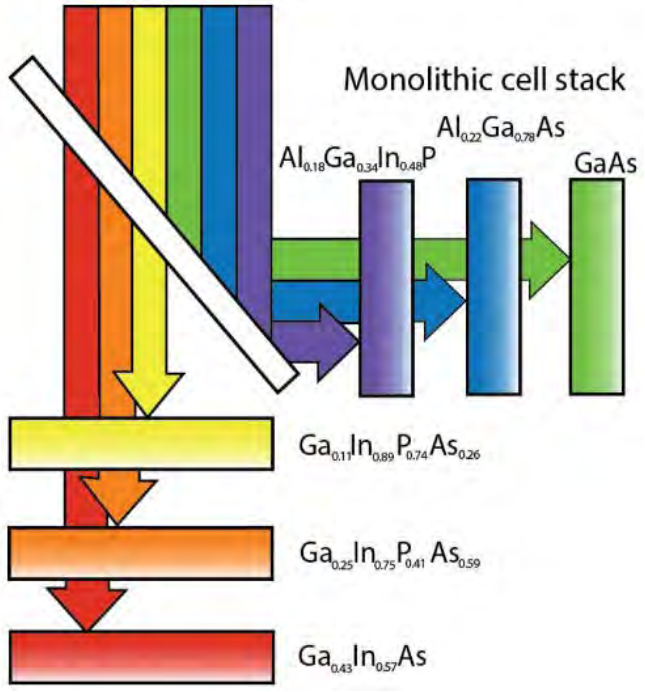

Figure 6.44.3: Conceptual design of a 3J + 3J spectrum splitting receiver using a long-pass filter and two 3J cells on GaAs and InP substrates, capable of achieving 50% efficiency (Green 2017).

The seed funding provided by this small ACAP grant has enabled us to develop various pathways to the ideal 3J + 3J = 6J receiver, in close consultation with official project partners CETC-18 and RayGen, as well as potential new partners IQE (the world's largest III-V compound semiconductor foundry, UK), SolAero (a leading provider of III-V solar cells and panels for satellite and aerospace applications, US), Azur Space (Europe's premier supplier of space and CPV solar cells, Germany) and NREL (a leading renewables research laboratory, US). This ACAP grant has also enabled the team to apply for the larger funding required to achieve the 50% efficiency result.

Highlights

- Conceptual design of 50% efficient receiver.
- Omega Optical design of a suitable dielectric long-pass filter.
- Global Innovation Linkage grant application with RayGen, UNSW and IQE, for project "Advanced III-V solar cell manufacturing and 50% efficient PV receiver" (submitted November 2018, unsuccessful April 2019).
- ARENA R&D grant application with UNSW, IQE, CETC-18 and RayGen, for project "Ultimate solar power conversion using III-V materials: efficiency, colour & cost" (submitted February 2020, unsuccessful July 2020).
- ACAP Collaboration Grant application with UNSW, IQE, SolAero and RayGen, for project "Development of III-V cells on GaAs & InP for a 50% efficient spectrum splitting CPV receiver" (submitted September 2020, successful November 2020, commences Q2 2021).
- Ongoing development of UNSW capabilities for III-V solar cell simulation, fabrication, packaging and testing.

Future Work

Progress along the development path towards a landmark 50% efficient PV receiver, including work on a 3J-on-GaAs + 1, 2 then 3J-on-InP spectrum splitting receiver. This work will be supported by an ACAP Collaboration Grant commencing Q2 2021.

References

GREEN, M.A. 2017. 15 November 2017. Landmark 50% efficient solar module design. Information Sheet MAG/ACAP1705 (confidential).

GREEN, M. A., KEEVERS, M. J., THOMAS, I., LASICH, J. B., EMERY, K. & KING, R. R. 2015. 40% efficient sunlight to electricity conversion. *Progress in Photovoltaics: Research and Applications*, 23, 685-691.

6.46 MANIPULATING THE PROPERTIES OF OXYGEN-RELATED DEFECTS FOR RECORD EFFICIENCY CELLS

Lead Partner

UNSW

UNSW Team

Dr Fiacre Rougieux

Academic Partners

Fraunhofer Institute for Solar Energy Systems ISE: Prof. Martin Schubert
University of Freiburg: Dr Wolfram Kwapil

Australian National University: Prof. Daniel Macdonald, Manjula Siriwardhana

Funding Support

ACAP

Aim

This project aimed to understand and control the properties of defects limiting high efficiency silicon solar cells, focusing on oxygen-related defects. This class of defect was poorly understood and current defect-engineering techniques were particularly inadequate at annihilating such defects.

Progress

This project took place between April 2018 and April 2020. As part of this project, Dr Fiacre Rougieux from UNSW spent a month at Fraunhofer ISE in September 2018. Manjula Siriwardhana from ANU spent a month at Fraunhofer ISE in September 2019 and a month at UNSW in October 2019. The project achieved its objective and generated a total of 10 publications.

In this project, we explored the impact of oxygen-related defects in their various forms in silicon wafers. Oxygen traditionally sits in an interstitial position in the silicon lattice. In its interstitial position, oxygen is harmless to the solar cell efficiency. However, oxygen can react to form a range of harmful defects. These include: (1) oxygen precipitates; (2) oxygen thermal donors; and (3) the boron-oxygen defect. Our work investigated the properties of each of these three classes of defects and devised defect-engineering processes to mitigate their impact.

1. Boron-oxygen defect: We demonstrated that the boron-oxygen defect may not be proportional to the net-doping or the boron concentration (Rougieux et al. 2020a). Detailed modelling enabled us to propose a new model for the recombination activity of the boron-oxygen defect (Rougieux et al. 2020b). We unraveled the latent form of the boron-oxygen defect via photoconductance measurements (Jafari 2020). We demonstrated that full passivation of the boron-oxygen defect is possible in compensated n-type silicon (Sun 2019).

2. Oxygen precipitates: We demonstrated the growth of oxygen precipitates at oxygen thermal donor growth temperatures (Basnet 2021). Our results showed that Tabula Rasa is key in mitigating the growth of oxygen precipitate in silicon and that growth in nitrogen ambient conditions increases the formation rate of precipitates (Basnet et al. 2020). Via high-resolution micro-PL and micro-Raman mapping, we demonstrated a new capability to detect individual oxygen precipitates (Basnet 2018).
3. Oxygen thermal donors: We invented a new technique to image thermal donors and trap in solar wafers and solar cells (Rougieux 2019). We developed new techniques to measure the electronic properties of oxygen-related defects (Siriwardhana 2018). We devised a new method to measure the capture properties and temperature dependence of thermal donors related traps in silicon (Siriwardhana 2021).

We also developed new defect-engineering techniques to increase the open-circuit voltage of commercial silicon solar cells by manipulating the properties of defects (Tan et al. 2018).

In summary, the project achieved and surpassed its initial objectives. The learnings from this project are being used for current cell processes and are contributing to more efficient and oxygen-resilient industrial solar cells.

Highlights

- Devise new model to describe the recombination activity of the boron-oxygen defect.
- Invention of a new technique to image the concentration of slow traps in silicon wafers.
- Invention of a new technique to measure the capture properties of traps via photoconductance.
- Development of a new technique to determine the electronic capture properties of oxygen-related defects.
- Development of new thermal processes to increase the open-circuit voltage of solar cells limited by defects.

Future Work

- The success achieved in this ACAP seed project has enabled us to firmly establish an ongoing collaboration between UNSW, Fraunhofer ISE and ANU on the theme of recombination active oxygen defects. There are now several students involved in this work with ongoing activities.

References

BASNET, R., PHANG, S. P., SUN, C., ROUGIEUX, F. E. & MACDONALD, D. 2020. Onset of ring defects in n-type Czochralski-grown silicon wafers. *Journal of Applied Physics* 127, 153101.

BASNET, R., SIO, H., SIRIWARDHANA, M., ROUGIEUX, F. E. & MACDONALD, D. 2021. Ring-Like Defect Formation in N-Type Czochralski-Grown Silicon Wafers during Thermal Donor Formation. *Phys. Status Solidi* A 2000587.

ROUGIEUX, F. E., KWAPIL, W., HEINZ, F., SIRIWARDHANA, M. & SCHUBERT, M. C. 2019. Contactless transient carrier spectroscopy and imaging technique using lock-in free carrier emission and absorption. *Scientific Reports*, 9(1) 1-5.

ROUGIEUX, F. E., SUN, C. & JUHL, M. 2020a. The Boron-Oxygen Defect: Does its Concentration Really Depends [sic] on the Boron/Dopant Concentration? 47th IEEE Photovoltaic Specialists Conference (PVSC), Calgary, OR, 2020, pp. 2522-2524.

ROUGIEUX, F. E., SUN, C. & JUHL, M. 2020b, Light-induced-degradation defect independent of the boron concentration: Towards unifying admittance spectroscopy, photoluminescence and photoconductance lifetime spectroscopy results. *Solar Energy Materials and Solar Cells*, 210, 110481.

SAMAN JAFARI, S., YAN ZHU, Y., ROUGIEUX, F. E., DE GUZMAN, J. A. T., MARKEVICH, V. P., PEAKER, A. R. & HAMEIRI., Z. 2020. Boron-oxygen related light-induced degradation of Si solar cells: Transformation between minority carrier traps and recombination active centers. 2020 47th IEEE Photovoltaic Specialists Conference (PVSC), Calgary, pp. 0689-0692.

SIRIWARDHANA, M., MACDONALD, D., HEINZ, F. D. & ROUGIEUX, F.E. 2018. Slow minority carrier trapping and de-trapping in Czochralski silicon: Influence of thermal donors and the doping density. 2018 IEEE 7th World Conference on Photovoltaic Energy Conversion (WCPEC). pp. 3312–3314.

SIRIWARDHANA, M., ZHU, Y., HAMEIRI, Z., MACDONALD, D. & ROUGIEUX, F. 2021. Photoconductance Determination of Carrier Capture Cross Sections of Slow Traps in Silicon Through Variable Pulse Filling. *IEEE Journal of Photovoltaics*, 1-9. DOI: 10.1109/JPHOTOV.2020.3043835.

SUN, D., CHEN, D., ROUGIEUX, F. E., BASNET, R., HALLAM, B. & MACDONALD, D. 2019. Kinetics and dynamics of the regeneration of boron-oxygen defects in compensated n-type silicon. *Solar Energy Materials and Solar Cells*, 195, 174-181.

TAN, X., CHEN, R., LEE CHIN, R., CHEN, D. & ROUGIEUX, F. E. 2018. Defect Engineering of n-type bifacial silicon solar cells using dark annealing. 2018 IEEE 7th World Conference on Photovoltaic Energy Conversion.

6.48 ITO-FREE PV PRINTED DIRECTLY ONTO FLEXIBLE BARRIER FILMS

Lead Partner

CSIRO

CSIRO Team

Dr Doojin Vak, Mrs Fiona Glenn

Academic Partners

Chonbuk National University (CBNU): A/Prof. Seok-In Na

Pukyong National University: Prof. Dong-Wook Chang

UNSW: Dr Nathan Chang

Funding Support

ACAP

Aim

Printed PV produced by roll-to-roll (R2R) printing is flexible, lightweight and semi-transparent (in some cases), creating access to new PV markets, especially for portable applications. However, some materials and process steps are costly and make the technology heavier and less flexible. This project aims to produce PV printed directly onto barrier films, resulting in lighter weights, improved flexibility and lower potential manufacturing costs.

Challenge

Finding printable and low-cost transparent conductive electrodes (TCEs) to replace commonly used indium tin oxide (ITO) has long been a great interest to the research community and wider flexible and printed electronics (FPEs) industry, which includes flexible solar cells. Producing practically high conductivities (that is low sheet resistance) economically while managing surface roughness and transparency has been a challenge.

Progress

Two types of printed TCEs have been developed over the last two years. One is low-cost mid-performance TCEs based on the PEDOT:PSS polymer followed by a R2R-compatible post-treatment. Another is mid-cost high-performance TCEs based on a silver nanowire and PEDOT:PSS composite. Properties of the TCEs have been confirmed to be suitable for flexible printed solar cells, and the cost compared to conventional vacuum-based TCEs has also been confirmed. The key aim of the last project year was to produce a high-performance device fabricated on the printed TCEs using formulations that were particularly developed to tolerate the rough surface of printed TCEs. An international collaboration project with a visiting student was made to achieve the goal. Unfortunately, the collaboration was significantly impacted by COVID-19. The student could only access the laboratory for a small fraction of his visiting period, and due to the restrictions the optimisation of ITO-free organic PV was not completed. However, preliminary results with a PCE of up to 5.2% were obtained by using previously developed recipes. As discussed in the next section, a promising printed TCE-friendly formulation has been developed, but the formulation could not be tested with the printed TCEs. The activity will be followed up as a PP2 activity of the ACAP project.

Printed TCE-friendly solar inks

Printed TCEs are typically much rougher than commercial TCEs fabricated by costly vacuum-deposition techniques and require robust solutions to produce high performance PV. The key requirement is thickness tolerance. Typical organic PV devices show the best performance with the thickness in the range of 100–150 nm. This thickness range is easily fabricated by spin-coating, an un-scalable laboratory technique, but difficult to achieve over a very large area (>m^2) by industrial deposition techniques. Therefore, thick-film organic PV with an optimised thickness of 200–300 nm is preferred for industrial production for commercial applications. Moreover, the thin films of OPV are more susceptible to defect formation, especially on rough printed TCEs. Figure 6.48.1 shows device results of R2R- produced organic PV developed through the collaboration with Prof. Dong-Wook Chang (Pukyong University, Korea) in this project (Yang et al. 2020). The formulation showed an exceptional thickness tolerance and the devices showed the highest PCE from R2R-produced organic PV in the literature. The data also show how thickness affects the yield of devices. The devices with a thickness of less than 200 nm show a much larger deviation in efficiency due to defect formation during the R2R process. In this case, the devices were fabricated on smooth commercial TCEs. The problem would be more serious on rough printed TCEs.

The previous highest PCE was also developed in this project and reported in last year's report (Lee et al. 2019). Although the improvement in efficiency from our own record was not significant, the new formulation showed outstanding thermal stability and thickness tolerance. Therefore, the formulation would be more suitable for commercial applications in the future. Moreover, the high PCE was obtained using a hot deposition technique (Na et al., 2018). The technique enables high performance without using solvent additives, which boost efficiencies but cause long-term stability issues. Therefore, high long-term stability is also expected from the device.

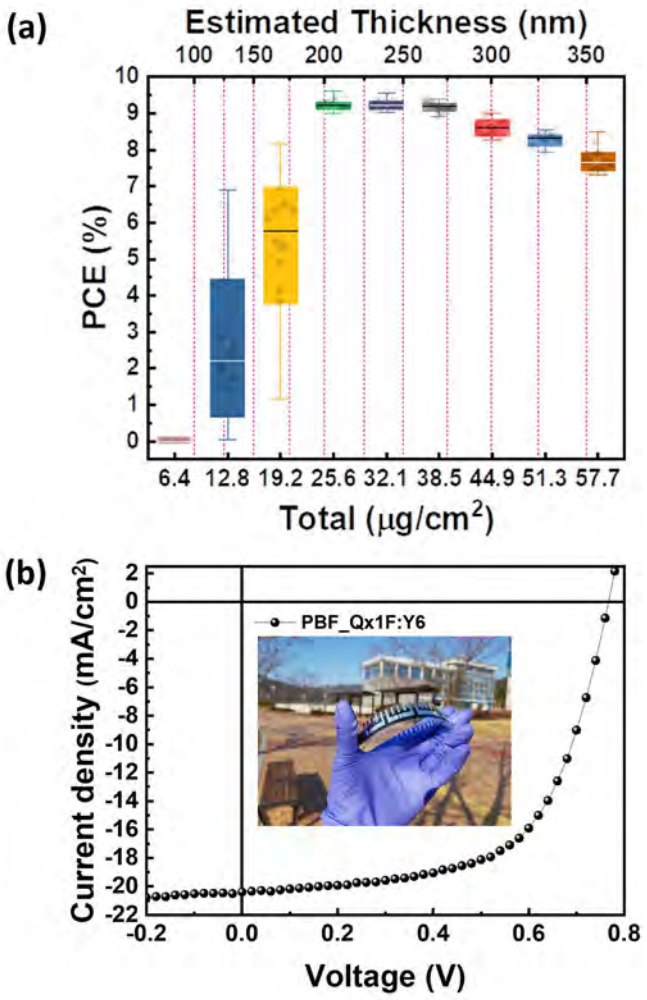

Figure 6.48.1: (a) PCEs of R2R-produced flexible organic PVs with the configuration of PET/TCE/ZnO/PBT_Qx1F:Y6/MoOx/Ag. (b) J-V curve of the best device with 9.63% PCE, the highest efficiency from R2R-processed organic PV in literature.

Cost benefit

The cost benefit of printed TCEs was reported in the 2019 annual report. In this case, the cost of the TCE was calculated using the actual purchase cost for a research quantity, i.e. a much higher cost than the potential cost for manufacturing. The projected manufacturing cost of ITO-free organic PV was calculated this year through a collaboration with Dr Nathan Chang (UNSW) using the model developed to calculate the manufacturing cost of R2R-produced perovskite PV (Chang et al. 2018) and also compared the projected manufacturing cost in the literature.(Machui *et al.*, 2014). The results are shown in figure 6.48.2. The following four sequences were used in the calculation: A: literature sequence; B: literature sequence with the low-cost TCE developed in this project; C: the low-cost TCE with the highest PCE (10%) demonstrated by the R2R process in CSIRO; and D: the low-cost TCE with highest PCE (18%) in literature.

The figure shows the new TCE can slightly reduce the manufacturing cost per unit area. It was expected that the introduction of more expensive high performance photo-active materials would increase the manufacturing cost significantly, however, we found the increase of the overall manufacturing cost was not significantly higher. Figure 6.48.2(c) clearly shows the benefit of high performance materials in cost per power generation. The result indicates ITO-free OPV would be competitive for R2R-produced perovskite PV, as well as commercial products in the portable PV market. However, no performance reduction due to the upscaling process was considered in this calculation. A more realistic calculation will be carried out when large-scale production is demonstrated through the ACAP project.

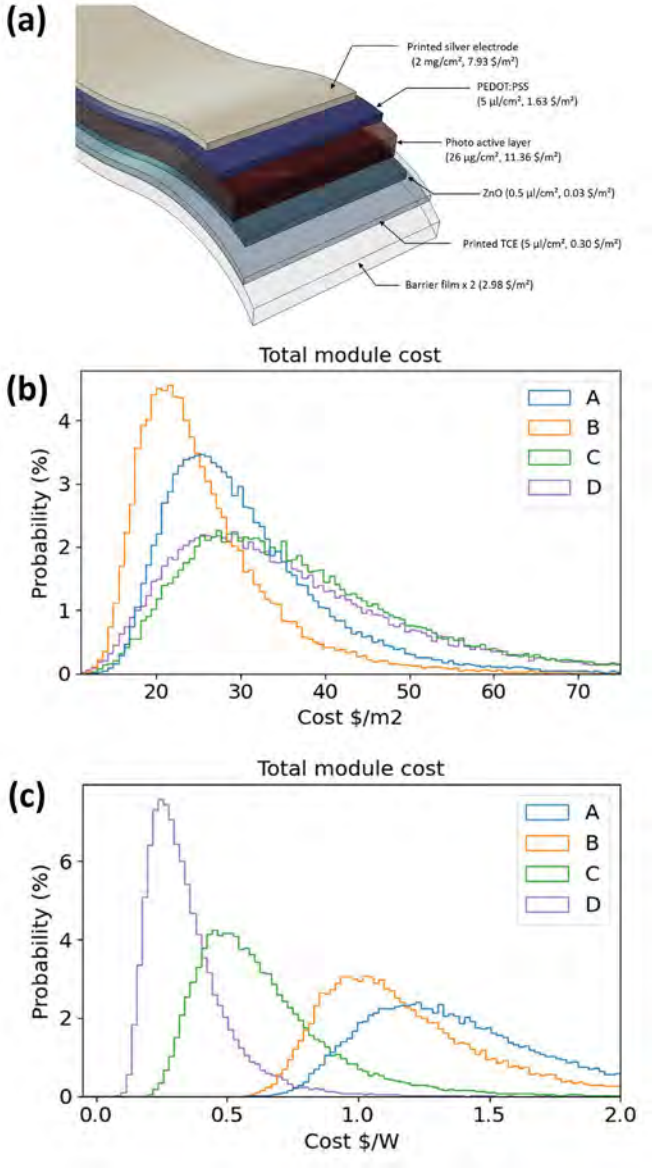

Figure 6.48.2: (a) Device configuration, material usage and cost of each component of the ITO-free organic PV used in the sequence D. (b) Projected manufacturing cost per unit area of four sequences. (c) Projected manufacturing cost per watt of four sequences.

Highlights

- Development of a printing-friendly formulation demonstrating the highest PCE from R2R-processed organic PV in literature, outstanding thickness tolerance and thermal stability.
- Calculation of manufacturing cost of printed organic PV indicating promising market potential of the technology.

References

CHANG, N. L., HO-BAILLIE, A. W. Y., VAK, D., GAO, M., GREEN, M. A. & EGAN, R. J. 2018. Manufacturing cost and market potential analysis of demonstrated roll-to-roll perovskite photovoltaic cell processes. Solar Energy Materials and Solar Cells, 174, 314-324.

LEE, J., SEO, Y. H., KWON, S. N., KIM, D. H., JANG, S., JUNG, H., LEE, Y., WEERASINGHE, H., KIM, T., KIM, J. Y., VAK, D. & NA, S. I. 2019. Slot-Die and Roll-to-Roll Processed Single Junction Organic Photovoltaic Cells with the Highest Efficiency. Advanced Energy Materials, 9.

MACHUI, F., HOSEL, M., LI, N., SPYROPOULOS, G. D., AMERI, T., SONDERGAARD, R. R., JORGENSEN, M., SCHEEL, A., GAISER, D., KREUL, K., LENSSEN, D., LEGROS, M., LEMAITRE, N., VILKMAN, M., VALIMAKI, M., NORDMAN, S., BRABEC, C. J. & KREBS, F. C. 2014. Cost analysis of roll-to-roll fabricated ITO free single and tandem organic solar modules based on data from manufacture. Energy & Environmental Science, 7, 2792-2802.

NA, S. I., SEO, Y. H., NAH, Y. C., KIM, S. S., HEO, H., KIM, J. E., ROLSTON, N., DAUSKARDT, R. H., GAO, M., LEE, Y. & VAK, D. 2019. High Performance Roll-to-Roll Produced Fullerene-Free Organic Photovoltaic Devices via Temperature-Controlled Slot Die Coating. Advanced Functional Materials, 29.

YANG, M. H., KO, S.-J., AN, N. G., WHANG, D. R., LEE, S.-H., AHN, H., KIM, J. Y., VAK, D., YOON, S. C. & CHANG, D. W. 2020. Roll-to-roll compatible quinoxaline-based polymers toward high performance polymer solar cells. Journal of Materials Chemistry A.

6.50 DEVELOPMENT AND IMPLEMENTATION OF INORGANIC TRANSPORT LAYERS IN THE PEROVSKITE CELLS OF PEROVSKITE/SILICON TANDEM STRUCTURES

Lead Partner

ANU

ANU Team

A/Prof. Klaus Weber, Mr Yiliang Wu, Ms Nandi Wu

Academic Partner

Peking University (PKU): A/Prof. Huanping Zhou

Funding Support

ACAP, ANU, PKU

Aim

The aim of the project is to develop hole transport layers (HTLs) that enable perovskite/silicon tandem devices with high efficiency and stability.

Specifically, in the project the partners will further develop the processes for synthesis and application of inorganic HTLs; carry out detailed optical characterisation to determine the complex refractive index dispersion, and dependence on processing conditions; implement optical and electronic modelling as a guide to cell optimisation and fabricate tandem cells incorporating all inorganic transport layers. The project will contribute to the goal of ultimately pushing tandem efficiencies to 30% and beyond.

Progress

Building on previous work where we developed advanced cells using NiO_X films deposited by sputtering as the HTL, we further optimised both the NiO_X film (in collaboration with project partners at Peking University) and an SnO_2 film deposited by atomic layer deposition (ALD) as the electron transport layer. This resulted in a cell efficiency of 21.8%, with a short circuit current density of 18.9 $mAcm^{-2}$ (Figure 6.50.1).

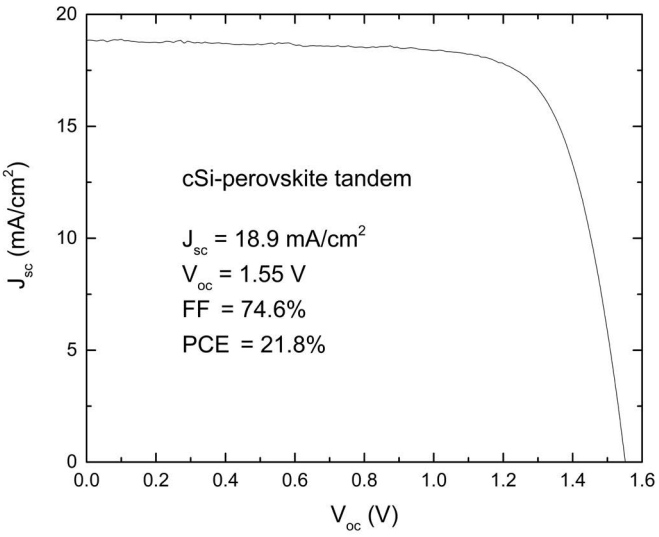

Figure 6.50.1: I-V curve of perovskite/Si tandem cell.

Substantial further improvements are anticipated which should boost the efficiency to 24%. Importantly, we continued with our approach to use industrially feasible processes. The cell was based on a conventional silicon solar cell fabricated on p-type Cz silicon rather than exotic, high quality material as is used for most tandem efficiency results that are reported in the literature. Furthermore, the silicon cell used only mass production techniques and the top cell surface was not polished. We used a planar (rather than textured) silicon cell to allow solution-processing techniques for the perovskite cell rather than requiring very slow evaporation processes.

We have carried out extensive modelling and characterisation to understand how to optimise the device structure for high efficiency. For the top ETL stack, C60/SnO_x/TCO, it was found to be critical to reduce the thickness of C60 to minimise the associated absorption loss. In addition, the thickness of the ITO layer needs to be carefully tuned to minimise reflection, as can be seen from the modelling result (Figure 6.50.2) which shows great sensitivity of reflectivity with changing ITO layer thickness. With such optimisation, modelling indicates that a short circuit current density of 40.2 $mAcm^{-2}$ and efficiency over 24% will be achieved.

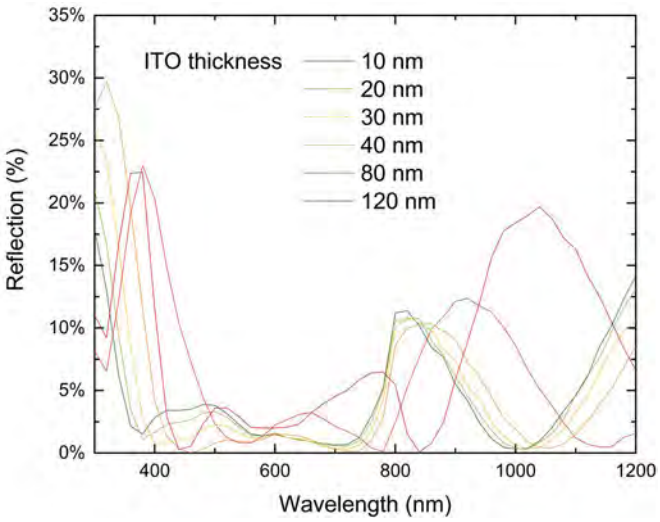

Figure 6.50.2: Variation of reflectivity with changes in the ITO layer thickness.

Highlights

- Comprehensive optimisation of all the layers for the top perovskite cell of a perovskite/silicon tandem.
- Demonstration of high efficiency tandem cells featuring inorganic transport layers for the perovskite cell and commercial c-Si cells.
- Further increases in short circuit current density to over 40 $mAcm^{-2}$ and efficiency to >24% expected.

6.51 HIGH EFFICIENCY SEMI-PLANAR PEROVSKITE CELLS COMBINING NANO-TEXTURED ELECTRON TRANSPORT LAYERS AND INORGANIC HOLE TRANSPORT MATERIALS

Lead Partner

ANU

ANU Team

A/Prof. Thomas White, Dr Jun Peng

Academic Partner

Sun Yat-Sen University (SYSU), Guangzhou, China

Funding Support

ACAP

Aim

This project aimed to develop efficient and stable semi-planar perovskite solar cells (PSCs) using a combination of nanostructured TiO_2 electron-transport layers (ETLs) and NiO_x hole transport layers (HTLs). The first objective was to investigate the use of nanopatterned TiO_2 ETLs as an alternative to the common mesoporous TiO_2 structure used for high performance perovskite solar cells. The second objective was to develop novel doping approaches to tailor the electronic property (e.g. work function and conductivity) of NiO_x HTLs, therefore substituting the widely used, but unstable doped Spiro-OMeTAD and PTAA HTLs for highly efficient and stable PSCs and perovskite/silicon tandem solar cells.

Progress

The initial concept of a nanopatterned ETL was based on the observation that planar PSCs with interface passivation layers can achieve higher open circuit voltages than equivalent cells with a mesoporous ETL, but planar cells suffer from low fill factors compared to mesoporous cells. This is indicative of resistive losses introduced by the poorly conducting polymer blend (PMMA:PCBM) passivation layers. Taking inspiration from local contact technologies used in high performance Si cells to overcome the voltage fill-factor trade-off, we have developed a novel approach to form nanoscale localised contacts in a perovskite solar cell for the first time, achieving a record efficiency for perovskite cells of area >1 cm^2.

The nanoscale contacts are formed by spin-coating the ultra-thin polymer passivation layer over a TiO_2 ETL layer patterned with nanorods, such that the tops of the nanorods remain unpassivated, forming effective charge extraction pathways through the poorly conducting passivation layer. The remaining polymer-coated interface regions provide excellent passivation, maintaining the excellent voltages exhibited by planar cells, while the local contacts reduce the average series resistance, thereby boosting the fill factor. The height, diameter and spacing of the nanorods were optimised using a combination of numerical simulations and experimental studies. The nanopatterned ETL was integrated into semi-planar PSCs with a device structure of ITO/compact-TiO_x/TiO_2 nanorods/PMMA:PCBM/CsFAMA triple cation perovskite /PMMA/HTL/Gold (see Figure 6.51.1).

Through detailed characterisation and numerical modelling, we have demonstrated that the nanostructured TiO_2 ETL can facilitate efficient collection, extraction and transportation of electrons compared to conventional mesoporous TiO_2 ETLs or fully planar devices. In addition, we have developed a dopant-free P3HT:CuPc blend HTL that significantly improves the stability of the PSCs compared to commonly used HTL Spiro-OMeTAD, where the P3HT and CuPc respectively represent poly(3-hexylthiophene-2,5-diyl) and copper phthalocyanine.

The cell fabrication was a joint undertaking of ANU and SYSU. The fabrication of nanopatterned TiO_2 layers was performed at SYSU; the rest of the device fabrication, including the deposition of the compact TiO_2 layer, perovskite active layer, P3HT:CuPc HTL and gold electrode was conducted at ANU. J-V characterisation was then performed at ANU. ANU researcher Jun Peng also visited SYSU to perform X-ray and UV photoelectron spectroscopy (XPS-UPS) measurements and analysis to optimise the TiO_2 nanopatterned layer.

As seen in Figure 6.51.1, a power conversion efficiency (PCE) of 21.956% (measured by reverse scan (V_{OC} to J_{SC}) at a scan rate of 20 mVs^{-1}) with V_{OC} = 1.205 V, J_{SC} = 21.804 $mAcm^{-2}$ and FF = 0.836 was obtained for the champion cell (effective area ~1.02 cm^2), where the corresponding forward scan efficiency is 22.030%. An efficiency of 21.6% was certified by CSIRO for the 1 cm^2 semi-planar perovskite cell. This is the highest certified performance for a perovskite solar cell with area >1 cm^2.

To evaluate thermal stability of these cells, we performed a damp heat test (85°C/85% RH, under dark) (see Figure 6.51.1). The results show that the control cell (with Spiro-OMeTAD) exhibited stark degradation within 240 hours due to severe deterioration at the interface between the perovskite and Spiro-OMeTAD HTL, which is most likely caused by diffusion of lithium ions (used as a dopant for the Spiro-OMeTAD). In contrast, the P3HT:CuPc-based cell retained >91% of its initial efficiency after 1000 hours of exposure. Thus, it is evident that the hydrophobic and thermally stable nature of P3HT:CuPc HTLs can effectively preserve the longevity of the perovskite cells.

In progress towards the second major project objective, we have developed an effective sputter-deposition process for depositing nickel oxide (NiO_x) HTLs. The original project plan was to focus on solution-deposition of NiO_x nanoparticles, but this was replaced with sputtering due to superior control over the quality (such as thickness, conformity and compactness) of the NiO_x layer. Most importantly, sputtering is already widely used in the photovoltaic and electronics industries and is therefore a promising deposition method for commercial fabrication of PSCs.

As part of this work we have optimised the concentration of extrinsic dopants (e.g. copper, Cu^{2+}) to tune and stabilise the proportion of Ni^{2+} and Ni^{3+} in NiO_x films, thus tailoring their work function and conductivity. As can be seen in Figure 6.51.2, we have achieved some preliminary results for p-i-n PSCs using those sputter-deposited NiO_x HTLs, yielding a PCE of over 22% and 20% for 0.16 cm^2 and 1 cm^2 active area PSCs, respectively. The un-encapsulated cell retained over 90% of its initial efficiency after 1000 hours of maximum power (V_{mpp}) tracking under continuous one-sun condition illumination, demonstrating the superiority of the sputtered NiO_x for use as HTLs in p-i-n PSCs.

Although we have achieved very high efficiencies for the nanostructured TiO_2-based n-i-p PSCs and NiO_x-based p-i-n PSCs, exploiting both inorganic transport layers (TiO_2 and NiO_x) in a single cell is challenging due to process constraints (thermal, chemical, physical) imposed by the need to deposit the second transport layer directly onto the perovskite. As a follow-up study we are therefore planning to investigate the use of remote plasma sputtering deposition (RPD) of NiO_x as a "gentle" deposition method to deposit NiO_x directly onto the perovskite active layer with minimal damage.

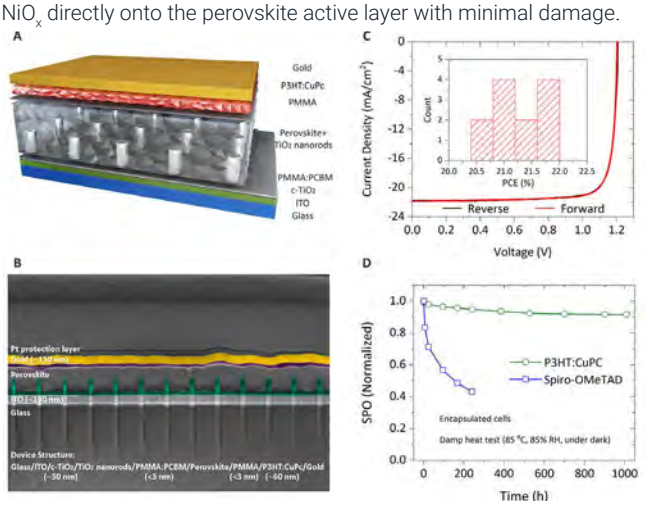

Figure. 6.51.1: (a) and (b) Schematic of nanopattern semi-planar perovskite solar cell and its corresponding cross-sectional scanning electron microscopy (SEM) image studied in this project. (c) and (d) J-V performance of the best semi-planar perovskite solar cell and the corresponding stability measurement in this project.

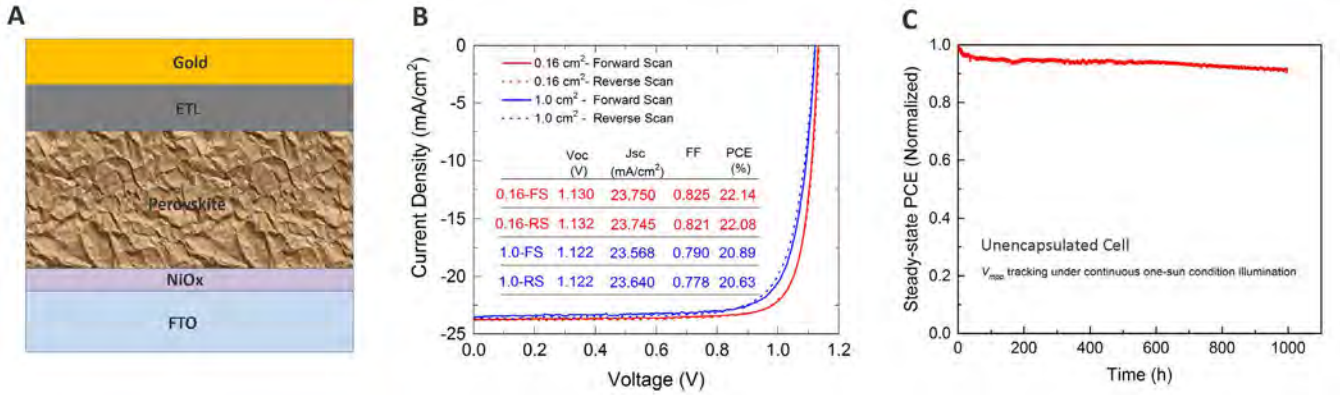

Figure. 6.51.2: (a) Schematic of NiO_x-based p-i-n perovskite solar cell. (b) and (c) J-V performance of the best p-i-n perovskite solar cell and the corresponding stability measurement in this project.

Highlights

- Optimised nanostructured TiO_2 electron transport layers to demonstrate a localised contact structure in perovskite solar cells for the first time.
- Achieved a world record efficiency of 21.6% (certified) for 1 cm^2 perovskite cell.
- The cell retained over 91% of its initial efficiency after 1000 hours of damp heat (85ºC and 85% RH) test.
- Optimised NiO_x HTLs for 1 cm^2 p-i-n perovskite cell with over 20% efficiency.

Future Work

- Optimise the deposition of NiO_x HTLs via remote plasma deposition (RDP) to substitute organic HTLs in n-i-p PSCs.
- Construct/optimise the performance of n-i-p PSCs using nanostructured TiO_2 ETLs and sputtered NiO_x HTLs.
- Test the perovskite cell's stability.

6.52 MICROSTRUCTURE CHARACTERISATION OF THERMALLY EVAPORATED PEROVSKITE SOLAR CELLS FOR THE APPLICATION OF MONOLITHIC PEROVSKITE/SILICON TANDEM SOLAR CELLS

Lead Partner
Monash University

Monash Team
Prof. Udo Bach

Academic Partner
Wuhan University of Technology (WHUT), China: Dr Wei Li, Prof. Yi-Bing Cheng

Funding Support
ARENA, Monash, WHUT

Aim

This project aims to combine complementary expertise at Monash and WHUT in the field of microstructure characterisation of materials for solar cells. In particular, the ultra-low dose transmission electron microscope techniques developed at Monash will be applied to some outstanding thermally evaporated perovskite solar cells, especially in relation to understanding the microstructure in perovskite solar cells.

Progress

This two-year project was commenced in January 2019. Due to the interruption of COVID-19, Dr. Wei Li from WHUT could not visit Monash in 2020. However, we still achieved the following progress during 2020.

1. Perovskite solar cells (PSCs) show excellent power conversion efficiencies (PCEs), long carrier diffusion lengths and low recombination rates. This encourages a view that intra-grain defects are electronically benign with little impact on device performance. Here we vary methylammonium (MA)/formamidinium (FA) composition in $MA_{1-x}FA_xPbI_3$ (x=0-1) and compare the structure and density of intra-grain planar defects with the device performance, otherwise keeping the device nominally the same. We find charge carrier lifetime, open-circuit voltage deficit, and current-voltage hysteresis correlate with the density and structure of $\{111\}_c$ planar defects (x=0.5-1) and $\{112\}_t$ twin boundaries (x = 0-0.1). The best performance parameters are found when essentially no intra-grain planar defects are evident (x = 0.2). Similarly, reducing the density of $\{111\}_c$ planar defects using MASCN-vapour-treatment of $FAPbI_3$ (x~1), also improved performance. These observations suggest that intra-grain defect control can provide an important route for improving PSCs' performance, in addition to well-established parameters, such as grain boundaries and heterojunction interfaces.
2. Mixed halide perovskites with the ability to tune bandgaps show attractive application in tandem solar cells, building integrated photovoltaic and wavelength tunable light-emitting devices. However, halide "demixing" under illumination or in the dark with charge carrier injection in both hybrid and inorganic perovskites results in bandgap instability and current density-voltage (J-V) hysteresis, which can significantly hamper their application. Here, we demonstrate that halide segregation and J-V hysteresis in mixed halide inorganic $CsPbIBr_2$ solar cells can be effectively mitigated by introducing an intermediate phase-enhanced Ostwald ripening through controlling the chemical composition in the $CsPbIBr_2$ precursor solution. "Excess" amounts of either $PbBr_2$ or CsI are incorporated into originally even molar amounts of $PbBr_2$ and CsI precursor solution. With excess $PbBr_2$, we observe enlarged perovskite grain size, no detectable halide phase segregation at grain boundaries nor the perovskite/TiO_2 interface, increased minority carrier lifetime, reduced J-V hysteresis, and improved the solar cell performance. However, different CsI:$PbBr_2$ stoichiometric ratios have different effects on perovskite solar cell performance. Excessive lead phase is reactive with dimethyl sulfoxide (DMSO) in precursor solution to form $Pb(I, Br)_2$·DMSO complex and quasi-two-dimensional $CsPb_2(I, Br)_5$, which are conducive to Ostwald maturation and defect extinction. Finally, the $CsPbIBr_2$ solar cell with a $PbBr_2$ excess precursor composition reaches a PCE of 9.37 % (stabilised PCE of 8.48 %) and maximum external quantum efficiency (EQE) over 90%.

Highlights

1. We demonstrated that planar defects can play a significant role in major impact on the performance of PSCs, providing further scope for optimisation of this exciting PV technology via planar defect control.
2. We also demonstrated the perovskite precursor chemical composition plays an important role in enhancing crystal growth, reducing defect, and mitigating halides segregation and J-V hysteresis of inorganic perovskite solar cells.

Future Work

We will continue to study the role of intra-grain defects, such as dislocations, twins and stacking faults on the performance and long-term stability of perovskite solar cells.

References

1. BACH, U. et al. The critical role of composition-dependent planar defects in the performance of $MA_{1-x}FA_xPbI_3$ perovskite solar cells. (under review, *Nature Energy*).
2. BACH, U. et al. Intermediate phases enhanced Ostwald ripening for elimination of phase segregation in efficient inorganic $CsPbIBr_2$ perovskite solar cells. (under review, *Science China Materials*).

6.53 MAGNETIC FIELD IMAGING FOR PHOTOVOTAIC CELLS AND MODULES

Lead Partner
UNSW

UNSW Team
Dr Oliver Kunz, Prof. Thorsten Trupke, Dr Appu Paduthol

Industry Partners
DENKweit GmbH, Halle (Saale) Germany
("Nur wer anders denkt, kann Neues schaffen!")

Funding Support
ACAP

Aim

UNSW photoluminescence (PL) imaging has revolutionised photovoltaic research and manufacturing by making it possible to visualise electronic material quality, while similarly, lock-in thermography has made it possible to identify power losses through the visualisation of the resulting heat patterns. Magnetic field (MF) imaging represents the missing link that allows visualising three-dimensional current flows in solar cells, modules and solar materials. The proposed project aims at pioneering the field of MF imaging at UNSW.

Progress

(A) Deliverable: Setting up of a prototype system for MF imaging at SPREE

As the basis of this work a measurement system needed to be established at our UNSW labs to perform magnetic field imaging (MFI) and to be able to develop this technology and to compare it to our in-house PL and electroluminescence (EL) capabilities. This deliverable has been achieved.

Figure 6.53.1(a) depicts the imaging system, a three-dimensional robotic measuring system with a linear magnetic sensor array attached to it. We are using this tool now to routinely perform MFI measurements. The system can reliably measure magnetic fields down to 1 µT magnetic resolution and any spatial resolution required. In Figure 6.53.1(b) we see an EL image of a multicrystalline silicon solar cell with three busbars under 5A current injection. The same solar cell was imaged using our in-house MFI tool as seen in Figure 6.53.1(c). During the imaging the scanning direction was chosen to be perpendicular to the busbar direction in order to get a very high spatial resolution in the direction perpendicular to busbars where the biggest magnetic field gradient is expected. The magnetic field component displayed is the component in x-direction, Bx, i.e. the component perpendicular to the busbars. The system, however, measures simultaneously the magnetic fields in all three spatial directions.

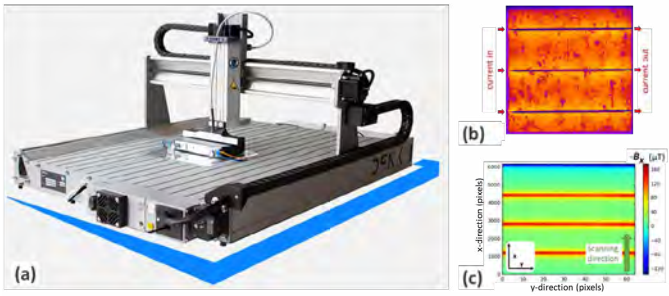

Figure 6.53.1. (a) Magnetic field imaging (MFI) measurement system at UNSW with a DENKweit linear magnetic sensor array attached; (b) EL image taken at our labs of a multicrystalline silicon solar cell with three busbars; (c) equivalent MF image of the same solar cell when scanned from bottom to top.

(B) Deliverable: Setting up MF measurement capabilities for field measurements

Magnetic field imaging is particularly interesting to detect faults in operating solar power plants. Faults like bypass diodes in short circuit or missing/faulty solder connections can conveniently be detected using this technique without the need for disrupting the operation of the solar power plant.

The hand-held sensor array that can be used for such purposes is depicted in Figure 6.53.2(a). It is similar in design and has the same magnetic measurement capabilities as the sensor array that is mounted on the MFI robotic system in Figure 6.53.1(a). However, it can be used on large-area photovoltaic modules in the lab or to measure current flows on solar power plants during normal operation.

Further enhancement of our measurement capabilities has been achieved via using a high performance MF sensor (Memsic – MMC5883MA) that has an approximately 50 times improved magnetic measurement sensitivity compared to our linear sensor arrays (Figure 6.53.2(b). This point sensor can be used where for example very small currents in solar grid lines need to be detected or for precise imaging of regions of interest that were previously identified with our standard line sensor array. In Figure 6.53.2(c) we show the high performance sensor mounted on our robotic x-y stage performing a measurement on a monocrystalline mini-module. This deliverable has been achieved.

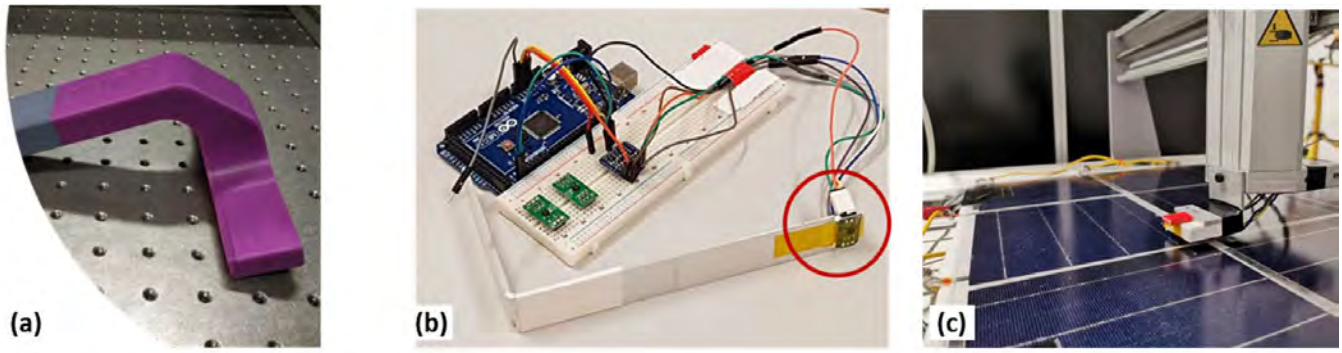

Figure 6.53.2: (a) Hand-held MFI line sensor array for inspection of large solar modules or field work; (b) point sensor (red circle) with 50 x higher MF sensing capability and the corresponding peripheral readout electronics; (c) shows the high sensitivity sensor attached to the x-y measurement system when in use.

(C) Deliverable: Presenting at two or more major PV conferences on MF imaging

At the 2019 IEEE 46th Photovoltaic Specialist Conference (PVSC) we had one oral presentation by Paduthol et al. (2019) and one poster presentation by Kunz et al. (2019) on the topic of Magnetic Field Imaging. The results obtained were also presented at the 2019 APVI APSRC Conference in Canberra as an oral presentation ("Investigating metal-semiconductor contacts in solar cells using magnetic field imaging"). In the latter work we measure and model current flows in solar cells when current is injected and extracted using contacts from one solar cell polarity only. Figure 6.53.3(a) (left) shows the results of our measurements for different current flow patterns ((A)–(C)). These images were then modelled using the circuit simulation software LT SPICE. The modelling results are displayed to the right of the measurements. The electronic circuit underlying this modelling is schematically displayed in Figure 6.53.3(b). This deliverable has been achieved.

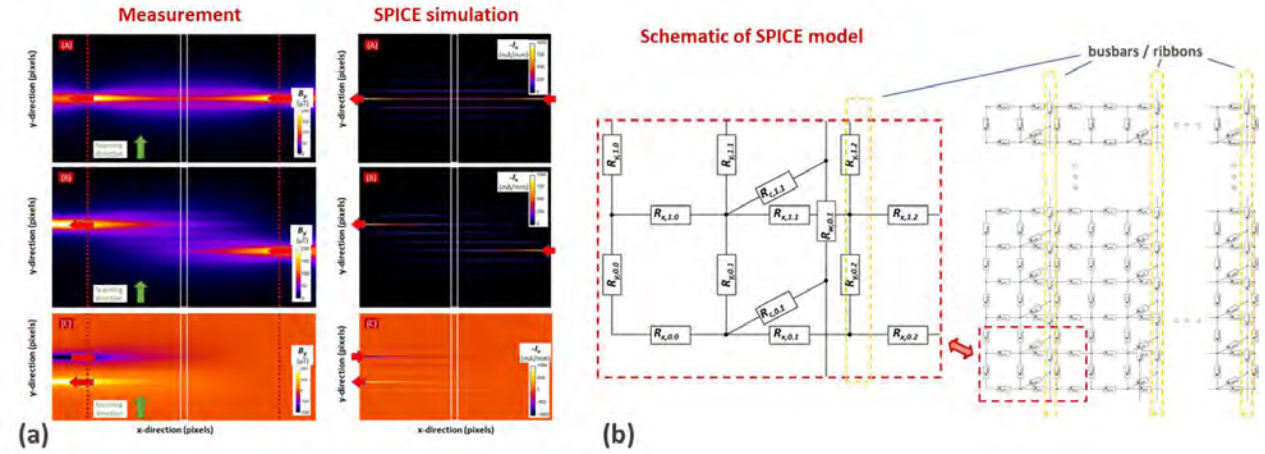

Figure 6.53.3: (a) left: Magnetic field images (By) of a multi-wire contacted silicon solar cell for different current injection patterns; (a) right: SPICE electronic network simulations of the measured current flows; (b) schematic display of the equivalent circuit SPICE model used to obtain the simulation results.

(D) Deliverable: Publishing of at least three research publications in the course of this project

We published our work in the proceedings of the 46th PVSC IEEE specialist conference in Chicago in 2019. Two much more detailed journal publications on this topic are now in preparation and expected to be submitted to journals by end of April and end of J une 2021, respectively.

Due to COVID-19 we have not been able to do as much lab work and we have also had unexpected problems getting access to samples from external partners (solar modules). Therefore, we were delayed in the measurements for our planned journal publication. The measurements are now completed, and we are in the process of writing a journal publication. We expect a paper to be submitted to Solar Energy at the beginning of 2021.

Some of our latest measurement results are presented in Figure 6.53.4 which also demonstrates our most recently acquired capabilities of measuring full PV modules. This deliverable has been almost achieved.

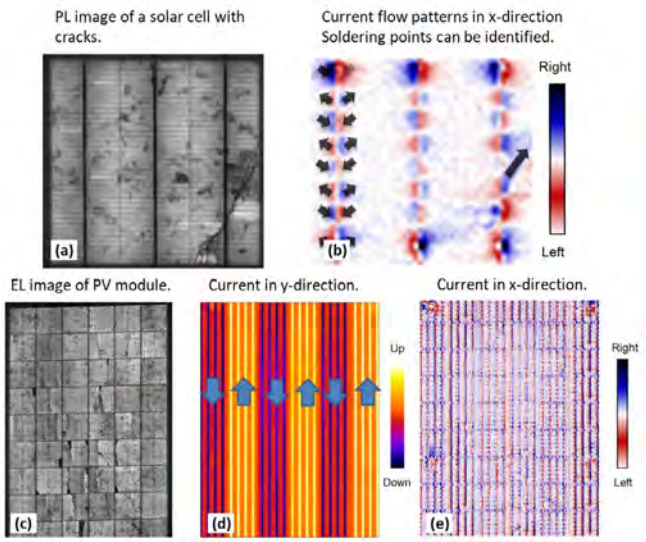

Figure 6.53.4: Recent measurement results from our labs: (a) PL image of a solar cell with pronounced cracks; (b) current flow pattern in x-direction of cell from (a) where the soldering points can be identified and the anomaly resulting from the cracks; (c) EL image of a solar module; (d) current flow patterns in y-direction of the module from (c); (e) current flow patterns in x-direction of the module from (c).

Highlights

- We have successfully established magnetic field imaging capabilities for lab and field measurements for solar cells and modules. Additionally, we have installed a high performance point sensor on our system which substantially enhances the sensitivity for measurements of small currents and smaller regions of particular interest ("MFI zoom images"). We are now also capable of measuring the magnetic fields and current flow patterns of full solar modules in a repeatable fashion.
- MF images of cells and modules from a wide range of technologies were studied.
- We have presented on this work at the IEEE specialist conference in Chicago in 2019 via an oral and a poster presentation. We also have orally presented this work at the annual APVI APSRC conference in Canberra in December 2019.
- We have to date published two conference papers on this work Kunz et al. (2019) and Paduthol et al. (2019) and a journal publication is currently in preparation which will summarise our work and also include the latest solar module results.

Future Work

- One journal publication is currently in preparation and expected to be submitted in 2021. The paper will discuss the basic theory of magnetic field imaging for solar applications, its strengths and weaknesses. It will feature measurement results from the course of this project.
- Progress this work with higher sensitivity sensor array and local laser illumination which will lead to magnetic field images with significantly improved spatial resolution and sensitivity.

Lessons Learned

- The technology is very promising but it also became clear in the course of this work that the standard MFI system provided by DENKweit has two major limitations,
  (i) it can only be used on small samples such as individual solar cells and mini-modules, and
  (ii) it has significant sensitivity limitations for solar cell applications and mainly shows currents that are flowing in the busbars and interconnecting ribbons (high current density).
  We are now building our own sensor board based on highly sensitive sensors (Sensitec, AFF756) to overcome the sensitivity limitations and to be able to add this capability to our line-scanning PL tool which can scan entire modules.
- We are pursuing further work on solar module measurements via a collaboration with Canadian Solar at the moment. The aim of this work is the exploring of defects in shingled modules. We expect that this work will lead to a further conference or journal publication.

Summary

We have added a completely new measurement capability to our research: magnetic field imaging. This allows us to now perform measurements of magnetic fields and current flow patterns in solar cells and solar modules.

Apart from a slight delay caused by a challenging year 2020 we have achieved all milestones. In particular, we have not only achieved the set-up of a standard measurement system but we have extended its use by adding highly sensitive measurement capabilities and we can now also measure on large areas, i.e. entire PV modules.

We believe that this measurement technique will be particularly useful in the current phase of solar technology development, where a large number of novel PV modules are developed with often challenging connection and layout schemes.
Being able to measure irregularities and faults in these novel module technologies using magnetic field imaging can be highly valuable and we will therefore keep pursuing and extending this body of work.

References

KUNZ, O., PADUTHOL, A., SLADE, A., EDWARDS, M., KAUFMANN, K., PATZOLD, M., LAUSCH, D. & TRUPKE, T. Investigating metal-semiconductor contacts in solar cells using magnetic field measurements. 2019 IEEE 46th Photovoltaic Specialists Conference (PVSC), 16–21 June 2019. 2764-2768.

PADUTHOL, A., KUNZ, O., KAUFMANN, K., PATZOLD, M., LAUSCH, D. & TRUPKE, T. Magnetic Field Imaging: Strengths and limitations in characterising solar cells. 2019 IEEE 46th Photovoltaic Specialists Conference (PVSC), 16–21 June 2019. 0822-0824.

6.54 INVESTIGATION OF PERFORMANCE DEGRADATION PATHWAYS IN SILICON PHOTOVOLTAIC MODULES ARISING FROM COPPER-PLATED METALLISATION

Lead Partner

UNSW

UNSW Team

Prof. Alison Lennon, Ben Phua

Academic Partner

Arizona State University (ASU), USA: Dr André Filipe Rodrigues Augusto, Prof. Stuart Bowden

Funding Support

ARENA, UNSW

Aim

The aim of this project was to investigate possible degradation pathways in silicon photovoltaic modules arising from copper-plated contacts on cells. The project used cross-sectional imaging and material analyses of fabricated modules to identify the physics and chemistry associated with degradation pathways in both copper-plated p-type cells (Al BSF and PERC). The project involved the fabrication and environmental testing of one and/or two cell modules from copper-plated silicon solar cells. Electrically degraded regions of the modules were then identified using electroluminescence (EL) imaging and cross-sections were prepared from the identified regions and analysed using plasma-focused ion beam (PFIB) imaging and electron dispersive X-ray spectroscopy (EDS). Potential degradation pathways that were of particular interest to this study included:

- Cu diffusion through the commonly used barriers and capping layers
- void formation due to metal interdiffusion
- weak adhesion of cell metallisation.

Progress

This two-year project commenced in January 2019. Cross-sectional analyses have been performed on one cell mini-modules, fabricated at ASU with copper-plated p-type back-surface field solar cells, and exposed to 2000 hours of damp heat treatment (Karas et al., 2017).

Electroluminescence (EL) imaging was used to detect regions which had been degraded by the exposure to damp heat and compared to regions where no degradation was observed (see Figure 6.54.1(a)). We have demonstrated that copper can out-diffuse through tin capping layers and be in direct contact with the EVA encapsulant. This out-diffusion is frequently associated with voids in the encapsulant as shown in Figure 6.54.1(b)–(f). Copper out-diffusion through the tin capping has also been detected in regions where no electrical degradation is observed suggesting that some Cu out-diffusion can occur without electrical degradation.

Copper in-diffusion has also been detected in UNSW fabricated modules comprising copper-plated ps laser ablated p-type PERC cells (Phua et al., 2019).

For these modules, the very narrow contact opening widths (<15 mm) make it challenging to achieve strong adhesion and it is hypothesised that weak interfacial adhesion between the copper-plated fingers and the silicon can result in a pathway for copper diffusion into the silicon, and subsequent electrical degradation. These modules were exposed to 1000 hours of damp heat. Figure 6.54.2(a) shows the EL image of a module after 1000 hours of damp heat exposure, the red box identifying a degraded region that was used for cross-sectional analysis. Figure 6.54.2(b)–(e) show that voids exist in the degraded region between the plated finger and Si wafer and that Cu has diffused into the silicon. This indicates that weak interfacial adhesion between the plated finger and Si may have resulted in dislodgement of the finger during the damp heat test. A closer examination of the damaged interface using EDS shows copper penetration into the silicon (Figure 6.54.2(e)). This result suggests that poor interfacial adhesion between plated fingers and silicon may predispose regions to copper in-diffusion.

As expectations of longer module operating life increase for ongoing reduced PV-generated electricity costs, 1 x IEC module environmental tests will most likely be insufficient and increased durability will be required. Although copper-plated p-type modules have been demonstrated to be able to pass the 1 x IEC tests, attention will need to be focused on identifying materials and processes that limit durability. This will require an improved understanding of the physical processes of metal interdiffusion and is of particular importance for copper-plated modules due to copper's propensity to inter-diffuse in metals. This

project has successfully demonstrated both copper out-diffusion through capping layers and in-diffusion into wafers. In both cases, these interdiffusion processes have resulted in localised degraded electrical performance after 1000 hours of damp heat exposure. Further research will require more extensive laboratory testing and additional supporting field studies to further the understanding of the physics of the failure of copper-plated modules. Similar investigations may be necessary for screen-printed modules.

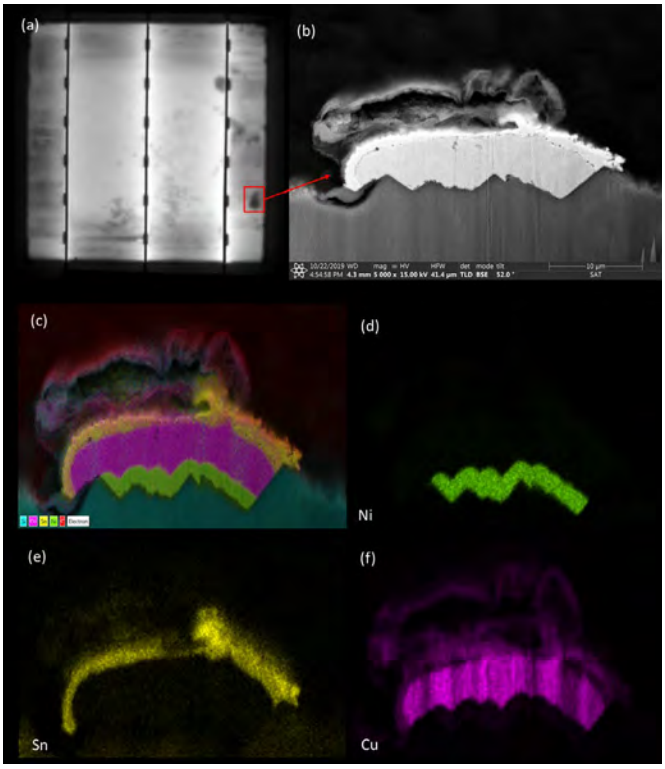

Figure 6.54.1: (a) Electroluminescence images of an ASU-fabricated mini-module comprising a p-type BSF cell showing electrical degradation with damp heat testing and the regions selected for cross-sectional analysis. (b) Cross-sectional EDS maps of a copper-plated finger in the indicated region in (a). (c)–(f) EDS analysis of (b) showing copper out-diffusion through a tin capping layer and the formation of a void in the EVA encapsulant.

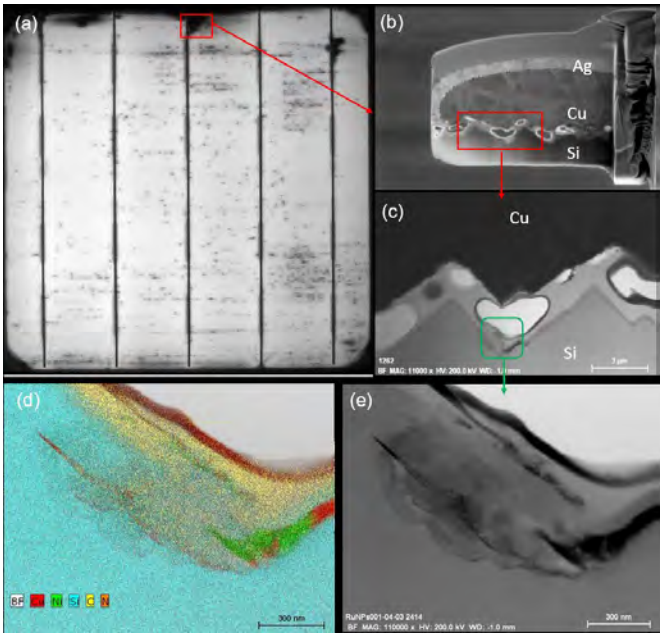

Figure 6.54.2: (a) Electroluminescence image of a UNSW mini-module comprising a p-type PERC cell showing electrical degradation with damp heat testing and the region selected (red box) for cross-sectional analysis. (b)–(c) Cross-sectional FIB image of a Ni/Cu/Ag-plated finger from the degraded region. The green box identifies the region where EDS analysis shown in (d) was performed. (d)–(e) EDS analysis of the degraded region (c) showing Cu (red) penetration into Si substrate.

Highlights

- Demonstrated the ability to perform cross-sectional imaging and elemental analysis of modules (even with tempered glass) using plasma FIB imaging and EDS.
- Copper out-diffusion through tin capping layers has been demonstrated and has been shown to occur at electrically degraded regions of copper-plated p-type BSF modules.
- Copper in-diffusion has been identified in modules comprising ps laser ablated cells.
- Results of this project were presented at the Australian Pacific Solar Research Conference in December 2019, and have been published in the following paper:
    - PHUA, B., SHEN, X., HSIAO, P., KONG, C., STOKES, A. & LENNON, A., 2020. Degradation of plated silicon solar module due to copper diffusion: The role of capping layer formation and contact adhesion. *Sol. Energy Mater. Sol. Cells* 215, 110638.
- Presently, UNSW and ASU researchers are writing a joint manuscript on copper out-diffusion to be published in 2021.

Future Work

The project has been successful in building a collaboration between the ASU and UNSW researchers in the area of durability of silicon PV modules comprising copper-plated cells. Further collaborations could also look to include field studies to ensure that lab results are consistent with degradation which may occur in the field. Future work could also consider the longer-term durability of silver screen-printed modules which employ very narrow finger widths in the cell metallization.

References

KARAS, J., MICHAELSON, L., CASTILLO, M. L., MUNOZ, K., BAILLY, M., JAIN, H., AKEY, A., RAND, J., TYSON, T., BUONASSISI, T. & BOWDEN, S. Addressing adhesion and reliability concerns of copper-plated c-Si solar cells and modules. 2017 IEEE 44th Photovoltaic Specialist Conference, PVSC 2017, 2017. 1-5.

PHUA, B., SHEN, X., MO, A., HSIAO, P.-C., KARAS, J., AUGUSTO, A. F. R., BOWDEN, S. & LENNON, A. 2019. Performance degradation pathways in silicon photovoltaic modules arising from copper-plated metallisation *Australian Pacific Solar Research Conference.* Canberra, ACT.

6.55 COMPUTATIONAL MATERIALS DISCOVERY: AB INITIO MODELLING OF NEW HIGH PERFORMANCE SEMICONDUCTORS FOR TOP CELLS IN MULTI-JUNCTION TANDEMS ON SILICON SOLAR CELLS

Lead Partner

UNSW

UNSW Team

Dr Rob Patterson, Dr Judy Hart, A/Prof. Xiaojing Hao, Prof. Martin Green

Academic Partners

University of Bristol, United Kingdom: Neil Allan

Beijing Computational Science Research Center: Su-Huai Wei

Funding Support

ARENA, ACAP

Aim

Challenges associated with the scalability of III-V semiconductors and stability of Pb-halide perovskite materials for multi-junction tandem solar cells on silicon (silicon tandems) motivates that search for alternative semiconductors that have the potential for high performance. In 2020, the project aimed to refine theoretical investigations into transition metal compounds. In particular, the electronic structure of stable semiconductors was computed using the spin-polarised DFT+U technique (Hu 2012). Knowledge of the properties of the stable sulfide perovskites was expanded with a particular focus on quantities that affect heterojunction devices, using the DFT+U technique. A comprehensive study of alloys in the CIGS family of materials has been performed, aiming to determine strategies to combat anti-site defects.

Progress

Novel multi-component compounds

Building on work from the first year of the project, increased understanding of novel transition metal compounds has led to an improvement in terms of material crystal structure and simulation approach. Though previous attempts to simulate the "defect-adamantine" structure for bulk $ZnIn_2S_4$ did not perform well computationally, $ZnIn_2S_4$ in the spinel crystal structure performed excellently, consistent with recently obtained experimental structural information. In this spinel structure, doping or alloying of transition metals of interest, Co and Ni, may sit on Zn sites. Of these two elements, Co has been observed experimentally to diffuse readily into $ZnIn_2S_4$ in preliminary studies conducted at UNSW, implying that a relatively high degree of alloying is possible on the Zn sites.

Computational techniques relevant to transition metals are still actively being developed and improved. Spin-polarised calculations using local spin density approximations (LSDA), coupled to the generalised gradient approximation with a Hubbard U value (GGA+U/DFT+U) applied to the d-orbitals of transition metal, are among the more sophisticated and generally increase the accuracy of the predictions. Analogous to experimental work on new materials where stability is a major issue, the challenge with the spin-polarised GGA+U technique is numerical stability. In 2020, the first simulations of spinel compounds alloyed with transition metals has been successfully performed in the supercell configuration to allow for the appropriate number of spin degrees of freedom. A result from this is shown in Figure 6.55.1.

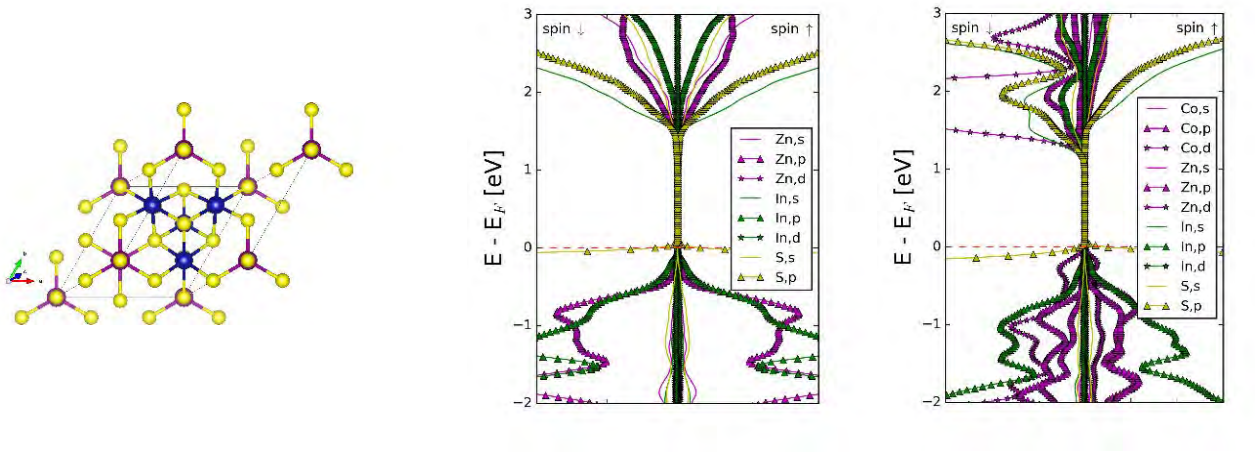

Figure 6.55.1: Unit cell structure (a) and projected density of electronic states (pDOS) from a spin-polarised GGA+U simulation of (b) bulk $ZnIn_2S_4$ and (c) cobalt alloyed $Co_{0.5}Zn_{0.5}In_2S_4$. Preliminary work conducted at UNSW showed that experimental bandgaps for the parent compound $ZnIn_2S_4$ are above 2 eV. Here, the simulation yields a bandgap prediction of ~1.7 eV. Indium s-orbitals and sulfur p-orbitals dominate the conduction and valence bands respectively, suggesting the potential for good absorption and defect tolerance for the In-S states making up the conduction band. No net magnetisation is observed in the pDOS, as seen by the symmetry of the data about the y-axis. Significant changes in the conduction band can be seen in the cobalt-doped case (c) where cobalt d-orbitals dominate the conduction band and lower the predicted bandgap to ~1.3 eV at a doping level of 50% atomic of cobalt. Also in the cobalt-doped case, asymmetries in the pDOS are indicative that a net magnetisation should be expected for the material. A Hubbard U value of 3.1 eV was applied to the Co d-states for the cobalt-doped simulations.

Stable perovskite compounds

The main effort coming from the work in 2020 was focused on developing the stable sulfide perovskite $BaZrS_3$. Many of the results require calculations on large numbers of atoms, i.e. for surfaces. These large supercell calculations ideally require highly efficient calculations. A good compromise between efficiency and accuracy in this case is to use the GGA+U technique and a Hubbard U value of 6.0 eV was found to widen the material's bandgap sufficiently so as to get an indication of the effects of any surface passivating layers. Supercells with oxygen substitution for sulfur were also simulated, with bandgaps estimated using a very computationally efficient correction technique (GLLB-SC functional) (Castelli 2014). A first estimate of this sulfide perovskite's work function was also estimated using a dipole-layer correction technique.

These results are encouraging, suggesting that heterojunction devices can be built from this material in ways analogous to well-developed state-of-the-art devices. In particular, the conduction band edge at -4.1 eV is very convenient for heterojunction device fabrication, as shown in Figure 6.55.2(b). Either TiO_2 or ZnO can be used as an electron transport layer and a variety of common p++ hole transporting layers can be used to make the final device.

a)

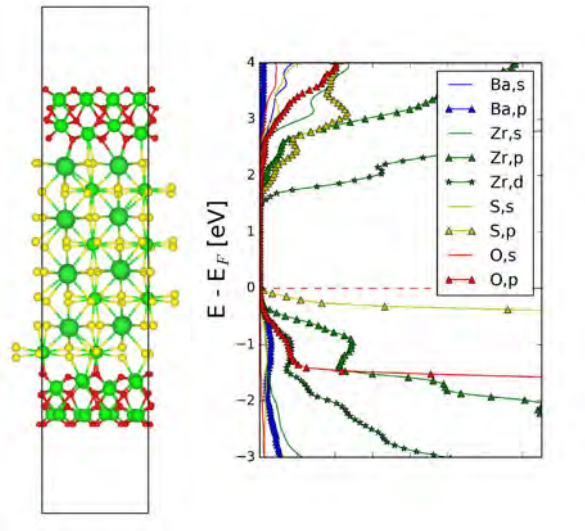

b)

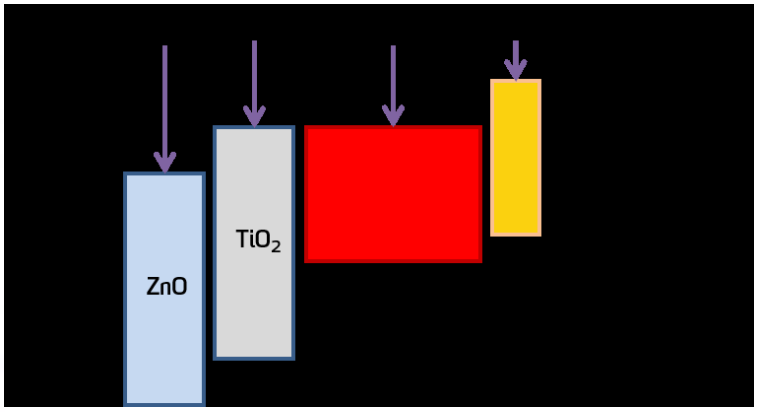

Figure 6.55.2: (a) It is likely that the native oxide, ZrO_2, provides excellent passivation to $BaZrS_3$ (Ba-large green, Zr-small green, O-red, S-yellow) as no deep levels appear in the bandgap of the material. (b) The work function predicted suggests band offsets for the sulfide perovskite that lend themselves readily to well-developed device configurations, such as those belonging to Pb-halide perovskites. (c.ii) Oxygen substitution on sulfur sites does not appear to lead to deep defects in $BaZrS_3$, relative to the bulk compound (c.i), though effective masses appear to increase. This is consistent with the continuous increase in band edge photoluminescence observed experimentally (Niu 2017).

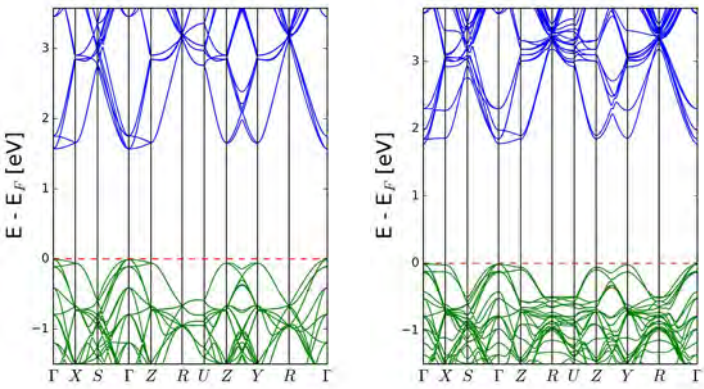

c.i) c.ii)

$CuInS_2$ and CIGS variations

Anti-site defects occur when two atoms swap positions during crystal growth. This can produce deep electronic defects well known in $Cu(In,Ga)Se_2$ compounds where they involve Cu substituting for Ga (Wei 1998). This problem tends to worsen in the wide bandgap sulfide compounds that are of interest in this project. Anti-site defects in the wide bandgap sulfide CIGS were comprehensively addressed through extensive simulations in 2020. The defect formation energy of multiple anti-site defect pairs was calculated for systems with different alloyed elements, with Na and Ag substituting for Cu as well as Al and La substituting for indium. It was hypothesised that alloying with an element that had the maximum difference in atomic radius from Cu and Ga would lead to the biggest increase in the defect formation energy, making anti-site defects significantly harder to form.

However, to date, relatively small changes in the defect formation energy were observed in most cases. A slightly stronger trend was observed when Na was substituted for Cu, rather than Ag. The absolute change in the ionic radius for Ag and Na is quite similar. As such, the larger defect formation energy change on the introduction of Na may suggest that increased ionicity in the compound can have a positive impact on reducing anti-site defect formation in the compound.

Highlights

- Spin-polarised GGA+U calculations for transition metal oxides implemented, to improve prediction accuracy.
- Multiple device design relevant properties predicted for $BaZrS_3$.
- Increased ionicity in CIGS alloys may have an impact on anti-site defect formation.

Future Work

The growth of $BaZrS_3$ is known to be quite slow. Going forward we intend to investigate surface diffusion of constituent atoms on different $BaZrS_3$ crystal facets using sophisticated nudged elastic band (NEB) calculations. Additional techniques will be developed to attempt to assess grain boundaries with the maximum possible computational efficiency. This will likely require multi-scale modelling using semi-empirical molecular dynamics to obtain a good initial crystal structure. Other stable nitride perovskite compounds will be investigated as well.

References

CASTELLI, I. E., GARCIA-LASTRA, J. M., THYGESEN, K. S. & JACOBSEN, K. W. 2014. Bandgap calculations and trends of organometal halide perovskites. *APL Materials,* 2. doi: 10.1063/1.4893495.

HU, J., ZHANG, Y., LAW, M. & WU R. 2012. First-principles studies of the electronic properties of native and substitutional anionic defects in bulk iron pyrite. *Physical Review B*, 85. doi: 10.1103/PhysRevB.85.085203.

NIU, S. Y., HUYAN, H. X., LIU, Y., YEUNG, M., YE, K., BLANKEMEIER, L., ORVIS, T., SARKAR, D., SINGH, D. J., KAPADIA, R. & RAVICHANDRAN, J. 2017. Bandgap Control via Structural and Chemical Tuning of Transition Metal Perovskite Chalcogenides. *Advanced Materials*, 29.

WEI S., ZHANG S. B. & ZUNGER A. 1998. Effects of Ga addition to $CuInSe_2$ on its electronic, structural, and defect properties. *Applied Physics Letters*, 72. doi: 10.1063/1.121548.

6.56 TOWARDS A MULTIPLE EXCITON GENERATING SILICON SOLAR CELL

Lead Partner

UNSW

UNSW Team

Dr Murad Tayebjee, Prof. Dane McCamey

Academic Partners

Harvard University, USA: Dr Daniel Congreve
Columbia University, USA: A/Prof. Luis Campos

Funding Support

ARENA, UNSW

Aim

This project will create new ACAP partnerships with Columbia University and Harvard University to develop an organic layer which will augment the current of existing silicon solar cell technologies. The potential energy conversion efficiency of these devices exceeds 35% (Tayebjee et al. 2014). The project brings together world leaders in singlet fission synthesis (Campos Group, Columbia University); fabrication of multiple exciton generating devices (Congreve Group, Harvard University); and optical and magnetic resonance spectroscopies (Tayebjee and McCamey Groups, UNSW).

A key outcome of this project is the use of magnetic resonance and THz spectroscopy to identify and characterise singlet fission in working devices. This will provide benchmarks and screening for potential singlet fission silicon tandem candidate materials.

Progress

COVID-19 has significantly hampered progress in 2020, and we were glad to accept a one-year extension to the work. Harvard's labs were shut down for a large portion of the year, and Tayebjee's teaching commitment was increased to account for the rapid transition to online teaching. Further, during 2020 our collaborator, Congreve, at Harvard has moved to Stanford University In a tenured position. Our collaboration will continue on-track, and his new labs have been established. All Chief Investigators are in regular email contact and we expect to achieve the stated aims of the project by its extended closing date.

Highlights

- Upgrade to the existing UNSW THz pump-probe setup to get a ~100x data collection speed-up. This higher throughput will allow for us to make up for lost time due to COVID-19 delays.
- Submission of paper with Campos Group to JACS on a magnetic resonance study of singlet fission materials.
- Internal UNSW–USA networks funding obtained to maintain this collaboration past the lifetime of the ACAP funding.

Future Work

- Initial magnetic resonance experiments will be carried out and results are expected in the first quarter of 2021.
- The spectroscopy from this work is being used as part of a larger DP22 application (re-bid from DP21).
- A "Singlet Fission Summit" was being planned in Sydney in 2020, however plans for this have changed given the current travel restrictions. We hope to use the UNSW–USA Networks funds to do this once travel restrictions are lifted.

References

PUN, A. B., ASADPOORDARVISH, A., KUMARASAMY, E., TAYEBJEE, M. J. Y., NIESNER, D., MCCAMEY, D. R., SANDERS, S. N., CAMPOS, L. M. & SFEIR, M. Y. 2019. Ultra-fast intramolecular singlet fission to persistent multiexcitons by molecular design. Nature Chemistry, 11, 821-828. doi: 10.1038/s41557-019-0297-7.

TAYEBJEE, M. J. Y., SOUFIANI, A. M. & CONIBEER, G. J. 2014. Semi-Empirical Limiting Efficiency of Singlet-Fission-Capable Polyacene/Inorganic Hybrid Solar Cells. Journal of Physical Chemistry C, 118, 2298-2305. doi: 10.1021/jp4101637.

6.58 MICROWAVE PROCESSING: FOR SILICON SOLAR CELLS AND BEYOND

Lead Partner

UNSW

UNSW Team

A/Prof. B. Hallam, A/Prof. S. Huang

UNSW Student

Yuchao Zhang

Academic Partner

Macquarie University

Macquarie University Team

Dr B. Puthen Veettil, Dr D Payne

Funding Support

ARENA, ACAP

Aim

This project aims to investigate the potential of microwave processing techniques for advanced hydrogenation of silicon solar cells and further this study to investigate the potential role of microwave processing for solution-processed solar cell materials. Through this project, we aim to establish microwave processing as an efficient alternative to conventional processing steps.

Progress

In the previous year, we custom-designed and installed a microwave cavity that has a continuous operating temperature at 1800°C. In 2020, we looked deeper into the interaction between material and microwaves in order to maximise the heating and to find suitable operating frequencies. Our experiments identified that eddy current effects in the presence of microwave frequencies heats up silicon at a much more rapid pace as compared to dielectric heating. Figure 6.58.1 (left) shows the rapid heating of a silicon sample in microwave. The sample heats up from room temperature to 500°C in 2 seconds. This experiment used dummy loads (silicon carbide) in addition to silicon samples to absorb the excessive microwave radiation and to protect the magnetron. Figure 6.58.1 (right) shows the difference in heating of the silicon carbide susceptor and silicon samples. The controlled heating of silicon samples is at a much higher rate as compared to the slower silicon carbide heating which follows logarithmic heating and cooling rates. This is also a demonstration of selective heating that will be exploited when processing heterojunction solar cells, whereby the surface dielectrics are temperature sensitive.

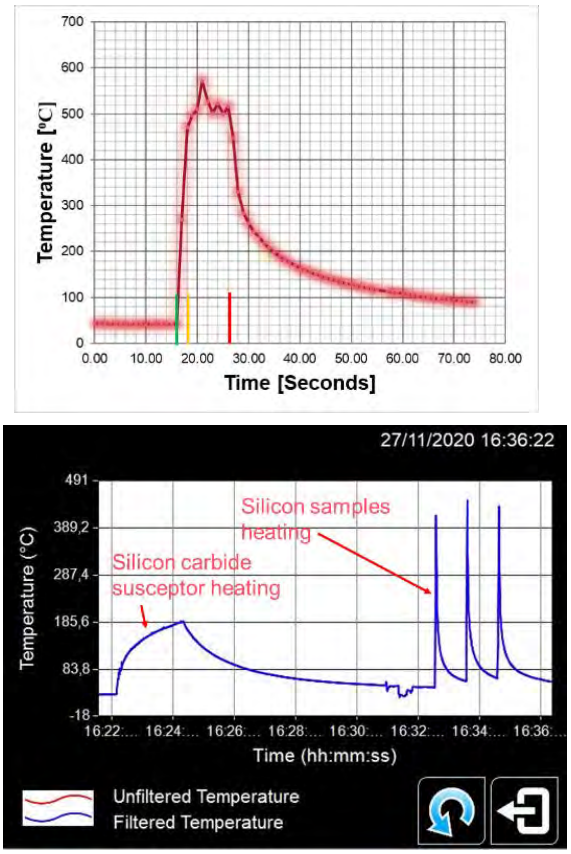

Figure 6.58.1: Rapid heating of silicon samples in the microwave (left) with a heating rate as high as 250°C.s^{-1} and (right) the comparison of the heating profiles of silicon carbide by dielectric heating and silicon by eddy current heating.

Another important progress is the development of our capability to measure the complex permittivity of semiconductor materials. As the imaginary part of permittivity (ε``) determines the heating by microwave radiation, it is critical to be able to quantify the real and imaginary components of dielectric constants for a range of frequencies. We developed a vector network analyser (VNA) technique to measure our samples by broadband-probe as well as cavity-perturbance methods. Figure 6.58.2 shows the real and imaginary permittivity of three silicon samples – original, after light soaking, and after hydrogenation. The samples were measured from 20 MHz to 20 GHz frequencies. It was observed that, microwave absorption (or the imaginary part of permittivity) increases for a narrow range of frequencies around 1 GHz for light-soaked samples. This is ascribed to the presence of the highly polar B-O bonds and other dangling bonds. The peak disappears after hydrogenation, further corroborating our assumptions of the origin of the peak.

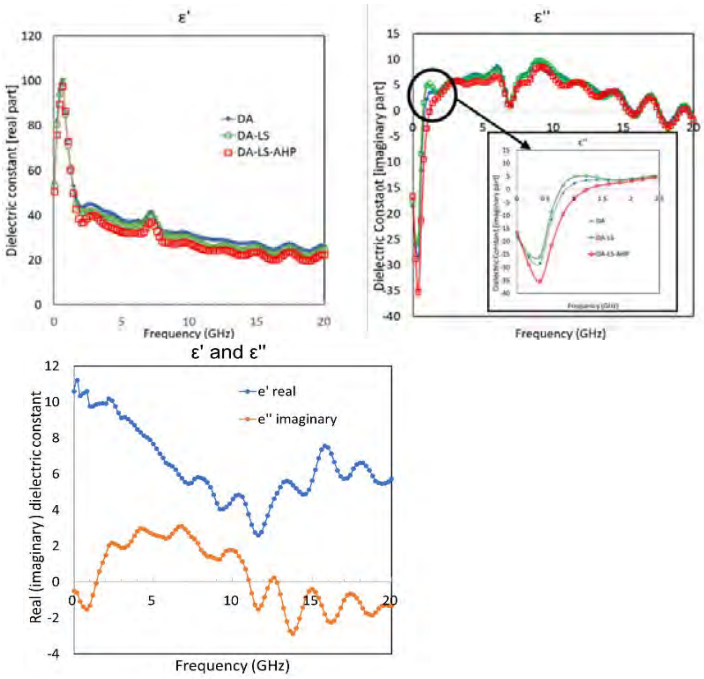

Figure 6.58.2: The real (left) and imaginary (middle) components of the complex permittivity of silicon samples – original (DA), after light soaked (DA-LS) and after hydrogenation (DA-LS-AHP) measured for broadband of frequencies – from 20 MHz to 20 GHz. No significant changes observed for the real part of the dielectric constant. A distinct peak at lower frequencies was observed for the imaginary part of the dielectric constant, indicating the presence of microwave-responsive (polar) bonds. Real and imaginary (right) components of the complex permittivity of a CsPbBrI perovskite sample.

Several new materials and material combinations are under investigation for developing new solar cell absorbers. Being able to model and predict the microwave response of materials is critical for the wider deployment of microwave processing techniques. We have developed capability and the know-how of molecular dynamic simulation using a Large-scale Atomic/Molecular Massively Parallel Simulator (LAMMPS) to simulate the heating of silicon and novel materials under microwave radiation. We have tested the model successfully with a well-studied microwave absorber-water. Figure 6.58.3 shows the simulation of heating of defective silicon under two electric field strengths.

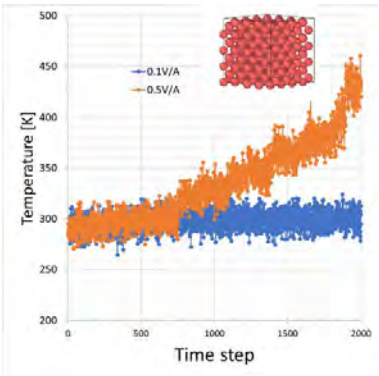

Figure 6.58.3: LAMMPS simulation of heating of silicon under two microwave field strengths. The microwave frequency used here is 20 GHz which is the highly absorbed frequency by water. The inset shows the unit structure used for this simulation – silicon atoms with 2% porosity (2% missing atoms) to emulate non-polar bonds.

Highlights

- Rapid heating rate 250°C.s-1 obtained for larger silicon samples. Is able to go to higher heating rate for smaller samples but with higher risks of arcing.
- Completed the development of techniques to directly measure the complex permittivity of materials using network analyser. Measured the complex permittivity of silicon and CsPbBrI perovskite.
- Completed the development of molecular dynamics models for simulating heating of materials under microwave radiation. Successfully tested and calibrated with water and tested on defective silicon samples.
- This work was selected for an oral presentation at the APSRC 2020 conference conducted on 2 December.
- This proof-of-concept was one of the three major technology streams that formed the basis of our successful ARENA funding (total 490K AUD) in 2020. All CIs of this project are also the CIs of the ARENA project, continuing the successful collaboration.
- Drafting is underway for a manuscript to be submitted to a Q1-ranked journal, Material Science in Semiconductor Processing.

Future Work

Microwave processing is a promising approach for heterojunctions and metal contact processing steps. At the APSRC conference, we received invitations for collaborations from researchers investigating heterojunctions. We will explore these avenues by translation and application of the outcomes of this project. We will continue this project work under the new umbrella of an ARENA project with a broader scope. This includes calculating the CAPEX and OPEX of microwave processing against standard industrial processes for benchmarking and aiming for future funding in collaboration with the renewable energy industry.

6.60 SILICON SOLAR CELLS WITH SILICON CARBIDE PASSIVATED CONTACTS

Lead Partner

UNSW

UNSW Team

Dr Ning Song, Dr Udo Römer, Prof. Alison Lennon, Mr Shuo Deng

UNSW Student

Car Lin Ng

Industry Partners

Trina Solar Ltd. China.

Funding Support

ACAP

Aim

This project aims to conduct fundamental research into the passivation properties of doped silicon carbide (SiC_x) passivated contacts for silicon solar cells.

Progress

The use of doped polysilicon (poly-Si) for electrical contacts is attracting significant interest in both PV research institutes and silicon PV manufacturing companies due to the record high efficiency (26.1%) achieved with this contacting technology (Green et al. 2019; Haase et al. 2018). Meanwhile, SiC_x as an alternative to poly-Si also draws more attention due to its greater resilience to blistering when deposited on SiO_x, low thermal budget for dopants activation, high chemical and thermal stability and high transparency and conductivity (Nogay et al. 2017; Xu et al. 2020; Pomaska et al. 2020). This project investigates a new silicon rich SiC_x material for contacting of both polarities of silicon instead of/ or in combination with poly-Si.

In order to study the carbon content on the properties of the SiC_x films, we have successfully fabricated SiC_x thin films with a thickness of ~28 nm on quartz substrate with varied C content of 0%, 2.5%, 5%, 7.5%, 10%, 20% and 30% by co-sputtering from a carbon and an intrinsic Si target. Then these films were subject to post annealing at 550°C, 650°C, 750°C, 850°C, 900°C and 950°C in N_2. The microstructure and optical properties of the thin films have been investigated by Raman spectroscopy and ellipsometry. The films were found to stay amorphous and start to crystallise at above 750°C. As shown in Figure 6.60.1, the crystallinity was found to decrease with the increase of the carbon content. The bandgaps determined from ellipsometer data are shown in Figure 6.60.2. Finally, an optical simulation with SunSolve on PV Lighthouse is carried out to gauge the parasitic absorption it would have when applying the as-prepared SiC_x thin films to the front contact. The parasitic absorption was plotted against carbon content at different annealing temperatures as shown in Figure 6.60.3. Overall, comparing the bandgap values in Figure 6.60.2 with the associated parasitic absorption in Figure 6.60.3 shows reasonable results in which samples with higher bandgap values at higher annealing temperatures show lower parasitic absorption due to them having a higher amount of crystalline silicon carbide domains.

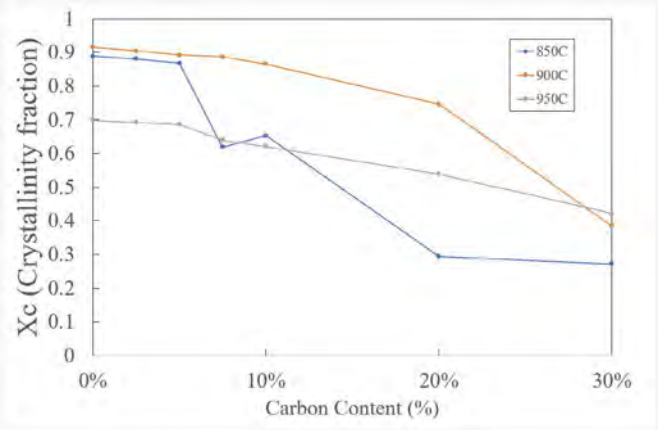

Figure 6.60.1: Crystallinity of sample at 850°C, 900°C and 950°C.

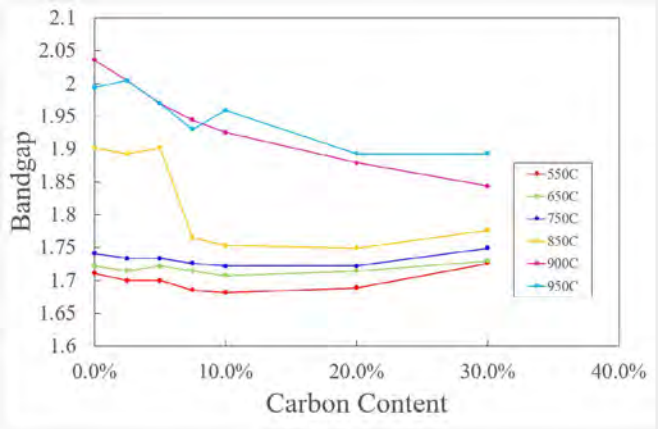

Figure 6.60.2: The bandgap of different samples determined from E_{04} method.

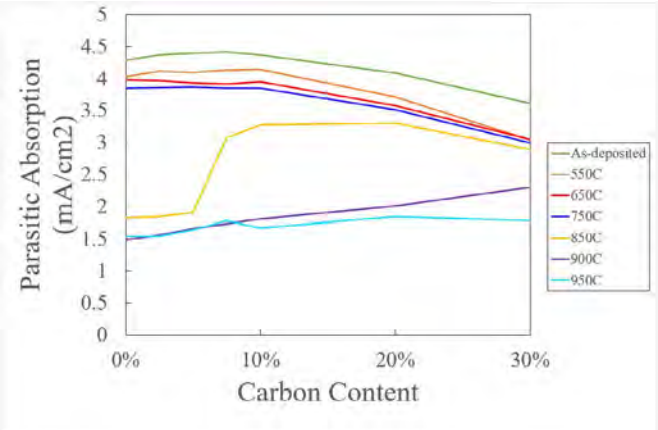

Figure 6.60.3: Parasitic absorption versus carbon content at different annealing temperatures.

Highlights

- SiC_x films with different C content have been fabricated by co-sputtering.
- The effects of the C content and post-annealing temperature were studied.

Future Work

- Study the composition, optical, structural and electrical properties of the highly doped SiC_x.
- Fabricate silicon solar cells with doped SiC_x passivated contacts.

References

GREEN, M. A., DUNLOP, E. D., LEVI, D. H., HOHL-EBINGER, J., YOSHITA, M. & HO-BAILLIE, A. W. Y. 2020. Solar cell efficiency tables (Version 55). *Progress in Photovoltaics*, 28, 3-15.

HAASE, F., HOLLEMANN, C., SCHAFER, S., MERKLE, A., RIENACKER, M., KRUGENER, J., BRENDEL, R. & PEIBST, R. 2018. Laser contact openings for local poly-Si-metal contacts enabling 26.1%-efficient POLO-IBC solar cells. *Solar Energy Materials and Solar Cells*, 186, 184-193.

NOGAY, G., STUCKELBERGER, J., WYSS, P., RUCAVADO, E., ALLEBE, C., KOIDA, T., MORALES-MASIS, M., DESPEISSE, M., HAUG, F. J., LOPER, P. & BALLIF, C. 2017. Interplay of annealing temperature and doping in hole selective rear contacts based on silicon-rich silicon-carbide thin films. *Solar Energy Materials and Solar Cells*, 173, 18-24.

POMASKA, M., KÖHLER, M., PROCEL MOYA, P., ZAMCHIY, A., SINGH, A., KIM, D. Y., ISABELLA, O., ZEMAN, M., LI, S., QIU, K., EBERST, A., SMIRNOV, V., FINGER, F., RAU, U. & DING, K. 2020. Transparent silicon carbide/tunnel SiO2 passivation for c-Si solar cell front side: Enabling Jsc > 42 mA/cm2 and iVoc of 742 mV. *Progress in Photovoltaics: Research and Applications*, 1– 7. https://doi.org/10.1002/pip.3244.

XU, Z., TAO, K., JIANG, S., JIA, R., LI, W., ZHOU, Y., JIN, Z. & LIU, X. 2020. Application of polycrystalline silicon carbide thin films as the passivating contacts for silicon solar cells. *Solar Energy Materials and Solar Cells*, 206, 110329.

6.61 ALL-SCREEN-PRINTED NANOPARTICLE CONTACTS

Lead Partner

UNSW

UNSW Team

Dr Malcolm Abbott

Industry Partner

Bert Thin Films, USA: Dr Thad Druffel, Dr Ruvini Dharmadasa

Funding Support

ARENA, UNSW, BTF

Aim

This project aims to develop next generation crystalline silicon contacting technology to enable higher efficiency and lower cost solar cells. Specifically, the program aims to develop novel screen-printable pastes containing nanoparticles that will be combined with laser processing to form layers of doped silicon-carbide contacted via a thick film copper conductor. The project aims to develop these processes and integrate them with working solar cells in collaboration with a US company Bert Thin Films (BTF).

Progress

The second year of the project has not seen significant progress towards developing the new contacting technology. The positive developments have been the successful implementation at the BTF site of a commercial firing profile on the inhouse oven (a goal identified as important from 2019) and the scaling up of the printing process to M2. Large-area laser doped selective emitter solar cells (Figure 6.61.1) were successfully fabricated at the BTF site using industry cell precursors. The development of the laser doped silicon-carbide contact regions has only been completed in the initial stages. Chemicals were sourced and the lab infrastructure and methods have been established to store and apply the nanoparticles onto polished silicon test wafers. Figure 6.61.2 demonstrates the application of a water-based silicon-carbide nanoparticle solution to a polished wafer using a spinner. Before spinning (Figure 6.61.2(a)) the solution spreads unevenly on the surface, after spinning (Figure 6.61.2(b)) a uniform coating is achieved. Spin settings were optimised to achieve layer continuity, the best spin setting was found to be 3000 rpm for 40 seconds (Figure 6.61.2(c)) which gave a uniform film (when viewed under microscope). This is only an early starting point and much more work is required to better characterise the films and their impact on laser doping results.

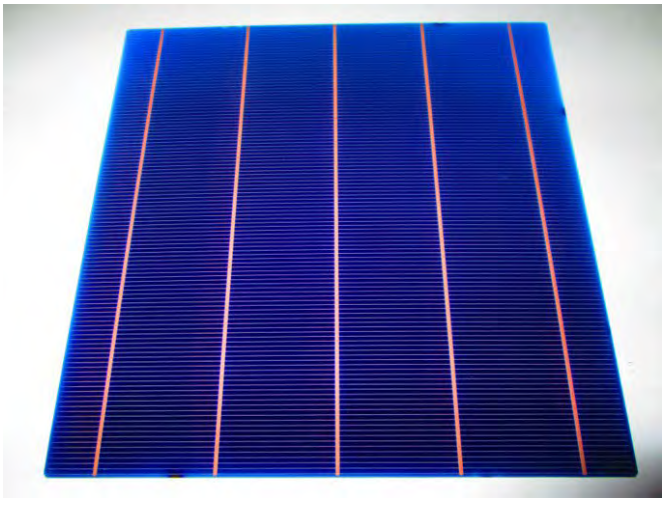

Figure 6.61.1: Optical image of M2-sized solar cell printed with copper metal paste.

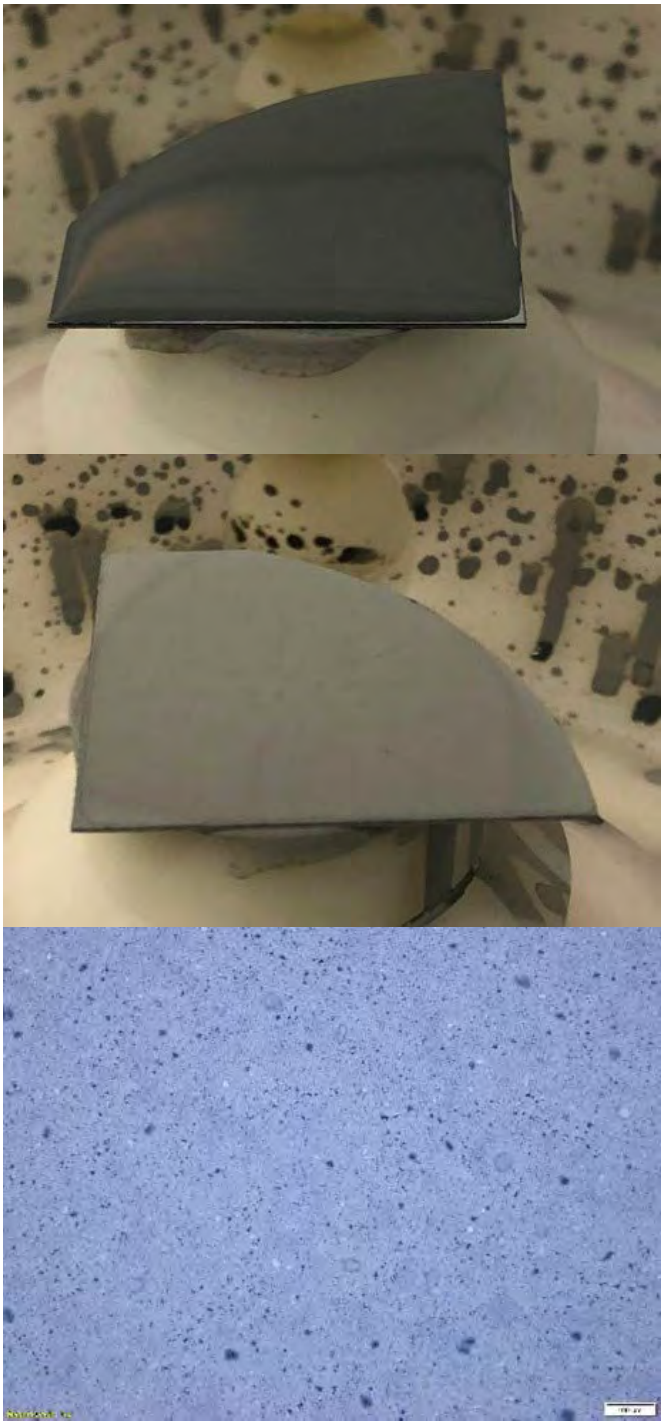

Figure 6.61.2: Image of silicon-carbide nanoparticles applied to a polished wafer surface from water-based solution, (a) deposited on wafer prior to spinning, (b) post-spinning, (c) microscope image of sample surface using optimal spin settings of 3000 rpm for 40 seconds.

Highlights

- Screen-print copper process scaled up to M2 wafers.
- Silicon-carbide nanoparticle solution sourced and laboratory infrastructure to store and process it installed. Process to apply particles to polished silicon surface established.

Future Work

Future work will focus on the further development of the silicon-carbide laser doping process. Variations in laser settings and their impact on layer formation need to be studied. Similarly, to improve the contact between copper paste and laser doped regions it is necessary to run some further experiments with variations in doping strength and depth of the laser doped regions.

6.62 DEVELOPMENT OF QUANTUM DOTS SOLAR INKS FOR ECONOMICAL MASSIVE-SCALE PRODUCTION OF THIN-FILM PHOTOVOLTAIC CELLS

Lead Partner

UNSW

UNSW Team

Dr Shujuan Huang, Prof. Gavin Conibeer, Dr Robert Patterson, Dr Lin Yuan

UNSW Students

Mr Zhi Li Teh, Mr Yijun Gao

Academic Partner

AMOLF

AMOLF Team

Prof. Albert Polman, Mr Stefan Tabernig

Aims

This project aims to develop economical high-throughput quantum dot (QD) "solar ink" technology for high efficiency thin-film solar cells. This technology will be enabled by two innovations, liquid-phase surface chemistry modification to improve QD deposition and advanced optical optimisation to further improve efficiencies through light trapping at strategically chosen wavelengths.

Progress

In this project, we have developed innovative surface chemistry to improve QD "ink" deposition. A champion cell with an efficiency of 11.9% was achieved in 2019 (ACAP Annual Report 2019). Continuing effort on surface passivation has led to a new champion device with an efficiency of 12.1% in 2020 (Figure 6.62.1) (Long et al. 2021). This has been achieved by eliminating the under-charged Pb atoms and dangling bond of S sites, simultaneously building robust PbI_2 and K shells on PbS QDs during the ligand exchange process by KI_3 additives. As a result, the surface trap states of the QDs have been significantly reduced and the thermal stability has been enhanced.

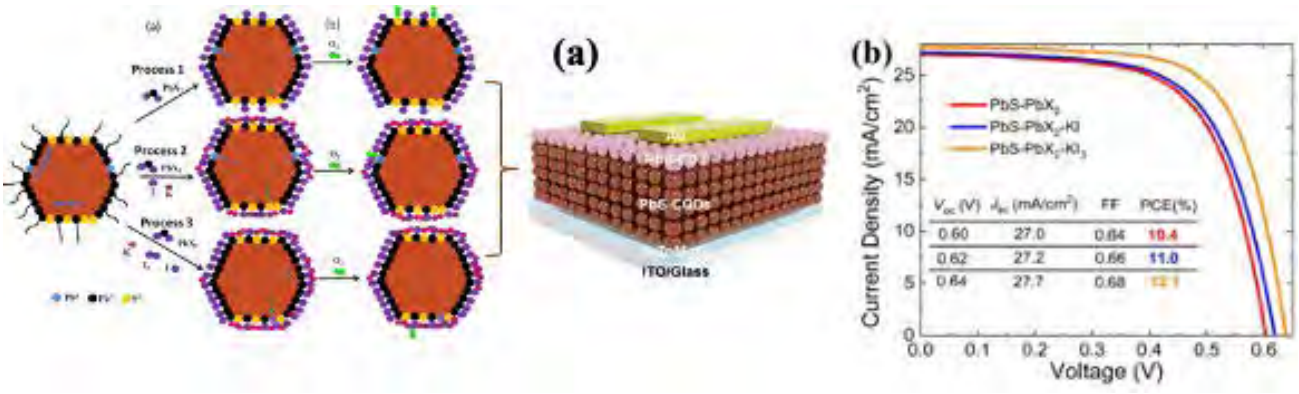

Figure 6.62.1: (a) Schematics of KI3 passivation mechanism and QD cell structure. (b) J-V curves of the champion devices fabricated by the three processes shown in (a).

The research focus in 2020 was on the light trapping and optical management aspect, the patterning process of the ZnO electron transport layer has been optimised. Initially, substrate conformal imprint lithography layer (SCIL) was used to fabricate a SiO_2 mask. This SiO_2 mask was used for patterning the ZnO layer using reactive ion etching (RIE). However, the slow etching rate and strong ion-bombardment have degraded the ZnO electronic property. To address this issue, a simple and direct patterning process has been developed, successfully producing a uniformly patterned ZnO layer on an ITO (Figure 6.62.2a) using a PDMS stamp.

The PbS QD solar cells were fabricated by spin coating the QD ink on the patterned ZnO layer. As shown in Figure 6.62.2(b), the QDs have filled up the holes of the ZnO patterned layer and formed a counter-patterned QD layer as the solar absorbing layer. Compared with the QD cell fabricated on a planar ZnO layer, the EQE spectrum of the patterned cell is flatter between 400 and 700 nm wavelength (Figure 6.62.2(c)) due to reduced interference. The patterned cell also shows higher response at around 800 nm and longer wavelength >1000 nm, which is attributed to the light trapping effect of the patterned structure (ACAP Annual Report 2019). As a result, the J_{SC} has been enhanced from 23.96 to 24.72 $mA.cm^{-2}$, consistent with the J_{SC} obtained by current-voltage (IV) measurement (Tabernig et al. 2020). However, the losses in fill-factor (FF) and open-circuit voltage (V_{oc}) lead to a final efficiency that is comparable to the planar reference device. The results suggest that fabricating a cell with a thinner active layer might be more beneficial to the device performance, as the influence of the patterned ZnO layer is expected to be stronger.

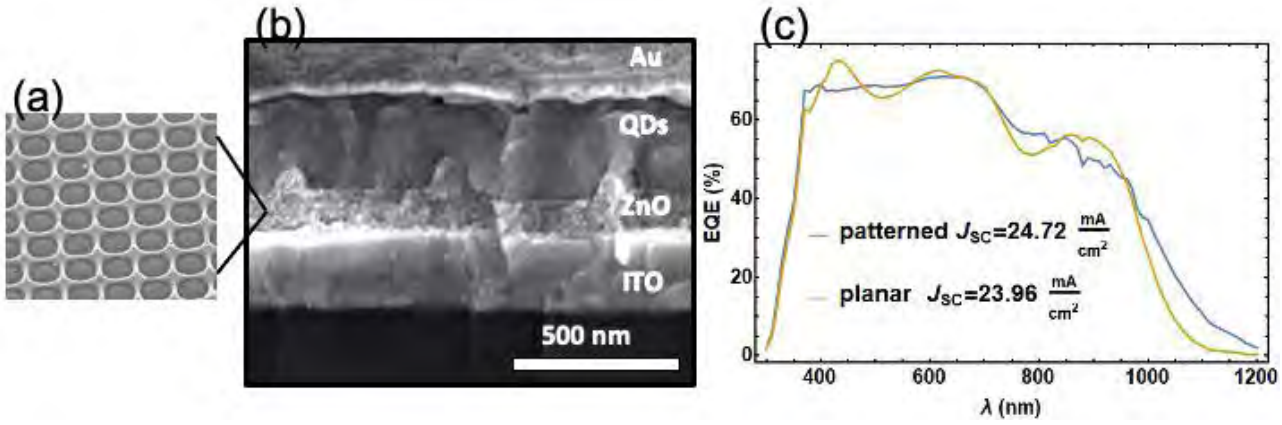

Figure 6.62.2: (a) SEM image of a patterned ZnO layer. (b) Cross-sectional SEM image of a PbS QD solar cell fabricated on the patterned ZnO, showing the QDs have filled up the ZnO pockets completely. (c) EQE-spectrum of patterned and planar QD solar cells. The spectrum of the patterned cell is much flatter and shows an improved response above 1000 nm wavelength as well as towards the left of the first exciton peak at ~800 nm.

Highlights

- Liquid-phase ligand exchange of PbS QDs has been developed, providing stable QD solar ink for the fabrication of an absorbing layer.
- Based on the QD ink deposition, an average efficiency of 11.8% has been achieved. The champion cell reached an efficiency of 12.1%. The work has been published with high impact journal Advanced Science.
- A novel nanophotonic structure for light trapping of the QD solar cell has been designed and optimised by employing optical as well as electronic simulation methods.
- The nanophotonic structure has been integrated with PbS QD solar cells, demonstrating improved current owing to the light trapping effect.

Future Work

This project has demonstrated that PbS QDs have great potential for low-cost and high efficiency solar cells. Incorporating a nanophotonic light trapping structure can further enhance the efficiency and reduce material usage.

To further improve the device performance, future work should:

- further optimise a nanophotonic structure based on optical simulation of a PbS QD device structure
- reduce QD absorber thickness to increase Voc and FF without sacrificing device performance
- apply the nanophotonic light trapping strategy developed in this project to other thin-film solar cells.

References

1. HU, L., LEI, Q., GUAN, X., PATTERSON, R., YUAN, J.Y., et al. 2021. Optimizing Surface Chemistry of PbS Colloidal Quantum Dot for Highly Efficient and Stable Solar Cells via Chemical Binding. *Advanced Science* 8, 2003138.
2. TABERNIG, S., TEH Z.-L., CORDARA, A., PATERSON, R., CONIBEER, G., et al. 2020. Carrier collection in optically resonant nanostructures for quantum dot solar cells. The 30th International Photovoltaic Science and Engineering Conference (PVSEC-30) & Global Photovoltaic Conference 2020 (GPVC 2020), Jeju, Korea, 8–13 November 2020..

6.63 ENGINEERING INTERFACES FOR HIGH PERFORMANCE SILICON TANDEM CELL STRUCTURES

Lead Partner

CSIRO, Energy, Newcastle

CSIRO Team

Dr Gregory Wilson, Dr Timothy Jones, Dr Terry Yang, Dr Chris Fell, Dr Benjamin Duck, Dr Jacob Wang (left CSIRO)

Academic Partner

UNSW: A/Prof. Anita Ho-Baillie

Funding Support

ACAP

Aim

This project has revised objectives to fabricate and assess four- and two-terminal configurations of perovskite/silicon tandem devices using evaporated processes and inorganic materials and down select preferred top-cell architecture and processes for next stage of work program.

Progress

In the latter stages of this project, it was evident the project team would not be able to screen and assess preferred passivation compounds. The status of required equipment and facilities (ALD, evaporator systems) although under commissioning were not fully operable for the purposes of meeting project objectives as proposed. Compounding this was the unsuccessful bid for competitive funds from ARENA to support the progress of this all-evaporated device configuration, limiting availability of technical resources and operational funds.

Despite this being an interesting, and suitable area of research, review of current research progress in the international community and the technology status of materials used in the top-cell configuration, including electron transport materials (ETMs) and hole transport materials (HTMs) identified preferred layer materials and configurations that would, preferably, lead to enhanced stability via an inorganic materials pathway rather than surface passivation as originally proposed. These outcomes were captured and published as two review articles, in *Advanced Energy Materials* and *Advanced Functional Materials*, with both articles receiving recognition with artwork selected for publication in the respective published issues of the journals.

The following is a summary and concluding report on the project progress, demonstrating proof-of-concept for the baseline device configurations (spin-cast perovskite materials) in both a four-terminal and two-terminal design. The results show promise for the down-selected top-cell configuration, supported by the four-terminal results, and promising options for further optimisation of the layered structures in the two-terminal configuration. Two-terminal cell

performance indicated later thickness optimisation and the silicon-perovskite interface requiring a more focused study on the interface transparent conductor.

Next steps in an expanded project scope would include development of a preferred methodology for the TCO (ALD), optimised layer thickness (via ALD, evaporated methods) and incorporation of the atmospheric chemical vapour deposition (ACVD) under development by CSIRO to demonstrate an all-evaporated tandem cell using industry-relevant equipment and process steps.

Fabrication of four-terminal tandem device

The upper performance limit of our proposed two-terminal device structure can be approximated using a four-terminal stack where each junction is independently connected to the external performance monitoring circuit. This configuration allows both junctions to achieve maximum power conversion efficiencies without being influenced by the performance characteristics of the companion junction.

Top-cell fabrication

The top perovskite solar cell was fabricated on patterned 30 x 30 x 1.0 mm^2, 7-15 Ohm/□ substrates from (Kintec, Hong Kong). Firstly 20 nm of NiO as the hole transport layer was deposited via RF magnetron sputtering in a NANO-MASTER NTE-3000 dual thermal evaporator/sputtering system (base pressure <1.5 × 10^{-5} Torr, working pressure <2.5 × 10^{-3} Torr with injection of 20 sccm of Ar, the 2" NiO target (Rearth Technology) was set at 150 W which produced a deposition rate of 0.5 Å/s). The NiO was then annealed on a hotplate at 400˚C for 10 minutes (relative humidity ~20%). The perovskite solution $Cs_{0.17}FA_{0.83}PbBr_{0.1}I_{0.9}$ was prepared by mixing separate solutions of $FAPbI_3$, $CsPbI_3$ and $Cs_{0.17}FA_{0.83}PbBr_3$. The $FAPbI_3$ solution was prepared by dissolving PbI2 (1.3M) with FAI (1.2M) in anhydrous DMF:DMSO (4:1 by volume). The $CsPbI_3$ solution was prepared by dissolving PbI_2 (1.3M) and CsI (1.2M) in anhydrous DMSO. The $Cs_{0.17}FA_{0.83}PbBr_3$ was prepared by dissolving $PbBr_2$ (1.3M), CsBr (0.2M) and FABr (1.2M) in anhydrous DMSO. The three separate solutions were stirred for >2 hours, following which $FAPbI_3$ and $CsPbI_3$ were mixed in a volume ratio of 5:1 to form $Cs_{0.17}FA_{0.83}PbI_3$. Then, the $Cs_{0.17}FA_{0.83}PbI_3$ was mixed with $Cs_{0.17}FA_{0.83}PbBr_3$ at a ratio of 9:1 to obtain the desired $Cs_{0.17}FA_{0.83}PbBr_{0.1}I_{0.9}$ perovskite solution composition. Spin-coating was run with a two-step program (step 1: 2000 rpm with 200 rpm/s acceleration for 10 seconds; followed by step two: 4000 rpm with 1000 rpm/s for 20 seconds). 400 uL of chlorobenzene was dropped onto the sample 3 seconds before the end of the two-step spin-coating program. The device was then annealed at 100˚C for 30 minutes in an N_2 atmosphere. Next 1.0 nm of LiF (99.98%, Sigma-Aldrich) was deposited via thermal evaporation in an Angstrom thermal evaporator system (base pressure <2.0 × 10^{-6} Torr, working pressure <2.0 × 10^{-6} Torr, deposition rate 0.1 Å/s) followed by 20.0 nm of C60 (99.5%, Lumtec) electron transport layer (ETL) in the same evaporator (base pressure <2.0 × 10^{-6} Torr, working pressure <2.0 × 10^{-6} Torr, deposition rate 0.2-0.8 Å/s (start to end)). An ABC nm wavelength laser at 0.1 mW (ABC laser systems) was then used to ablate the perovskite to create laser openings for the contact to the conductive FTO layer underneath. Finally, 160 nm of Ag was deposited with the Angstrom thermal evaporator system (base pressure <2.0 × 10^{-6} Torr, working pressure <2.0 × 10^{-6} Torr, deposition rate 0.2-2.0 Å/s (start to end)). Six cells, each with an aperture area of 0.156 cm^2 are fabricated per 30 x 30 x 1.0 mm^2 FTO substrate (Figure 6.63.1).

Bottom-cell .preparation

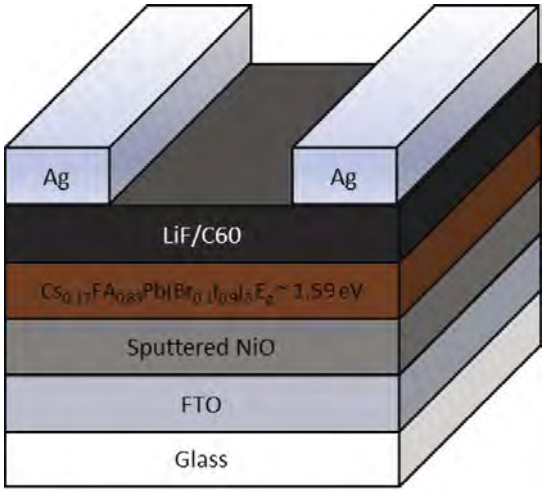

Figure 6.63.1: Schematic of the top perovskite solar cell device.

The standard PERC (passivated emitter and rear cell) silicon bottom cells were procured from SIRF UNSW. The precursor silicon cells were obtained from an unnamed Tier 1 Chinese solar cell manufacturer. In summary, the cells were fabricated on 175 µm thick p-type Cz M2 wafers (156.75 mm × 156.75 mm in size) with a resistivity of 0.5 to 3 Ωcm. The wafers were textured in KOH-based solution to produce ~2 µm pyramids. The front emitter was formed by $POCl_3$ diffusion (130 Ω/□ sheet resistance) followed by the formation of a selective emitter using a 532 nm pulsed DR laser tool to melt through and incorporate dopants from the phosphosilicate glass. A dielectric stack was deposited on the rear and a 70–85 nm hydrogenated silicon nitride (SiN_x:H) on the front to both act as an anti-reflection coating and provide surface passivation in the form of a hydrogen source. A 532 nm pulsed DR laser tool was then used to create openings in the rear dielectric stack. Aluminium was screen-printed on the rear-side, with silver front fingers and five busbars screen-printed on the front aligned to the selective emitter. Cells were fired in a belt furnace at a peak temperature of 810–830˚C for the front contacts and to create local rear doping. An advanced hydrogenation process was then carried out after firing using a laser hydrogenation system.

Results and discussion

The results for the four-terminal tandem equivalent are shown in Figure 6.63.2 and summarised in Table 6.63.1. Here the perovskite sub-cell has been measured as fabricated with an aperture area of 0.156 cm^2. The silicon sub-cell has been measured with a dummy perovskite device placed on top consisting of the perovskite layers deposited onto an ITO substrate. A shadow mask with an aperture of ~1 cm^2 has been used to define the active area of the silicon sub-cell.

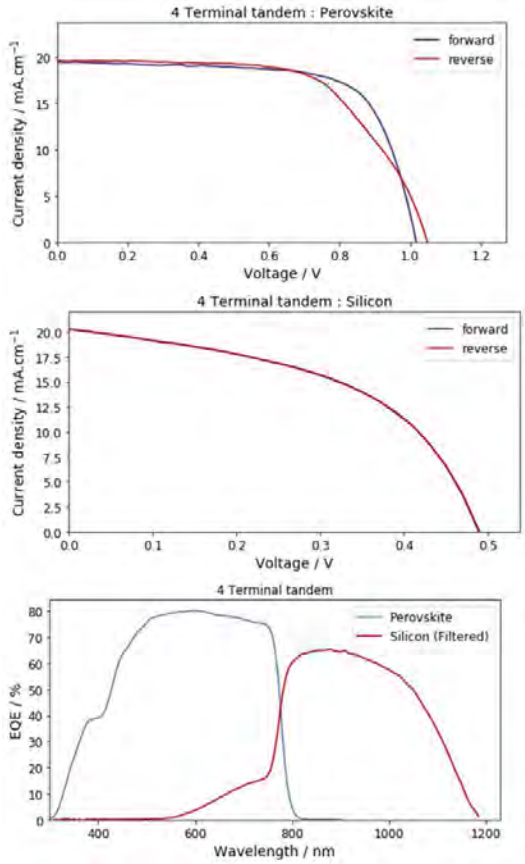

Figure 6.63.2: Characterisation results for four-terminal tandem equivalent.

Table 6.63.1: Four-terminal device characteristics summary.

	Silicon	Perovskite	
Quantity		Reverse	Forward
J_{sc} / mAcm^{-1}	20.25	19.46	19.50
V_{oc} / V	0.49	1.02	1.05
Efficiency / %	4.90	13.95	12.92

The filtered silicon device shows a significant reduction in performance above what is expected due to masking of a much larger device area ~9 cm^2 (which is effectively measured in the dark). This reduction artificially impacts the overall potential of the tandem device limiting its maximum efficiency to ~18% with the current structure, however when appropriate steps are made to limit the active area of the silicon substrate (e.g. isolation or simply cutting the substrate down to size) this value is expected to improve significantly with V_{OC} approaching that of typical PERC cells >650 mV. The I-V results show that the generated current densities for both devices are well matched indicating the chosen perovskite formulation is suitable for a two-terminal device.

Fabrication of two-terminal tandem device

Initial fabrication of a working two-terminal tandem device has been successfully completed (Figure 6.63.3a).

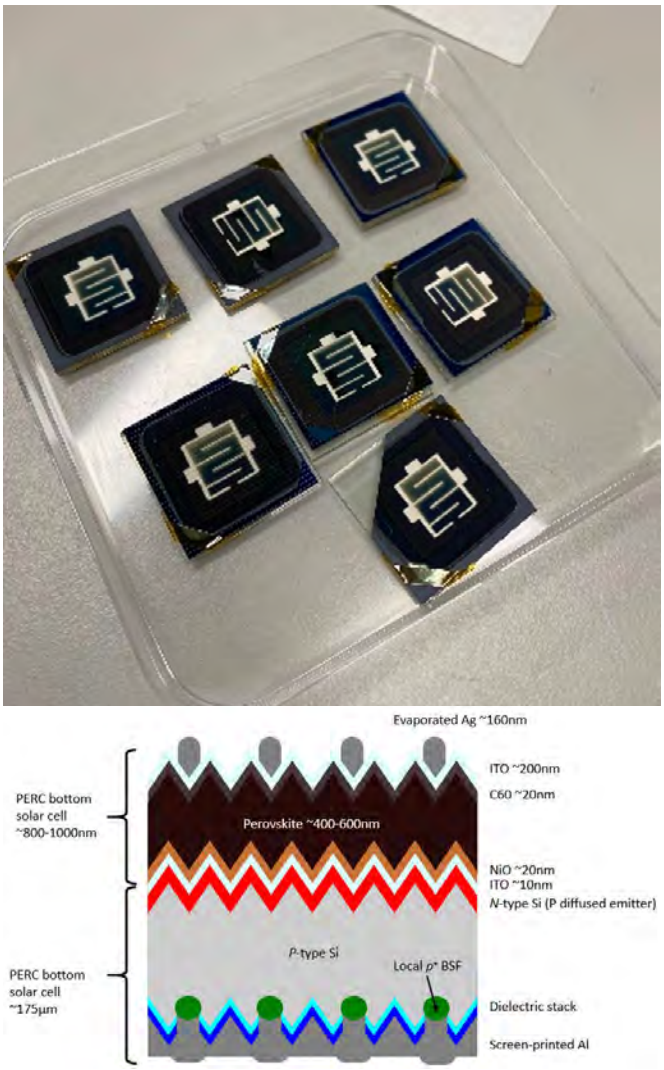

Figure 6.63.3: (a) Initial simple two-terminal perovskite/PERC silicon device fabricated. (b) Structure of the basic two-terminal device stack.

The fabrication of the initial Perov-PERC tandem solar cell device as shown in Figure 6.63.3(b), was achieved by using mostly vacuum-based deposition techniques standard to perovskite solar cell fabrication in conjunction with an industrially sourced PERC solar cell from a Tier 1 Chinese photovoltaic manufacturer. The method for the PERC solar cell as detailed above was adjusted by removing the front dielectric layer via HF solution to obtain a bare *N*-type Si (P diffused front emitter), as shown in red in Figure 6.63.3(b). The full M2-sized (156.75 mm × 156.75 mm) PERC precursors were then cut into 30 x 30 mm substrates with a 1080 nm laser (Universal Laser Systems).

Two-terminal cell fabrication

Firstly, 17 nm of ITO as the recombination junction was deposited on the PERC precursor via RF magnetron sputtering in a Nanomaster NTE-3000 dual thermal evaporator/sputtering system (base pressure of 2.5×10^{-5} Torr, working pressure of 3.0×10^{-3} Torr with injection of 20 sccm of Ar, the 2" ITO target (Rearth Technology) was set at 150 W which produced a deposition rate of 0.5 Å/s). Then 34 nm (equivalent to 20 nm on the textured pyramids) of NiO as the hole transport layer was deposited via RF magnetron sputtering in the NTE-3000 (base pressure of 1.2×10^{-6} Torr, working pressure $<2.5 \times 10^{-3}$ Torr with injection of 20 sccm of Ar, the 2" NiO target (Rearth Technology) was set at 150 W which produced a deposition rate of 0.4 Å/s). The NiO was then annealed on a hotplate at 400˚C for 10 minutes (relative humidity ~20%). The perovskite layer was formed with a hybrid two-step technique starting with the thermal evaporation of a powder mixture PbI_2 + CsBr (Greatcell Solar Materials) at a molar ratio of 4:1. The powders of PbI_2 and CsBr were ground up with a pestle and mortar for 20 minutes in an N_2 atmosphere. The PbI_2 + CsBr powder mixture was then evaporated in the NTE-3000 with a film thickness of 400 nm (equivalent to 235 nm on the textured pyramids) (base pressure of 2.0×10^{-6} Torr, working pressure $<2.0 \times 10^{-3}$ Torr, deposition rate up to 3.0 Å s^{-1}). Subsequently, a mixture of formamidinium bromide (FABr) and iodide (FAI) (in 1 to 2 molar ratio, 0.5 M in ethanol, Greatcell Solar Materials) was spin-coated onto this template layer. This step was performed using a dynamic solution dispensing at a spin speed of 4000 rpm during 30 seconds in an N_2 atmosphere. The layers were then annealed at 100°C for 25 minutes in air (RH ~20%) to crystallise the perovskite absorber. The C60 ETL was evaporated in the NTE-3000 with a film thickness of 34 nm (equivalent to 20 nm on the textured pyramids) (base pressure of 2.2×10^{-6} Torr, working pressure $<2.2 \times 10^{-3}$ Torr, deposition rate up to 0.3 Å s^{-1}). Then another ITO layer was deposited via sputtering in the NTE-3000 with a film thickness of 200 nm (equivalent to 118 nm on the textured pyramids) (base pressure of 2.5×10^{-5} Torr, working pressure of 2.5×10^{-3} Torr with injection of 20 sccm of Ar, the 2" ITO target (Rearth Technology) was set at 150 W which produced a deposition rate of 0.3 Å s^{-1}). The bulk resistivity of the ITO films were ~1.5×10^{-3} Ωcm. Finally, a serpentine grid design (aperture area: 11.00 x 12.50 mm) was used for the 272 nm (equivalent to 160 nm on the textured pyramids) Ag evaporation in the NTE-3000. A shadow mask with an aperture area of ~1 cm^2 was used on the device to define the active area for all measurements.

Results and discussion

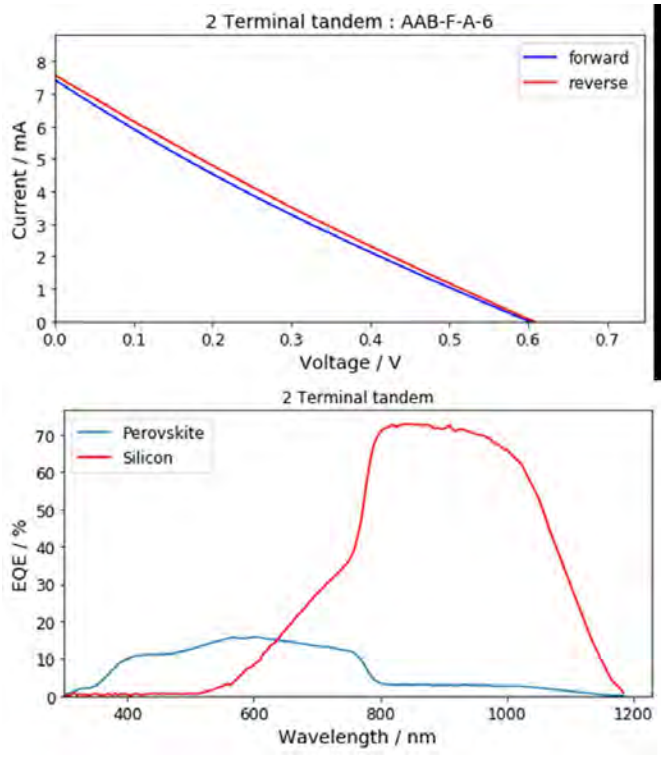

Figure 6.63.4: Characterisation results for two-terminal tandem.

Table 6.63.2: Two-terminal device characteristics summary.

	Two-Terminal	
Quantity	Reverse	Forward
J_{sc} / mAcm^{-1}	7.58	7.44
V_{oc} / V	0.61	0.60
Efficiency / %	1.05	0.99

Device I-V and EQE characterisation measurements are shown in Figure 6.63.4 and summarised in Table 6.63.2. The device requires significant further optimisation as evident in its I-V curve which shows results characteristic of a device with a large amount of shunting of one or both junctions. The open circuit voltage (V_{OC}) indicates that the device performance is currently dominated by the Si junction. Results for the spectral responsivity of the device confirm the functionality of both junctions and the response at longer wavelengths (above 800 nm) exhibited by the perovskite junction demonstrates that this junction is shunted. The shunting of this junction explains the poor I-V performance for the entire device but is expected to be improved with improved deposition methods made available using the new ALD capability. Shunting is likely derived from the difficulties associated with depositing the perovskite as conformal layers onto the pyramidal surface structure of the silicon substrate. If even deposition is not achieved across these peaks then these areas will have thinner material coverage leading to poorer electrical properties. In a worst case these areas may have very little or no perovskite deposited leading directly to a shunting of the junction.

Highlights

- Atomic layer deposition (ALD) capability, commissioned – ready for next stage.
- Initial two-terminal tandem device fabrication has been successful with perovskite deposited on supplied Si substrates.

Future Work

- Proposal for additional small grant funding, ARENA proposal for scale-up to larger area (subject to funding availability).
- Incorporate ALD capabilities for the optimisation of transparent perovskite devices and fabrication of the two-terminal tandem.
- Optimisation of the device stack using optical and electrical modelling to identify the most promising configurations and ALD fabrication capabilities to verify their potential.

Publications

LIN, L., JONES, T. W., YANG, T. C.-J., DUFFY, N. W., LI, J., ZHAO, L., CHI, B., WANG, X. & WILSON, G. J. Inorganic Electron Transport Materials in Perovskite Solar Cells. *Advanced Functional Materials*, 2008300. https://doi.org/10.1002/adfm.202008300
Highlight: selected as Frontispiece of Journal Issue (in press) in Hot Topic Solar Cells.

PHAM, H. D., YANG, T. C.-J., JAIN, S. M., WILSON, G. J. & SONAR, P. 2020. Development of Dopant-Free Organic Hole Transporting Materials for Perovskite Solar Cells. *Advanced Energy Materials*, 10, 1903326. https://doi.org/10.1002/aenm.201903326.
Highlight: selected as Cover of Special Issue (vol 10, issue 13) "Advances in Perovskite Optoelectronics"

6.64 DEVELOPMENT OF UPSCALING TECHNOLOGY FOR MONOLITHIC PEROVSKITE/SI TANDEM PHOTOVOLTAICS

Lead Partner

ANU

ANU Team

Dr Heping Shen (lead), Prof. Kylie Catchpole

Academic Partner

IMEC, Belgium: Dr Tom Aernouts , Dr Manoj Jaysankar, Dr Weiming Qiu

Funding Support

ARENA, ACAP, ANU, IMEC

Project Background

Monolithic perovskite/Si tandem solar cells have resulted in efficiencies as high as ~29.5%, much higher than the record efficiency for the conventional single-junction c-Si solar cell. Nevertheless, the high efficiencies of perovskite/Si tandem devices to date have been restricted to approximately 1 cm^2, which is far away from the 6-inch plus size usually used for Si solar cells and the m^2 scale required for modules. To realise the commercialisation of perovskite/Si tandem technology, scaling up the perovskite technology and maintaining high efficiency over large areas are thereby crucial.

Aim

This project targets the development of upscaling technologies for high efficiency monolithic perovskite/Si tandems by building on the demonstrated expertise of IMEC, Belgium (perovskite upscaling technology) and ANU (monolithic perovskite/Si tandem). This will be achieved through systematic work on the following aspects: simulations to achieve optimised layout of a tandem device; development of appropriate techniques for the front and back contact designs in the tandem device; development of fabrication processes for making high efficiency large-scale perovskite solar cells; and integration into high efficiency perovskite/Si mini-modules.

Progress:

- Developed vacuum deposition process for hole transport layer that is compatible for fabricating large-area perovskite solar cells and resulted in high efficiency (>21%) for single-junction perovskite solar cells, comparable to those based on Spiro-OMeTAD.
- Systematic optoelectronic simulations have been performed on established high efficiency monolithic perovskite/Si solar cells to provide a clear route to minimise losses in the device thus improving the tandem efficiency.
- Optical simulations on established high efficiency perovskite/Si tandem solar cells led to tandem current densities of ≈20

mAcm^{-2} with front-side texture. The simulation pointed out two effective approaches to reducing the optical losses in the tandem solar cells, including incorporating low absorptive hole transport material like NiO_x and developing an ultrathin hole transport layer (such as 15 nm PTAA).

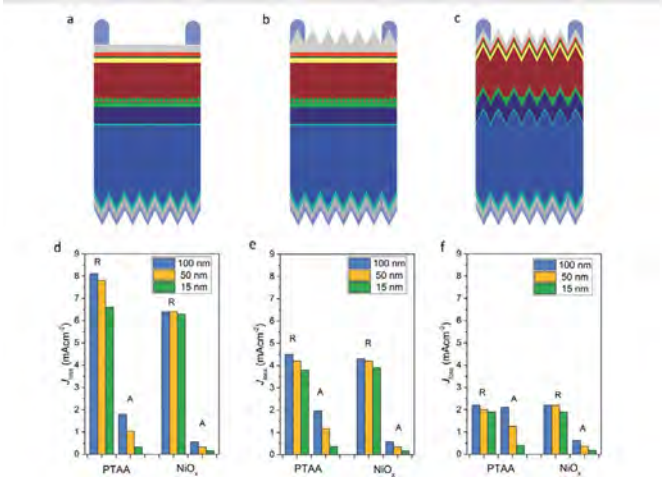

Figure 6.64.1: Schematic of the interlayer-free tandem based on a poly-Si/SiO_x passivating cell and an n-i-p PSC with (a) fully flat front side (blue) (b) attaching textured foil at the front (yellow) and (c) textured Si front side (green), (d)–(f) simulated reflectance of the tandem and absorption losses in HTM (PTAA or NiO_x) by varying their thicknesses in the three structures, respectively.

- Electrical modelling on the Si sub-cell predicts an absolute efficiency increase by 1% through joint improvements to the bulk lifetime, which exceeds 4 ms, and improving the surface passivation quality to saturation current densities below 10 fAcm^{-2}. Polycrystalline-Si/SiO_x passivating contacts are proposed as a promising alternative to partial-area rear contacts, with the potential for further simplifying cell fabrication and improving device performance.
- Optoelectronic simulations point out a great potential to achieve an over 30% perovskite/Si tandem within the short term. If a normal bandgap perovskite (1.6 eV) is used, an efficiency of 18.8% can be achieved for a perovskite solar cell and can lead to a tandem efficiency of 30.8% by being coupled with the proposed poly-Si/SiO_x passivated cell with an efficiency of 12% under filtered light. Instead, if a high bandgap perovskite was used (taking 1.72 eV, for example), the perovskite solar cell efficiency has a potential to reach 20.1%, based on a V_{OC} of 1.31 V and fill factor of 0.78, which would translate to a tandem efficiency of 32.1%.

Highlights

- Developed vacuum deposition technology for a high-quality, large-area carrier transport layer.
- Optical simulation points out effective approaches to achieving tandem current density of over 20mAcm^{-2}.
- Electrical simulation on a Si solar cell indicates an absolute efficiency gain of ~1% as compared to our previous design.
- Optoelectronic simulation provides effective approaches to achieving a perovskite/Si tandem with efficiency of >30%.

Future Work

- Incorporate a high-quality hole transport layer deposited by vacuum method to a high efficiency large-area perovskite solar cell and the perovskite/Si tandem cell.
- Optimise the Si bulk and surface properties to improve the Si solar cell efficiency and apply it to the tandem, with the guidance from the optoelectronic simulation.
- The team will upgrade the current tandem technology on the 4 cm^2 device.

References

SHEN, H., WALTER, D., WU, Y., FONG, K. C., JACOBS, D. A., DUONG, T., PENG, J., WEBER, K., WHITE, T. P. & CATCHPOLE, K. R. 2020. Monolithic Perovskite/Si Tandem Solar Cells: Pathways to Over 30% Efficiency. *Advanced Energy Materials*, 10, 1902840.

SHEN, H. P., OMELCHENKO, S. T., JACOBS, D. A., YALAMANCHILI, S., WAN, Y. M., YAN, D., PHANG, P., DUONG, T., WU, Y. L., YIN, Y. T., SAMUNDSETT, C., PENG, J., WU, N. D., WHITE, T. P., ANDERSSON, G. G., LEWIS, N. S. & CATCHPOLE, K. R. 2018. In situ recombination junction between p-Si and TiO2 enables high-efficiency monolithic perovskite/Si tandem cells. *Science Advances,* 4, 12.

6.65 ADVANCED LUMINESCENCE CHARACTERISATION FOR DOPED POLY AND PASSIVATION FILMS IN SILICON PHOTOVOLTAICS

Lead Partner

ANU

ANU Team

Dr Hieu Nguyen (lead), Thien Truong, Mike Tebyetekerwa, Prof. Daniel Macdonald

Academic Partner

Fraunhofer ISE (Fh-ISE), Germany: Dr Martin Schubert

Funding Support

ARENA, ACAP, ANU, Fh-ISE

Aim

This project aims to combine complementary leading expertise at the Australian National University (ANU) and the Fraunhofer Institute for Solar Energy Systems (Fh-ISE), Germany, in the development of novel luminescence-based techniques for characterising silicon (Si) materials and solar cells. This will primarily be achieved through the investigation and application of luminescence of doped poly-silicon films and other passivation layers. The scientific findings will improve our understanding of the impacts and performances of various solar cell components, whereas the technique inventions will provide tools to characterise and optimise Si solar cells.

Progress

This project was commenced in November 2018. Between 2018 and 2019, the ANU team led by Dr Hieu Nguyen discovered that at low temperatures the doped polycrystalline silicon (poly-Si) films, employed in passivating contact solar cells, emitted a characteristic broad photoluminescence (PL) peak at energies lower than the crystalline Si (c-Si) bandgap. Based on such phenomenon, they demonstrated several applications to understand the behaviour of poly-Si/SiO_x passivating contacts in terms of carrier recombination and transport: (i) the films contain radiative defects whose energy levels continuously stretch from the band edges to deep levels inside the poly-Si bandgap; (ii) even though UV light generates carriers inside the poly-Si films, these carriers cannot contribute usefully to the solar cell current, since they are blocked by the ultra-thin oxide layer; (iii) it is possible to detect hydrogen introduced in the passivating contact stacks by analysing the PL emission from its partial amorphous phase. Notably, the team developed a luminescence-based method to quickly track hydrogen content inside the poly-Si films. The technique relies on various PL features from doped poly-Si films and their mixed-phase nature (amorphous and crystalline). The method and its various potential applications were then reported in a series of four journal papers (Nguyen et al. 2018; Truong et al. 2019a and b; Truong et al. 2020a).

In 2020, the team continued exploring luminescence properties of different poly-Si film technologies and their applications to the development of high quality passivation films. Particularly, they combined the luminescence-based method with various optical and microscopy techniques to unlock the structural and optoelectronic characteristics of ex-situ boron-doped poly-Si/SiO_x passivating contacts, formed from sputtered intrinsic amorphous silicon (a-Si) deposited at different pressures on top of SiO_x/c-Si substrates and subjected to a high-temperature boron diffusion step. They found that the deposition rate and density of the as-deposited a-Si films increased with reducing pressure. Low-temperature PL spectra captured from the as-deposited samples at different pressures did not show typical emissions from hydrogenated a-Si. Meanwhile, their Fourier-transform infrared absorption spectra all showed Si–H stretching modes, indicating that hydrogen had been initially incorporated into the chemical SiO_x layers and eventually hydrogenated the a-Si/SiOx interfaces during the sputtering process. After the high-temperature boron-diffusion step, all hydrogen-related peaks disappeared. The team also found that lower pressure films (1.5 and 2.5 mTorr) showed more-consistent improved performance after hydrogen treatments, compared to higher pressure films (4 and 5 mTorr). The resultant passivating contacts at 2.5 mTorr achieved a low single-side recombination current density J_0 of ~9 fAcm^{-2}, whereas their contact resistivity was still low at 15 mΩ cm^2. These results were published in a journal paper (Truong et al. 2020b).

Figure 6.65.1: Recombination current density J_0 of different poly-Si samples diffused at 890 (A), 860 (B) and 830 (C) ºC, with various a-Si deposition pressures, and before and after hydrogen treatments. The J_0 was measured using a quasi-steady state photoconductance (QSSPC) technique. Reference J_0 results from Yan et al. (Appl. Phys. Lett. 2018, 113, 061603) for in situ boron-doped samples with the poly-Si layer thicknesses of ~40 and ~70 nm, sputtered at 2.7 mTorr and annealed at 800, 850 and 900 ºC, are also given. The legends are the same for all figures.

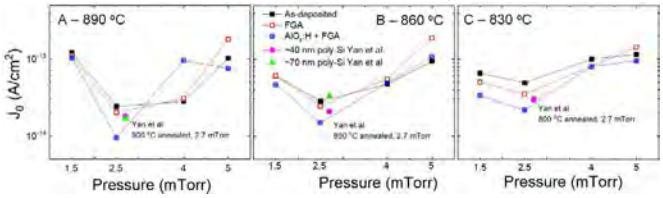

Highlights

- Poly-Si films contain both amorphous and crystalline phases, each of which yields distinct luminescence peaks at low temperatures (2018).
- The luminescence signatures can be used to understand the behaviour of poly-Si/SiO_x passivating contacts in terms of carrier recombination and transport (2019).
- Luminescence from the amorphous Si phase in poly-Si films can be used to track the hydrogen content inside the films (2019).
- High quality ex-situ boron-doped poly-Si/SiO_x passivating contacts based on sputtered amorphous silicon films (2020).
- Five journal papers (Nguyen et al. 2018; Truong et al. 2019a and b; Truong et al. 2020a and b) and seven conference oral presentations (Nguyen 2019a, b and c; Nguyen 2020a and b; Truong 2019; Truong 2020).
- Fh-ISE support (AU$60k in-kind plus equipment access) for Dr Nguyen's ACAP Fellowship Round 3.

Future Work

- This project is almost finished with all scientific milestones successfully achieved. The team will use the remaining time to consolidate their techniques and scientific findings to support high efficiency silicon solar cell teams at ANU and UNSW. A final report will be submitted to ACAP in early 2021 to officially close the project.

References

NGUYEN, H. T. 2019a. Luminescence from poly-Si films and its applications in Si PV. 46th IEEE Photovoltaic Specialists Conference, Chicago, June 2019.

NGUYEN, H. T. 2019b. Luminescence from poly-Si films and its applications in Si PV. 29th International Photovoltaic Science and Engineering Conference, Xi'an, November 2019.

NGUYEN, H. T. 2019c. Luminescence from poly-Si films and its applications in Si PV. 6th Asia-Pacific Solar Research Conference, Canberra, December 2019.

NGUYEN, H. T. 2020a. Spectral Luminescence: Science and Applications in Silicon Photovoltaics. 37th European Photovoltaic Solar Energy Conference and Exhibition, Lisbon, September 2020.

NGUYEN, H. T. 2020b. Recent Progress in the Characterization of PV Materials (silicon, perovskite, tandem, and 2D materials). 7th Asia-Pacific Solar Research Conference, Melbourne, December 2020.

NGUYEN, H. T., LIU, A. Y., YAN, D., GUTHREY, H., TRUONG, T. N., TEBYETEKERWA, M., LI, Z. Y., LI, Z. F., AL-JASSIM, M. M., CUEVAS, A. & MACDONALD, D. 2018. Sub-Bandgap Luminescence from Doped Polycrystalline and Amorphous Silicon Films and Its Application to Understanding Passivating-Contact Solar Cells. *Acs Applied Energy Materials*, 1, 6619-6625.

TRUONG, T. N. 2019. Effects of hydrogenation on poly-Si/SiOx passivating contacts for silicon solar cells. 6th Asia-Pacific Solar Research Conference, Canberra, December 2019.

TRUONG, T. N. 2020. Doped Poly-Si/SiOx Passivating Contacts: Hydrogenation and Its Mechanisms. 7th Asia-Pacific Solar Research Conference, Melbourne, December 2020.

TRUONG, T. N., YAN, D., SAMUNDSETT, C., BASNET, R., TEBYETEKERWA, M., LI, L., KRERNER, F., CUEVAS, A., MACDONALD, D. & NGUYEN, H. T. 2019a. Hydrogenation of Phosphorus-Doped Polycrystalline Silicon Films for Passivating Contact Solar Cells. *ACS Applied Materials & Interfaces*, 11, 5554-5560.

TRUONG, T. N., YAN, D., SAMUNDSETT, C., LIU, A. Y., HARVEY, S. P., YOUNG, M., DING, Z. T., TEBYETEKERWA, M., KREMER, F., AL-JASSIM, M., CUEVAS, A., MACDONALD, D. & NGUYEN, H. T. 2019b. Hydrogen-Assisted Defect-Engineering of Doped Poly-Si Films for Passivating Contact Solar Cells. *ACS Applied Energy Materials*, 2, 8783-8791.

TRUONG, T. N., YAN, D., CHEN, W. H., TEBYETEKERWA, M., YOUNG, M., AL-JASSIM, M., CUEVAS, A., MACDONALD, D. & NGUYEN, H. T. 2020a. Hydrogenation Mechanisms of Poly-Si/SiOx Passivating Contacts by Different Capping Layers. *Solar RRL*, 4, 1900476.

TRUONG, T. N., YAN, D., CHEN, W., WANG, W., GUTHREY, H., AL-JASSIM, M., CUEVAS, A., MACDONALD, D. & NGUYEN, H. T. 2020b. Deposition Pressure Dependent Structural and Optoelectronic Properties of Ex-situ Boron-Doped Poly-Si/SiOx Passivating Contacts Based on Sputtered Silicon. *Solar Energy Materials and Solar Cells*, 215, 110602.

6.67 SINGLET FISSION–ENHANCED SOLAR CELLS

Lead Partner

UoM

UoM Team

Dr David Jones, Dr Jegadesan Subbiah, Ms Ruoxuan Shi

Academic Partner

KIT (Germany): Dr Alexander Colsmann, Mr Lorenz Graf von Reventlow

Funding Support

AUSIAPV, UoM, KIT

Aims

- Scale up synthesis of high performance FHBC(TDPP)2 singlet fission (SF) material.
- Demonstrate EQE enhancement in solar cell devices (QD).
- Identify SF material energy matched to silicon.
- One patent or publication.

Progress

Progress has been delayed by COVID-19 and an extension has been approved. Multiple exciton generation (MEG) in organic semiconductors through singlet fission (SF) is a process that produces multiple charge carrier pairs from a single excitation. MEG is a viable route to overcome the Shockley-Queisser limit in single-junction solar cells, and hence to enhance their performance to generate third generation solar cells.
Therefore, any proof of principle of this concept has the potential to substantially change the field of solar energy harvesting. Yet, as of today, it remains challenging to harvest charge carrier pairs generated by MEG in working photovoltaic devices. Initial yields of additional carrier pairs may be reduced due to ultrafast intra-band relaxation processes that compete with MEG at early times. We have recently developed a new class of SF materials based on an acceptor-donor-acceptor (A-D-A) design to promote intra-molecular SF. We designed these materials to remove local order constraints normally required for molecular SF materials, like acenes, and have designed materials that are solution processible, promote SF in the solid state, and surprisingly show little order in spin-cast thin films. The key aim of this project is to understand this new material and its behaviour in devices, especially routes to charge extraction.

Definitive proof for enhanced efficiency due to SF is to record EQEs above 100%, which has rarely been achieved in the literature in real systems. It is possible to incorporate SF materials into devices either through direct electrical connection or through energy transfer. Direct electrical connection is predicted to give higher overall efficiencies.

We have chosen to investigate homojunction solar cells, where we use only the SF material, in the first instance in anticipation of inclusion through direct electrical contact with silicon to gain a better understanding of the SF material properties, and a direct measurement of the EQE from the SF material.

We have previously reported that the known material was synthesised on a large scale. Device and synthesis work expected to be completed in 2020 has not been possible due to COVID-19 impacts. We have examined enhanced device architectures for inclusion of SF materials and these will be examined in 2021.

Highlights

- Dr David Jones has been awarded a Distinguished Visiting Fellowship to undertake SF device research at KIT in 2021.
- Travel required for the project was unable to be taken in 2020.
- The Masters student who is synthesising new materials for evaluation in Germany was unable to travel back to Australia after returning to China for her New Year holiday to complete the synthesis.

Future Work

- Fundamental studies on FHBC$(TDPP)_2$ directed material design for silicon compatible materials.
- Optimise homojunction solar cells to demonstrate EQEs of greater than 100%.
- Assemble SF-enhanced solar cell devices.

References

MASOOMI-GODARZI, S., LIU, M., TACHIBANA, Y., MITCHELL, V. D., GOERIGK, L., GHIGGINO, K. P., SMITH, T. A. & JONES, D. J. 2019. Liquid Crystallinity as a Self-Assembly Motif for High-Efficiency, Solution-Processed, Solid-State Singlet Fission Materials. *Advanced Energy Materials*, 9(31), 1901069.

6.68 ORGANIC ELECTRON TRANSPORT LAYER TOWARDS UPSCALING OF HIGH-EFFICIENCY PEROVSKITE SOLAR CELLS

Lead Partner
CSIRO

CSIRO Team
Dr Dechan Angmo, Dr Doojin Vak, Dr Andrew Scully

Academic Partner
Chinese Academy of Sciences (CAS), Beijing: Prof. Jin-Hui Hou
University of Cambridge, UK: Dr Samuel Stranks

Funding Support
ARENA, CSIRO, University of Cambridge, Chinese Academy of Science

Project Aim

State-of-the-art organic non-fullerene molecules from the field of organic solar cells have great potential as electron transport layers (ETLs) in industrial roll-to-roll (R2R) manufacturing of perovskite solar cells (PSCs). Organic non-fullerene molecules demonstrate superior film-forming properties, compatibility with non-hazardous industry-relevant solvents, and strong interfacial adhesion with perovskites imparting higher device stability. Through this project, we aim to investigate organic non-fullerene materials further to find optimum electronic properties suitable for R2R printed perovskites to improve device power conversion efficiency (PCE) and stability.

Project Status Update

Deliverables (D), Milestones (M), and Conference (C)	Delivery	Current Status
D1: Manuscript on process transfer from spin-coating to R2R coating of the mixed cation of PSCs.	Y2Q2	Completed (Angmo 2020)
D2: Manuscript on R2R compatible fabrication of PSCs incorporating non-fullerene electron transport materials with an in-depth characterisation of films and interface quality comparing lab versus R2R fabrication method.	Y2Q4	Broken down into two manuscripts. D2.1 First one focusing on the characterisation of R2R processed perovskite films based on mixed cation composition is under progress (addresses M2). D2.2 Second one based on non-fullerene ETL will be completed at the end of the project. Lab-scale device study is completed. Non-fullerene ETL identified. R2R fabrication is underway.
M1: Demonstrate mixed cation perovskite enabling power conversion efficiency over 13% in devices fabricated under ambient conditions using spin-coating to benchmark subsequent upscaling experiments.	Y1Q4	Completed
M2: Stable variants of perovskites such as mixed cation processed with scalable printing/coating methods enabling efficiency within 20% of the benchmark spin-coated devices (M1) on the same device area (benchtop S2S and R2R methods).	Y2Q2	Completed
M3: In-depth characterisation of layers and interfaces of devices in M2, comparing film processing through spin-coating versus scalable fabrication methods.	Y2Q4	Experimental and characterisation completed. Manuscript in progress (D2.1).
C1: APSRC/ACAP conferences.	Dec 2020	Completed.
C2: Oral Presentation at MRS conference.	Nov 2021	Cancelled due to COVID19.

Progress

1. Process transfer from spin-coating to roll-to-roll fabrication of perovskite solar cells

1.1 Process optimisation under ambient environment: The laboratory-scale fabrication of high efficiency PSCs typically utilises an inert glovebox environment during the deposition of the functional layers. Maintaining an inert environment is neither technically nor commercially realistic in large-scale manufacturing. Thus, R2R fabrication requires the development of humidity-tolerant film fabrication processes. Humidity interferes with the perovskite film formation mechanism and impacts film uniformity and optoelectronic properties (Kamat 2020; Angmo 2018). Hence, Milestone 1 was initially formulated to assess perovskite materials and their deposition processes under an ambient humidity environment using spin-coating to set up a benchmark for subsequent upscaling activities under the same fabrication environment. Addressing this milestone, we delved into process optimisation of mixed cation perovskites for compatibility with an ambient processing environment with devices fabricated with spin-coating. We used the common anti-solvent method, which is the most used laboratory method (Figure 6.68.1(a)). The anti-solvent was optimised for ambient compatibility. We studied various anti-solvents in lab-scale spin-coated cells and found ethyl acetate is best for the mixed cation perovskite. We have achieved a PCE of 15.12%, which is the highest reported performance for PSCs processed under a non-inert environment with relative humidity over 30% (Figure 6.68.1(b)).

1.2 R2R compatible printing and coating processes: In addition to the inert glovebox environment, the laboratory-scale devices reported in the literature are typically fabricated using spin-coating. Spin-coating is not a scalable method. The film formation mechanism with spin-coating is vastly different from the film formation mechanism using industrial-scale printing/coating methods such as slot-die or micro-gravure. As such, results reported in the literature based on spin-coated devices often cannot be reproduced with R2R printing/coating methods. To transfer a process developed using spin-coating to scalable and R2R-compatible fabrication methods requires significant process engineering and development. For this reason, Milestone 2 was set up to assess and optimise the process transfer of perovskite film fabrication from spin-coating to R2R compatible printing/coating methods.

The spin-coated cells were fabricated using the anti-solvent method. We attempted to translate the anti-solvent method to R2R fabrication. We investigated various scalable deposition methods to apply anti-solvents in-line during R2R fabrication of the perovskites. Perovskite solution is best deposited with slot-die coating in an R2R manufacturing set-up, which is a scalable deposition method (Figure 6.68.2(c)). However, the in-line application of anti-solvent while the perovskite is being printed proved highly challenging. We attempted several methods, including dip-coating, double slot-die, and spray-coating using a range of nozzles. However, the anti-solvent process was not suitable to upscale through R2R coating as consistent film quality could not be achieved when combined with slot-die coating of perovskites. Hence, an alternative method based on the hot deposition of perovskite solution was employed. In this method, perovskite films can be deposited by slot-die coating perovskite solution on a hot substrate (>130°C) (Figure 6.68.1(c)). The perovskite precursor solution was engineered to result in smooth and uniform films. Such a method is easily applicable in R2R manufacturing (Figure 6.68.2(a), (c)). We compared the films' characteristics and photovoltaic performance of slot-die coated films and devices through the hot-deposition method against the spin-coated laboratory benchmark cells. The champion cell efficiencies are given in Figures 6.68.1(b) and (d). The device structure and energy level diagrams are shown in Figures 6.68.1(e) and (f). A PCE of 13.36% was achieved with hot-deposition using slot-die coating, which is only 11% lower than the spin-coated devices based on the anti-solvent method (15.12%). Thus, this result surpasses the target of Milestone 2, where we aimed to get PCE of perovskite printed with a scalable method within 20% range of PCE of laboratory spin-coated PSCs.

1.3 R2R fabrication (process transfer from glass-to-flexible)

Most laboratory cells are fabricated on glass substrates. R2R fabrication requires continuous flexible substrates. Perovskite deposition processes need to be robust to changes in substrate. The anti-solvent method employed lab-scale perovskite film fabrication induces nucleation-driven film fabrication. In this method, dense perovskite grains generally less than 500 nm in size are formed. In contrast, the hot-deposition with slot-die coating induces crystal-growth film formation, which leads to large clusters of grains that are typically >1 µm to millimetre size. We studied the process transferability of the nucleation-driven method (anti-solvent method) and the crystal-growth driven method (the hot-deposition method) from glass-to-flexible substrates. Doing so would enable us to identify the best R2R upscaling pathway for perovskite film formation. For the nucleation-driven method, we used the anti-solvent method with spin-coating on both glass and flexible substrate. Whereas, we had to use a benchtop slot-die coater for hot-deposition on a glass substrate and R2R processing for hot-deposition on a flexible substrate (R2R) for crystal-growth driven film formation (Figure 6.68.2(a), (c)).

We found the anti-solvent method is highly sensitive to the substrate. We observed PCE drops by 50% on a flexible substrate with all materials and processing being the same as glass-based devices, which gave a champion PCE of 15.12%. In contrast, the highest R2R-processed perovskite films using the hot-deposition process led to 11.2% champion efficiency, a drop of only 16% compared to the glass-based champion cell (13.32%) (Figure 6.68.2(b)). We expect significantly higher efficiency if the poorer conductivity of commercial ITO on flexible substrate compared to ITO on glass substrate can be addressed. Currently, the sheet resistance of ITO on a flexible substrate (50 ohms/sq) is an order of magnitude higher than ITO on glass (5 ohms/sq). As flexible substrates with higher conductivity become available, higher PCE of R2R-fabricated PSCs can be achieved. Nonetheless, the result of the R2R-processed devices is promising. We characterised the R2R-processed perovskite films' quality on a flexible substrate and compared them against glass-based films – both processed with the hot-deposition method. The hot-deposition method led to similar perovskite film quality irrespective of the substrate (glass or flexible). The R2R-processed perovskite film also demonstrated consistent quality across different experiments conducted on different days (varying ambient environment conditions) and throughout the length of coated films. This is evidenced in R2R devices having superior reproducibility than lab devices based on glass substrates (Figure 6.68.2(d)). Thus, the hot-deposition method is highly promising for upscaling of larger-area devices and for higher technical yield. It needs to be developed further to improve PCE.

2. Non-fullerene electron transport layer

2.1 Literature review

An extensive literature review was carried out compiling opto-electronic properties of all promising non-fullerene materials as COVID impacted partner materials, which was communicated through the ACAP COVID Impact Report. Several materials were identified as highly promising for mixed cation perovskite formulation based on energy level matching and carrier mobilities. A sample of some of the potential materials is shown in Figure 6.68.3(a). We have equally identified a plethora of promising organic materials that can be used as printable hole-transport material as well.

2.2 Preliminary tests

Primary tests were conducted on a material known as Y7 as ETL in p-i-n type PSCs based on mixed cation formulation. The photovoltaic performance was similar to cells containing a fullerene-based PCBM (Phenyl-C61-butyric acid methyl ester) layer. Critically, the open-circuit voltage (V_{OC}) of Y7-based cells was only marginally lower than cells with PCBM, which suggests Y7 is a strong alternative (Figure 6.68.3(b)). Devices with intermixed PCBM and Y7 result in higher Voc than PCBM-only devices. The intermixing strategy could be more effective in controlling the aggregation of PCBM in printed film. Unlike indacenodithiophene-based ETL layers that react with solution-processed buffer layers based on polyethylene amine (PEIE), Y7

did not show any noticeable incompatibility with PEIE. It must be noted that the replacement materials considered in this project are also more cost-effective than fullerene-based ones. Instead of a concentration of 15–20 mg/ml required of fullerene compounds, these organic non-fullerene materials require a low concentration of 2–3 mg/ml. In addition, the organic materials are also compatible with non-toxic and non-halogenated solvents, whereas fullerenes tend to form large aggregates in non-halogenated solvents, in which they have poor solubility.

Based on these preliminary results in lab-scale cells, we have progressed to screening and optimisation of the ETL alternatives to PCBM in R2R processing. Further in-depth characterisation in conjunction with the University of Cambridge including long-term stability will be carried out.

Highlights

- A master's engineering student, Remy Leroudier from the University of Marseilles, joined the project from 1 March 2020 to 30 June 2020.
- With limited or no access to laboratories during the COVID-19 lockdown in Victoria (April–July 2020 and September–November 2020), a literature survey of potential ETL materials was completed, and a manuscript on the lab-to-fab study of printed perovskite solar cells was completed (Angmo 2020).
- A second publication based on the characterisation of R2R-printed perovskite films based on stable mixed cation composition is under preparation.
- Research results were presented at the ACAP Conference 2020.
- The second internship position was advertised in November/December 2020. Research master's student Mostafa Othman from Monash University accepted the position. He will join the project from 11 January 11 2021 until 30 June 2021.

Future work

- Completion of manuscript on characterisation of roll-to-roll fabricated perovskite films.
- Optimisation of ETL replacement in R2R-processed PSCs and characterszation at University of Cambridge.

References

ANGMO, D., DELUCA, G., SCULLY, A. D., CHESMAN, A. S. R., SEEBER, A., ZUO, C., VAK, D., BACH, U. & GAO, M. 2021. A Lab-to-Fab Study toward Roll-to-Roll Fabrication of Reproducible Perovskite Solar Cells under Ambient Room Conditions. Cell Reports *Physical Science*, 2, 100293.

MANSER, J. S., SAIDAMINOV, M. I., CHRISTIANS, J. A., BAKR, O. M. & KAMAT, P. V. 2016. Making and Breaking of Lead Halide Perovskites. *Accounts of Chemical Research*, 49, 330-338.

ANGMO , D., PENG, X., SEEBER, A., ZUO, C., GAO, M., HOU, Q., YUAN, J., ZHANG, Q., CHENG, Y.B. AND& VAK, D., 2019. Controlling Homogenous Spherulitic Crystallization for High-Efficiency Planar Perovskite Solar Cells Fabricated under Ambient High-Humidity Conditions. *Small*, 15(49), p.1904422

Captions

Figure 6.68.1: (a) A schematic illustration of the anti-solvent method used for spin-coated devices. (b) J-V curve and MPP stabilisation trend of the champion spin-coated devices on glass substrates under ambient fabrication environment (25°C, 38% RH) measured under 1000 $W.m^{-2}$, AM1.5G. (c) A schematic illustration of the hot-deposition method with scalable slot-die coating. (d) J-V curve and MPP stabilisation trend of the champion hot-deposited device on glass substrates under ambient fabrication environment (25°C, 42% RH) measured under 1000 $W.m^{-2}$, AM1.5G. (e)–(f) Perovskite solar cell device structure used in this study and the corresponding energy level diagram, respectively.

Figure 6.68.2: (a) A schematic illustration of the hot-deposition method with slot-die coating in a roll-to-roll (R2R) fabrication. (b) J-V curve and MPP stabilisation trend of the champion hot-deposited R2R devices on flexible substrates under ambient fabrication environment (25°C, 45% RH) measured under 1000 $W.m^{-2}$, AM1.5G.(c) Photographs highlighting the scalability of the slot-die coating method. (d) Bar graph showing the statistics of photovoltaic parameters. All R2R devices were measured without pre-screening across 20 cm length (48 cells).

Figure 6.68.3: (a) Various non-fullerene organic molecules/polymers and their energy level alignment with perovskite formulation used in this study. All green ones are suitable candidates.

(b) Comparison of open-circuit voltage of solar cells with PCBM and non-fullerene Y7 electron transport layers. The chemical structure of PCBM and Y7 are shown on the right.

FELLOWSHIPS

ACAP's competitively selected Fellowships, are reported online at http://www.acap.net.au/annual-reports.

F1 TECHNO-ECONOMIC ANALYSIS OF PHOTOVOLTAIC CELL AND MODULE FABRICATION TECHNOLOGIES

Fellowship Holder
Dr Nathan L. Chang

Supervisor
Prof. Renate Egan

Funding Support
ACAP Fellowship

Aims

This Fellowship has two broad aims. The first is to focus on individual technologies that are being developed, and to apply techno-economic analysis with the expectation that insightful understanding will be obtained of the technology's particular strengths and weaknesses.

The second is to develop and improve the innovative cost analysis methodology so that it can analyse each successive technology with greater effectiveness.

This Fellowship has its primary focus on contributing to ACAP's PP4 Manufacturing Issues, and there is some overlap between this report and the PP4 report.

Progress

PV Cell and Module Technologies

Collaboration with the CZTS group at UNSW (Ao Wang, Kaiwen Sun). A cost analysis was completed of the copper-zinc-tin-sulfide (CZTS) technology, which is a potentially lower cost relative to the commercialised copper-indium-gallium-selenide (CIGS) solar cell. The CZTS thin-film technology, like many non-commercialised PV technologies, is expected to struggle to compete on pure cost ($/W) terms with the established PV technologies, in particular c-Si cells. For this reason, this work included market identification and analysis to consider the potential market niches where CZTS could have competitive advantages over other alternatives. This work considered (i) the traditional rooftop PV market segment, identifying the "lightweight roof" niche – roofs that are not strong enough to hold standard rigid glass-based PV, (ii) the internet of things (IOT) market niche, and the steel roof integrated PV (BIPV) market niche. It identified features of CZTS (deposited on glass, plastic and steel) that brought competitive advantage in these market segments, and areas that must be developed (in particular efficiency) in order to compete in these areas. This work was included in the meeting of ACAP milestones for 2020, and additional information and figures from this work are shown in the PP4.1 report, section A. This work has been recently published (Wang 2021).

Collaboration with CSIRO (Doojin Vak). Building on previous work (Chang 2018), where the cost of producing perovskite PV using roll-to-roll techniques was reported, this work focused on the related technology of organic photovoltaics (OPV). Analysis was completed on newly developed processes for OPV (i) an alternative low-cost ITO-free substrate, and (ii) two higher efficiency photo-active layers that are also expected to be more expensive (per module) than the standard OPV layers. This work was also included in meeting the ACAP milestones for 2020, and additional information and figures are shown in the PP4.1 report, section B.

Collaboration with the perovskite groups at UNSW and ANU (Jianghui Zheng, Yiliang Wu, Heping Shen, Anita Ho-Baillie). The work reported in last year's report analysing the cost of perovskite/silicon tandem (SPT) cells has been extended and published (Chang 2020a) and was presented as an oral presentation at the APSRC in December 2020. The extension included an analysis of SPTs from other institutes that used more expensive but higher efficiency heterojunction silicon bottom cells. Figure F1.1 shows how the sequences from UNSW (Seq A and Seq C), ANU (Seq B and Seq D), Colorado University and NREL (Seq E) and CSEM/EPFL (Seq F) compare with each other on levelized cost of electricity (LCOE) terms, based on the reported efficiency and estimated cost. This shows how improvements in efficiency and cost can be assessed in terms of improved LCOE.

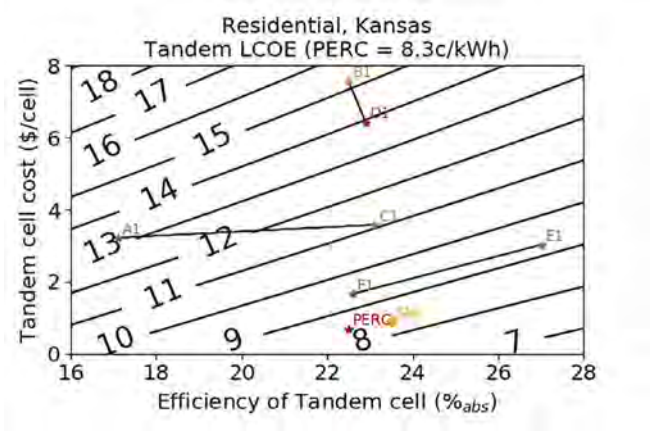

Figure F1.1 LCOE of each SPT sequence analysed based on reported efficiency and estimated manufacturing cell cost ($/cell).

Collaboration with the hydrogenation group at UNSW (Matthew Wright, Brett Hallam). The analysis of silicon heterojunction (SHJ) cell technology applied to lower cost p-type wafers that was described in previous years has been extended and published (Chang 2020b). Figure F1.2 shows some guidance to researchers regarding the relative cost of n-type wafers and the cost of the SHJ processing on the relative cost benefit of using p-type wafers.

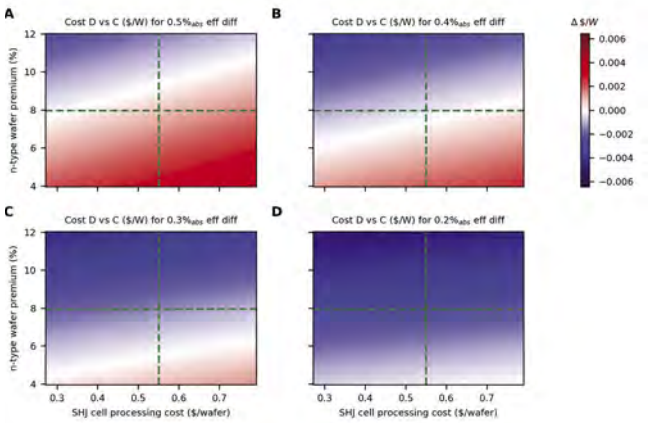

Figure F1.2 Relative cost of using p-type wafers (Seq D) compared to using n-type wafers (Seq C), where blue indicates an improved cost of the new process.

PV Module Recycling

Moving beyond PV manufacturing analysis, two bodies of work were completed in collaboration with UNSW researchers working on PV module recycling.

The first built on previous work at UNSW (Deng 2019), where analysis was completed to determine the allowable cost and efficiency trade-off of reusing recycled silicon as either metallurgical-grade silicon, solar-grade silicon or intact wafers. This work was included in meeting the ACAP 2020 milestones, and further information and figures are shown in the PP4.1 report, section C. This work has been published (Deng 2020).

The second was in collaboration with Pablo Dias (also UNSW), analysing the cost of a full sequence recycling process incorporating a toluene process to separate the PV module. This work was included in meeting the ACAP 2020 milestones, and further information and figures are shown in the PP4.2 report, section A. This work was also published this year (Dias 2020).

Wider application of techno-economic analysis

The work on PV-driven hydrogen generation (JonathonYates, UNSW SPREE and collaboration with Rahman Daiyan ,UNSW Chemical Engineering) reported last year has been published (Yates 2020)

The future cost model (collaboration with TNO, Netherlands, Bonna Newman) has been extended. It was presented as a poster presentation at the IEEE PVSC (Chang 2020c), and a paper is currently under review (Chang, review).

Highlights

- Continuing wide collaboration with different institutions in Australia and internationally.
- Techno-economic analysis of CZTS and OPV technologies.
- Techno-economic analysis of recycling technologies.
- Dissemination of work via publications and conferences.

Future Work

- Analysis of additional PV technologies and processes.
- Development of the methodology as required for new analyses.
- Continuing dissemination of the methods via collaboration and the creating of tools to enable effective collaboration.

References

CHANG, N. L., HO-BAILLIE, A. W. Y., VAK, D., GAO, M., GREEN, M. A. & EGAN, R. J. 2018. Manufacturing cost and market potential analysis of demonstrated roll-to-roll perovskite photovoltaic cell processes. *Solar Energy Materials and Solar Cells*, 174, 314-324. https://doi.org/10.1016/j.solmat.2017.08.038.

CHANG, N. L., ZHENG, J., WU, Y., SHEN, H., QI, F., CATCHPOLE, K., HO-BAILLIE, A. & EGAN, R. J. A bottom-up cost analysis of silicon–perovskite tandem photovoltaics. *Progress in Photovoltaics*, 1– 13. https://doi.org/10.1002/pip.3354.

CHANG, N. L., WRIGHT, M., EGAN, R. & HALLAM, B. 2020. The Technical and Economic Viability of Replacing n-type with p-type Wafers for Silicon Heterojunction Solar Cells. *Cell Reports Physical Science*, 1, 100069. https://doi.org/10.1016/j.xcrp.2020.100069.

Chang, N.L., Newman, B.K. & Egan, R.J. 2020c. 2020. Assessing the Competitiveness of Metallization Cell Schemes with a Future-Cost Uncertainty Model. 47th IEEE Photovoltaic Specialists Conference (PVSC) 2020 (pp. 1992-1995). IEEE.

Chang, N.L., Newman, B. & Egan, R. Under Review. Future Cost Projections for Photovoltaic Module Manufacturing Using a Bottom-up Cost and Uncertainty Model. Paper Under Review.

DENG, R., CHANG, N. L., OUYANG, Z. & CHONG, C. M. 2019. A techno-economic review of silicon photovoltaic module recycling. Renewable and Sustainable Energy Reviews, 109, 532-550. https://doi.org/10.1016/j.rser.2019.04.020.

DENG, R., CHANG, N., LUNARDI, M. M., DIAS, P., BILBAO, J., JI, J. & CHONG, C. M. Remanufacturing end-of-life silicon photovoltaics: Feasibility and viability analysis. *Progress in Photovoltaics: Research and Applications*. 1– 15. https://doi.org/10.1002/pip.3376

DIAS, P., SCHMIDT, L., MONTEIRO LUNARDI, M., CHANG, N. L., SPIER, G., CORKISH, R. & VEIT, H. 2021. Comprehensive recycling of silicon photovoltaic modules incorporating organic solvent delamination – technical, environmental and economic analyses. *Resources, Conservation and Recycling*, 165, 105241.

WANG, A., CHANG, N. L., SUN, K., XUE, C., EGAN, R. J., LI, J., YAN, C., HUANG, J., RONG, H., RAMSDEN, C. & HAO, X. 2021. Analysis of manufacturing cost and market niches for Cu2ZnSnS4 (CZTS) solar cells. *Sustainable Energy & Fuels*. https://doi.org/10.1039/D0SE01734E

YATES, J., DAIYAN, R., PATTERSON, R., EGAN, R., AMAL, R., HO-BAILLE, A. & CHANG, N. L. 2020. Techno-economic Analysis of Hydrogen Electrolysis from Off-Grid Stand-Alone Photovoltaics Incorporating Uncertainty Analysis. Cell Reports Physical Science, 1, 100209. https://doi.org/10.1016/j.xcrp.2020.100209

F2 DEVELOPMENT OF PRACTICAL HIGH EFFICIENCY PEROVSKITE/SILICON TANDEM MODULES

Lead Partner

ANU

ANU Team

Dr The Duong

UNSW Team

A/Prof. Anita Wing Yi Ho-Baillie

Academic Partners

Peking University: A/Prof. Huanping Zhou

Funding Support

ACAP

Aim

This project aims to develop complete and practical perovskite/silicon tandem modules in the mechanically stacked configuration with an efficiency of ≥25% for large-area devices (over 1 cm^2) and stability passing the damp heat test as described in the IEC-61646 standard.

Progress

1. Encapsulation method for perovskite solar cells and perovskite/silicon tandem solar cells

We developed an encapsulation method for perovskite solar cells and perovskite/silicon tandem solar cells. The solar cells were sandwiched between two glass substrates and a butyl rubber seal was applied on the edges of the glass substrates. The temperature and time were optimised at 90°C and 30 minutes, respectively, to obtain a uniform edge seal with no air bubble. As illustrated in Figure F2.1(a)–(b), we designed a jig to assist with the encapsulation process. A layer of thermal insulator was used to minimise the temperature effect on the devices and four screws were used to press the stack down during the heating and curing. The resulting encapsulated devices were shown in Figure F2.1(c)–(d) from both the perovskite side and silicon side. The encapsulated devices were stored inside a dry environment (glove box) for 1 week before testing.

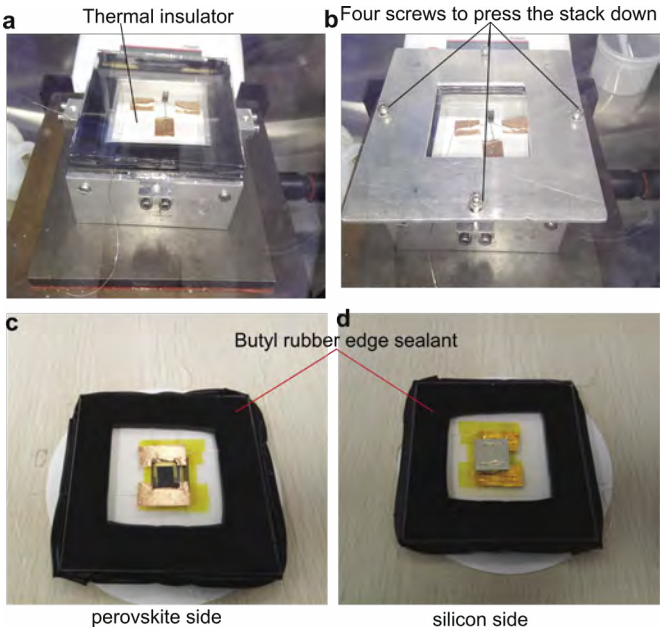

Figure F2.1: (a), (b) Custom-built jig to encapsulate the perovskite/silicon tandem solar cell. (c) Picture of the encapsulated perovskite/silicon tandem solar cell from the perovskite top cell side. (d) Picture of the encapsulated perovskite/silicon tandem solar cell from the silicon bottom cell.

We tested the encapsulated perovskite solar cells at 85% relative humidity (RH) / 85°C for over 1400 hours. This is slightly longer than the duration of 1000 hours as defined for the damp heat test in the IEC-61646 standard. As shown in Figure F2.2, the open circuit voltage (V_{OC}) and short circuit current (J_{SC}) of the device remained stable throughout the test, however the fill factor (FF) dropped notably to ~90% of the initial value. As a result, the efficiency of the device retained ~90% of the initial efficiency after over 1400 hours. The results indicate that the encapsulated device was stable during the damp heat test, surpassing the requirement from the IEC-61646 standard.

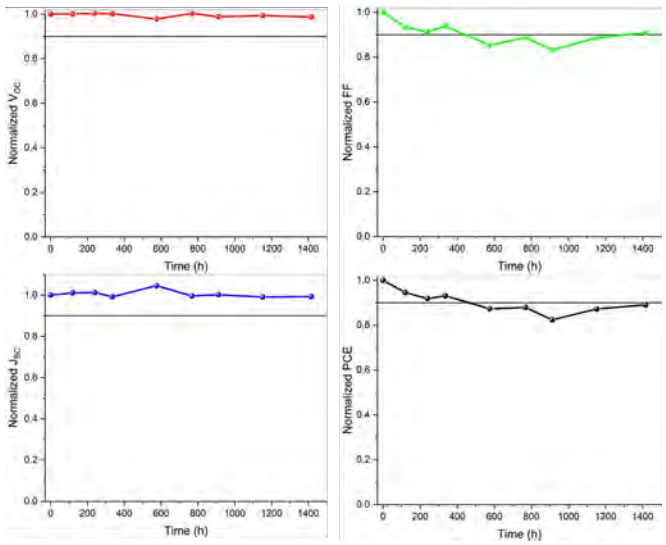

Figure F2.2: Normalised open circuit voltage (V_{OC}), short circuit current (J_{SC}), fill factor (FF) and efficiency of the device after over 1400 hours at 85% relative humidity (RH) and 85°C.

2. Enhancing the efficiency of the optimised bandgap 1.72 eV perovskite solar cells

We employed the method of passivating the perovskite surface with different aliphatic alkylammonium bulky cations such as n-butylammonium bromide to further enhance the efficiency of the perovskite top cell. We found that the 2D layer passivates the defects on the perovskite surface and significantly reduces the surface recombination. In addition, the electronic structure of the perovskite film was modified greatly with the passivation layer including the reduction in the work function (WF) and the downward movement of the valence band energy level (E_V) (Duong et al., 2020). This caused more band bending at the perovskite/hole transport layer interface and improved the extraction of holes inside the devices. As shown in Figure F2.3, the V_{OC} was significantly increased from ~1.23 V to ~1.27 V and FF was increased from ~0.72 to ~0.76. The J_{SC} remained almost unchanged upon passivation. As a result, the passivation method improved the efficiency from ~16.9% to ~17.9%. In addition, the hysteresis phenomenon was almost eliminated in the passivated devices.

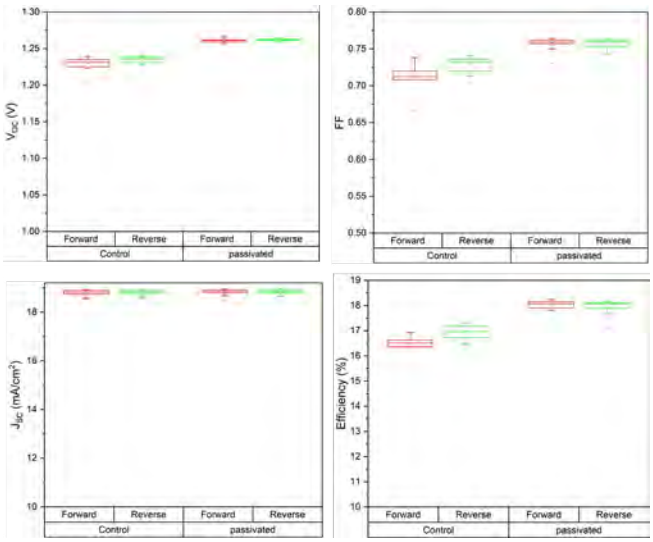

Figure F2.3: Open circuit voltage (V_{OC}), short circuit current (J_{SC}), fill factor (FF) and efficiency of the control perovskite cells and perovskite cells passivated with n-butylammonium bromide.

We carried out a light stability test of a passivated perovskite solar cell for 5 day/night cycles (12 hours under light and 12 hours in the dark for each cycle) in an inert environment. The perovskite cell was held at fixed voltages close to its maximum power points and J-V curves were recorded every hour. We found that in each cycle, after 12 hours operating under light, the efficiency of the perovskite cell retained around 95% of the initial efficiency recorded at the start of the cycle. The efficiency then recovered to about 98–99% of the efficiency recorded at the start of the previous cycle after the cell stayed in the dark for 12 hours. After 5 day/night cycles, the efficiency of the perovskite cell retained 96% of the original efficiency. The result indicates that the passivated perovskite cell was relatively stable under operating conditions, however more stability improvement is needed to achieve a fully robust device.

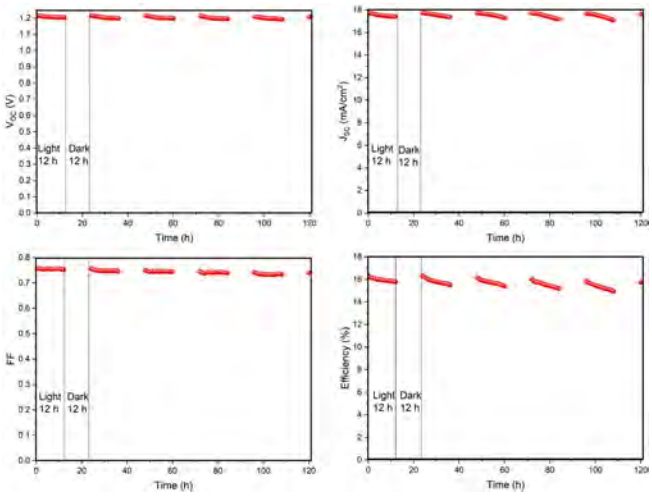

Figure F2.4: Stability of a passivated perovskite solar cell after 5 day/night cycles.

3. Improving the large-area semitransparent perovskite solar cells and perovskite/silicon tandem solar cells

We fabricated large-area perovskite cells with an active layer of 1.32 cm^2 using a vacuum flash method. The perovskite layer was first spin coated on the substrates (2.15 x 2.15 cm). After spin coating, the films were transferred into a vacuum chamber and the air inside the chamber was quickly evacuated to get the chamber pressure down to 150 mTorr for 10 seconds. The perovskite films were then annealed at 100°C on a hot plate for 30 minutes. The vacuum flash method enabled us to fabricate efficient and reproducible large area semitransparent perovskite solar cells. We utilised the passivation strategy using alkyl ammonium organic cation n-BABr to fabricate semitransparent perovskite solar cells to be used in perovskite/silicon tandem solar cells. In semitransparent cells, the opaque Au contact was replaced by a semitransparent contact stack MoO_3/indium zinc oxide (IZO). The use of the passivation layer reduced the surface roughness of the perovskite layer from ~16 nm to ~11 nm. This enabled us to further reduce the thickness of the Spiro-MeOTAD to ~120 nm and the thickness of the MoO_3 layer was reduced to ~5 nm without impacting the reproducibility of the semitransparent perovskite cells. The transparency of the semitransparent device was boosted to over 84% in the long wavelength following the changes. We combined the large area semitransparent perovskite solar cells with 1 cm^2 passivated emitter rear locally-diffused (PERL) solar cell in a mechanically stacked four-terminal tandem configuration (Yan et al., 2019). As shown in Figure F2.5, the efficiency of the champion perovskite solar cell is 18.19% and the efficiency from the reverse scan is the same as the efficiency from the forward scan. The PERL silicon cell efficiency is 22.51% while performing alone and the efficiency is 10.22% while operating under the semitransparent perovskite solar cell. Overall, the four-terminal perovskite tandem efficiency is 28.41%, outperforming the record efficiency of the single-junction silicon cell.

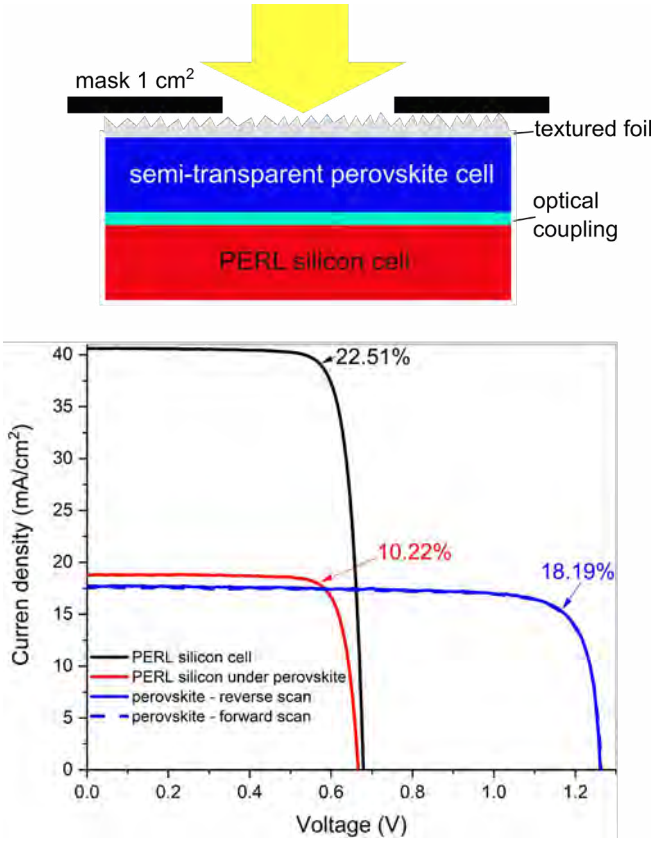

Figure F2.5: Schematic showing the four-terminal perovskite/silicon tandem in the four-terminal tandem configuration and J-V curves of a perovskite-PERL silicon tandem.

Highlights

- Developed an encapsulation method for perovskite solar cells and perovskite/silicon tandem solar cells using a butyl rubber edge seal.
- The encapsulated perovskite solar cells retained ~90% of the initial efficiency after over 1400 hours at 85% RH / 85°C, passing the damp heat test as defined in the IEC-61646 standard.
- Established a passivation method for perovskite solar cells using alkylammonium organic cation to enhance the cell performance.
- Achieved an efficiency of 28.41% for a 1 cm^2 area-matched four-terminal mechanically stacked perovskite/silicon tandem. A manuscript reporting this result is under preparation.

Summary

In this project, we have developed high efficiency large-area (over 1 cm^2) perovskite/silicon tandem solar cells with a champion efficiency of 28.41%, greatly exceeding the record efficiency of single-junction silicon solar cells. We also developed an encapsulation method for the devices using a butyl rubber edge seal, enabling the devices to pass the damp heat test as defined in the IEC-61646 standard. Overall, this project has successfully demonstrated the great potential of perovskite/silicon tandem solar cells and paves the way for the commercialisation of the technology.

References

DUONG, T., PHAM, H., KHO, T. C., PHANG, P., FONG, K. C., YAN, D., YIN, Y., PENG, J., MAHMUD, M. A., GHARIBZADEH, S., NEJAND, B. A., HOSSAIN, I. M., KHAN, M. R., MOZAFFARI, N., WU, Y., SHEN, H., ZHENG, J., MAI, H., LIANG, W., SAMUNDSETT, C., STOCKS, M., MCINTOSH, K., ANDERSSON, G. G., LEMMER, U., RICHARDS, B. S., PAETZOLD, U. W., HO-BALLIE, A., LIU, Y., MACDONALD, D., BLAKERS, A., WONG-LEUNG, J., WHITE, T., WEBER, K. & CATCHPOLE, K. 2020. High Efficiency Perovskite-Silicon Tandem Solar Cells: Effect of Surface Coating versus Bulk Incorporation of 2D Perovskite. 10, 1903553.

YAN, D., PHANG, S. P., WAN, Y., SAMUNDSETT, C., MACDONALD, D. & CUEVAS, A. 2019. High efficiency n-type silicon solar cells with passivating contacts based on PECVD silicon films doped by phosphorus diffusion. *Solar Energy Materials and Solar Cells*, 193, 80-84.

F3 TRANSPARENT DOPED LPCVD POLYSILICON

Fellowship Holder

Dr Kean Chern Fong

Supervisor

Prof. Andrew Blakers

Funding Support

ACAP

Aim

Polysilicon-oxide (poly-ox) passivated contact is among the most promising solutions towards high efficiency Si solar cells due to its excellent electrical performance and compatibility with standard industrial fabrication processes. Most prominently, the potential of this technology has been demonstrated when applied on the rear surfaces of both IBC and front contact single-junction Si cells reaching above 25% efficiencies.

This technology is typically applied on non–light facing surfaces due to its high parasitic optical absorption combined with poor contact resistivity. Parasitic absorption is undesirable for obvious reasons, while having a high contact resistance makes it incompatible with metal fingers which typically cover only 2–5% of the surface.

This project has the ambitious aim to develop an optically optimised poly-ox contact for application on a light facing surface, by having a combination of: (1) high optical transparency; (2) anti-reflection properties; (3) compatibility with transparent conductive oxides; (4) ultra-low contact resistivity; and (5) retains the promising electrical qualities of poly-ox contacts.

The rewards for successfully developing an optically optimised poly-ox technology are tremendous as it would provide passivation, contact, and anti-reflection in an extremely elegant process sequence.

Such a technology is particularly relevant within the near future for application in bifacial solar cells, and as a carrier transport layer between Si and a top cell in Si-tandem devices.

Progress

The processes developed within this project currently exhibit among the best combinations of surface passivation as measured via saturation current density (J_0) 1 fAcm^{-2}, and contact resistivity (ρc) < 1 mΩcm^2. As plotted in Figure F3.1, very low ρc values of less than 1 mΩcm^2 were measured for a wide range of processing conditions owing to the excellent control of the in situ low-pressure oxidation deposited between 700 and 800°C in a pure oxygen ambient under low pressures of 600 mTorr. TEM imaging of this stack shows a well intact Si-oxide layer with a thickness of approximately 1.2 nm

Optical characterisation, and derivation of the n-k values of the polysilicon film has been carried out, identifying the optical losses of its application to light facing surfaces. Subsequent analysis indicates a full-area polysilicon contact is highly applicable for Si-tandem devices due to its transparency to long wavelength light. However, local polysilicon via patterning, is likely the best suited strategy for non-tandem single-junction Si cell application such as on bifacial silicon solar cells.

The focus of the project is now to demonstrate a working device applying polysilicon passivated contacts on a light facing surface. Specifically, processes are being developed for formation of a recombination junction for perovskite/silicon tandem devices, as well as masking and patterning methods for formation of local polysilicon in application for bifacial solar cells.

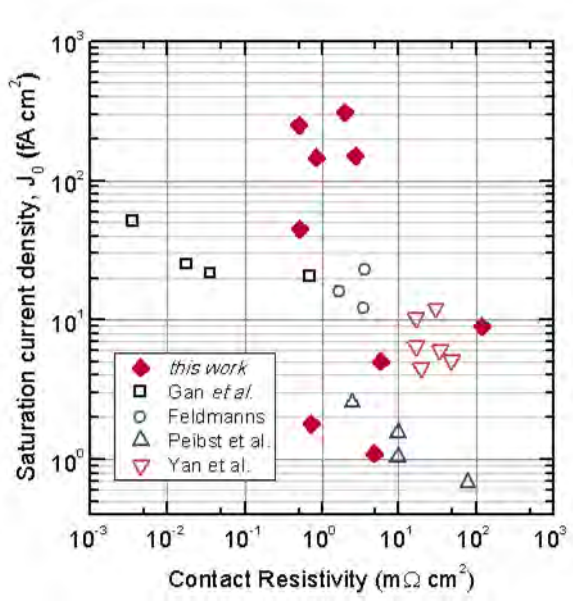

Figure F3.1: Comparison of J_0 and ρ_c to other recent work on poly-ox contacts in literature.

Additionally, this project is developing polysilicon-metal oxide recombination junctions for application to monolithic Si-tandem applications. Several key publications have demonstrated recombination junction contacts using heterojunction technology, achieving excellent carrier transport efficiency. A similar implementation using polysilicon contacts represents further progression of this implementation as polysilicon contacts have significant advantages in terms of optical properties, electrical characteristics and their long-term stability over amorphous Si-based hetero contacts.

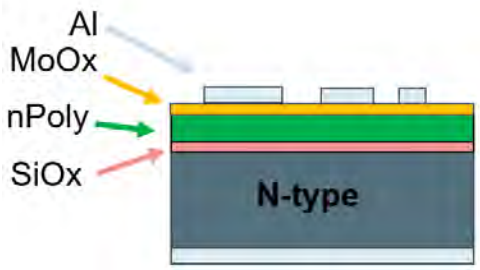

Figure F3.2: Illustration of Cox and Strack test structure for characterisation of the ohmic contact in the SiO_2/n-Poly/MoO_x/Al recombination junction layer.

Experiments conducted at ANU have successfully demonstrated implementation of a recombination junction contact consisting of a chemically grown tunnel-oxide (~1.5 nm), ex-situ phosphorus-doped PECVD polysilicon, and thermally evaporated molybdenum-oxide layer. Lifetime measurements via photoconductance-decay indicates excellent surface passivation <10 fAcm^{-2} is achieved for the electron selective contact (n-contact) and maintained after thermal evaporation of MoO_x. Importantly, electrical measurement via evaporated Pd/Al contact dots shows a highly efficient recombination junction contact as the resistance through the Cox and Strack metal dot structures shows linear ohmic response and measured to be near-identical between samples with direct metal contact to the polysilicon and samples with contact through the polysilicon-MoO_x recombination junction, with an estimate contact resistivity of less than 10 mΩcm^2. This represents significant advancement in polysilicon-based recombination junction contact technology, and is intended for application in ongoing projects in the field of hybrid IBC solar cells and perovskite/silicon tandem devices.

The near-future plan is to examine compatibility, and electrical performance of high work-function electron and hole metal oxides when deposited on heavily doped polysilicon layers with the goal of developing stable, and efficient recombination junction layers.

A. Masking layer over doped polysilicon

A key requirement to the development of local heavily doped polysilicon is the ability to mask, pattern, and etch the polysilicon layers without adversely affecting the electrical (passivation and contact) properties.

This project has previously demonstrated that it is possible to perform selective texturing through the doped polysilicon layers. This specifically refers to the ability to mask selected regions with a silicon-nitride mask, while submerging the wafer in a KOH texturing solution, which has been shown to successfully etch through the polysilicon layers and subsequently to form high quality random-pyramid texturing.

This report now presents in Table F3.1, the electrical characterisation of the surface passivation of the masked regions, as examined using a set of four viable masking recipes which withstand the chemical etching. In this data, the chemically resistant SiN_x layer is kept constant, while the oxide growth on the polysilicon layer is varied. The minority-carrier excess carrier density is measured after removal of the mask, and a 400°C forming-gas annealing. Chemically grown oxide is shown to be the only viable process for retaining good surface passivation in n-type polysilicon samples, while p-type polysilicon is significantly more robust in masking as various processes of chemically grown and thermally grown oxide have shown to be effective in further reducing the surface passivation from the original state of the p-type polysilicon structure.

The results indicate the most promising combination to likely be the use of chemical oxide/SiN_x masking layer, which retains 13.5 and 15.5 $fAcm^{-2}$ passivation for n-type and p-type polysilicon respectively after deposition, removal of the mask, and forming gas annealing. This is consistent with passivated contact quality necessary for over 720 mV implied-V_{OC} solar cells.

Table F3.1: Passivation quality of n-type and p-type polysilicon layers after deposition and removal of chemically resistant masking SiN_x, followed by a forming gas annealing at 400°C.

	J_{0s} ($fAcm^{-2}$)	
	n-type SiO_2/PolySi	p-type SiO_2/ PolySi
Optimised poly-Ox layer	6.3	22
Chem-SiO_2/SiN_x & removal	13.5	15.5
600°C SiO_2/SiN_x & removal	54	46
650°C SiO_2/SiN_x & removal	53	17.5
700°C SiO_2/SiN_x & removal	52	13.4

The key importance of the combination of demonstration of patterning on polysilicon wafers (in previous report), and the ability to retain excellent surface passivation after mask removal, represents significant advancement towards a patterning strategy of doped polysilicon contact layers, highly relevant to implementation of local polysilicon under front contacts for front contact cells, and application of local polysilicon passivated contacts on the rear surface of IBC and bifacial solar cells.

Highlights

- Excellent J0 and contact resistivity <1 $fAcm^{-2}$ and <1 $m\Omega cm^2$ was achieved.
- Development of texture-through process for formation of local doped polysilicon regions.
- Development of tunnel-junction MoOx/n-polysilicon contact.

Future Work

- Demonstration of texture-through-polysilicon process on an operational solar cell.
- Incorporation of tunnel-junction MoOx/n-polysilicon contact on PV device.

References

FONG, K. C., KHO, T. C., LIANG, W., CHONG, T. K., ERNST, M., WALTER, D., STOCKS, M., FRANKLIN, E., MCINTOSH, K. & BLAKERS, A. 2018. Phosphorus diffused LPCVD polysilicon passivated contacts with in-situ low pressure oxidation. *Solar Energy Materials and Solar Cells*, 186, 236-242.

FONG, K. C., KHO, T. C., LIANG, W., CHONG, T. K., ERNST, M., WALTER, D., STOCKS, M., FRANKLIN, E., MCINTOSH, K. & BLAKERS, A. Optimization and Characterization of Phosphorus Diffused LPCVD Polysilicon Passivated Contacts with Low Pressure Tunnel Oxide. 2018 IEEE 7th World Conference on Photovoltaic Energy Conversion (WCPEC) (A Joint Conference of 45th IEEE PVSC, 28th PVSEC & 34th EU PVSEC), 10–15 June 2018. 2002-2005.

F4 HYDROGEN DRIFT AND DIFFUSION IN SILICON SOLAR ARCHITECTURES AT INTERMEDIATE TEMPERATURES

Lead Partner

UNSW

UNSW Team

Dr Phillip Hamer, Dr Catherine Chan, Chandany Sen, Daniel Chen, Dr Michael Pollard, Prof. Renate Egan, Diana Koh, Dr Li Wang

Academic Partner

The University of Oxford, Department of Materials: Dr Sebastian Bonilla, Prof. Peter Wilshaw

Aim

This project aims to create a model for the transport of hydrogen within silicon solar cell structures. This involves both the creation of a software program to perform the simulations and experiments to obtain more accurate values for some of the physical parameters involved. The understanding gained from the model can then be used to develop improved processes for controlling the behaviour of hydrogen in solar cells.

Progress

Previous work has shown that the use of an applied bias can either enhance or mitigate an increase in contact resistance for PERC (passivated emitter and rear cell) solar cells during thermal annealing. In 2019 a reverse bias annealing process was developed which could mitigate LeTID (light and elevated temperature induced degradation) in multicrystalline solar cells, while avoiding any reduction in efficiency due to series resistance. This was backed up by simulations of hydrogen distributions across a p-n junction under bias, showing a reduced concentration at the surface when a reverse bias was applied. The aim for 2020 was to progress this work by improving our understanding of the process through simulation and demonstrating a viable process in an industrial tool.

The main progress in improving the capabilities for hydrogen simulation came from the development of a more complete Sentaurus TCAD model. The initial Sentaurus model, which ran solely in S-Process, could not handle externally applied currents or fixed surface charges. By integrating the S-Process model with electrostatic modelling in S-Device a much wider range of conditions can now be simulated. Furthermore, simulations can now be performed for 2D structures. This is important for the simulation of hydrogen transport during the reverse biased annealing processes developed in this project. Figure F4.1 shows the potential, hole density and interstitial hydrogen distribution in the first micron of a cell with a reverse bias applied to the contact at 400°C. It can clearly be seen that the applied bias results in a quite narrow current flow across the emitter, and greatly reduces the hydrogen concentration in this region. The rest of the device which is not under the contact shows very little impact from the applied bias. This is important for understanding the reverse bias process. Our previous hypothesis has been that processes at these temperatures reduce the hydrogen concentration (and hence LeTID) by allowing hydrogen to move back to the surfaces, unfortunately resulting in an increase in contact resistance at the contact. The action of an applied reverse bias is so localised that it allows hydrogen to move back to the surface in the regions covered by the nitride layer but protects the contacts themselves.

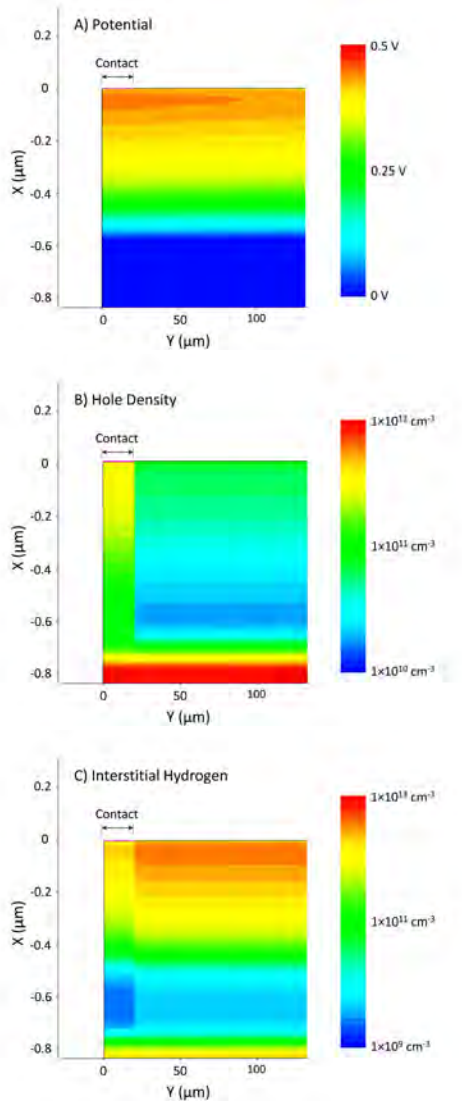

Figure F4.1: (a) Potential; (b) hole density; and (c) interstitial hydrogen concentration across the first 1 µm of a solar cell with a localised front contact and diffused emitter during a reverse bias annealing process at 400°C.

On the experimental side trials have been performed on using an industrial-scale biased annealing tool to mitigate LeTID using these reverse bias processes. The tool is a modified version of commercial "coin-stackers", with a very small footprint and a 400 wafer batch size. A stack of 10 multicrystalline PERC cells was annealed at 319°C under a 30 V reverse bias for two hours, followed by an optimised cooling process. Figure F4.2 shows a median improvement in cell efficiency of 0.2% absolute, largely driven by an increase in the open-circuit voltage. Importantly the fill factor did not drop as a result of the process, indicating there were no series resistance issues. Light soaking showed no significant decay in performance with open-circuit voltages remaining above "before process" values through over 200 hours at 80°C. The commercial viability of the process was also evaluated, with the power consumption during the process identified to be the main cost driver. As such significant work has been done to reduce power consumption with a reduction of over 80% achieved on the initial best known method.

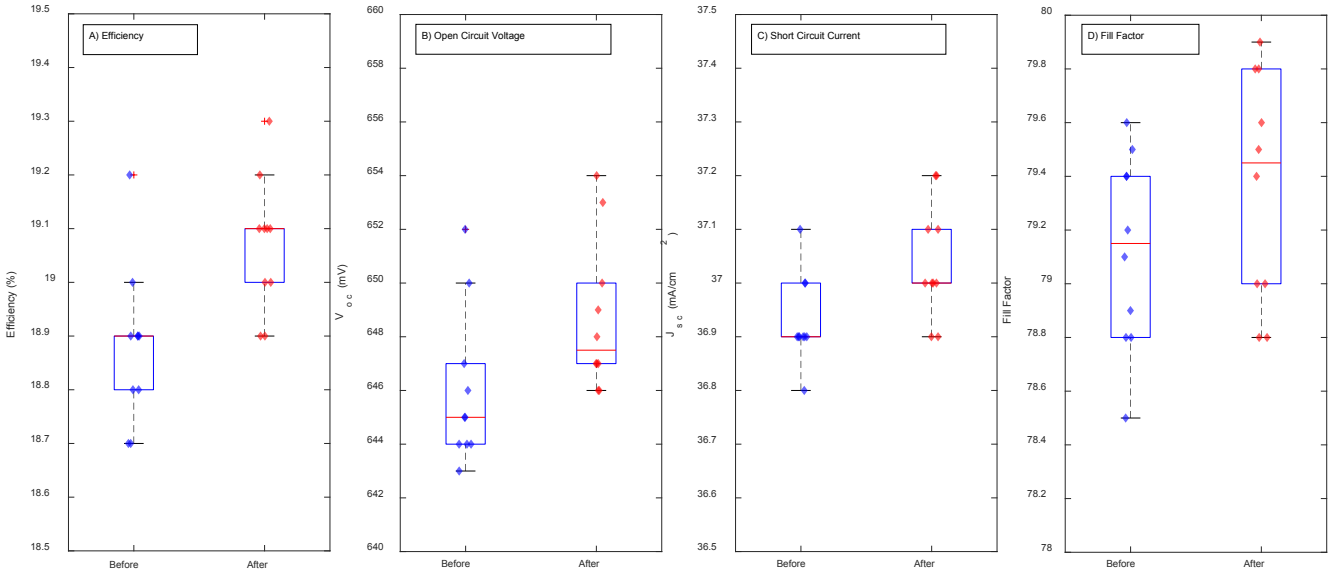

Figure F4.2: (a) Efficiency: (b) open-circuit voltage; (c) short-circuit current; and (d) fill factor of multicrystalline cells before and after reverse biased annealing process.

Highlights

- Sentaurus TCAD model improved and updated to more accurately simulate UNSW processes.
- Reverse bias annealing process demonstrated to eliminate LeTID and improve performance with a greatly reduced power consumption.

Future Work

- Publication of a number of studies on surface-related degradation.
- Project work will cease end March 2021.

F5 CHARACTERISATION OF MICROSTRUCTURE FORMATION IN SOLUTION-PROCESSED PHOTOVOLTAIC PEROVSKITE THIN FILMS WITH SYNCHROTRON-BASED X-RAY SCATTERING TECHNIQUES

Lead Partner

Monash University

Monash Team

Dr Wenchao Huang, Prof. Christopher R. McNeill, Prof. Udo Bach

Academic Partners

Wuhan University of Technology: Prof. Fuzhi Huang, Prof. Yi-Bing Cheng

Funding Support

ACAP

Aim

Here, a novel cation phenylmethylamine bromide (PMABr) is used to post-treat a wide bandgap perovskite $FA_{0.8}Cs_{0.2}Pb(I_{0.7}Br_{0.3})_3$ to form a 3D/2D heterojunction structure, which can simultaneously enhance device performance and stability. The complex morphology of 3D/2D bilayer perovskite films is comprehensively investigated with a combination of synchrotron-based characterisation techniques. The hierarchical morphology is observed, consisting of a highly stable pure 2D (n = 1) perovskite layer on the top of a quasi-2D (n = 2) perovskite layer that caps an underlying 3D perovskite film.

By precisely controlling the surface structure and thickness of 2D perovskites, the wide bandgap perovskite solar cell (PSC) achieves an efficiency of 18.5% with the negligible hysteresis and a significantly enhanced device stability.

Progress

In recent few years, the discovery of mixing structurally stable 2D perovskites with 3D perovskites with a bilayer structure provides a plausible solution to potentially overcome stability-related issues (Huang et al., 2020, Grancini and Nazeeruddin, 2019). The 2D perovskite capping layer is spontaneously formed via cation exchange via post-treating the underlying 3D perovskite layer. Because of the large formation energy, 2D perovskite materials are intrinsically more stable than their 3D counterparts (Quan et al., 2016). The formation of structurally stable 2D perovskites with hydrophobic organic cations on the top of 3D perovskites may also act as a barrier to inhibit water and oxygen diffusion into 3D perovskites, resulting in the significantly improved stability. The morphology and thickness of the 2D perovskite layer plays an important role in determining device performance and stability. However, due to the limited characterisation techniques, there is still a lack of understanding of the 2D perovskite morphology after the post-treatment. It is also still difficult to precisely control the interfacial morphology at 3D/2D heterojunction. In this study, we introduce a simple and novel post-treatment of PMABr onto a wide bandgap formamidinium/cesium lead halide ($FA_{0.8}Cs_{0.2}Pb(I_{0.7}Br_{0.3})_3$) perovskite film to form a 3D/2D bilayer perovskite layer which simultaneously improve the efficiency and stability of solar cell devices (Bu et al., 2020). We also comprehensively study the morphology of 3D/2D bilayer perovskites by using synchrotron-based characterisation techniques and then establish the relationship between 3D/2D bilayer morphology and device performance.

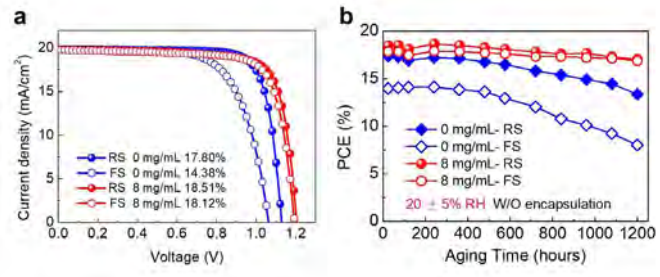

Figure F5.1: Device performance of 3D/2D bilayer perovskite solar cells. (a) J-V curves of perovskite solar cells with and without post-treatments. (b) Long-term stability of perovskite solar cells with and without post-treatments under 20% RH.

PSCs are fabricated with an n-i-p planar structure, with a device architecture of FTO/SnO_2/perovskite/Spiro-OMeTAD/Au. After the optimisation of solution concentration in the post-treatment, the champion device is fabricated with an 8 mg/mL PMABr/IPA solution. The wide bandgap perovskite solar cell with the post-treatment exhibits an efficiency of 18.5% under reverse scan (RS) and 18.1% under forward scan (FS) with a negligible hysteresis (Figure F5.1a). Moreover, the post-treated devices also demonstrate a significantly improved stability under the low humidity environment (20% RH) for over 2000 hours (Figure F5.1b).

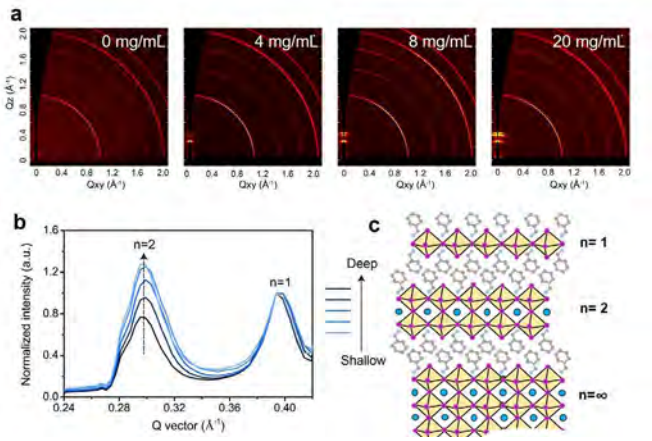

Figure F5.2: (a) 2D grazing incidence wide angle X-ray scattering (GIWAXS) patterns of perovskite films treated with different concentration of PMABr/IPA solution. (b) 1D out-of-plane line profiles extracted from 2D GIWAXS of perovskite treated with 8 mg/mL PMABr/IPA solution as a function of X-ray incident angles. (c) Schematic structure of perovskite films post-treated with 8 mg/mL PMABr/IPA solution.

A combination of synchrotron-based techniques, including grazing incidence wide angle X-ray scattering and near edge X-ray absorption fine structure (NEXAFS) spectroscopy are used to provide an in-depth understanding of the microstructure of 2D perovskite layers formed on the top of 3D perovskite layers. From the GIWAXS measurement (as shown in Figure F5.2a), it is found that organic precursors can react with the 3D perovskite and form different microstructures, which are strongly dependent on the concentration of the post-treatment solution. A pure perovskite (n = 1) layer first grows on the top surface at low concentration, which transforms to a quasi-2D perovskite (n = 2) with the higher concentration. As the concentration of PMABr salt solution further increases, a thicker 2D perovskite as well as a large amount of unreacted salts forms at the surface of the 3D perovskite, both of which are detrimental to charge transport. In order to further investigate the microstructure of 2D perovskites in the optimised perovskite film (post-treated with 8 mg/mL PMABr solution), GIWAXS patterns taken from different X-ray incident angles were measured, shown in Figure F5.2b. As the X-ray incident angle increases from 0.05° (below the critical angle) to 0.13° (close to the critical angle), the ratio of quasi-2D perovskite (n = 2) to 2D perovskite (n=1) systematically increases with increasing penetration depth. This indicates that the pure 2D perovskite (n=1) is located on the surface, while the quasi-2D (n = 2) perovskite is located deeper within the structure (Figure F5.2c).

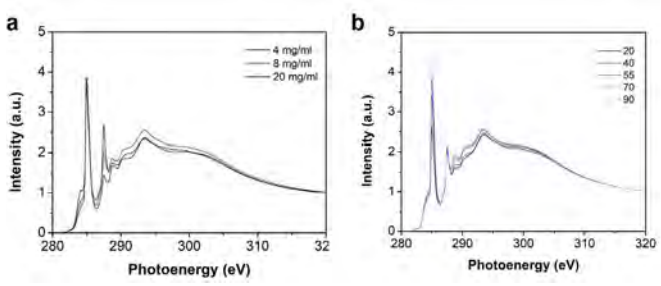

Figure F5.3: (a) Carbon K-edge NEXAFS spectra of different concentration of PMABr/IPA solution–treated perovskite films. (b) Angel-resolved carbon K-edge NEXAFS spectra of a perovskite film treated with 8 mg/mL PMABr/IPA solution.

Moreover, the NEXAFS spectroscopy is also used to investigate the composition and molecular orientation after the post-treatment. Figure F5.3a shows the carbon K-edge NEXAFS spectra (taken at 55° to mitigate the orientation effects) of perovskite films treated with different concentrations of PMABr solution. The intensity of peak located at 287.5 eV which is corresponding to the 3D perovskite exhibits a continuous decrease as a function of PMABr concentration. The fraction of the 3D perovskite at the surface becomes smaller due to the formation of the 2D perovskite layer and residual PMABr. The molecular orientation of PMA in the 2D perovskite was also investigated by using angle-resolved NEXAFS spectroscopy (Figure F5.3b). The intensity of the π* peak (located at ~285 eV) increases as the X-ray incident angle changes from 20° to 90°, indicating that PMA molecules have an edge-on surface orientation which could inhibit the ingress of the water molecules to improve the moisture resistance of the film.

Highlights

- A 3D/2D bilayer device structure is developed to simultaneously improve device efficiency and stability of perovskite solar cells through exploring.
- The morphology of 3D/2D bilayer perovskite films is comprehensively investigated by using a combination of synchrotron-based techniques, unravelling a hierarchical structure.
- A novel phenylmethylamine bromide (PMABr) salt is developed and the microstructure of 2D perovskite films is precisely controlled by the optimisation of solution concentration.
- A high efficiency of 18.5% is achieved in wide bandgap perovskite solar cells, with negligible hysteresis and excellent stability.

Future Work

- New bulky organic cations and methods to control the microstructure of 3D/2D perovskite films will be developed for further improving the efficiency and stability of perovskite solar cells.
- Thermodynamic and kinetic behaviours behind this transformation (cation exchange during the post-treatment) will be studied.

References

BU, T., LI, J., LIN, Q., MCMEEKIN, D. P., SUN, J., WANG, M., CHEN, W., WEN, X., MAO, W., MCNEILL, C. R., HUANG, W., ZHANG, X.-L., ZHONG, J., CHENG, Y.-B., BACH, U. & HUANG, F. 2020. Structure engineering of hierarchical layered perovskite interface for efficient and stable wide bandgap photovoltaics. *Nano Energy*, 75, 104917.

GRANCINI, G. & NAZEERUDDIN, M. K. 2019. Dimensional tailoring of hybrid perovskites for photovoltaics. *Nature Reviews Materials*, 4, 4-22.

HUANG, W., BU, T., HUANG, F. & CHENG, Y.-B. 2020. Stabilizing High Efficiency Perovskite Solar Cells with 3D-2D Heterostructures. *Joule*, 4, 975-979.

QUAN, L. N., YUAN, M., COMIN, R., VOZNYY, O., BEAUREGARD, E. M., HOOGLAND, S., BUIN, A., KIRMANI, A. R., ZHAO, K., AMASSIAN, A., KIM, D. H. & SARGENT, E. H. 2016. Ligand-Stabilized Reduced-Dimensionality Perovskites. *Journal of the American Chemical Society*, 138, 2649-2655.

F6 HIGH DIELECTRIC CONSTANT SEMICONDUCTORS FOR HOMOJUNCTION ORGANIC SOLAR CELLS

Lead Partner
UQ

UQ Team
Dr Hui Jin, Prof. Paul Burn

Academic Partner
None

Funding Support
ACAP

Aim

The objective of this project is to develop organic semiconductors that possess high (optical frequency) dielectric constants at both low and high frequencies and minimise the energy losses in free charge carrier generation in homojunction organic photovoltaic devices.

Progress

High dielectric constant of organic semiconductors can dramatically lower the exciton binding energy and reduce geminate and non-geminate recombination to minimise energy losses and lead to improvement in the performance of homojunction photovoltaic devices (Koster, Shaheen et al. 2012). In principle when the exciton binding energy is low enough to dissociate excitons into free charges in a single organic semiconductor, the efficiency of homojunction organic solar cells could be comparable to inorganic and hybrid solar cells. One of the most studied strategies developed for high dielectric constant organic semiconductors is replacing the alkyl solubilising

groups with ethylene glycol groups to enhance the dipole polarisability (Donaghey, Armin et al. 2016). The flexibility of glycol side chains can lead to less steric hindrance due to the C-O bond rotation (Meng, Song et al. 2015) and results in closer π-π stacking of the electroactive chromophores and thus a higher film density (Armin, Stoltzfus et al. 2017). High film density is a contributing factor to the increase of optical frequency dielectric constant, which can also lead to a redshift in the absorption. Apart from adopting ethylene glycols, high dielectric constant organic semiconductor materials design has also focused on structures capable of adopting a 2D planar geometry with extended π-conjugation for long-range π-electron delocalisation. In the annual report of 2019, a crown-ether substituted co-planar material was proposed with π-electron delocalisation enabled by aromatic ring fusion. The crown-ether containing material suffered difficulties during its synthesis, particularly the cleavage of the crown ether in the presence of strong base and Lewis acids. The ring fusion further limited the solubility of the material. To resolve the chemical stability and solubility issues, the material design was changed towards creating co-planar structural conformations using non-covalent inter-chromophore interactions. As shown in Figure F6.1(a), difluorobenzothiadiazole (FBT) was employed, with the fluorine substitution enabling co-planarity between the FBT and the thienothiophene (TT) moieties. The planarity was induced by strong F-S interactions or F-H bonding. This has been confirmed by the calculated semi-empirical model shown in Figure 1(b) in which the diagram clearly shows the lowest-energy configuration is obtained when the two components that make up the chromophore are co-planar. Furthermore, DFT calculations (Figure F6.1(c)) also show the geometry of the proposed material adopts a planar conformation at its lowest energy configuration. It thus can be speculated that the novel material will lead to high film density and an extended absorption spectrum in the long wavelength region, and thus a large optical-frequency dielectric constant. The well-defined intramolecular interactions could also lead to less conformational diversity, which would contribute to more ordered alignment of molecules and stronger edge-on orientation (McDowell, Narayanaswamy et al. 2018). Scheme 1 shows the optimised synthetic route – a double-site Stille cross coupling was carried out followed by formylation using a Vilsmeier-Haack reaction, and finally a Knoevenagel condensation in chlorobenzene to give the desired material as a dark blue powder. An n-nonylene solubilising group

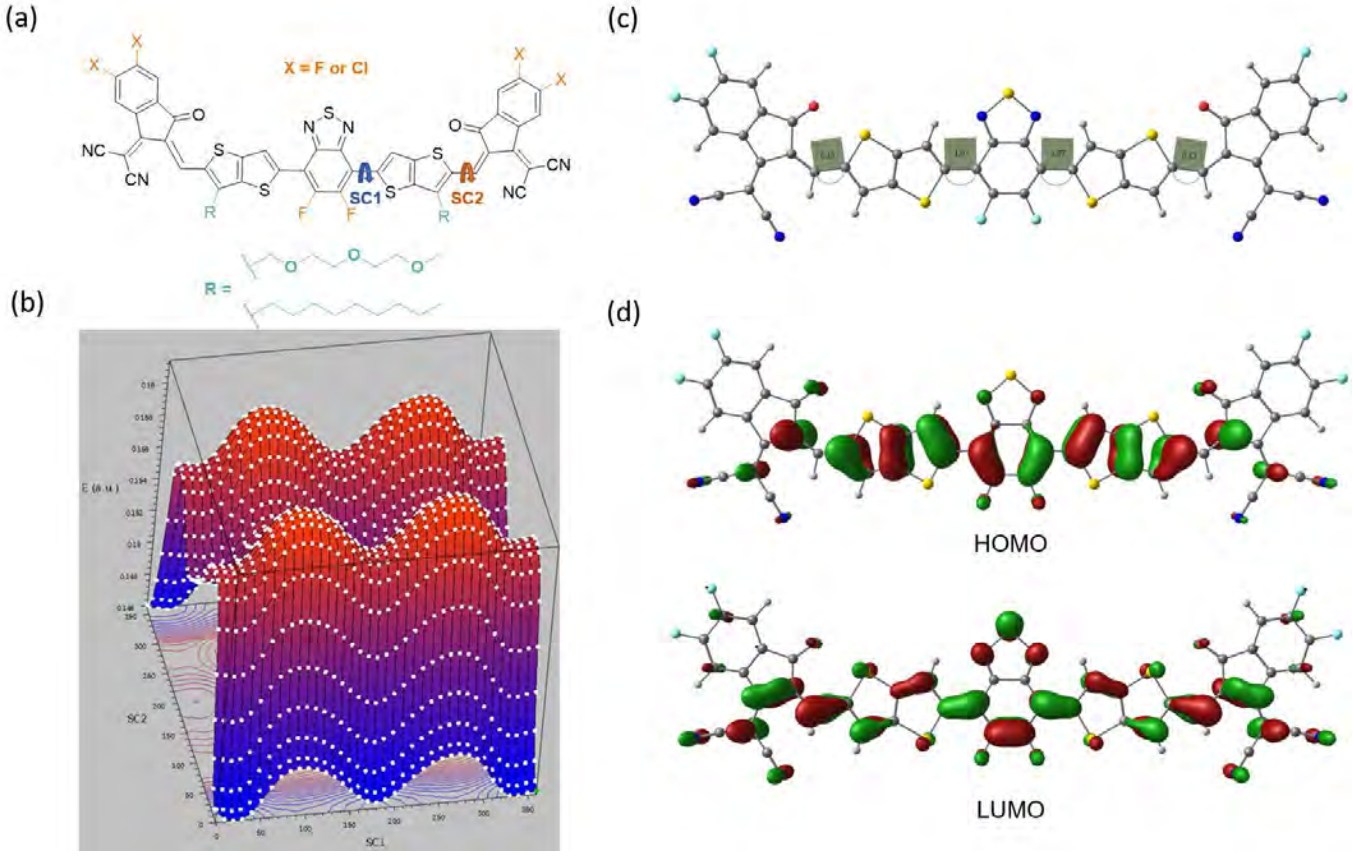

Figure F6.1: (a) Molecular structures of the target material; (b) semi-empirical energy diagram illustrates the energy changes when changing dihedral angle around bonds SC1 and SC2 of the compound shown in (a); (c) calculated molecular geometry (top and side view) at the ground state; (d) calculated molecular orbital distribution (HOMO = highest occupied molecular orbital and LUMO = lowest unoccupied molecular orbital).

($-C_9H_{19}$) was initially attached to the TT moiety as it tends to have a limited effect on the overall molecular geometry. However, it led to very poor solubility of the material in many common solvents used for solution processing. Widely used n-lauryl ($-C_{11}H_{23}$) substitution was also attempted but failed to lead to an improvement in the solubility. The strategy to increase the solubility was therefore converted to employing a branched solubilising group, which has a component perpendicular to the conjugated chromophore. As shown in Scheme F6.1, a branched alkyl solubilising group ($-C_{10}H_{21}$) was chosen with the length expected not to substantially reduce the glass transition temperature of the material. Difficulties also arose during the synthesis. For example, the steric hindrance created by the branched alkyl chain resulted in incomplete reactions, the conditions of which have since been optimised. To demonstrate the effect of fluorine-substitution on BT unit on the molecular conformation and solubility, the fluorine-less compound has also been developed using n-nonylene solubilising groups following the synthetic route shown in Scheme F6.2. However, the solubility of the material was also found to be poor, which nonetheless suggests that the observed solubility issue has not arisen by the fluorine-substitution.

Highlights

- With the deeper understanding gained from the previously prepared materials, a new series of compounds with co-planar molecular geometry enabled by non-covalent bonding has been designed and synthesised.
- An oral presentation was given in the 2020 ACAP annual meeting on the correlation between the molecular geometry and dielectric constant of organic semiconductors.
- A manuscript is being prepared on the results.

Future Work

- The focus is still to develop novel organic/hybrid materials aiming at simultaneously increasing the low- and optical-frequency dielectric constant.

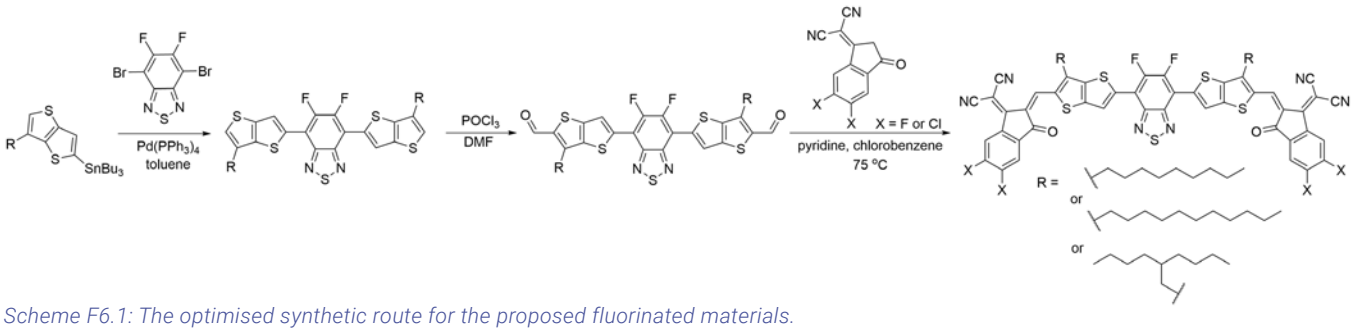

Scheme F6.1: The optimised synthetic route for the proposed fluorinated materials.

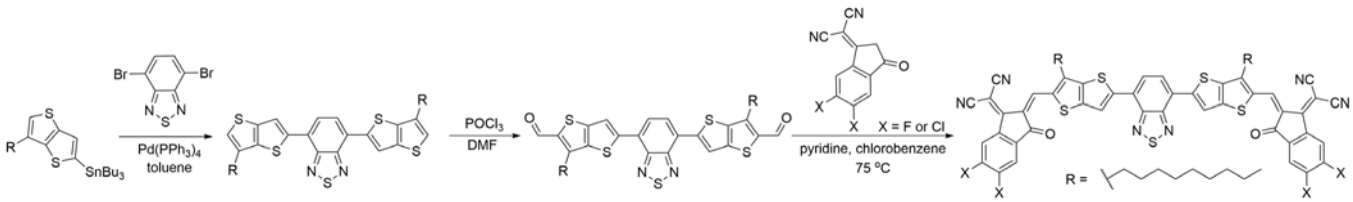

Scheme F6.2: The synthesis of fluorine-less BT centred material.

References

ARMIN, A., STOLTZFUS, D. M., DONAGHEY, J. E., CLULOW, A. J., NAGIRI, R. C. R., BURN, P. L., GENTLE, I. R. & MEREDITH, P. 2017. Engineering dielectric constants in organic semiconductors. *Journal of Materials Chemistry* C, 5, 3736-3747.

DONAGHEY, J. E., ARMIN, A., STOLTZFUS, D. M., BURN, P. L. & MEREDITH P. 2016. Correction: Dielectric constant enhancement of non-fullerene acceptors via side-chain modification. Chemical Communications, 52, 13714-13715.

KOSTER, L. J. A., SHAHEEN, S. E. & HUMMELEN, J. C. 2012. Pathways to a new efficiency regime for organic solar cells. *Advanced Energy Materials*, 2, 1246-1253.

MCDOWELL, C., NARAYANASWAMY, K., YADAGIRI, B., GAYATHRI, T., SEIFRID, M., DATT, R., RYNO, S. M., HEIFNER, M. C., GUPTA, V., RISKO, C., SINGH S. P. & BAZAN G. C. 2018. Impact of rotamer diversity on the self-assembly of nearly isostructural molecular semiconductors. *Journal of Materials Chemistry* A, 6, 383-394.

MENG, B., SONG, H., CHEN, X., XIE, Z., LIU, J. & WANG, L. 2015. Replacing alkyl with oligo(ethylene glycol) as side chains of conjugated polymers for close π–π stacking. *Macromolecules*, 48, 4357-4363.

F7 PRACTICAL 50% EFFICIENT SPECTRUM SPLITTING CPV RECEIVERS USING INTERMEDIATE BRAGG REFLECTORS

Lead Partner

UNSW

UNSW Team

Dr Yajie Jiang, Dr Mark Keevers, Scientia Prof. Martin Green

Industry Partners

AZUR SPACE Solar Power, RayGen Resources Pty Ltd

Funding Support

ACAP

Aim

The aim of this project is to demonstrate the advantages of the distributed Bragg reflector (DBR) assisted spectrum splitting concept compared with discrete dielectric filters. We are also workingtowards world record system efficiency exceeding 50% using spectrum splitting between two triple-junction solar cells (TJSCs) under standard concentrator photovoltaic (CPV) test conditions, including all optical losses.

Progress

We investigated the use of DBRs in both lattice-matched (LM) and metamorphic (MM) TJSCs for spectrum splitting photovoltaics. An optical model of an LM GaInP/GaInAs/Ge TJSC with intermediate DBR is developed, in good agreement with measured reflectance. By modifying the DBR layer number, composition and thickness to broaden the reflectance band, we show that a DBR can provide suitable 900–1050 nm reflectance for spectrum splitting from the LM TJSC to a Si cell, resulting in a more efficient four-junction receiver. We also propose that the buffer layers in MM TJSCs could additionally function as a DBR for spectrum splitting applications. We propose several DBR designs to achieve a suitable spectrum splitting reflectance band from MM TJSCs to a Si cell, again resulting in a more efficient four-junction receiver.

For better practicality and cost effectiveness, minimum DBR layers should be used to achieve a broad reflection band. Chirping the periodicity of the DBR structure is an effective way to achieve a wide reflection range. The idea of chirped DBR can be dated back to 1974 (Hill, 1974). The most common chirping structure is using a linear chirp design (Wu et al., 2009). We compared the performance of standard single DBR, double DBR and chirped DBR in a TJSC in this project.

The state-of-the-art one-sun terrestrial III-V on Ge TJSC is a 34.1% modified space cell, developed by AZUR SPACE for solar car racing (Bett et al., 2009). We measured the spectral specular reflectance of such an LM $Ga_{0.51}In_{0.49}P/Ga_{0.99}In_{0.01}As/Ge$ TJSC using a Perkin-Elmer Lambda 1050 UV-Vis-NIR spectrophotometer with a universal reflectance accessory (URA) at the minimum (8°) angle of incidence (AOI). We developed an optical model of this TJSC by adapting published structures (Shvarts et al., 2012) so that the simulated and measured reflectance are a close match. Optical analysis software WVASE® was used to fit the modelled reflectance to the measured data, by allowing the layer thicknesses to be automatically adjusted (within sensible bounds). An Al_2O_3/TiO_2 double-layer anti-reflection coating (ARC) was assumed, with optical constants from recently published literature (Boidin et al., 2016, Siefke et al., 2016). The optical constants of Ge and Al are from the Palik handbook (Palik, 1985) and the ternary alloys AlInP (window layer), GaInP (top sub-cell) and AlGaAs (DBR layers) are from the New Semiconductor Materials (NSM) Archive semiconductors database. For intermediate alloys, values are determined using the effective medium approximation. Linear interpolation and/or extrapolation are used for missing wavelengths. For the $Ga_{0.99}In_{0.01}As$ (middle sub-cell) layer, the extinction coefficient *k* is determined from the absorption coefficient of GaAs with p-type doping 4.9 x 10^{17} cm^{-3} (Casey et al., 1975), with a rigid 20 meV shift to lower energy due to the 1% In content. These optical constants are shown in Figure F7.1.

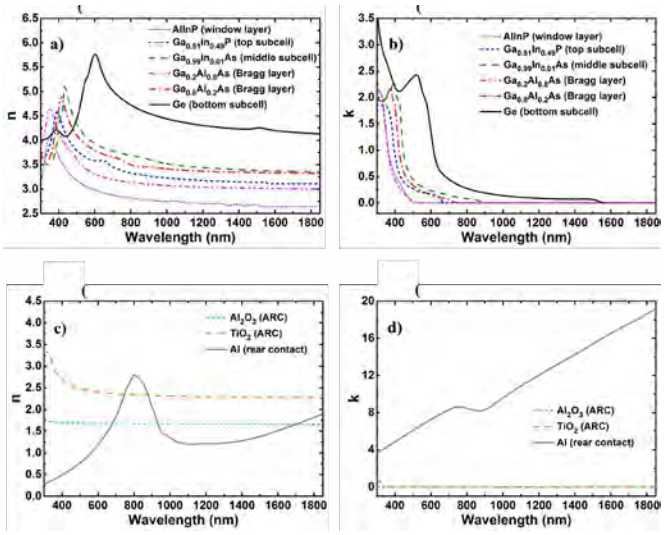

Figure F7.1: Complex refractive index of the (a), (b) top, middle, bottom sub-cells and DBR layers, and (c), (d) ARC layers and rear Al contact in the modelled LM TJSC.

An optical model of the GaInP/GaInAs/Ge TJSC was established based on the above extracted optical constants values. To simulate the performance of an integrated CPV receiver consisting of the LM TJSC and a Si cell, the reflectance and light IV characteristics of the different TJSC designs were modelled assuming an incident AM1.5D spectrum concentrated 350x incident at 45° AOI on the TJSC. Light reflected from the TJSC is incident normally on the Si cell. DBR parameters were optimised to achieve the highest total efficiency in each configuration. The photocurrent densities of the top, middle and bottom sub-cells of the LM TJSC with intermediate DBR and the efficiencies of all cells are shown in Table F7.1. The J_{SC} of the top and middle sub cell are not affected by the various DBR designs. The Si cell efficiencies and total receiver efficiencies show a clear increasing trend using double DBR designs (Table F7.1(c)–(f)), compared with single DBR designs (Table F7.1(a) and (b)). The 2 x 12 bilayer design (Table F7.1(c) and (d)) is sufficient to divert excess photons away from the Ge bottom sub-cell ($J_{SC\ bottom}$ reduced to 12.8 $mAcm^{-2}$, same with $J_{sc\ middle}$) without detriment to the top or current-limiting sub-cells, therefore a further increase of DBR layers to 2 x 16 (Table F7.1(e) and (f)) bilayers does not show significant enhancement. The chirped DBR designs provide promising results as the standard DBR designs.

Figure F7.2 shows the modelled external quantum efficiency (EQE) of TJSCs with various DBR designs, and the modelled EQE of an additional Si cell. For a 1 x 16 bilayer DBR design, the chirped DBR (Figure F7.2 (b)) reflects a much broader band to the Si cell compared a with standard 1 x 16 bilayer DBR design (Figure F7.2 (a)). However, the reflectance intensity was reduced with the broadening therefore similar overall efficiency is achieved. Standard double DBR designs already give a broad enough reflection band (Figure F7.2 (c) and (e)), therefore, chirping (Figure F7.2 (d) and (f)) does not provide any further broadening.

Table F7.1: Calculated sub-cell photocurrent densities and LM TJSC + Si cell efficiencies for various DBR designs.

Device structure	J_{SC} top sub-cell ($mA.cm^{-2}$)	J_{SC} middle sub-cell ($mA.cm^{-2}$)	J_{SC} bottom s ub-cell ($mA.cm^{-2}$)	Efficiency LM TJSC (%)	Efficiency Si cell (%)	Efficiency total (%)
(a) TJSC with 1 × 16 bilayer DBR	12.4	12.7	14.2	40.04	3.45	43.5
(b) TJSC with 1 × 16 bilayer chirped DBR	12.4	12.8	13.8	40	3.69	43.7
(c) TJSC with 2 × 12 bilayer DBR	12.4	12.8	12.8	39.73	4.42	44.2
(d) TJSC with 1 × 24 bilayer chirped DBR	12.4	12.8	12.9	39.79	4.31	44.1
(e) TJSC with 2 × 16 bilayer DBR	12.4	12.9	12.6	39.67	4.61	44.3
(f) TJSC with 2 × 16 bilayer chirped DBR	12.4	12.9	12.6	39.64	4.58	44.2

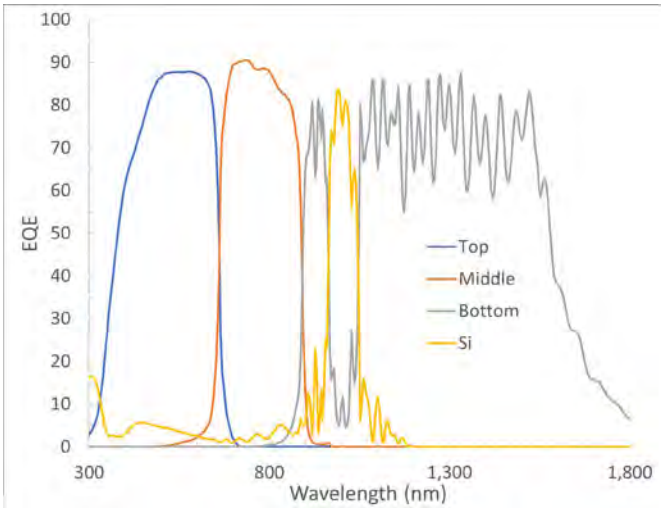

Figure F7.2: Modelled EQE of (a) TJSC with 1 × 16 bilayer DBR + Si cell; (b) TJSC with 1 × 16 bilayer chirped DBR + Si cell; (c) TJSC with 2 × 12 bilayer DBR + Si cell; (d) TJSC with 1 × 24 bilayer chirped DBR + Si cell; (e) TJSC with 2 × 16 bilayer DBR + Si cell; and (f) TJSC with 2 × 16 bilayer chirped DBR + Si cell.

Highlights

- For better practicality and cost-effectiveness, we demonstrated that TJSC with a 2 × 12 bilayer DBR design is sufficient to achieve the desired efficiency with less bilayers.
- A linear chirped DBR also shows promising results for spectrum splitting applications.

Future Work

- Fabricate and characterise the optimised TJSCs with double DBR.
- Further progress along the development path towards a 50% efficient PV receiver.

References

BETT, A. W., DIMROTH, F., GUTER, W., HOHEISEL, R., OLIVA, E., PHILIPPS, S. P., SCHÖNE, J., SIEFER, G., STEINER, M., WEKKELI, A., WELSER, E., MEUSEL, M., KOSTLER, W. & STROBL, G. Highest efficiency multi-junction solar cell for terrestrial and space applications. EU PVSEC, Hamburg, 21-25 September, 2009. 1-6.

BOIDIN, R., HALENKOVIČ, T., NAZABAL, V., BENEŠ, L. & NĚMEC, P. 2016. Pulsed laser deposited alumina thin films. *Ceramics International,* 42, 1177-1182.

CASEY, H. C., SELL, D. D. & WECHT, K. W. 1975. Concentration dependence of the absorption coefficient for n− and p−type GaAs between 1.3 and 1.6 eV. *Journal of Applied Physics,* 46, 250-257.

HILL, K. O. 1974. Aperiodic Distributed-Parameter Waveguides for Integrated Optics. *Applied Optics,* 13, 1853-1856.

PALIK, E. D. 1985. Handbook of Optical Constants of Solids. Academic Press: Orlamdo.

SHVARTS, M. Z., ARONOVA, E. A., EMELYANOV, V. M., KALYUZHNYY, N. A., LANTRATOV, V. M., MINTAIROV, S. A., SOLUYANOV, A. A. & TIMOSHINA, N. K. 2012. Multijunction solar cell with intermediate IR reflector. *AIP Conference Proceedings,* 1477, 28-31.

SIEFKE, T., KROKER, S., PFEIFFER, K., PUFFKY, O., DIETRICH, K., FRANTA, D., OHLÍDAL, I., SZEGHALMI, A., KLEY, E.-B. & TÜNNERMANN, A. 2016. Materials Pushing the Application Limits of Wire Grid Polarizers further into the Deep Ultraviolet Spectral Range. *Advanced Optical Materials,* 4, 1780-1786.

WU, C. J., CHU, B. H., WENG, M. T. & LEE, H. L. 2009. Enhancement of Bandwidth in a Chirped Quarter-Wave Dielectric Mirror. *Journal of Electromagnetic Waves and Applications,* 23, 437-447.

F8 DETERMINATION OF DEFECT ENERGY LEVELS FROM INJECTION-DEPENDENT TRAPPING

Lead Partner

UNSW

UNSW Team

Dr Mattias K. Juhl, Prof. Thorsten Trupke

Academic Partners

Australian National University: Prof. Daniel Macdonald

Arizona State University: Prof. Stuart Bowden

Fraunhofer ISE: Dr Martin Schubert

Funding Support

ACAP Fellowship

Review

This Fellowship investigated the use of transient photoconductance for the identification of defects via measuring "trapping" effects present in transient photoconductance data. We outlined the relationship for a simple defect and it's trapping time constant and demonstrated that this can be greatly simplified if no re-trapping of carriers occurs:

$$\frac{1}{\tau_{pc}} = e_{mj} + e_{mn} + c_{mj}N_{dop} \quad \text{(Eq. F8.1)}$$

where τ_{pc} is the time constant of the photoconductance decay, c_{mj} is the majority capture coefficient, e_{mn} is the minority carrier emission coefficient, e_{mj} is the majority carrier emission coefficient, c_{mn} is the minority carrier capture coefficient, and N_{dop} dopis the doping density. An important outcome of this derivation is that, especially for standard solar-grade material at room temperature, the trapping time constants is more likely to be determined by the capture time rather than the emission time of defects. This suggests that recent analysis performed on such signals is incorrect, as it is often assumed that

the time constant represents an emission process. The trapping time of interstitial iron was measured and confirmed to match the capture time, supporting the above conclusion.

In our last year we focused on analysis and the cause of trapping signals that appear in current mono and multicrystalline solar-grade silicon. The trapping signal in multicrystalline silicon has been studied for many years and is often assumed to be directly related to bulk defects changing their charge state. Our work focused on determining if this is really true by testing the competing theory (Glaenzer and Jordan 1969; Seager 1985), that the trapping-like signal is a result of grain boundaries that have large number defects which cause a local reduction of the majority carrier density when the sample is in the dark but are restored when the sample is illuminated. The lower carrier density in the dark causes a depletion region, and a high barrier to current flow, in effect decreasing the entire sample's lateral dark conductance by a few per cent. Upon illumination the defects change their charge state, restoring the majority carrier density at the grain boundary and restoring this "hidden" dark conductance. It is this restoration of this dark conductance that would cause the "trapping" signal in a photoconductance measurement. The testable predictions of this theory are that (a) a wafer with "trapping" should have slightly lower dark conductance than a sister sample without "trapping", where this difference should roughly be the magnitude of trapping, and (b) the trapping signal should only be observed when there is illumination as the time constant of the defects should be much faster than the time constant of the light source, that is, if the light quickly turns off the conductance should return to its dark state value.

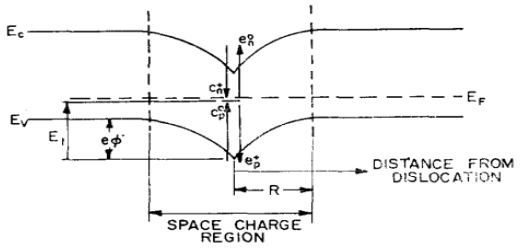

FIG. 1. Electron energy band diagrams as a function of distance from a dislocation for *n*-type and *p*-type material showing carrier transitions involved in the recombination process.

Figure F8.1: Reproduced figure showing the double depletion layer forming at a grain boundary, referred to in the image as a dislocation (Glaenzer and Jordan 1969)

To test these predictions 155 x 155 mm cast-monocrystalline wafers from the side of an ingot were studied as they have varying regions of crystallography across a single wafer. The samples were alkaline textured to visibly highlight the different grain orientations. Samples were chosen that had large regions of multi and monocrystalline regions. The wafer was split into 9 tokens, still large enough to be measured on a Sinton WCT-120. The sample's conductivity was measured with the sample in the dark and under a known photon flux. An example PL image of a sample is shown in Figure F8.2 (Left), with different grain orientations appearing in different colours. Large trapping-like signals were observed in photoconductance measurements on tokens 1, 2 and 8 taking ~30 ms, similar to the time of the flash lamp. The dark conductance across the wafer varies strongly, but upon illumination the measured conductance was the same. This agrees with what the tested theory predicts, and was observed on all samples tested. Finally, transient measurements were performed on the sample with both an eddy current and microwave-based lifetime system when the light was turned off, it was not observed in the microwave-based system. This is as the microwave-based system only probed a local region of the sample, which did require current to flow laterally and is less impacted by the depletion region formed at the grain boundaries. The right image in Figure F8.2 shows transient measurements on token 1 taken with a microwave-based system at different points on wafer 1, it is clear no trapping is observed.

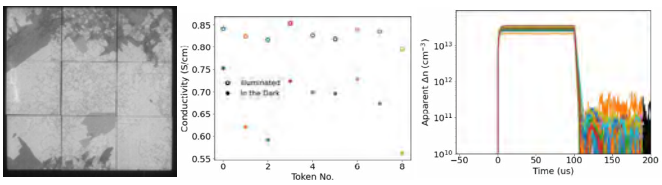

Figure F8.2: Trapping at grain boundaries. Left – PI image of a cast-mono wafer, tokens number left to right then top to bottom. Middle – Comparison of measured conductivity in the dark and under illumination. Right – Transient measurements on token 1, showing no trapping.

For monocrystalline silicon we investigated the claim that the boron-oxygen defect, as measured by DLTS, (a) would act as a trap in solar-grade silicon and (b) could prevent accurate measurements of lifetime. To test these claims a custom photoconductance tool, and digital signal process was established to enable more sensitive measurement. This enabled measurement of carrier densities down to 10^{11} cm^{-3}.

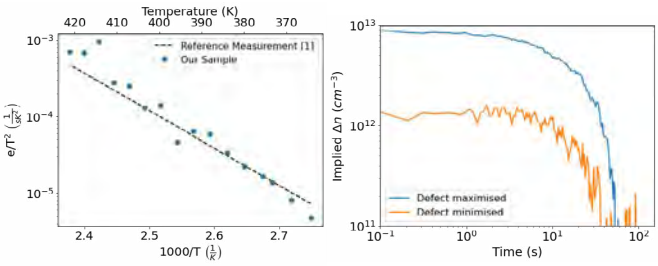

Figure F8.3: Measurements of the precursor of the boron oxygen–related defect with left) DLTS confirming the same defect is in the material (Markevich et al. 2019; Vaqueiro-Contreras et al. 2019) and right) Photoconductance confirming it is modulated in the same manner.

To determine if the same BO-related defect was measured as in previous studies photoconductance measurements were compared to DLTS measurements. The samples were then taken through thermal treatments, which are known to either create or destroy the boron-oxygen defect, and the measurement compared between the techniques. The measurement result highlights are shown in Figure F8.3. Figure 3 (left) shows DLTS measurements confirming the same defect is observed in our material as in the previous studies

(Markevich et al. 2019; Vaqueiro-Contreras et al. 2019). The magnitude of the defect, when maximised, was similar in both measurements, being ~10^{13} cm^3. The defect concentration increases or decreases according to the repeated thermal processing. This confirms the first claim that the boron oxygen defect does act as a trap in solar-grade silicon. However, the second claim about making lifetime measurement incorrect should be considered false as the defect has a time constant significantly different from the excess carrier density (minutes compared to milliseconds), as its magnitude is representing carrier densities below 5 *x* 10^{13} cm^{-3}, a region an order of magnitude below what is looked at in standard measurements representing illumination intensities well below 0.1 sun for typical solar cells.

Highlights

- Reanalysed trapping in photoconductance measurements in silicon.
- The trapping time constants of simple defects in PV material are dominated by capture not emission of carriers, confirmed using intentional contaminated samples with iron.
- Common trapping signals in Cz silicon and multicrystalline silicon were analysed.
    - The trapping in p-type Cz silicon is related to the DLTS measured defect associated with the BO defect or thermal donors (oxygen-related defect).
    - The trapping in multicrystalline /cast-mono silicon has been linked to an effect at grain boundaries rather than defects within grains. The trapping is associated with an incorrect measurement of the sample's dark conductance caused by a significant reduction in the majority carrier density at grain boundaries causing a large barrier to lateral current flow within the sample.

References

GLAENZER, R. H. & JORDAN, A. G. 1969. The electrical properties of dislocations in silicon—I: The effects on carrier lifetime. Solid-State Electronics, 12, 247-258. https://doi.org/10.1016/0038-1101(69)90006-9

MARKEVICH, V. P., VAQUEIRO-CONTRERAS, M., DE GUZMAN, J. T., COUTINHO, J., SANTOS, P., CROWE, I. F., HALSALL, M. P., HAWKINS, I., LASTOVSKII, S. B., MURIN, L. I. & PEAKER, A. R. 2019. Boron–Oxygen Complex Responsible for Light-Induced Degradation in Silicon Photovoltaic Cells: A New Insight into the Problem. *Phys. Status Solidi* A 216, 1900315. https://doi.org/10.1002/pssa.201900315

SEAGER, C. H. 1985. Grain Boundaries in Polycrystalline Silicon. *Annual Review of Materials Science*. 15, 271-302. https://doi.org/10.1146/annurev.ms.15.080185.001415

VAQUEIRO-CONTRERAS, M., MARKEVICH, V. P., COUTINHO, J., SANTOS, P., CROWE, I. F., HALSALL, M. P., HAWKINS, I., LASTOVSKII, S. B., MURIN, L. I. & PEAKER, A. R. 2019. Identification of the mechanism responsible for the boron oxygen light induced degradation in silicon photovoltaic cells. *Journal of Applied Physics*. 125, 185704. https://doi.org/10.1063/1.5091759

F10 TOWARDS A 50% EFFICIENT MULTIJUNCTION PV SYSTEM

Lead Partner
UNSW

UNSW Team
Dr Dongchen Lan

Funding Support
ACAP

Aim

The objective of this project is to find industrially viable methods able to take photovoltaic (PV) energy conversion efficiencies to levels beyond present worldwide expectations. The project is planned to assess existing limitations in state-of-the-art solar cell technologies (e.g., the world record spectrum-splitting modules) and suggest improvements. This will include two main aspects, namely, designing new cell architectures and investigating novel photovoltaic materials. In particular, perovskite solar cells as potential building blocks for next generation multi-junction PV systems will be investigated.

Progress

A. Next generation spectrum-splitting approach

UNSW holds the current efficiency record for spectrum-splitting photovoltaics (Green et al. 2016). In order to find feasible methods capable of enhancing the efficiency further, we first analysed the primary power losses in the existing system, where an external filter directed a portion of the sunlight normally wasted by commercial InGaP/InGaAs/Ge triple-junction cells to a silicon cell. We identified two primary efficiency loss mechanisms which are expanded as follows.

First, we realised that emissions from high- to low-bandgap cells are detrimental to the emitting cell's voltage. This is due to the cell's rear emissions increasing its dark saturation current (Lan and Green 2014). Our analysis shows that, if such rear emissions are reflected back for reabsorption, in the radiative limit where only radiative recombination occurs, the top two cells will have an increase of 0.067 V in each of their voltages with a total increase of 0.134 V for the tandem device (Lan and Green 2018a: Lan and Green 2018b; Lan and Green 2018c). This would give an absolute increase of ~1.8% in the tandem efficiency. For good real cells with radiative efficiencies of ~30%, the tandem voltage will have an increase of ~0.08 V, corresponding to an absolute increase of ~1.1% in the tandem efficiency part. Noticeably, the above data are for cells using concentrated sunlight and the relative improvements will be larger for one-sun modules since each cell operates at a lower voltage but with the same absolute improvement.

Second, we noticed that the current band-pass filter directs out light from 880 to 1030 nm (1.41 to 1.206 eV) only, suggesting that the Ge cell is still generating more photocurrent than the top two cells hence still dissipating some power. The wavelength range for the directed

light can be extended further to ~1190 nm (1.04 eV) where the Ge cell can generate just matched photocurrent, unless it has significant defects resulting in too much bend in its I-V curve before reaching its maximum power point voltage. Noting that silicon has a bandgap of 1.11 eV, corresponding to 1120 nm, light of wavelengths above 1120 nm cannot be harnessed by a silicon cell. Hence, replacing the silicon cell with another high-quality cell with a 1.04 eV or slightly lower bandgap, such as an InPAs cell, may improve the efficiency further. Compared with the old scheme where only light from 880 to 1030 nm is directed to the silicon cell, the current will be increased by ~85.7% and the voltage will be decreased by ~6.3%. This can boost the detached single cell efficiency by ~74%, corresponding to an absolute increase of ~3.3% in the detached cell efficiency part.

Hence, addressing the two power losses identified above can increase the overall photovoltaic energy conversion efficiency to 45% (40.6% + 1.1% + 3.3%).

Interestingly, filters with suitable optical windows built into the rear of the cells themselves can address the above two power loss mechanisms simultaneously. For instance, as shown in Figure F10.1, a filter capable of reflecting light of 750–1190 nm built into the rear of the 1.41 eV GaInAs cell can both reflect its rear emissions (750–900 nm) back for reabsorption and direct the extra light (900–1190 nm) to another cell for additional photovoltaic power production. Such built-in filters may be realised through Bragg-type structures that are essentially stacked thin-film layers of alternating high and low refractive indices. They use light interference to reflect certain wavelengths but transmit others. Key requirements of these thin-film optical layers include transparency to the wavelengths of interest and good conductivity of electricity.

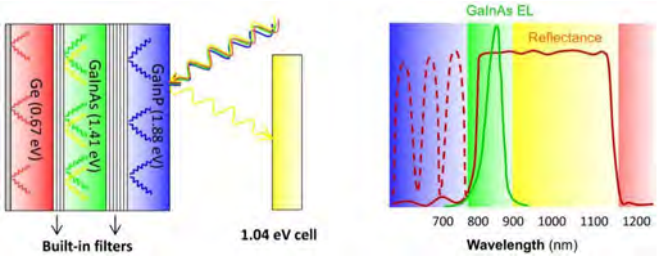

Figure F10.1: Schematics of (a) a proposed new spectrum-splitting system with built-in filters and the silicon cell replaced by a slightly lower gap (1.04 eV) cell; and (b) the GaInAs electroluminescence and an effective rear filter's reflectance. Colours are indicative only (Lan and Green 2018b).

The above concept may be further generalised by having two monolithic tandem cells with built-in filters, where a second tandem absorbs light directed out from the first tandem (Figure F10.2). This can improve the overall efficiency on two accounts. First, sunlight may be better harnessed with an increased number of cells of appropriate bandgaps. Second, splitting a long cell stack into two short stacks can reduce a range of mismatch issues that limit the performance of series-connected cells. Note that these include more than photocurrent mismatching. For instance, the lowest-bandgap cell normally has the largest dark saturation current which can move the operating points of the other series-connected cells away from their maximum power points. This can have a most severe impact on the performance of the highest-bandgap cell that normally has the smallest dark saturation current. Having two electrically separate tandems ensures that the lowest-bandgap cell can only lightly impact its series-connected medium-bandgap cells instead of all other cells with higher bandgaps.

Figure F10.2 shows an optimal design using the dual tandem concept where two monolithic cell stacks are lattice-matched to the GaAs and InP wafer substrates. As one of our interests is to predict its practical performance, we conducted a realistic assessment for cells of ~1-cm2 area based on real data. With the state-of-the-art cell technologies, this design was predicted to have a practical efficiency of 51.0% at 300 suns and 51.7% at 500 suns, with an absolute further improvement of ~1% possible using built-in filters.

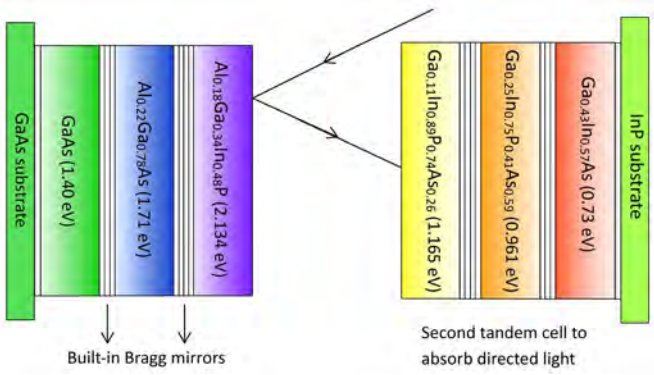

Figure F10.2: Conceptual design of a next generation spectrum-splitting module consisting of two monolithic cell stacks lattice-matched to GaAs and InP wafers. Each stack has built-in filters and is current-matched (though not necessarily to the same value). Colours are indicative only (Lan and Green 2018b).

We evaluated the feasibility of the above two developments, namely application of built-in filters and generalisation of concept, as a crucial step before eventual fabrication.

For the design of rear Bragg-type mirrors, current industrial facilities can deposit at least 32 optical layers onto the rear of a cell, which is sufficient to make an effective built-in filter. However, provided the filters can divide light appropriately, a minimal number of optical layers is desired as this would improve the electrical conductivity and lower the potential fabrication cost. This can be realised by noting two points. First, the built-in feature allows the requirements of filter properties over some wavelengths to be relaxed compared with external ones. Taking the 1.41 eV GaInAs cell in Figure F10.1 as an example, its rear filter's reflectivity for wavelengths below 800 nm would not matter because incident light of these wavelengths is largely absorbed before reaching its rear and the cell does not have appreciable self-emissions in this wavelength range. Second, instead of using repeated periods of optical layers, we may design chirped Bragg reflectors by tuning the thicknesses and refractive indices of certain optical layers for more desired reflection patterns.

For the implementation of dual tandem concept, each cell stack is designed to be current-matched, though not necessarily to the same value. The first cell stack is lattice-matched to a GaAs wafer substrate and the second is lattice-matched to an InP wafer substrate.

For the cells on the GaAs wafer, bandgaps between 1.40 and 2.30 eV are accessible using lattice-matched solid solutions of GaAs, GaP, InP, AlP and AlAs (Vurgaftman et al. 2001). For the cells on the InP wafer, bandgaps between 0.73 and 1.40 eV are accessible using lattice-matched solid solutions of GaAs, InAs, InP, AlAs and GaSb (Vurgaftman et al. 2001). Figure F10.2 shows a rather sophisticated 6-cell module that can take photovoltaic conversion of sunlight to efficiency levels beyond present worldwide expectations. But a much simpler four-cell module consisting of 1.89/1.40 eV cells on the GaAs wafer and 1.041/0.73 eV cells on the InP wafer, is predicted to deliver an over 48% efficiency under 500 suns, which can already beat the current efficiency record for solar cells of any type.

Notably, the dual tandem approach will not only make better use of the solar spectrum but allow more flexibility in the filter design since the requirement on the spectral shape of the directed light can be significantly relaxed. In particular, the spectrum of the light directed out from the first tandem no longer needs to be a continuous band. It can even be two discrete parts with irregular shapes, which can still be well utilised by a second tandem cell with suitable band gaps (Figure F10.3). A more flexible requirement on the reflectance spectrum is likely to lead to even fewer optical layers required to make an effective filter, which can result in both improved efficiencies and reduced fabrication costs.

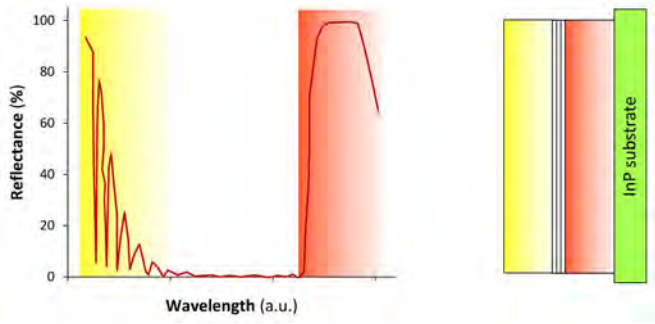

Figure F10.3: A schematic example of a reflected spectrum consisting of two distinct parts (left) that can be well harnessed by a two-cell tandem stack (right). Colours are indicative only (Lan and Green 2018b).

Compared with the monolithic architecture, having physically separate cells is also more compatible with future generation photovoltaics in the sense that low-cost photovoltaics often involve combining materials of vastly different properties (e.g., silicon and perovskites), where the traditional monolithic approach may be more restricted in some aspects.

B. Perovskite-based photovoltaic devices

Perovskite solar cells promise to reach the highest efficiencies at the lowest costs but the mobile ions create challenges in both cell measurements and performance improvement. Being able to understand the ion migration mechanism and its impacts would help to solve relevant issues and may open up opportunities for further development. Here, familiar knowledge in device physics is used to explain a range of ion-related issues in perovskite devices.

Figure F10.4(a) (left) shows a schematic of the electronic and ionic charge distributions under the dark equilibrium condition. Figure F10.4 (b) (left) shows a schematic of how electrons move immediately after light turns on, when ionic charges have not moved much yet. Upon light illumination, the depletion region near contacts shrinks immediately under open-circuit conditions. This suggests that the bulk region becomes wider and some ionic charges that were previously inside the depletion region are now in the bulk region. Before these bulk ionic charges move to their new equilibrium positions, electrons move rapidly to screen these ionic charges to make the bulk region remain quasi-neutral, in a direction opposing the photo-generated current if the cell were connected to an external circuit. The electron screening reduces much of the ionic drift due to Coulomb force and suggests that the bulk ionic charges move to their new equilibrium positions through diffusion mainly. As the screening can reduce the Coulomb attraction between negative and positive ionic charges, it can make the ionic migration even slower. After sufficient illumination time, the mixed ionic-electronic system will reach a new equilibrium with new ionic and electronic distributions (Figure F10.4(c) (left)).
The continuing electron redistribution with the ion migration helps to keep the bulk neutrality, in a way similar to the more familiar screening process in plasmonics but with much slower speed. This electron redistribution process has great implications for the impact on device characterisation and performance.

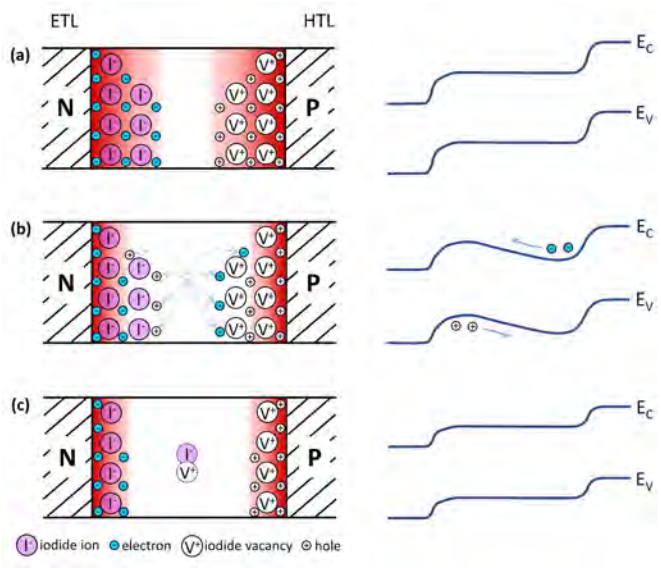

Figure F10.4: Schematics of ionic and electronic carrier distributions (left) and corresponding band diagrams (right) for three situations of interest: (a) the dark equilibrium; (b) immediately after light turns on; and (c) after prolonged illumination. The red-colour shaded region is the depletion region with the shade grading indicating the electric field strength (Lan 2020).

The hysteresis in I–V curves can be well understood following above considerations of the depletion edge moving during the scanning process and the resulting time-varying ionic and electronic distributions. Noting the depletion region width will reduce with an increasing forward bias, scanning from short-circuit to forward-bias under illumination will cause the depletion region to shrink towards the contact during the process, thereby widening the bulk region. Hence,

an increasing volume of ionic charges that were in the depletion region before will become in the bulk region that expands with the scanning. Before these ionic charges move slowly to new equilibriums, electrons and holes move rapidly in response to the ionic fields. Most of the redistributed electrons and holes are actually semi-bounded due to their mobilities being significantly limited by the ionic field. This causes a bending in the perovskite band diagram (see the right of Figure. F10.4(b)) and macroscopically a reduction in the overall currents, which can recover as ionic charges move to new equilibriums.

Slow time-evolution of PL exhibited by perovskite cells has attracted great attention since the rapid emergence of this area. This feature has been experimentally shown to be related to ion migration but the physics is not well understood yet. Figure F10.4 shows that ion migration causes electron redistribution. The electron redistribution will affect the Shockley-Read-Hall and Auger processes differently. Depending on which one of the two non-radiative processes changes more, it may lead to either an increase or a decrease in the overall non-radiative recombination rate, hence either PL quenching or PL enhancement over time as ionic charges move to new equilibriums.

Ion migration can also impact cell performance by affecting the electron distribution inside the perovskite layer. On one side, the depletion edge movement due to a change in the cell operating condition will cause ions to move slowly to their new equilibriums. Consistently, the electron distribution will change over time with the slow ion migration as argued previously. This can at least partly explain why perovskite solar cells are unstable with their properties changing over time. On the other hand, whether ionic charge distribution should positively or negatively affect the cell performance depends on a range of factors such as the material quality and cell operating conditions, consistent with how it affects non-radiative processes discussed previously. One thing for sure is that the bulk ionic charge distribution can lead to spatially varying bulk electron-hole distributions due to charge balance. This is likely to suppress non-radiative recombination when the Shockley-Read-Hall process dominates, thereby improving the cell performance; but it is likely to increase non-radiative recombination when the Auger process dominates, thereby reducing the cell performance. As the bulk ion distribution changes with the cell operating condition, the impact of bulk ion distribution on cell performance discussed above reveals one previously unaddressed mechanism for variations in the perovskite cell performance when the operating condition changes.

In 2020, we show how ion migration may result in anomalously large ideality factors (e.g., >4) in perovskite cells, hence impacting the device performance in another way than those already known such as causing current-voltage (J–V) hysteresis. This is an important aspect but has been overlooked. Based on a quasi-equilibrium treatment, we derive the electric field penetration depth (λ_D) into perovskite layers in the presence of ion migration

$$\lambda_D = \sqrt{\frac{2kT\varepsilon_r\varepsilon_0}{q^2(n_s + N_s)}}\ , \qquad \text{(Eq. F10.1)}$$

where ε_r is the dielectric constant of the bulk material, $\varepsilon_0 = 8.85 \times 10^{-14}$ F cm^{-1} is the vacuum permittivity, n_s and N_s are the electronic and ionic charge densities at the Pero/CTL interface, with N_s being the sum of the concentrations of all ionic charge carriers including charged ions and vacancies multiplied by the number of elementary charges each ion or vacancy carries, and show how ion migration leads to electrostatic decoupling of the two perovskite contact interfaces (Figure F10.5). This leads to an equivalent circuit pointing toward the likely origin of large ideality factors, whose analytical solutions illustrate how the measured ideality factor can exceed 4 or even 5.

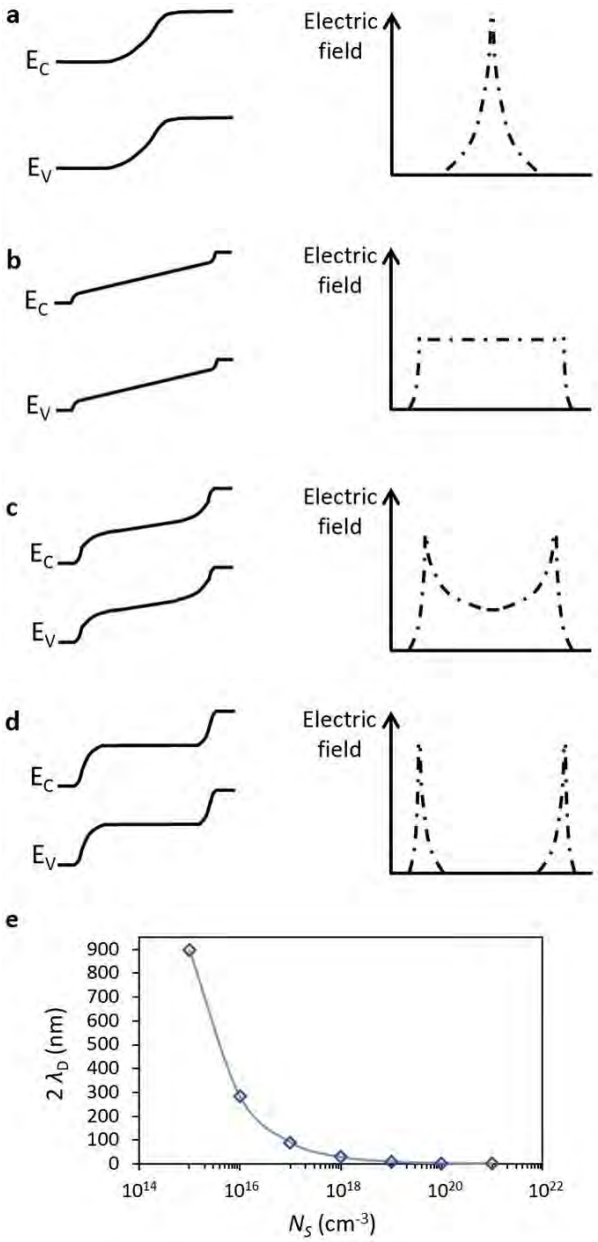

Figure F10.5: Energy band diagrams and electric field distributions for some representative solar cell structures: (a) p–n junction solar cell; (b) p–i–n junction solar cell; (c) perovskite solar cell with moderate ion migration; (d) perovskite solar cell with significant ion migration; and (e) the total range of electric fields from two Pero/CTL interfaces as a function of the same ionic charge density at both interfaces, assuming $\varepsilon_r = 70$ (Lin et al. 2015), $T = 300\ K$ and $N_S >> n_S$ for appreciable ion migration.

Highlights

- Built-in filters can both divide the sunlight appropriately for sub-cells and reduce voltage losses due to rear emissions, pushing the efficiency to ~45%.
- Two tandem cell stacks can make 50% system efficiency a realistic task with state-of-the-art technologies.
- Tardy ionic charges can distort the perovskite bands hence reduce the net currents before they move to new equilibriums, causing the hysteresis effect.
- Ion migration affects the Shockley-Read-Hall and Auger processes differently, hence may either reduce or increase the ratio of radiative to non-radiative recombination.
- Ion migration may lead to PL quenching, enhancement or staying the same, depending on which recombination process changes more as ions migrate.
- Ion migration may lead to device performance improvement and degradation due to the same mechanism as for the PL enhancement and quenching.
- Ion migration is a possible reason for large ideality factors in perovskite solar cells.

Future Work

- Investigate perovskite devices at the module level.
- Investigate how ion migration can be incorporated into the present solar cell model.
- Investigate how perovskite diode ideality factors vary with ion migration.

References

GREEN, M. A., KEEVERS, M. J., CONCHA-RAMON, B.,JIANG, J., VERLINDEN, P.J., YANG, Y. & ZHANG, X. 2016. 37% Efficient One-Sun Minimodule and over 40% Efficient Concentrator Submodules, 32nd EU PVSEC. Munich, June 2016.

LAN, D. 2020. The physics of ion migration in perovskite solar cells: Insights into hysteresis, device performance, and characterization. *Progress in Photovoltaics: Research and Applications*, 28, 533-537.

LAN, D. & GREEN, M. A. 2014. Ideal solar cell equation in the presence of photon recycling. *Journal of Applied Physics*, 116, 174511.

LAN, D. & GREEN, M. A. 2018a. Pathways towards a 50% efficiency spectrum-splitting photovoltaic system: Application of built-in filters and generalization of concept. *Energy Procedia*, 150, 83-86.

LAN, D. & GREEN, M. A. 2018b. The potential and design principle for next-generation spectrum-splitting photovoltaics: Targeting 50% efficiency through built-in filters and generalization of concept. *Progress in Photovoltaics: Research and Applications*, 1-6.

LAN, D. & GREEN, M. A. 2018c. The potential and design principle for next-generation spectrum-splitting photovoltaics: Targeting 50% efficiency through built-in filters and generalization of concept. 35th EU PVSEC. Brussels, September 2018, 951-955.

LIN, Q., ARMIN, A., NAGIRI, R. C. R., BURN, P. L. & MEREDITH, P. 2015. Electro-optics of perovskite solar cells. *Nature Photonics*, 9, 106.

VURGAFTMAN, I., MEYER, J. & RAM-MOHAN, L. 2001. Band parameters for III–V compound semiconductors and their alloys. *Journal of Applied Physics*, 89, 5815-5875.

F11 NEW IMPURITY REMOVAL TECHNOLOGIES FOR LOW-COST, HIGH EFFICIENCY SILICON SOLAR CELLS

ACAP Fellow

Dr AnYao Liu, ANU

Academic Partners

Fraunhofer Institute for Solar Energy Systems, Germany: Dr Frank Feldmann

Leibniz University Hannover, Germany: Dr Jan Krügener

A/Prof Ziv Hameiri

Funding Support

ACAP

Aim

The aim of this project is to understand and develop new gettering technologies in silicon solar cells, namely gettering by dielectric films, and gettering by polysilicon-based passivating contacts.

Progress

Polysilicon-based passivating contacts can be fabricated, in a robust fashion, by a range of techniques (Schmidt et al. 2018). There are multiple ways to grow the thin SiO_x interlayer, to deposit the poly-Si film, and to dope and form the heavily doped poly-Si/SiO_x structure. These different techniques can induce very different impurity gettering effects (Liu et al. 2018a; Krügener et al. 2017; Hayes et al. 2019; Wang et al. 2020). To quantify and assess the different gettering effects, we prepared a range of poly-Si/SiO_x samples on intentionally Fe-contaminated silicon wafers, in collaboration with Fraunhofer-ISE and LUH. This will allow a direct comparison of the gettering effectiveness. An example is shown in Figure F11.1, which is only a subset of the test conditions.

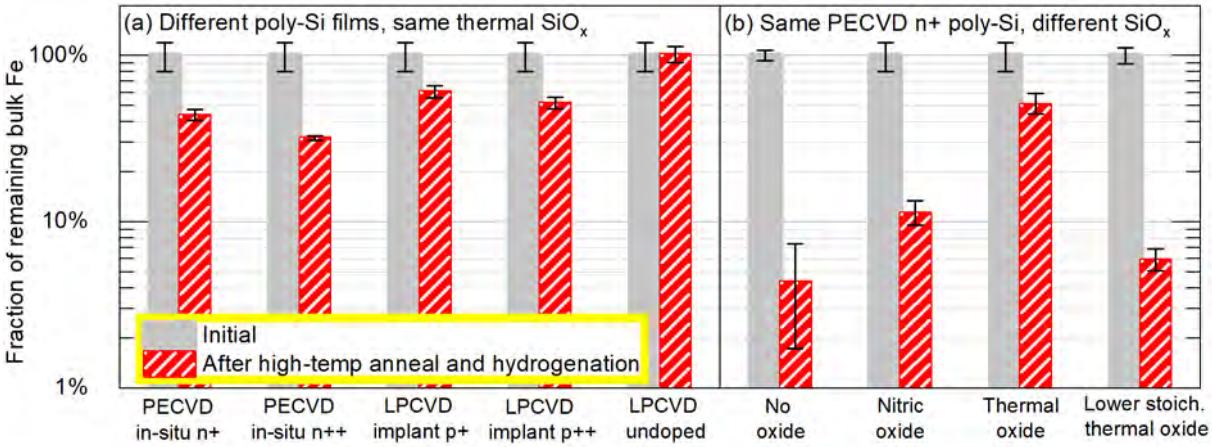

Figure F11.1: Fraction of the remaining impurity (iron in this case) concentration in the silicon wafer bulk after a typical poly-Si/SiO_x formation process (high temperature anneal and hydrogenation): (a) samples with different poly-Si films but the same thermal SiO_x interlayer; (b) samples with different SiO_x interlayers but the same PECVD in situ phosphorus-doped poly-Si film.

To further understand the different gettering effects and to enable predictive modelling of the gettering effect in the future, a new experimental approach was proposed and a simulation model was developed to separate and quantify the individual impact of each component on the overall gettering effect of the poly-Si/SiO_x structure. These components include the doped poly-Si layer, which acts as the main gettering region (Liu et al. 2018b); the thin SiO_x interlayer, which partially blocks impurity transport from the silicon wafer bulk to the poly-Si gettering layer (Liu et al. 2018a); and the dopant in-diffused silicon surface region directly beneath the SiO_x interlayer, which has a small gettering effect due to heavy doping. For the poly-Si/SiO_x samples shown in Figure F11.1(b), the findings in Figures F11.2 and F11.3 break down the whole structure and show the individual effect of the doped poly-Si layer (in terms of its gettering capability, as quantified by segregation coefficient) and the SiO_x interlayer (in terms of its blocking effect for impurity diffusion). The results also provide insights into the properties of ultrathin SiO_x layers, which seem to differ from thick SiO_2 with regard to impurity diffusion (Figure F11.3). A manuscript is in preparation to disseminate this new analysis method and model.

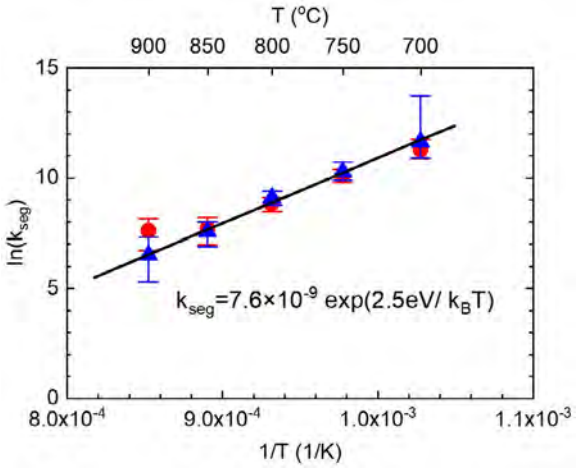

Figure F11.2: Temperature-dependent segregation coefficient of a PECVD in situ phosphorus-doped poly-Si film.

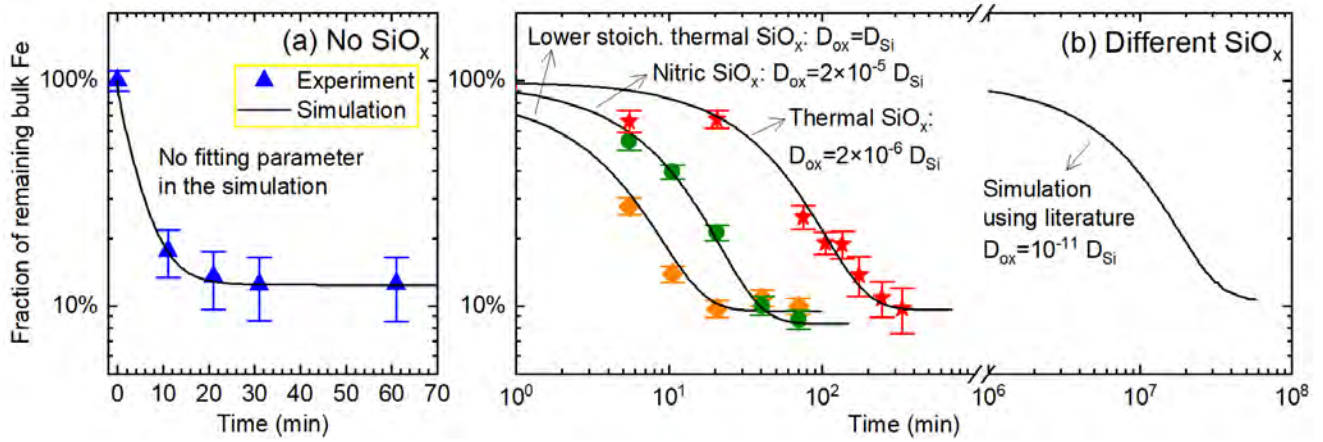

Figure F11.3: Gettering kinetics at 700°C, for samples with different SiO_x interlayers and the same PECVD in situ phosphorus-doped poly-Si film. Solid lines are simulation results, which enable us to quantify the different blocking effects of the SiO_x interlayers.

This project also aims to further our understanding of the gettering effects and mechanisms of silicon nitride (SiN_x) films. A detailed analysis of the gettering kinetics was carried out, for a range of SiN_x films, from laboratory- and industrial-scale PECVD and LPCVD. The gettering effect of LPCVD SiN_x at cell-processing temperatures (below 900°C) is illustrated and studied for the first time. Results confirm that SiN_x gettering occurs through a segregation mechanism, with different SiN_x films demonstrating different gettering capacities and rates, as shown in Figure F11.4. We further quantified the gettering capacities and extracted the activation energy for the segregation gettering process, as shown in Figure F11.5. To understand the different gettering rates, a model was proposed to reproduce the gettering kinetics, as shown in Figure F11.4. A manuscript is currently under preparation to report these new findings.

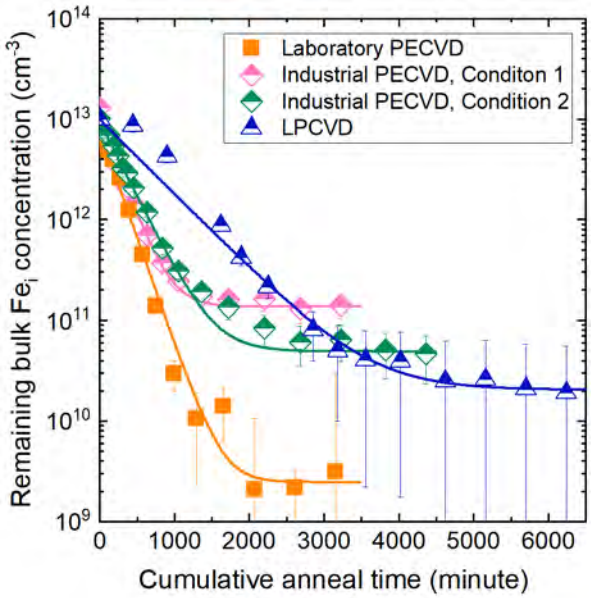

Figure F11.4: Gettering kinetics at 400°C for different SiN_x films. Solid lines are simulated kinetics, which provide new insights into the gettering process.

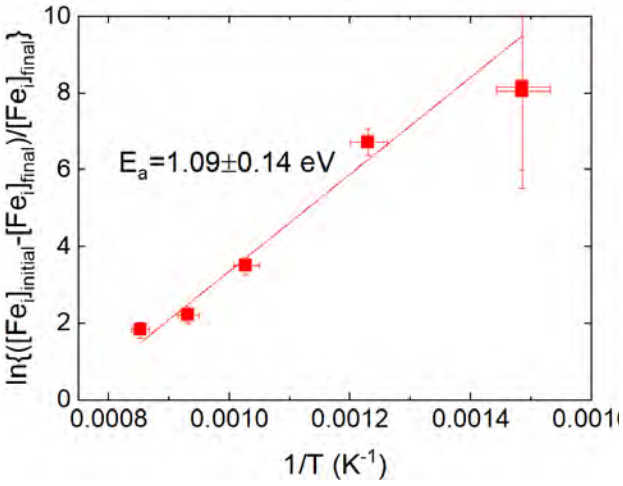

Figure F11.5: Temperature-dependent gettering capacities of a PECVD SiN_x film.

Due to much-reduced laboratory access this year (hailstorm and COVID), some efforts were diverted into preparing a comprehensive and updated review article on the topic of impurity gettering in silicon photovoltaics.

Highlights

- A new simulation model was developed to separately quantify the impact of each component on the overall gettering effect of doped poly-Si/SiO_x passivating contact structures. This will enable better predictive modelling of the gettering effect of poly-Si/SiO_x from different fabrication techniques.
- Diffusion of iron through different thin SiO_x layers was quantified and activation energies extracted.
- The mechanism of SiN_x gettering was identified, and the activation energy for the gettering process was estimated.
- The gettering effect of LPCVD SiN_x at low temperatures was demonstrated for the first time.
- A new model was proposed to explain the gettering kinetics of different SiN_x films.

Future Work

- Provide a direct experimental comparison of the different gettering effects of poly-Si/SiO_x passivating contact structures that are fabricated by a wide range of techniques. Demonstrate a simulation model to accurately reproduce the gettering results.
- Identify and investigate factors that hinder impurity diffusion through the thin SiO_x interlayer to reach the poly-Si gettering layer.
- Understand the gettering mechanisms and kinetics of ALD AlO_x films.
- Further investigate the effect of gettering on the passivation quality of ALD AlO_x films.
- Finalise a review article on impurity gettering in silicon solar cells.

References

HAYES, M., MARTEL, B., ALAM, G. W., LIGNIER, H., DUBOIS, S., PIHAN, E. & PALAIS, O. 2019. Impurity Gettering by Boron- and Phosphorus-Doped Polysilicon Passivating Contacts for High-Efficiency Multicrystalline Silicon Solar Cells. *physica status solidi (a),* 216, 1900321.

KRÜGENER, J., HAASE, F., RIENÄCKER, M., BRENDEL, R., OSTEN, H. J. & PEIBST, R. 2017. Improvement of the SRH bulk lifetime upon formation of n-type POLO junctions for 25% efficient Si solar cells. *Solar Energy Materials and Solar Cells,* 173, 85-91.

LIU, A., YAN, D., PHANG, S. P., CUEVAS, A. & MACDONALD, D. 2018a. Effective impurity gettering by phosphorus- and boron-diffused polysilicon passivating contacts for silicon solar cells. *Solar Energy Materials and Solar Cells,* 179, 136-141.

LIU, A., YAN, D., WONG-LEUNG, J., LI, L., PHANG, S. P., CUEVAS, A. & MACDONALD, D. 2018b. Direct Observation of the Impurity Gettering Layers in Polysilicon-Based Passivating Contacts for Silicon Solar Cells. *ACS Applied Energy Materials,* 1, 2275-2282.

SCHMIDT, J., PEIBST, R. & BRENDEL, R. 2018. Surface passivation of crystalline silicon solar cells: Present and future. *Solar Energy Materials and Solar Cells,* 187, 39-54.

WANG, Z., LIU, Z., LIAO, M., HUANG, D., GUO, X., RUI, Z., YANG, Q., GUO, W., SHENG, J., SHOU, C., YAN, B., YUAN, Z., ZENG, Y. & YE, J. 2020. Effective gettering of in-situ phosphorus-doped polysilicon passivating contact prepared using plasma-enhanced chemical-vapor deposition technique. *Solar Energy Materials and Solar Cells,* 206, 110256.

F13 MULTISCALE AND DEPTH-RESOLVED SPECTRAL PHOTOLUMINESCENCE FOR CHARACTERISING SOLAR CELLS

Lead Partner

ANU

ANU Team

Dr Hieu Nguyen

Academic Partners

National Renewable Energy Laboratory (NREL), UNSW

NREL Team

Dr Mowafak Al-Jassim

UNSW Team

Prof. Thorsten Trupke

Funding Support

ACAP

Aim

The objective of this project is to develop a class of novel spectral photoluminescence (PL) mapping and imaging techniques to identify and characterise important properties of various materials and structures employed in photovoltaics (PV) with ultra-high spatial resolution.

Progress

A. Silicon

The first topic was to explore luminescence properties of doped polycrystalline silicon (poly-Si) films employed in passivating contact Si solar cells, and their applications to the development of high quality passivation films. In 2018, the ANU team found that their doped poly-Si films contained both amorphous and crystalline phases, each of which yielded distinct luminescence peaks at low temperatures (Figure F13.1). In 2019, they discovered that after high temperature diffusion processes to form the doped poly-Si films, most of the hydrogen content had effused out of the films, leaving them un-hydrogenated. Un-hydrogenated amorphous Si (a-Si) contained a very high density of non-radiative defects, yielding no PL signal. Once hydrogenated, the a-Si:H phase emitted a strong PL peak in which the intensity was proportional to the hydrogen content inside the films. Tracking the a-Si:H PL emission, the team could study the effectiveness and mechanisms of various hydrogenation techniques on different poly-Si films. Their findings and the various applications of their method were reported in a series of four journal papers (Nguyen et al. 2018; Truong et al. 2019a and b; Truong et al. 2020a). Also, the work in Truong et al. 2020a was selected as an issue frontispiece.

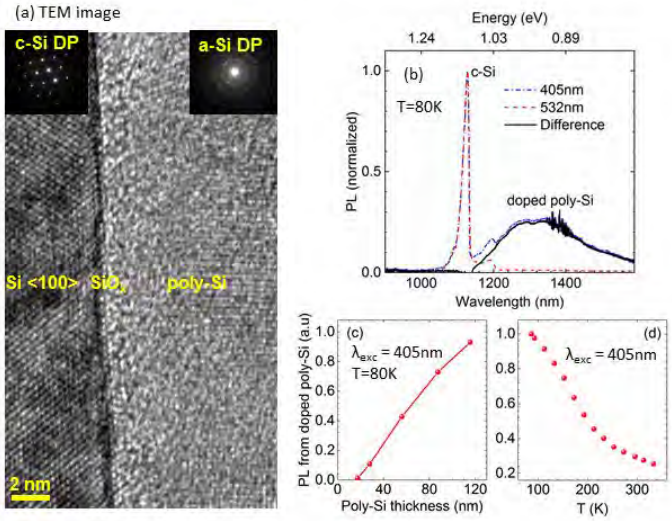

Figure F13.1: (a) Cross-sectional transmission electron microscope (TEM) image of a phosphorus-doped poly-Si/SiO_x/c-Si structure reveals both amorphous and crystalline phases in the poly-Si layer. (b) Normalised PL spectra with various excitation wavelengths at 80K. (c) Integrated PL intensity from poly-Si films versus their thicknesses. (d) Temperature dependence of the poly-Si film's PL intensity.

In 2020, the team combined the PL-based method with various optical and microscopy techniques to unlock the structural and optoelectronic characteristics of ex-situ boron-doped poly-Si/SiO_x passivating contacts, formed from sputtered intrinsic a-Si deposited at different pressures on top of SiO_x/c-Si substrates and subjected to a high temperature boron diffusion step. They found that the deposition rate and density of the as-deposited a-Si films increased with reducing pressure. Low temperature PL spectra captured from the as-deposited

samples at different pressures did not show typical emissions from hydrogenated a-Si. Meanwhile, their Fourier-transform infrared absorption spectra all showed Si–H stretching modes, indicating that hydrogen had been initially incorporated into the chemical SiO_x layers and eventually hydrogenated the a-Si/SiO_x interfaces during the sputtering process. After the high temperature boron-diffusion step, all hydrogen-related peaks disappeared. The team also found that lower pressure films (1.5 and 2.5 mTorr) showed more consistent improved performance after hydrogen treatments, compared to higher pressure films (4 and 5 mTorr). The resultant passivating contacts at 2.5 mTorr achieved a low single-side recombination current density J_0 of ~9 fAcm^{-2}, whereas their contact resistivity was still low at 15 mΩ cm^2. These results were then published in *Solar Energy Materials and Solar Cells* (Truong et al. 2020b).

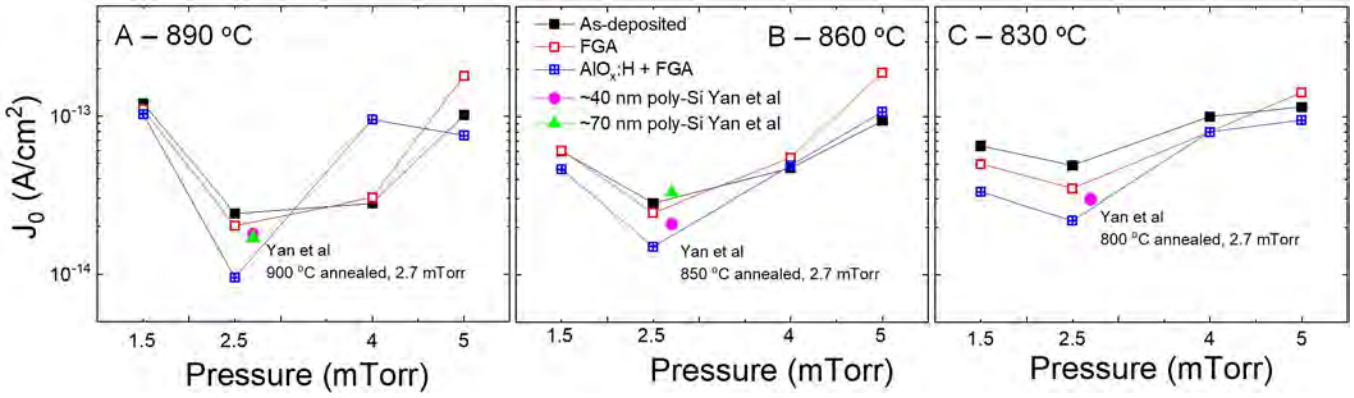

Figure F13.2: Recombination current density J_0 of different poly-Si samples diffused at 890 (A), 860 (B) and 830 (C)°C, with various a-Si deposition pressures, and before and after hydrogen treatments. The J_0 was measured using a quasi-steady state photoconductance (QSSPC) technique. Reference J_0 results from Yan et al. (Appl. Phys. Lett. 2018, 113, 061603) for in-situ boron doped samples with the poly-Si layer thicknesses of ~40 and ~70 nm, sputtered at 2.7 mTorr and annealed at 800, 850 and 900°C, are also given. The legends are the same for all figures.

The second topic was to develop a PL-based technique to determine dopant profiles of localised boron-diffused regions in c-Si wafers and solar cell precursors. It was fast, contactless and non-destructive. The measurements could be performed at room temperature with micron-scale spatial resolution. The technique employed relative changes in PL spectral shape between two different excitation wavelengths to extract the doping profiles. The ANU team applied the technique to reconstruct dopant profiles of a large-area boron-diffused sample (Figure F13.3a) and heavily doped regions (30 µm in diameter) of passivated emitter rear locally (PERL) diffused solar cell precursors (Figure F13.3b). The reconstructed profiles were confirmed with the well-established electrochemical capacitance voltage (ECV) technique. The developed technique helped quickly determine boron dopant profiles in small doped features employedin c-Si solar cells. This work was published in *Scientific Reports* (Nguyen et al. 2019).

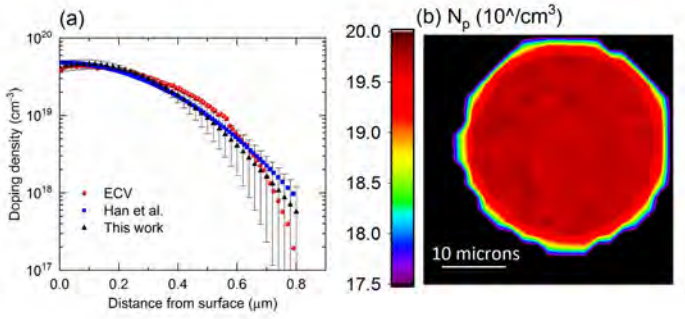

Figure F13.3: (a) Comparison between the ECV measured and reconstructed dopant profiles by Han et al.'s method (IEEE JPV 2017, 7, 1693-1700) and this work of a large-area boron-diffused region in a c-Si wafer. (b) Peak doping density N_D map of a localised p+ region in a PERL solar cell precursor, determined by the µ-PLS method at room temperature.

B. Perovskites

The first topic was to develop a fast, non-destructive, camera-based method to capture optical bandgap images of perovskite solar cells (PSCs) with micron-scale spatial resolution. This imaging concept utilised well-defined and relatively symmetrical band-to-band luminescence spectra emitted from perovskite materials, whose spectral peak locations coincided with absorption thresholds and thus represented their optical bandgaps. The technique was employed to capture relative variations in optical bandgaps across various PSCs, and to resolve optical bandgap inhomogeneity within the same device due to material degradation and impurities. Degradation and impurities were found to both cause optical bandgap shifts inside the materials. The team confirmed their results with other independent optical-based techniques including absorption and PL spectroscopy.

As an example, the team applied the technique to investigate the implications of PSC instability on the optical bandgap by measuring a PSC degraded after a long period of storage in a nitrogen environment without humidity control (>2 months). Figure F13.4(a) and F13.4(b) show electroluminescence (EL) intensity and extracted optical bandgap images of this solar cell, respectively. From the figure, the edge region severely degraded and the perovskite optical bandgap energy decreased around the cell edges. The bandgap non-uniformity was confirmed by the μ-photoluminescence spectroscopy (μ-PLS) map in Figure F13.4(c). A combination of two images (F13.4(a) and F13.4(b)) allowed the team to relate the material optical bandgaps to EL intensities, as shown in Figure F13.4(d). The degraded signal was strongly correlated with the optical bandgap shift. However, this optical bandgap shift was not obvious until the cell had been severely degraded (more than one order of magnitude reduction in EL intensities).

This new method could also provide information on the mechanisms of degradation taking place under various conditions (temperature, voltage, light, storage, etc.) across a broad type of samples, from large-area PSCs to cell precursors. For example, the optical bandgap variation should relate to a change in material composition. However, in Figure F13.4(d), the EL intensity reduction does not necessarily correlate to the optical bandgap variation unless the sample is severely degraded. As EL emission can be strongly affected by the current injection (and extraction) efficiency, the initial degradation suggests that the interface between the perovskite layer and the transport layer and/or the transport layers themselves are likely to be degraded before the absorber during the storage. Therefore, combining both luminescence intensity and optical bandgap images could be useful for the study of how the degradation happens (e.g. in the absorber or at interfacial layers). This research was published in *Advanced Energy Materials* (Chen et al. 2019) and selected as an issue's back cover.

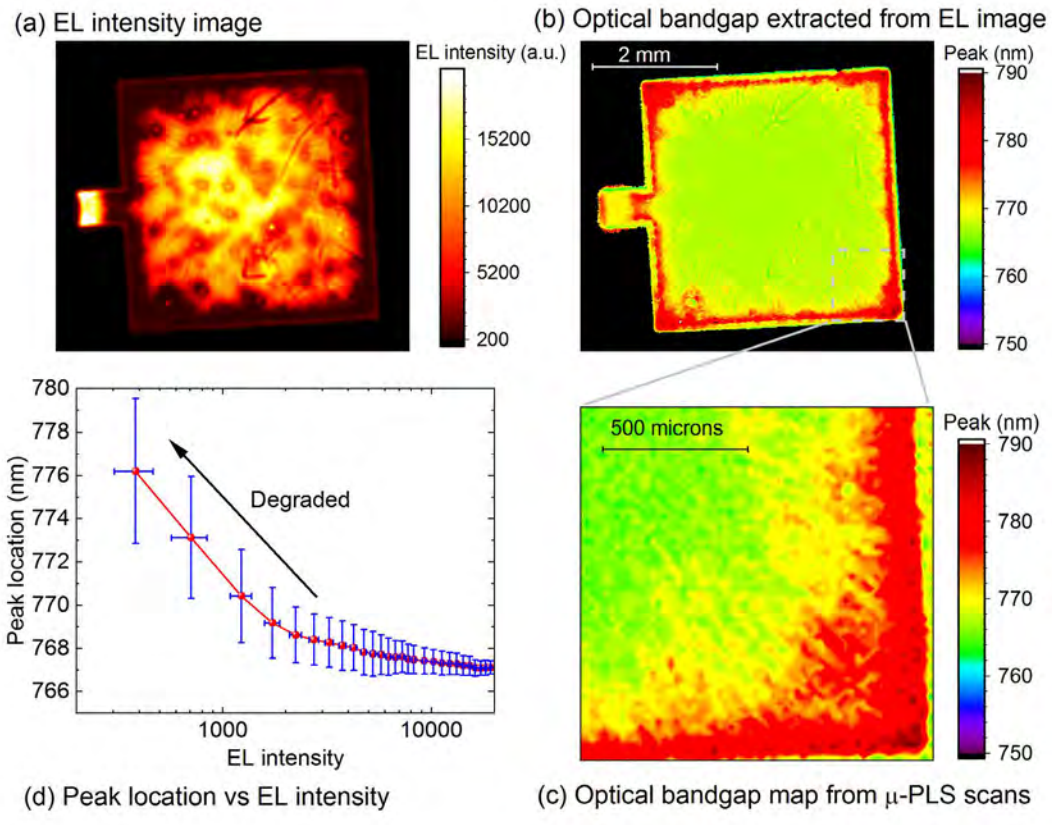

Figure F13.4: (a) EL intensity image of a degraded perovskite solar cell. (b) Extracted optical bandgap image from the EL intensity image. (c) Optical bandgap map extracted from μ-PLS scans, confirming the results from the EL-imaging method. (d) Peak locations (i.e. optical bandgaps) versus EL intensities.

The second topic was to develop a contactless, non-destructive approach to study early degradation across perovskite and perovskite/silicon tandem solar cells. The technique employed spectrally and spatially resolved absorptivity at sub-bandgap wavelengths of perovskite materials, extracted from their PL spectra, as shown in Figure F13.5. Parasitic absorption in other layers, carrier diffusion, and photon smearing phenomena were all demonstrated to have negligible effects on the extracted absorptivity. The absorptivity was demonstrated to reflect real degradation in the perovskite film and was much more robust and sensitive than its PL spectral peak position, representing its optical bandgap, and intensity. The technique was applied to study various common factors which induced and accelerated degradation in PSCs including air and heat exposures and light soaking. Also, it was employed to extract the individual absorptivity component from the perovskite layer in a monolithic perovskite/silicon tandem structure. The results demonstrated the value of this approach for monitoring degradation mechanisms in perovskite and perovskite/silicon tandem cells at early stages of degradation and various fabrication stages. This research was published in *Advanced Energy Materials* (Nguyen et al. 2020) and selected as an issue's inside back cover.

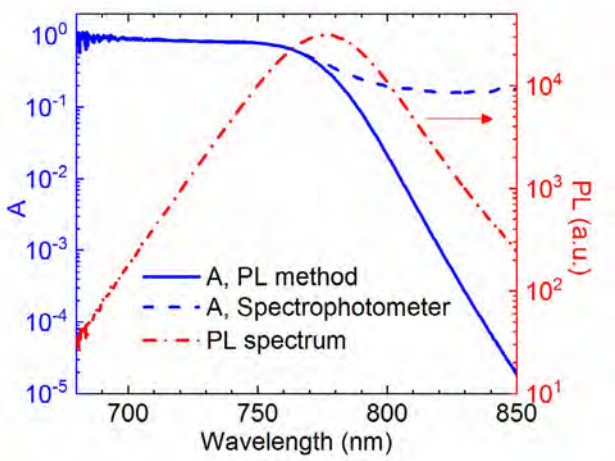

Figure F13.5: Comparison of spectrophotometer-based and PL-based absorptivity spectra. The spectrophotometer-based curve was captured at the centre of a PSC with a spot size of ~2 mm in diameter. The PL-based curve was averaged from the centre of a PL map (2 mm × 2 mm).

As an example, Figure F13.6 shows evolutions of PL intensities, spectral peak locations (i.e. approximate optical bandgaps), and absorptivity at various wavelengths from a PSC left at room condition (~25°C, 35% ± 15% relative humidity). The sub-bandgap absorptivity map (row 4) clearly shows that the air slowly invaded the solar cell through the edge of the gold contact when the cell was exposed in the atmosphere. Various localised degraded regions can also be observed, as indicated by the white circles (row 4, absorptivity at 800 nm). Both the edges and localised regions display similar evolutions with time. Therefore, the localised spots must have been affected by the air exposure over time due to pinholes on the gold contact as this is the only way that air can penetrate the locations without passing across the edge.

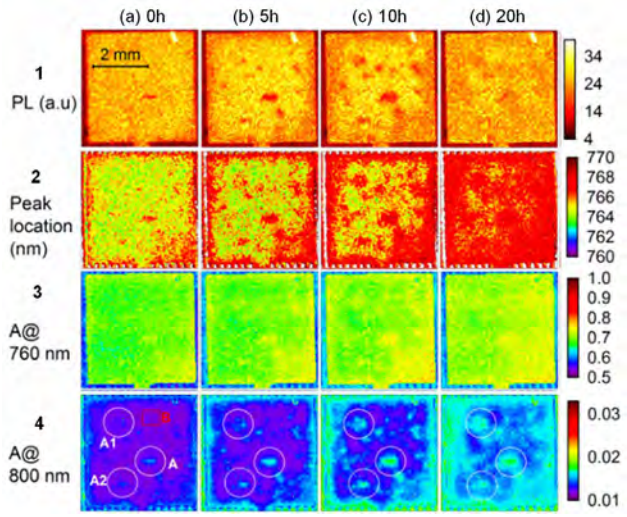

Figure F13.6: PL intensity, spectral peak location and extracted absorptivity maps of a perovskite solar cell versus exposure time in a room atmospheric environment.

C. 2D Materials

The first topic was to calculate the potential of two-dimensional (2D) transition metal dichalcogenides (TMDs) for solar cells. 2D TMDs are currently receiving some attention for photovoltaic applications due to their very strong light-matter interaction, atomic thickness and naturally occurring surface passivation. Also, there has been a rapid improvement in their large-scale material processing capability and quality. This signals that in the next few years, large-area (millimetres to centimetres) solar cells based on TMDs could be fabricated. Therefore, it is crucial to understand and quantify the potential of these future solar cells using experimental and/or theoretical means in early days.

By quantifying light absorbed and emitted from the TMDs, the ANU team developed a method to predict the possible open circuit voltages (V_{oc}) that could be achieved from TMD-based solar cells, at the material stage. The team applied the technique to quantify the upper limits of V_{oc} that could possibly be achieved from monolayer WS_2, MoS_2, WSe_2 and $MoSe_2$-based solar cells, and compared them with other thin-film technologies. Their results showed that V_{oc} values of ~1.4, ~1.12, ~1.06 and ~0.93 V could be potentially achieved from solar cells fabricated from WS_2, MoS_2, WSe_2 and $MoSe_2$ monolayers at one-sun illumination, respectively, as shown in Figure F13.7. The results suggested that the requirements of high-voltage, flexibility, ultralight, transparency and stability for future solar cells were possible with 2D TMDs. More significantly, the established limits could be a reference for future works on fabricating TMD-based photovoltaic devices.

The team also observed that the predicted V_{oc} values were inhomogeneous across different regions of these monolayers. Therefore, they attempted to engineer the observed V_{oc} heterogeneity by electrically gating the TMD monolayers in a metal-oxide-semiconductor (MOS) structure which effectively changed the doping level of the monolayers electrostatically and improved their V_{oc} heterogeneity (Figure F13.8). These preliminary results demonstrated

that indeed both the predicted V_{oc} and its homogeneity could be manipulated by the doping levels inside monolayer TMDs. This work was published in *Advanced Materials* (Tebyetekerwa et al. 2019) and selected as an issue's frontispiece.

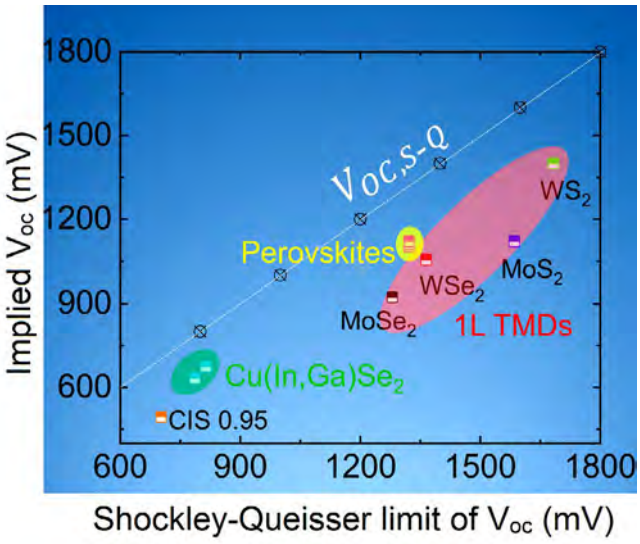

Figure F13.7: 2D TMD-based solar cells could potentially yield high voltages, very competitive to other thin film technologies.

The second topic was to develop a class of air-stable vertical organic-inorganic (O-I) heterostructures comprising of a monolayer of TMDs, including WS_2, WSe_2 and $MoSe_2$, on top of tetraphenylethylene (TPE) core-based aggregation-induced emission (AIE) molecular rotors. This glass of O-I heterostructures presented synergistic and enhanced optoelectronic properties with a high tunability. The created O-I heterostructures yielded a PL enhancement of up to ~950%, ~500% and ~330% in the top monolayer WS_2, $MoSe_2$ and WSe_2 as compared to PL in their pristine monolayers, respectively. The strong PL enhancement was mainly attributed to the efficient photo-generated carrier process in the AIE luminogens (courtesy of their restricted intermolecular motions in the solid state) and the charge transfer process in the created type-I O-I heterostructures. Moreover, they observed an improvement in photovoltaic properties of the TMDs

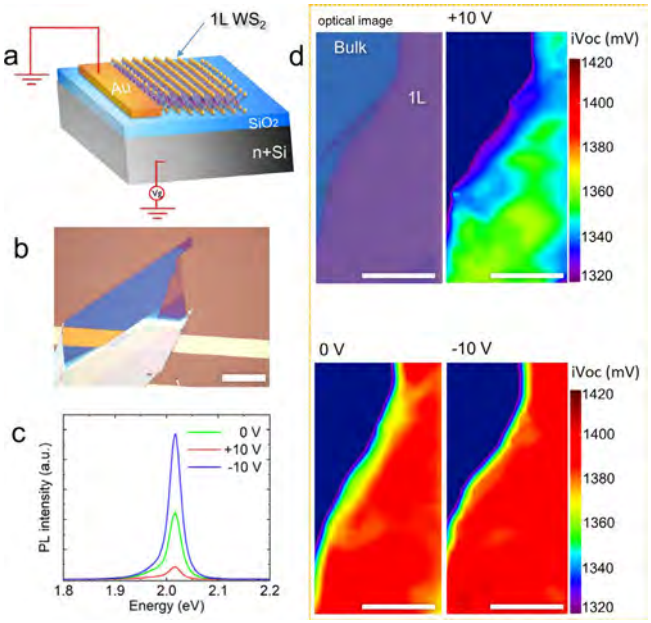

Figure F13.8: Effects of electrical gating on predicted V_{oc} of the monolayer WS_2. (a) Schematic assembly of the monolayer-based MOS structure with electrical connections. (b) Optical microscope image of the analysed monolayer on the MOS setup (scale bar 50 µm). (c) Photoluminescence spectra obtained from the monolayer WS_2 with back gate voltages of -10, 0 and +10 V. (d) The corresponding mapping of predicted V_{oc} across the monolayer WS_2 (scale bar 10 µm).

in the heterostructures including the quasi-Fermi level splitting Δµ, minority carrier lifetime and light absorption (Figure F13.9). This work presented an inspiring example of combining stable, highly luminescent AIE-based molecules, with rich photochemistry and versatile applications, with atomically thin inorganic semiconductors for multifunctional and efficient optoelectronic devices. The results were published in *ACS Nano* (Tebyetekerwa et al. 2020a).

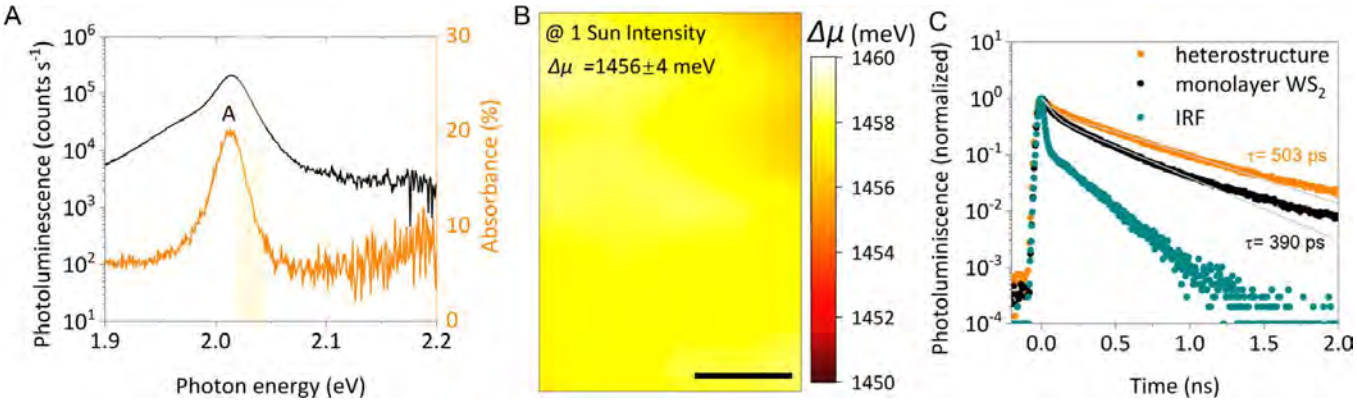

Figure F13.9: Photovoltaic properties of the AIEgen-WS_2-based O-I heterostructure. (A) Representative PL and absorption spectra from the heterostructure at room temperature. Using the generalised Planck law, the quasi-Fermi level splitting Δµ under excitation can be extracted. "A" denotes the A-excitonic peak. (B) The resultant Δµ map of an AIEgen-WS_2 heterostructure-based solar cell. The scale bar is 2.5 um. (C) Lifetime measurements of the heterostructure and pristine WS_2 regions, excited with a 522-nm femto-second laser.

Highlights

- Poly-Si films contained both amorphous and crystalline phases, each of which yielded distinct luminescence peaks at low temperatures. Luminescence from the amorphous Si phase in poly-Si films could be used to track the hydrogen content inside the films. Various applications were reported.
- Development of a fast, contactless, non-destructive luminescence-based method to extract boron doping profiles of localised heavily doped regions in silicon solar cells at room temperature.
- Development of a fast bandgap imaging method for process monitoring and degradation studies in perovskite solar cells.
- Development of a spectrally and spatially resolved absorptivity mapping method to study early degradation in perovskite and perovskite/silicon tandem solar cells.
- 2D TMDs could yield very high implied open circuit voltages of more than 1V, and could be engineered by doping to improve their uniformity and implied open circuit voltages.
- Development of a class of air-stable vertical organic-inorganic heterostructures comprising of a monolayer of TMDs on top of tetraphenylethylene core-based aggregation-induced emission molecular rotors.
- Publication of eleven high-quality journal papers (three as first-author and eight as last-author). Four of them were the journal feature articles (Chen et al. 2019; Nguyen et al. 2020; Tebyetekerwa et al. 2019; Truong et al. 2020a).
- Nine oral presentations delivered by Dr Hieu Nguyen at international conferences (2019a, b; 2019a–e; 2020a, b).

Summary

The project has been completed. The knowledge and techniques developed from the project are being employed by researchers at the ANU and UNSW to understand and optimise photovoltaic devices across various technologies. The project has also fortified the solid, strategic, long-term collaboration among the three world-class solar characterisation teams – ANU, NREL (Dr Mowafak Al-Jassim, principal scientist) and UNSW (Professor Thorsten Trupke) with numerous joint journal publications, conference presentations and successful grants.

References

c HEN, B., PENG, J., SHEN, H., DUONG, T., WALTER, D., JOHNSTON, S., AL-JASSIM, M. M., WEBER, K. J., WHITE, T. P., CATCHPOLE, K. R., MACDONALD, D. & NGUYEN, H. T. 2019. Imaging Spatial Variations of Optical Bandgaps in Perovskite Solar Cells. *Advanced Energy Materials*, 9, 1802790.

Nguyen, H. T 2018a. Characterizing heavily-doped regions in Si solar cells with spectral photoluminescence. 7th World Conference on Photovoltaic Energy Conversion, Hawaii, June 2018.

Nguyen, H. T 2018b. Luminescence from poly-Si films and its applications in Si PV. 5th Asia-Pacific Solar Research Conference, Sydney, December 2018.

NGUYEN, H. T. 2019a. Luminescence from poly-Si films and its applications in Si PV. 46th IEEE Photovoltaic Specialists Conference, Chicago, June 2019.

NGUYEN, H. T. 2019b. Imaging spatial variations of optical bandgaps in perovskite solar cells. 46th IEEE Photovoltaic Specialists Conference, Chicago, June 2019.

NGUYEN, H. T. 2019c. Luminescence from poly-Si films and its applications in Si PV. 29th International Photovoltaic Science and Engineering Conference, Xi'an, November 2019.

NGUYEN, H. T. 2019d. Imaging spatial variations of optical bandgaps in perovskite solar cells. 29th International Photovoltaic Science and Engineering Conference, Xi'an, November 2019.

NGUYEN, H. T. 2019e. Luminescence from poly-Si films and its applications in Si PV. 6th Asia-Pacific Solar Research Conference, Canberra, December 2019.

NGUYEN, H. T. 2020a. Spectral Luminescence: Science and Applications in Silicon Photovoltaics. 37th European Photovoltaic Solar Energy Conference and Exhibition, Lisbon, September 2020.

NGUYEN, H. T. 2020b. Recent Progress in the Characterization of PV Materials (silicon, perovskite, tandem, and 2D materials). 7th Asia-Pacific Solar Research Conference, Melbourne, December 2020.

NGUYEN, H. T., LIU, A. Y., YAN, D., GUTHREY, H., TRUONG, T. N., TEBYETEKERWA, M., LI, Z. Y., LI, Z. F., AL-JASSIM, M. M., CUEVAS, A. & MACDONALD, D. 2018. Sub-Bandgap Luminescence from Doped Polycrystalline and Amorphous Silicon Films and Its Application to Understanding Passivating-Contact Solar Cells. *ACS Applied Energy Materials*, 1, 6619-6625.

NGUYEN, H. T., LI, Z. F., HAN, Y. J., BASNET, R., TEBYETEKERWA, M., TRUONG, T. N., WU, H. T., YAN, D. & MACDONALD, D. 2019. Contactless, nondestructive determination of dopant profiles of localized boron-diffused regions in silicon wafers at room temperature. *Scientific Reports*, 9, 1-8.

NGUYEN, H. T., GERRITSEN, S., MAHMUD, M. A., WU, Y. L., CAI, Z. Y., TRUONG, T., TEBYETEKERWA, M., DUONG, T., PENG, J., WEBER, K., WHITE, T. P., CATCHPOLE, K. & MACDONALD, D. 2020. Spatially and Spectrally Resolved Absorptivity: New Approach for Degradation Studies in Perovskite and Perovskite/Silicon Tandem Solar Cells. *Advanced Energy Materials*, 10, 1902901.

TEBYETEKERWA, M., ZHANG, J., LIANG, K., DUONG, T., NEUPANE, G. P., ZHANG, L. L., LIU, B. Q., TRUONG, T. N., BASNET, R., QIAO, X. J., YIN, Z. Y., LU, Y. R., MACDONALD, D. & NGUYEN, H. T. 2019. Quantifying Quasi-Fermi Level Splitting and Mapping its Heterogeneity in Atomically Thin Transition Metal Dichalcogenides. *Advanced Materials*, 31, 1900522.

TEBYETEKERWA, M., CHENG, Y., ZHANG, J., LI, W., LI, H., NEUPANE, G. P., WANG, B., TRUONG, T. N., XIAO, C., AL-JASSIM, M. M., YIN, Z., LU, Y., MACDONALD, D. & NGUYEN, H. T. 2020a. Emission Control from Transition Metal Dichalcogenide Monolayers by Aggregation-Induced Molecular Rotors. *ACS Nano,* 14, 7444-7453.

TEBYETEKERWA, M., ZHANG, J., XU, Z., TRUONG, T. N., YIN, Z., LU, Y., RAMAKRISHNA, S., MACDONALD, D. & NGUYEN, H. T. 2020b. Mechanisms and Applications of Steady-State Photoluminescence Spectroscopy in Two- Dimensional Transition-Metal Dichalcogenides. *ACS Nano*, 14, 14579-14604.

TRUONG, T. N., YAN, D., SAMUNDSETT, C., BASNET, R., TEBYETEKERWA, M., LI, L., KRERNER, F., CUEVAS, A., MACDONALD, D. & NGUYEN, H. T. 2019a. Hydrogenation of Phosphorus-Doped Polycrystalline Silicon Films for Passivating Contact Solar Cells. *ACS Applied Materials & Interfaces*, 11, 5554-5560.

TRUONG, T. N., YAN, D., SAMUNDSETT, C., LIU, A. Y., HARVEY, S. P., YOUNG, M., DING, Z. T., TEBYETEKERWA, M., KREMER, F., AL-JASSIM, M., CUEVAS, A., MACDONALD, D. & NGUYEN, H. T. 2019b. Hydrogen-Assisted Defect-Engineering of Doped Poly-Si Films for Passivating Contact Solar Cells. *ACS Applied Energy Materials*, 2, 8783-8791.

TRUONG, T. N., YAN, D., CHEN, W. H., TEBYETEKERWA, M., YOUNG, M., AL-JASSIM, M., CUEVAS, A., MACDONALD, D. & NGUYEN, H. T. 2020a. Hydrogenation Mechanisms of Poly-Si/SiOx Passivating Contacts by Different Capping Layers. *Solar RRL*, 4, 1900476.

TRUONG, T. N., YAN, D., CHEN, W., WANG, W., GUTHREY, H., AL-JASSIM, M., CUEVAS, A., MACDONALD, D. & NGUYEN, H. T. 2020b. Deposition Pressure Dependent Structural and Optoelectronic Properties of Ex-situ Boron-Doped Poly-Si/SiOx Passivating Contacts Based on Sputtered Silicon. *Solar Energy Materials and Solar Cells*, 215, 110602.

F14 OVERCOMING THE MATERIAL LIMITATIONS OF CAST-GROWN MULTICRYSTALLINE AND MONO-LIKE SILICON FOR HIGH EFFICIENCY SOLAR CELLS

ACAP Fellow

Dr Hang Cheong Sio

Supervisor

Prof. Daniel Macdonald

Funding Support

ACAP Fellowship

Academic and Industrial Partners

Jinko Solar

Fraunhofer Institute for Solar Energy Systems AF Simulations

Aims

The objective of this project is to provide a holistic assessment of the material quality, cell potential, and stability of different types of cast-grown silicon materials, including both p-type and n-type high performance multicrystalline silicon (HP mc-Si) and mono-like Si, and correspondingly develop solutions to improve the efficiency and reliability of solar cells from a material perspective.

Progress

A. Light and elevated temperature induced degradation (LeTID)

An extensive study has been performed to evaluate LeTID behaviours in various types of silicon materials, including cast-grown Si (HP mc-Si and mono-like Si), Cz-Si materials grown by Jinko Solar, and FZ-Si materials, for both p-type and n-type. It was found that LeTID can be observed on different materials, and their occurrence depends heavily on the processing conditions, in particular the PECVD SiN_x deposition conditions, the diffusions and the firing profile. Our key experimental findings are summarised below.

- P-type materials suffer a higher degradation extent than their n-type counterparts, whereas mono-like Si wafers degrade more severely than FZ-Si samples (Figure F14.1(a)).
- LeTID activities are triggered by the rapid cooling after the firing process, with minimal degradation detected on samples fired with slow ramp down rate (Figure F14.1(b)).
- Degradation is found to be affected by diffusions, with the phosphorus-diffused sample showing the lowest degree of degradation compared to the non-diffused and boron-diffused samples (Figure F14.1(c)).
- Maximum degradation magnitude correlates strongly with the refractive index of the SiN_x films, measured using ellipsometry (Figure F14.1(d)).

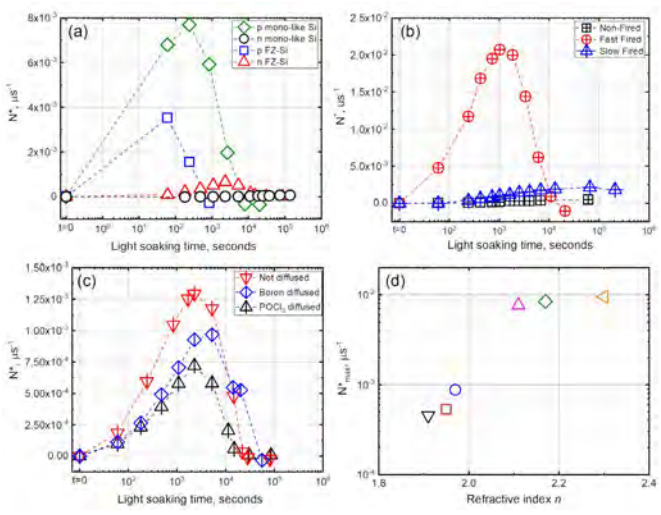

Figure F14.1: (a) Evolution of normalised defect density (N) during light soaking for various Si materials. (b) Evolution of normalised N* during light soaking for p-type mono-like Si samples fired with different cooling profiles. (c) Evolution of N* during light soaking for n-type mono-like Si samples with and without receiving phosphorus or boron diffusions. (d) Relationship between N* at the maximum degradation stage (N^*_{max}) and the refractive index n of the SiN_x films. N* is calculated as* $N^* = 1/\tau_{eff}(t) - 1/\tau_{eff}(t = 0)$.

Based on the experimental data acquired, a model is developed to describe the LeTID behaviours. In our model, as illustrated in Figure F14.2, it is proposed that hydrogen atoms originally bound in the SiN_x layer are released into the Si bulk above a certain firing temperature, which then interact with some other species in the Si bulk under illumination, causing the LeTID degradation. During the cooling ramp of the firing process or extended annealing, hydrogen in the Si bulk starts to out-diffuse into the ambient, altering the amount of hydrogen remaining in the Si bulk. The amount of hydrogen remaining in the Si bulk, and the resulting LeTID behaviour, then depends on the properties of the dielectric films, the peak firing temperature, the cooling rate, the sample thickness, the diffusion treatments, and dopant type, which govern the balance between in-diffusion and effusion of hydrogen.

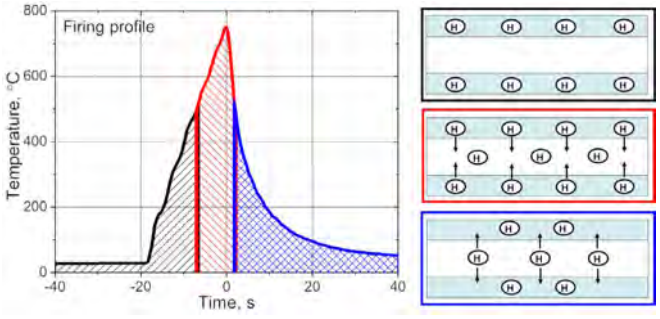

Figure F14.2: Proposed model correlating LeTID, firing and hydrogen.

B. Defect passivation with fluorine

While the benefits of hydrogenation are known in solar cell fabrication for improving interfaces and bulk quality, hydrogen does not always fully passivate the recombination activities, and as shown above, an excess amount of hydrogen in the silicon bulk can lead to LeTID. This project investigates the use of fluorine as an alternative passivating agent for defects in silicon, through annealing the sample with a thin thermally evaporated fluoride overlayer.

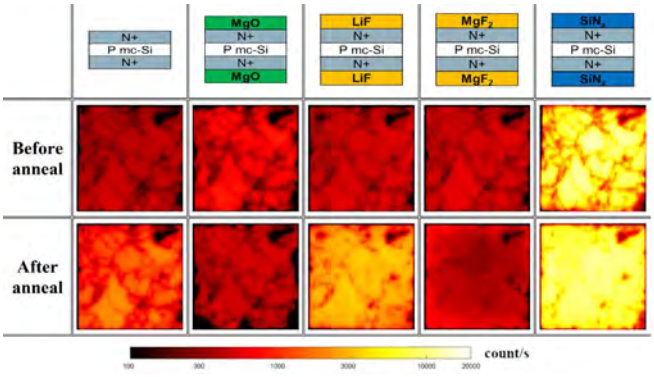

Figure F14.3: PL images of sister mc-Si wafers coated with MgO, LiF, MgF_2 or SiN_x, before and after a 5-minute annealing at 600°C. A logarithmic scale is used for the PL intensity. The images were taken at around 0.85-sun excitation condition.

Figure F14.3 shows PL images of sister mc-Si wafers coated with MgO, LiF, MgF_2 or SiN_x, before and after a 5-minute annealing at 600°C in a nitrogen ambient. The samples feature different surface films with different surface passivation quality, and hence the PL images should only be used for qualitative comparison. Most of the GBs were recombination active after phosphorus diffusion. The GBs remained recombination active on the samples annealed without any coating or with MgO. In contrast, annealing the samples coated with LiF and MgF_2 resulted in the deactivation of GBs, with a similar passivation extent as the hydrogenated SiN_x-coated sample. It is believed that the observed passivation effect is caused by fluorination, given the fact that the passivation was observed in a sample coated with MgF_2, but not seen in a sample coated with MgO, where both films were evaporated with the same tool in the same chamber. The involvement of hydrogen, unintentionally introduced into the samples during annealing or film deposition, can also be excluded given that no passivation effect was observed in the uncoated and MgO-coated control samples.

Our results demonstrate the potential of fluorine for passivating defects and interfaces in silicon. Although the detail of the fluorination mechanism remains unclear, it is possible that the passivation mechanism is different from hydrogenation, given the distinct electronic properties of fluorine and hydrogen such as their charge state distribution and electronegativity. Hence, it might be possible to use fluorine to complement hydrogenation to yield a better overall defect passivation effect. For example, fluorination might be useful for passivating dislocation clusters in mc-Si and mono-like Si where hydrogen passivation is found to be less effective.

Highlights

- Propose a LeTID model correlating LeTID with the properties of the dielectric films, the peak firing temperature, the cooling rate, the sample thickness, the diffusion treatments and the dopant type.
- Develop a method to incorporate fluorine into silicon bulk and interfaces for defect passivation.

Future Work

- Explore other applications for fluorination to improve solar cell performance.

F15 DEVICE ARCHITECTURE DESIGN FOR COMMERCIAL KESTERITE SINGLE-JUNCTION AND MULTI-JUNCTION SOLAR CELLS

Lead Partner

UNSW

UNSW Team

Dr Kaiwen Sun, Prof. Martin Green, A/Prof. Xiaojing Hao, Dr Jialiang Huang, Dr Chang Yan, Xin Cui, Heng Sun, Ao Wang

Academic Partner

Nanyang Technological University (NTU): A/Prof. Lydia Helena Wong

Funding Support

ACAP

Aim

The objective of this project is to develop the specific device architecture for Cu_2ZnSnS_4 (CZTS) solar cells to enhance the device performance. The project planned to optimise the optical design of the window/buffer layer, conduct interface engineering of the heterojunction and explore Cd free buffer alternatives.

Progress

Device simulation for guiding the architecture design of CZTS solar cells

A complete 2D device model in Sentaurus TCAD was initially constructed and then was used to evaluate the J-V and EQE characteristics of our fabricated CZTS devices to understand the loss mechanism. A variety of optical and electrical characterisation (such as EBIC, CV, PL, TRPL, ellipsometry, J-V, EQE, TEM) were employed to extract empirical parameters (Gokmen et al. 2014). This, together with other parameters from literature, formed a complete materials library from which our model was constructed. The model was verified against actual device performance. Based on this model, the major V_{OC} loss mechanism of our fabricated CZTS solar cells was analysed (Pu et al. 2017). As shown in Figure F15.1, V_{OC} can be improved to 917 mV by reducing the heterojunction interface recombination velocity below 10 cm/s. This can be realised by optimising the conduction band offset of heterojunction and carrier concentration ratio between buffer and absorber layers. From modelling, further improvement in V_{OC} beyond 1000 mV could be achieved by reducing the bulk disorder.

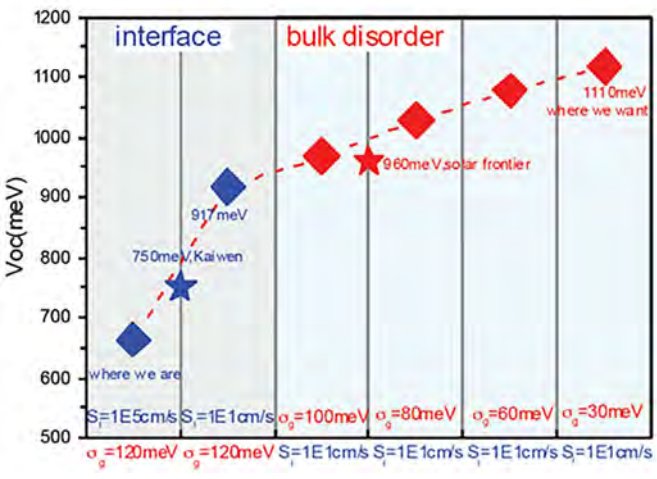

Figure F15.1: The impact of interface recombination velocity and bulk disorder on open circuit voltage of pure sulfide CZTS solar cells by device simulation.

In the ultimate device model as shown in Figure F15.2, heterojunction interface recombination, together with disorder induced bandgap fluctuation contributed to 97% of V_{OC} loss. Therefore, we identified these two as major bottlenecks of CZTS device V_{OC}. The simulation results provided theoretical guidelines for further improving the device performance of this project.

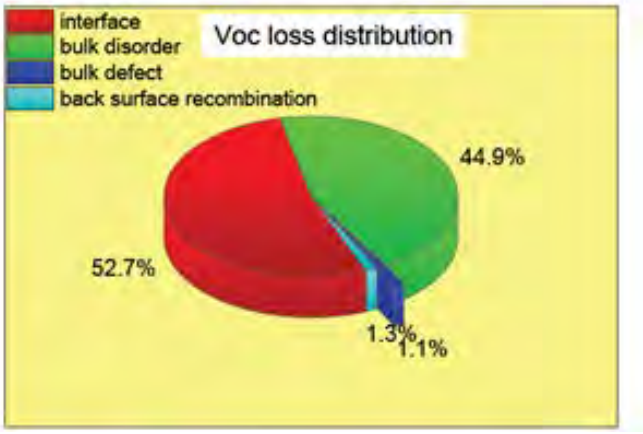

Figure F15.2: Fraction of V_{OC} loss pertains to mechanisms including heterojunction interface, bulk disorder, bulk deep level defects and back contact recombination parameterised into the device model. The V_{OC} loss is calculated comparing it to that of an ideal device without any loss mechanisms.

Post-annealing of the TCO layer for performance enhancement

As a transparent conductive oxide (TCO) electrode for thin-film solar cells, the performance of indium tin oxide (ITO) including conductivity, carrier concentration, mobility and transmittance can be affected by the oxygen vacancy, indium/tin ratio, and preparation conditions such as sputtering power, atmosphere, temperature, and so forth (Ishibashi et al. 1990). To further improve the quality of ITO thin film, we annealed ITO thin films under Ar atmosphere at different temperatures and the performance of ITO films was measured, as shown in Figure F15.3(a). Obviously, the carrier density, transmittance and mobility are greatly improved with increasing temperatures. In order to obtain the effect of annealed ITO on device performance, we carried out the post-annealing process on devices with ITO thin films, in which the whole devices (glass/Mo/CZCTS/CdS/ITO) were annealed at 25, 100, 200, 300 and 400°C for about 8 minutes under Ar atmosphere conditions. After post-annealing to a device with an ITO layer, the V_{OC} can be enhanced significantly with increasing annealing temperatures, as can be seen from Figure F15.3(b), and the V_{OC} enhancement caused by the increase of carrier density of the ITO film can be calculated. However, the increase of calculated V_{OC} is far less than the increase of experimentally measured V_{OC}, which indicates that there are other reasons besides ITO for the improvement of V_{OC} after post-annealing.

Nevertheless, via post-annealing (at 300°C) with the ITO layer, our optimised device yields an efficiency of 12.6% (active area efficiency), with V_{OC}, J_{SC} and FF of 640 mV, 27.8 $mA.cm^{-2}$, and 71%, respectively. The photovoltaic (PV) parameters and J-V curves of CZCTS thin-film solar cells with different post-annealing processes (devices 1, 2, and 3) are shown in Figure 15.3(c).

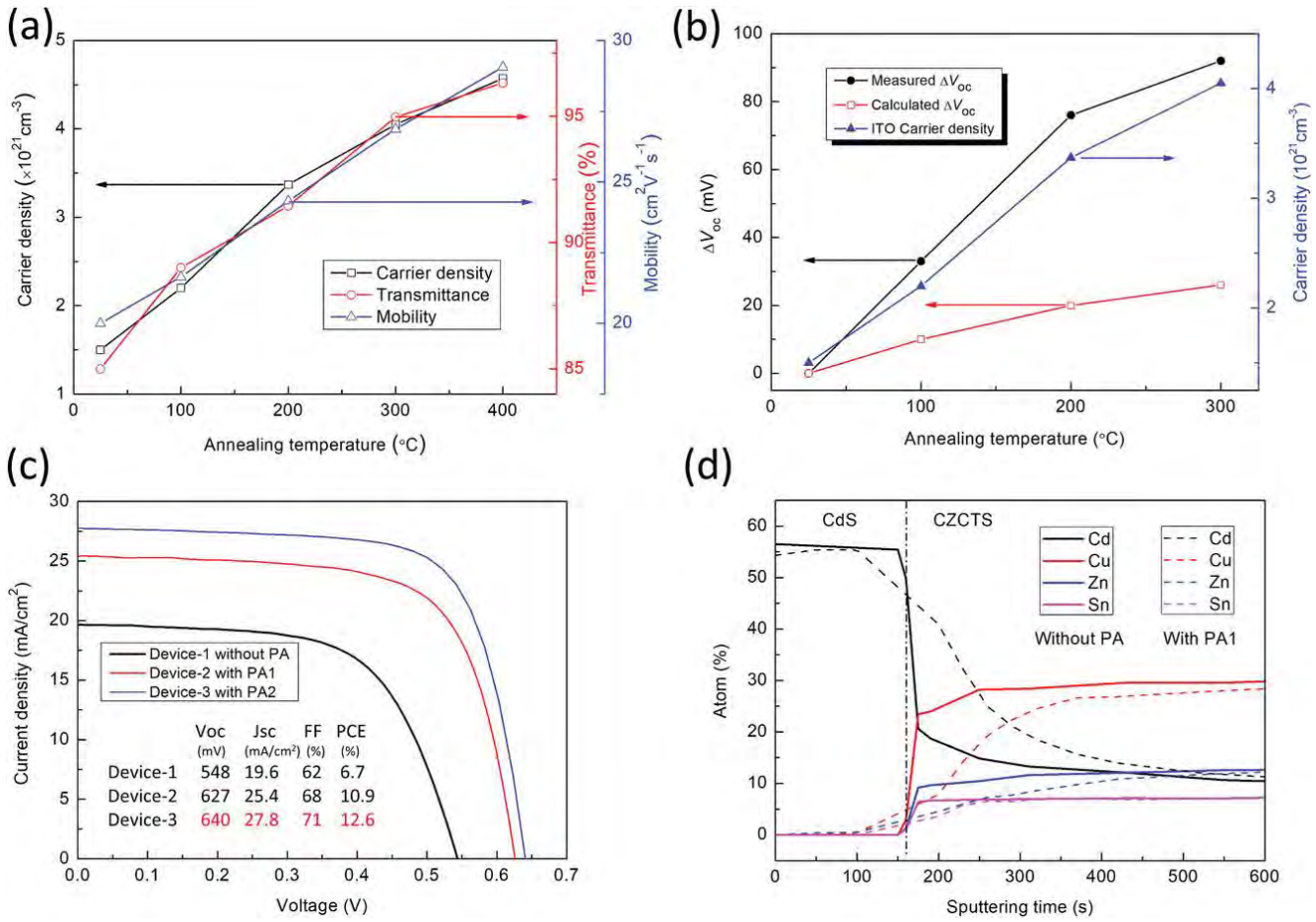

Figure F15.3: (a) The performance of ITO thin film with different annealing temperatures (the transmittance measured at wavelength of 555 nm). (b) Left: The measured and calculated V_{OC} variation (difference with the V_{OC} of device without post-annealing) as a function of annealing temperatures; right: the carrier density of ITO versus annealing temperatures. (c) The J-V curves for three CZCTS devices with different post-annealing processes (device-1 is prepared with the structure of Mo/CZC-TS/CdS/ITO and without any post-annealing; device-2 is prepared with post-annealing the structure of Mo/CZTS/CdS and then deposited with ITO thin film (PA1); device-3 is prepared with post-annealing the structure of Mo/CZTS/CdS/ITO (PA2)). (d) XPS elemental profiling of CdS/CZCTS heterojunctions without and with post-annealing (device-1 and device-2).

One of the main purposes of annealing the entire device (with ITO) is to promote the interdiffusion of elements between layers in CZTS devices. As can be seen from Figure F15.3(d), XPS results can show the significant difference of elemental diffusion for devices without post-annealing and with PA1. In the layer of CdS, little up diffusion of elements from CZTS, such as Cu, Zn and Sn, can be observed upon PA1 and PA2 post-annealing. This means that within the heterojunction region, Cu, Zn and Sn are slightly increased in the CdS layer, while reduced in the CZTS side except for Cd. As for Zn, after PA1 annealing, it can be found that Zn diffuses obviously from the CZTS side to the CdS side, but after PA2 annealing, the content of Zn in the CdS side is reduced while there is a little increase on the CZTS side. As a result of the element diffusion, the interfacial electron and hole densities are improved, leading to the achievement of a suitable band alignment for carrier transport. The post-annealing also reduces the interface traps and deep-level defects, contributing to decreased non-radiative recombination.

Highlights

- Device loss mechanism simulation provides theoretical guidelines for further improving the device performance.
- The post-annealing of the complete device improves the properties of the ITO layer and promotes the element diffusion, enhancing the device performance.

Future Work

- Further optimisation of the architecture of the device according to the simulation results.
- Exploration of an alternative Cd free buffer layer for CZTS solar cells.
- Investigation of additional doping in ZnCdS buffers to improve the device performance.

Reference

GOKMEN, T., GUNAWAN, O. & MITZI, D. B. 2014. Semi-empirical device model for Cu2ZnSn(S,Se)4 solar cells. *Applied Physics Letters*, 105, 033903.

ISHIBASHI, S., HIGUCHI, Y., OTA, Y. & NAKAMURA, K. 1990. Low resistivity indium–tin oxide transparent conductive films. I. Effect of introducing H2O gas or H2 gas during direct current magnetron sputtering. *Journal of Vacuum Science & Technology* A, 8, 1399-1402.

PU, A., MA, F., YAN, C., HUANG, J., SUN, K., GREEN, M. & HAO, X. 2017. Sentaurus modelling of 6.9% Cu2ZnSnS4 device based on comprehensive electrical & optical characterization. *Solar Energy Materials and Solar Cells*, 160, 372-381.

F16 COMPREHENDING CHARGE TRANSPORT IN PEROVSKITE-SILICON TANDEM SOLAR CELLS

ACAP Fellow

Daniel Walter

Supervisor

Prof. Klaus Weber

Funding Support

ACAP

Aim

This project aims to develop the theoretical foundation for the interpretation of optoelectronic measurements of perovskite and perovskite-tandem solar cells.

Progress

This project has continued to explore the fundamental optoelectronic properties of perovskite semiconductors, with a focus on how ionic movement can manifest in measurements of perovskite materials and solar cells (PSCs), and the implications for cell behaviour, design and optimisation. This project is capped by a co–first author publication in *Science* (Peng et al. 2021), which employed the most self-consistent set of numerical simulations yet described for PSCs to identify optimal geometries for a nanostructured local contact PSC in support of a new world record for a 1 x 1 cm PSC.

But to begin, there are fundamental questions as to the origin of hysteresis in perovskite-based devices: is it intrinsic to the perovskite material or does it emerge through interaction with transport layers? Time series characterisation of the spatial distribution of luminescence intensity of bare perovskite films suggests that hysteresis is indeed intrinsic (Figure F16.1) (Walter et al. 2018). As showed earlier in this project, the characteristic of this transient photoluminescence intensity (or the electrochemical potential of the film) follows directly from ion migration moderating non-radiative recombination (Schubert et al. 2020). These experiments thus show that ion migration will occur upon illumination. Numerical modelling discounted the Dember effect as insufficient to drive this migration, suggesting a role instead for changing charge states of interface traps, or potentially a light-induced generation of ions. Regardless, the data shows the challenge in quantified analysis of luminescence intensity from perovskite films. Intensity can vary with time and space, and in the egregious example presented below, can demonstrate an inversion of the heterogeneity over longer time periods (Figure F16.1(f)).

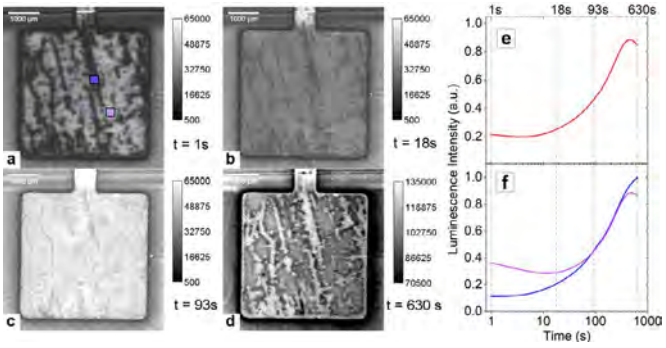

Figure F16.1: Photoluminescence intensity images on a bare $MAPbI_3$ perovskite film at time equal to 1 s (a), 18 s (b), 9 3s (c) and 630 s (d). The mean intensity across the cell area (e) demonstrates the extent of the hysteresis in the photoluminescence intensity, while (f) illustrates how initially low-emission regions (blue) can eventually exceed high-emission regions (magenta) after longer periods.

Returning to cell-level behaviour, numerical simulations explored the recovery of a PSC following a period of reverse bias. This analysis pointed towards a potentially serious negative-feedback loop: a transiently shaded cell can remain pinned in reverse bias if the recovery of the photocurrent after returning to forward bias is sufficiently slow (Figure F16.2) (Qian et al. 2020). Ionic accumulation at voltages below the built-in potential (V_{bi} typically around 0.8 V for common transport layer combinations) can amplify non-radiative recombination currents, likely at or near the transport layer interfaces (Qian et al. 2020). This is the explanation for the archetypical JV hysteresis in which reverse voltage sweeps are more efficient than forward sweeps. Following reverse bias, the ions migrate slowly back to the forward bias steady state and photocurrent increases comparably slowly. If the photocurrent diminishment is beyond a certain threshold, the cell can be returned to reverse bias, in a potentially destructive cycle. Given that results in Figure F16.1 suggest that hysteresis is intrinsic to the perovskite material, reverse bias tolerance in PSCs will be vital to reliable long-term yields.

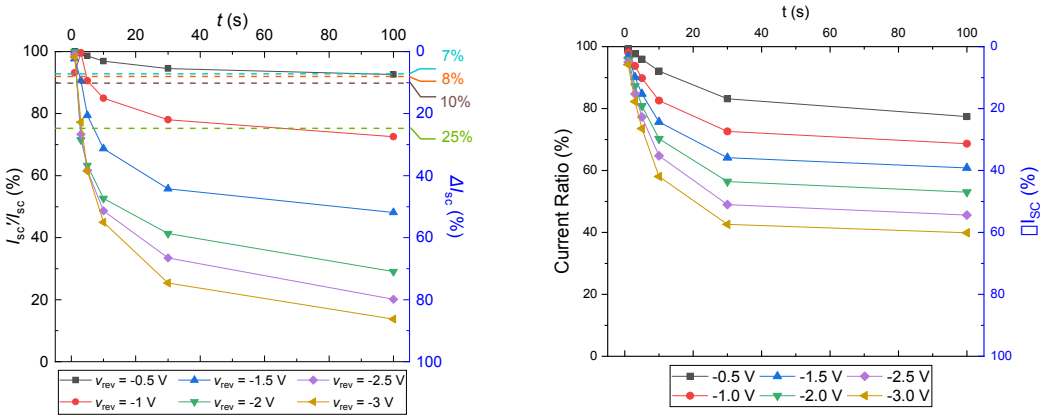

Figure F16.2: Photocurrent ratio following periods of reverse bias at increasing voltage and time. Experimental data (left) agrees closely with the simulation results (right) suggesting that "standard" hysteresis (as opposed to "inverted" hysteresis) could be correlated with slow recovery from reverse bias, with significant implications for long-term stability of PSC-based modules.

Finally, a major challenge in perovskite research is parameterising key material properties (such that we can predict eventual device performance). In silicon PV, it is taken for granted that a reliable, repeatable measurement (e.g. photoconductance decay) can quantify material properties for a silicon wafer, which in turn can predict the efficiency potential of the eventual solar cell. In a first step towards developing such a capability for perovskite research, this project developed simulation tools that (1) extracted bulk and interface defect parameters and charge carrier mobility from transient photoluminescence (TRPL) measurements (Figure F16.3); (2) used these parameters to quantify resistance at interface passivation layers based on performance from planar control cells; and (3) implemented these fits into a three-dimensional representation of a nanostructured solar cell to determine the optimal geometry (Figure F16.4). Cells fabricated with this optimal nanostructure achieved a world record efficiency for 1 x 1 cm PSCs, which was published in *Science* (Peng et al. 2021).

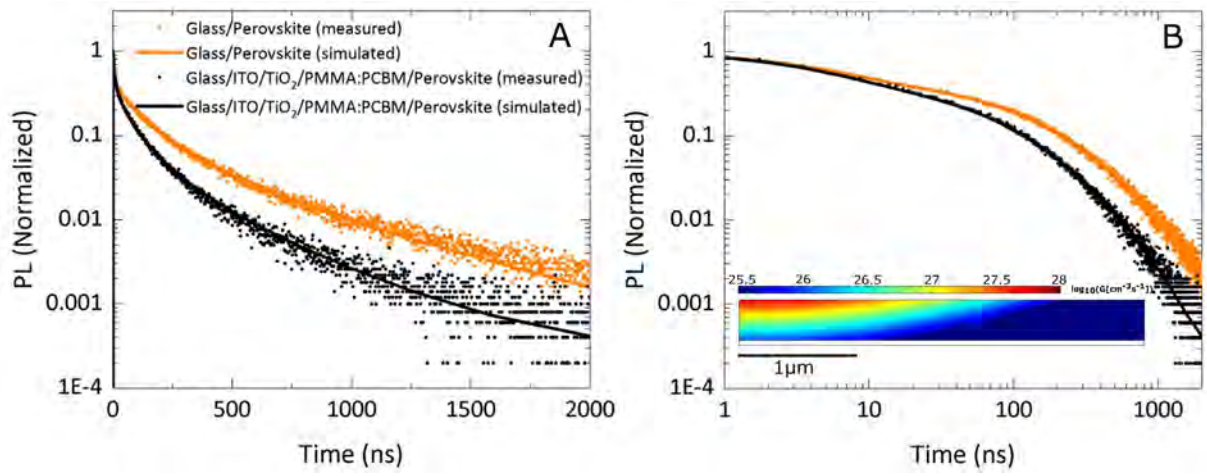

Figure F16.3: Experimental data (scatter plots) and simulated best-fits using time-dependent numerical simulation (solid line). The numerical model incorporates the fully generalised Shockley-Read-Hall recombination model, and dynamics of charge transport across interfaces. This produced close agreement across logarithmic time (right). Inset figure presents the model geometry showing photo-generation of the Gaussian laser pulse (in scale log10(G)), and the corresponding fits to experimental data in linear (left) and log10(t) scales (right).

This project also demonstrated the significant improvement in efficiency on PSCs using insulating passivation layers via local contacts. This approach is of course familiar to those working in high efficiency silicon PV, but charge carrier diffusion lengths in even the best perovskite materials are of the order of 1–5 µm, roughly 10^3 times smaller than diffusion lengths in high quality silicon wafers. Thus, the size of local contacts must be comparably smaller. Indeed, the local, periodic nanorods were only 50 nm in diameter (Figure F16.4(g)).

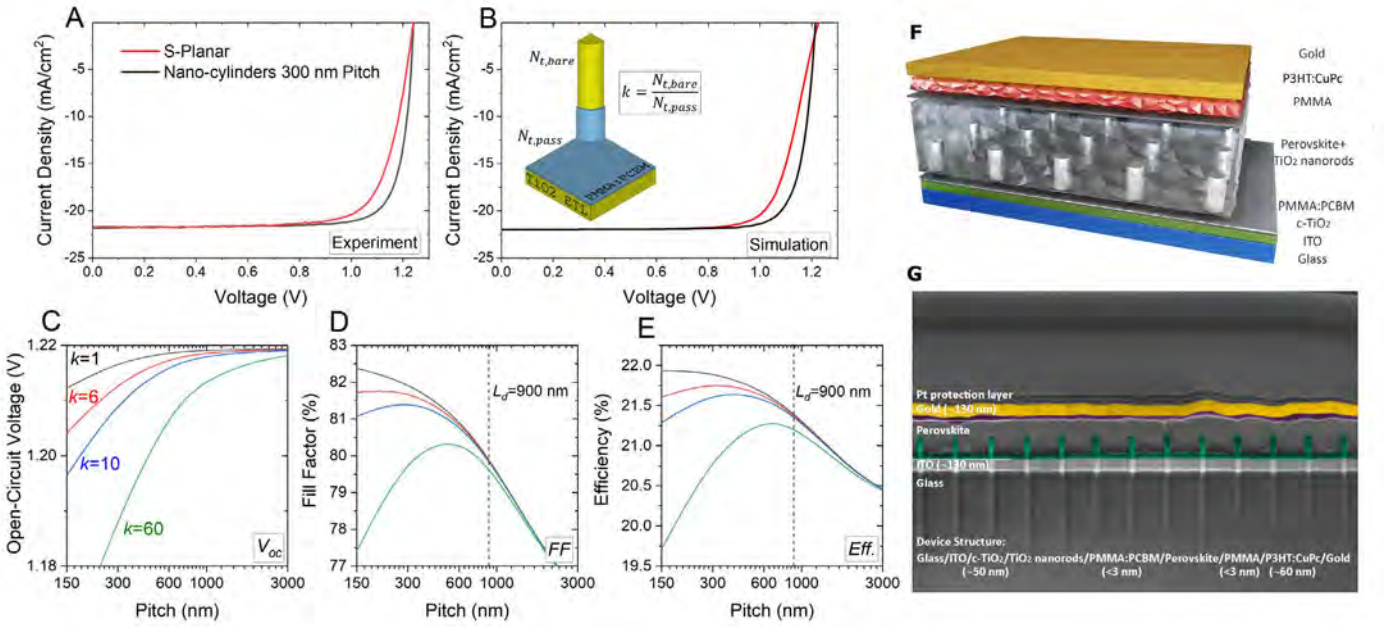

Figure F16.4: Comparison between experimental (a) and simulated (b) JV curves using a nanostructured TiO_2 electron transport layer as illustrated by the inset figure in (b). The influence of the contact geometry on V_{OC} (c), FF (d) and overall efficiency (e) was used to identify the optimal geometry. A schematic representation of the cell structure (f) and a cross-section electron microscope image (g).

Highlights

- Strong evidence now supports the conclusion that hysteresis, in its myriad forms, is fundamentally an expression of ion-mediated influence on non-radiative recombination. It is intrinsic to the perovskite film and will affect even the simplest of experimental measurements.
- The models demonstrate an inescapable conclusion: a period of reverse bias may temporarily diminish photocurrent from a perovskite cell in a fashion that keeps a cell trapped in reverse bias even after shading is removed. This can prolong the period of reverse bias with potentially catastrophic implications for the cells.
- A self-consistent set of device models demonstrated agreement with experiment from fundamental TRPL measurements on perovskite cell precursors, through to complex three-dimensional nanostructured devices. This is a first step in using material-level characterisation to predict final device performance. This analysis demonstrated that a novel nanostructured TiO_2 electrode was functioning as a local contact in a polymer passivation layer, pointing a way towards PSCs that exhibit high (passivated) V_{OC}, and fill factor.

Future Work

- Investigation will continue into the further methods of characterisation of perovskite materials that yield data predictive of eventual cell results. This will include capacitance-based measurements that are complicated by ion migration.
- Stability of PSCs under reverse bias will be of major importance in the future. Given the potential for increased RB exposure periods, resistance to destructive breakdown will be paramount.
- Work will continue to understand the fundamental mechanism driving ion migration in perovskite materials, and thus how it may be mitigated to improve stability of performance in the short, and long, terms.

References

PENG, J. & WALTER, D. et al. 2021. Nanoscale localized contacts for high fill factors in polymer-passivated perovskite solar cells. Science, 371, 390-395.

QIAN, H., ERNST, M. & WALTER, D., et al. 2020. Destructive reverse bias pinning in perovskite/silicon tandem solar modules caused by perovskite hysteresis under dynamic shading. *Sustainable Energy and Fuels*, 4, 4067-4075.

SCHUBERT, M. C., MUNDT, L. E., WALTER, D., FELL, A. & GLUNZ S. W. 2020. Spatially Resolved Performance Analysis for Perovskite Solar Cells. *Advanced Energy Materials*, 10, 1904001.

WALTER, D., FELL, A., WU, Y., DUONG, T., BARUGKIN, C., WU, N., WHITE, T. & WEBER, K. 2018. Transient Photovoltage in Perovskite Solar Cells: Interaction of Trap Mediated Recombination and Migration of Multiple Ionic Species. *Journal of Physical Chemistry C*, 122, 11270-11281.

F18 TOWARDS 20% EFFICIENCY CU_2ZNSNS_4 THIN-FILM SOLAR CELL BY DEFECT ENGINEERING AND BAND GRADING ENGINEERING

Lead Partner

UNSW

UNSW Team

Dr Chang Yan, Prof. Martin Green, A/Prof. Xiaojing Hao, A/Prof. Nicholas (Ned) Ekins-Daukes, Dr Jialiang Huang, Dr Kaiwen Sun, Mr Guojun He

Academic Partner

National Renewable Laboratories (NREL): Dr Steven Johnston

Funding Support

ACAP

Aim

Kesterite Cu_2ZnSnS_4 (CZTS), a non-toxic and Earth-abundant compound, has been considered as the most promising candidate for next generation cost-effective, environmentally friendly and stable photovoltaics. CZTS not only can be applied to building and vehicle integrated PV but also provides excellent promises as an upper cell candidate for kesterite/silicon tandem solar cells. The aim of this project is to increase the efficiency of CZTS solar cells through reducing the non-radiative recombination and V_{OC} deficit by using cation substitution and control the defects of CZTS via a modified annealing process.

Progress

The current bottleneck for CZTS development is well recognised to be the large V_{OC} deficit. Among many reported V_{OC} deficit contributing factors, the Sn-related defects are relatively deep level as well as the most detrimental ones according to first principles calculations (Chen et al., 2013). The oxidation state of Sn in precursor, either Sn^{2+} or Sn^{4+} was found to determine the reaction pathway for solution-processed CZTSSe (Gong et al., 2020). Sn^{4+} precursor facilitates the formation of CZTS in precursor, leading to compositional uniform absorber and higher device performance with the record lowest V_{OC} deficit for kesterite solar cells (Gong et al., 2020). Recently, Jianjun Li et al. (Li et al., 2020) reported the oxidation state of Sn is critical during initial formation of kesterite. This is because in this stage, the local environment during the formation of kesterite determines the defects state. Oxidation of Sn as Sn^{4+} is confirmed to effectively suppressing the detrimental intrinsic defects and activating the desirable shallow acceptor V_{Cu} (Li et al., 2020). The baseline process at UNSW currently uses sputtering followed by a sulfurisation two-stage process, which already enable 11% record efficiency for CZTS (Yan et al., 2018). However, the precursor in such record cell processing is composite of co-sputtered Cu/SnS/ZnS, in which the Sn precursor consists of an Sn^{2+} oxidation state. Hence, the focus for the current work is to investigate the effectiveness of Sn^{4+} in precursor and how it influences the CZTS solar cell efficiency.

The SnS_2 target (AJA International) was used as the Sn^{4+} source. The precursor is deposited by co-sputter Cu/SnS_2/ZnS simultaneously. The sulfurisation processes were carried out by using a Rapid Thermal Processor (AS-One 100) with combined sulfur and SnS. ZnSnO buffer layers were deposited by ALD approach in a Fiji G2 ALD system (Cambridge Nanotech). The deposition of ALD ZnSnO use of diethylzinc [$Zn(C_2H_5)_2$ DEZ, Sigma-Aldrich], tetrakis(diethylamido)tin(IV) [$Sn(N(CH_3)_2)_4$ or TDMASn, Strem Chemicals] as Zn, Sn precursor, and water as an oxidant, respectively. The Zn to Sn sub-cycles with a 3:1 ratio was employed, and the substrate temperature was kept at 150°C. A transparent front contact of i-ZnO/ITO (50 nm/210 nm) bi-layer was then deposited by radio frequency sputtering before Al grids were deposited using evaporation. A stainless-steel anti-template was used for the thermal evaporated Al patterning with a height of ~1.5 µm as the top contact for the device. The total area of the final cells is ~0.23 cm^2 defined by mechanical scribing.

Precursors with three different compositions were deposited with the corresponding metal ratios and are illustrated in Table F18.1. Cu-poor Cu/Sn ratios, in the range of 1.55~1.65, were adopted in this investigation. The Zn/Sn ratio was controlled closed to the stoichiometric ratio. The annealing processes were conducted at 560 °C for 3 minutes, with a ramping rate of 10 °C /minute which enables record CZTS, was initially use for sulfurisation (Yan et al., 2018). Then the corresponding CZTS solar cells were fabricated. Figure F18.1 illustrates the device performance parameter statistic box chart. The device with the highest precursor copper content (precursor A) demonstrates the highest V_{OC} in both average and peak value. The V_{OC} of the device with the lower Cu content (B and C) shows 10–20 mV lower than that of the device with the higher Cu content (sample A). The J_{SC} shows a clear negative trend with the copper content in precursors. Note that sample C with the lowest Cu content not only demonstrates a lower J_{SC} average value but also with a much wider distribution. In terms of FF, sample B with mediate copper content displays the higher average value, and sample C displays a deleterious FF. Consequently, sample A with a higher Cu content shows the highest efficiency with average of 6.9% and peak at 7.9%. Sample C with the lowest Cu content demonstrates a much lower average efficiency of 4.7% with a very large efficiency distribution, which indicates the slow sulfurisation of a low Cu content precursor led to inhomogeneity for CZTS film and corresponding device. This inhomogeneity may be due to the volatile SnS phase escaping from

the SnS_2 matrix precursor compound due to very slow ramping rate. The evaporated SnS would leave a large void at the bottom of the absorber with huge vertical and lateral random inhomogeneity. In order to reduce the possible decomposition of the SnS_2 precursor and resulting escape of SnS phases, a higher ramping rate is favoured and required.

Table F18.1: The composition for three CZTS precursors deposited by co-sputter Cu/SnS_2/ZnS. (ICP)

Precursor	Cn/Sn	Zn/Sn	Cu/(Zn+Sn)
A	1.62	1.05	0.79
B	1.59	1.05	0.78
C	1.55	1.03	0.76

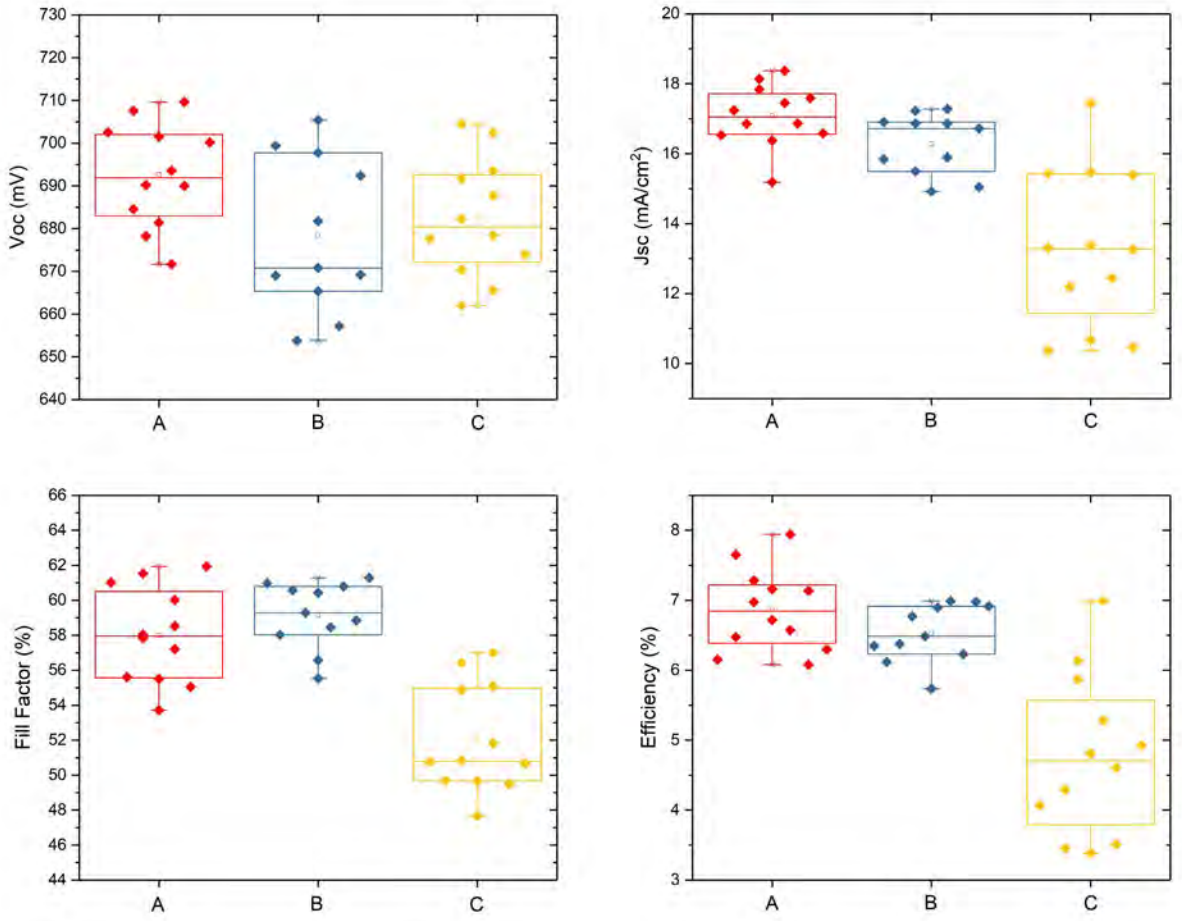

Figure F18.1: Statistical performance parameters of the CZTS devices with different precursor composition. The annealing processing was conducted at 560°C for 3 minutes with 10°C /minutes.

Then a faster ramping rate of 30°C /minute was utilised for the sulfurisation annealing process and solar cell devices were fabricated accordingly. The corresponding solar cell performance parameter statistics are shown in F18.2. To our surprise, the relationship of efficiency and Cu content with ramping rate of 30°C /minute is opposite to what we previously observed for the samples with 10°C /minute. All the efficiency performance parameters demonstrate a negative relationship with Cu content, which is, the higher Cu content, the lower device performance parameters. To be specific, the sample with the lower Cu content shows a slightly higher average V_{OC} with a narrowed distribution compared to a sample with a high Cu content. The boost of J_{SC} and FF is much more significant for the sample with a lower Cu content. The average J_{SC} and FF for sample C reach 19 $mAcm^{-2}$ and 61%, respectively. Finally, the efficiency illustrates a monotonous increase with the decrease of the Cu content, with peak average efficiency of 8.1% and peak efficiency of 8.6% without an MgF_2 anti-reflection coating. The tin sulfide phases would act as a protection layer to prevent defect formation at the surface, the sample with a lower Cu content would result in more tin sulfide generated at the surface of the sample during the sulfurisation annealing, preventing the surface decomposition and associated generated defects during the annealing process (Rudisch et al., 2020). At the final stage of CZTS these tin sulfides would evaporate at the surface of CZTS and help preserve a low-defect surface.

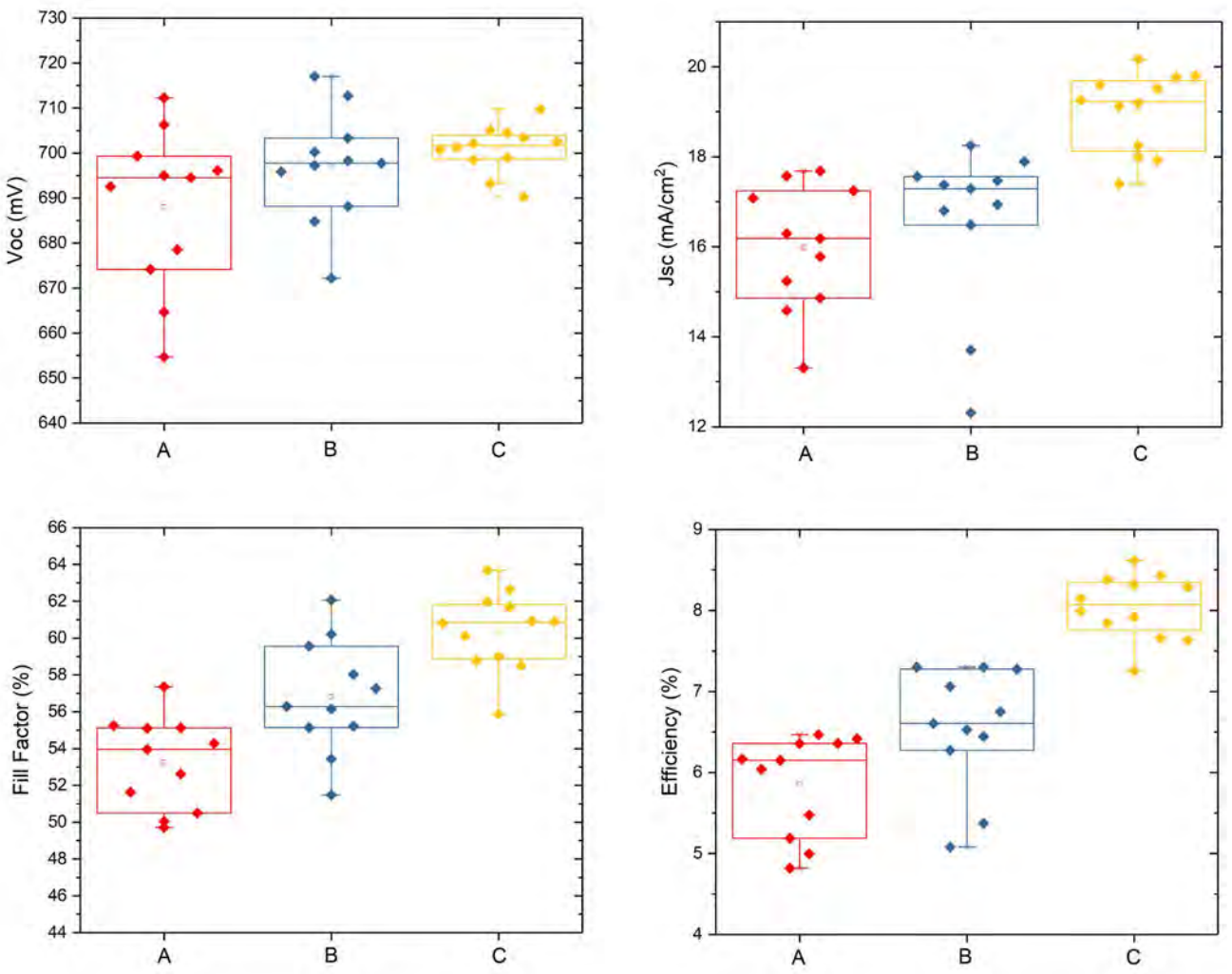

Figure F18.2: Statistical performance parameters of the CZTS devices with different precursor compositions. The annealing process was conducted at 560°C for 3 minutes with 30°C /minute.

After optimisation of the annealing process for the SnS_2 precursor, we compare the device performance between the Sn^{4+} precursor and Sn^{2+} precursor, as shown in Figure F18.3. Note that the annealing conditions (Sn^{2+} using 10 °C /minute ramping rate and Sn^{4+} using 30 °C /minute ramping rate) were used according to their own optimised processes. The V_{OC} for both the Sn^{2+} and Sn^{4+} precursors shows similar average V_{OC}, however, the distribution of Sn^{4+} precursor samples set demonstrates a narrower distribution, which indicates CZTS from the Sn^{4+} precursor should have a better lateral and vertical homogeneity than the device with the Sn^{2+} precursor. This homogeneity issue can be further confirmed by FF that the device with Sn^{4+} precursors demonstrates a higher overall FF than that with the Sn^{2+} precursors. Unlike V_{OC} and FF, the J_{SC} shows a large increment, around 2 $mAcm^{-2}$ increase, when swapping the precursor from Sn^{2+} to Sn^{4+}. Consequently, the average efficiency for the Sn^{4+} precursor set is 8.1% whereas that for the Sn^{2+}precursor set is 7.4%. Despite that the highest efficiency of 8.8% was achieved by using Sn^{2+} precursor, the overall/ average device performance for Sn^{4+} precursor set is 0.7% (absolute value) outperformed than that for Sn^{2+} precursor set.

In summary, Sn^{4+} precursor (SnS_2) has been used to synthesise CZTS film and fabrication of the corresponding device performance. A Cu-rich precursor demonstrates a better device performance by using normal/lower ramping rate during the sulfurisation annealing process whereas a Cu-poor precursor benefits from a higher ramping rate during the sulfurisation annealing process. After optimisation of the precursor composition and annealing condition, average efficiency of 8.1% has been achieved by using Sn^{4+} precursors, which is higher than that by using Sn^{2+} precursors. These results show the effectiveness by using Sn^{4+} precursors and its potential need to be further explored by further optimisation of annealing processes.

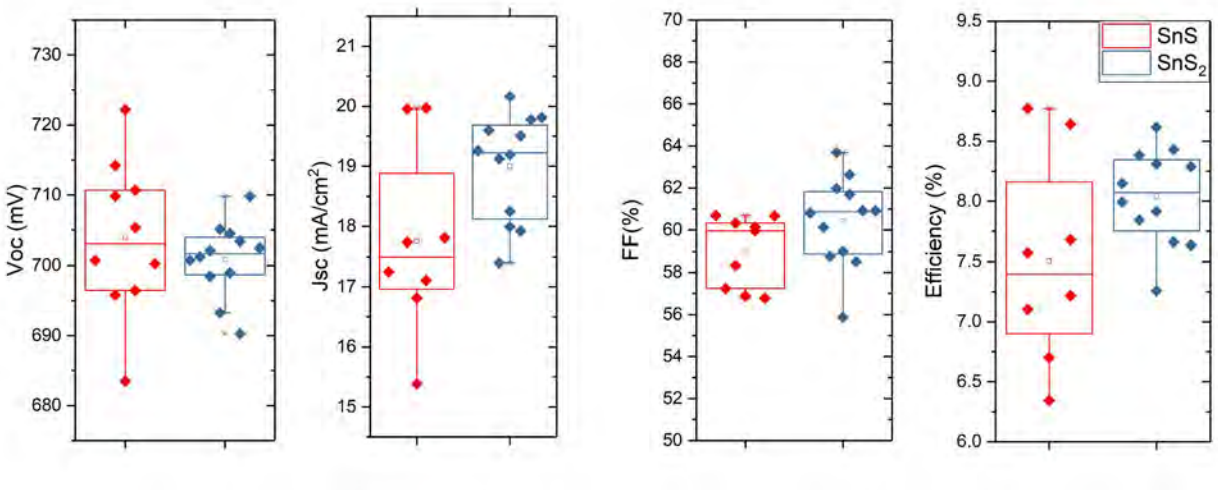

Figure F18.3: Statistical performance parameters of the CZTS devices with Sn^{2+} (SnS) and Sn^{4+} (SnS_2) precursors, respectively.

Highlights

- Slow ramping rate during annealing process favors Cu-rich composition whereas fast ramping rate during annealing contributes to Cu-poor composition for Sn^{4+} precursor.
- Sn^{4+} precursor shows its effectiveness in boosting the CZTS efficiency with achieved average efficiency of 8.1%.
- Device from Sn^{4+} precursor not only possesses a better overall performance but also shows a much-narrowed distribution.

Future Work

- The sulfurisation annealing temperature should be further optimised for an Sn^{4+} precursor.
- All sulfide precursors need to be investigated with a faster ramping rate.
- The processing and structure to facilitate an Ag front grading and Ge back grading based on Sn^{4+} precursor need to be studied.

References

CHEN, S., WALSH, A., GONG, X.-G. & WEI, S.-H. 2013. Classification of Lattice Defects in the Kesterite Cu2ZnSnS4 and Cu2ZnSnSe4 Earth-Abundant Solar Cell Absorbers. 25, 1522-1539.

GONG, Y., ZHANG, Y., JEDLICKA, E., GIRIDHARAGOPAL, R., CLARK, J. A., YAN, W., NIU, C., QIU, R., JIANG, J., YU, S., WU, S., HILLHOUSE, H. W., GINGER, D. S., HUANG, W. & XIN, H. 2020. Sn4+ precursor enables 12.4% efficient kesterite solar cell from DMSO solution with open circuit voltage deficit below 0.30 V. Science China Materials.

LI, J., HUANG, Y., HUANG, J., LIANG, G., ZHANG, Y., REY, G., GUO, F., SU, Z., ZHU, H., CAI, L., SUN, K., SUN, Y., LIU, F., CHEN, S., HAO, X., MAI, Y. & GREEN, M. A. 2020. Defect Control for 12.5% Efficiency Cu2ZnSnSe4 Kesterite Thin-Film Solar Cells by Engineering of Local Chemical Environment. 32, 2005268.

RUDISCH, K., DAVYDOVA, A., RIEKEHR, L., ADOLFSSON, J., QUAGLIA CASAL, L., PLATZER-BJÖRKMAN, C. & SCRAGG, J. 2020. Prospects for defect engineering in Cu2ZnSnS4 solar absorber films. Journal of Materials Chemistry A, 8, 15864-15874.

YAN, C., HUANG, J., SUN, K., JOHNSTON, S., ZHANG, Y., SUN, H., PU, A., HE, M., LIU, F., EDER, K., YANG, L., CAIRNEY, J. M., EKINS-DAUKES, N. J., HAMEIRI, Z., STRIDE, J. A., CHEN, S., GREEN, M. A. & HAO, X. 2018. Cu2ZnSnS4 solar cells with over 10% power conversion efficiency enabled by heterojunction heat treatment. Nature Energy, 3, 764-772.

F19 ADVANCED NANOSCALE CHARACTERISATION OF LOCAL STRUCTURES AND DEFECTS FOR LARGE BANDGAP MATERIALS FOR TANDEM SOLAR CELLS

Lead Partner
UNSW

UNSW Team
Dr Jae Sung Yun, Prof. Martin Green, Dr Jongsung Park, A/Prof. Xiaojing Hao, A/Prof. Ziv Hameiri, Dr Arman Soufiani, Prof. Jan Seidel

Academic Partner
Green Energy Institute: Dr Jongsung Park
The University of Tennessee: Dr Dohyung Kim
School of Materials and Science Engineering, UNSW: Prof. Jan Seidel

Funding Support
ACAP, Green Energy Institute

Aim

We aim to study local charge separation properties of long-cation chained cation passivated 3D large bandgap perovskite solar cells (PSCs) using scanning probe microscopy techniques. Recently, the long-chain passivation deposition onto the 3D absorber layer has been widely applied in PSCs. This reduces non-radiative recombination activity of the device that has been confirmed by macroscopic characterisation tools such as photoluminescence or transient photoconductance. With our high resolution (<10 nm) scanning probe

microscopy technique, we aim to elucidate morphology-dependent charge transport properties in the phenethylammonium iodide (PEAI) passivated 3D PSCs.

Progress

Figure F19.1 depicts an energy level diagram of a PSC that consists of an electron transport layer (ETL), a large bandgap perovskite ($Cs_{0.05}FA_{0.6}MA_{0.4}Pb(I_{0.6}Br_{0.4})_3$), a PEAI layer, a hole transport layer (HTL), and a gold contact. As can be seen, the PEAI layer is expected to have a higher valence energy level compared to the perovskite layer, thus, facilitates the hole transfer. We also examined the surface morphology of the perovskite films with different amounts of PEAI additives by scanning electron microscopy (SEM) shown in Figures F19.2(a)–(d), as well as the crystalline phases formed using X-ray diffraction patterns in Figure F19.2(e). As illustrated in Figure F19.2(a), a nicely packed polycrystalline film is formed (reference sample). The perovskite film has two main peaks at 14.1° and 28.1°, which are indexed to the (100) and (200) planes, respectively, and there is no presence of a PbI_2 peak. When 2 mg of PEAI was deposited, PEAI was conformally coated on the surface in its salt form with still distinguishable apparent grains. The PEAI signature (4.7°) was yet absent in the associated XRD pattern (Figure F19.2(e)). When the PEAI amount was increased to 5 mg, a PEAI peak (4.7°) appears in XRD pattern and the perovskite surface coverage started to show inhomogeneities, forming regions of interconnected grains (Figure F19.2(c)).

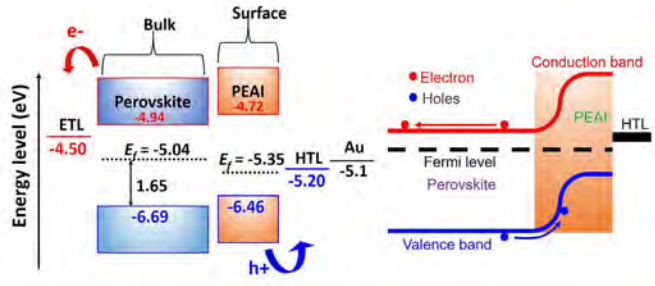

Figure F19.1: Energy level diagram of the PSC used in this work. The ETL and HTM used in this work is SnO_2 and Spiro-OMeTAD respectively (Lee et al. 2021).

It is interesting that there was no PbI_2 initially, but it has appeared with a low-dimensional perovskite $(PEA)_2PbI_4$ (5.4°, 10.9°, 16.4°, 21.9°, 27.4°, 33.1°) peak. We speculate that the excessive amounts of PEAI decomposes the original perovskite structure into a halide salt and lead halide and reacts with the lead halide to form 2D $(PEA)_2PbI_4$. However, this reaction does not occur uniformly, thus, there is always unreacted lead halide left as well as unreacted PEAI. Figure F19.2(f) displays CPD pixel distribution plots of each sample. Full width half maximum (FWHM) of Gaussian fitted curves of each sample are also presented. As expected, the FWHM is relatively much larger for the 5 mg and 7.5 mg samples compared to the reference and 2 mg samples in Figure F19.2(f). This indicates that there is a non-uniform work function distribution that is harmful for the charge transport. Also, it is noticeable that the average CPD decreases as the amount of PEAI increases. Given that the work function of the tip (Φtip) is -5.1 eV (gold), the CPD indicates the decrease of work function, according to the CPD equation, CPD= Φsample -5.1 eV.

Next, the impact of different amounts of PEAI additives on the device performance, particularly on the potential suppression of non-radiative recombination losses and thus voltage gains, was evaluated through Suns-VOC measurements. The device configuration is the same as what is described in Figure F19.1. Figure F19.2(g) shows the corrected VOC as a function of illumination intensity. At an intensity range between 0.1- to one-sun, little or no change in VOC is observed for each sample. The sample containing 2 mg of PEAI showed the highest VOC at both one-sun and at lower illumination intensities (<0.04-sun). At such low intensities, solar cell performance is more vulnerable to the presence of recombination active traps due to a limited amount of the excess carriers. Therefore, the higher VOC of the 2 mg PEAI sample under such low illumination intensities implies a reduced recombination activity of the charge carrier traps. We will further explore the electrical properties of 2 mg PEAI samples later. The devices fabricated with 5 mg and 7.5 mg PEAI performed worse than the reference sample which could be due to the inhomogeneous electrical properties of the surface as evident from the SEM images .

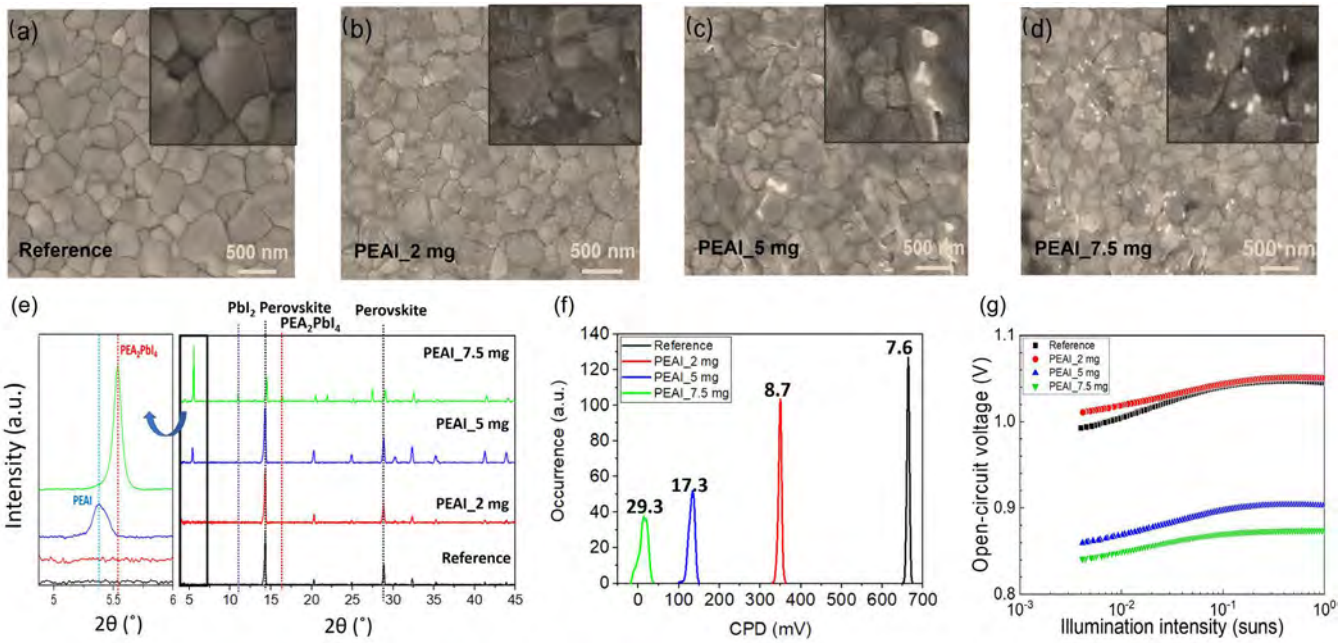

Figure F19.2: SEM images of perovskite films without PEAI deposition (a), with 2 mg (b), 5 mg (c), and 7.5 mg (d) PEAI deposition. (e) XRD patterns of the perovskite films with deposition of different PEAI concentrations. (f) CPD distribution plots of each sample with full width half maximum (FWHM) values. (g) Suns-V_{OC} curves of the corresponding solar cells (Lee et al. 2021).

Given that morphological variation has substantial effects on the performance of PSCs, investigation of the spatial distribution of photo-generated charge carriers at the nanoscale is crucial to understand the device operation mechanisms. We used Kelvin probe force microscopy (KPFM) to measure the contact potential difference (CPD) in the dark as well as under indoor relevant illumination for the reference and the 2 mg PEAI deposited 3D perovskite films both deposited on SnO_2/ITO. Figure F19.3(a) shows the schematic of the KPFM measurement setup used. A topography map can be obtained in the first pass scan and the CPD is spatially resolved in the second pass scan (Figures F19.3(d)–(g)). Considering that there are no excess carriers generated in the absorber, the CPD measured in the dark represents the work function (WF) difference between the metal cantilever and the sample surface. As shown in Figure F19.3(a), the white LED is used to illuminate the samples from the glass side so as to investigate the charge carrier dynamics like the real operating condition. Upon illumination, photo-generated electrons are transported towards the cathode (ITO) through the ETL, whereas photo-excited holes can diffuse to the surface of the film and accumulate there.

Figures F19.3(b) and (c) display CPD distribution graphs under dark and light for the reference and the 2 mg PEAI passivated samples, respectively, obtained from Figures F19.3(d)–(g). The peak CPD value of the deposited sample in the dark is smaller than the reference sample by about 310 mV. Since CPD is the difference between the cantilever tip WF (ΦAu = -5.1 eV) and the sample Fermi level energy position ($\Phi_{sample} - \Phi_{tip}$), the decrease in the CPD implies a decrease in Φ_{sample}. This indicates that the top surface of the 2 mg PEAI deposited sample is more p-type compared to the reference sample. Under illumination, the CPD peak value for 2 mg PEAI deposited sample shifts to 663 mV, as shown in Figure F19.3(c), while that of the reference film is 844 mV, shown in Figure F19.3(b). A relevant band diagram in the dark and under light for the reference and PEAI deposited sample is shown in Figure F19.3(h) and (i). By subtracting the dark CPD (CPD_{dark}) from the measured values under illumination (CPD_{light}), the surface photovoltage (SPV) parameter is calculated, which is an indication of the extent of charge carrier accumulation (here, holes) at the top surface.

The average SPV value of ~320 mV for the 2 mg PEAI deposited sample is about 120 mV higher than that of the reference sample (~200 mV) under 200 lux illumination. This suggests that more photo-excited holes are accumulated at the surface of the PEAI deposited film inducing a greater shift in the holes quasi-Fermi level towards the valence band, due likely to the reduced non-radiative recombination in the interface passivated sample, compared to the reference film. The CPD maps in the dark for the reference and the PEAI deposited samples are shown in Figures F19.3(d) and (e), respectively. The grain boundaries of the reference sample have lower CPD than the grain interiors and individual grains can be clearly identified by the CPD variation between the grain interiors and the grain boundaries, indicative of variation in the Fermi level between the grain boundaries and the grain interiors. Previously, we reported that defects, which create energy levels near the valence band (VB) (cation vacancies or halide interstitials) can be segregated at the grain boundaries (Yun et al. 2015). After the deposition of 2 mg of PEAI on the surface, the CPD variation between the grain interiors and the grain boundaries almost diminishes, indicating that the surface electronic properties become more homogeneous. Figures F19.3(f) and (g) show CPD maps taken under the 200-lux light (LED). As can be seen, the grain boundaries exhibit higher CPD than the grain interiors for the reference sample, which indicates higher SPV ($CPD_{light} - CPD_{dark}$) given that the

CPD at the grain boundaries was lower in the dark. Average CPD at the grain boundaries and the grain interiors in the dark and under the light are plotted in Figure F19.3(h) and (i) for the reference and PEAI deposited samples, respectively. The SPV of the grain boundaries (207 mV) is slightly higher compared to the grain interiors (200 mV) for the reference sample. Higher SPV at the grain boundaries has been previously observed in lead halide–based PSCs, which was attributed to either a larger bandgap (i.e. bandgap fluctuation between the grain interiors and the grain boundaries) or change in local Fermi level due to the segregation of different types of halides or lead halides. After the PEAI deposition (Figure F19.3(g)), CPD does not vary across the grain boundaries and the grain interiors and exhibits high uniformity similar to the case of CPD in the dark and under light. The calculated average SPVs for the grain boundaries and the grain interiors differ only by 1 mV. These results also suggest that the PEAI deposition results in homogeneous charge separation, which is attributed to the homogeneous interface properties.

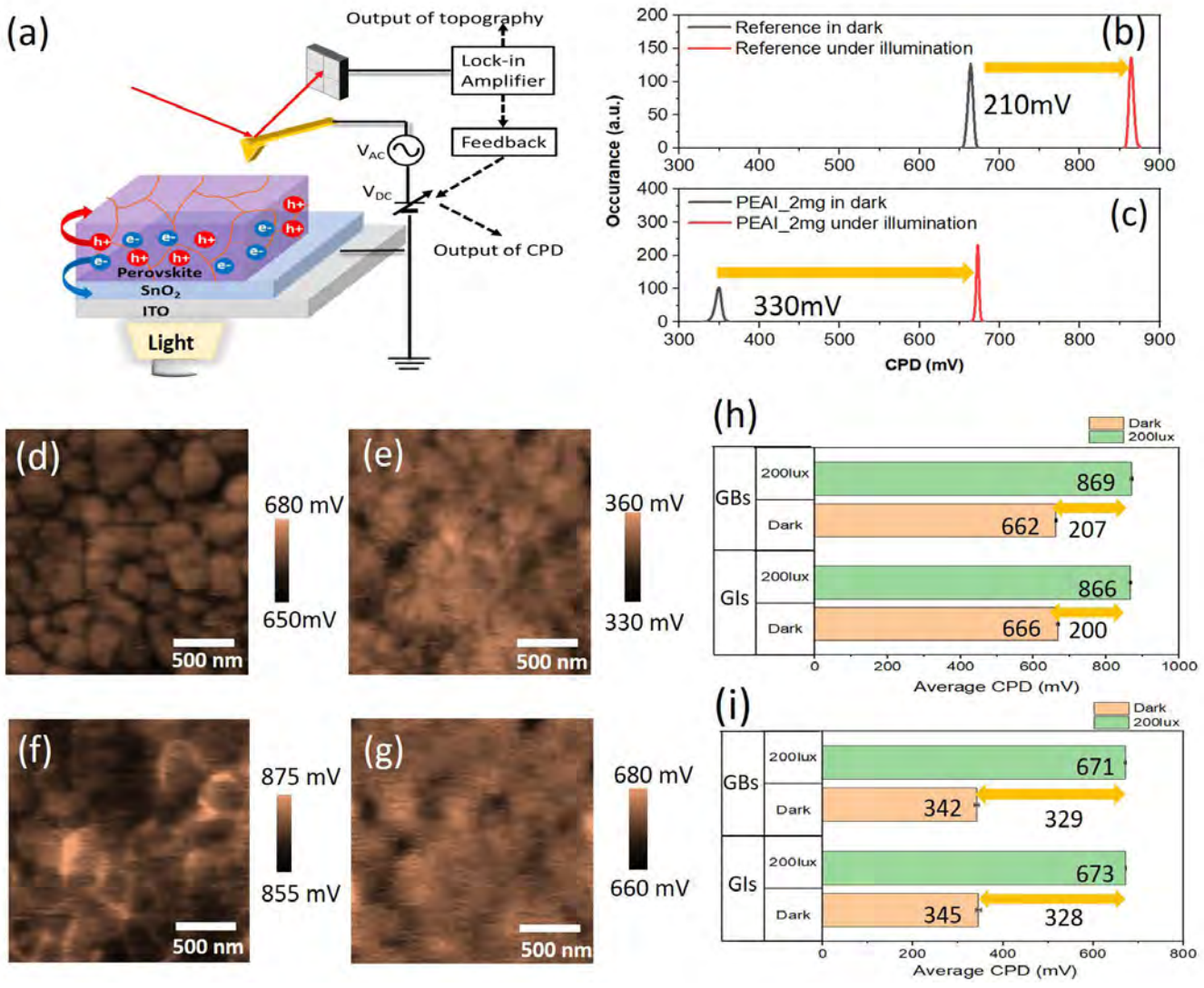

Figure F19.3: (a) Schematic of the KPFM setup with LED illumination from the glass side. CPD distribution curves in the dark and under illumination for (b) the reference sample and (c) the 2 mg PEAI deposited sample. Contact potential difference distribution maps measured in the dark for (d) the reference sample and (e) the 2 mg PEAI deposited sample and under 200 lux illumination for the (f) reference sample and (g) the 2 mg PEAI deposited sample. Average CPD measured at the grain boundaries and the grain interiors under the dark and light for (h) the reference sample and (i) the 2 mg PEAI deposited sample (Lee et al. 2021).

Highlights

- Appropriate post-deposited amount of PEAI (2 mg) strongly interacts with the perovskite surface forming a conformal coating of PEAI on the perovskite film surface which improves the crystallinity and absorption of the film. Consequently, improved device performance is demonstrated.
- Our KPFM results indicate that the potential difference across the grain boundaries and grain interiors diminishes after the PEAI deposition, constructing an electrically and chemically homogeneous surface. This increases the SPV and uniformity of the charge transport under the light illumination.

Future Work

- Investigate charge separation and ion migration properties of the long-chained cations and 2D perovskites.
- Compare and elucidate the charge transport mechanisms between the long-chain cations and 2D perovskites.
- Perform stability tests using KPFM to observe nanoscale degradation processes in these materials.

References

Yun, J.S., Ho-Baillie, A., Huang, S., Woo, S.H., Heo, Y., Seidel, J., Huang, F., Cheng, Y.B. & Green, M.A. 2015. Benefit of grain boundaries in organic–inorganic halide planar perovskite solar cells. The journal of physical chemistry letters, 6(5), 875-880.

LEE, M., CHOI, L., SOUFIANI, A., LIM, J., KIM, M., CHEN, D., GREEN, M., SEIDEL, J., LIM, S., KIM, J., DAI, X., LEE-CHIN, R., ZHANG, B., HAMEIRI, Z., PARK, J., hAO, X., & Yun, J.S. 2021. Enhanced hole-carrier selectivity in wide bandgap halide perovskite PV devices for Indoor IoT Applications. Advanced Functional Materials, in press.

Closing Report

- Summary of the overall project

- Potential wide bandgap materials, halide perovskites and CZTS, for the Si-based tandem solar cells, have been characterised using scanning probe microscopy techniques.
- Charge transport properties of nanoscale topological defects such as grain boundaries and ferroic domains have been investigated.

- Outcomes and learnings

- Impact of these defects on the device performance was explained which can lead to further device performance improvement.
- New microscopic techniques have been developed to elucidate the ionic motion and charge transport properties in halide perovskites.
- 23 journal publications have been made during the Fellowship period.
- External fundings of ~$450K have been acquired from a company (Daeyeon C&I) and a research institute (Green Energy Institute).

F20 SEMITRANSPARENT FLEXIBLE PEROVSKITE SOLAR CELLS FOR LAMINATED TANDEM CELL

Lead Partner

CSIRO

CSIRO Team

Dr Chuantian Zuo, Dr Mei Gao, Dr Doojin Vak

Funding Support

ACAP

Aim

The objective of this project is to develop semitransparent flexible perovskite solar cells for laminated perovskite/silicon tandem cells. The project focuses on how to create semitransparent flexible perovskite solar cells using scalable methods – either slot-die coating or a roll-to-roll (R2R) continuous process. Ultimately, the semitransparent cells will be integrated to form perovskite/silicon tandem cells.

Progress

In our previous work, we developed a slot-die coating compatible drop-casting method to prepare perovskite solar cells. Following the previous work, we tried to use different recipes and optimise preparation conditions to improve device performance. We found that the drop-casting method can be used as a facile and time-saving method to screen materials and preparation conditions for the R2R process. To find the best recipe, we tried 3D $MAPbI_3$ and various 2D perovskites with different cations, then the optimised recipe was successfully applied to the R2R process. PCEs of 15.0% and 8.5% were achieved by drop casting and the R2R process, respectively.

Figure F20.1 shows the chemical structure and abbreviation for the cations used in this work. These cations have been used in the spin coating. But the in-depth study of these cations in the drop-casting method has not been reported yet. We found that the perovskite films using these cations show a quite different crystallisation process, resulting in different film morphology.

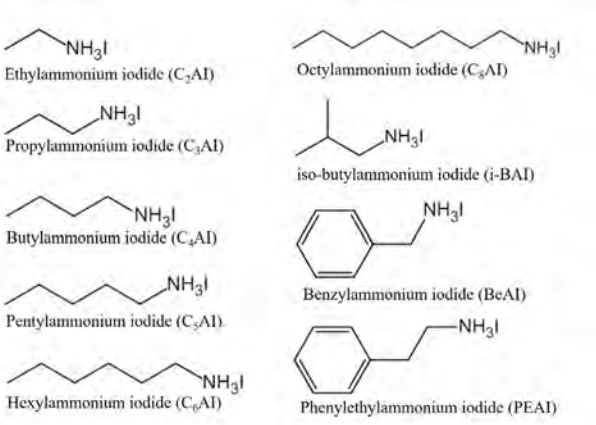

Figure F20.1: Chemical structure and abbreviation for the cations used in this work.

Figure F20.2 shows the photos for drop-cast 3D $MAPbI_3$ and 2D/3D perovskite films using different cations. It can be seen that the films show different appearances. Both the type of the cations and the ratio of the cations in the solution have significant impact on film morphology. The film prepared using a BA cation with n=5 show relatively better morphology than the other films.

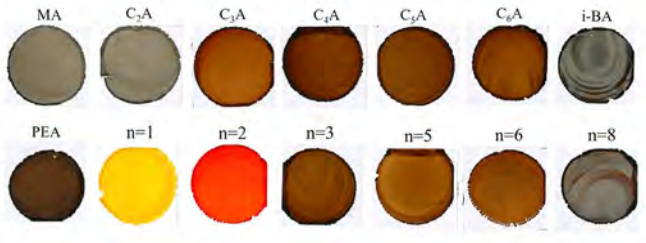

Figure F20.2: Photographic images of drop-cast 3D $MAPbI_3$ perovskite film, 2D X2MA3Pb4I13 perovskite films prepared by using different cations (X), and BA2MAn−1PbnI3n+1 2D perovskite films with different n.

To verify the compatibility between the drop casting and the R2R-process we applied the optimised conditions obtained from the drop casting to the R2R process. Figure F20.3 shows a photo of the R2R processed perovskite film on flexile substrate. The film is smooth, uniform, and no pin hole. Then we made perovskite solar cells using the flexible film and obtained a PCE of 8.5%.

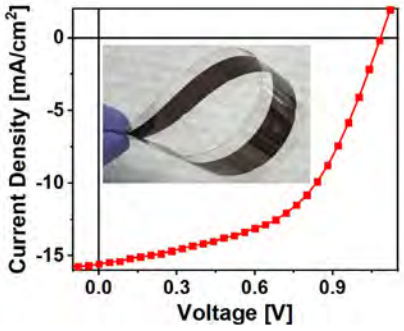

Figure F20.3: J-V curve of a perovskite solar cell prepared using R2R-processed $BA_2MA_4Pb_5I_{16}$ perovskite film on flexible substrate (inset).

Highlights

- A facile method is developed to screen materials and preparation conditions for the R2R process.
- The optimised condition obtained from the drop casting is successfully applied to the R2R process.

Future Work

- Improve the PCE of perovskite solar cells using drop-cast perovskite layer.
- Prepare four-terminal perovskite/silicon solar cells.

References

- ZUO, C. T., SCULLY, A., VAK, D., TAN, W. L., JIAO, X. C., MCNEILL, C. R., ANGMO, D., DING, L. M. & GAO, M. 2019. Self-Assembled 2D Perovskite Layers for Efficient Printable Solar Cells. *Advanced Energy Materials*, 9, 1803258.
- ZUO, C. T., SCULLY, TAN, W. L., ZHENG F., GHIGGINO K. P., VAK D., WEERASINGHE H., MCNEILL C. R., ANGMO, D., CHESMAN A. S.R. & GAO M. 2020. Crystallization control of drop-cast quasi-2D/3D perovskite layers for efficient solar cells, *Communications Materials*, 1, 33.

F21 THE ROLE OF SOLAR PHOTOVOLTAICS IN A 100% RENEWABLE ENERGY FUTURE

ACAP Fellow

Bin Lu

Supervisor

Prof. Andrew Blakers

Funding Support

ACAP

Aim

Large-scale deployment of solar photovoltaics supplemented by wind energy and other renewables presents the most promising prospect for tackling climate change. In this project, the role of solar photovoltaics in full decarbonisation of the energy systems is explored through high-resolution modelling of energy generation, storage and transmission in a set of 100% renewable energy scenarios.

Progress

In 2020, a new modelling tool, FIRM, was developed. This tool enables simulations of high-level energy balancing through a synergy of: (i) flexible energy sources; (ii) interconnection of electricity grids over large geographic areas; (iii) response from demand-side participation;

and (iv) mass energy storage in energy balancing and electricity grid stabilization – (acronym: FIRM). Energy generation, storage and transmission are co-optimised based on long–term (10-40 years), high-resolution (hourly or half-hourly intervals) meteorological and energy demand data. In this way, the inter-annual variability of renewable energy resources can be effectively captured, together with the weather events which occur occasionally with extremely low availability of solar and wind energy supply.

As the first application of the modelling tool, a journal article entitled "A zero-carbon, reliable and affordable energy future in Australia" has been published in *Energy* (Lu et al. 2021). This study demonstrated that a zero-carbon, reliable and affordable electrical energy system can be built in Australia, based on: (i) solar photovoltaics, wind turbines, existing hydropower and biomass for power generation; (ii) pumped hydro (off-river) and electric car batteries for energy storage; and (iii) high-voltage direct-current and alternating-current for electricity transmission. All of these energy technologies are commercially available today and have already been deployed on a large scale worldwide. The variability and uncertainty of renewable energy resources were addressed using short-term off-river energy storage (STORES) from pumped hydro and distributed energy storage (DES) from the smart charging of electric vehicles. A set of three 100% renewable energy scenarios for Australia were modelled in this work:

- Scenario 1: "7 Grids". This is the baseline scenario in which the regional electricity markets were assumed to be operated separately in seven Australian states and territories: New South Wales (NSW), Northern Territory (NT), Queensland (QLD), South Australia (SA), Tasmania (TAS), Victoria (VIC) and Western Australia (WA).
- Scenario 2: "Super Grid". In this scenario, energy systems in NSW, QLD, SA, TAS and VIC were fully integrated as a National Electricity Market (NEM), along with three potential extensions (sub-scenarios 2.1–2.8) to Far North Queensland (FNQ, 1,500 km), NT/Alice Springs (1,200 km) and WA/Perth (2,400 km).
- Scenario 3: "Smart Grid". This scenario (comprising sub-scenarios 3.1–3.8) was built based on the Super Grid scenario, with an additional assumption that distributed energy storage such as electric car batteries contributed large demand flexibility to the electricity system, enabled by smart grid technology.

Figure F21.1 illustrates a snapshot of the load profiles and generation mix for a day with low availability of wind energy in New South Wales. The levelised costs of electricity (LCOE) and the energy storage requirements are shown in Figure F21.2. As demonstrated, in the 7 Grids scenario, the LCOE ranges from A$52–124/MWh in QLD, NSW, NT, SA, TAS, VIC and WA with a volume-weighted average of A$99/MWh. The storage requirements are 65 GW, 2,049 GWh in total. By contrast, in the Super Grid scenario, the LCOE of an integrated National Electricity Market (including QLD, NSW, SA, TAS and VIC) is in the range of A$75–88/MWh depending on whether connections to FNQ, NT and WA are built. The total storage requirements in the Super Grid scenario decrease to 481–746 GWh – only equivalent to the storage requirement in a single state, NSW or VIC, in the 7 Grids scenario. In the Smart Grid scenario, with flexible charging of electric cars, the LCOE reduces further still to A$70–82/MWh and the total storage requirements range from 321 to 493 GWh. Large-scale grid interconnection in the Super Grid scenario and the introduction of demand-side participation in the Smart Grid scenario help to reduce the cost of 100% renewables by A$11–24/MWh and A$17–29/MWh, respectively.

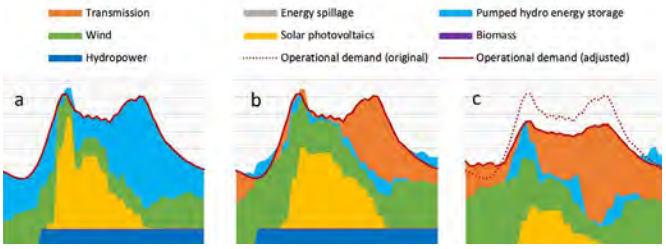

Figure F21.1: Load profiles and generation mix for a day with low availability of wind energy in New South Wales in the 7 Grids (a), Super Grid (b) and Smart Grid (c) scenarios.

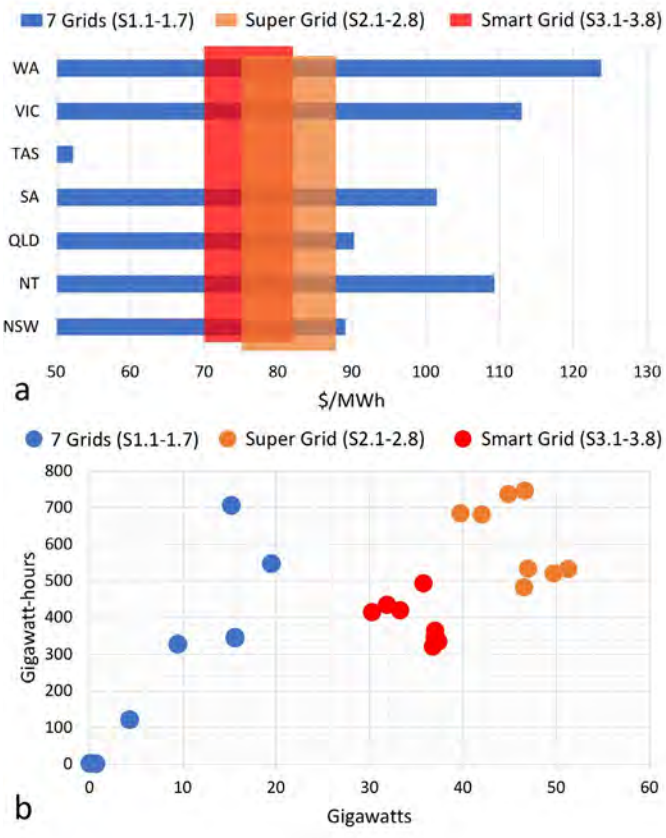

Figure F21.2: Levelised costs of electricity (a) and storage requirements (b) in the 7 Grids (blue), Super Grid (orange) and Smart Grid (red) scenarios. The volume-weighted average of LCOE in the 7 Grids scenario is $99/MWh. The total storage requirements in the 7 Grids scenario are 65 GW and 2,049 GWh.

In 2020, I have delivered a series of talks at the following events:

- ANU public lecture *Imagining Australia with 100% renewable energy: how do we get there?* (17 February 2020 in Canberra)
- ANU 100% renewable futures workshop (18 February 2020 in Canberra)
- 4th Pumped Hydro & Battery Storage Conference (25 February 2020 in Sydney)
- ANU Grand Challenge *Zero-carbon energy for the Asia-Pacific* workshops (6 April, 26 June, 20 July and 17 September 2020 online)
- 2020 Asia-Pacific Solar Research Conference (2 December 2020 online).

Despite the significant impact of COVID-19, these presentations attracted an audience of >500 in total. I had a short conversation with the 29th Prime Minister Malcolm Turnbull regarding a submarine power cable to Singapore. Over the course of my ACAP Fellowship in 2019–2020, I have co-authored another three journal articles which have been published in *Joule* (Stocks et al. 2020), *IEEE Journal of Photovoltaics* (Blakers et al. 2019) and *Global Energy Interconnection* (Cheng et al. 2019). I'm supervising and co-supervising two PhD students and a number of Engineering Honours students extending the study to Japan, Indonesia, Bolivia, Singapore, Malaysia and the United States (California).

About three-quarters of the world's population lives in the Sunbelt (lower than +/- 35 degrees of latitude), where the solar radiation is high, and the seasonal variations of solar resource are relatively low. Unlike much of Europe, North America and Northeast Asia, there is no significant heating load in winter, and the demand for cooling is generally in alignment with the high solar irradiance in summer. Consequently, deployments of renewable energy and storage, primarily solar photovoltaics with support provided by STORES and DES, can be a rapid and generic pathway towards zero-carbon energy futures within the Sunbelt.

Highlights

- Large-scale deployment of solar photovoltaics, with support provided by STORES and DES, can be a cost-effective pathway towards 100% renewable energy futures in Australia and the Sunbelt.
- The levelised cost of 100% renewable energy in Australia is in the range of A$70–A$99 (US$49-US$69) per megawatt-hour based on the current technology costs.
- A US$30–90 billion solar photovoltaics market is expected in Australia to fully decarbonise electricity generation, along with electrification of heating, transportation and industry to displace fossil fuels.

Future Work

- A journal article entitled "Low-cost, low-emission 100% renewable electricity in Southeast Asia" is in preparation. This study investigates the potential for solar energy and storage to support the rapidly growing demand for electricity in Southeast Asia. The initial results show that solar energy can be the major source of electricity in the 100% renewable energy scenarios, which contributes to 30–99% in the energy mix across Southeast Asia with a volume-weighted average of 82%. It is highly likely that solar photovoltaics will dominate the market for future renewable energy development in Southeast Asia, due to a lack of constraints relating to cost competitiveness, environmental impact, raw material supply, resource availability, security concerns and social factors.

References

BLAKERS, A., STOCKS, M., LU, B., CHENG, C. & STOCKS, R. 2019. Pathway to 100% Renewable Electricity. IeeeEEE Journal of Photovoltaics, 9, 1828-1833. https://doi.org/10.1109/JPHOTOV.2019.2938882.

CHENG, C., BLAKERS, A., STOCKS, M. & LU, B. 2019. Pumped hydro energy storage and 100% renewable electricity for East Asia. Global Energy Interconnection, 2, 387-393. https://doi.org/10.1016/j.gloei.2019.11.013.

LU, B., BLAKERS, A., STOCKS, M., CHENG, C. & NADOLNY, A. 2021. A zero-carbon, reliable and affordable energy future in Australia. Energy, 220. https://doi.org/10.1016/j.energy.2020.119678.

STOCKS, M., STOCKS, R., LU, B., CHENG, C. & BLAKERS, A. 2020. Global Atlas of Closed-Loop Pumped Hydro Energy Storage. Joule. https://doi.org/10.1016/j.joule.2020.11.015.

F22 DEVELOPMENT OF THERMAL STABLE HOLE TRANSPORT LAYERS FOR HIGHLY EFFICIENT AND STABLE PEROVSKITE SOLAR CELLS

ACAP Fellow

Jun Peng

Supervisor

A/Prof. Thomas P. White

Funding Support

ACAP

Aim

This project aims to develop thermally stable hole transport layers (HTLs) for high efficiency perovskite solar cells (PSCs) and to demonstrate PSCs that pass the damp heat (85°C and 85%RH) test.

The first objective of this project is to develop ionic-dopant-free organic HTLs to substitute unstable ionic-doped Spiro-OMeTAD and PTAA for n-i-p structured PSCs. The second objective of this project is to develop novel doping approaches to tailor the electronic properties (e.g. work function and conductivity) of nickel oxides (NiO_x) for use as HTLs for p-i-n structured PSCs.

Progress

We have developed the ionic-dopant-free poly(3-hexylthiophene) (P3HT) HTLs by manipulating the π-π stacking of the P3HT side-chains using solvent annealing and copper phthalocyanine (CuPc) additive to improve the morphology and crystallinity of the P3HT films. Figure F22.1 shows that the crystallinity and conductivity of the pure P3HT film is clearly improved by solvent annealing, and then further improved with the addition of CuPc in a 10:1 ratio. Further increases in the CuPc content result in the crystallinity and conductivity being reduced. When incorporated into a baseline mesoporous TiO_2 PSC process as a substitute for Spiro-OMeTAD, the best results were obtained for a 10:1 (v/v) ratio blend of P3HT (12 mg/ml):CuPc (5 mg/ml) (Figure F22.1).

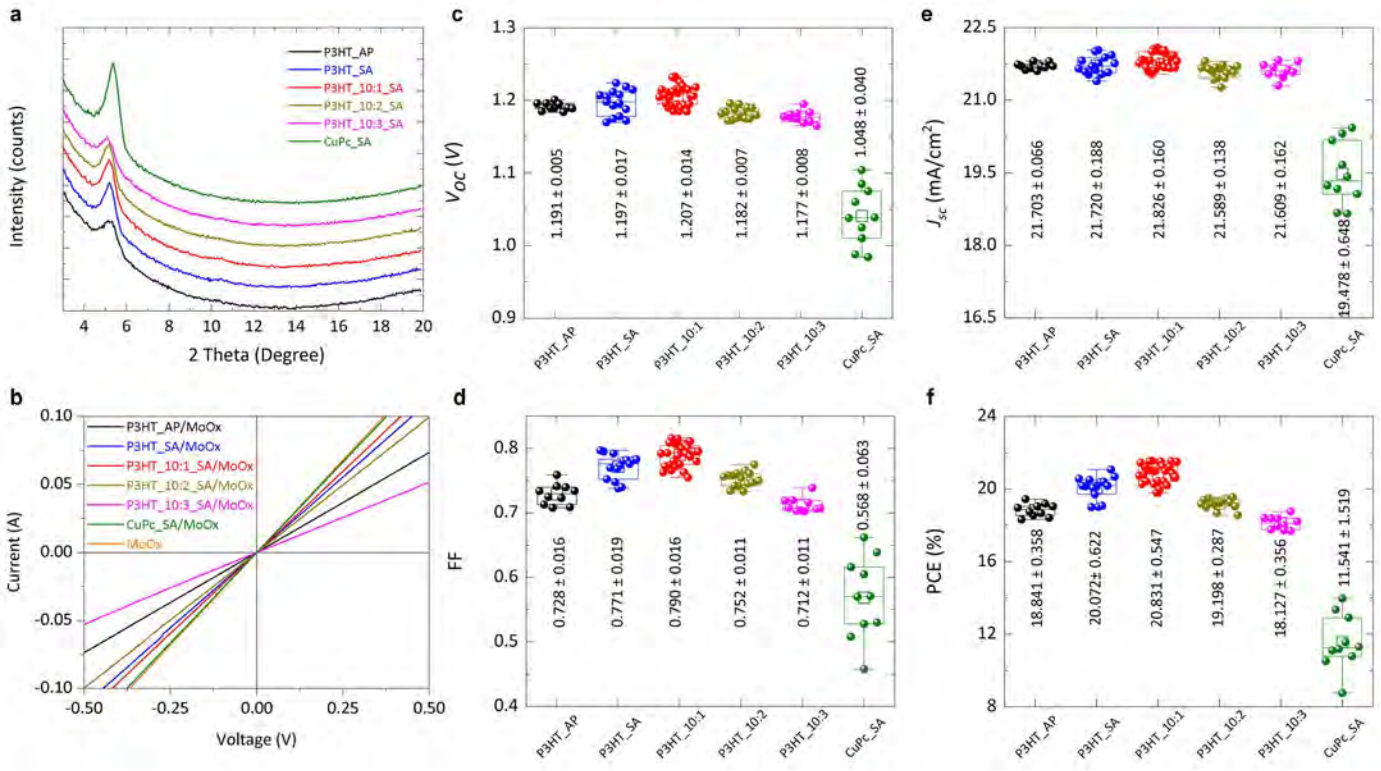

Figure F22.1: (a) Grazing incidence X-ray diffraction (GIXRD) spectra of the different HTL films deposited on glass substrates. (b) Dark I-V curves of the hole-dominated device with a structure of Glass/ITO/HTLs (~60 nm)/MoO_x (~30 nm)/Gold [note that the legend of "AP" and "SA" represent as-prepared and with solvent annealing treatment]. (c)–(f) Statistical distribution of the photovoltaic parameters for mesoporous perovskite cells based on different HTLs. Data from Peng et al., Science, (2021).

To further boost the performance of our PSCs, we then used a nanostructured TiO_2 electron transport layer to substitute the mesoporous TiO_2 layer. As shown in Figure F22.2, our champion 1 cm^2 PSC yielded a PCE of 21.96% (21.86%) with V_{OC} ~ 1.205 V (1.204 V), J_{SC} ~ 21.80 $mA.cm^{-2}$ (21.86 $mA.cm^{-2}$), and FF ~ 0.836 (0.836) from reverse (forward) J-V scans. In order to confirm the device performance measured in-house, another cell submitted to an independent photovoltaic testing centre (CSIRO PV Performance Lab, Newcastle) obtained a certified PCE of ~21.698 ± 0.555% with an FF of 83.87 ± 1.16%.

Two extended degradation tests were conducted to determine the light and thermal stability of the cells: a steady-state power output (SPO) measurement and a damp heat test (Figure F22.2). The results show that the cell with the P3HT:CuPC HTL retained ~95.3% of its initial efficiency ($PCE_{initial}$ ~21.45%) after 260 hours, whereas the control cell with a Spiro-OMeTAD HTL dropped to ~76.1% of its initial efficiency ($PCE_{initial}$ ~ 19.50%) after 250 hours. In the damp heat test results, the P3HT:CuPc–based cell retained ~91.7% of its initial efficiency after 1009 hours of damp heat exposure, whereas the cell with the Spiro-OMeTAD HTL exhibited substantial degradation after only 240 hours, which we attributed to the severe deterioration at the interface between perovskite and Spiro-OMeTAD caused by lithium ion diffusion. The detailed analysis and discussion can be found in our recent *Science* paper (Peng et al. 2021).

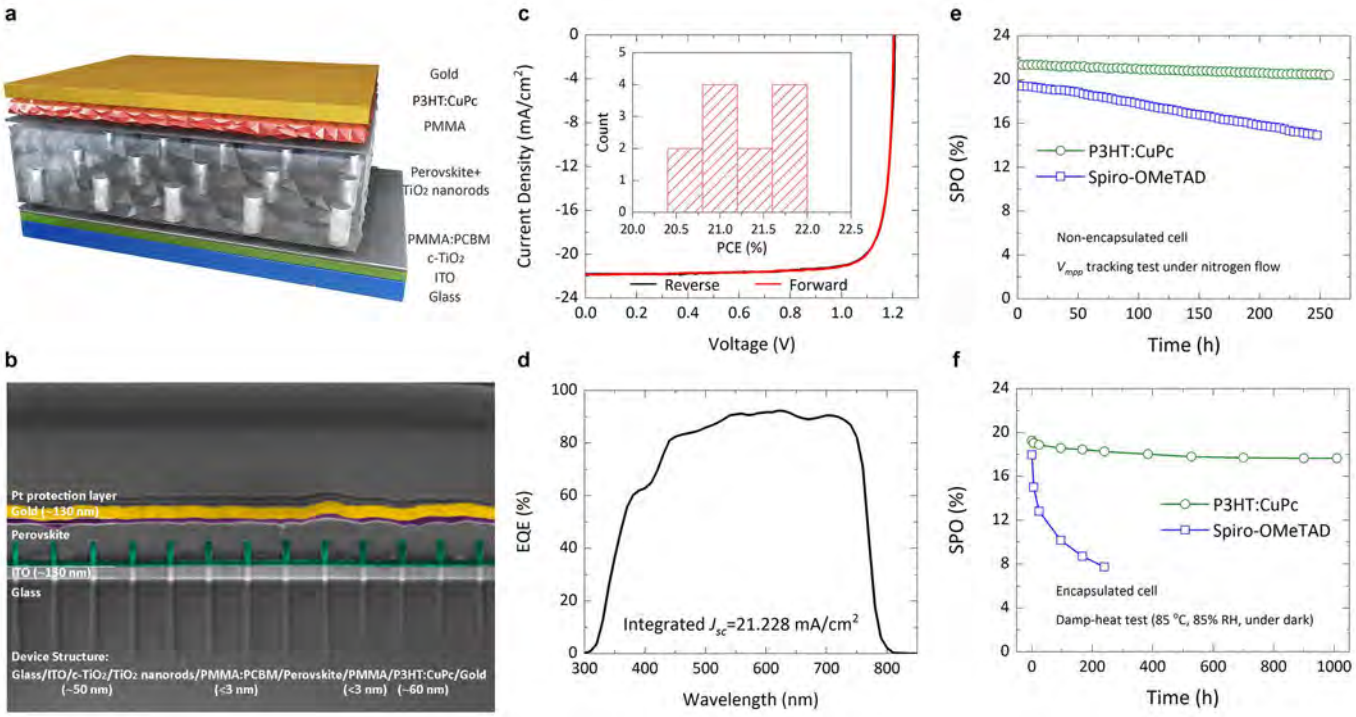

Figure F22.2: (a) Schematic of nanopattern perovskite cell studied in this work. (b) Cross-sectional SEM image of the nanopattern cell structure [note that the perovskite layer was fabricated using ~1 mol/ml diluted precursor solution instead of the standard ~1.3 mol/ml (for cells); the Pt protection layer was only used to prepare the focused ion beam SEM cross-sectional image]. (c) J-V performance. (d) EQE measurement. (e) SPO of non-encapsulated cells based on P3HT:CuPc and Spiro-OMeTAD HTL measured by V_{mpp} tracking under continuous one-sun illumination intensity. (f) SPO of encapsulated cells based on P3HT:CuPc and Spiro-OMeTAD HTL [note that the cell structure for the damp heat tests included a MoO_x-ITO barrier between the HTL and the gold electrode: ITO/c-TiO_2/TiO_2 nanorods/PMMA:PCBM/ $Cs_{0.05}FA_{0.88}MA_{0.07}PbI_{2.56}Br_{0.44}$/PMMA/P3HT:CuPc (or Spiro-OMeTAD)/MoO_x (~10 nm)/IZO (~40 nm)/gold; the optimisation of PMMA:PCBM and PMMA passivation layers can be found in Peng et al. (2017) and Peng et al. (2018). Data from Peng et al. (2021).

We also have developed a Cu-doped NiO_x (Cu-NiO_x) HTL by optimising the concentration of extrinsic dopants (Cu^{2+}) to tune and stabilise the proportion of Ni^{2+} and Ni^{3+} in NiO_x films, therefore tailoring their work function and conductivity. As shown in Figure F22.3, we have achieved some preliminary results for p-i-n structured PSCs using those sputter deposited Cu-NiO_x HTLs, yielding a PCE above 22% and 20% for 0.16 cm^2 and 1 cm^2 active area PSCs, respectively. The un-encapsulated cell retained over 90% of its initial efficiency after 1000 hours of maximum power (V_{mpp}) tracking under continuous one-sun condition illumination, demonstrating the superiority of the sputtered Cu-NiO_x for use as HTLs in p-i-n PSCs.

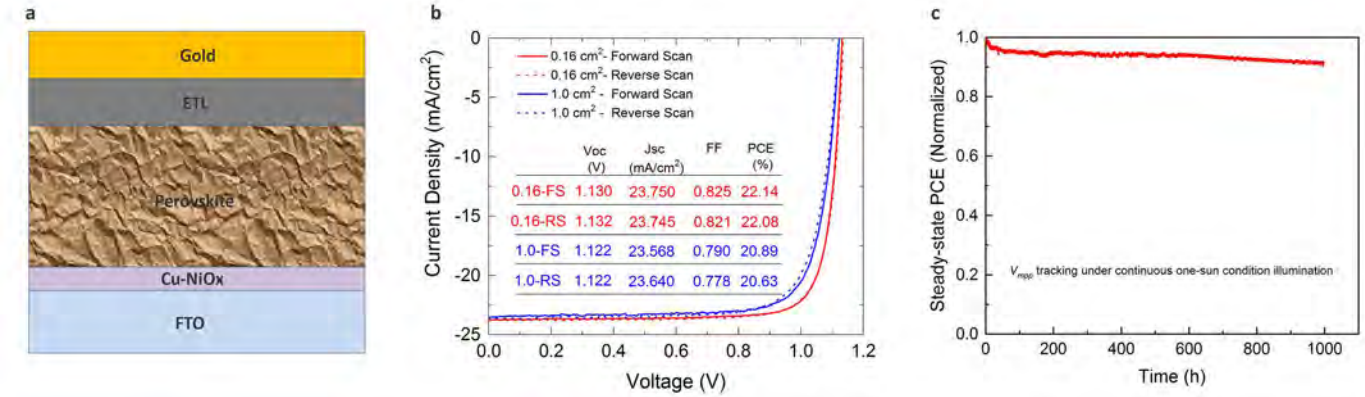

Figure F22.3: (a) Schematic of Cu-NiO_x-based p-i-n perovskite solar cell. (b) and (c) J-V performance of the best p-i-n perovskite solar cell and the corresponding stability measurement in this project.

Highlights

- Optimised ionic dopant-free P3HT:CuPc HTLs.
- Achieved a high efficiency of 21.6% (certified) for 1 cm^2 perovskite cells (a new efficiency record for PSCs of area >1 cm^2).
- The encapsulated cell retained over 90% of its initial efficiency after 1000 hours of damp heat (85°C and 85% RH, under dark) test.
- Optimised Cu-NiO_x HTLs for 1 cm^2 p-i-n perovskite cell with an efficiency of over 20%.
- Published one paper in the journal *Science*.

Future Work

- Optimise the ionic dopant-free organic HTLs for 1 cm^2 n-i-p structured low bandgap PSCs with efficiencies of over 23%.
- Optimise the NiO_x HTLs via doping technology for 1 cm^2 p-i-n structured PSCs with efficiencies of over 22%.
- Test the perovskite cell's stability.

References

PENG, J., KHAN, J. I., LIU, W., UGUR, E., DUONG, T., WU, Y., SHEN, H., WANG, K., DANG , H., AYDIN, E., YANG, X., WNA, Y., WEBER, K. J., CATCHPOLE, K. R., LAQUAI, F., WOLF, S. D. & WHITE, T. P. 2018. A universal double-side passivation for high open-circuit voltage in perovskite solar cells: role of carbonyl groups in poly(methyl methacrylate). *Advanced Energy Materials*, 8, 1801208.

PENG, J., WALTER, D., REN, Y., TEBYETEKERWA, M., WU, Y., DUONG, T., LIN, Q., LI, J., LU, T., MAHMUD, M. A., LEM, O. L. C., ZHAO, S., LIU, W., LIU, Y., SHEN, H., LI, L., KREMER, F., NGUYEN, H. T., CHOI, D. -Y., WEBER, K. J., CATCHPOLE, K. R. & WHITE, T. P. 2021. Nanoscale localized contacts for high fill factors in polymer-passivated perovskite solar cells. *Science*, 371, 390-395.

PENG, J., WU, Y., YE, W., JACOBS, D. A., SHEN, H., XIAO, F., WAN, Y., DUONG, T., WU, N., BARUGKIN, C., NGUYEN, H.T., ZHONG, D., LI, J., LU, T., LIU, Y., LOCKERY, M. N., WEBER, K. J., CATCHPOLE, K. R. & WHITE, T. P. 2017. Interface passivation using ultrathin polymer-fullerene films for high-efficiency perovskite solar cells with negligible hysteresis. *Energy & Environmental Science*, 10, 1792-1800.

F23 INSIGHTS INTO HYDROGENATION OF DEFECTS IN SILICON SOLAR CELLS

ACAP Fellow

Chang Sun

Supervisor

Prof. Daniel Macdonald

Funding Support

ACAP

Aim

This project aims to provide new insights into the hydrogenation of defects in silicon solar cells, and develop new hydrogenation techniques.

Progress

WP1.1 aims to provide direct experimental evidence for bulk hydrogen incorporation at low temperatures by the silicon heterojunction (SHJ) solar cells–related a-Si stacks, observed in my previous works (Sun et al. 2018; Sun et al. 2019) through the regeneration of boron-oxygen defects. The experimental idea is: we deposit H-lean sputter a-Si on one side of a wafer, and deposit H-rich a-Si stacks on the other side. During annealing, hydrogen will effuse out of the a-Si stacks, diffuse through the wafer thickness, and be captured by the H-lean, defective sputter a-Si. The captured H can be measured by SIMS measurements. In the beginning, we had planned to use deuterated a-Si stacks for the experiment; however, the lab at Arizona State niversity (ASU) which provides SHJ cells to us was badly affected by the pandemic, and deuterium could not be connected. So we did the experiments with hydrogen. H concentrations measured by SIMS are shown in Figure F23.1. The peaks in the data are caused by the periodic stops during the deposition of sputter a-Si. We can see that more [H] was detected from the i/p$^+$ stack than the i/n$^+$ stack, in agreement with previous findings. However, we are not able to fully interpret the results at the moment: first, we expected the 30 second H_2 plasma treatment would result in higher [H] than the 15 second treatment for the i/p$^+$ stack; second, we expected the bare Si case to have lower [H] than all of the other cases. We suspect that the results are affected by the intrinsic H content in the sputter a-Si films, so in the future we need to deposit a-Si films containing less H to replace this sputter a-Si. We are considering the a-Si created by implantation at the moment and some tests are being conducted.

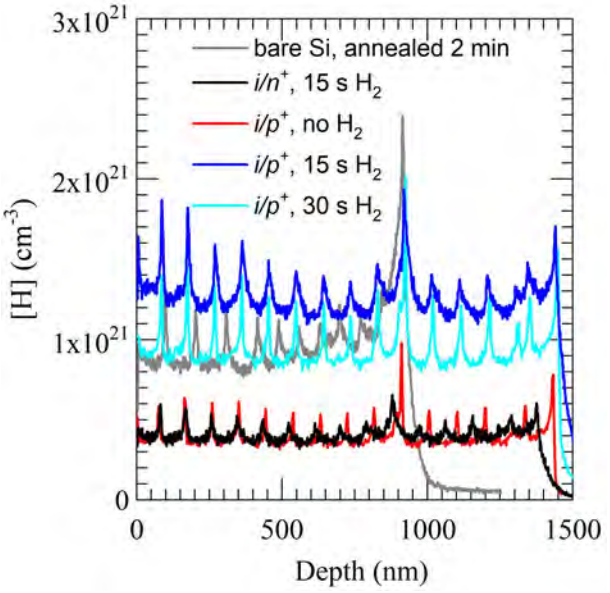

Figure F23.1: [H] measured by SIMS in the sputter a-Si film, with bare Si, a-Si (i/n$^+$), or a-Si (i/p$^+$) with different durations of H_2 plasma treatment on the other side of the wafer.

In WP1.2, we investigated how grain boundaries (GBs) in high performance multicrystalline Si (HP mc-Si), dislocation clusters in cast-grown mono-like Si, and ring defects in UMG Cz Si react to the hydrogenation by the SHJ cell a-Si stacks. Wafers containing the three types of defects respectively, were prepared at ANU and sent to ASU to make the SHJ cell structure without ITO or metal. We observed very similar results on the three types of defects. Figure F23.2 gives the PL images and lifetimes at $\Delta n = 1\times10^{15}$ cm^{-3} of two HP mc-Si wafers during the processes. We did not observe pronounced passivation of GBs after the deposition of the a-Si stacks, or subsequent 200–300°C dark anneals. The lifetime even degraded during these dark anneals, indicating the effusion of H from the stacks or bulk. We then sent another as-deposited wafer ((d), without any dark annealing) to UNSW, for a firing at 500–570°C, 6 seconds firing in a belt furnace. As the high temperature would damage the a-Si passivation, we removed the a-Si stacks and passivated the wafer with SiN_x films at ANU. We observed the passivation of a lot of GBs as well as an improvement in lifetime (>2 times higher). This means that the high temperature (>500°C) is required for the passivation reaction between GBs and H. In conclusion, for GBs, dislocations and rings, pre-fabrication defect engineering as described in (Hallam et al. 2018) is more viable for SHJ cells. These defects not only require the presence of H in the bulk, but also high temperature for H to bind with them. This is very different from the boron-oxygen defects, which, as described in (Sun et al. 2018), can be deactivated at lower temperatures in finished SHJ cells.

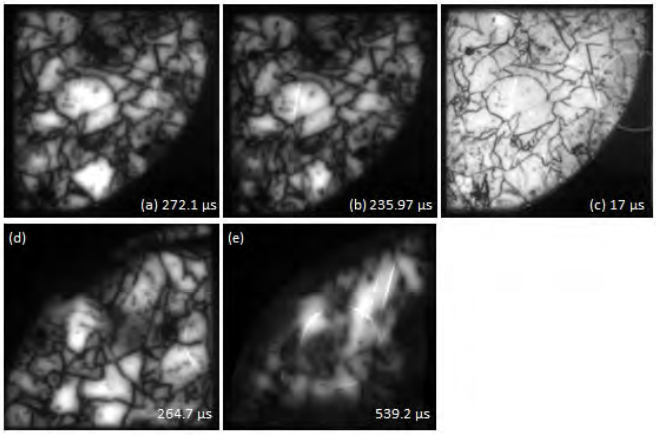

Figure F23.2: PL image and lifetime at Δn = 1×10^{15} cm^{-3} of GBs in two HP mc-Si wafers: (a) the first wafer, after deposition of the a-Si stacks, and then (b) dark annealed at 200°C for 20 minutes, to simulate the screen-printing-curing dark annealing during the SHJ cell processes, and then (c) dark annealed at 300°C for 20 minutes. (d) The second wafer, after deposition of the a-Si stacks, and then (e) fired in a belt furnace at UNSW, at 500–570°C for 6 seconds, followed by removal of a-Si stacks and SiN$_x$ passivation on both sides.

WP3.1 aims to investigate/verify the theoretical charge state model through experiments on the charge state of interstitial Fe (Fe$_i$) in p-type silicon. The dissociation of FeB pairs in p-type silicon under injection is often explained by the charge state change of interstitial Fe (Fei) from positive to neutral. However, it is also sometimes interpreted as a Recombination-Enhanced Defect Reaction (REDR) mechanism. We have designed and performed experiments to distinctly separate and compare the two effects. The results of this study were published as a journal paper (Sun et al. 2021). The main findings are: (1) the rigorous charge state model (Sun et al. 2015) is verified by the experimental observations to be more reasonable than the quasi-Fermi level approximation which is frequently used in the literature. This can be seen from Figure 23.3(d): almost all the pairs are predicted based on the approximation to be dissociated from an injection level as low as 10^{11} cm^{-3}, which disagrees with the experimental observations. (2) The comparison of the charge effect and the REDR effect showed that the REDR effect is the dominant effect in most cases in dissociating FeB pairs under injection. This is also shown in Figure F23.3: the REDR effect is much stronger than the charge effect over most of the injection range shown in the figure. Greater details of this study can be found in Sun et al. 2021.

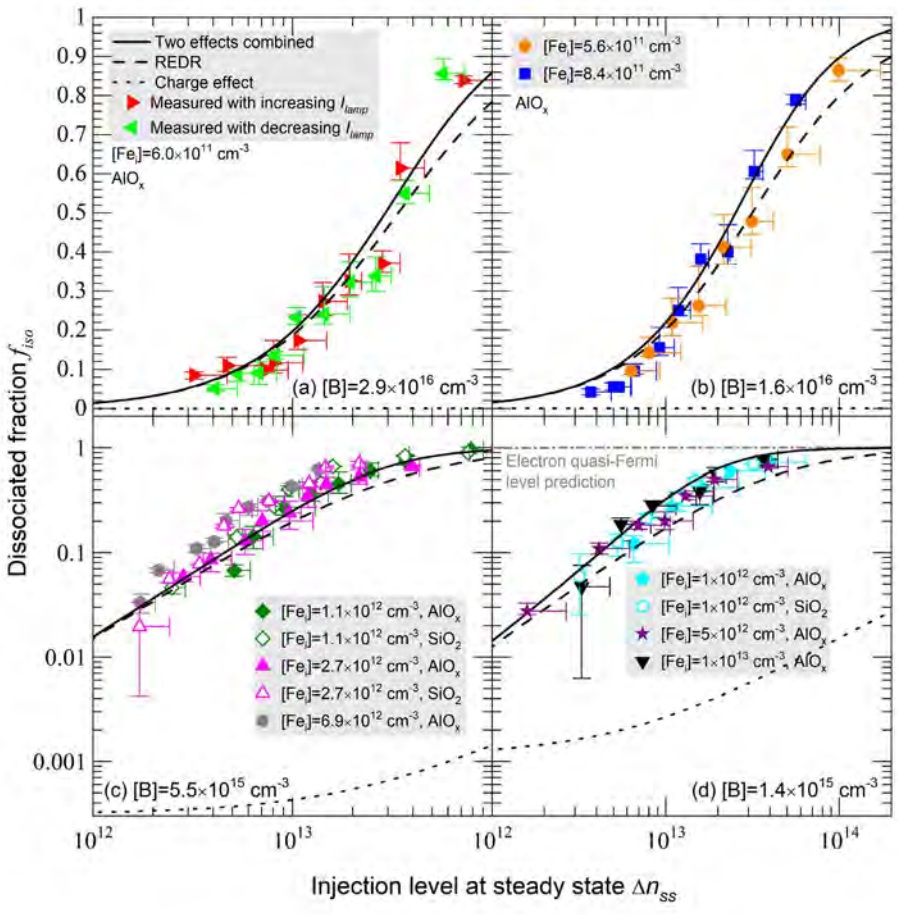

Figure F23.3: Dissociated fraction f_{iso} as a function of injection level at the steady state Δn_{ss}. Data points were calculated from the measurements. The lines are the predicted dissociated fractions under only the charge effect, and only the REDR effect, and both effects. The results predicted based on the electron quasi-Fermi level approximation are shown in (d).

WP3.2 aims to further develop this charge state model in WP3.1, and investigate the charge state of H experimentally. In the passivated contact solar cell processes at ANU, we observed some interesting results comparing the n^+ polysilicon layer and the p^+ polysilicon layer: the n^+ layer usually provides better passivation in comparison with the p^+ layer, but is less firing stable. This can be potentially explained by different charge states of H in the two layers. So we decided to model the charge distribution of H in the two layers. Based on some preliminary SIMS results, [H] can be up to 10^{21} cm^{-3} in the polysilicon layers, which is comparable with the doping concentration. In this condition, the simplified SRH model which assumes that the concentration of the defect N_t << doping level does not hold any more, so we developed a more general charge state model based on the general SRH model, in which the previous assumption N_t << doping level is not required. Two significant differences of this general charge state model from the previous model described in Sun et al. 2015 are: (1) now the charge distribution will depend on N_t (which is [H] for the case of H); and (2) N_t will also affect the equilibrium carrier concentrations n_0 and p_0, and the injected carrier concentrations Δn and Δp in a non-equilibrium steady state. An example of the modelling results is shown in Figure F23.4. The [B] was measured by ECV in a B-doped p^+ poly-Si–passivated Si wafer (as an input of the model). The model assumes the total [H] to be 10^{21} cm^{-3}. A very interesting observation is that H has compensated the heavy p^+ doping to light n-type, as shown by the results of n_0. Similarly, in n^+ poly-Si layer, a high [H] could compensate the doping to light p-type. This compensation effect of H and the charge distribution can potentially explain the different passivation quality and firing stability of n^+ and p^+ poly silicon layers. A conference abstract (Kang et al. 2021) has been submitted, and more investigation on this topic is underway.

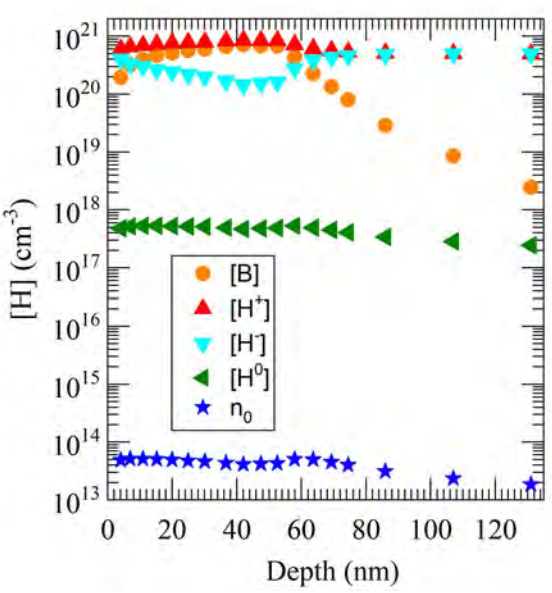

Figure F23.4: Measured [B], and modelled n_0, $[H^+]$, $[H^-]$, $[H^0]$ in a B-doped p^+ polysilicon layer, and the near-surface region of the bulk (the thin SiO_2 film is neglected in the modelling) in thermal equilibrium at 300 K. The total [H] in the modelling was assumed to be 10^{21} cm^{-3}, based on some preliminary SIMS measurements.

Highlights

- For GBs, dislocations and rings, a pre-fabrication hydrogenation step before the SHJ processes is more viable, as they require temperatures >500°C. This is very different from the boron-oxygen defects, which do not require high temperature to be regenerated, and can be regenerated in finished SHJ cells.
- The rigorous charge state model (Sun et al. 2015) is verified by some experimental results on FeB dissociation in p-Si, to be more reasonable than the quasi-Fermi level approximation which is frequently used in the literature. In the dissociation of FeB in p-Si under injection, REDR plays a more dominant role than the charge effect.
- A more general charge state model based on the general SRH model was developed, in which the previous assumption Nt << doping level is not required any more. Some preliminary modelling results indicate that hydrogen has a significant compensation effect in both n^+ and p^+ poly silicon layers. The compensation effect and the charge distribution of hydrogen can potentially explain the different passivation quality and firing stability of n+ and p+ polysilicon layers.

Future Work

- We will deposit and test implanted a-Si as the caption layer in WP1.1.
- Finalise developing and testing the hydrogen effusion system at ANU and conduct measurements in PP2.
- Continue the modelling and experimental work in WP3.2: a more thorough investigation of how the charge state of H impacts the passivation and firing stability of a poly-Si layer will be conducted.

References

HALLAM, B., CHEN, D., SHI, J., EINHAUS, R., HOLMAN, Z. C. & WENHAM, S. 2018. Pre-Fabrication Gettering and Hydrogenation Treatments for Silicon Heterojunction Solar Cells: A Possible Path to> 700 mV Open-Circuit Voltages Using Low-Lifetime Commercial-Grade p-Type Czochralski Silicon. *Solar RRL,* 2.

KANG, D., SIO, H. C., YAN, D., STUCKELBERGER, J., SUN, C., TRUONG, T. N., PHANG, S. P., LIU, R. & MACDONALD, D. Firing Stability of Polysilicon Passivating Contacts: The Role of Hydrogen. IEEE PVSC-48, Miami, submitted, 2021.

SUN, C., CHEN, D., WEIGAND, W., BASNET, R., PHANG, S. P., HALLAM, B., HOLMAN, Z. C. & MACDONALD, D. 2018. Complete regeneration of BO-related defects in n-type upgraded metallurgical-grade Czochralski-grown silicon heterojunction solar cells. *Applied Physics Letters,* 113, 152105.

SUN, C., ROUGIEUX, F. E. & MACDONALD, D. 2015. A unified approach to modelling the charge state of monatomic hydrogen and other defects in crystalline silicon. *Journal of Applied Physics,* 117, 045702.

SUN, C., WEIGAND, W., SHI, J., YU, Z., BASNET, R., PHANG, S. P., HOLMAN, Z. C. & MACDONALD, D. 2019. Origins of hydrogen that passivates bulk defects in silicon heterojunction solar cells. *Applied Physics Letters*, 115, 252103.

SUN, C., ZHU, Y., JUHL, M., YANG, W., ROUGIEUX, F., HAMEIRI, Z. & MACDONALD, D. 2021. The Role of Charge and Recombination-Enhanced Defect Reaction Effects in the Dissociation of FeB Pairs in p-Type Silicon under Carrier Injection. *physica status solidi (RRL) – Rapid Research Letters*, 2000520.

F24 NOVEL APPROACH FOR THE INTEGRATION OF CARRIER-SELECTIVE PASSIVATING CONTACTS ON THE FRONT OF INDUSTRIAL SILICON SOLAR CELLS

ACAP Fellow

Josua Stuckelberger

Supervisor

Prof. Daniel Macdonald

Funding Support

ACAP

Aim

The project aims to locally implement polysilicon contacts below the metallisation on the front side of n-type silicon solar cells with maximal one diffusion step per dopant species.

Progress

To date, polysilicon structures are applied on the rear side of c-Si solar cells thanks to their excellent passivating properties. Therefore the boron-diffused front side becomes the efficiency limiting factor, particularly the recombination losses at the contact openings. Applying a polysilicon contact on the front side as well targets these losses directly. However, a patterned polysilicon layer below the metallisation is necessary to outperform the low parasitic absorption of Al_2O_3/SiN_x. In this project we focus on two different pathways to reach this goal: (i) develop a self-limiting wet etching process enabling the removal of the highly doped polysilicon locally, whilst stopping at the wafer/SiO_x interface, maintaining the shallow-doped region at the wafer surface; (ii) develop fabrication processes using alternative doping sources, which allow localised variations in dopant concentration.

Self-limiting wet etching approach

This approach is based on a self-limiting wet etching process enabling the removal of the highly doped polysilicon layer locally, whilst stopping at the wafer/SiO_x interface, maintaining the shallow-doped region at the wafer surface. This opens up a broad range of lean processes achieving the generation of highly performing patterned polysilicon layers with only one diffusion step. In our experiments, we chose tetramethylammonium hydroxide (TMAH) as the etching solution. TMAH is known for its high selectivity in etching silicon versus SiO_2, which is needed to etch the boron-doped polysilicon layer stopping at the ultrathin SiO_2 layer (~1–2 nm thick) at the wafer surface. Firstly we developed a masking layer that can be easily patterned while resisting the TMAH etching solution. After testing a broad range of different layers, a stack of SiO_x/SiN_x was found to withstand the TMAH solution without the formation of pinholes. In a second step, the etching time of the polysilicon layers is analysed keeping part of the polysilicon protected by the SiO_x/SiN_x etch-mask. In Figure F24.1 SEM micrographs are shown after etching the polysilicon locally and removing the etch-mask and the remaining SiO_x at the wafer surface using diluted hydrofluoric acid. Figure F24.1 shows three different etching times (20 s, 160 s and 360 s), in top-view (a)–(f) and cross-section (g)–(i). It can be seen that 20 s etching (Figure F24.1(a), (d) and (g)) already removes the 100 nm polysilicon completely, but it leaves remaining Si crystals/grains present in the etched area. These remnants on the wafer surface will be highly recombination active and difficult to passivate and therefore will limit the final cell performance remarkably. After 160 s (Figure F24.1(b), (e) and (h)), the etched surface is smooth and no remaining polysilicon crystals can be found. At the same time only a few pinholes (circled in red) can be detected, meaning that the ultrathin interfacial SiO_x was able to resist the etching, in contrast to the 360 s etching where a high density of pinholes is found.

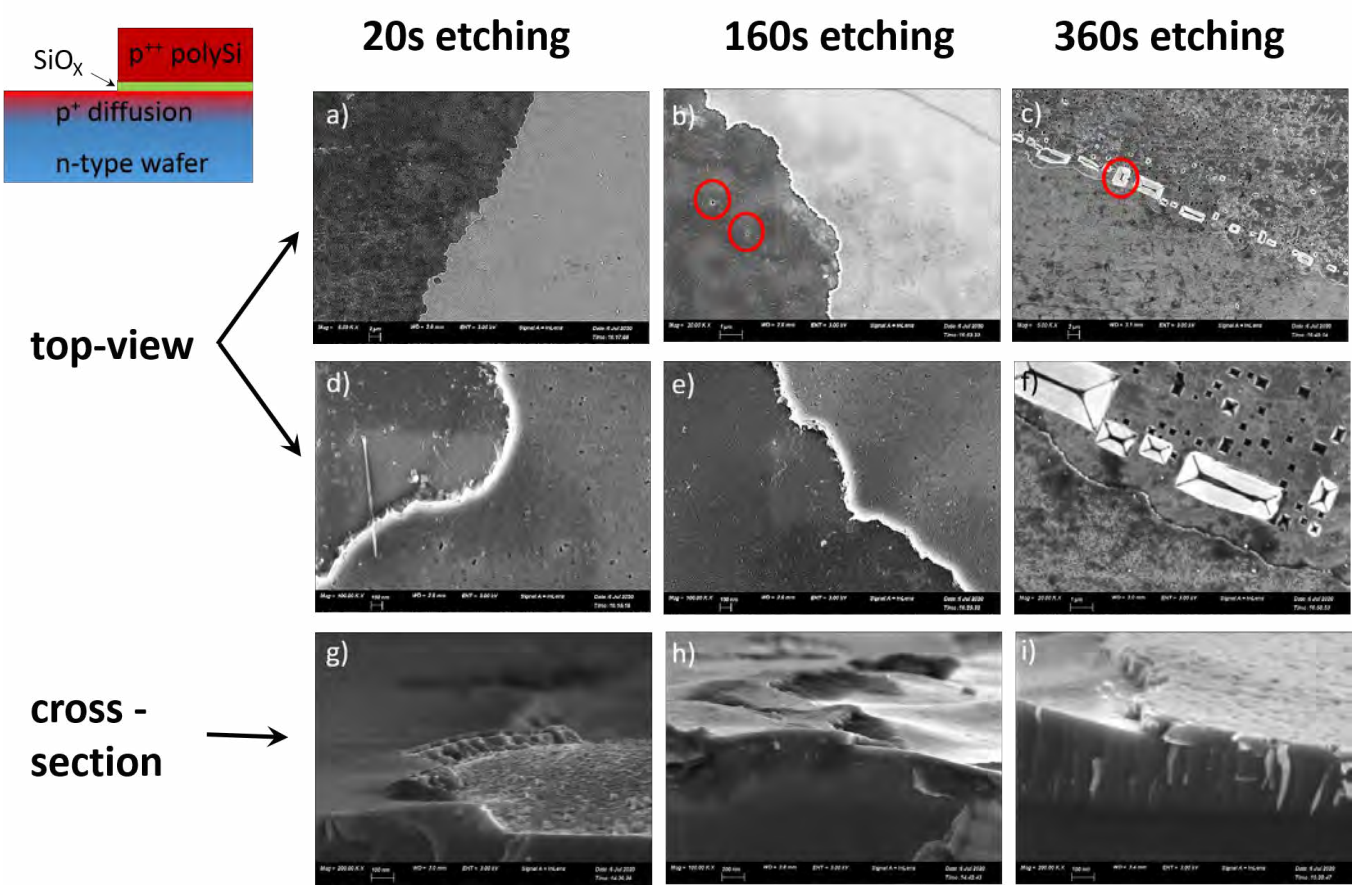

Figure F24.1: SEM micrographs after etching the polysilicon layer locally. A sketch of the remaining structure is shown in the top left corner.

These findings were integrated in the fabrication of first batches of cells containing polysilicon under the finger leading to preliminary results with a conversion efficiency of 13.1%. It is clear that these results are not yet competitive, but the main limitations are identified as high series resistance (low fill factor) and low open-circuit voltage (V_{OC}). The high series resistance results from a suboptimal lateral conductivity in the shallow diffused region. This was expected and can be tuned changing the annealing conditions, which is part of the optimisation process now that the cell process is determined. The same holds for the low open-circuit voltage. A promising implied open-circuit voltage (iV_{OC}) of 710 mV was achieved after the patterning and re-passivation by AlO_X/SiN_X, but an unexpectedly detrimental hydrogenation process led to losses in iV_{OC} of over 50 mV.

Until this stage, our main focus was the determination of a cell fabrication process that enables polysilicon fingers under the metallisation using only one annealing per dopant. As this is now established, the next steps will be the optimisation of said processes pushing the efficiency to be able to compete with the state-of-the-art.

Alternative doping sources

The second approach is based on liquid doping sources either as spin-on doping or via inkjet printing. Liquid doping sources have several advantages: (i) they involve less dangerous materials; (ii) the liquid dopant inks can contain a wide variety of chemical elements (dopant species) with different concentrations; and (iii) the doped regions can be patterned easily.

We developed the spin-on doping process directly on industrially fabricated symmetrical polysilicon samples provided by Jinko Solar. For n-type passivating contacts (phosphorus doped), we were able to reach a high iV_{OC} of above 730 mV together with a low contact resistivity below 4 mΩ·cm^2 for 100–230 nm thick polysilicon layers after a thermal treatment at 975°C for 60 minutes followed by a forming gas annealing (FGA). In Figure F24.2 the iV_{OC} (a) and the contact resistivity (b) are shown as functions of the drive-in temperature. We also analysed the underlying recombination mechanism and separated the Auger recombination from recombination occurring at the SiO_X interface using advanced simulations. These promising results imply that phosphorus spin-on doping can be an effective doping method alternative to conventional POCl3 diffusion.

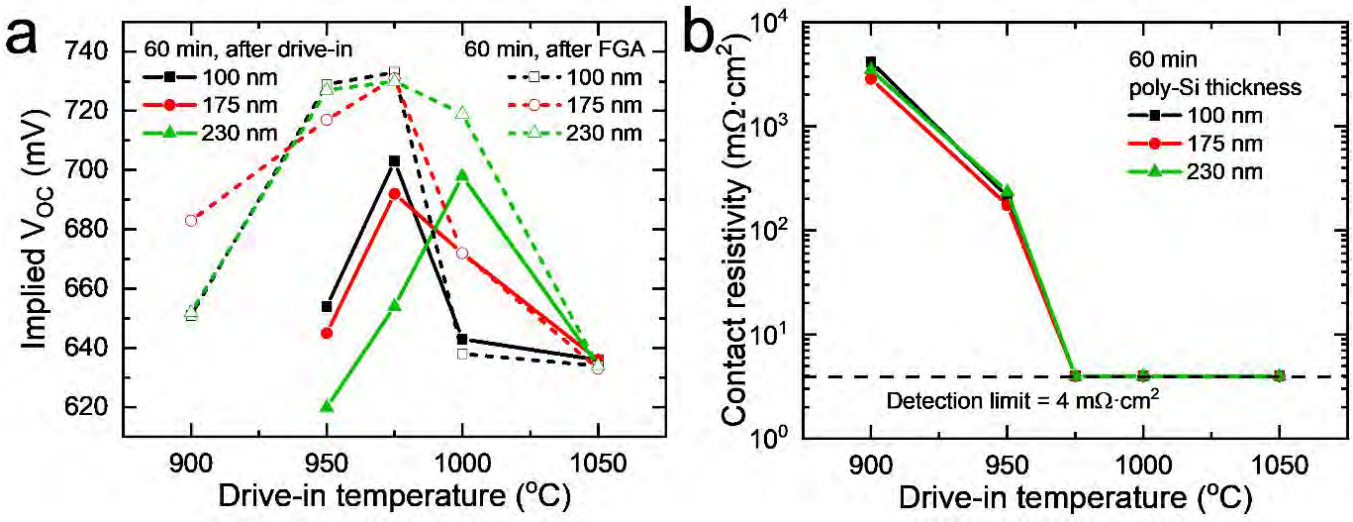

Figure F24.2: Implied open-circuit voltage (a) and contact resistivity (b) as functions of drive-in temperature for n-type polysilicon passivating contacts doped with phosphorus via spin-on doping method. Data from Ding et al. Sol. Energy Mater Sol. Cells (2021).

For p-type passivating contacts (boron-doped), a similar study and optimisation was performed leading to an optimal iVoc >720 mV, together with a contact resistivity (ρc) below 5 mΩ.cm^2 for 100–230 nm thick polysilicon layers after a thermal treatment at 950°C for 60 minutes. In Figure F24.3 the iV_{OC} (a) and the contact resistivity (b) are shown as functions of the drive-in temperature. Whereas for the phosphorus-doped polysilicon molecular hydrogen from FGA led already to excellent passivation, the boron-doped polysilicon contacts benefit when atomic hydrogen is provided via an AlO_X/SiN_X capping layer acting as a hydrogen donor during a subsequent annealing. These results demonstrate that boron spin-on doping is a promising alternative to the conventional BBr3 diffusion for the fabrication of p-type polysilicon passivating contacts.

To further improve the p-type passivating contacts, we tested the influence of gallium as a dopant. We made use of one of the advantages of liquid doping sources and mixed the boron and the gallium containing doping solutions together with varying ratios. A trade-off is found between the Ga and the B doping. Purely Ga-doped samples provide the best passivation (atomic hydrogenation is key) but suffer from a higher contact resistivity. In Figure F24.4 the iV_{OC} (a) and the contact resistivity (b) are shown as functions of the percentage of Ga in the B-Ga mixed solution.

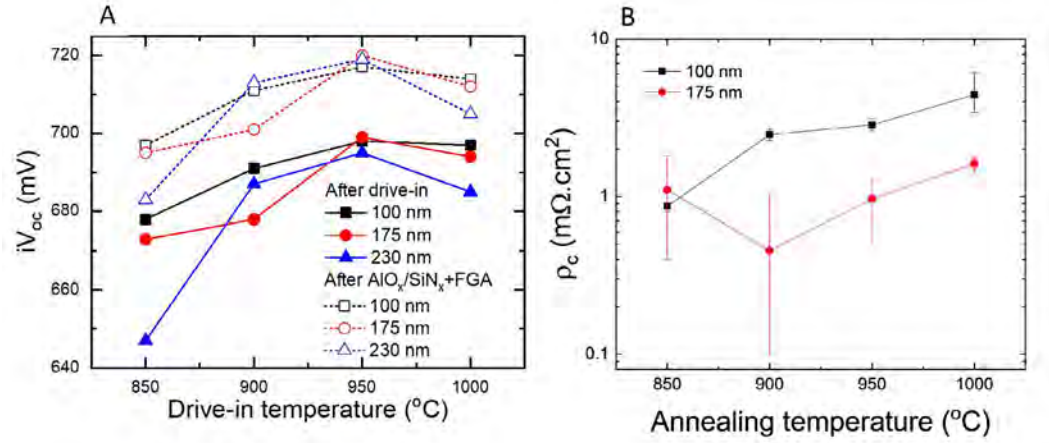

Figure F24.3: Implied open-circuit voltage (a) and contact resistivity (b) as functions of drive-in temperature for p-type polysilicon passivating contacts doped with boron via spin-on doping method.

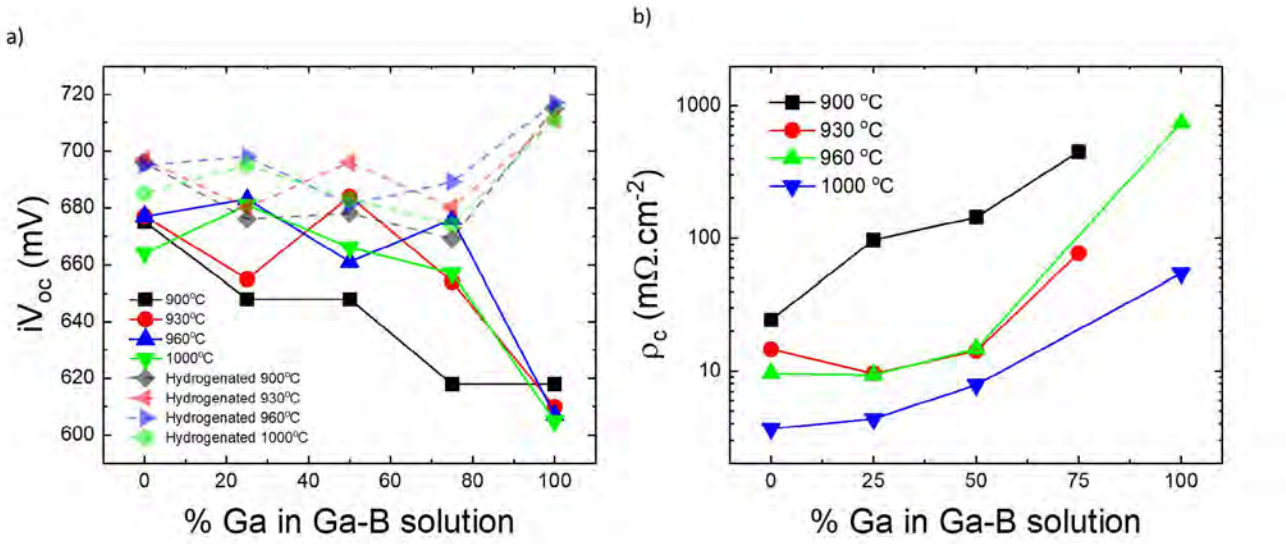

Figure F24.4: Implied open-circuit voltage (a) and contact resistivity (b) as functions of percentage of Ga in the B-Ga mixed solution.

Finally, the liquid phosphorus doping solutions were adjusted to meet the requirements to be printed using an inkjet printer. In first tests, we were able to reach iV_{oc} above 705 mV and to print lines with a width below 100 µm which is promising for more advanced cell structures.

In addition to the work directly related to the goals of the Fellowship, the newest results on the impact of pre-annealing on p-type polysilicon contacts was presented at the APRSC (Stuckelberger et al.2020), we fabricated interfacial SiO_x layers in situ by PECVD before the growth of the polysilicon layer (Chen et al., 2020), and we deepened our understanding of how to characterise the localised polysilicon structures using micro-photoluminescence spectroscopy (Wu et al. 2020).

Highlights

- Development of a process sequence integrating localised polysilicon passivating contacts below the metallisation with one single thermal treatment per doping.
- Spin-on doping processes for n- as well as p-type polysilicon contacts have shown their potential as an alternative for conventional gas diffusion with iV_{oc}'s over 730 mV and 720 mV, respectively.
- The localised inkjet printing of doping sources reached competitive passivation above 705 mV.

Future Work

- Having a cell fabrication process that enables polysilicon fingers under the metallisation developed, the next steps will be the optimisation of said processes pushing the efficiency to be able to compete with the state-of-the-art.
- The n- as well as p-type polysilicon passivating contacts doped from liquid doping sources will be integrated in devices proving the potential of this technology on high efficiency silicon solar cells.

References

CHEN, W., STUCKELBERGER, J., WANG, W., PHANG, S. P., KANG, D., SAMDUNDSETT, C. & MACDONALD, D., (2020) Influence of PECVD Deposition Power and Pressure on Phosphorus-Doped Polysilicon Passivating Contacts. *IEEE J. PHOTOVOLT*. 10. https://doi.org/10.1109/JPHOTOV.2020.3001166.

DING, Z., YAN, D., STUCKELBERGER, J., PHANG, S. P., CHEN, W., SAMUNDSETT, C., YANG, J., WANG, Z., ZHENG, P., ZHANG, X., WAN, Y. & MACDONALD, D., 2021. Phosphorus-doped polycrystalline silicon passivating contacts via spin-on doping. *Solar Energy Materials and Solar Cells*. 221. https://doi.org/10.1016/j.solmat.2020.110902.

STUCKELBERGER, J., YAN, D., PHANG, S. P., SAMUNDSETT, C., ANTOGNINI, L., HAUG, F.-J., WANG, Z. YANG, J. ZHENG, P., ZHANG, X. & MACDONALD, D. (2020) Impact of Pre-Annealing on Industrially LPCVD Deposited PolySi Hole-selective Contacts. Asia-Pacific Solar Research Conference – visual presentation.

WU, H., NGUYEN, H. T., YAN, D., STUCKELBERGER, J., CHEN, W., WANG, W., & MACDONALD, D., 2020. Micro-Photoluminescence Studies of Shallow Phosphorus Diffusions below Polysilicon Passivating Contacts. *Solar Energy Materials and Solar Cells*. 218. https://doi.org/10.1016/j.solmat.2020.110780.

F25 SOLUTION-PROCESSED MULTI-JUNCTION ARCHITECTURES FOR HIGH-THROUGHPUT, FLEXIBLE AND PRINTABLE SOLAR CELLS

ACAP Fellow

David McMeekin

Supervisor

Prof. Udo Bach

Funding Support

ACAP

Aim

The focus of our research is geared towards the design and fabrication of fully solution-processable and stable multi-junction all-perovskite solar cells for high-throughput application.

Progress

Silicon-based solar cells are currently commercially available and leading today's solar energy market. However, as their efficiencies converge towards their maximum theoretical limit, price reductions will soon become increasingly difficult to achieve. Multi-junction architectures can overcome this single-junction efficiency limit – by absorbing various portions of the solar spectrum using different materials, we can reduce thermalisation losses. Perovskite materials are solution-processable, which allows for compatibility with existing low-cost, high-throughput printable deposition techniques such as roll-to-roll or inkjet printing. This disruptive next generation technology would allow for the first low-cost, flexible and highly efficient solar cells.

Our recent work focuses on the design and fabrication of multi-junction perovskite solar cells for high-throughput application. These architectures consist of two or more absorbing materials, which allows us to move beyond the Shockley–Queisser limit. By integrating novel perovskite materials in tandem and multi-junction architectures, significant solar energy price reduction could potentially be obtained. However, today, all-perovskite multi-junction solar cells are fabricated using expensive, high-vacuum deposition techniques such as atomic layer deposition (ALD) and magnetron sputtering (Bush et al. 2017). These deposition steps may ultimately negate any cost benefit from having greater efficiency. Furthermore, mixed-halide perovskite solar cells suffer from an increase in open-circuit losses due to a combination of halide redistribution and an increase in energetic disorder under illumination. Lattice disorder can lead to non-radiative recombination pathways. Moreover, narrow-bandgap perovskite materials, comprised of a mixture of tin and lead, are prone to oxidation from a Sn^{2+} state to a Sn^{4+} state (Eperon et al. 2016). [This oxidation process creates deep trap states within the semiconductor, which induces an unwanted p-type behaviour that promotes high levels of recombination. Suppressing these mechanisms to obtain greater performance and stability is vital to the success of perovskite solar cells in tandem applications.

Lastly, the choice of cation, occupying the A-site in the ABX_3 structure, has a crucial impact on stability of the perovskite material. A formamidinium-based perovskite is a viable approach towards long-term stability. However, in order to fabricate a fully solution-based perovskite-perovskite tandem, an acetonitrile/methylamine (ACN/MA) solvent-system is needed to process the narrow-bandgap perovskite on top of an existing wide-bandgap perovskite solar cell. Using an orthogonal solvent-system, we can sequentially deposit a perovskite layer on top of an existing perovskite without any solvent damage, to create a monolithic two-junction tandem solar cell. Although we have previously demonstrated this stacking ability (McMeekin et al. 2019), we have yet to incorporate the more stable formamidinium (FA^+) cation into this solvent system. This would allow for the deposition of a stable narrow-bandgap perovskite junction to improve the thermal stability of the entire tandem solar cell stack.

The ACAP Fellowship enabled us to progress on solving the "fully solution-processed tandem solar cell" problem. As shown in Figure F25.1 and Figure F25.2, we were able to create a mixed-cation mixed-metal ($FA_xMA_{1-x}Pb_xSn_{1-y}I_3$) perovskite using an ACN/MA solvent-system to process the perovskite. As shown in Figure. F25.1(a), this partial cation substitution from methylammonium (MA^+) to formamidinium allowed us to slightly narrow the bandgap, while simultaneously providing a greater thermal and phase stability to the perovskite structure. In Figure F25.1(b), we show the partial metal substitution at the B-site, where the Sn^{2+} is substituting the Pb^{2+} cation. This allows for a significant bandgap reduction in the perovskite semiconductor.

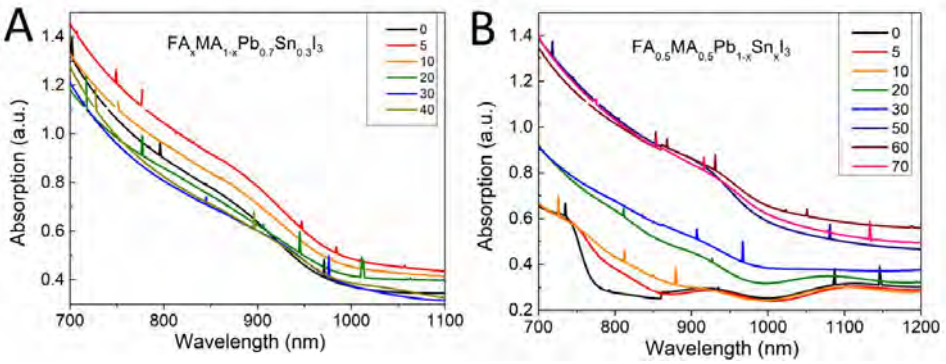

Figure F25.1: UV-Vis absorption spectra of the (a) $FA_xMA_{1-x}Pb_{0.7}Sn_{0.3}I_3$ and the (b) $FA_{0.5}MA_{0.5}Pb_{1-x}Sn_xI_3$ perovskite systems.

Furthermore, as shown in Figure F25.2, we conducted an X-ray diffraction study for both of these systems. We observed that the addition of FA^+ resulted in a significant increase in preferred orientation in the (100) direction. We obtained the highest level of texturing when substituting 20% MA with FA. However, as we increased the FA^+ content in the $FA_xMA_{1-x}Pb_{1-y}Sn_yI_3$ perovskite system, we observed lower angle peaks appearing. These lower angle peaks do not usually appear in the standard DMF/DMSO solvent system, hence additional information will be needed to identify these peaks. When varying the metal content in the $FA_{0.5}MA_{0.5}Pb_{1-x}Sn_xI_3$ perovskite system, we obtained a highest texturing with 60% Sn and 40% Pb. Fine tuning of both the A-site and B-site content is crucial to obtain the highest material quality possible.

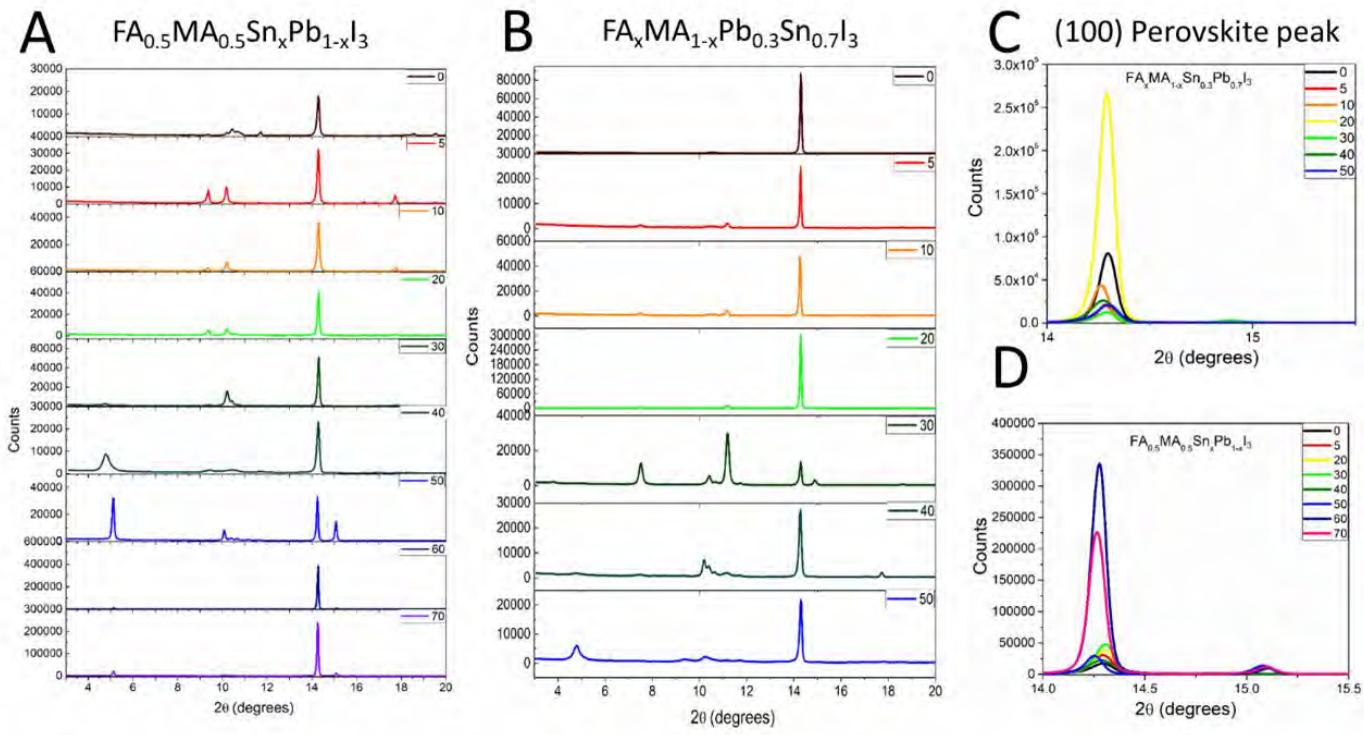

Figure F25.2: X-ray diffraction patterns of the(a) $FA_xMA_{1-x}Pb_{0.7}Sn_{0.3}I_3$ and the (b) $FA_{0.5}MA_{0.5}Pb_{1-x}Sn_xI_3$ perovskite systems. A zoom of the (100) perovskite peak for the (c) $FA_xMA_{1-x}Pb_{0.7}Sn_{0.3}I_3$ and the (d) $FA_{0.5}MA_{0.5}Pb_{1-x}Sn_xI_3$ perovskite systems.

We then proceeded to incorporate this $FA_xMA_{1-x}Pb_{1-y}Sn_yI_3$ perovskite system into perovskite/perovskite multijunction architectures as a wide-bandgap perovskite absorber. We incorporated this material into a Spiro-MeOTAD-free p-i-n structure that utilises poly(triaryl amine) (PTAA) instead. This "inverted" p-i-n structure resulted in a stable solution-processed multi-junction architecture, offering significantly greater operational stability over its n-i-p architecture counterpart. In Figure F25.3, we show a cross-sectional scanning electron microscope (SEM) of a solution-processed tandem solar cell.

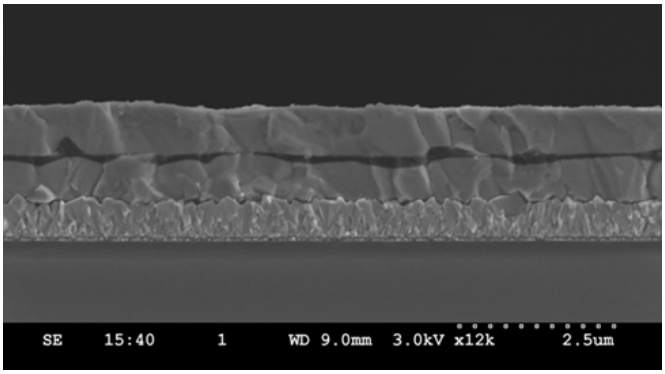

Figure F25.3: A cross-sectional scanning electron microscope (SEM) of a solution-processed tandem solar cell.

Finally, we believe that these progresses will result in stability improvements in the overall tandem. By tuning the ionic composition of the $FA_xMA_{1-x}Pb_{1-y}Sn_yI_3$ perovskite system, we could obtain a highly ordered and oriented narrow-bandgap perovskite. Furthermore, these thermally stable ions were successfully solubilised via the ACN/MA solvent complex, which allowed us to construct the first p-i-n solution-processed tandem solar cell, including the recombination layer. However, significant progress is still needed to achieve similar power conversion efficiencies (PCEs) reached using a tin oxide/indium-thin-oxide (SnO_2/ITO) interlayer.

Highlights

- The successful incorporation of the formamidinium cation in the ACN/MA solvent system.
- This incorporation has allowed us to form a narrow-bandgap $FA_xMA_{1-x}Sn_yPb_{1-y}I_3$ perovskite system that can be processed on top of an existing wide-bandgap perovskite junction.
- We have successfully fabricated a solution-processed tandem solar cell with a p-i-n architecture.
- Replacement of the Spiro-MeOTAD hole-accepting layer with a poly(triaryl amine) (PTAA) layer allowed for improvements in the overall the architecture.

Future Work

- In-depth structural and thermal characterisation to assess the improvements from the ionic composition.
- Operational degradation study of an encapsulated solution-processed tandem solar cell device.
- Addition of reducing agents to suppress the undesired oxidative behaviour of the Sn-based perovskite from Sn^{2+} to Sn^{+4}.
- Identification and suppression of the lower angle XRD peak found in the FA-based ACN/MA perovskite system.

References

BUSH, K. A., PALMSTROM, A. F., YU, Z. J., BOCCARD, M., CHEACHAROEN, R., MAILOA, J. P., MCMEEKIN, D. P., HOYE, R. L. Z., BAILIE, C. D., LEIJTENS, T., PETERS, I. M., MINICHETTI, M. C., ROLSTON, N., PRASANNA, R., SOFIA, S., HARWOOD, D., MA, W., MOGHADAM, F., SNAITH, H. J., BUONASSISI, T., HOLMAN, Z. C., BENT, S. F. & MCGEHEE, M. D. 2017. 23.6%-efficient monolithic perovskite/silicon tandem solar cells with improved stability, Nature Energy, 2, 17009.

EPERON, G. E., LEIJTENS, T., BUSH, K. A., PRASANNA, R., GREEN, T., WANG, J. T., MCMEEKIN, D. P., VOLONAKIS, G., MILOT, R. L., MAY, R., PALMSTROM, A., SLOTCAVAGE, D. J., BELISLE, R. A., PATEL, J. B., PARROTT, E. S., SUTTON, R. J., MA, W., MOGHADAM, F., CONINGS, B., BABAYIGIT, A., BOYEN, H. G., BENT, S., GIUSTINO, F., HERZ, L. M., JOHNSTON, M. B., MCGEHEE, M. D. & SNAITH, H. J. 2016. Perovskite-perovskite tandem photovoltaics with optimized band gaps, Science, 354, 861-865.

MCMEEKIN, D. P., MAHESH, S., NOEL, N. K., KLUG, M. T., LIM, J., WARBY, J. H., BALL, J. M., HERZ, L. M., JOHNSTON, M. B. & SNAITH, H. J. 2019. Solution-Processed All-Perovskite Multi-junction Solar Cells, Joule, 3, 387-401.

F26 TOWARDS SINGLE-CRYSTALLINE PEROVSKITE SOLAR CELLS

ACAP Fellow

Wenxin Mao

Supervisor

Prof. Udo Bach

Funding Support

ACAP

Aim

This project aims to develop the method to fabricate bandgap-stable single-crystalline mixed halide perovskite solar cells and suppress light-induced phase segregation.

Progress

In our previous work, we studied photoinduced halide-ion segregation (PHS) effect in mixed halide perovskite single crystals, where we observed that PHS is able to happen at both crystal edges (grain boundaries) and crystal interior (Mao et al., 2019, Chen et al., 2019). Here we demonstrate that photo-induced halide-ion segregation can be actively controlled in situ with light and investigate the driving mechanisms using fluorescence microspectroscopy. We develop a two-dimensional lattice model that reproduces the experimental results by assuming that the driving force for photo-induced phase segregation is dependent on carrier-induced strain gradients that

vanish at sufficiently high carrier densities. The ability to control ion segregation could become key to solving the issue of halide demixing and to harness the exceptional opportunities associated with a bandgap tunable semiconductor material. Our work creates a new pathway for the application of mixed-halide perovskites in photovoltaics, including tandem solar cells and concentrator solar cells.

For this study we use single crystal microplatelets to visualise and probe PHS away from grain boundaries. We fabricated single-crystal $MAPb(Br_{0.8}I_{0.2})_3$ microplatelets following our reported procedure (Chen et al., 2019, Mao et al., 2019). The crystals have an average size of 30 µm and thickness of 0.5-0.8 µm. The I:Br ratio in the as-grown single crystals was confirmed to be 2:8 with X-ray photoelectron spectroscopy (XPS).

The complete time-dependent spectral information is provided in Figure F26.1(a). After resting in the dark, upon exposure to low intensity light an emission peak appears at ~550 nm and slowly red-shifts to ~710 nm over the first 60 seconds. Immediately after the intensity is increased to 200 W cm^{-2}, three emission peaks centred at 545 nm, 610 nm and 710 nm are observed. Over time the peaks at 545 nm and 610 nm red- and blue-shift, respectively, to form a single peak at ~555 nm, whereas the peak at 710 nm decays to zero. When the intensity is reduced to 10 W cm^{-2} for another 80 seconds the emission peak at 555 nm again red-shifts, reproducing the initial phase-segregated emission. The red-shift over the first 60 seconds is characteristic of the formation of I-rich domains, and is a clear signature of PHS. At 200 W cm^{-2}, emission from Br-rich, I-rich and intermediate halide compositions is observed. The decay of the peak at 710 nm and the growth of a high-bandgap peak at 555 nm suggests the I-rich domains decompose and the as-grown low-I composition is restored at high intensity This is further supported by the red-shift of the Br-rich peak at 545 nm to 555 nm, indicating that a mixed composition material is formed. By tuning the input excitation power (Figure F26.1(b)), a range of stable PL energies can be reached, indicating that the distribution of halide ions is highly correlated with the excitation power. From here onwards we term this process photo-induced halide-ion mixing (PHM). The experiment setup is illustrated in Figure F26.1 (C).

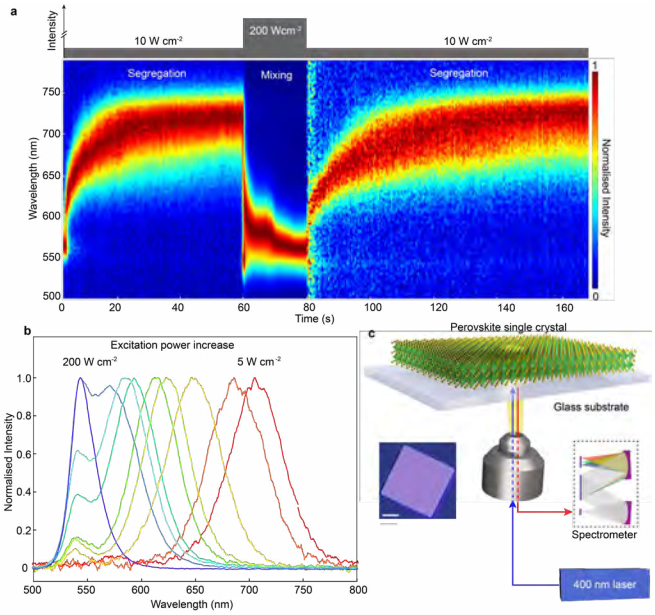

Figure F26.1: Photo-induced halide-ion segregation (PHS) and mixing (PHM) within a $MAPb(Br_{0.8}I_{0.2})_3$ single crystal microplatelet. (a) Normalised PL emission spectra recorded upon illumination with a pulsed laser with low excitation intensity (10 W cm^{-2}) over 60 seconds, followed by high intensity (200 W cm^{-2}) over 20 seconds, and back to low intensity (10 W cm^{-2}) over 80 seconds. (b) Normalised power-dependent PL emission spectra recorded with a range of excitation powers. The arrow indicates the shift in peak position as the excitation power increases. Each steady-state spectrum, recorded at the same crystal position, is reached after 20 seconds of laser illumination. The excitation intensity was sequentially increased from 5 to 200 W cm^{-2}. (c) Schematic of the confocal photoluminescence (PL) microspectroscopy system. Excitation was provided by a 400 nm pulsed laser with a repetition rate of 2.7 MHz. The beam was focused on the centre of the microplatelet in a non-scanning mode. Fluorescence from the illuminated spot was collected and spectrally resolved. The inset shows an optical image of a perovskite microplatelet. The scale bar is 5 µm. (Mao et al., 2020)

Several mechanisms have been proposed to describe PHS in mixed halide perovskites. However, none of these models describes PHM observed under high photon flux, at least not in their current form. Instead, we have developed a lattice model, which builds on the concept of polaron-induced segregation, to model changes in halide distribution in response to a wide range of illumination powers. The model considers three driving forces: (i) a force which locally attracts iodides towards polarons due to the strain gradients which they generate; (ii) a force which attracts carriers/polarons towards iodide-rich regions due to the reduction (or funnel) in the bandgap; and (iii) a force which drives the halides to mix homogeneously in the absence of strong strain gradients (see Figure F26.2(a)). With this physical picture, and a reasonable limit on how strongly polarons can overlap, remixing will naturally occur under strong illumination due to the reduction in strain gradient where the polarons overlap or merge. This model qualitatively accounts for all phenomena observed from low to high excitation intensities and rationalises the change in halide distribution (in both time and space) in terms of the local polaron density. The key results for different excitation regimes, after the model has reached a

steady state, are presented in Figure F26.2(b)–(d). The positions of the I^- and Br^- and corresponding photoluminescence spectra information are shown in Figure F26.2(e)–(g) and Figure F26.2(h)–(j), providing insight into the coupling between the polaron and halide distributions.

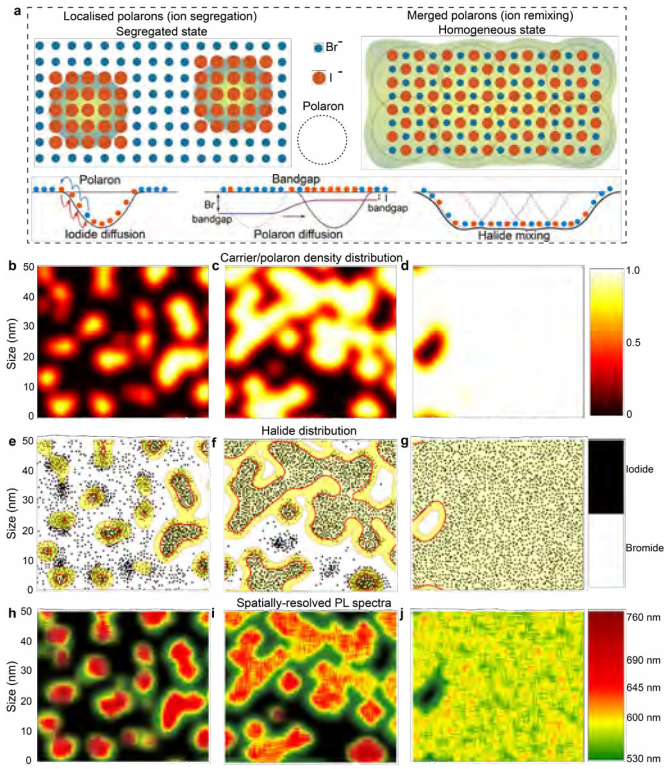

Figure F26.2: Modelling of halide segregation and mixing in response to polaron density (steady state). (a) Illustration of halide ion distribution for a MAPb($Br_{0.8}I_{0.2}$)$_3$ perovskite lattice in response to low carrier density (left) and high carrier density (right). The lattice model includes three driving mechanisms: (i) iodide diffusion along polaron strain gradients; (ii) polaron diffusion along iodide concentration gradients; and (iii) halide mixing in the absence of strong strain gradients. (b)–(j) Simulation results for the lattice model: (b)–(d) Polaron distributions at different carrier densities (b-low, c-medium, d-high); e-g, halide distributions in (b), (c) and (d) respectively; (h)–(j) corresponding spatially resolved PL emission peak wavelength. The model shows how the local halide composition and bandgap can be controlled by the carrier density. (Mao et al., 2020)

Highlights

- Reversing photo-induced halide-ion segregation back into homogeneous phase with concentrated excitation.
- Simulations confirm the driving force for photo-induced phase segregation is dependent on carrier-induced strain gradients that vanish at sufficiently high carrier densities.
- The ability to control ion segregation could become key to solving the issue of halide demixing and to harness the exceptional opportunities associated with a bandgap tunable semiconductor material.

Future Work

- As we have shown, we can extract significant information about the interaction between input photons and perovskite lattice through optical measurements for a MAPb(I_xBr_{1-x})$_3$ perovskite system. However, the state-of-the-art perovskite solar cells are fabricated through multiple cations, i.e. Cs, FA and MA. Future work will focus on the analysis of light-induced ion distribution dynamics in more complicated double-cation and triple-cation perovskite systems.
- Another major future work is to fabricate mixed halide perovskite solar cell devices with single crystalline structures to study their device performance under concentrated light illumination.

References

CHEN, W., MAO, W., BACH, U., JIA, B. & WEN, X. 2019. Tracking Dynamic Phase Segregation in Mixed-Halide Perovskite Single Crystals under Two-Photon Scanning Laser Illumination. *Small Methods*, 3, 1900273.

MAO, W., HALL, C. R., BERNARDI, S., CHENG, Y.-B., WIDMER-COOPER, A., SMITH, T. A. & BACH, U. 2020. Light-induced reversal of ion segregation in mixed-halide perovskites. *Nature Materials*.

MAO, W., HALL, C. R., CHESMAN, A. S. R., FORSYTH, C., CHENG, Y.-B., DUFFY, N. W., SMITH, T. A. & BACH, U. 2019. Visualizing Phase Segregation in Mixed-Halide Perovskite Single Crystals. *Angewandte Chemie International Edition*, 58, 2893-2898.

F27 A LOW-COST STRATEGY FOR P-DOPED AND STABLE HOLE-TRANSPORT-MATERIAL LAYER FOR HIGH PERFORMANCE STABLE SINGLE-JUNCTION PEROVSKITE AND/OR SI-PEROVSKITE TANDEM SOLAR CELLS

Lead Partner

UNSW

UNSW Team

Xu Liu; A/Prof. Xiaojing Hao

Funding Support

ACAP Fellowship

Aims

This Fellowship aims to devise a low-cost strategy to enable (i) controlled oxidation (p-dope the hole-transport-material (HTM) layer); and (ii) improved moisture stability, thermal stability, and illumination stability of an HTM layer for more stable low-temperature-processed planar perovskite and/or perovskite/Si tandem solar cells.

Progress

A. P-dope an HTM layer by compositional engineering and its role in solar cells

In 2020, we firstly incorporated cheap additive into the most common Spiro-OMeTAD HTM layer and thence into negative-intrinsic-positive (n-i-p) photovoltaic devices, increasing the device efficiencies. We observed an obvious p-type doping induced by this additive for Spiro-OMeTAD HTM. Our best planar PSCs show a champion efficiency of 21.8% (certified efficiency is 21.63%) using a one-step method.

(i) Traditional humidity-controlled air treatment (namely, storage in a humidity-controlled air box for several days) is critical for the most common Spiro-OMeTAD HTM films comprising Spiro-OMeTAD, tBP (4-tert-butylpyridine), LiTFSI (bis(trifluoromethane)sulfonimidelithium) due to the optimised energy level alignment, minimised recombination, and maximised carrier extraction during the air-treatment period (Hawash et al., 2018). The reaction between Spiro-OMeTAD and Li^+-$TFSI^-$ involves an uncontrollable oxidation of Spiro-OMeTAD [Eq. (1) and (2)] (Jeon et al., 2018)

$$\text{Spiro-OMeTAD} + O_2 \rightleftharpoons \text{Spiro-OMeTAD}^{\cdot+} + O_2^{\cdot-} \quad (1)$$

$$\text{Spiro-OMeTAD}^{\cdot+} + O_2^{\cdot-} + Li^+\text{-}TFSI^- \rightarrow \text{Spiro-OMeTAD}^{\cdot+}TFSI^- + Li_XO_Y \quad (2)$$

Here, we added a novel additive into the HTM layer. We carried out UV-vis absorption spectroscopy and kelvin probe force microscopy (KPFM) to investigate the electronic properties of as-prepared Spiro-OMeTAD films (we have denoted samples before undergoing the air treatment as "as-prepared"). We observed an increased intensity in the film absorption with the maximum peak at around 480 nm (Figure F27.1(a)), consistent with the formation of oxidised Spiro-$OMeTAD^{\cdot+}TFSI^-$. From the KPFM (Figure F27.1(b)), we observed a pronounced contact potential difference (CPD), where the additive changes the fermi energy level of the as-prepared Spiro-OMeTAD film – from 4.94 eV to 5.09 eV – with respect to vacuum. This means the additive-tailored film has a lower HOMO energy level by 0.15 eV than that of the control counterpart, in that the fermi level for doped Spiro-OMeTAD lies very close to the edge of the HOMO level. These results confirm the additive induces the p-doping progress of the HTM layer.

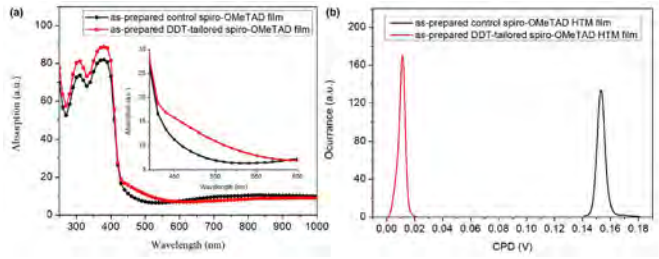

Figure F27.1 (a)UV-vis absorption of the as-prepared control and the additive-tailored Spiro-OMeTAD HTM films on quartz substrates. (b) Contact potential difference (CPD) at each pixel distribution of freshly prepared control and additive-tailored Spiro-OMeTAD films coated on a glass substrate. We employ an Au-coated tip which has a work function of −5.1 eV. A scan over a 25 μm² area is taken for each sample. The average isolated CPDs of additive-tailored Spiro-OMeTAD film and control Spiro-OMeTAD film came to −20 mV and −160 mV respectively, corresponding to Fermi levels of −5.08 eV and −4.94 eV.

(ii) We incorporated the additive-tailored HTM layers into our previously reported n-i-p planar solar cell structure(Liu et al., 2018, Liu et al., 2019), using tin oxide (SnO_2), perovskite via one-step, and potassium chloride (KCl) along with poly(methyl methacrylate) (PMMA) as, respectively, the n-type charge-extraction layers, the absorbers, and the interfacial passivation materials (Figure F27.2(a)). We observed enhanced efficiencies in the complete photovoltaic cells comprising 0.25–1.0 volume% (v%) of the additive with respect to 1 mL precursor volume (Figure F27.2(b)). We noticed an improved performance for devices before undergoing traditional humidity-controlled air treatment (namely, storage in a humidity-controlled air box for several days) (Figure F27.2(c)). For our typical device via one-step method, comprising 0.25% of additive, we measure an open-circuit voltage (V_{OC}) of 1.15 V, a short-circuit photocurrent density (J_{SC}) of 22.0 $mAcm^{-2}$, and a fill factor (FF) of 79.4%, yielding an efficiency of 20.0%. Further humidity-controlled air treatment gives a slight increase in V_{OC} and FF values, exhibiting an efficiency of 21.2% with a V_{OC} of 1.16 V, a J_{SC} of 22.5 $mAcm^{-2}$, and an FF of 81.5%. In contrast, the as-prepared control cell exhibits a poor initial PCE of 8.7%, owing to a low V_{OC} of 1.0 V, a J_{SC} of 20.9 $mAcm^{-2}$, and an inferior FF of 41.4%. Efficiency jumps after humidity-controlled air treatment as expected, reaching a PCE of 20.2% with a V_{OC} of 1.13 V, a J_{SC} of 22.7 $mAcm^{-2}$, and an FF of 78.5%. Our champion device shows a PCE of 21.8% with a V_{OC} of 1.16 V, a J_{SC} of 23.0 $mAcm^{-2}$, and an FF of 81.6% after using an anti-reflection layer with little hysteresis as shown in Figure F27.2(d) (certificated efficiency is 21.63%).

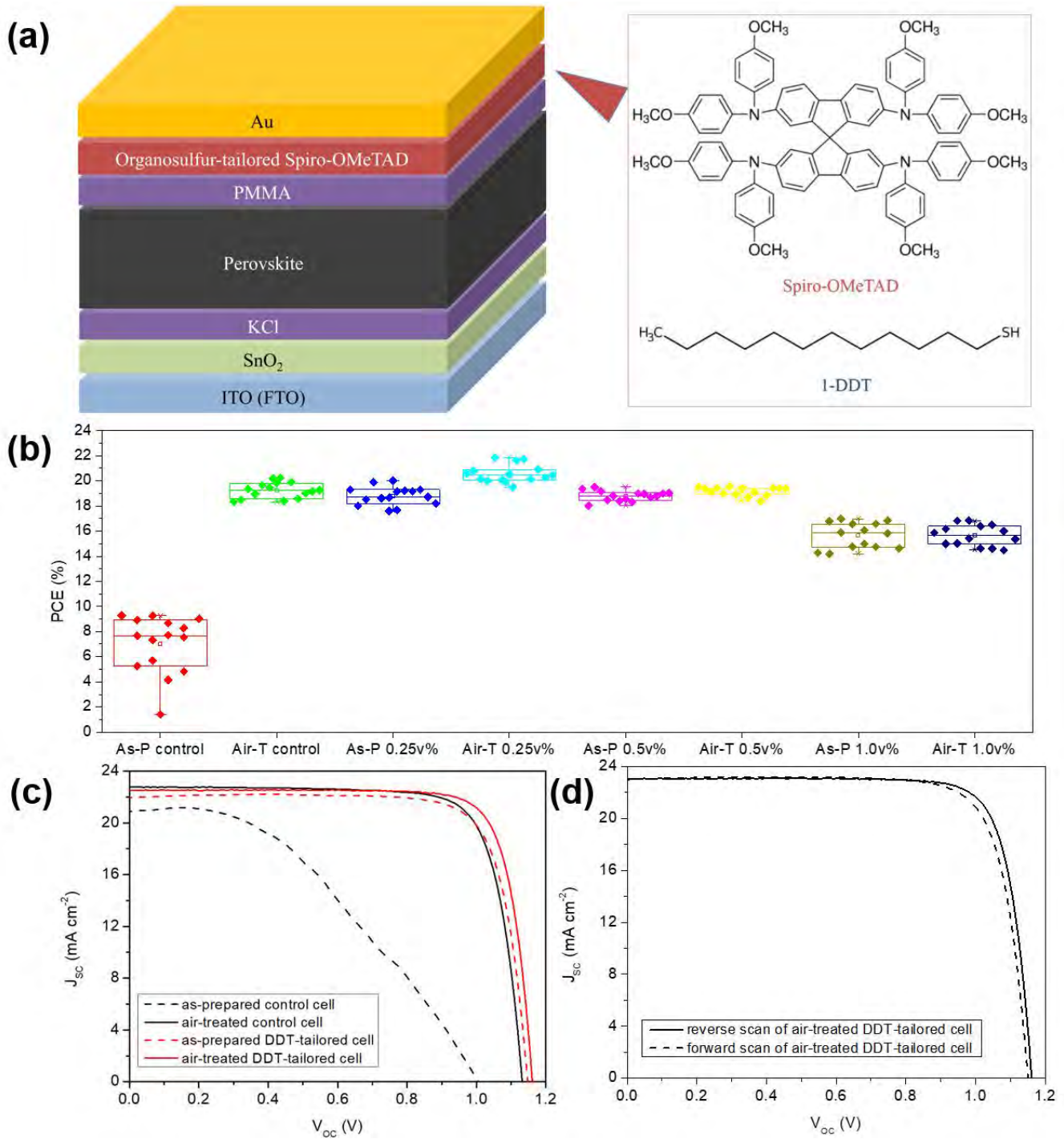

Figure F27.2 (a) Architecture of our planar negative-intrinsic-positive perovskite solar cell, and the molecule structures of Spiro-OMeTAD andadditives. (b) Impacts of additive concentration and humidity-controlled air-treatment on device performance. As-P represents the as-prepared sample, Air-T represents the air-treated sample. (c) J-V curves of the typical control cell and the typical additive-tailored cell before and after air-treatment. (d) J-V curves of air-treated additive-tailored device measured under the reverse- and forward-bias scan directions, respectively, between −0.1 V and 1.2 V.

B. Stabilise the HTM layer by molecule engineering and its role in solar cells

Spiro-OMeTAD must be chemically doped with hygroscopic dopants (LiTFSI and tBP) to attain sufficient conductivity and good hole extraction. These dopants negatively influence the devices' stability, impeding the true commercialisation of PSCs. Inspiringly, we observed that additive positively influences the long-term stability for Spiro-OMeTAD HTM and thence PSCs owing to the reduced pinhole size, the increased hydrophobicity, and the suppressed crystalline growth. Unencapsulated PSCs retain 96% of peak efficiency after 530 hours in wet conditions and retain 94% of peak efficiency after 2200 hours in air. A five-fold enhanced thermal stability at 50–85°C for unencapsulated devices was observed. Upon continuous one-sun illumination, PSCs without encapsulation retain 93% of peak efficiency after 2000 hours under open-circuit conditions and retain 90% of peak efficiency after 1000 hours of operation at the maximum power point (MPP), respectively.

(i) We found a stark reduced pinhole size for the additive-tailored HTM film in atomic force microscopy (AFM) images (Figure F27.3(a)). Contact-angle measurements are conducted to determine the surface water resistance of the Spiro-OMeTAD films with dopants. The water droplet contact angle of 101° on the additive-tailored film is larger than that of 35° on the control film (Figure F27.3(b)), indicating reduced hygroscopicity of the additive-tailored HTMs. Under different ageing stresses including the wetting, the thermal, and the continuous illumination conditions, the formation of a crystalline domain is observed in the control films (Figure F27.3(c1),(c3),(c5)), whereas it is not found in the additive-tailored counterpart (Figure F27.3(c2), (c4), (c6)),.

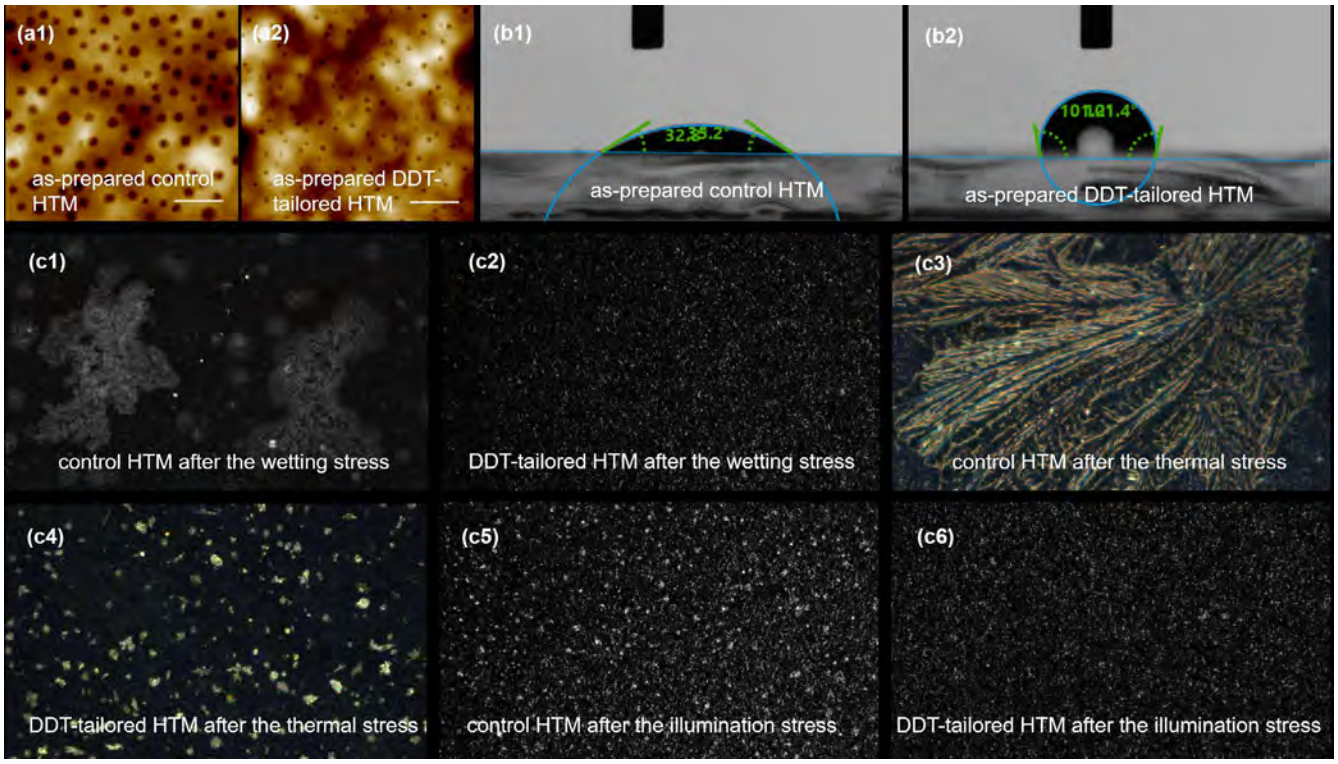

Figure F27.3(a) AFM images of the as-prepared control Spiro-OMeTAD HTM film and the as-prepared additive-tailored Spiro-OMeTAD HTM film. Scale bar is 1μm. (b) Contact-angle measurement of a water droplet on the surface of the as-prepared control Spiro-OMeTAD HTM film and the as-prepared additive-tailored Spiro-OMeTAD HTM film. (c) Microscope photographs of the as-prepared control Spiro-OMeTAD HTM film and the as-prepared additive-tailored Spiro-OMeTAD HTM film under different ageing stresses, including under ~50% RH over 500 hours, at 50–85°C over 144 hours in an N_2 atmosphere, and under continuous one-sun illumination stresses over 2000 hours in an N_2 atmosphere.

(ii) We proceeded to investigate the stability of complete photovoltaic cells under the wetting, the thermal, and the continuous one-sun illumination stresses. We firstly conducted long-term stability tests on the devices without encapsulation under ~50% RH (Figure F27.4(a)). For the control device, we observed a slow degradation of PCE during the first 100 hours, followed by a quick degradation, decreasing to 68% of its peak efficiency after another 430 hours. In comparison, the device with additive-tailored HTM demonstrates greatly improved moisture stability, retaining a high efficiency up to 97% over the same measurement period.

We then proceeded with stability tests on the devices without encapsulation under 50–85°C in an N_2 atmosphere (Figure F27.4(b)), where the performance of additive-tailored PVSK also excels. We observed an as high as 63% decrease with respect to the peak efficiency after 120 hours at 50°C for the control device. In comparison, the device fabricated with additive-tailored HTM has a high PCE retention up to 95% over the same ageing period. We then allowed the device temperature to rise to 85°C, and again evaluated the device stability. We measured a faster degradation of another 16% drop for the control cell after 24 hours, whereas the device fabricated with additive-tailored Spiro-MeOTAD HTM showed a slower degradation of only another 5% drop over the same ageing period.

We finally conducted long-term stability tests on the devices without encapsulation under continuous one-sun illumination stress including the open-circuit condition and the operation at the MPP in an N_2 atmosphere (Figure F27.4(c) - (d)). Under the open-circuit condition, we observe an as high as 90% decrease with respect to the peak PCE after 2000 hours for the control device. In comparison, the device with additive-tailored HTM has a high PCE retention up to 93% over the same measurement period. Similar enhanced stability of additive-tailored PSCs is also obtained under the continuous operation condition. The device with additive-tailored HTM retains 90% of its peak PCE after 1000 hours under the operation at the MPP.

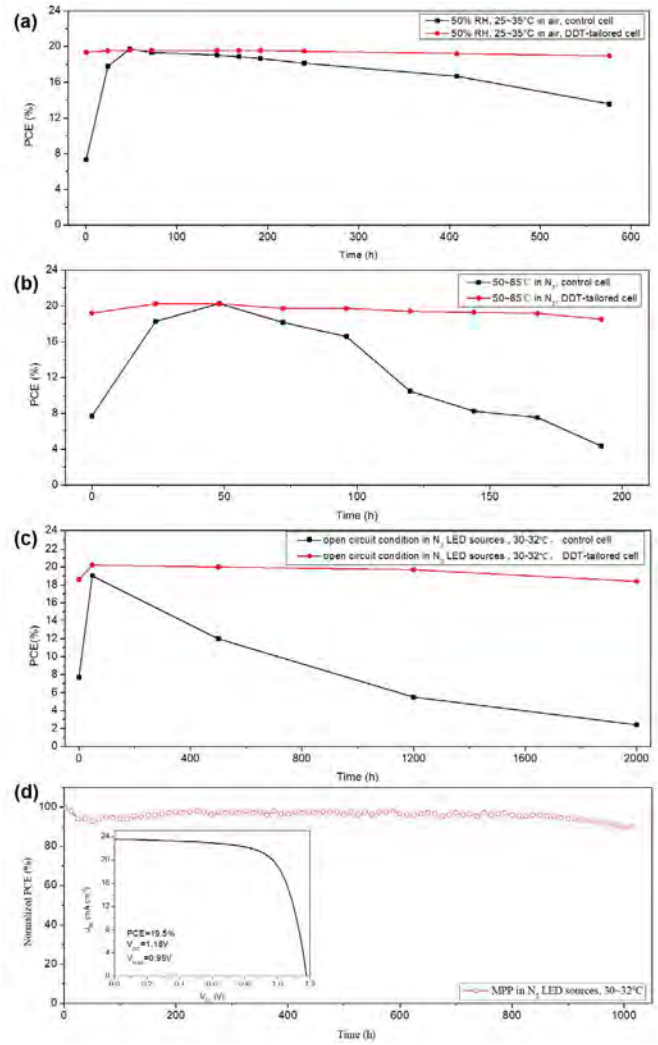

Figure F27.4 Device stability under different stresses. (a) Evolution of cells' PCEs on wetting ageing at ~50% RH. (b) Evolution of cells' PCEs on thermal ageing at 50–85°C in an N_2 atmosphere. (c) Evolution of cells' PCEs under continuous one-sun illumination stress at the open-circuit condition. (d) Evolution of cells' PCEs under continuous one-sun illumination stress at the operational MPP condition.

C. Achievement on highly efficient solar cells

More recently, we developed a two-step method to fabricate the perovskite absorber layers. By optimising all the technologies used in the one-step method, our champion device via the two-step method shows a PCE of 24.3% with a V_{OC} of 1.19 V, a J_{SC} of 26.0 $mAcm^{-2}$, and an FF of 79.0%, as shown in Figure F27.5. However, we observed the obvious hysteresis issue that will be solved in the future.

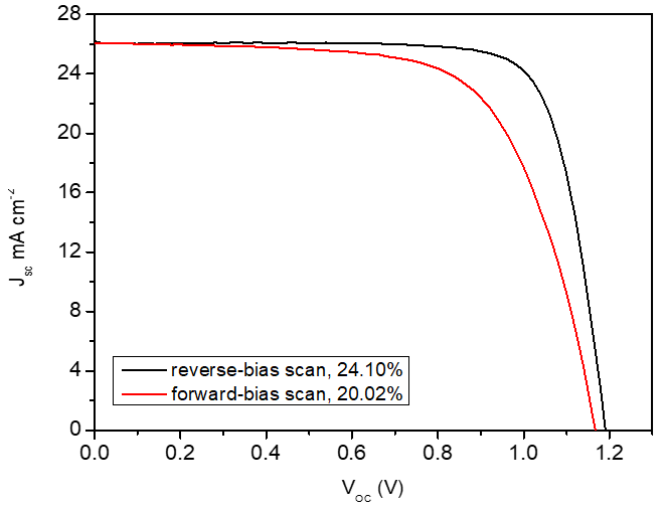

Figure F27.5. J-V curves of air-treated additive-tailored device measured under the reverse- and forward-bias scan directions, respectively, between 0 V and 1.2 V.

Highlights

- Additive induces the p-doping progress of the Spiro-OMeTAD HTM layer.
- Additive stabilises the Spiro-OMeTAD HTM layer and thence the PSCs.
- Stale additive-tailored PSCs without encapsulation under ~50% RH.
- Stale additive-tailored PSCs without encapsulation under 50–85°C.
- Stale additive-tailored PSCs without encapsulation under continuous one-sun illumination.
- PSCs with efficiency beyond 24%.
- One manuscript titled "Recent advances on interfacial engineering of perovskite solar cells" with me as the co-author has been submitted to Advanced Functional Materials.
- One manuscript titled "Unencapsulated planar perovskite solar cells with long-term stability using additive-tailored hole-transport-material layers" is in preparation for the submission to Nature.
- One relevant patent titled "Perovskite solar cell and method of making the same" (Application No. 2020900488).

Future Work

- Obtain the optimum strategy, enabling HTL that spontaneously has p-doping effect, improved moisture stability, improved thermal stability, and improved illumination stability.
- Achieve stable unencapsulated solar cells that can maintain 20% efficiency at 50% relative humidity, 50°C, and continuous one-sun illumination combined ageing condition.
- Develop encapsulation technology and target encapsulated samples that maintain 20% efficiency at 85% relative humidity, 85°C, and continuous one-sun illumination combined ageing stress.
- Mitigate the hysteresis issue of PSCs via a two-step method, targeting the device of efficiency beyond 25% and a new world record.

References

HAWASH, Z., ONO, L. K. & QI, Y. 2018. Recent Advances in Spiro-MeOTAD Hole Transport Material and Its Applications in Organic–Inorganic Halide Perovskite Solar Cells. 5, 1700623.

JEON, I., UENO, H., SEO, S., AITOLA, K., NISHIKUBO, R., SAEKI, A., OKADA, H., BOSCHLOO, G., MARUYAMA, S. & MATSUO, Y. 2018. Lithium-Ion Endohedral Fullerene (Li+@C60) Dopants in Stable Perovskite Solar Cells Induce Instant Doping and Anti-Oxidation. 57, 4607-4611.

LIU, X., SHI, L., HUANG, J., LIU, Z., ZHANG, P., YUN, J. S., SOUFIANI, A. M., SEIDEL, J., SUN, K., HAMEIRI, Z., STRIDE, J. A., ZHANG, Y., GREEN, M. A., LIN, H. & HAO, X. 2019. Improvement of Cs-(FAPbI3)0.85(MAPbBr3)0.15 Quality Via DMSO-Molecule-Control to Increase the Efficiency and Boost the Long-Term Stability of 1 cm^2 Sized Planar Perovskite Solar Cells. *Solar RR*L, 3, 1800338.

LIU, X., ZHANG, Y., SHI, L., LIU, Z., HUANG, J., YUN, J. S., ZENG, Y., PU, A., SUN, K., HAMEIRI, Z., STRIDE, J. A., SEIDEL, J., GREEN, M. A. & HAO, X. 2018. Exploring Inorganic Binary Alkaline Halide to Passivate Defects in Low-Temperature-Processed Planar-Structure Hybrid Perovskite Solar Cells. *Adv. Energy Mater.*, 8, 1800138.

F29 HYDROGEN PASSIVATION OF $SI_{1-X}GE_X$ FOR $SI_{1-X}GE_X$/SI TANDEM SOLAR CELLS

Lead Partner

UNSW

UNSW Team

Dr Li Wang, Mr Fukun Lei, A/Prof. Brett Hallam

Funding Support

ACAP Fellowship

Aims

This project aims to passivate the material defects in the $Si_{1-x}Ge_x$ solar cell grown on silicon substrates using advanced hydrogenation techniques. This will provide a better platform with improved quality for the III-V solar cell growth, and eventually improve the efficiency of the tandem solar cells grown on silicon substrates. The aims of the project are:

- to study the impact of hydrogenation on $Si_{1-x}Ge_x$ solar cells grown on silicon substrates
- to develop advanced hydrogenation processes to improve the $Si_{1-x}Ge_x$ solar cells grown on silicon substrates.

Progress

Fabrication process and characterisation methods for $Si_{1-x}Ge_x$ have been designed, developed and tested. Initial results for two types of hydrogen passivation processes, including SiN_x with thermal annealing and a-Si with thermal annealing, have been demonstrated and discussed. Detailed progress is as follows.

A. $Si_{1-x}Ge_x$/Si cell fabrication process development:

i) Fabrication process for SiGe solar cells with SiN_x layer as hydrogen source has been developed using a photolithography technique. The SiN_x layer was deposited in PECVD. SiN_x was selectively etched where Ti/Pd/Ag front metals were evaporated to form ohmic contact, then Al was evaporated as the rear metal contacts on a Si substrate. This was followed by a cell being isolated using RIE dry etch. The cross-sectional structure of such a fabricated $Si_{1-x}Ge_x$/Si cell is illustrated in Figure F29.1. Two different Ge concentrations of 77% and 85% have been fabricated.

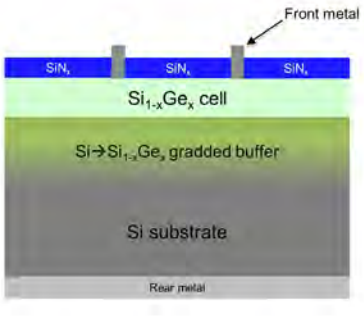

Figure F29.1: Cross-sectional structure of fabricated $Si_{1-x}Ge_x$/Si cell.

ii) Fabrication process for SiGe solar cells with an a-Si layer as the hydrogen source has been started to develop, since the key process is to precisely control the etching thickness of the a-Si layer. Due to the tool upgradation, this process is still being developed.

B. New characterisation method/procedure development:

i) Ellipsometry fitting models have been built to extract thickness and optical constants of the passivation layer, such as SiN_x and a-Si materials.

ii) Microsecond PL setup has been built to characterise PL changes of $Si_{1-x}Ge_x$ materials, since such low bandgap material cannot be measured using the existing setup for Si material.

iii) Other material characterisation methods such SIMS and DLTS measurements have also been tested.

C. Experiments, results and analysis:

i) SiN_x layer as a hydrogen source for passivation.
Fabricated $Si_{1-x}Ge_x$ cells with 77% and 85% Ge% have been characterised, including EQE, R, IV. Thermal annealing was conducted in RTP at 350°C for 2 minutes on fabricated $Si_{0.23}Ge_{0.77}$/Si and $Si_{0.15}Ge_{0.85}$/Si cells, respectively. Initial IQE and V_{OC} results before and after the annealing have been shown in Figure F29.2. As shown in this figure, IQE and V_{OC} for both
77% and 85% SiGe cells have been improved – the improvement was more significant for the $Si_{0.23}Ge_{0.77}$ than that of the $Si_{0.15}Ge_{0.85}$ cells.

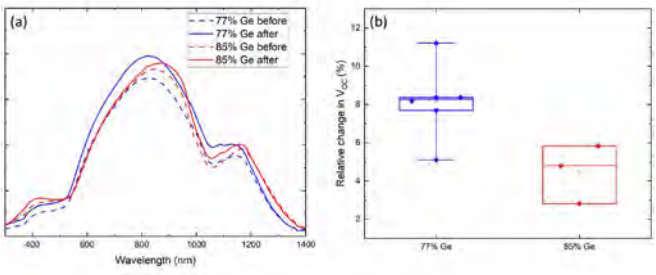

Figure F29.2: IQE (a) and V_{OC} (b) results before and after annealing for $Si_{0.23}Ge_{0.77}$ and $Si_{0.15}Ge_{0.85}$ cells with SiN_x layer, respectively.

Analysis on the reasons why $Si_{1-x}Ge_x$ cells with lower Ge% achieved more obvious improvement after the low temperature annealing has been conducted. A possible cause of the differing behaviour is the transition from Si-like to Ge-like behaviour of the alloy at approximately 85% Ge composition. Figure F29.3 shows the bandgap of $Si_{1-x}Ge_x$ alloy as a function of Ge compositions (Braunstein 1958).

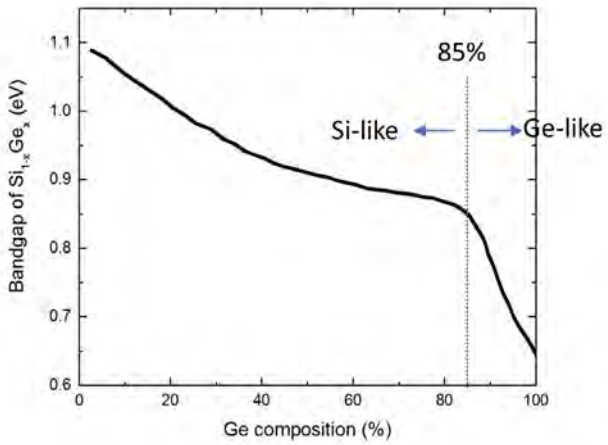

Figure F29.3: Bandgap of SiGe with different Ge% (Braunstein 1958).

In addition, an explanation for the different behaviour under annealing in the presence of hydrogen may be developed based on the differing behaviour of hydrogen passivation in Si and Ge. The charge states of hydrogen and defects have a significant impact on the defect passivation (Hamer 2014). Figure F29.4 shows the charge state transition levels for isolated dangling bond defect and interstitial hydrogen in Si, SiGe and Ge (Herring 2001; Weber 2007; Weber 2013). The red lines represent the charge state transition levels for dangling bonds. The green lines represent the charge state transition levels for hydrogen. As can be seen, both the charge state transition levels for dangling bond and interstitial hydrogen in Si are within the conduction band minimum and valance band maximum. In contrast, as can be seen in the same figure, the charge state transition levels of dangling bonds in Ge are lower than the valance band maximum. This suggests the dangling bonds' defects will always be negatively charged. Thus hydrogen passivation will not be effective since most of the hydrogen is also negatively charged. The dashed lines in Figure F29.4 represent the interpolated charge state transition level of dangling bonds and hydrogen in SiGe. As can be seen, the charge state transition levels move above the valance band maximum with the decrease of Ge composition. Thus, the fractional concentration of the positive charge state of hydrogen will increase. Eventually with the decrease of Ge composition, the alloy will become more Si-like and hydrogen passivation becomes more likely.

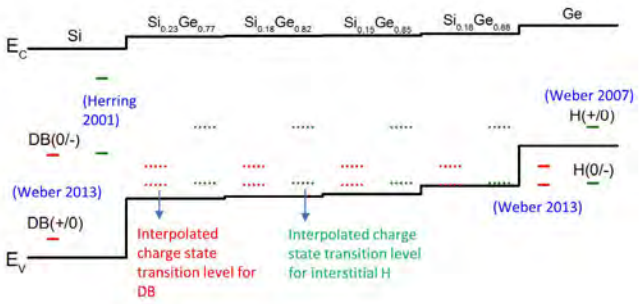

Figure F29.4: The charge state transition levels for dangling bonds and interstitial hydrogen in Si, SiGe and Ge (Li 2016).

ii) A-Si layer as hydrogen source for passivation:
Hydrogen passivation effect using a-Si layers as the hydrogen source has also been investigated. A-Si layers with different thicknesses were deposited at 250°C on FZ Si wafers. Here FZ Si wafers have been used first to examine effectiveness of the hydrogenation passivation. PL was measured before and after the thermal annealing at 300°C for an accumulated 30 minutes in RTP. PL counts as a function of annealing time for three different a-Si thicknesses have been plotted in Figure F29.5. As shown in this figure, a thicker a-Si layer led to more dramatic PL counts increasing after annealing. However, a thicker a-Si layer results in larger optical losses. Therefore, the thickness needs to be determined by balancing the passivation effectiveness and optical losses.

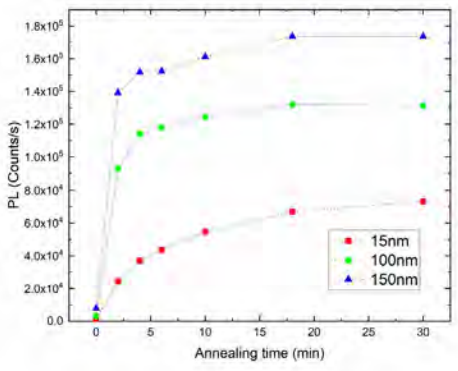

Figure F29.5: PL counts at different annealing times for different a-Si thicknesses.

Highlights

- A poster entitled "Hydrogen passivation of $Si_{1-x}Ge_x$ for $Si_{1-x}Ge_x$ /Si tandem solar cells" was presented at the ACAP stream of the 2020 Asia-Pacific Solar Research Conference, Melbourne.
- Initial experimental results have demonstrated effectiveness of hydrogen passivation on $Si_{1-x}Ge_x$ solar cells, especially on those with a lower Ge concentration.

Future Work

- Optimisation of the hydrogen passivation process using SiN_x as the hydrogen source.
- Development of the cell fabrication process and hydrogen passivation process using a-Si as the hydrogen source.
- Investigation and development of other hydrogen passivation techniques, such as illuminated annealing and a hydrogen plasma process.
- Material and defect characterisation to further evaluate the effectiveness of different hydrogen passivation processes on $Si_{1-x}Ge_x$ solar cells.

References

BRAUNSTEIN, R., MOORE, A.R. & HERMAN, F. 1958. Intrinsic optical absorption in germanium-silicon alloys, *Phys. Rev.*, 109, 695-710.

HAMER, P., HALLAM, B., WENHAM, S. & ABBOTT, M. 2014. Manipulation of hydrogen charge states for passivation of P-type wafers in photovoltaics, *IEEE J. Photovolt.*, 4, 1252-1260.

HERRING, C., JOHNSON, N.M. & VAN DE WALLE, C.G. 2001. Energy levels of isolated interstitial hydrogen in silicon, *Physical Review B*, 64, 125209.

LI, D. 2016. Material Characterization and Device Optimization of Silicon Germanium Solar Cells Grown on Silicon Substrates, PhD thesis, UNSW, Sydney.

WEBER, J.R., JANOTTI, A., PINKE, P. & VAN DE WALLE, C.G.2007. Dangling-bond defects and hydrogen passivation in germanium, Appl. Phys. Lett., 91, 142101.

WEBER, J.R., JANOTTI, A. & VAN DE WALLE, C.G. 2013. Dangling bonds and vacancies in germanium, *Physical Review B*, 87, 035203.

F30 DEVELOPMENT OF HIGH PERFORMANCE PEROVSKITE/SI TANDEM AND ITS APPLICATIONS

Lead Partner
UNSW

UNSW Team
Dr Jianghui Zheng, Prof. Shujuan Huang, Prof. Anita Wing Yi Ho-Baillie

Academic Partners
University of Wisconsin—Madison: Prof. Song Jin, Dr Wenjie Li
Peking University: Prof. Rui Zhu

Funding Support
ACAP Fellowship

Aims

This fellowship aims to develop high performance monolithic perovskite/Si tandem solar cells with high stability and demonstrate the potential practical applications of tandem cells with our partners.

Progress

Monolithic perovskite/Si-homojunction tandem solar cell for application in high performance solar flow battery

Here, we developed a perovskite/silicon-homojunction tandem solar cell with high efficiency and suitable photovoltage for high performance solar flow battery applications with our partner from the University of Wisconsin—Madison. A homojunction Si solar cell is the bottom cell of choice because homojunction Si solar cells dominate ~90% of the world market and there is great potential to achieve high efficiency and low cost with such bottom cell integration. The detailed structure is shown in Figure F30.1 and the cross-sectional scanning electron microscopy (SEM) image of the perovskite/Si tandem junction solar cell is shown in Figure F30.2. The top perovskite cell consists of a standard nip structure perovskite cell with the $(FAPbI_3)_{0.83}(MAPbBr_3)_{0.17}$ composition. For solar flow battery application, a thin (100 nm) layer of gold was deposited on the Si bottom cell by thermal evaporation, since Au has been demonstrated to be a robust protection material for protecting the silicon bottom cell from corrosion in an aqueous electrolyte (Figure F30.1).

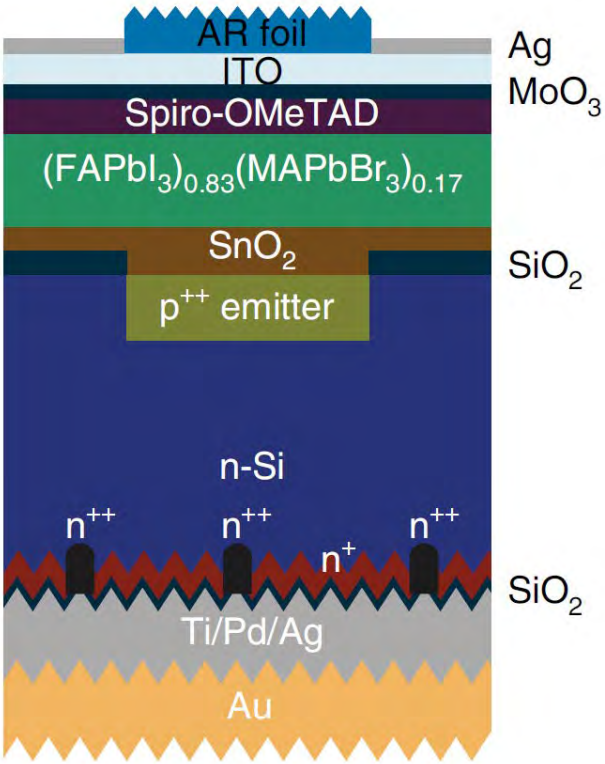

Figure F30.1: The schematic perovskite/Si tandem solar cell. The composition of the perovskite in the top cell is $(FAPbI_3)_{0.83}(MAPbBr_3)_{0.17}$. The Si bottom cell has a 100 nm Au bottom protection layer.

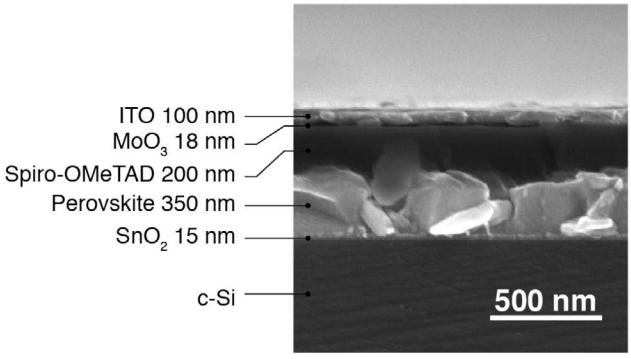

Figure F30.2: Cross-sectional scanning electron microscopy (SEM) image of the perovskite top cell on a Si cell.

Photos of the tandem cells with and without a shadow mask are shown in Figures F30.3(a) and F30.3(b) respectively. The best cell produced an open circuit voltage (V_{oc}) of 1.68 V, a short circuit current density (J_{sc}) of 15.8 mAcm^{-2}, a fill factor (FF) of 80.2% and a PCE of 21.3 % (Figure F30.3(d)) with or without the shadow mask. This is due to the well-defined 1 cm^2 emitter for the Si bottom cell masked by the SiO_2 passivating layer as shown in Figure F30.3(c). The composition of the perovskite is $(FAPbI_3)_{0.83}(MAPbBr_3)_{0.17}$ such that the output voltage of the tandem (V_{MPP} of 1.38 V) is optimal for an aqueous organic solar flow battery.

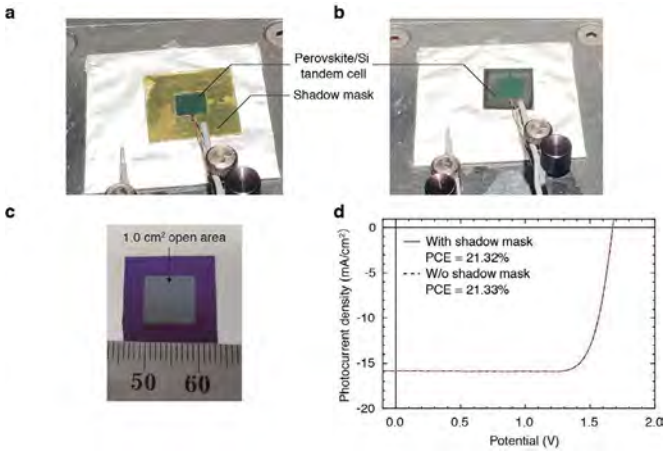

Figure F30.3: Photographs of a perovskite/Si tandem solar cell (a) with and (b) without a shadow mask. (c) Photograph of the silicon bottom cell prior to perovskite cell fabrication showing a 1.0 cm^2 opening for p++ diffusion masked by a passivating SiO_2 layer. (d) Current density-voltage curve of perovskite/Si solar cell measured with and without shadow mask.

The current density versus voltage performance of the perovskite/Si tandem solar cell under different light illumination intensities (with simulated solar irradiance of 0.010, 0.051, 0.098,0.020, 0.030, 0.040, 0.0502, 0.060, 0.071, 0.082, 0.899 and 1.001 Sun) are shown in Figure F30.4. It is clear that the tandem solar cell can maintain high voltage output under low illumination intensities, therefore maintaining charging for the solar flow battery.

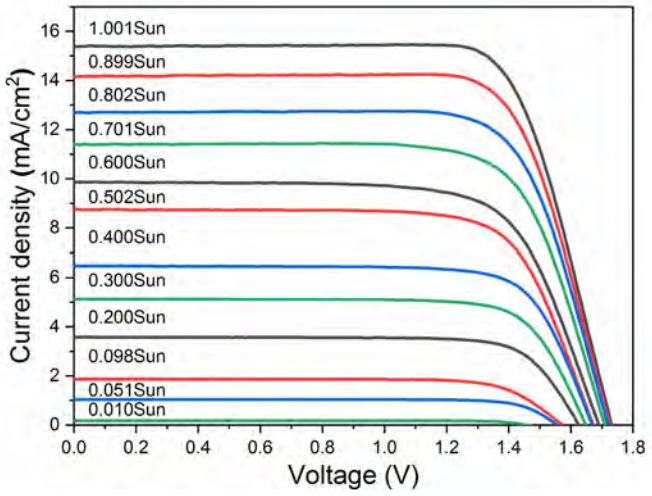

Figure F30.4: Current density-voltage curves of perovskite/Si tandem cell as a function of intensities.

Table F30.1: Current-voltage parameters of the perovskite/Si tandem cell at different intensities.

Light Condition	V_{OC} (V)	$_{SC}$(mA/cm^2	FF (%)	V_{MPP}(V)	PCE(%)
1.001Sun	1.73	15.4	74.9	1.35	19.95
0.899Sun	1.72	14.2	74.6	1.35	18.23
0.802Sun	1.72	12.7	74.1	1.35	16.17
0.701Sun	1.71	11.4	73.1	1.35	14.22
0.600Sun	1.69	9.9	71.1	1.33	11.86
0.502Sun	1.67	8.74	73.3	1.33	10.71
0.400Sun	1.67	6.47	76.2	1.37	8.22
0.300Sun	1.65	5.13	76.8	1.36	6.49
0.200Sun	1.63	3.57	77.5	1.35	4.5
0.098Sun	1.57	1.87	76.2	1.28	2.34
0.051Sun	1.55	1.04	80.1	1.33	1.3
0.010Sun	1.46	0.16	82.3	1.27	0.2

Figure F30.5 schematically shows the configuration of our solar flow battery device integrating a perovskite/Si cell as the photoelectrode and BTMAP-Vi/N^{Me}-TEMPO as redox couples. The cycling test of the SFB was performed by first charging the device under solar recharge mode with simulated solar irradiation until the cell potential reaches the upper cutoff potential of 1.5 V. The device was then discharged galvanostatically until the cell voltage reaches the lower cut-off potential of 0.8 V. The solar flow battery was continuously cycled for 426 cycles (516 hours) and maintained a very stable performance during the whole time of operation. We observed a slight increase of solar-to-output electricity efficiency in the first 51 cycles from 18.9% to 20.1%, which then stabilised around 20.1% during the rest of the cycling period (Figure F30.6). Importantly, the average solar-to-output electricity efficiency of 20.1% achieved by this SFB is >40% higher than the previous record efficiency of 14.1% for the integrated solar rechargeable battery devices (Li et al. 2018). Another significant result from this work is the demonstrated stability of our perovskite/Si-homojunction tandem operating for >500h under continuous light illumination for the solar flow battery.

The above progress constitutes a significant advance towards a practical approach of using a perovskite/Si tandem powered integrated solar flow battery for solar home systems and other distributed solar power generation and storage applications.

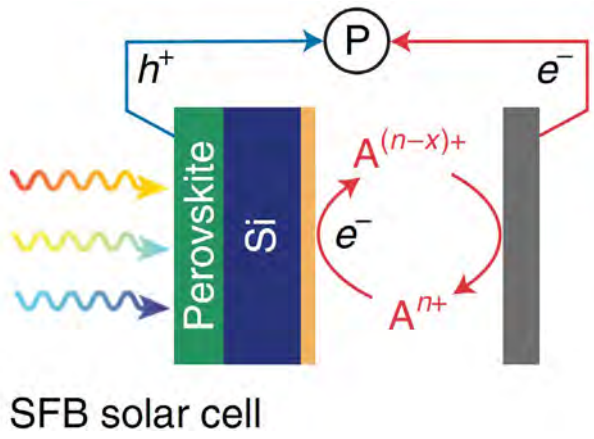

Figure F30.5: Configuration of the solar flow battery solar cell. Note that only the gold bottom protection layer of the tandem cell is exposed to the electrolyte.

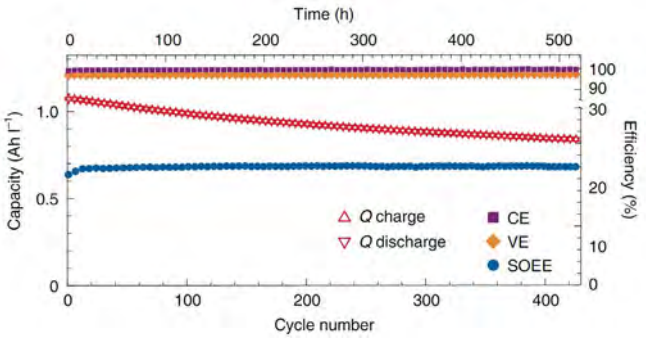

Figure F30.6: Charge and discharge capacity, Columbic efficiency (CE), voltage efficiency (VE) and solar-to-output electricity efficiency of solar flow battery over 426 cycles. The data are down sampled to show one data point in every five cycles for better visibility.

Highlights

- A monolithic perovskite/Si tandem solar cell with a suitable V_{OC} has been developed for the application of a high performance solar flow battery.
- The photovoltaic performance of the perovskite/Si tandem solar cell under different illumination intensity has been investigated.
- A new solar-to-output electricity efficiency record of 20.1% for a solar flow battery has been achieved.

Future Work

- Further development of the high performance tandem solar cells with nip structure.
- Development of large-area high performance tandem solar cells on 100-mm and 150-mm wafers.
- Further improvement of the stability of tandem solar cells and measurement of their stability using MPP tracking under continuous illumination.
- Development of tandem cells for water splitting applications.

References

LI, W., FU, H.-C., ZHAO, Y., HE, J.-H. & JIN, S. 2018. 14.1% Efficient Monolithically Integrated Solar Flow Battery. Chem, 4, 2644-2657.

LI, W., ZHENG, J., HU, B., FU, H.-C., HU, M., VEYSSAL, A., ZHAO, Y., HE, J.-H., LIU, T. L. , HO-BAILLIE, A. & JIN, S. 2020. High-performance solar flow battery powered by a perovskite/silicon tandem solar cell. Nature Materials, 19, 1326-1331.

F31 INTERFACE ENGINEERING BY ATOMIC LAYER DEPOSITION FOR HIGH PERFORMANCE EARTH-ABUNDANT SOLAR CELLS

Lead Partner

UNSW

UNSW Team

Dr Xin Cui, A/Prof. Xiaojing Hao, Prof. Bram Hoex

Funding Support

ACAP, ARENA

Aims

The ultimate aim of the project is to develop high performance Earth-abundant solar cells through interface engineering by atomic layer deposition (ALD). This is being perused with the following steps.

- The first is to conduct design and computational research to predict novel metal oxide materials as sustainable functional layers for emerging Earth-abundant solar cells.
- The second is the synthesis of functional materials by using ALD and analysis of those materials with an in situ characterisation method.
- The third is to apply the theoretically predicted materials synthesised by ALD to improve the device performance of the emerging Earth-abundant solar cells.

This Fellowship has its primary focus on contributing to ACAP's PP2 O Thin-Film, Third generation and Hybrid Devices, and this report highlights the development of high bandgap Earth-abundant solar cells without any toxic element involved.

Progress

Design and computational research of sustainable functional layers

High bandgap solar cells including Cu_2ZnSnS_4 (CZTS), Sb_2S_3, $Cu_2BaSn(Se,S)_4$, and $CuSbS_2$ have recently witnessed rapid progress and demonstrated their potential as the top cell in silicon tandem solar cells, albeit their efficiencies are currently not yet high enough. It has been identified that the performance of these Earth-abundant solar cells is mainly hampered by a large open-circuit voltage (V_{OC}) loss due to defect recombination. Specifically, the interface recombination can be suppressed effectively through nanolayer engineering. ALD is a technique that enables nanoscale engineering and forming ultrathin, dense and continuous layers with a sub-nanometer scale, providing a great opportunity to mitigate defect recombination within or between layers. A record power conversion efficiency of 9.3% was achieved for Cd-free CZTS cells by using ALD ZnSnO to replace toxic CdS in 2018 (Cui et al., 2018). In 2019, we further enhanced the performance of Cd-free CZTS one step further to 10.2% (Cui et al., 2019), bringing this low-cost and green absorber one step closer to commercial practicality. Based on the previous work of developing high-efficient CZTS solar cells through ALD nanolayer implementation, this project has focused on the novel design of the buffer/window/TCO layers in Earth-abundant solar cells with minimum electrical and optical loss.

- **Material predication via first-principles modelling**

Band alignment is a critical research point as it helps us to understand the carrier transportation and recombination mechanism at the interface of solar cells. Therefore, the work function of alternative metal oxides with suitable band alignment in the CZTS solar cell is needed. We performed first-principles density functional theory (DFT) calculations to predict electronic properties of novel ternary materials as functional buffer/window/TCO layers. The study of defect chemistry and electronic properties of the as-designing materials were also carried out to understand the underlying mechanisms. Potential alternatives include Cd-free buffer layers such as ZnSnO, ZnSnO/ZnMgO and Zn(O,S) and window layers with a higher bandgap such as ZnTiO, ZnMgO:Al and InZrO. We modelled the ZnMgO (ZMO) using the molecular dynamics (MD) simulations followed by the first-principles DFT calculations to reveal the electronic band structure properties with a varied composition ($Zn_{1-x}Mg_xO$, x = 0.0 - 0.4). (Hossain et al. 2020)

- **CZTS structure design via SCAPS simulation**

The structure design of solar cell electrical simulation was performed using SCAPS 1D. Combinations of the buffer layer, window layer and anti-reflection layer with different thicknesses, and optical and electrical properties are investigated to discover the optimised parameters. As an example, the device structure of the CZTS/ZTO/ZMO model with built-in SCAPS is shown in Figure F31.1(a) and the corresponding band diagram of the model is demonstrated in Figure F31.1(b). Here, a flat band approximation was used for the 1D simulation due to the bandgap fluctuation in the disordered CZTS triggered by the band tail states. From Figure F31.1(d), it can be observed that the highest efficiency was achieved in the region with lower ZMO electron affinity and higher ZMO doping density. When $3.9 < x_{ZMO} < 4.2$ eV, the efficiency decreased slightly with decreased carrier concentration in ZMO mainly due to the V_{OC} change. It should be noted that V_{OC} changes independent of ZMO electron affinity, which means the recombination rate does not increase due to the quasi-Fermi level for electrons at the CZTS surface lay sufficiently below the trap position.

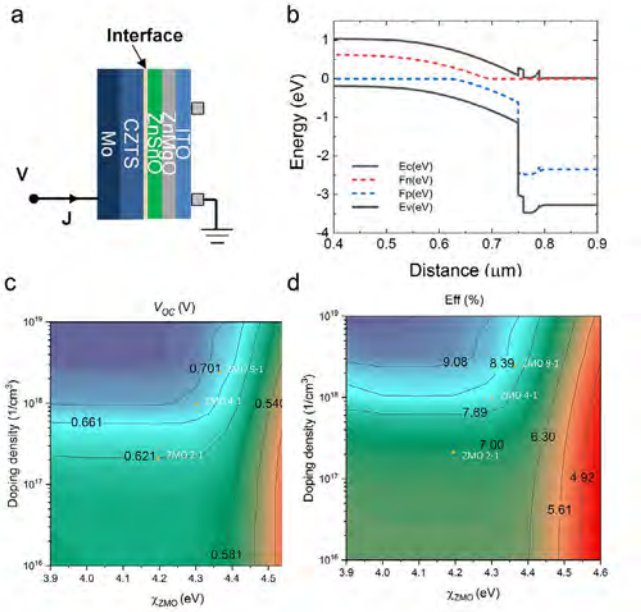

Figure F31.1: (a) Illustration of device structure used for CZTS/ZTO/ZMO model. (b) Schematic band diagrams under light at short circuit conditions for CZTS/ZTO/ZMO baseline model. Calculated contour plots of (c) open-circuit voltage and (d) efficiency for CZTS/ZnSnO/ZnMgO devices with the variation of ZMO properties.

In situ characterisation and analysis of the functional layers deposited by ALD

In situ measurement was implemented in the development of the ALD process to minimise the optimisation time and material consumption. The dynamic measurements allow for evaluating the basic properties of the deposited films, thus providing precise control of the growth of desired materials. In this project, in situ quartz crystal microbalance (QCM) and spectroscopic ellipsometry (SE) were utilised as the dynamic measurements. The schematic representation of Fiji G2 ALD used in this project is shown in Figure F31. 2.

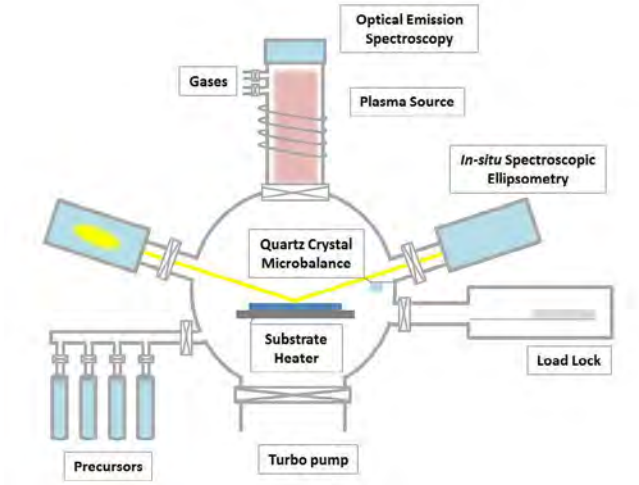

Figure F31. 2: Schematic representation of Fiji G2 ALD chamber equipped with in situ SE, OES and QCM.

Figure F31. 3 shows the growth property of ALD ZnO:Al as measured by in situ spectroscopic ellipsometry. ZnO:Al films with different metal ratios were deposited by the super-cycle method. It indicates that the growth values of ZnO cycles were different from the values for pure ZnO and Al_2O_3 films. A nucleation delay was observed for ZnO after one cycle of Al_2O_3 which can be explained by the etching of surface Zn atoms via ligand exchange during the Al_2O_3 cycles. In the case of ZMO deposition, in situ ellipsometry measurement revealed the different growth behaviour for ZMO films deposited by thermal ALD and PE-ALD and correlated them with the different fundamental properties of the films.

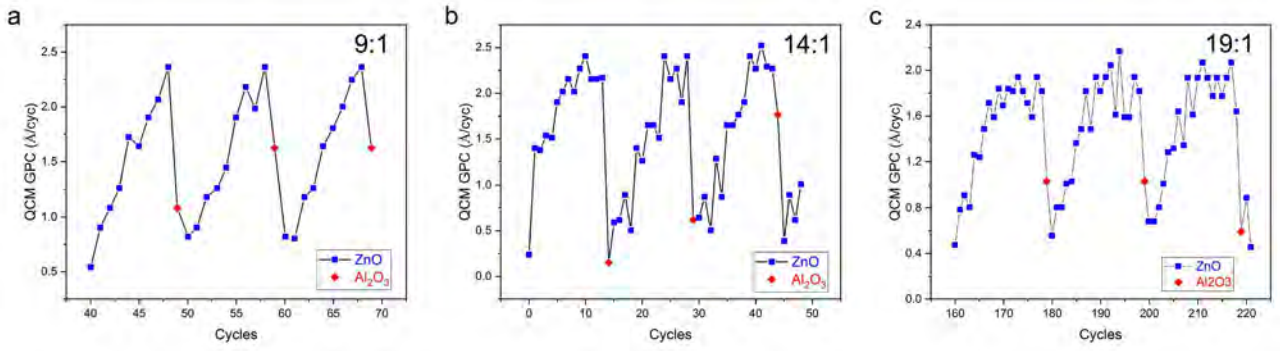

Figure F31. 3: Growth per cycle of consecutive ZnO and Al_2O_3 cycles of ALD ZnO:Al as measured by in situ spectroscopic ellipsometry.

Application of ALD functional layers for high performeanceCZTS solar cells

Window layer management is essential to minimise the optical loss as well as prevent shunt paths in CZTS thin-film solar cells. The wider bandgap of ZMO layers minimised the optical loss from the window layer and led to an enhanced J_{SC}. A more favourable conduction band alignment is believed to contribute to the improvement in V_{OC}. The CZTS solar cells with ZnSnO buffer and ZnMgO window layers were fabricated following the process described in Figure F31.4.

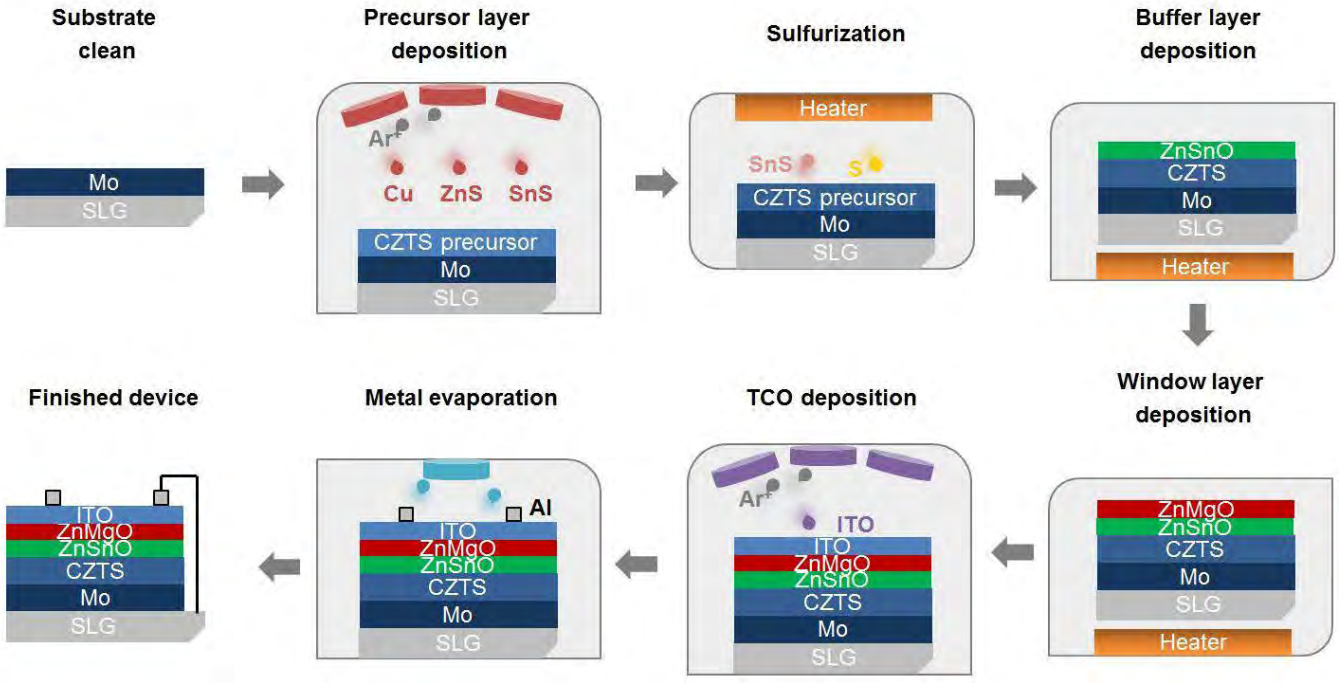

Figure F31.4: Schematic of the fabrication of CZTS/ZnSnO/ZnMgO thin-film solar cell.

To this end, both thermal ALD (T-ALD) and plasma-enhanced ALD (PE-ALD) were implemented to synthesise a wide range of $Zn_{1-x}Mg_xO$ (ZMO, $0 \le x \le 0.4$) films for application as a window layer in CZTS solar cells. The device with the $Zn_{0.8}Mg_{0.2}O$ layer showed a relatively higher efficiency although the fill factor (FF) still needs improvement. Further study was carried out by comparing T-ALD and PE-ALD processed ZMO as an alternative window layer due to their difference in band alignment and electrical properties. As shown in Figure F31.5, the CZTS solar cells with a PE-ZMO device window layer showed a higher efficiency, mainly due to a higher V_{OC} and J_{sc}. The reduced cliff-like CBO between the absorber and window layer was believed to be beneficial for the V_{OC} of CZTS/ZTO/PE-ZMO devices. However, the relatively higher roughness of PE-ZMO could deteriorate the FF of the device. Finally, a champion 9.2% efficient PE-ZMO device was fabricated without anti-reflection coating thanks to the significantly enhanced J_{sc}, primarily because of the lesser optical loss in the thinner window layer with a large bandgap.

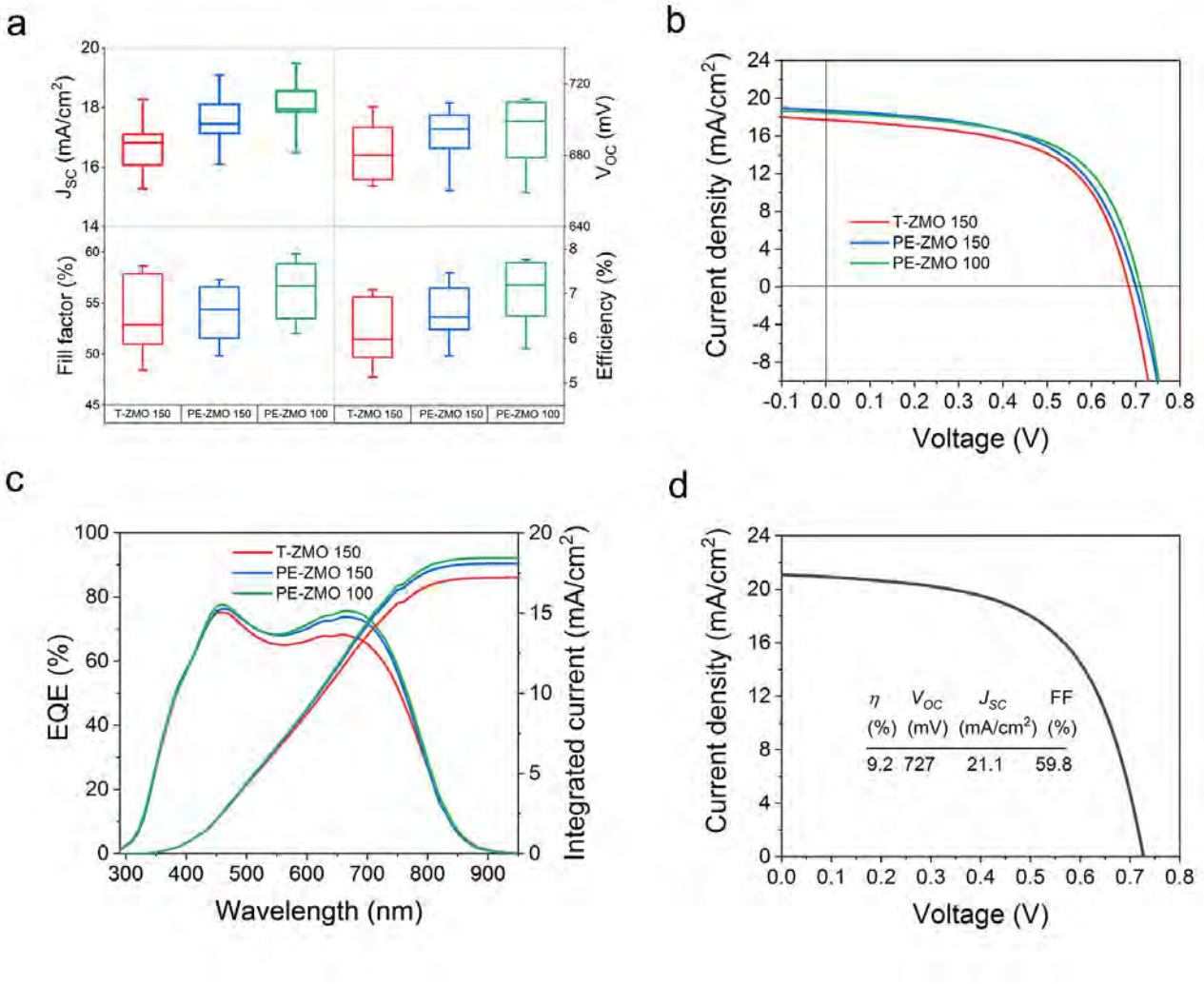

Figure F31.5: (a) Box-plots of performance parameters; (b) the current density-voltage; (c) external quantum efficiency of the CZTS solar cells with ZMO window layer deposited from T-ALD and PE-ALD; and (d) J-V characteristics of the champion CZTS/ZTO/PE-ZMO solar cell without anti-reflection coating.

Highlights

- Novel Cd-free CZTS structure design.
- In situ characterisation and analysis of the functional layers deposited by ALD.
- Comparison study between thermal ALD and plasma-enhanced ALD for ternary material deposition.
- A 9.2% efficient CZTS/ZTO/PE-ZMO device was fabricated without anti-reflection coating.

Future Work

- Continuing the optimisation of Cd-free CZTS devices with CZTS/ ZTO/ ZMO structures.
- Design, computational research, and application of alternative functional layers such as ZnTiO, ZnMgO:Al and InZrO for Earth-abundant solar cells.
- Exploring the capability of ALD tools for large-area applications with good uniformity and high throughput.

References

CUI, X., SUN, K., HUANG, J., LEE, C.-Y., YAN, C., SUN, H., ZHANG, Y., LIU, F., HOSSAIN, M. A., ZAKARIA, Y., WONG, L. H., GREEN, M., HOEX, B. & HAO, X. 2018. Enhanced Heterojunction Interface Quality To Achieve 9.3% Efficient Cd-Free Cu2ZnSnS4 Solar Cells Using Atomic Layer Deposition ZnSnO Buffer Layer. *Chemistry of Materials*.

CUI, X., SUN, K., HUANG, J., YUN, J., LEE, C.-Y., YAN, C., SUN, H., ZHANG, Y., XUE, C. & EDER, K. 2019. Cd-free Cu2ZnSnS4 solar cell with an efficiency greater than 10% enabled by Al2O3 passivation layers. *Energy & Environmental Science*.

F32 OPTIMISATION OF MANUFACTURING METROLOGY AND ANALYTICS FOR IMPROVED SOLAR CELL AND MODULE PERFORMANCE AND QUALITY

Lead Partner

UNSW

UNSW Team

Dr Rhett Evans

Funding Support

ACAP Fellowship

Aims

There are two general aims to this Fellowship. The first is to identify improved analytical tools and characterisation methods to control PV cell and module production lines. The second is to identify relationships between methods of improved manufacturing control and improved field performance outcomes, such as the minimisation of risk of field failure or underperformance.

Progress

Investigating end-of-line PL and IV performance relationships

The primary point of progress for this investigation is that paired cell IV and cell line scanning PL data has been obtained from a cell manufacturing line in South-East Asia with the intention of collecting data related to the comparative PL and IV performance of standard production cells. Large data sets have been collected consisting of PL images (well in excess of 1 million cells), paired with convention IV cell performance data.

At this initial stage of the project, the data collected is still considered commercial in confidence and cannot be widely shared, although the techniques that are being investigated and developed can be shared. It is anticipated that as the project develops and as the data becomes older, commercial sensitivities will be relaxed.

Motivation for the approach

Every solar cell produced on a manufacturing line in 2021 will have its full electrical characteristics measured to some level of assumed accuracy. These electrical characteristics are known as the IV properties of the cell. The primary outcome of interest from the measurement of electrical characteristics is the cell power or efficiency. This power is itself composed of information related to the voltage produced by the cell, the current produced by the cell, the resistive properties of the cell (series and shunt) and the diode behaviour of the cell. Every cell produced will have performance metrics within some range. This range represents the variance of the performance of a cell produced on the production line and the range provides insight into the quality of the output of the production line. Work completed prior to the start of this project concentrated on modelling the variance properties of the cells, as determined using the electrical characteristics, in order to provide insight into the performance and operation of the production line.

There are significant shortcomings with the conventional approach of measuring IV cell characteristics. The contention of the work in this project is that PL data is at least as good, and in some regards far superior, for the purpose of tightly controlling and also troubleshooting a cell production line. If this can be conclusively demonstrated, this will provide a significant point of disruption for solar cell manufacturing.

Overall Approach and Progress Results

It is well known and well established that the voltage properties of a cell primarily determine the luminescent properties of that cell. Existing approaches that attempt to predict efficiency data from luminescent data primarily rely on the extent to which the voltage data is itself predictive of the efficiency data. A more nuanced approach is taken here. A variance analysis is done on the cell electrical data to decompose this data into four primary sources of variance. These are shown in table F32.1, together with the typical expected significance of each variance source from public domain analyses. Table F32.1 represents a simplistic analysis that investigates only the variance components that are not correlated to V_{OC}. The objective of the analysis is then to use the PL data – either using image parameterisation approaches or machine learning / regression style approaches – to try to predict the variance component data. The success or otherwise of this initial approach will provide the basis for targeting ongoing investigations or analysis.

Table F32.1: Four typical variance components for PV cell manufacturing data and the typical significance of each. Note that some known pre-existing correlations (e.g. a strong V_{oc} – I_{sc} correlation related to underlying material properties), are removed first in order to provide an unambiguous calculation of the significance of each component.

Variance Component	% of the overall cell efficiency variance that would be expected to be explained by this component in a modern cell manufacturing line
1. Open-Circuit Voltage (V_{oc})	50-75%
2. Short-Circuit Current (uncorrelated to V_{oc})	10-25%
3. Series resistance (uncorrelated to V_{oc})	10-25%
4. High ideality factor recombination (uncorrelated to V_{oc})	2-5%

Only limited results can be reported owing to commercial sensitivities, but PL image data can be used to explain over 90% of the open-circuit voltage variance (variance component 1 in Table F32.1). Approximately 10–20% of variance component 2 can be explained using the PL data. This is an area where PL would be expected to perform poorly. Significant opportunities remain to improve this predictive power, and it should also be noted that a large amount of IV tester measurement error is contained within this data stream. Variance component 3 from Table F32.1 also contains significant tester error, but the PL data can still be used to explain nearly 50% of the series resistance data. Significant opportunities remain to improve the analysis of the PL data to better predict the cell IV data.

Further development of new analysis techniques for end-of-line electrical data

Other areas of work are under ongoing development and will be the subject of future reports. These areas of work include

- analysis of time-based variance and autocorrelation to isolate source of process variance in the data
- use of mass data set analysis to develop self-calibration and correction algorithms for cell series resistance. The series resistance estimation from many modern production cell testers can be highly inaccurate.

Highlights

- Development of an approach and benchmark for analysing end-of-line cell performance using PL and EL data.
- Ongoing development of novel analysis techniques for analysing end-of-line electrical data.

Future Work

- Further develop the image parameterisation and analysis techniques to improve the predictability of electrical performance data using the PL imaging data.
- Include the correlating variance sources in the analysis because they represent identifiable performance characteristics of the cell.
- Secure data sources for use in open public domain discussion of the results and outcomes.
- Publishing of analytical methods developed to date.
- Co-supervision of postdoctoral and PhD students to progress some of the aims and outcomes of this research.

F33 RECYCLING END-OF-LIFE SILICON PHOTOVOLTAIC MODULES USING LOW-COST AND LOW-EMISSION PROCESSES

Lead Partner

UNSW

UNSW Team

Dr Pablo R. Dias, Dr Marina M. Lunardi, Dr Nathan L. Chang, Dr Richard Corkish, Prof. Renate Egan, Prof. CheeMun Chong

Funding Support

ACAP Fellowship

Academic Partners

Federal University of Rio Grande do Sul (UFRGS), Brazil

Aims

This fellowship aims to develop processes in order to separate and recover materials from waste photovoltaic (PV) modules. It aims to fully recover the main materials present in waste PV using first-stage recycling processes, so as to allow small industries to undertake such processes without the need of large investments.

This Fellowship has its primary focus on contributing to ACAP's PP4 Manufacturing Issues (including both subcategories PP4.1 and PP4.2), and this report should be read in conjunction with the PP4 report.

Progress

Motivation for development of recycling processes

Global installed PV is expected to rise 11-fold in the next 30 years; coupled to this rise in infrastructure is the increase of PV waste, which is expected to reach 78 million tons by 2050 (Chowdhury et al. 2020), this sharp rise was in large part registered in China (Figure F33.1).

Crystalline silicon cells (c-Si) dominate the market with approximately 95% of the market share. This figure is up from 80–90% in 2010–2015 (IEA PVPS 2020; Paiano 2015). Therefore, crystalline silicon modules remain the main challenge in the recycling front, given these panels will translate into the largest volume of waste in the foreseeable future.

The 20–25-year lifespan of the modules indicates that this technology will still dominate the recycling efforts for the next 30–40 years. The motivation of this Fellowship is to address the upcoming PV waste stream and to transition the photovoltaic industry into the circular economy model, that is, to recover materials from end-of-life modules so that these materials can find their way back into the supply chain.

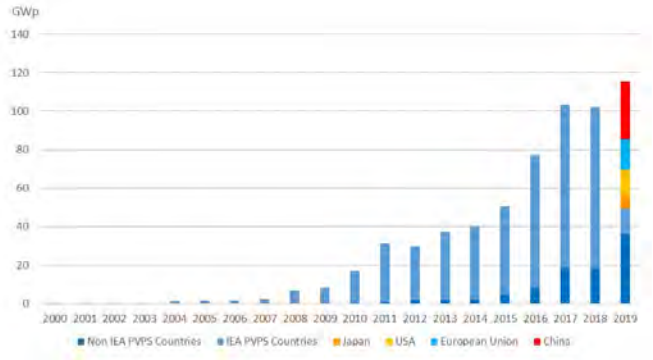

Figure F33.1: Evolution of annual photovoltaic installations worldwide (IEA PVPS 2020).

Crystalline silicon photovoltaic modules have a variety of components, each made with different materials chosen to comply with specific requirements. The main materials in weight, however, are glass, aluminum, ethylene-vinyl acetate (EVA), polyvinyl fluoride (PVF), silicon and copper. In addition, there are metals found in small quantities, but with large intrinsic value because of their financial importance (e.g. silver) or their toxicity (e.g. lead) (Dias and Veit 2018; Latunussa et al. 2016). In order to achieve a circular economy model, the materials contained in waste PV need to be processed back into the supply chain.

However, recent reviews indicate that the process can only become financially viable by reducing the total recycling processing costs of $400–500 per tonne for mechanical processes and $700–800 per tonne for thermal processes (Deng et al. 2019). Given there is an international industry set up to work with downstream processing of valuable materials such as the ones contained in waste PV (e.g. Umicore), it then becomes apparent the need for a technology capable of supplying such industry with the materials that can be processed and recycled. It is also crucial to evaluate the financial and environmental cost of such technology to ensure it meets the market requirements without polluting the ecosystem further

Recycling processes

Initial experiments to recycle waste PV modules were carried out using organic solvents as a way to separate the components contained in commercial panels. The organic solvent would partially dissolve and partially swell the encapsulant layers (namely EVA) and allow for the separation of the remaining laminate layers (Figure F33.2). Further downstream processes included thermal decomposition of the polymers and chemical separation of the metals, resulting in a high efficiency separation and the recovery of different materials.

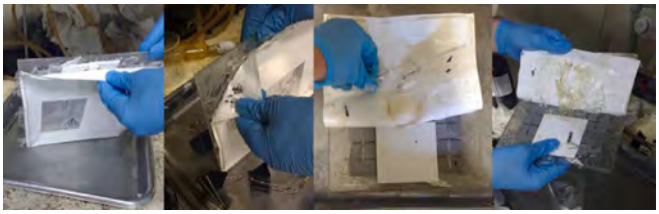

Figure F33.2: Effect of the immersion of photovoltaic modules in organic solvents. Layers can be seen being separated.

The experimental works yielded efficiency results and the cost of running such a process. These data were then used to envision an industry-scale process. Both laboratory and industrial-scale processes were analysed using life cycle assessment (LCA) (environmental impact tool) and life cycle costing (LCC) (financial impact tool). These analyses revealed that the process had a positive environmental impact, but was not economically feasible, even when benefiting from economies of scale (Figure F33.3). The results have been published in the *Resources, Conservation and Recycling* journal (Dias et al. 2021).

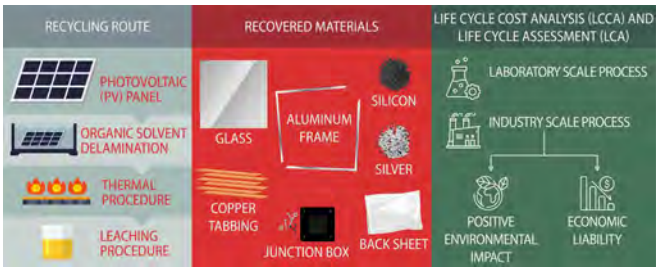

Figure F33.3: Summary of the assessment of the recycling process using organic solvents.

Efforts were then turned to the development of a new process using electrostatic separation as opposed to organic solvents. Preliminary results show an effective separation with the concentration of more than 94% of the silver and copper. The process is scheduled to be assessed in terms of financial cost (LCC) to ensure it is economically feasible and that it is under the benchmark proposed by Deng et al. (Deng et al. 2019). Furthermore, the process will also be assessed in terms of its environmental impacts (LCA). Preliminary results indicate this can be a way forward in shifting the PV industry into a circular economy.

Highlights

New recycling process for waste PV using organic solvents was proposed and tested.

The viability of the proposed process was evaluated in respect to the technical, economic and environmental aspects.

- Organic solvent recycling process has a positive environmental impact.
- Electrostatic separation method has yielded high material concentration results.

Future Work

- Analysis of additional PV recycling technologies and processes.
- Development of a commercial model for the newly created electrostatic process.
- Financial and environmental analysis of newly created electrostatic process.

References

CHOWDHURY, MD. S., RAHMAN, K. S., CHOWDHURY, T., NUTHAMMACHOT, N., TECHATO, K., AKHTARUZZAMAN, MD., TIONG, S. K., SOPIAN, K. & AMIN, N. 2020. An overview of solar photovoltaic panels' end-of-life material recycling. *Energy Strategy Rev.* 27, 100431. https://doi.org/10.1016/j.esr.2019.100431.

CORCELLI, F., RIPA, M. & ULGIATI, S. 2017. End-of-life treatment of crystalline silicon photovoltaic panels. An emergy-based case study. *J. Clean. Prod*. 161, 1129-1142. https://doi.org/10.1016/j.jclepro.2017.05.031.

DENG, R., CHANG, N. L., OUYANG, Z. & CHONG, C. M. 2019. A techno-economic review of silicon photovoltaic module recycling. *Renew. Sustain. Energy Rev*. 109, 532-550. https://doi.org/10.1016/j.rser.2019.04.020.

DIAS, P., SCHMIDT, L., MONTEIRO LUNARDI, M., CHANG, N. L., SPIER, G., CORKISH, R. & VEIT, H. 2021. Comprehensive recycling of silicon photovoltaic modules incorporating organic solvent delamination – technical, environmental and economic analyses. *Resour. Conserv. Recycl*. 165, 105241. https://doi.org/10.1016/j.resconrec.2020.105241.

DIAS, P. & VEIT, H. 2018. Recycling Crystalline Silicon Photovoltaic Modules, in: Kurinec, S. K. (Ed.), *Emerging Photovoltaic Materials*. John Wiley & Sons, Inc., Hoboken, NJ, USA, pp. 61-102. https://doi.org/10.1002/9781119407690.ch3.

IEA PVPS, 2020. Snapshot of Global PV Markets – 2020. https://doi.org/10.13140/RG.2.2.24096.74248.

LATUNUSSA, C. E. L., ARDENTE, F., BLENGINI, G. A. & MANCINI, L. 2016. Life Cycle Assessment of an innovative recycling process for crystalline silicon photovoltaic panels. *Sol. Energy Mater. Sol. Cells*, 156, 101–111. https://doi.org/10.1016/j.solmat.2016.03.020.

MATHUR, N., SINGH, S. & SUTHERLAND, J. W., 2020. Promoting a circular economy in the solar photovoltaic industry using life cycle symbiosis. *Resour. Conserv. Recycl*. 155, 104649. https://doi.org/10.1016/j.resconrec.2019.104649.

PAIANO, A., 2015. Photovoltaic waste assessment in Italy. *Renew. Sustain. Energy Rev*. 41, 99-112. https://doi.org/10.1016/j.rser.2014.07.208.

F34 PRINTED SELECTIVE CONTACTS FOR HIGH EFFICIENCY SILICON SOLAR CELLS

ACAP Fellow

James Bullock

Funding Support

ACAP

Aim

This project is aimed at the exploration of carrier-selective contact structures deposited by scalable, industry applicable techniques for use in crystalline silicon solar cells.

Progress

During the first year of this Fellowship a focus was made on the development of metal compound electron contacts. Work was broken into two streams. The first stream explored three new electron extraction layers for use with crystalline silicon: cesium bromide CsBr, aluminum fluoride AlF_3 and lanthanum hexaboride LaB_6. The best performing candidate from this subset, CsBr, was then combined with conventional electron contact buffer layers, including TiO_x and *a*-Si:H to gauge its performance and stability. The second stream was based around the optimisation of thermal stability for TiO_x electron contact layers and the trial of TiO_x using ultrasonic spray pyrolysis printing. Highlights from these studies are provided below.

Exploration of novel electron contact candidates

Some metal halides, such as LiF_x and MgF_x, are known to exhibit very low work functions when stacked with aluminum. As such, when integrated into the contacts of silicon solar cells these materials have shown an impressive ability to extract electrons (Bullock et al. 2016; Wan et al. 2016). The AlF_3/Al and CsBr/Al systems may also exhibit similar behaviour. In the past, aluminum fluoride drew interest as a passivating layer for silicon (König et al. 2014), and CsBr has been utilised as an interface modification interlayer in metal halide perovskite solar cells. Similarly, LaB_6 is well known as a thermionic emitter coating material, exhibiting a stable, low work function, which also suggests its potential use for electron collection in silicon solar cells. Figure F34.1(a) shows the contact resistivity ρ_c, extracted using the transfer length method (TLM), of AlF_3-, CsBr- and LaB_6-based electron contacts on moderately doped n-type silicon. It can be seen that CsBr presents the lowest ρ_c with a value approaching 10 $m\Omega cm^2$ for CsBr thicknesses above 2 nm. The other two candidates, AlF_3 and LaB_6, reached optimum values of 40 and 200 $m\Omega cm^2$, for thicknesses of 1.7 and 0.5 nm respectively. Figure F34.1(b) shows the time stability (unencapsulated storage in air) of a select set of samples from Figure F34.1(a), revealing that CsBr is also the most stable, especially for the 2 nm thickness interlayer.

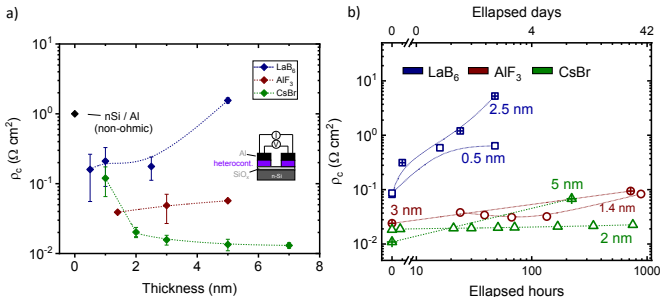

Figure 34.1. (a) Contact resistivity versus thickness for AlF_3, CsBr and LaB_6 electron contact candidate materials measured on n-type 2 Ωcm wafers with Al electrodes. Note that points are an average of multiple samples.(b) Time stability of AlF_3, CsBr and LaB_6 electron contacts measured on n-type 2 Ωcm wafers with Al electrodes. Note that points are from individual samples (i.e. not averages).

Excess carrier lifetime measurements performed on the AlF_3-. CsBr- and LaB_6-based electron contacts revealed negligible passivation, see for example Figure F34.2(a). As such, these films were combined with *a*-Si:H- and TiO_x-based buffer layers which are well known as successful passivating layers in electron contacts. The level of surface passivation improvement is also shown in Figure F34.2(a). Of the three new candidate materials only the CsBr yielded convincing results when combined with passivating interlayers, for example stable ρ_c values as low as 10 mΩcm^2 were obtained for TiO_x (5 nm)/CsBr (2 nm)/Al contacts after a short anneal. Similarly, promising results were obtained with a-Si:H interlayers, see Figure F34.2(b). This figure shows the performance of a conventional silicon heterojunction cell with CsBr applied at the rear in the place of the a-Si:H(n) layer. An impressive "hybrid" cell result of ~20.5% efficiency indicates the promising potential of CsBr. This sample was prepared with the help of collaborators at École Polytechnique Fédérale de Lausanne. Some of these results were presented at the 2020 Asia-Pacific Solar Research Conference (Ibarra et al. 2020).

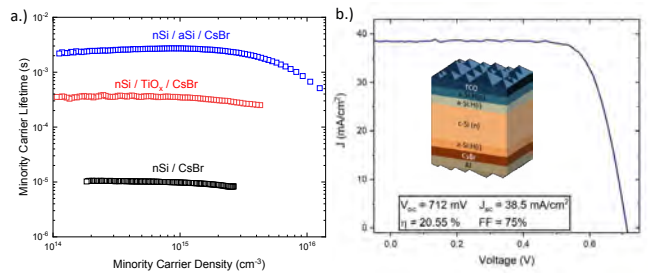

Figure F34.2 (a) Excess carrier lifetime recorded at a carrier density of 10^{15} cm^{-3} for CsBr, TiO_x/CsBr and a-Si:H/CsBr passivating layers on n-type 2–4 Ωcm wafers. (b) One-sun light current-voltage curve of a hybrid silicon heterojunction cell made with an a-Si:H/CsBr/Al rear contact.

Improving stability and initial printing trials of TiO_x

As it currently stands, TiO_x is perhaps the most promising metal compound electron buffer layer for crystalline silicon solar cells. However, several challenges remain before TiO_x could be considered industry viable, for example the poor passivation stability of TiO_x when directly contacted with a metal. With the help of collaborators at the Australian National University we studied the influence of an LiF interlayer, sandwiched between the TiO_x and Al layers. In our previous studies, we found this LiF was indispensable in obtaining excellent results without fully understanding the mechanism (Bullock et al. 2019). Figure F34.3(a) shows the improvement in ρ_c for TiO_x / LiF / Al contacts upon annealing in air, reaching values of 20 mΩcm^2 for TiO_x (5 nm)/ LiF (1 nm)/Al contacts. The inset of the same figure shows a set of photoluminescence (PL) images taken through the rear side of the TLM test structures. The top row shows the low PL intensity of directly metallised TiO_x samples, which do not recover upon annealing. The bottom row, representative of samples with an LiF interlayer, shows a comparatively higher PL intensity, which reduces with temperature, but remains higher than the directly metallised case. This suggests the LiF plays an active role in the protection of the TiO_x passivation which could be further optimised to realise higher performance at the cell level. Another factor which could improve viability of TiO_x-based contacts is the demonstration of inline printed layers. With the help of our collaborators at RMIT university we have begun initial trials on the use of ultrasonic spray pyrolysis to deposit electron contact buffer layers including SnO_x and TiO_x. Figure F34.3(b) shows preliminary (from our first trial) passivation results of 30 nm TiO_x layers printed symmetrically on a moderately doped n-type silicon wafer. Although low, the change in lifetime upon annealing suggests the possibility of further optimisation.

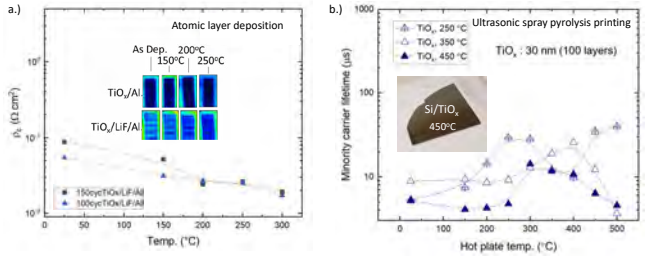

Figure F34.3 (a) Evolution of contact resistivity with temperature for TiO_x/LiF/Al contacts on n-type 2 Ωcm wafers. Inset shows PL images of the TLM test structures taken after each anneal step. (b) Evolution of excess carrier lifetime for n-type 2 Ωcm wafers with TiO_x passivating layers deposited by ultrasonic spray pyrolysis. The image shows a photograph of a TiO_x printed sample.

Highlights

- Trial of multiple new electron contact materials and the identification of CsBr as a promising candidate.
- Demonstration of CsBr with both TiO_x- and a-Si:H-based passivating interlayers, leading to the fabrication of a prototype solar cell with an efficiency of ~20.5% featuring an a-Si:H/CsBr/Al rear contact.
- Identification of the positive role of LiF interlayers in the protection of TiO_x buffer layers and demonstrated first results for printed TiO_x buffer layers.

Future Work

- Further exploration of electron contacts including the continuation of CsBr optimisation and TiO_x printing. Trialling a broader range of printed electron metal oxide materials such as SnO_x and transparent conductive oxides.
- Exploration of printed hole contacts, trialling both metal oxide and polysilicon-based materials. Following this, printed hole contacts will be combined in cell structures with the electron contacts outlined above.

References

BULLOCK, J., WAN, Y., HETTICK, M., ZHAORAN, X., PHANG, S. P., YAN, D., WANG, H., JI, W., SAMUNDSETT, C., HAMEIRI, Z., MACDONALD, D., CUEVAS, A. & JAVEY, A. 2019. Dopant-Free Partial Rear Contacts Enabling 23% Silicon Solar Cells. *Advanced Energy Materials*, 9, 1803367.

BULLOCK, J., ZHENG, P., JEANGROS, Q., TOSUN, M., HETTICK, M., SUTTER-FELLA, C. M., WAN, Y., ALLEN, T., YAN, D., MACDONALD, D., DE WOLF, S., HESSLER-WYSER, A., CUEVAS, A. & JAVEY, A. 2016. Lithium Fluoride Based Electron Contacts for High Efficiency n-Type Crystalline Silicon Solar Cells. *Advanced Energy Materials*, 6, 1600241.

Ibarra, J., Wang, S. & Bullock, J. Dopant-Free Electron Heterocontacts for Silicon Solar Cells. 2020. In Asia-Pacific Solar Research Conference; Melbourne, Australia, December 2020.

KÖNIG, D., ZAHN, D. R. T. & EBEST, G. 2004. Field effect of fixed negative charges on oxidized silicon induced by AlF3 layers with fluorine deficiency. *Applied Surface Science*, 234, 222-227.

WAN, Y., SAMUNDSETT, C., BULLOCK, J., ALLEN, T., HETTICK, M., YAN, D., ZHENG, P., ZHANG, X., CUI, J., MCKEON, J., JAVEY, A. & CUEVAS, A. 2016. Magnesium Fluoride Electron-Selective Contacts for Crystalline Silicon Solar Cells. *ACS Applied Materials & Interfaces*, 8, 14671-14677.

F35 THE DEVELOPMENT OF HIGH-EFFICIENCY QUANTUM DOT-ORGANIC TANDEM SOLAR CELLS FOR NEW GENERATION WEARABLE AND LIGHTWEIGHT PHOTOVOLTAICS

Lead Partner

UQ

UQ Team

Dr. Peng Chen, Prof. Lianzhou Wang, Prof. Paul Burn

Funding Support

ACAP Postdoctoral Fellowship (P. Chen), ARC Laureate Fellowship (L. Wang)

Aim

The objective of this project is to develop hybrid quantum dot-organic tandem devices with high efficiency and good operational stability towards practical application in wearable and lightweight photovoltaics.

Progress

Owing to the passivation effect and suppressed dot-to-dot ion migration from abundant surface ligands, nanometer-sized colloid quantum dots (QDs) show high defect tolerance and good stability against various external stimuli (Swarnkar et al. 2016; Sanehira et al 2017). Employing mixed-cation halide perovskite nanocrystals as the light-absorbing materials, the state-of-the-art quantum dot solar cells (QDSCs) have shown a low open-circuit voltages (V_{oc}) loss of 0.45 V and tunable bandgaps (1.6–1.8 eV), which makes them ideal candidates as the front cells to construct efficient tandem photovoltaic (PV) devices (Hao et al. 2020). In the synthesis of colloid perovskite QDs, the introduced surface-coordinated ligands such as oleate (OA^-) and oleylammonium (OLA^+) play a vital role in stabilising the meta-stable octahedral crystal structure of metal halide perovskites ($CsPbI_3$/$FAPbI_3$, FA is formamidinium) at room temperature by relaxing their lattice strains (Moot et al. 2020). However, these insulating long carbon-chain ligands (OA^-/OLA^+) attached to the surface of perovskite QDs need to be partially replaced by acetate/FA^+ in a following ligand exchange process, enabling efficient dot-to-dot charge carrier extraction for PV applications (Wheeler et al. 2018). Therefore, the selection of appropriate ligand exchange agents that can well manage the surface chemistry of perovskite QDs determines the final PV performance of perovskite QDSCs. To attain high efficiency QDSCs, one of the main tasks of this project is to find an effective and mild ligand exchange solvent to treat the deposited mixed-cation perovskite QD films. After screening the solvent library in terms of polarity and boiling point, we have tried various mild, volatile and green solvents, including methyl acetate, ethyl acetate and acetonitrile, et al., as ligand

exchange agents to fabricate perovskite QDSCs with a conventional device architecture on indium-doped tin oxide (ITO) glass substrates (ITO/SnO_2/QDs/Spiro-OMeTAD/Au). As shown in Figure F35.1(a), the fabricated lab-scale perovskite QDSCs (active area is 0.08 cm^2) treated by ethyl acetate showed the highest short-circuit current density (J_{sc}) of 18.78 $mAcm^{-2}$ with a V_{oc} of 1.12 V and a fill factor (FF) of 0.71, yielding a champion power conversion efficiency (PCE) of 14.8%. However, the PCE of perovskite QDSCs experienced a dramatic drop to 9.1% when increasing the active area by an order of magnitude to 1.008 cm^2 (Figure F35.1(b)). Such a significant PV performance loss is mainly attributed to the low J_{sc} of 14.52 $mAcm^{-2}$, which is probably due to the non-uniform and sufficient ligand exchange across the large active area of over 1 cm^2.

To narrow the efficiency gap between small-area and large-area QDSCs, we developed a scalable blade-coating technique for the fabrication of uniform perovskite QD films with more controllable ligand exchange processes. As illustrated in Figure F35.2(a), the meniscus of QD ink on a substrate can be continuously sheared by a moving blade at a constant speed of 1 cm s^{-1} with a flow channel height of 80 μm, leading to the formation of compact and pinhole-free QD films on flat substrates after the quick evaporation of a volatile solvent (octane) at room temperature. The thickness of QD films can be tuned by the concentration of the employed QD inks. For instance, the use of QD inks with concentrations of 50, 75 and 100 mg mL^{-1} would result in QD film thicknesses of 160, 240 and 300 nm, respectively (Figure F35.2(c)–(d)). As a proof-of-concept, a large-area QD film was deposited on a fluorine-doped tin oxide (FTO) glass substrate of 36 cm^2 by using the developed blade-coating technique, showing good uniformity and semi-transparent property (Figure F35.3(a)–(b)). Besides, we also demonstrate the compatibility of this scalable coating method with flexible substrates, such as polyethylene naphthalate (PEN) of 2.25 cm^2 and polyethylene terephthalate (PET) of 30 cm^2, as shown in Figure F35.3(c)–(d). Then, using the developed blade-coating method for both QD film deposition and the following ligand exchange process, we built up around 300 nm-thickness QD film as the light-absorbing layer to construct large-area QDSCs. Compared to that (8.0%) of their spin-coated counterparts, the blade-coated QDSCs with an active area of 1.008 cm^2 showed a much higher average PCE of 9.4% (Figure F35.4(a)). As shown in Figure F35.4(b), the champion large-area QDSCs based on the blade-coating technique exhibited a J_{sc} of 15.76 $mAcm^{-2}$, a V_{oc} of 1.11 V and an FF of 0.59, yielding a high PCE of 10.4%, which is the highest among all the reported QDSCs with an active area of over 1 cm^2. In this scenario, the successful establishment of this blade-coating method may pave the way for the future fabrication of an efficient QD flexible solar module based on a more rational electrode pattern design.

As we have demonstrated the capability for making efficient QDSCs, more attention will be paid to the optimisation of transparent metal electrodes (Au or Ag) as well as the robust interconnection recombination layer such as sputtered ITO and solution-processed PEDOT:PSS in the next step. Meanwhile, low-bandgap (1.1–1.3 eV) organic photovoltaics (OPV) based on bulk heterojunction comprised of non-fullerene acceptor and polymer donor will be developed in the following 12 months, acting as bottom cells to construct efficient QDSC-OPV tandem cells on either rigid glass or flexible plastic substrates.

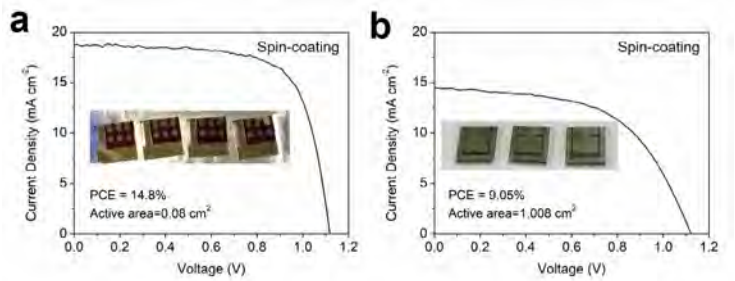

Figure F35.1: The J-V curve of spin-coated QDSCs: (a) active area is 0.08 cm^2; and (b) active area is 1.008 cm^2, the inset shows the digital pictures of the completed QDSCs with different active areas.

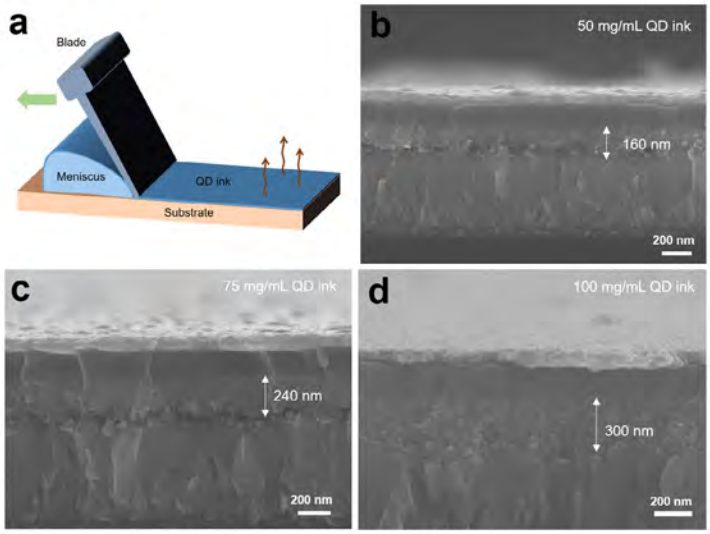

Figure F35.2: (a) Schematic illustration of scalable blade-coating technique; completed QDSCs using different concentrations of QD inks via blade coating: (b) 50 mg/mL, (c) 75 mg/mL, and (d) 100 mg/mL.

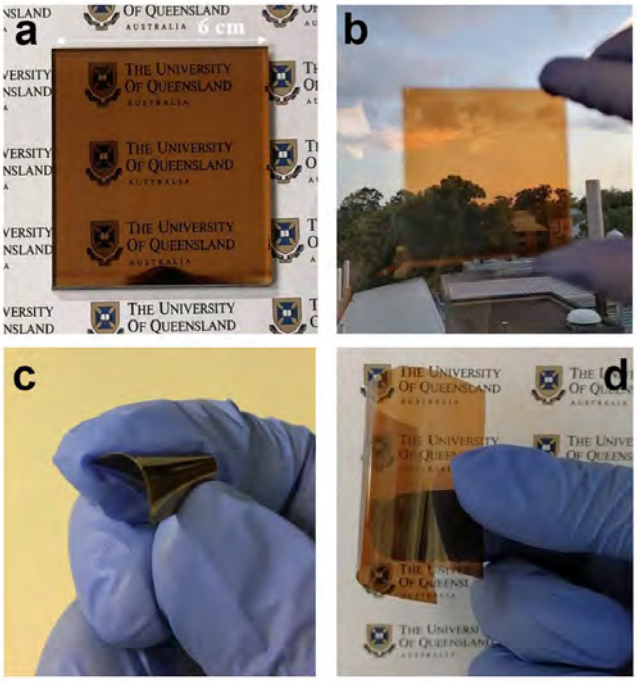

Figure F35.3: Pictures of (a)–(b) blade-coated QD film on FTO glass (36 cm²); (c) blade-coated QD film on a flexible PEN substrate (2.25 cm²); (d) blade-coated QD film on a flexible PET substrate (30 cm²).

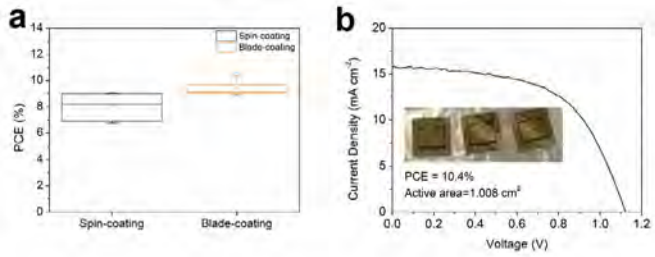

Figure F35.4: (a) The statistic distributions of the photovoltaic performance of large active area QD solar cells via spin-coating a nd blade-coating methods; (b) the J-V curve of the champion blade-coated QDSC with an active area of 1.008 cm², the inset shows the digital picture of the completed device.

Highlights

- Ethyl acetate was selected as an effective and mild solvent to facilitate a ligand exchange process of QD films and promote the charge carrier transport of QDSCs.
- A PCE of 14.8% was achieved in small active area QDSCs (0.08 cm²) via spin-coating on rigid ITO glass substrates.
- A scalable blade-coating technique was developed for the fabrication of uniform and pinhole-free large-area QD films on rigid glass (36 cm²) and flexible substrates (30 cm²).
- The large active area QDSCs (>1 cm²) via the optimised blade-coating protocol achieved a PCE of 10.4%, which is the highest among all the reported QDSCs with an active area of ~1 cm².

Future Work

- The fabrication of efficient QDSCs on flexible PEN substrates.
- The development of high efficiency non-fullerene OPV cells with a narrow bandgap (1.1–1.3 eV).
- The investigation on the appropriate interconnection recombination layers between the top QDSCs and the bottom "OPV cell.
- The demonstration of tandem cells on flexible PEN substrates with an active area of over 1 cm².

References

HAO, M., BAI, Y., ZEISKE, S., REN, L., LIU, J., YUAN, Y., ZARRABI, N., CHENG, N., GHASEMI, M., CHEN, P., LYU, M., HE, D., YUN, J.-H., DU, Y., WANG, Y., DING, S., ARMIN, A., MEREDITH, P., LIU, G., CHENG, H.-M., & WANG, L. 2020. Ligand-assisted cation-exchange engineering for high-efficiency colloidal $Cs_{1-x}FA_xPbI_3$ quantum dot solar cells with reduced phase segregation. *Nature Energy*, 5, 79-88.

MOOT, T., DIKOVA, D. R., HAZARIKA, A., SCHLOEMER, T. H., HABISREUTINGER, S. N., LEICK, N., DUNFIELD, S. P., ROSALES, B. A., HARVEY, S. P., PFEILSTICKER, J. R., TEETER, G., WHEELER, L. M., LARSON, B. W. &, LUTHER, J. M. 2020. Beyond strain: controlling the surface chemistry of $CsPbI_3$ nanocrystal films for improved stability against ambient reactive oxygen species. *Chemistry of Materials*, 32, 7850-7860.

SANEHIRA, E. M., MARSHALL, A. R., CHRISTIANS, J. A., HARVEY, S. P., CIESIELSKI, P. N., WHEELER, L. M., SCHULZ, P., LIN, L. Y., BEARD, M. C., & LUTHER, J. M. 2017. Enhanced mobility $CsPbI_3$ quantum dot arrays for record-efficiency, high-voltage photovoltaic cells. *Science Advances*, 3, eaao4204.

SWARNKAR, A., MARSHALL, A. R., SANEHIRA, E. M., CHERNOMORDIK, B. D., MOORE, D. T., CHRISTIAN, J. A., CHAKRABARTI, T., & LUTHER, J. M. 2016. Quantum dot-induced phase stabilization of α-$CsPbI_3$ perovskite for high-efficiency photovoltaics. *Science*, 354, 92-95.

WHEELER, L. M., SANEHIRA, E. M., MARSHALL, A. R., SCHULZ, P., SURI, M., ANDERSON, N. C., CHRISTIANS, J. A., NORDLUND, D., SOKARAS, D., KROLL, T., HARVEY, S. P., BERRY, J. J., LIN, L. Y., & LUTHER, J. M. 2018. Targeted Ligand-Exchange Chemistry on Cesium Lead Halide Perovskite Quantum Dots for High-Efficiency Photovoltaics. *Journal of the American Chemical Society*, 140, 10504-10513.

F37 STABLE AND SCALABLE PEROVSKITE FILMS USING INDUSTRIALLY RELEVANT PROCESSES

Lead Partner

ANU

ANU Team

Dr Yiliang Wu, Prof. Klaus Weber

Funding Support

ACAP Fellowship

Aims

The first aim of this Fellowship is on developing large-area (smooth, pinhole free), high quality (highly oriented grain, low non-radiative recombination), and stable (CsFA dual cation composition, low tensile strain) perovskite films using industrially feasible processes. The second is to develop and improve the innovative cost analysis methodology so that it is able to analyse each successive technology with greater effectiveness.

This Fellowship has its primary focus on contributing to ACAP's PP1 and PP2, stable and high quality large-area perovskite films contributing to both high efficiency silicon-based tandem cells and high efficiency organic/inorganic hybrid cells.

Progress

Remove the strain of the perovskite film

The perovskite film is typically under tensile strain after annealing process owing to the large mismatch of the thermal expansion coefficient between the perovskite film and the substrate. There is also discussion regarding whether the lattice of the perovskite film expands with light, but the result is still under debate. However tensile strain is not desired for device fabrication. The perovskite film with a convex setup (tensile strain) was found to degrade significantly faster than the film with a concave setup (compressive strain), and the localised tensile strain is strongly associated with the non-radiative defects.

A. Solvent engineering

To remove the tensile strain inside the perovskite film, we started with efficiently removing the solvent in the wet film from spin coating and have the black phase perovskite film form at room temperature. Zhao et al. and Rolston et al. showed that once the perovskite film is fully crystallised, additional high temperature annealing will not change the strain status within the film. From our previous work, we found using a vacuum flash method, the black phase perovskite film can easily form after the gas quenching process with room temperature annealing for a few minutes. We used a simple metal halide perovskite composition FA0.3MA0.7PbI3 to test the principle. In this work, we used the classical sin2ψ analysis using relative peak positions to measure the residual strain in the poly-crystalline perovskite film with the X-ray diffraction (XRD) method. We found there is no significant change for the residual strain between the film fabricated with 100°C annealing, or room temperature (RT) + 100°C annealing, though the black phase perovskite was formed at room temperature without high temperature annealing. We found no trace of CH_3NH_3I–PbI_2–DMSO intermediate phase in the XRD scan. But with Fourier transform Infrared (FTIR) spectroscopy (Figure F37.1), we found with the room temperature annealed perovskite film, significant traces of DMSO complex still exist, indicating the DMSO solvent was not completely extracted by the vacuum flash followed by RT annealing process. Since the DMSO has strong coordination with Pb elements, and its high volatilisation temperature reduces the release rate of Pb, the crystallisation of the PbI_2 and perovskite was retarded. We speculated that the strain of the perovskite film was reconstructed by the conversion of the CH_3NH_3I–PbI_2–DMSO intermediate phase into perovskite after 100°C annealing. Hence, the film returned to tensile strain after cooled to room temperature due to the large mismatch of the thermal expansion coefficient between the film and the substrate.

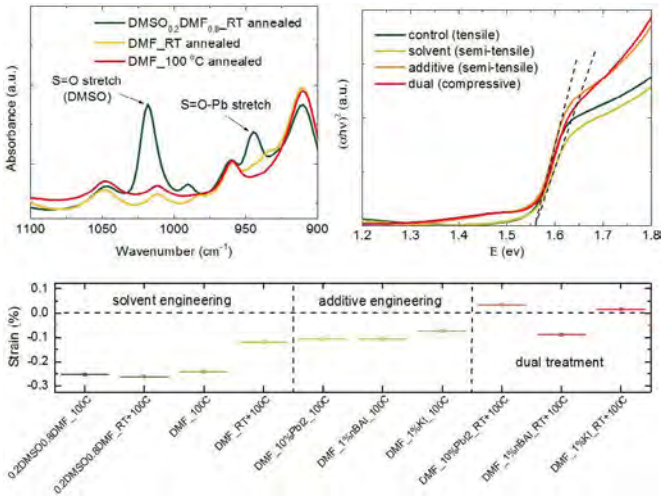

Figure F37.1: (a) FTIR spectra; (b) Tauc plot of the perovskite film with RT or 100°C annealing using DMF or DMF/DMSO as the solvent; and (c) XRD strain measurement result of the perovskite film fabricated on FTO substrates with solvent, additive engineering or dual treatments.

To cope with the problem, we removed the DMSO from the mixed solvent, and used the DMF (dimethylformamide) as the single solvent since it is more volatile and it has weaker coordination with Pb elements. We prepared the high quality perovskite film with a gas quenching process to effectively remove the solvent. After the gas quenching process, the perovskite film turned to black phase within 5 minutes under room temperature annealing. With room temperature plus 100°C annealing process, we successfully halved the tensile strain that remained inside the perovskite film compared to the film with only 100°C annealing process. However, there was still tensile strain found in the film and it was attributed to the small amount of DMF that remained inside the perovskite film after gas quenching and room temperature annealing, as can be seen from the FTIR result (C=O stretched from DMF at ~1650 cm^{-1}). The tensile strain formed may attribute to the small amount of DMF-induced intermediate phase. Interestingly, the trace of DMF was not found with the room

temperature annealed perovskite film fabricated with the DMF/DMSO mixed solvent, suggesting DMSO dominates the coordination with the Pb element and forms the majority of the intermediate phase.

B. Additive engineering

To further eliminate the residual tensile strain, we investigated the possibility of using additive engineering. From previous reports, by alloying octylammonium iodide at the perovskite top surface, the strain was relaxed at the perovskite/hole transport layer interface, which suggested interstitial additives can effectively reduce the macrostrain in the perovskite film. Here, we chose three commonly used interstitial additives for perovskite solar cell fabrication, including KI, PbI_2, and n-BAI to cover the A site, B site cation and 2D perovskite categories without introducing Br into the perovskite lattice. From the XRD strain measurements, we found all three additives we chose can effectively suppress the strain of the perovskite film compared to the control sample. The level of the suppression of the tensile strain is strongly dependent on the amount of additive doped in the perovskite precursor. Combining both solvent and additive engineering methods, as shown in Figure F37.1, with PbI_2 and KI as additive, dual treatment effectively eliminated the tensile strain in the perovskite film and pushed it into the compressive strain regime. However surprisingly, for the film with n-BAI, only a small decrease for the strain measured was observed compared with additive treatment only.

Highlights

Compressive strain of perovskite film was achieved with solvent and additive engineering.

Established collaboration with a variety of institutions in Australia and internationally.

Future Work

- Establishing the flow dynamics model of the vacuum flash procedure.
- Optimising the vacuum flash process for CsFA perovskite composition.
- Development of the large-area perovskite and tandem cell.

F39 PATHWAYS TO ACHIEVE A SOLAR CELL EFFICIENCY ABOVE 26%

Lead Partner

ANU

ANU Team

Dr Teng Choon Kho, Prof. Andrew Blakers

Funding Support

ACAP Fellowship

Aims

This Fellowship aims to achieve a solar cell efficiency of 26%, either by implementing a single silicon junction interdigitated back contact (IBC) solar cell with polysilicon passivated contacts or a mechanical tandem structure of silicon IBC with perovskite solar cell.

This report should be read in conjunction with the PP1 report.

Progress

Experiment with and design of hybrid IBC solar cell

A previous IBC cell with a conventional direct metal-Si contact design at the ANU achieved an efficiency of 25%. The proposed hybrid IBC solar cell design intends to achieve a higher efficiency of ≥26% by introducing phosphorus-doped polysilicon passivated contacts. A detailed simulation performed with Quokka3 shows that such cell efficiency with passivated contacts should be achievable. The introduction and implementation of phosphorus-doped polysilicon passivated contacts for the IBC solar cell will therefore be discussed in this section.

(i) Phosphorus diffused polysilicon passivated contact:

The thermally diffused phosphorus polysilicon passivated contact structure in this project consists of a chemical SiO_x / LPCVD aSi stack onto silicon wafer.

Phosphorus polysilicon passivated contact experiments with different thicknesses of LPCVD aSi and thermal phosphorus diffusion profiles were performed. Figure F39.1 shows a low J_0 of 3–5 fA.cm^{-2} can be achieved for all of the different aSi thicknesses. This observation is similar to n+ polysilicon passivated contact results with PECVD aSi (Yan et al., 2019). However, Cox and Strack (1967) measurements performed on all of the lowest J_0 (<5 fA.cm^{-2}) samples of different LPCVD aSi thicknesses showed high contact resistivity, ranging between 0.2 and 0.01 Ω.cm^2.

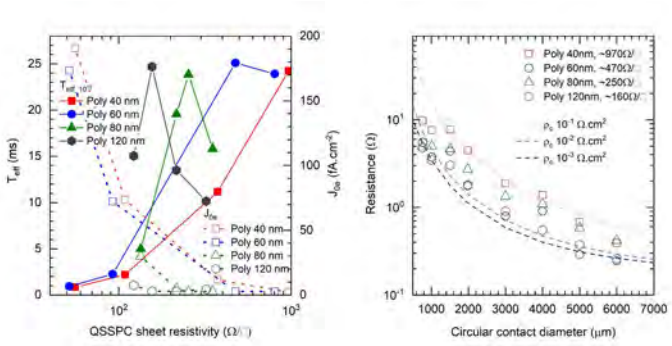

Figure F39.1: Measurement of different LPCVD polysilicon thicknesses and phosphorus diffusion for (a) T_{eff} at $\Delta n=10^{15}$ cm^3 and J_0; and (b) contact resistivity.

A light phosphorus diffusion of 800–1000 Ω/□ was performed prior to depositing a phosphorus-doped polysilicon passivated contact with a polysilicon thickness of ~80 nm. Lifetime and contact resistivity with the initial phosphorus diffusion in Figure F39.2 shows that the passivated contact is capable of obtaining a J_0 of ~4 fA.cm^{-2} with excellent contact resistivity of ≤10^{-3} Ω.cm^2.

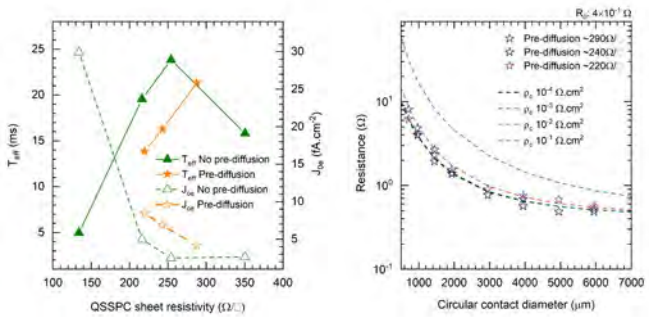

Figure F39.2: Measurement of different phosphorus diffusion on polysilicon passivation contact for (a) T_{eff} at $\Delta n=10^{15}\,cm^3$ and J_0; and (b) contact resistivity with and without phosphorus diffusion on silicon wafer prior to deposition of polysilicon.

(ii) Design of hybrid IBC solar cell

The cell fabrication process flow will be based on previous IBC cell development at ANU with slight modifications (Franklin et al., 2014). The cell design will be based on experimental results and simulation software using Quokka3 and ray tracing SunSolve.

Highlight

Light phosphorus diffusion on silicon wafer prior to deposition of polysilicon passivated contact improves the contact resistivity and achieves low J_0.

Future Work

- Optimisation of cell design and fabrication process is on-going
- Purchase of wafers and mask design and fabrication are on-going

References

COX, R. H. & STRACK, H. 1967. Ohmic contacts for GaAs devices, *Solid-State Electronics*, 10, 1213-1218.

FRANKLIN, E., FONG, K., MCINTOSH, K., FELL, A., BLAKERS, A., KHO, T., WALTER, D., WANG, D., ZIN, N. & STOCKS, M. 2014. Design, fabrication and characterisation of a 24.4% efficient interdigitated back contact solar cell. *Progress in Photovoltaics: research and applications*, 24.

F40 HIGH PERFORMING LEAD-FREE EARTH-ABUNDANT SOLAR CELLS

Lead Partners

Monash University

Monash Team

Narendra Pai, Nikhil Medhekar, Alexandr Simonov, Philip C Andrews, Udo Bach

CSIRO Team

Anthony Chesman

Funding Support

ACAP, ARENA, Monash

ACAP Partners

Melbourne Centre for Nanofabrication

Commonwealth Scientific and Industrial Research Organisation Manufacturing

Aims

Lead-free perovskite and perovskite-inspired materials are now gaining increased research attention due to well-understood toxicity and stability issues of organolead halide perovskites (Jena et al. 2019; Ke and Kanatzidis 2019). A search for new efficient light-harvesting compounds that (i) are thermodynamically stable under the conditions of an operating solar cell; (ii) can be fabricated as thin layers using scalable solution-processed methods; and (iii) contain only non-toxic, reasonably abundant and cheap elements led to the discovery of several compositions over the years. In recent years, the Monash team has made notable progress by unravelling the potential of some of the lead-free systems such as $Ag_aBi_bI_{a+3b}$ (Pai et al. 2019) and $Cs_2AgBiBr_6$ (Pai et al. 2019b), and demonstrating the possibility of improving the intrinsic light-harvesting efficiency and band structural misalignments. However, these systems' efficiency is still lower than their lead counterparts due to interfacial recombination, surface defects and wider bandgaps (E_g >1.8 eV). We aim to improve the interfacial band alignment, the films morphology, minimise the photovoltage-photocurrent losses, and comprehensively investigate the developed compositions. Extending these strategies to the discovery and characterisation of novel compositions was also intended.

Progress

The urge to find a reliable and stable lead-free system led us to introduce the $A_aBi_bX_{a+3b-2x}S_x$ family of sulfo iodobismuthates that outperform conventional bismuth iodide perovskites in these aspects eventuated with A^+ being a monovalent group 11 cation and X^- being a halogen anion. Among these perovskite-inspired three-dimensional edge-sharing octahedral crystal networks, silver bismuth sulfoiodides were extensively investigated by the Monash team in recent years. While further tuning of the bandgap or light-harvesting efficiency of these devices employing mixed chalcogenide-halide strategy was limited with the low solubility and induced phase segregation of chalcogenide complexes. The team has tackled this limitation by modifying the synthesis strategy of thiolates and employing hot-casting methods, leading to an increase in the amount of S^{2-} in $Ag_aBi_bI_{a+3b-2x}S_x$ to the previously unachievable x = 0.12 (see Figure F40.1(a)). To have ambiguous information on the structural and electronic changes by the anionic substitution, the team submitted a proposal for a detailed XANES/EXAFS investigation at synchrotron and were awarded beamtime in the middle of the year (Reference No: AS1/XAS/15944). While a thorough analysis of the results is undergoing,

the team proceeded with the construction of photovoltaic devices. Unfortunately, severe voltage losses in the system were observed despite the materials having wider bandgap than the tin/germanium perovskites, possibly due to the apparent surface defects induced by low film quality and non-radiative recombination rendered by reduced minority carrier lifetimes. The film quality and interfacial contact were improved by employing solvent vapour-assisted post-annealing, utilising an energetically favourable (band-aligned) hole transport layer (PTB7), and carbon counter electrode. While the strategy significantly improved the open-circuit voltage by ~200 mV, a proportionate increase in current was not achieved. Consequently leading to lower photovoltaic performance (Figure F40.1(b)).

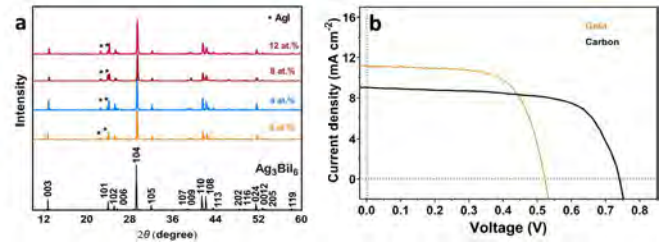

Figure F40.1: (a) XRD of the $Ag_aBi_bI_{a+3b-2x}S_x$ at different sulfide modification concentrations; and (b) photovoltaic performance of the PTB7/ $Ag_aBi_bI_{a+3b-2x}S_x$ + m-TiO_2/ c-TiO_2/ FTO with gold and carbon as counter electrodes (aperture 0.16 cm^2) under one-sun irradiation.

As per the research plan of extending the strategy to novel compositions, silver was replaced with cheaper copper(I) cation, developing $Cu_aBi_bI_{a+3b-2x}S_x$ systems. Unfortunately, very low intrinsic light-harvesting efficiency, positively shifted valence band levels, and wide bandgap limited the performance significantly (Figure F40.2(a), (b) and (c)). The specific focus was on assessing the possibility to produce target materials using solution-based low-temperature procedures and conformal copper bismuth sulfoiodide thin films were produced (Figure F40.2(d) and (e)).

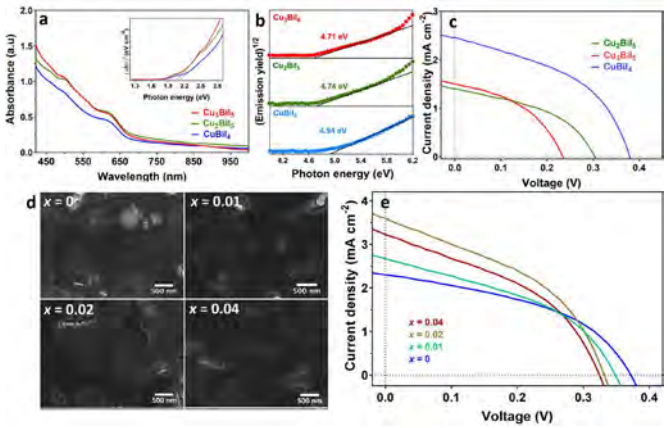

Figure F40.2: Optoelectronic properties of copper bismuth iodide films deposited onto m-TiO_2/c-TiO_2/FTO: (a) UV-Vis spectra and Tauc plots for direct band transition (inset). (b) PESA data of copper bismuth iodides having different Cu:Bi ratios. (c) Photovoltaic performance of the Au / P3HT/ $Cu_aBi_bI_{a+3b}$+ m-TiO_2/ c-TiO_2/ FTO non-encapsulated solar cells (aperture 0.16 cm^2) under one-sun irradiation. (d) Top-view SEM images of $Cu_aBi_bI_{a+3b-2x}S_x$ at different sulphide modification concentrations and corresponding (e) photovoltaic performance of the Au / P3HT/ $Cu_aBi_bI_{a+3b-2x}S_x$ + m-TiO_2/ c-TiO_2/ FTO non-encapsulated solar cells (aperture 0.16 cm^2) under one-sun irradiation.

The team have also explored the possibility of constructing titanium-based vacancy-ordered perovskites via a solution process. Considering there have been no reports on viable solution-processible synthesis of cesium iodotitanates, the preliminary results have demonstrated successful extraction of Cs_2TiI_6 crystals. Further purification of the crystals is necessitated with the observed CsI impurities on the crystal surfaces (Figure F40.3).

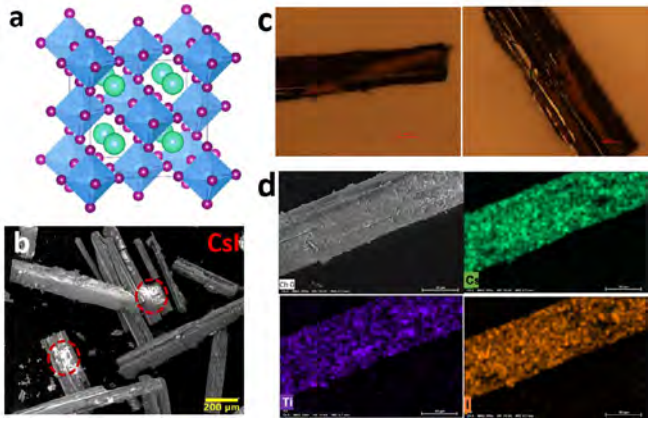

Figure F40.3: Crystal structure and compositional analysis of the titanium perovskites: (a) crystal structure of Cs_2TiI_6; (b) SEM image of the obtained crystals highlighting the presence of CsI impurities; (c) optical image of the crystals; and (d) EDX mapping image of the crystals for the confirmation of the composition.

The team have also found some novel lead-free compositions in collaboration with Professor Nikhil Medhekar's computational materials lab. This high-throughput computation of a lead-free system is still ongoing.

Highlights

- Improved open-circuit voltage and fill factor for sulfo iodobismuthate lead-free systems.
- Copper bismuth sulfoiodides constructed for the first time.
- Cesium iodotitanate perovskites are developed via a solution process for the first time.

Future Work

The team will build upon the current morphological advancement, explore surface treatment, and improve the sulfide-iodide modifications without compromising the performance. The team will further investigate the purification and film fabrication strategies for the titanium perovskites and develop a photovoltaic device with the improved systems and focus on developing more novel compositions, with the strong support of the computational team.

References

JENA, A. K, KULKARNI, A. & MIYASAKA, T. 2019. Halide Perovskite Photovoltaics: Background, Status, and Future Prospects. *Chemical Reviews*, 119, 3036.

KE, W. & KANATZIDIS, M. G. 2019. Prospects for low-toxicity lead-free perovskite solar cells. *Nature Communications*, 10, 965.

PAI, N., LU, J., GENGENBACH, T. R., SEEBER, A., CHESMAN, A. S. R, JIANG, L., SENEVIRATHNA, D. C., ANDREWS, P. C., BACH, U., CHENG, Y. -B. & SIMONOV, A. N. 2019a. Silver Bismuth Sulfoiodide Solar Cells: Tuning Optoelectronic Properties by Sulfide Modification for Enhanced Photovoltaic Performance. *Advanced Energy Materials*, 2019a, 9, 1803396.

PAI, N., LU, J., WANG, M., CHESMAN, A. S. R, SEEBER, A., CHEREPANOV, P. V., SENEVIRATHNA, D. C., GENGENBACH, T. R., MEDHEKAR, N. V., ANDREWS, P. C., BACH, U. & SIMONOV, A.N. 2019b. Enhancement of the intrinsic light-harvesting capacity of Cs2AgBiBr6 double perovskite: Via modification with sulphide. *J.L Material Chemistry A*. 8, 2008-2020.

F41 APPLICATION OF STABLE LEAD-FREE ABSORBER LAYERS IN PHOTOVOLTAICS

Lead Partner

Monash University

Monash University Team

Dr Nadja Glueck (Giesbrecht), Prof. Udo Bach

Funding Support

ACAP Fellowship

Aims

This Fellowship has the main aim to synthesise lead-free compounds with a perovskite-related structure suitable as absorber materials and to apply them in photovoltaic systems. The requirement criteria for the lead-free absorbers are a bandgap below 2 eV with preferably a direct transition and high stability towards moisture, temperatures above 80°C and oxidation.

This Fellowship has its primary focus on contributing to ACAP's PP2 Thin-Film, Third Generation and Hybrid Devices, and this report should be read in conjunction with the PP2 report.

Progress

To address the issue of toxicity of lead in perovskite photovoltaics, a metal cation replacement is required. Therefore, we suggested in our proposal an investigation and optimisations of the 2D antimony-based systems $A_{3+n}M^{II}_nSb_2X_{9+3n}$. This material class shows significant similarity to the lead-based perovskites: tunable bandgap sizes with often a direct transition and strong light absorption and high conductivity within the corner-sharing inorganic octahedra two-dimensional layers. With the inclusion of two-valent metal cations (M^{II}) and/or a halide variation, the dimensionality can be further increased and the bandgap size tuned. Synthesising highly crystalline bulk or thin films of these 2D $A_{3+n}M^{II}_nSb_2X_{9+3n}$ compounds is highly challenging due to their good stability towards high temperatures and moisture and, therefore, resulting low solubility in polar solvents.

A. Synthesis of $Cs_4CuSb_2Cl_{12}$ single crystals and thin films

In 2017 $Cs_4CuSb_2Cl_{12}$ (CCSC) was reported by Vargas et al. as a semiconductor with a direct bandgap of 1.0 eV (Vargas et al., 2017). This compound crystallises within seconds if all ions are in solution, resulting in small crystallites with high stability and low solubility in polar solvents. As proposed, we already established a two-step synthesis approach of highly crystalline CCSC bulk by first synthesising $Cs_3Sb_2Cl_9$ and then converting it to CCSC. In this research, the process was further altered to crystallise CCSC in one step using a copper acetate precursor and dissolving the precursors in a suitable solvent mixture. The compound slowly crystallises being controlled by annealing temperature, annealing time and cooling rate. Therefore, highly crystalline material can be synthesised with this approach. Figure F41.1 shows the scanning electron microscope (SEM) images of the fabricated crystalline bulk of CCSC and a large area's close-up with no visible defects. With the now obtained crystallites, further investigations of its physical properties are possible. So far, the characterisations on the physical properties of CCSC published are based on bulk powder samples and more crystalline material can more efficiently reveal its potential for solar cell applications of CCSC.

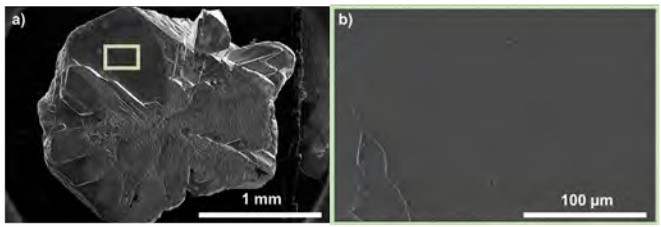

Figure F41.1: SEM images of: (a) millimetre-sized crystalline bulk of CCSC; and (b) area indicated in the green box in (a).

Thin-film synthesis of CCSC was also targeted. Here, the low solubility of especially CsCl in anything but water significantly complicates the thin-film fabrication through a precursor solution containing all the ions. Thus, we approached the thin-film synthesis similarly to our first bulk crystallisation approach by utilising $Cs_3Sb_2Cl_9$ as a precursor film and converting it to CCSC. To synthesise $Cs_3Sb_2Cl_9$, we used the method of converting a $Cs_3Sb_2I_9$ layer with $SbCl_3$ vapour published by (Singh et al., 2019). Afterwards, we added CsCl and $CuCl_2$ in an acidic solution as a top layer to convert the $Cs_3Sb_2Cl_9$ bottom layer. The resulting films show a significant increase and broadening of the absorption in the visible spectrum compared to the wide bandgap precursor film (see Figure F41.2(a)). However, the conversion only partially results in a phase mixture of $Cs_3Sb_2Cl_9$ and $Cs_4CuSb_2Cl_{12}$ as the thin-film XRD analysis in Figure F41.2(b) indicates. Further optimisation will be required to aim for CCSC phase purity and high quality morphologies, including smooth and homogeneous films.

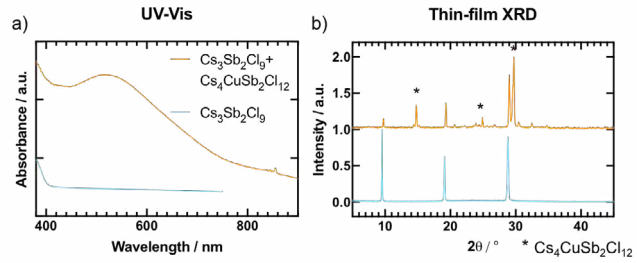

Figure F41.2: (a) UV-Vis; and (b) XRD analysis of $Cs_3Sb_2Cl_9$ and $Cs_4CuSb_2Cl_{12}$ thin films.

B. Tin inclusion to narrow the bandgap of 2D $MA_3Sb_2I_9$

In previous research, 2D $MA_3Sb_2I_9$ (MA = methylammonium) with a direct bandgap of 2 eV was synthesised using an antimony acetate precursor (Giesbrecht et al., 2020). With this approach, the pure iodide-based compound form in a 2D structure, whereas typically a chloride inclusion widening the bandgap is necessary to obtain the same structural result. In this research, we added to our 2D $MA_3Sb_2I_9$ synthesis approach different amounts of $SnCl_2$ with MAI in equivalent molar ratios to narrow the bandgap further to values below 1.7 eV (see Figure F41.3(a) and (c)). More narrow bandgaps with strong light-absorbing properties are preferable and can potentially improve the performance of solar cells utilising the absorber layer. The most substantial effect on the bandgap has the addition of more than 0.5 mol $SnCl_2$ to 1 mol $MA_3Sb_2I_9$ (see Figure F41.3(c)). According to the thin-film XRD analysis, the crystal structure remains similar for all amounts of added $SnCl_2$ besides the 1:1 ratio in the top pattern of Figure F41.3(b). Here, a chloride-rich second phase forms but further synthesis optimisation might avoid the second phase formation since the additional phase peak vanishes after one week of storage. With increasing amounts of $SnCl_2$ to the precursor mixture, some peaks become more intense in the XRD pattern indicating either preferential orientation of the crystallites of the $MA_3Sb_2I_9$ phase or the formation of an additional tin-based phase overlapping at the peak positions. The crystalline or tin-based phases' exact nature still needs to be investigated with a study on the oxidation state of tin since Sn^{2+} is prone to be oxidised to Sn^{4+}. The tin inclusion additionally improves the thin-film morphology in comparison to the initial $MA_3Sb_2I_9$ layers. With higher tin chloride amounts, the grain size slightly increases and the thin-film roughness reduces (see Figure F41.3(d)–(f)) but more quality thin-films are still required.

The exact composition and phase/phases still need to be specified and the suitability for photovoltaic applications confirmed. However, the material appears to be a very promising absorbing layer with a narrow bandgap and high environmental stability. In in situ XRD studies, the compound was stable at temperatures up to 80°C in air and around 40% relative humidity values.

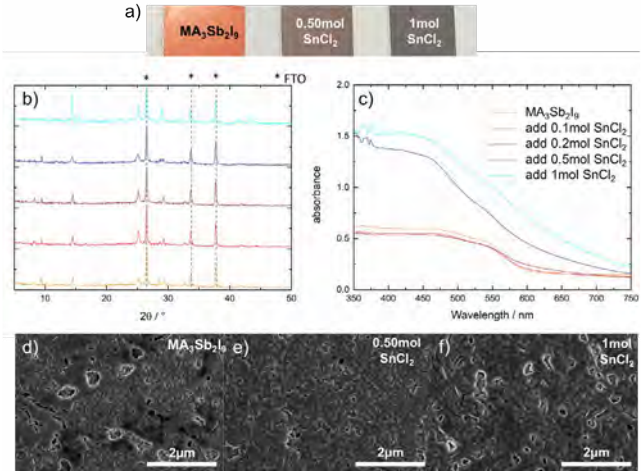

Figure F41.3: (a) Images of films with pure $MA_3Sb_2I_9$ and with an addition of 0.5 mol $SnCl_2$/MAI to 1 mol of $MA_3Sb_2I_9$ or an addition of 1 mol $SnCl_2$/MAI. (b) XRD analysis of the films with the different compositions indicated in (c). (c) UV-Vis analysis of the films with the different amounts of $SnCl_2$ added. (d)–(f) SEM images of the films from (a).

Highlights

- Highly crystalline $Cs_4CuSb_2Cl_{12}$ from one-step synthesis method.
- First thin-film synthesis approach of $Cs_4CuSb_2Cl_{12}$ based on $Cs_3Sb_2Cl_{12}$ precursor films.
- Bandgap below 1.7 eV with the addition of Sn^{2+} to the 2D $MA_3Sb_2I_9$ environmentally stable compound.

Future Work

- Synthesis of additional compounds based on the 2D $A_{3+n}M^{II}{}_nSb_2X_{9+3n}$ system.
- Fabrication of thin films of pure $Cs_4CuSb_2Cl_{12}$ and other suitable absorbers.
- Characterisation physical and optoelectronic properties of the absorber compounds.
- Application of the absorber layers in solar cells.

References

GIESBRECHT, N., WEIS, A. & BEIN, T. 2020. Formation of stable 2D methylammonium antimony iodide phase for lead-free perovskite-like solar cells*. *Journal of Physics: Energy*, 2, 024007.

SINGH, A., CHIU, N.-C., BOOPATHI, K. M., LU, Y.-J., MOHAPATRA, A., LI, G., CHEN, Y.-F., GUO, T.-F. & CHU, C.-W. 2019. Lead-Free Antimony-Based Light-Emitting Diodes through the Vapor–Anion-Exchange Method. *ACS Applied Materials & Interfaces*, 11, 35088-35094.

VARGAS, B., RAMOS, E., PÉREZ-GUTIÉRREZ, E., ALONSO, J. C. & SOLIS-IBARRA, D. 2017. A Direct Bandgap Copper–Antimony Halide Perovskite. *Journal of the American Chemical Society*, 139, 9116-9119.

F44 DEVELOPMENT OF ACCELERATED LID TESTING METHODS WITH IN SITU PL CHARACTERISATION AND NUMERICAL MODEL TO IMPROVE THE UNDERSTANDING OF DEGRADATION MECHANISMS IN SILICON SOLAR CELLS

Lead Partner

UNSW

UNSW Team

Moonyong Kim

Funding Support

ACAP Fellowship

Aims

This Fellowship has its primary focus on contributing to ACAP's PP4 Manufacturing Issues, and this report should be read in conjunction with the PP1 report.

This Fellowship has two broad aims. The first is to focus on understanding the behaviour of light induced degradation (LID) in crystalline silicon and implementation of rapid testing. To address this, experiments are conducted to understand the dependence of the testing condition and the LID changes. A new metric to more accurately quantify the defect concentration has been introduced. Moreover, a comprehensive understanding of injection dependence on light and elevated temperature induced degradation (LeTID) is demonstrated.

Progress

A. Developing a universal metric to quantify defect concentration

At the 2020 Asia-Pacific Solar Research Conference, which was held online, I presented a paper, entitled "A new universal metric called the relative defect concentration, β in c-Si solar cells and its application". This presentation aimed to demonstrate a new metric that can be used to quantify defect concentrations, particularly for light induced defects.

The motivation for the new metric for defect concentration: The normalised defect density (NDD) metric has been widely used to quantify the two common types of light induced degradation (LID): boron oxygen-related LID (BO-LID) (Bothe and Schmidt 2006); and light and elevated temperature induced degradation (LeTID) (Kersten et al. 2015). The NDD is calculated based on the difference in inverse effective lifetime (τ_{eff}) after ($\tau_{eff,f}$) and before lifetime degradation ($\tau_{eff,i}$) (Glunz et al. 2001; Herguth 2019). While it has been widely used to study LID in silicon, the value varies with injection level, Δn or doping density, N_{dop} as shown in Figure F44.1 for a given true defect concentration. The symbols show the reported range of Δn and N_{dop} from different studies. It is possible to make a relative comparison by comparing at the same ratio of Δn and N_{dop}, typically $\Delta n = 0.1 \times N_{dop}$. It is intuitively a simple approach to allow a relative comparison but not all studies followed the ratio, which will not allow direct comparison. Some examples do not follow the ratio where difference in NDD can be by orders of magnitude different. Therefore, a universal term is necessary for direct comparison.

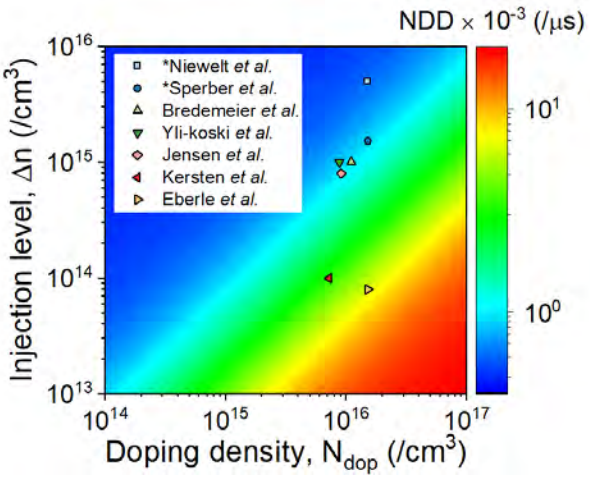

*Figure F44.1: An illustration of different value of normalised defect density (NDD) based on a given concentration of a defect as a function of doping density and injection level for p-type silicon. * Indicates that the indicated study only reported effective lifetime.*

Methods used in this project

A term for the relative defect concentration, β is introduced. Similar work has been done in a previous study, but it was used for BO-LID, and no further analysis was performed (Rougieux et al. 2020). Here, the conversion from NDD to β is introduced, based on the SRH equation. Typically, the NDD is calculated as follows:

$$\mathrm{NDD} = \frac{1}{\tau_{eff,d}} - \frac{1}{\tau_{eff,i}} \qquad \textit{Eq. 1}$$

Where $\tau_{eff,d}$ and $\tau_{eff,i}$ are the effective lifetimes after and before degradation, respectively. This value is typically compared at a fixed Δn but NDD is equivalent to the inverse of the Shockley-Read-Hall lifetime (τ_{eff}):

$$\mathrm{NDD} = \frac{1}{\tau_{SRH}} = \frac{p_0 + n_0 + \Delta n}{\tau_{p0}(n_0 + n_1 + \Delta n) + \tau_{n0}(p_0 + p_1 + \Delta n)} \qquad \textit{Eq. 2}$$

where τ_{n0} and τ_{p0} are the fundamental lifetimes of electrons and holes, respectively, and n_0 and p_0 are the equilibrium concentrations of electrons and holes, respectively. Both n_1 and p_1 are electron and hole densities when the Fermi energy coincides with the recombination centre energy, respectively (Macdonald and Cuevas 2001). τ_{p0} and τ_{n0} are given by:

$$\tau_{n0} = \frac{1}{N_t \sigma_n v_{th,n}} \text{ and } \tau_{p0} = \frac{1}{N_t \sigma_p v_{th,p}} = \frac{k}{N_t \sigma_n v_{th,p}}, \qquad \textit{Eq. 3}$$

where they are determined by the concentration of the defect (N_t), capture cross-section of holes (σ_p) and electrons (σ_n), and the thermal velocity of electrons ($v_{th,n}$ = 2.05 × 10^7 cm·s^{-1}) and holes ($v_{th,p}$ = 1.69 × 10^7 cm·s^{-1}) at 300 K (Green 1990) and capture cross-section ratio, $k = \sigma_n/\sigma_p$. We can define $\beta = N_t\sigma_n$ and combining Eq. 2 and Eq. 3, the conversion equation from NDD to β is as follows:

$$\beta = \left(\frac{\Delta n + n_1}{N_{dop} + \Delta n}\frac{k}{v_{th,p}} + \frac{N_{dop} + \Delta n + p_1}{N_{dop} + \Delta n}\frac{1}{v_{th,n}}\right) NDD. \quad Eq.\ 4$$

Using Eq. 4, the NDD is converted to β with different input values of Δn and N_{dop}. Only range $N_{dop} > 10^{14}$ cm^{-3} is shown since it is a more practical range value for industrial solar cells. We can see in Figure F44.2(a) that β is identical to β_{ref} with different N_{dop} and Δn values, unlike the NDD values. The symbols of examples all lie well within the range where β is unchanged, which indicates that the value of NDD from those studies can be converted to β to make direct comparisons on the concentration of N_t in the different materials. Using the β, the NDD from different literature studies at the maximum degradation extent (MDE) was converted into β and compared in Figure F44.2(b). The different values of NDD_{MDE} show it can be varied with different firing temperatures, testing conditions, degradation and recovery rates or the pre-annealing condition. However, despite the values of NDD_{MDE} varying by more than one order of magnitude across the several different studies (Bredemeier et al. 2017; Eberle et al. 2016; Kersten et al. 2016; Niewelt et al. 2017; Yli-koski et al. 2019) due to the different input value of $\Delta n/N_{dop}$, β_{MDE}, in contrast, typically lay within the range of ~(1–10) × 10^{-3} cm^{-1}. The other results that do not fall under this range tend to be the one with a lower firing temperature or the one that would likely have a lower hydrogen concentration in the dielectric layer. The agreement shows that β should be a more accurate value after Δn and N_{dop} correction. The small variations of β may indicate that the relative concentration of LeTID-related defects observed in various studies is far more similar than was previously possible to identify using the NDD metric without correction.

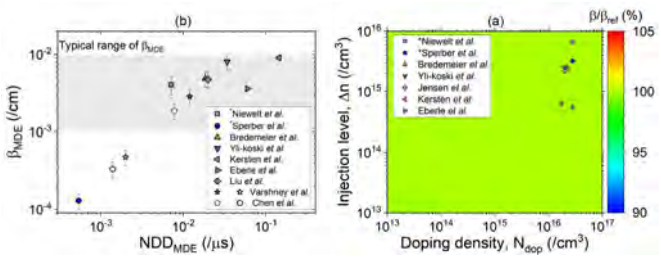

*Figure F44.2: (a) Plots of simulated result of the converted value of relative defect concentration, β, using Equation 6 with k = 35 to the reference value of β, β_{ref} (β/β_{ref}) as a function of doping density, N_{dop} in p-type silicon, and excess minority carrier concentrations, Δn. The symbols on the graphs show Δn where effective lifetimes (τ_{eff}) were extracted to calculate NDD and N_{dop} that are used in the studies of LeTID (Bredemeier et al. 2017; Eberle et al. 2016; Jensen et al. 2017; Kersten et al. 2015; Niewelt et al. 2017; Sperber et al. 2017; Yli-koski et al. 2019). (b) Converted value of NDD to β at the maximum degradation extents (MDE) from different literatures. Gray region indicates the typical range with high temperature. * Indicates that the study reported only τ_{eff}.*

A new term of relative defect concentration, β is introduced to correct the pitfall of NDD. This term overcomes issues with the use of NDD, which varies with both Δn and N_{dop}. It has a potential application to unify the defect concentration value to make a more quantitative conclusion among the studies.

B. Excess carrier concentrations, Δn dependence on LeTID

This covers a new method of normalising LeTID result in Δn to the light soaking time. It provides the potential to understand LeTID and how it changes with different parameters more comprehensively.

Δn normalised LeTID and recovery rates

A dependence of excess carrier concentration or injection level (Δn) exists and LeTID. The degradation rate constants of LeTID is linearly proportional to Δn (Kwapil et al, 2017). While the exact dependence of the LeTID recovery rate on Δn is unclear, studies have shown that the rate can be reduced when the light soaking is performed in short-circuit conditions compared to open-circuit conditions. Therefore a higher Δn accelerates the recovery (Kersten et al. 2015). Based on the Δn dependent lifetime curve, the Δn under a given intensity can be estimated. Different illumination intensities are used to investigate the link between Δn and LeTID-related reaction rates.

Sample preparation and testing condition

Industrial mc-Si PERC precursors with the resistivity of ~1.6 Ω·cm are used in this study. The samples are fired at the peak temperature ~740°C, which were then cleaved into ~39 mm × 39 mm pieces using a pulsed laser with frequency at 20 kHz, 1064 nm, 15 W. Samples were degraded under the accelerated light soaking condition with source being a fibre-coupled diode laser with the wavelength of 938 nm operated in quasi-continuous wave mode with a repetition frequency of 2 kHz and a pulse width of 0.5 ms (Payne et al. 2016) with different illumination intensities (equivalent to the generation rate, G of 1.2 × 10^{19} $cm^{-2}s^{-1}$ per sun) at a temperature of ~150°C. The injection-dependent lifetime was measured periodically using the quasi-steady state photoconductance tool (ex situ PC) from Sinton Instruments (WCT-120TS QSSPC) at 25°C (Sinton et al. 1996) and analysed using the generalised method (Nagel et al. 1999). The lifetime was measured at Δn = 10% of N_{dop}. The initial τ_{eff} was about 60-70 μs.
The measured τ_{eff} as a function of illumination time under different illumination intensities, I (0.6 sun and 17 suns), are shown in Figure F44.3. Lower intensity showed over two orders of magnitude slower rate to reach the maximum degradation extent time (t_{max}). Moreover, under the lower I, it showed stretched exponential and compressed exponential behaviours for degradation and recovery phases, respectively. At higher I, in comparison, the trends were more symmetrical.

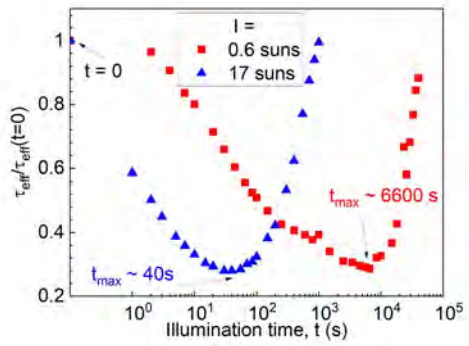

Figure F44.3: Normalised effective lifetime (τ_{eff}) to the initial τ_{eff} as a function of illumination time with different illumination intensities (0.6 sun and 17 suns). t_{max} indicates the time to reach the maximum degradation extent.

In order to estimate Δn at the given I, injection-dependent lifetime curves are analysed. Figure F44.4(a) shows the inverse lifetime curves where the dashed line shows the corresponding lifetime at the given intensities. At low I, Δn is reduced from ~4 × 10^{14} cm^{-3} to 7 × 10^{13} cm^{-3}. In comparison, Δn was not only higher at higher I but the variation was less significant (~1.2 × 10^{16} cm^{-3} to 7.4 × 10^{15} cm^{-3}). Based on the Δn at given I, Δn over time is shown in Figure F44.4(b). It shows that under low I, Δn is maintained at below 10^{14} cm^{-3} until it slowly starts recovering. This can then expect to reflect on the slower rate of LeTID, which can explain the trend that only lower I showed. Therefore, this is expected to occur on other studies that tested LeTID at low intensity (≤one sun) (Liu et al. 2018; Niewelt et al. 2017; Sperber et al. 2017; Ylikoski et al. 2019). However, note that may not necessarily occur if the defect amount at the maximum extent is not significant to vary Δn.

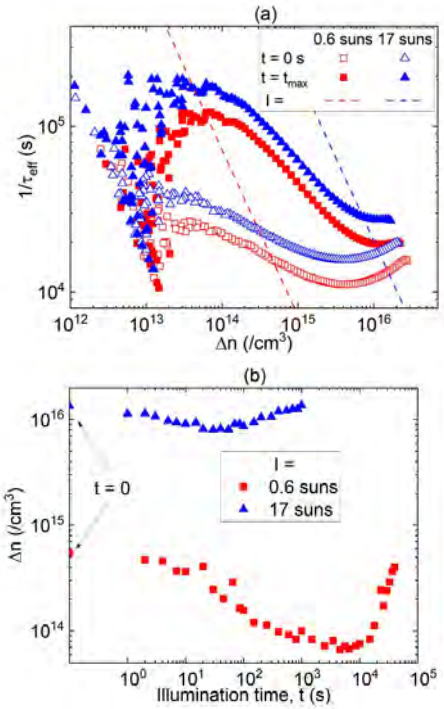

Figure F44.4: (a) Inverse effective lifetime (τ_{eff}) as a function of injection levels (Δn). Dashed line indicates the equivalent lifetime at different intensities. (b) Δn at given intensities as a function of illumination time, t.

Based on the estimated Δn and the τ_{eff} over time, Figure F44.5 shows the normalised τ_{eff} over Δn normalised time (Δn × t = Γ). Unlike the change in τ_{eff} over time, the normalised time showed very close agreement in both extent and the time scale. Moreover, the result with I = 0.6 sun showed mono-exponential degradation and recovery in Γ when Δn dependence is neglected. The result demonstrates a new approach to normalise the degradation and recovery cycles to Δn. The result has two implications. First, the recovery rate is linearly proportional to Δn. The closely matching result can only occur when the recovery is linearly proportional. Second, by knowing the Δn range during the operating condition, the accelerated testing result can already provide an insight into the performance change under different illumination intensity or operating conditions.

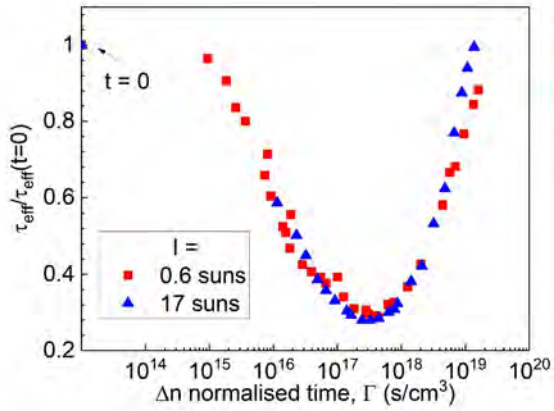

Figure F44.5: Normalised effective lifetime (τ_{eff}) to the initial τ_{eff} as a function of injection level normalised illumination time (Γ) with different illumination intensities (0.6 sun and 17 suns).

This section demonstrated an approach to normalise the illumination time to equivalent Δn. The normalisation excluded variation due to different illumination intensities. It shows the potential to isolate the dependence due to different initial lifetime or testing conditions. It can be applicable for understanding the dependence of LeTID on other parameters without being influenced by modulation of Δn. This understanding will help with developing the accelerated LID testing method in the future.

Highlights

- A new metric for the relative defect concentration identified and applied for understanding LeTID. This work has been submitted to the *IEEE Journal of Photovoltaics*.
- Illumination intensity dependence and the understanding of the influence of the variation of Δn on the LeTID cycle.
- Injection level normalised-time LeTID cycles used to determine a correlation between excess carrier concentration and reaction rates.

Future Work

- Simulating the injection level dependence on a LeTID cycle to compare to the experiment results.
- Compare the predicted result based on Δn normalised result using accelerated testing condition to the result under the operating condition on solar cells.
- Apply the application of LID on different structures of solar cells or lifetime precursors.

References

Bothe, K. & Schmidt, J. 2006. Electronically activated boron-oxygen-related recombination centers in crystalline silicon. *J. Appl. Phys*. 99, 013701. https://doi.org/10.1063/1.2140584.

Bredemeier, D., Walter, D. & Schmidt, J. 2017. Light-induced lifetime degradation in high-performance multicrystalline silicon: Detailed kinetics of the defect activation. *Sol. Energy Mater. Sol. Cells*, 173, 2-5. https://doi.org/10.1016/j.solmat.2017.08.007.

Eberle, R., Kwapil, W., Schindler, F., Schubert, M. C. & Glunz, S. W. 2016. Impact of the firing temperature profile on light induced degradation of multicrystalline silicon. *Phys. Status Solidi - Rapid Res. Lett.*, 10, 861-865. https://doi.org/10.1002/pssr.201600272.

Glunz, S. W., Rein, S., Lee, J. Y., Warta, W., Glunz, S. W., Rein, S., Lee, J. Y. &, Warta, W. 2001. Minority carrier lifetime degradation in boron-doped Czochralski silicon. *J. Appl. Phys*, 90, 2397-2404. https://doi.org/10.1063/1.1389076.

Green, M.A. 1990. Intrinsic concentration, effective densities of states, and effective mass in silicon. *J. Appl. Phys.*, 67, 2944-2954. https://doi.org/10.1063/1.345414.

Herguth, A. 2019. On the lifetime-equivalent defect density: Properties, application, and pitfalls. *IEEE J. Photovoltaics*, 9, 1182-1194. https://doi.org/10.1109/JPHOTOV.2019.2922470.

Jensen, M. A., Morishige, A. E., Hofstetter, J., Needleman, D. B. &, Buonassisi, T. 2017. Evolution of LeTID Defects in p-Type Multicrystalline Silicon during Degradation and Regeneration. *IEEE J. Photovoltaics*, 7, 980-987. https://doi.org/10.1109/JPHOTOV.2017.2695496.

Kersten, F., Engelhart, P., Ploigt, H. C., Stekolnikov, A., Lindner, T., Stenzel, F., Bartzsch, M., Szpeth, A., Petter, K., Heitmann, J. &, Müller, J. W. 2015. Degradation of multicrystalline silicon solar cells and modules after illumination at elevated temperature. *Sol. Energy Mater. Sol. Cells*, 142, 83-86. https://doi.org/10.1016/j.solmat.2015.06.015.

Kersten, F., Heitmann, J. &, Müller, J. W. 2016. Influence of Al2O3 and SiNx Passivation Layers on LeTID. *Energy Procedia*, 92, 828-832. https://doi.org/10.1016/j.egypro.2016.07.079.

Kwapil, W., Niewelt, T. &, Schubert, M. C. 2017. Kinetics of carrier-induced degradation at elevated temperature in multicrystalline silicon solar cells. *Sol. Energy Mater. Sol. Cells*, 173, 80-84. https://doi.org/10.1016/j.solmat.2017.05.066.

Liu, S., Chan, C., Chen, D., Kim, M., Sen, C., Varshney, U., Hallam, B., Abbott, M., Wenham, S. &, Payne, D. 2018. Investigation of temperature and illumination dependencies of carrier-induced degradation in p-type multi-crystalline silicon. AIP Conf. Proc. 1999, 130014. https://doi.org/10.1063/1.5049333.

Macdonald, D. &, Cuevas, A. 2001. Capture cross sections of the acceptor level of iron–boron pairs in p-type silicon by injection-level dependent lifetime measurements. *J. Appl. Phys*., 89, 7932-7939. https://doi.org/10.1063/1.1372156.

Nagel, H., Berge, C. &, Aberle, A. G. 1999. Generalized analysis of quasi-steady-state and quasi-transient measurements of carrier lifetimes in semiconductors. *J. Appl. Phys*., 86, 6218-6221. https://doi.org/10.1063/1.371633.

Niewelt, T., Schön, J., Schindler, F. &, Schubert, M. C. 2017. Understanding the light - induced degradation at elevated temperatures : Similarities between multicrystalline and floatzone p - type silicon. *Prog. Photovoltaics Res. Appl.*, 26, 533-542. https://doi.org/10.1002/pip.2954.

Niewelt, T., Selinger, M., Grant, N. E., Kwapil, W., Murphy, J. D. &, Schubert, M. C. 2017. Light-induced activation and deactivation of bulk defects in boron-doped float-zone silicon. *J. Appl. Phys.*, 121, 185702. https://doi.org/10.1063/1.4983024.

Payne, D. N. R., Chan, C. E., Hallam, B. J., Hoex, B., Abbott, M. D., Wenham, S. R. &, Bagnall, D. M. 2016. Acceleration and mitigation of carrier-induced degradation in p-type multi-crystalline silicon. Phys. Status Solidi - Rapid Res. Lett., 10, 237-241. https://doi.org/10.1002/pssr.201510437.

Rougieux, F. E., Sun, C. &, Juhl, M. 2020. Light-induced-degradation defect independent of the boron concentration: Towards unifying admittance spectroscopy, photoluminescence and photoconductance lifetime spectroscopy results. Sol. Energy Mater. Sol. Cells, 210, 110481. https://doi.org/10.1016/j.solmat.2020.110481.

Sinton, R.A., Cuevas, A. &, Stuckings, M., 1996. Quasi-steady-state photoconductance, a new method for solar cell material and device characterization, in: Conference Record of the Twenty Fifth IEEE Photovoltaic Specialists Conference - 1996. IEEE, pp. 457–460. https://doi.org/10.1109/PVSC.1996.564042

Sperber, D., Heilemann, A., Herguth, A. &, Hahn, G. 2017. Temperature and light-induced changes in bulk and passivation quality of boron-doped float-zone silicon coated with SiNx:H. IEEE J. Photovoltaics, 7, 463-470. https://doi.org/10.1109/JPHOTOV.2017.2649601.

Yli-koski, M., Serué, M., Modanese, C., Vahlman, H. &, Savin, H. 2019. Low-temperature dark anneal as pre-treatment for LeTID in multicrystalline silicon. Sol. Energy Mater. Sol. Cells, 192, 134-139. https://doi.org/10.1016/j.solmat.2018.12.021.

F45 PHOTOLUMINESCENCE IMAGING WITH SPATIALY NON-UNIFORM ILLUMINATION FOR THE CHARACTERISATION OF SILICON WAFERS AND SOLAR CELLS

Lead Partner

UNSW

UNSW Team

Yan Zhu, Oliver Kunz, Thorsten Trupke, Ziv Hameiri

UNSW Students

Shuai Nie, Jackson Moore

Funding Support

ACAP Fellowship

Academic partner

Fraunhofer Institute for Solar Energy Systems (Fh-ISE)

Industry partner

Jinko Solar, Griddler LLP

Aims

Photoluminescence (PL) imaging is a characterisation technique widely used for obtaining the spatial non-uniformity of silicon bricks, wafers, solar cells and modules. One of the main advantages of PL imaging is that no electrical contact is required. This reduces the potential damage of samples and also makes PL imaging suitable for in-line inspection. In conventional PL imaging measurement, uniform illumination light is used, for example the entire sample area is laterally excited under the same generation rate. As PL is directly correlated to the excess charge carrier concentration, lower counts in a PL image usually indicate regions with lower local electrical quality, such as lower minority carrier lifetime or local shunts.

However, resistance information is usually difficult to be extracted from conventional PL imaging. The resistance information such as series resistance is also important metric for quantifying the performance of solar cells. To get the resistance information, stimulation of lateral carrier flow is required, which is usually done by techniques that require electrical contact, such as electroluminescence (EL) imaging or PL imaging with current extraction. Lateral carrier flow can also be stimulated by using spatially non-uniform illumination, and no electrical contact is required. Therefore, in this project, we explore the potential of using spatially non-uniform illumination in PL imaging to extend its characterisation capability in silicon photovoltaics.

Additionally, this project aims to improve quantitative analysis of PL images by using non-unform illumination. In conventional PL imaging where uniform illumination is used, any non-uniformity in the sample quality will lead to a gradient of the quasi-Fermi level splitting. This gradient induces a net lateral carrier flow in the sample. It should be noted that this lateral carrier flow is usually not enough for resolving the resistance information mentioned above. On the contrary, this lateral carrier flow smears the resulted PL image and impedes an accurate quantitative analysis of PL images. By using spatially non-uniform illumination, it is possible to compensate the non-uniform quality of the sample and reach a uniform injection level in PL imaging. The spatially resolved sample quality information can be retrieved from the applied non-uniform illumination image.

Progress

1. Development of PL imaging setup with non-uniform illumination

The PL image setups with spatially non-uniform illumination have been developed by the UNSW team. The spatially non-uniform illumination is achieved by using a uniform light source and a digital micromirror device (DMD) chip or a liquid crystal display (LCD) chip. The DMD chip allows a higher contrast ratio than the LCD chip. However, the LCD chip allows pure steady-state illumination which is required for certain applications. A sketch of the developed PL imaging setup with spatially non-uniform illumination is shown in Figure F45.1.

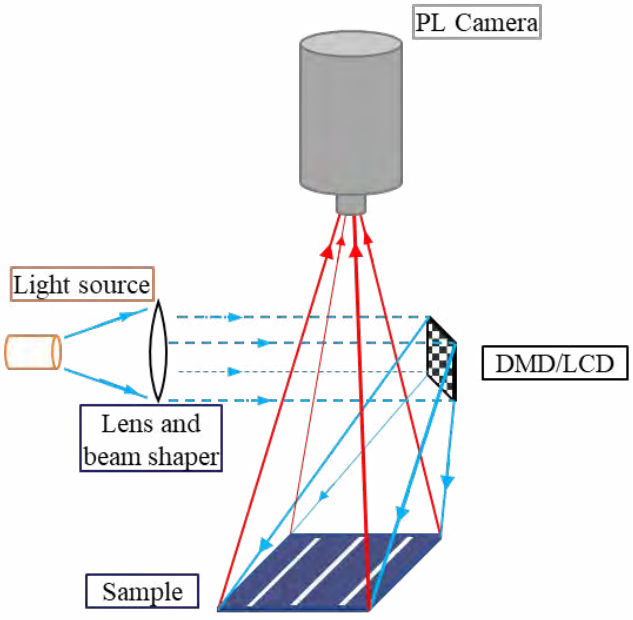

Figure F45.1: Sketch of the developed PL imaging setup with spatially non-uniform illumination.

2. PL imaging with contactless-induced lateral carrier flow

The developed DMD-based PL imaging with non-uniform illumination setup was first applied to induce lateral carrier flow into the samples while keeping the contactless feature of PL imaging.

For a silicon solar cell, the lateral carrier flow leads to local voltage drop cross local series resistance. The local voltage drop can be

reflected from PL imaging. Therefore, by using spatially non-uniform illumination to induce lateral carrier flow, it is possible to obtain a series resistance image in a contactless manner. In Figure 45.2, a demonstration of the contactless series resistance imaging method is shown for a six-inch silicon solar cell (only half of the cell is shown). Two PL images of the sample with partial illumination are obtained with the DMD-based setup (Figure 45.2 (b) and (c)). The division of these two partial illuminated PL images yields a qualitive series resistance image of the sample (Figure 45.2(e)). As can be seen, the high series resistance regions due to broken fingers are clearly shown. The resulting image also shows good agreement to the quantitative series resistance image obtained using a method by Kampwerth et al. (Figure 45.2(f)). However, the method by Kampwerth et al. is based on a PL image with current extraction, which requires electrical contact. Another series resistance image obtained by the method of Kasemann et al. is also shown (Figure 45.2(d)). The method of Kasemann et al. is also based on non-uniform illumination PL imaging. However, the non-uniform illumination is achieved by putting an opaque buffer on the sample. The physical contact adds the potential risk of damaging the samples. Furthermore, the PL beneath the buffer is not available. The DMD-based PL imaging setup in this project allows the PL from the non-illuminated area also to be captured by the camera and this information helps to increase the quality of the resulting PL image. As can be seen, the local low lifetime region marked by a red circle in Figure 45.2(a) is still observable in the series resistance image obtained by the method of Kasemann et al., whereas the series resistance image obtained by our DMD-based PL imaging setup does not show this impact of local non-uniformity of lifetime.

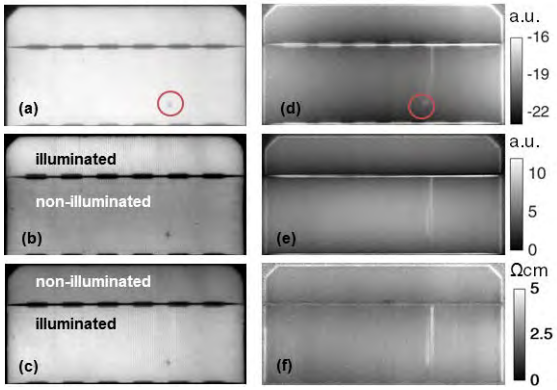

Figure F45.2: Contactless series resistance image of a silicon solar cell using non-uniform illumination PL imaging. (a) Conventional PL image with uniform illumination; (b) and (c) PL images of the sample with partial illumination; (d) contactless series resistance image using a method by Kasemann et al.; (e) contactless series resistance image using non-uniform illumination PL imaging method; and (f) series resistance image obtained with PL with current extraction using the method of Kampwerth et al.

The non-uniform illumination can also be used to stimulate lateral carrier flow in silicon wafers. For a diffused silicon wafer, the lateral carrier flow is impacted by the emitter sheet resistance ρ_{she}. The developed DMD-based PL imaging setup has thus also been used to extract emitter sheet resistance of diffused silicon wafers. The non-uniform illumination pattern used is simply a uniform large-area illumination with a dark circular mask in the centre. A series of samples with various emitter sheet resistance were measured. The rear surfaces of the samples were full area metallised to remove the impact of bulk conductivity on the measurement. A theoretical correlation between the maximum to minimal PL ratio and the product of ρ_{she} and photogenerated current was previously established by Juhl et al. via simulation. The measurement results by our DMD-based setup are compared to the theoretical correlation and good agreement is achieved.

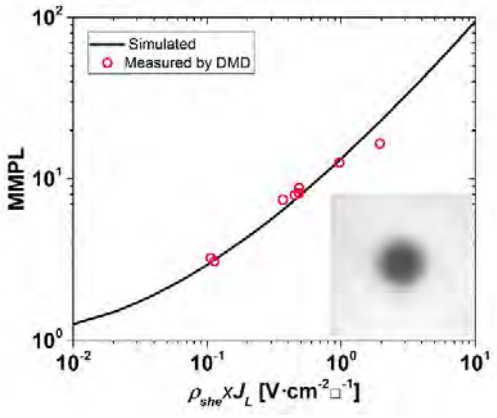

Figure F45.3: Extraction of emitter sheet resistance ρ_{she} from PL imaging with non-uniform illumination. The solid line indicates the theoretical correlation between maximum to minimal PL ratio (MMPL) and the product of ρ_{she} and photogenerated current J_J obtained by simulation. The circles indicate the experimental results.

For non-diffused silicon wafers, the lateral carrier flow is primarily dominated by diffusion. Therefore, it is possible to extract the diffusion length of a non-diffused silicon wafer with non-uniform illumination. We have demonstrated a proof-of-concept measurement of diffusion length using non-uniform illumination PL imaging for a high lifetime silicon wafer. Good agreement between the obtained result and the calculated diffusion length using charge carrier lifetime measured by photoconductance decay was obtained.

3. PL imaging at uniform excess carrier concentration

A different application of non-uniform illumination in PL imaging is to mitigate the lateral carrier flow due to the spatial non-uniform lifetime of the sample. The lateral carrier flow leads to inaccuracies in PL imaging–based quantitative analysis. For example, in carrier lifetime imaging, when lateral carrier flow is present, the lifetime is not simply the ratio of excess carrier concentration and generation rate, an additional term of the lateral carrier flow needs to be considered. This lateral carrier flow is difficult to quantify in practice. By using non-uniform illumination, we can minimise the lateral carrier flow in the sample by illuminating the low lifetime region with higher light intensity and illuminate the high lifetime region with lower light intensity. The modulation frequency of the DMD chip is not suitable for this application. Therefore, we use an LCD chip to achieve non-uniform illumination.

A proof-of-concept measurement is made on a silicon sample with non-uniform lifetime. To achieve a PL image at uniform excess carrier concentration (thus no lateral carrier flow), an adaptive iteration procedure is required. The iteration starts from the PL image with uniform illumination (conventional PL imaging). From the resulting PL image, a non-uniform illumination image can be calculated and applied to the next iteration. The iteration continues until a uniform PL image is obtained. This procedure is shown in Figure 45.4(a). As can be seen, a reasonably uniform PL image is obtained in the last iteration. The lifetime image of the sample can be obtained from the non-uniform illumination image in the last iteration. The lifetime profiles of the sample obtained from this adaptive PL imaging procedure and from a conventional PL image are compared in Figure 45.4(b). As can be seen, the lifetime profile obtained from the adaptive PL imaging shows a much sharper transition. This is expected as there is no smearing effect due to the lateral carrier flow. Moreover, the resulting lifetime image is under the same injection level across the whole sample.

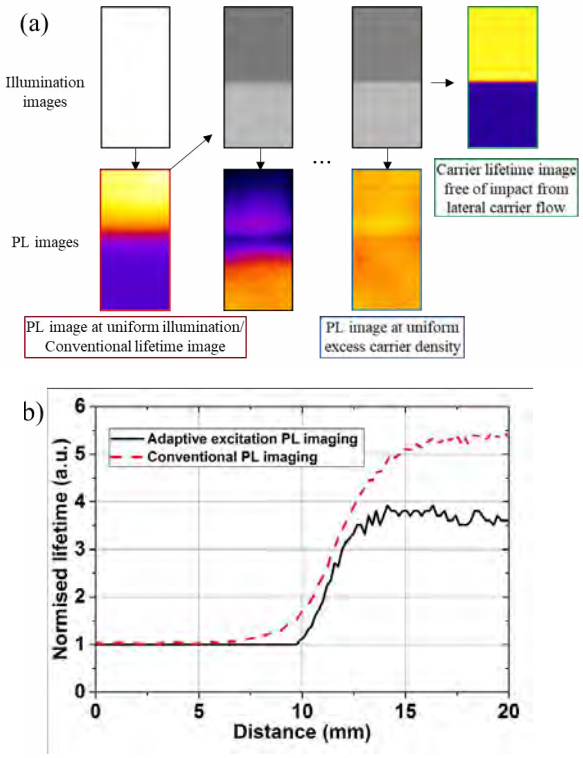

Figure F45.4: Demonstration of PL imaging at uniform excess carrier concentration on a non-uniform silicon wafer. (a) The adaptive iteration procedure; and (b) the resulting normalised lifetime profile from the PL imaging at uniform excess carrier and the conventional PL imaging.

Highlights

- PL imaging setups with the capability of arbitrary spatially non-uniform illumination is developed.
- Contactless series resistance imaging of silicon solar cells, emitter sheet resistance of diffused silicon wafers, and diffusion length of non-diffused silicon wafers were achieved using PL imaging with non-uniform illumination.
- PL image at uniform excess carrier concentration is achieved for a silicon wafer with spatially non-uniform quality.

Future work

The current setup of PL imaging with non-uniform illumination will be updated featuring higher illumination intensity (above one sun) and better mapping between the PL image and illumination image. Meanwhile, a few new applications of the developed methods will be made including: (1) the series resistance components in silicon heterojunction solar cells; (2) advanced parameterisation for solar cells; and (3) improved recombination analysis of ring defects in Czochralski grown silicon.

Reference

HEINZ, F. D., ZHU, Y., HAMEIRI, Z., JUHL, M., TRUPKE, T., & SCHUBERT, M. C., 2018. The principle of adaptive excitation for photoluminescence imaging of silicon: theory. physica status solidi (RRL) - Rapid Research Letters 12, 1800137.

JUHL, M., TRUPKE, T., & AUGARTEN, Y., 2013. Emitter sheet resistance from photoluminescence images. In: 39th IEEE Photovoltaic Specialists Conference. pp. 198–-202.

KAMPWERTH, H., TRUPKE, T., WEBER, J. W., & AUGARTEN, Y., 2008. Advanced luminescence based effective series resistance imaging of silicon solar cells. *Applied Physics Letters* 93, 202102.

KASEMANN, M., REINDL, L. M., MICHL, B., WARTA, W., SCHÜTT, A., & CARSTENSEN, J., 2012. Contactless qualitative series resistance imaging on solar cells. *IEEE Journal of Photovoltaics* 2, 181–-183.

ZHU, Y., HEINZ, F. D., JUHL, M., SCHUBERT, M. C., TRUPKE, T., & HAMEIRI, Z., 2018. Photoluminescence imaging at uniform excess carrier density using adaptive nonuniform excitation. *IEEE Journal of Photovoltaics* 8, 1787–-1792.

ZHU, Y., JUHL, M. K., TRUPKE, T., & HAMEIRI, Z., 2017. Photoluminescence imaging of silicon wafers and solar cells with spatially inhomogeneous illumination. *IEEE Journal of Photovoltaics* 7, 1087–-1091.

F46 CHARACTERISING THE PERFORMANCE, CONTRIBUTION, AND IMPACT OF DISTRIBUTED PV SYSTEMS IN AUSTRALIA'S ELECTRICITY GRIDS

Lead Partner

UNSW

UNSW Team

Dr Navid Haghdadi, Dr Anna Bruce, A/Prof. Iain MacGill

Funding Support

ACAP Fellowship

Aims

The aims of the research are to: (1) perform comprehensive operational performance, reliability and degradation analysis of distributed PV systems in Australia, quantifying the impact of factors including age, PV technology, inverter technology, grid conditions, compliance with grid connection standards, and installation characteristics including shading and weather conditions; (2) build a data-driven machine learning (ML) platform to characterise PV systems based on their generation data; (3) enhance existing generation upscaling methods using the ML models for "aggregate" PV characteristics; (4) develop advanced models to characterise aggregate PV system response to system security events including voltage and frequency excursion.

Progress

A. Literature review on the characterising of the performance and impact of distributed PV systems on the electricity grids

A review of the literature has been conducted examining the nowcasting methodologies for distributed PV (DPV) systems and those looking at the impact of DPV on low voltage networks. It found that methodologies and lessons learned relevant to Australia are sparse and while significant bodies of research have focused on forecasting and characterisation of utility PV, a relatively limited body of work is dedicated to DPV internationally and in Australian context. The literature review is currently being reviewed by the team and will be considered for publication in a relevant journal. A summary of the literature is provided here.

A.1 Regional nowcasting of distributed PV systems

Different bodies of work documented different approaches and each with different data input requirements. The approaches applied in the literature can be grouped under three broad categories, transposition model-based approaches, data driven approaches, and a hybrid of both (Vrettos et al., 2019), with the techniques applied in each category ranging in complexity from simple algorithms to complex machine learning tools. Transposition methodologies typically comprise GHI measurements which are transposed and applied to a representative PV model which are then upscaled to estimate power production for an area or region. Data-driven approaches do not appear within the Australian literature but are documented and applied in an overseas location, namely the United States.

Several gaps are identified in the literature including methods for upscaling, description and application of correction factors and finally the application of nowcasting in planning and operation of the electricity networks. Methods for forecasting solar irradiance prior to application to PV output models tended to focus on either satellite or deterministic forecasting approaches. While other approaches, such as the use of sky cameras, are demonstrated to be effective. These are more relevant to spatially constrained nowcasting used for utility scale arrays and less relevant for nowcasting DPV where regional forecasts are sought. In (Bright et al., 2017), a comprehensive description of upscaling based on the use of satellite is provided during which data from the Himawari-8 satellite's advanced Himawari Imager is processed and obtained from the Australian Bureau of Meteorology (BOM).

Artificial intelligence–based forecasting models have also been widely applied. A large existing body of literature examines these (Akhter et al., 2019, Mellit et al., 2020, Sobri et al., 2018), however, for the most part this work does not capture the variability in physical attributes of the DPV fleet. Instead focusing on prediction of irradiance and then using a generic input value to represent the characteristics of the PV plant (Sobri et al., 2018). Another area focuses on the description and quantification of variables influencing solar array output, which can be developed into correction factors and applied to upscaling models. The main approaches include understanding and modelling the factors influencing the performance and nowcasting of DPV and hence enhancing the overall accuracy (Bright et al., 2018, Killinger et al., 2016, Haghdadi et al., 2017)

A.2 Impact on low voltage networks

The challenges associated by high penetration of PV systems are documented to include reduced understanding of the native load and its interaction with DPV, voltage fluctuations due to DPV variability, increased wear and tear on transformer tap changers, spurious tripping of protection devices and voltage rises or changes to the voltage profile of the feeder (Engerer et al., 2019, Xue et al., 2017). The AEMO Renewable Integration Study, surveyed distribution network service providers (DNSPs) and documented the key impacts (AEMO, 2020a, AEMO, 2020b) then summarised these challenges as voltage regulation, thermal capacity and tap settings. These impacts are felt to differing degrees across the various Australian DNSPs with integration challenges tending to be location and network specific, influenced by the size and location of PV clusters with respect to network characteristics and load. However, it is noted that all of the surveyed DNSPs are experiencing voltage management challenges across the low voltage networks. This literature review studies the impact of DPV on feeder voltage regulation and substation characterisation. Broadly, few studies were identified using actual data, furthermore, some studies highlight the benefits of DPV in reducing and shifting peak loads to later periods of the day improving thermal deratings of infrastructure. Figure F46.1 shows a summary of the challenges faced by DNSPs based on the survey done by AEMO.

Level		Issue	SA	QLD		VIC					NSW/ACT				TAS
			SA Power Networks	Energex	Ergon Energy	CitiPower	Powercor	United Energy	AusNet Services	Jemena	Ausgrid	Evoenergy	Endeavour Energy	Essential Energy	Tas Networks
Behind meter	Customer premises	Over voltage complaints	●	●	●	●	●	●	●	●	●	●	●	●	●
		DPV inverter settings	●	●	●	●	●	●	●	●	●	●		●	●
		Under voltage	●	●	●	●			●				●		
		Other power quality	●	●				●		●	●	●			
LV	LV feeder	Voltage regulation	●	●	●	●	●	●	●	●	●	●	●	●	●
		Phase balance	●	●	●		●	●	●	●	●	●		●	●
		Thermal capacity	●	●	●	●	●	●	●	●		●			●
	Distribution substation transformer	Tap setting	●	●	●	●	●	●	●	●	●	●	●		●
		Thermal capacity	●	●	●	●	●	●	●	●		●			
MV	Zone substation feeder	Voltage regulation	●	●	●				●						
		Thermal capacity	●	●										●	
	Zone substation transformer	Tap range	●	●	●				●		●	●	●		
		Voltage set point	●	●	●			●	●		●	●	●		
HV	Sub trans. transformer	Voltage set point	●	●	●				●		●		●		
Protection		Low background fault level	●		●							●			
		Fault discrimination		●								●			

Figure F46.1: Summary of challenges experienced by DNSPs (AEMO's Renewable Integration Study, Appendix A).

A.3 Variability of the distributed PV systems:

The output power variability of distributed PV systems can have an important impact on the operation of the electricity grid. With an increasingly high number of small-scale PV systems in the grid, it is vitally important to characterise and quantify the variability of the DPV and its impact on the electricity networks. The aggregated size of variability depends on a number of factors including the local climate condition and spatial dispersion of PV systems in the area. Studies on characteristics of PV variability can be classified into three categories which are: (1) national level, which expands across large region or country (Wiemken et al., 2001, Murata et al., 2009, Klima et al., 2018) where it can be assumed that the PV variability is uncorrelated due to very large distances; (2) regional level, which expands across a region or hundreds of kilometres, at which distance PV variability exhibits some correlation depending on the temporal resolution of the studies (Mills and Wiser, 2011, Mills et al., 2011, Marcos et al., 2012); and (3) town or city level (< 100 km^2) (Lave et al., 2012, Elsinga and van Sark, 2015, Adye et al., 2018) which implies a denser area with higher correlation in PV output variability. Despite the number of studies on distributed PV variability, most of the studies presented a case for a single area due to limited data availability and the results are therefore, specific to the fleet. Some (Adye et al., 2018) used data from distributed irradiance sensors instead of PV output which differed from the real-world characteristics in terms of orientation and diversity of installations.

Often in the literature, the correlation is being studied to understand the spatial smoothing effect of aggregated distributed PV systems. This is provided that the distance between the systems is known. The results from these studies provide a quantitative estimation of at what distance and temporal resolution PV fleet would be most benefitted from spatial smoothing effect. However, there is a lack of study which attempts to understand the real-world characteristics of distributed PV variability resulting from random siting of the systems. Australia presents an interesting case study because it has high installations of distributed PV per area. It allows the comparison of different areas as well as different climate zones.

B. Research study on characterising the variability of the distributed PV systems in Australia

In this study, we aim to address two main research questions of (1) short-term characteristics of aggregated distributed PV variability in various areas, and (2) compare short-term and longer-term variability. The analysis is ongoing, and in this progress report we review the works done to answer the first question.

The data used in this study is 5-minute interval data from PV systems contributing to the publicly available website PVoutput.org. The data covers calendar year 2019. The systems with 5-minute interval data are considered, which comprise about 3000 systems across Australia. We analyse the characteristics of each 3-digit postcode area by the number of PV systems installed in the area. Each dot in Figure F46.2 represents 99th percentile of normalised aggregated PV output

variability (against total DC capacity in the area) for each 3-digit postcode region. The overall trend shows a strong correlation and decreasing size of variability as the number of systems increases. Even for a large distributed PV system, the coverage area is not enough to provide intra-plant spatial smoothing at this 5-minute temporal resolution of variability study. This is shown by the uncorrelated size of variability of individual PV systems at a range of sizes (Figure F46.2). In Figure F46.2, the lines are drawn according to the theoretical quantification defined by (Hoff and Perez, 2010) which characterise an area with PV systems as a spacious area where the variability of additional PV systems are uncorrelated.

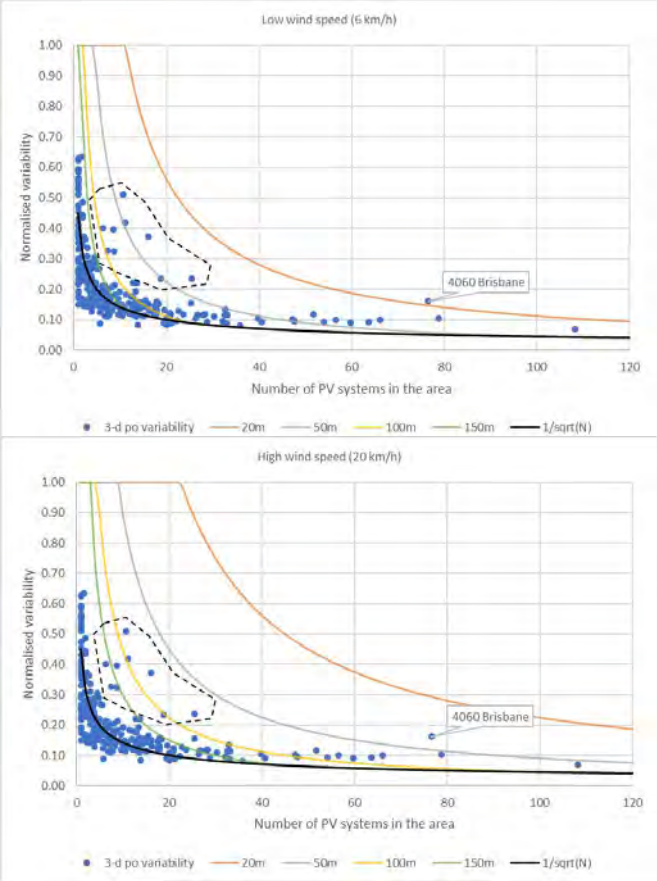

Figure F46.2: The normalised aggregated variability within each 3-digit postcode area at 99th percentile against the number of PV systems installed in the area with the lines indicating the density classification of PV systems defined by an average distance between the systems. Each dot represents a 3-digit postcode area. The value is normalised by the total capacity of PV systems installed in the area. The charts are for two scenarios: (1) low wind speed (i.e. slow cloud moving); and (2) high wind speed.

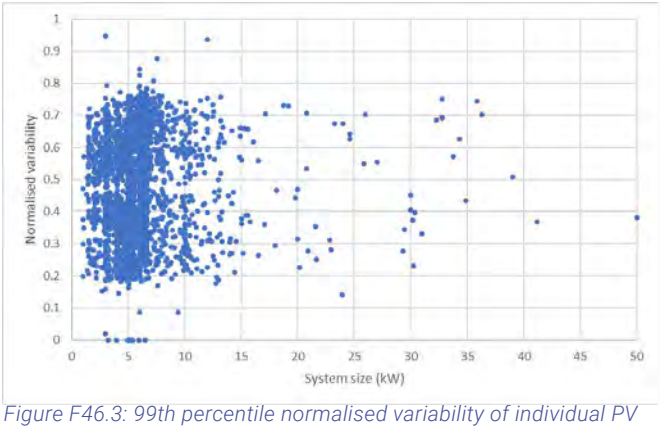

Figure F46.3: 99th percentile normalised variability of individual PV systems in this data set from PVoutput.org in 2019. The variability is normalised against the DC capacity of the system.

(Lave et al., 2017, Remund et al., 2015) demonstrated the difference in short-term variability due to climate. (Lave et al., 2017) analysed 30-second irradiance variability across different locations in the US and emphasised that the size of irradiance variability varies significantly. Although the study claimed the results as distributed PV variability, it did not reflect the impact of spatial smoothing as the model consisted of a 3 MW PV plant. (Remund et al., 2015) used BRSN irradiance measurement data to analyse variability in different climate zones including arid, equatorial and temperate and showed that they are different. These studies did not investigate how the impact is lessened with spatial smoothing. It was also found in (Islam and Waldl, 2016) that 5-minute variability in Queensland is highest compared to other cities in Australia and the authors claimed that it was due to climate. The analysis was performed with only a few PV systems (<40 systems) across a 110 km area.

Figure F46.3 shows the 99th percentile normalised variability of each 3-digit postcode area and these are classified by their climate zone. While each dot point in Figure F46.2 is the final aggregated variability of the postcode area and each dot point represents a unique 3-digit postcode area, the dots in Figure F46.3 are not unique. The dots are derived from random aggregation of the corresponding number of systems on the x-axis in each 3-digit postcode. This is to replicate as many data points per level of number of systems as possible to represent various distributed PV characteristics. In this figure we can again see the impact of spatial smoothing. Nonetheless, the average of these dots within the same climate zone (Figure F46.4) shows that there is almost no difference in the average variability between different climate zones. Although there might not be enough data to confirm in some climate regions such as equatorial and desert, the tropical, subtropical and temperate zones show very similar average variability. The grassland area is exceptional as it was only one 3-digit postcode area with more than 15 systems available and therefore, the impact cannot be concluded. The overall results imply that the impact of climate on irradiance variability is masked by spatial smoothing.

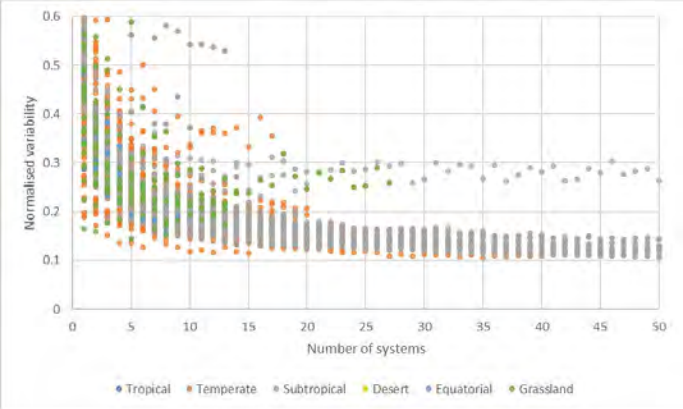

Figure F46.4: Normalised 99th percentile variability of aggregating number of systems (x-axis) within each 3-digit postcode classified by climate zones.

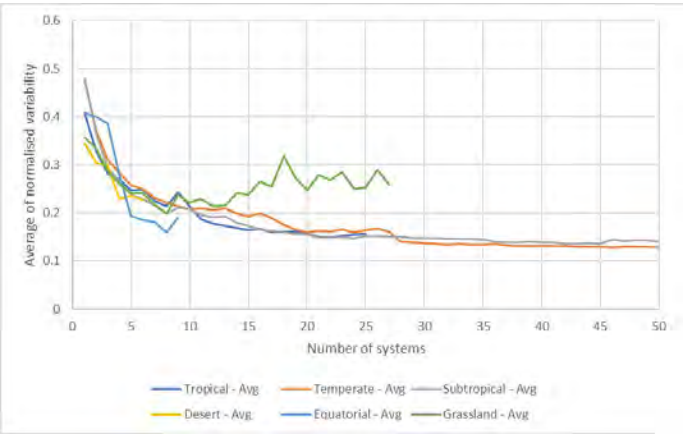

Figure F46.5: Average of normalised 99th percentile variability of aggregating number of systems (x-axis) within each 3-digit postcode averaging over each climate zone.

The analysis across many PV fleets reflects different characteristics of spatial smoothing observed in different postcode areas. While the majority of the areas demonstrate the trend towards spacious fleet, some areas tend to be crowded. The trend of reducing PV variability as the number of systems grows seems to be predictable however, a further study is required to confirm the effect of an additional system to the PV fleets. Moreover, analysis of longer-term variability needs to be conducted to estimate the impact of high distributed PV penetration on distribution and transmission grids, considering different aggregation level and change in the size of PV output ramps.

C. Ongoing enhancement to the Australian PV Institute PV mapping platform

The APVI's PV mapping online platform provides a series of useful PV analysis tools and dashboards. The website has been used by many different energy stakeholders in Australia as an independent source of information about the status and trend of PV systems in Australia in different spatial and temporal scales. We have been constantly working on enhancing the website as part of the ACAP project to help stakeholders understand the PV industry market and trend. Some of the enhancements include: (i) improving the SunSPoT tool user experience by expanding the areas covered by the tool to many more councils, enhancing the user interface, updating the list of tariffs, and addressing the issues raised by users; and (ii) improving the other mapping tools including the live and historical PV generation tools, Application Programming Interface (API), and the quarterly capacity update workflow.

Highlights

- A thorough literature review addressing the nowcasting methods for distributed PV systems, their impact on the electricity networks, and quantifying the variability of the distributed PV systems.
- A research study on characterising the variability of distributed PV systems.
- Ongoing support and enhancement to the Australian PV Institute's PV mapping platform.

Future Work

- Continue the analysis work on characterising the variability of distributed PV systems.
- Analysis of the operational performance of distributed PV systems, degradation analysis of them and quantifying the impact of factors including age, PV technology, inverter technology, grid conditions, compliance with grid connection standards, and installation characteristics including shading and weather conditions.
- Build a data-driven machine learning (ML) platform to characterise PV systems based on their generation data.
- Develop advanced models to characterise aggregate PV system response to system security events including voltage and frequency excursion.

References

ADYE, K., PEARRE, N. & SWAN, L. 2018. Contrasting distributed and centralized photovoltaic system performance using regionally distributed pyranometers. *Solar Energy*, 160, 1-9.

AEMO 2020a. Renewable Integration Study : Stage 1 report.

AEMO 2020b. Renewable Integration Study Appendix A : High Penetrations of Distributed Solar PV Important notice.

AKHTER, M. N., MEKHILEF, S., MOKHLIS, H. & SHAH, N. M. 2019. Review on forecasting of photovoltaic power generation based on machine learning and metaheuristic techniques. *IET Renewable Power Generation*, 13, 1009-1023.

BRIGHT, J. M., KILLINGER, S., LINGFORS, D. & ENGERER, N. A. 2017. Integration of distributed solar forecasting with distribution network operations in Australia. I*SES Sol. World Congr. 2015, Abu Dhabi, United Arab Emirates*, Oct. 29-Novemb. 2.

BRIGHT, J. M., KILLINGER, S., LINGFORS, D. & ENGERER, N. A. 2018. Improved satellite-derived PV power nowcasting using real-time power data from reference PV systems. *Solar Energy,* 168, 118-139.

ELSINGA, B. & VAN SARK, W. 2015. Spatial power fluctuation correlations in urban rooftop photovoltaic systems. Progress in *Photovoltaics: Research and Applications*, 23, 1390-1397.

ENGERER, N. A., TIDEMANN, C. E., BRIGHT, J. M., CONDIE, S., BROOKS, M. & VITHANA, S. Solar forecasting for low voltage network operations: Selected case studies in Australia. 2019 IEEE 46th Photovoltaic Specialists Conference (PVSC), 2019. IEEE, 2106-2110.

HAGHDADI, N., COPPER, J., BRUCE, A. & MACGILL, I. 2017. A method to estimate the location and orientation of distributed photovoltaic systems from their generation output data. *Renewable Energy*, 108, 390-400.

HOFF, T. E. & PEREZ, R. 2010. Quantifying PV power Output Variability. *Solar Energy*, 84, 1782-1793.

ISLAM, M. R. & WALDL, H.-P. I. Ramp rate analysis of roof-top PV on distribution grids for large cities in Australia. 2016 4th International Conference on the Development in the in Renewable Energy Technology (ICDRET), 2016. IEEE, 1-5.

KILLINGER, S., MÜLLER, B., SAINT-DRENAN, Y. M. & MCKENNA, R. Towards an improved nowcasting method by evaluating power profiles of PV systems to detect apparently atypical behavior. 2016 IEEE 43rd Photovoltaic Specialists Conference (PVSC), 5-10 June 2016 2016. 0980-0985.

KLIMA, K., APT, J., BANDI, M., HAPPY, P., LOUTAN, C. & YOUNG, R. 2018. Geographic smoothing of solar photovoltaic electric power production in the Western USA. *Journal of Renewable and Sustainable Energy*, 10, 053504.

LAVE, M., BRODERICK, R. J. & RENO, M. J. 2017. Solar variability zones: Satellite-derived zones that represent high-frequency ground variability. *Solar Energy*, 151, 119-128.

LAVE, M., STEIN, J. S. & ELLIS, A. Analyzing and simulating the reduction in PV powerplant variability due to geographic smoothing in Ota City, Japan and Alamosa, CO. 2012 IEEE 38th Photovoltaic Specialists Conference (PVSC) PART 2, 2012. IEEE, 1-6.

MARCOS, J., MARROYO, L., LORENZO, E. & GARCÍA, M. 2012. Smoothing of PV power fluctuations by geographical dispersion. *Progress in Photovoltaics: Research and Applications*, 20, 226-237.

MELLIT, A., MASSI PAVAN, A., OGLIARI, E., LEVA, S. & LUGHI, V. 2020. Advanced methods for photovoltaic output power forecasting: A review. *Applied Sciences*, 10, 487.

MILLS, A., AHLSTROM, M., BROWER, M., ELLIS, A., GEORGE, R., HOFF, T., KROPOSKI, B., LENOX, C., MILLER, N. & MILLIGAN, M. 2011. Dark shadows. *IEEE Power and Energy Magazine*, 9, 33-41.

MILLS, A. D. & WISER, R. H. Implications of geographic diversity for short-term variability and predictability of solar power. 2011 IEEE Power and Energy Society General Meeting, 2011. IEEE, 1-9.

MURATA, A., YAMAGUCHI, H. & OTANI, K. 2009. A method of estimating the output fluctuation of many photovoltaic power generation systems dispersed in a wide area. *Electrical Engineering in Japan*, 166, 9-19.

REMUND, J., CALHAU, C., PERRET, L. & MARCEL, D. 2015. Characterization of the spatio-temporal variations and ramp rates of solar radiation and PV. *Internation Energy Agency-Photovoltaic Power Systems Programme*.

SOBRI, S., KOOHI-KAMALI, S. & RAHIM, N. A. 2018. Solar photovoltaic generation forecasting methods: A review. *Energy Conversion and Management*, 156, 459-497.

VRETTOS, E., KARA, E., STEWART, E. & ROBERTS, C. 2019. Estimating PV power from aggregate power measurements within the distribution grid. *Journal of Renewable and Sustainable Energy*, 11, 023707.

WIEMKEN, E., BEYER, H., HEYDENREICH, W. & KIEFER, K. 2001. Power characteristics of PV ensembles: experiences from the combined power production of 100 grid connected PV systems distributed over the area of Germany. *Solar energy,* 70, 513-518.

XUE, Y., SHARMA, I., KURUGANTI, T., NUTARO, J., DONG, J., OLAMA, M. & FUGATE, D. Voltage impact analyses of solar photovoltaics on distribution load tap changer operations. 2017 North American Power Symposium (NAPS), 2017. IEEE, 1-6.

F47 LOW TEMPERATURE GRAPHENE OXIDE FILM PROPERTIES AND APPLICATIONS FOR ADVANCED AND HIGH PERFORMANCE PHOTOVOLTAICS

Lead Partner

UNSW

UNSW Team

Dr Michelle Vaqueiro Contreras

Funding Support

ACAP Fellowship

Aims

The main objectives of this Fellowship are:

- To investigate and understand the applicability of graphene oxide (GO) derivatives as selective passivating contacting materials in large-area silicon wafers.
- To study the effect of the various types of GO, such as variations in flake size, surface chemistry and doping levels, on the level of surface passivation of silicon-based photovoltaic devices and other innovative concept cells.
- To realise a feasibility study on the application of GO in the manufacture of solar cells to establish cost and efficiency targets for viable industrial applications.

Progress

Graphene oxide (GO) has been raised as a very flexible and appealing material for optoelectronic applications. The application of GO as a passivating material for silicon solar cells has been further demonstrated in this research. Despite some supporting staff disruptions in 2020, appropriate storage and deposition tools at the Solar Industrial Research Facility (SIRF, UNSW) have been set up as was intended for the initial six months of this Fellowship. A photograph of the new tools is shown in Figure F47.1, which includes an N_2 desiccator, spin coaters, precision hot plate, and fan forced refrigerator. A batch of high quality graphene oxide diluted in water with 23 mg.mL^{-1} concentration fabricated by our collaborators at the National Graphene Institute was received in October 2020. With this material the first set of passivated emitter and rear locally diffused (PERL) cells using thin layers of graphene oxide as the passivation material have been fabricated. Our results demonstrate that gains in open-circuit voltage and short-circuit current in excess of 5 mV and 3 mA, respectively are achievable with the GO films.

Figure F47.1: Graphene oxide storage and deposition set up at the Solar Industrial Research Facility.

Samples were prepared on industrially manufactured PERC precursors with ~1.2 Ω·cm p-type wafers, front phosphorous diffusion and SiN_x ARC layer, and AlO_x/SiN_x dielectric stack on the rear. The precursors were then screen-printed in the front with Ag paste and fired at 780°C at the SIRF. A set of samples of 4 by 4 cm dimensions were laser cut and prepared for laser doping and GO deposition. Laser doping through the AlO_x was carried out with a 950 nm continuous-wave laser (1500 W) on the rear before GO deposition. Three GO concentrations were investigated. The deposition is carried out by spin coating at room temperature followed by a 110°C step dry prior to Al rear evaporation.

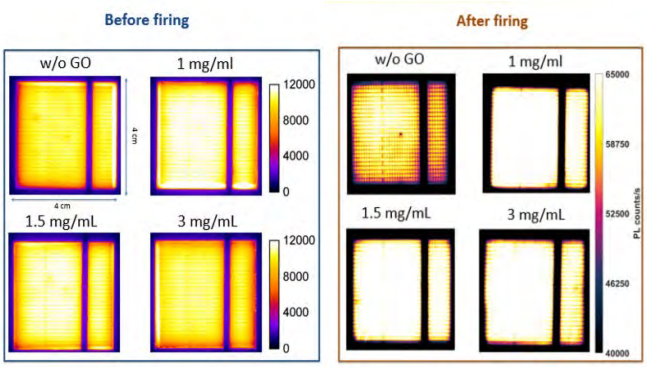

Figure F47.2: Photoluminescence maps of sample cells using passivating graphene oxide layers of different concentrations compared to a control (w/o GO) sample, before and after 780°C firing.

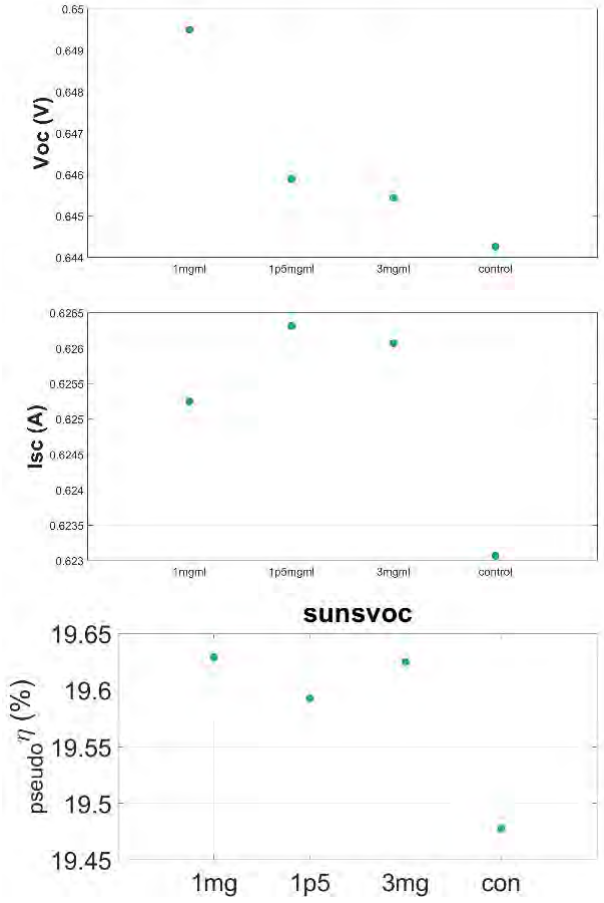

Figure F47.3: Open-circuit voltage, short-circuit current and pseudo-efficiency of the fabricated cells.

Figure F47.2 shows the obtained photoluminescence mapping taken from the samples before and after fast firing. An average of a 2000 increase in PL counts on the samples with the GO interlayer was observed in the "as-deposited" samples as the result of decreased recombination. Furthermore, and despite the known thermal instability of GO at high temperatures, we found that the film's passivation is sustained even after 780°C firing with further and more significantly improved cell performance.

Figure F47.3 shows the comparison of electrical characteristics of the different cells after rear contact firing. It is found that every measured cell containing the GO interlayer between the laser-doped region and the rear contact had increased open-circuit voltage (V_{OC}) and short-circuit current (J_{SC}) values compared to the control devices. The same figure includes the extracted values of the pseudo-efficiency of the cells obtained by the Suns-V_{oc} method. From those series-resistance-free measurements an increase of up to 0.14% efficiency from the GO-coated samples over the control sample was calculated. Even though the calculated absolute efficiency of the control sample of this experiment resulted in 0.06% over the champion GO-coated PERL cell due to some resistive losses, it is concluded that it was due to unoptimised deposition conditions that hindered the GO-PERL cell performance. Still the benefit of the GO deposition is evident by the increase in V_{OC} and J_{SC}, which is the highest on the sample with the largest GO concentration. Comparison between short UV (300–500 nm , ~40W.m^{-2}) and long UV (900–1100 nm, ~127 W.m^{-2}) wavelength illuminated IV curves showed that these gains were the result of decreased losses of IR-photo-generated carriers at the rear of the cell. To further validate these results a set of samples was prepared for spectral response analysis. Figure F47.4 shows the measured external quantum efficiency (EQE) of four cells made on sister wafers. Three cells, labelled GO1, GO2 and GO3 correspond to three cells containing graphene oxide films of different concentrations. Estimated gains on the GO-coated samples obtained by the spectral response integration in the excess of 1 mA.cm^{-2} were determined. Even though these 4 by 4 cm samples were prepared on sister wafers which are expected to have the same response at the low wavelength range due to the exact same front surface processing and metallisation, we observed a few discrepancies. Thus, another 4 cm by 4 cm sample cell was prepared with only a drop-casted solution of 1 mg/ml graphene oxide left to dry on an N_2 box before rear metallisation and firing. This was followed by a repetition of spectral measurements on the coated and uncoated area of this single sample. Results are shown in Figure F47.5.
With these results we have confirmed that not only have we reduced recombination with the GO films which increased the open-circuit voltage, but we have also improved carrier collection at the rear contacts.

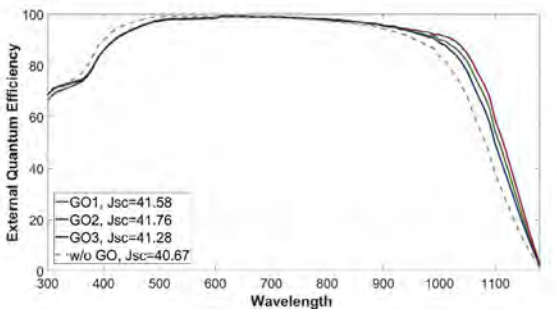

Figure F47.4: Quantum efficiency and estimated J_{sc} of four PERL measured cells, three of which had graphene oxide films as a passivation layer at the rear.

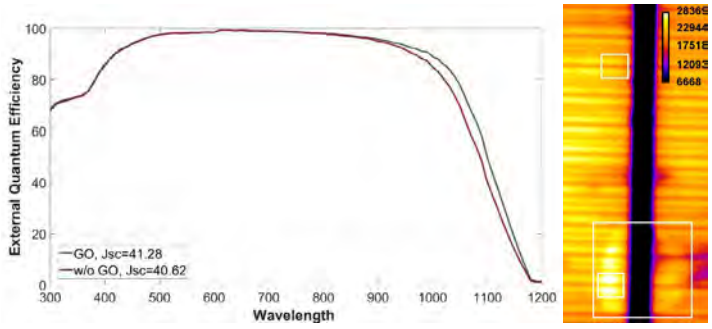

Figure F47.5: (Left) Quantum efficiency and estimated Jsc of one PERL cell with a graphene oxide deposited region. (Right) Photoluminescence image of the busbar section of the cell highlighting with a large square the region with drop-casted GO and with smaller squares the areas of the spectral response measurements shown on the left.

Tools and methods used thus far in this Fellowship and available at UNSW

Fabrication	***Characterisation***
Industrial screen printer	Photoluminescence imaging
Belt furnace	Suns-V_{oc}
532 nm laser (for doping)	Photoconductance lifetime tester
Sputterer	Optical Microscope
Spin coater	Spectral Response System (QEX7)
High precision hot plate	Dektak profilometer
	Four-point probe
	Scanning Electron Microscope
	X-ray photoelectron spectroscope

Highlights

- Demonstration of graphene oxide films as passivation material for solar cells.
- Demonstration of the first fabricated passivated emitter and rear locally diffused (PERL) working solar cell using graphene oxide as the passivation material.
- Demonstration of the scalability of the graphene oxide passivated solar cell using room temperature deposition.
- Collaboration with international institutions.
- Presentation of groundbreaking results on graphene oxide passivation at the 30th International Photovoltaic Science and Engineering Conference (PVSEC-30) and Global Photovoltaic Conference 2020 (GPVC 2020).

Future Work

- Study of graphene oxide films as selective contacts.
- Study the stability of the graphene oxide passivation on finished cells.
- Begin feasibility studies in relation to cost/stability on the application of GO at large scale.

References

VAQUEIRO-CONTRERAS, M., WALTON A.S., BARTLAM, C., BYRNE C., BONILLA R.S., MARKEVICH V.P., HALSALL M.P., IJAYARAGHAVAN, A. & PEAKER A.R. The surface passivation mechanism of graphene oxide for crystalline silicon. 2019 IEEE 46th Photovoltaic Specialists Conference, Chicago, USA, 2019.

VAQUEIRO-CONTRERAS M., HALSALL M.P. & IJAYARAGHAVAN, A. Graphene Oxide Films for Higher Open Circuit Voltage Silicon Solar Cells. 30th International Photovoltaic Science and Engineering Conference and Global Photovoltaic Conference 2020, Jeju, Republic of Korea, 2020 (online conference).

F48 OPTICAL CHARACTERISATION TECHNIQUES AND RECOMBINATION ANALYSIS ROUTINES FOR UNDERSTANDING CARRIER DYNAMICS OF EMERGING PHOTOVOLTAIC MATERIALS AND DEVICES

Lead Partner

UNSW

UNSW Team

Dr Weijian Chen, Prof. Martin Green, A/Prof. Xiaojing Hao, A/Prof. Nicholas (Ned) Ekins-Daukes

Academic Partner

King Abdullah University of Science and Technology (KAUST): Prof. Omar F. Mohammed

Swinburne University of Technology (SUT): Prof. Baohua Jia, Dr Xiaoming Wen

Funding Support

ACAP Fellowship

Aims

Photophysics in novel materials and devices are keys to photovoltaics research to improve efficiency, reduce cost and enhance stability. Perovskite and adamantine (such as kesterite, chalcopyrite) thin-film materials are the most promising materials. Interface and bulk defect engineering in perovskite and kesterite solar cells are the most viable approaches to improving their stability and efficiency. The microscopic physical mechanism of charge carriers in working condition solar cells is the key to guide engineering strategies.

This project aims to develop three-dimensional optical characterisation techniques and recombination analysis routines for emerging PV materials in operational single-junction and tandem solar cells. Photoluminescence (PL)-spectroscopy characterisation routine methods and numerical models are to be developed for perovskite, kesterite, and other adamantine thin-film solar cells with superior temporal, spatial and spectral resolutions, and methodological generalisation for other adamantine thin films in operational single-junction solar cells and tandem silicon solar cells. With a thorough understanding of carrier dynamics, fundamental limitations to devices performance (i.e., stability of perovskite and efficiency of kesterite/adamantine/$Sb_2(S,Se)_3$) will be investigated to accelerate the development of high quality PV materials for silicon-based tandem cells.

This work directly contributes to the ACAP program PP2 Thin-Film, Third Generation and Hybrid Devices and PP3 Optics and Characterisation by developing advanced spectroscopy characterisation methods analysing and optimising emerging

solar cells. With the characterisation methods aiming at analysing complicated structures in tandem solar cells, it also contributes to PP1 Silicon Solar Cells with a focus on PP1.3 Silicon Tandem Cells.

Progress

A. Illumination-induced mobile ion dynamics in perovskite solar cells

Motivation

Dynamic processes of mobile ions and the interaction between charge carriers and mobile ions, are intimately correlated to the observed slow response in perovskites. PL and time-resolved PL (TRPL) imaging are unique tools to probe the dynamic processes of the slow response and the corresponding microscopic and temporal physical mechanisms. Therefore, investigation of mobile ions in perovskite using time-resolved micro-spectroscopy is essential not only for the perovskite community, but also for the broader semiconductor research community interested in ionic transports in polycrystalline materials.

Progress

The dynamic effect of mobile ions in halide perovskites is studied via time-resolved micro-spectroscopy (Chen, Gan et al. 2021). PL quenching and fluorescence blinking are induced by mobile ion migration and accumulation in a single perovskite grain. The ion accumulation at the interface impacts the carrier extraction and the efficiency of perovskite solar cells. Using the PL-TRPL imaging technique, the light soaking effect has been dynamically monitored in a nanoscale, which exhibits a tight correlation to the performance of a perovskite solar cell. A comprehensive understanding of ionic dynamics is not only critically important for stable solar cells but also for new applications based on ionic properties. Micro-spectroscopic techniques, combining confocal microscope and TRPL, have been demonstrated as a powerful way to reveal the dynamic of mobile ions in both macroscopic and microscopic range.

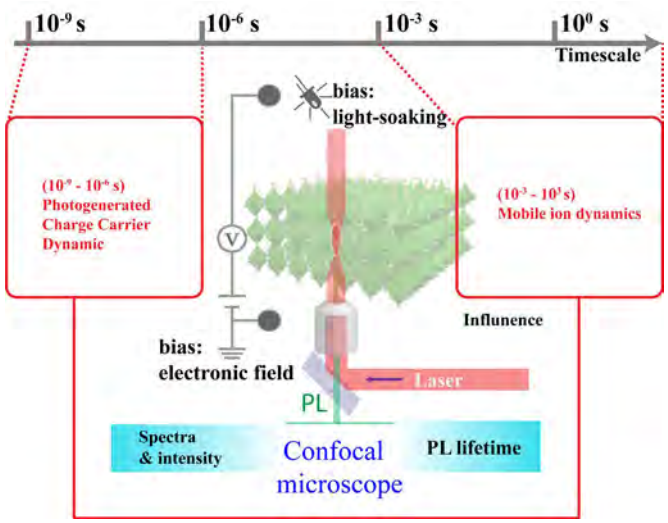

Figure F48.1: Diagrams of the methodology of probing ion dynamics using time-resolved spectroscopic techniques.

B. Interface dynamics study on carrier extraction of perovskite solar cell

Motivation

For high photo-conversion efficiency and long-term stability, charge carrier transfer must be stable and efficient. Spiro-OMeTAD doped with Li-TFSI is the most widely used solid-state hole transport material in perovskite solar cells. However, the additive Li-TFSI is a highly hygroscopic material that affects long-term performance. High mobility of Li^+ ions can also affect the stability of the PSCs, for example, I-V hysteresis. Therefore, alternative additives to Li-TFSI in Spiro-OMeTAD is essential.

Progress

In this work, Li-TFSI additive in the Spiro-OMeTAD is replaced by TFSI-salts (Mg-$TFSI_2$, Ca-$TFSI_2$), and the corresponding PSCs demonstrate higher efficiency with significantly boosted photostability. Spectroscopic investigations provide insights into efficient and stable hole transfer mechanisms of substituting Mg-$TFSI_2$ and Ca-$TFSI_2$ for Li-TFSI. The PSC's photoluminescence dynamics are monitored under continuous illumination, which reveals the behaviours of mobile ion accumulations at the perovskite/Spiro-OMeTAD interface. (Chen, Pham et al. 2021) The mobile ion accumulation is mitigated in the cases of Mg-$TFSI_2$ and Ca-$TFSI_2$, which ascribes to the improved hole mobilities of the Spiro-OMeTAD. Additives engineering in Spiro-OMeTAD provides a strategy to improve stability and photo-conversion efficiency. The spectroscopic study in this study concludes that higher hole mobility in hole transport layers plays a vital role in suppressing mobile ion accumulation. With optimal engineering of conductive additives, a more efficient charge transfer can be attained, together with improved photostability.

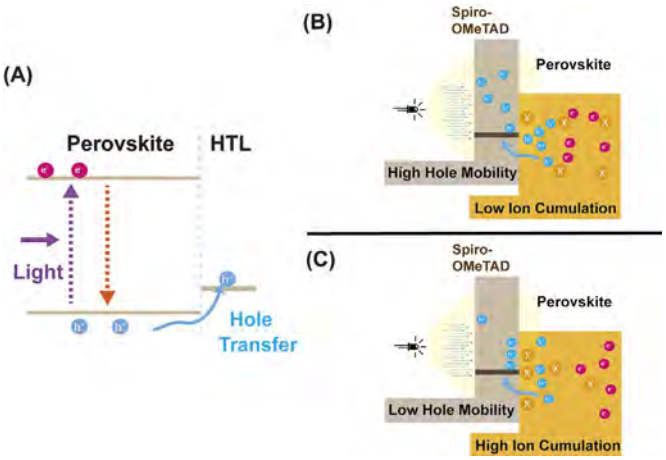

Figure F48.2: Schematic of the (A) hole extraction dynamics for the interface of Spiro-OMeTAD and perovskite with (B) high hole mobility and (C) low hole mobility.

C. Photophysics of two-dimensional (2D) organic-inorganic hybrid lead halide perovskites

2D layered perovskites have recently attracted significant attention owing to their excellent environmental stability, a high degree of electronic tunability, and natural multi-quantum-well structures. This part of the project aims to study the special photophysics of 2D

perovskites that are different from the conventional 3D congeners. Unlike the conventional inorganic quantum wells, the organic cationic ligands in the 2D perovskites can be flexibly modified. The design of organic sites has afforded a versatile platform for the modulation and functionalisation of the 2D perovskites.

Highlights

- Promising Earth-abundant materials for high efficiency next-generation PV technology.
- Advanced multi-dimensional imaging spectroscopy and microscopies for emerging materials both for single-junction solar cells and tandem solar cells.
- Collaboration with a variety of institutions in Australia and internationally.

Future Work

- Design and develop characterisation routine for active layers in tandem cell structure.
- Generalisation of developed characterisation methods and models and apply on tandem solar cells.
- Numerical modelling and completed design of multi-dimensional microscopies

References

CHEN, W., GAN, Z., GREEN, M. A., JIA, B. & WEN, X. 2021. Revealing Dynamic Effects of Mobile Ions in Halide Perovskite Solar Cells Using Time-Resolved Microspectroscopy, *Small Methods*, 5, 2000731. doi: 10.1002/smtd.202000731.

CHEN, W., PHAM, N. D., WANG, H., JIA, B. & WEN, X. 2021. Spectroscopic Insight into Efficient and Stable Hole Transfer at the Perovskite/Spiro-OMeTAD Interface with Alternative Additives, *ACS Applied Materials & Interfaces*.

F49 IN SITU BACK SURFACE FIELD ENHANCED HIGH EFFICIENCY $CU_2ZNSN(S,SE)_4$ SOLAR CELLS WITH SURFACE DEFECT PASSIVATION

Lead Partner

UNSW

UNSW Team

Dr Jianjun Li, A/Prof. Xiaojing Hao, Prof. Martin A. Green, Dr Jialiang Huang, Dr Kaiwen Sun, Dr Chang Yan, Mingrui He, Xiaojie Yuan, Ao Wang

Funding Support

ACAP Fellowship

Aims

This Fellowship is aimed to substantially boost the power conversion efficiency of environmentally friendly, Earth-abundant and low-cost kesterite (CZTSSe) thin-film solar cells by engineering an in situ P+ back surface field (BSF) with passivated surface defects, squeezing more potential out of this PV technology based on the imperfect material to a commercially viable level.

Progress

A. 12.5% new world record efficiency for pure-selenide CZTSe thin-film solar cells

To improve the bulk quality of the kesterite absorber, we investigated the intrinsic defect formation mechanism based on first-principle calculation with collaborators and developed a robust growth process based on our previous baseline (Figure F49.1). We unveiled that the defect formation mechanism is mainly governed by the local chemical environment at the point in time when the synthesis of CZTSSe phase initiates.

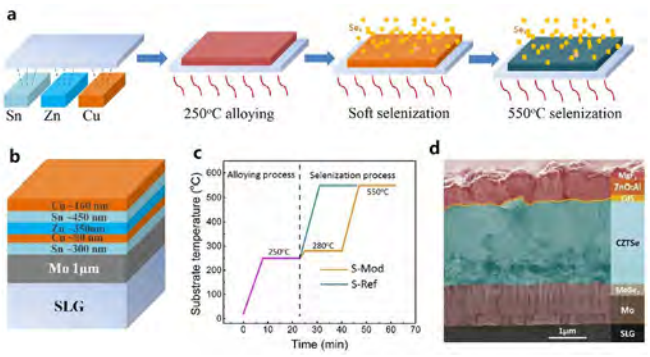

Figure F49.1: Fabrication of CZTSe films and devices. (a) Schematics of sputtering, annealing, and two-step selenisation processes. (b) Stacking structure of metal precursors. (c) Temperature profiles of the fabrication of reference sample S-Ref and sample S-Mod with modified growth process. (d) Cross-section image of a finished CZTSe device.

The modified growth process improved the previous baseline (up to 10% efficiency CZTSe solar cells) to a much higher level (>12% efficiency) (Figure F49.2). An independently confirmed total area (0.2397 cm^2) efficiency of 12.5% is achieved, which is the new record of pure-selenide CZTSe solar cell (previous record is 11.6% achieved by IBM in 2014) and very close to IBM's12.6% record efficiency in the whole area of kesterite solar cells. This device significantly reduced the V_{oc} loss and firstly demonstrated a high V_{oc} comparable to the record counterpart $CuInSe_2$ solar cell (Table F49.1).

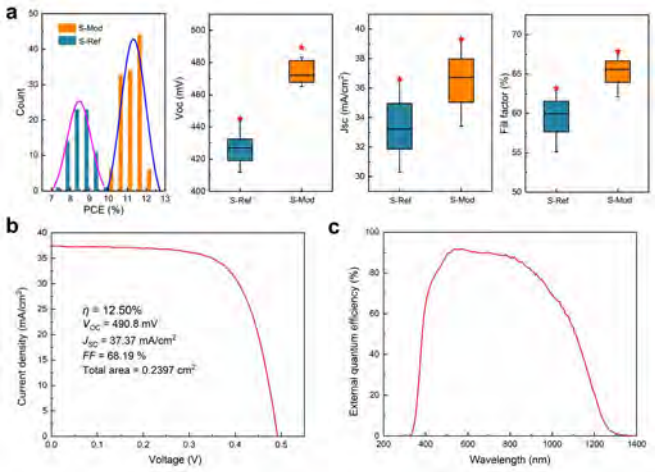

Figure F49.2: Photovoltaic performance. (a) Statistical box and histogram plots of device performance parameters of S-Mod and S-Ref. The sample size is 124 cells for S-Mod and 73 cells for S-Ref. All the photovoltaic performance parameters are measured based on total-area devices. (b) Certified J-V data. (c) EQE data of the champion CZTSe solar cell from S-Mod.

*Table F49.1: Device performance parameters of the state-of-the-art kesterite solar cells and the record low bandgap $CuInSe_2$ solar cell. Only total-area efficiencies are included. The PCE values marked by * were independently confirmed.*

Cell	Doping /alloying	PCE (%)	V_{oc} (mV)	J_{sc} ($mAcm^{-2}$)	FF (%)	E_g (eV)	$E_g/q-V_{oc}$ (V)	Area (cm^2)	Institute
CZTSSe		12.62*	541	35.4	65.9	1.13	0.589	0.48	DGIST
CZTSSe		12.6*	513	35.2	69.8	1.13	0.617	0.42	IBM
CZTS		11.0*	731	21.7	69.3	1.50	0.769	0.23	UNSW
CZTGSe	Ge	12.3	527	32.3	72.7	1.11	0.583	0.52	AIST
CZTSSe	Li	11.6	531	33.7	64.8	1.13	0.599	0.28	EMPA
CZCTS	Cd	11.0	650	26.7	66.1	1.38	0.730	0.22	UNSW
CZTSe	Na	11.6*	423	40.6	67.3	1.00	0.577	0.43	IBM
CZTSe		**12.5***	**491**	**37.4**	**68.2**	**1.04**	**0.546**	**0.24**	**UNSW**
$CuInSe_2$		14.5*	491	41.1	71.9	1.0	0.509	0.447	NREL

The modified CZTSe absorber demonstrates very encouraging characteristics comparable to high performance CIGS solar cells, including greatly suppressed bandgap/potential fluctuation, long minority carrier lifetime (>10 ns), highly effective minority carrier collection, activated shallow acceptor VCu (as shown in Figure F49.3) and consequently greatly improved hole mobility. These greatly improved properties indicate a potential for an over 14% efficiency device if better window layer with higher conductivity and higher transmittance is employed. The analysis of performance loss mechanisms of the modified devices is in progress to identify effective strategies for further efficiency advances. This work has been recently published in the prestigious journal *Advanced Materials*.

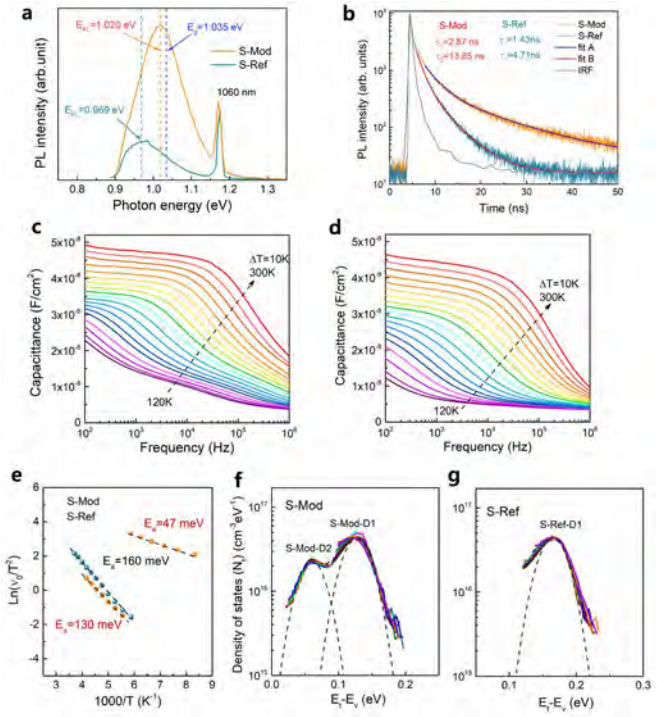

Figure F49.3: Carrier recombination mechanisms and defect profiles. (a), (b) PL and TRPL spectra for S-Mod and S-Ref. The PL peaks at 1060 nm in a are the binary- divided frequency signals of the 530 nm laser. (c), (d) Admittance (C-f-T) spectra of S-Mod and S-Ref, respectively. (e) Arrhenius plots for S-Mod and S-Ref obtained from admittance spectra. (f). (g) Energy profiles of the defect states in S-Mod and S-Ref, respectively.

B. B. 12.1% efficient Se-S mixed CZTSSe devices

We also employed similar growth process to the sulfuro-selenide process for sulfur-contained CZTSSe solar cells and demonstrated 12.1% total area efficiency (Figure F49.4). This efficiency is among the highest efficiencies in the kesterite field. However, the inclusion of S and SeS_2 in the chalcogenide source makes the reactive atmosphere difficult to control. Particularly, the vapour pressure of S at a relatively low temperature (significant evaporation at 80°C) makes the alloying process very difficult to be realised in the same furnace. Moreover, the incorporation of S also reduces the grain size, leading to more grain boundary recombination. Replacing the elemental S with SeS_2 (evaporation around 140°C) enables better control of the pre-alloying process, but still not good enough. Therefore, more effective atmosphere control and strategies to facilitate the grain growth may give further improvements of device performance.

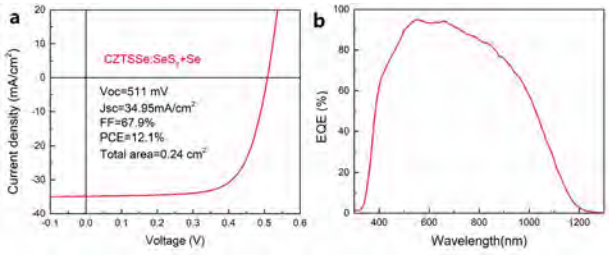

Figure F49.4: J-V and EQE data of the best performance CZTSSe solar cell prepared with a metallic precursor and newly developed sulfuro-selenisation process. This device demonstrated 12.1% total area efficiency.

Highlights

- An effective strategy to control the detrimental intrinsic defects is developed.
- The bandgap/potential fluctuation is greatly suppressed and the minority carrier lifetime is improved to >10 ns.
- 12.5% record efficiency for CZTSe is demonstrated.
- 12.1% efficiency CZTSSe device is demonstrated with a similar strategy.

Future Work

- Identify the loss mechanisms of the high efficiency CZTSe and CZTSSe solar cells.
- Develop new strategies to control the S/Se atmosphere for high quality CZTSSe films.
- Develop effective strategies for surface defect passivation.
- Develop the method for in situ back surface field.

References

LI, J., HUANG, Y., HUANG, J., LIANG, G., ZANG, Y., REY, G., GUO, F., SU, Z., ZHU, H., CAI, L. SUN, K.,SUN, Y., LIU F.,CHEN, S., HAO, X., MAI, Y. & GREEN, M.A. 2020. Defect Control for 12.5% Efficiency Cu2ZnSnSe4 Kesterite Thin-Film Solar Cells by Engineering of Local Chemical Environment. Advanced Materials, 32(52), p.2005268.

F50 TWO EXCITONS FOR THE PRICE OF ONE PHOTON: TOWARDS BETTER UNDERSTANDING OF SINGLET FISSION

Lead Partner

The University of Melbourne

UNIVERSITY OF MELBOURNE Team

Dr Saghar Masoomi-Godarzi, Prof. Trevor Smith

Funding Support

ACAP Fellowship

Aim

The aim of this Fellowship is to improve the efficiency of highly optimised solar cells without introducing substantial complexity or cost. The strategy is reducing the thermalisation loss in PV devices by using singlet fission (SF) material in conjugation with the PV device. SF is an exciton multiplication process in organic semiconductors which converts one high energy photon to two low energy photons, so it has the potential to double the electric current produced by the device. This Fellowship is contributing to ACAP's PP2 (Thin-Film, Third Generation and Hybrid Devices) and this report should be read in conjunction with the PP2 report.

Progress

SF-enhanced PV can be achieved in two ways: energy/charge transfer and photon multiplication. In the energy/charge transfer method, the SF-generated triplets undergo triplet energy transfer or dissociation at a heterojunction between the SF material and the inorganic semiconductor, and electron and holes are collected at the electrodes (Dexter 1979; Rao and Friend 2017) as shown in Figure F50.1(a). In the SF photon multiplication method, the SF-generated triplet energy is transferred to an emissive intermediate like quantum dots, thereby generating two low energy photons from a single high energy photon (Figure F50.1(b)). The efficiency limit of the SF photon multiplier approach matches the efficiency limit for a two-junction tandem solar cell. However, this method is more stable against changing irradiation, spectral change and temperature than tandem solar cells. Futscher et al. (2018) demonstrated that for silicon solar cells with a PCE of 26.6%, the photon multiplier approach has the potential to increase the efficiency by up to 4.2% absolute in a realistic case, however directly coupling the SF to the silicon PV was still projected to increase the efficiency up to 38%.

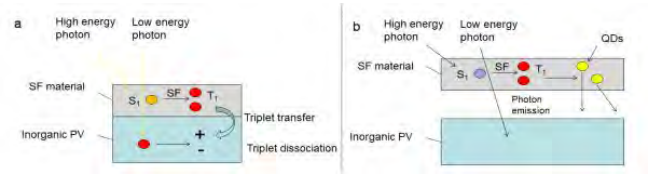

Figure F50.1: Schematic illustration of (a) SF-enhanced PV through energy/charge transfer; and (b) SF photon multiplier system.

A. SF-enhanced PV via energy/charge transfer

For efficient energy or charge transfer between SF and inorganic semiconductors, the SF material requires having the right energy levels so it might be necessary to tune its bandgap while SF properties should remain intact. It is a really challenging problem since singlet fission is very sensitive to molecular ordering and packing (Smith and Michl 2010). To overcome this challenge, we decided to use metal halide perovskite nanostructures since the bandgap of metal halide perovskite is widely tunable with light emission ranging from ultraviolet to near-infrared wavelength (Ou et al. 2019). It can be achieved by tuning the mixing ratio of halides. As a result, there is no need to tune the bandgap of the singlet fission material.

For this purpose, we studied energy/charge transfer of SF-generated triplets for the first time in diketopyrrolopyrroles (DPP, Figure F50.2), a well-known SF material (Mauck et al. 2016), to a series of metal halide perovskite nanostructures. We spent some time optimising the crystallinity of DPP thin films to achieve the highest SF-generated triplet yield by trying different annealing conditions as no accurate measures were reported in the literature although the SF process is highly sensitive to the molecular packing and crystallinity of the film. Figure F50.3 shows the generation of triplets via SF in crystalline film in contrast to the as-cast film in which there is no sign of triplet generation.

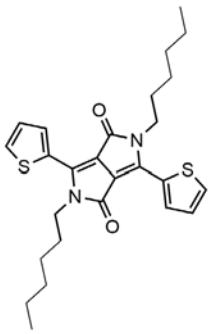

Figure F50.2: Chemical structure of 3,6-di(thiophen-2-yl)pyrrolo[3,4-c] pyrrole-1,4- (2H,5H)-dione (DPP).

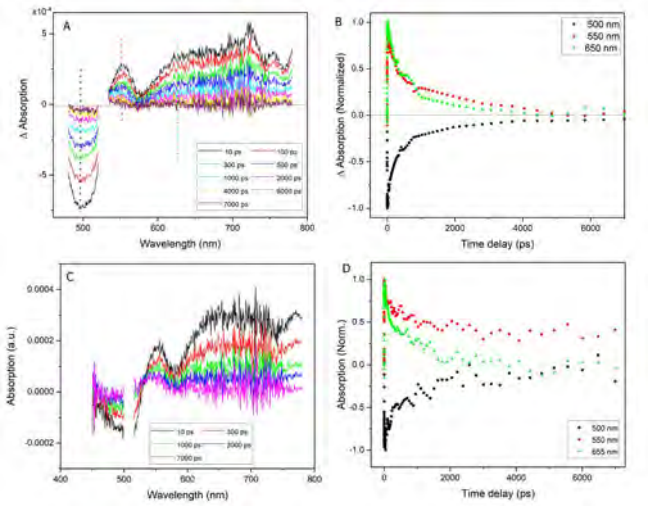

Figure F50.3: Transient absorption spectra and kinetic traces of (A-B) as cast and (C-D) thermally annealed thin film of DPP in Vis region.

A series of metal halide perovskite nanostructures with different absorption and emission spectra has been synthesised and characterised for this work. Figure F50.4(a) and (b) show the broad absorption and emission range across the entire visible spectrum of the typical $MAPbX_3$ perovskite by controlling the composition of Br and I.

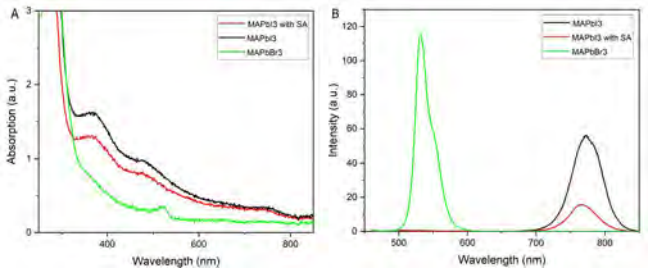

Figure F50.4: The (a) absorption and (b) emission spectra of $MAPbI_3$, $MAPbI_3$ with Sulfamic acid (SA) and $MAPbBr_3$.

To study the energy/charge transfer mechanism of SF-generated triplets in DPP to metal halide perovskite nanostructures, steady state and time-resolved spectroscopy such as absorption, photoluminescence, time-correlated single photon counting (TCSPC) and ultrafast transient absorption (fs-TA) have been performed on the binary film. The detailed analysis and modelling of the data are under further investigation. The preliminary analysis of data was promising for showing charge transfer at the heterojunction of DPP and perovskite nanocrystals. Although the two perovskite nanostructures were quenched in the presence of DPP, that is the singlet energy transfer from perovskite to DPP happened in both cases, one of the films behaved differently and not only has it not been quenched but also it forms a long-lived species in the presence of DPP, as shown in Figure F50.5. Further study and analysis of TA data is in progress.

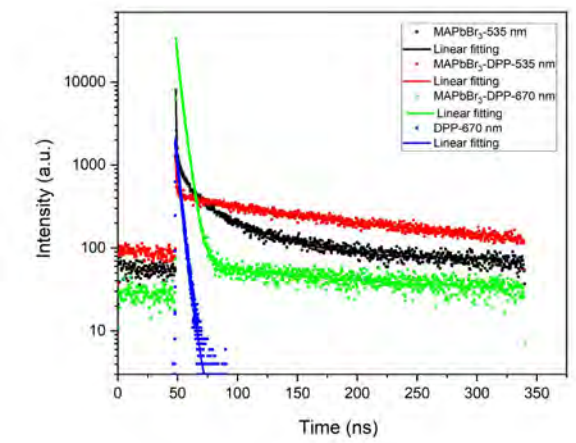

Figure F50.5: Fluorescence decay profiles of DPP/perovskite film after exciting at 400 nm.

B. SF-enhanced PV via photon multiplication

The photon multiplier approach is a very interesting technique as it can be integrated into the existing PV technologies such as silicon, CIGS, CdTe or perovskites with little extra cost or complexity (Rao and Friend 2017). One of the problems with this approach is that the SF yield for most current materials is highly sensitive to the molecular packing and the presence of quantum dots is disruptive for the chromophore packing. Therefore, we designed a new system for the photon multiplier approach where an intramolecular SF is used in conjugation with QDs. The new system is less sensitive to the molecular packing and should still act as SF material even in the presence of QDs. The aim of this project is to use carboxylic acid functionalised-tetracene dimer (figure 6) which has been reported as an efficient iSF material (Mauck et al. 2016) on the surface of PbS QDs.

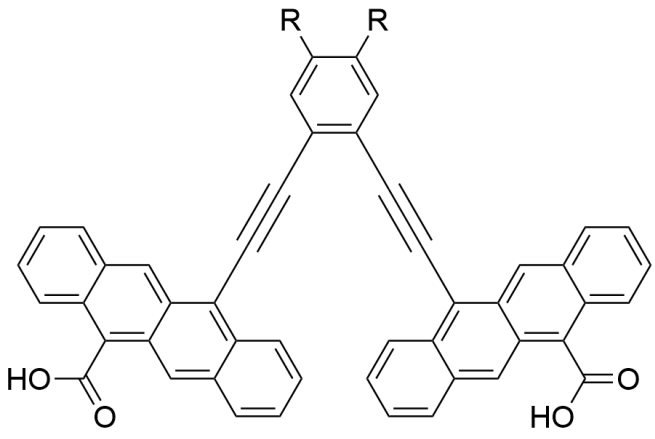

Figure F50.6: The chemical structure of carboxylic acid functionalised-tetracene dimer.

The synthesis approach for the carboxylic acid functionalised-tetracene dimer and PbS QDs have been determined and the starting materials will arrive soon. After the synthesis, the triplet transfer to QDs needs to be investigated using spectroscopic tools including transient absorption and time-resolved photoluminescence measurements.

Highlights

- Optimising the crystallinity of DPP thin films to achieve the highest SF-generated triplet yield by trying different annealing conditions.
- A series of metal halide perovskite nanostructures with different absorption and emission spectra has been synthesised.
- The preliminary analysis of data was promising for charge transfer at the heterojunction of DPP and perovskite nanocrystals.
- A new system is designed for the photon multiplier approach where an intramolecular SF is used in conjugation with QDs.
- The synthesis approach for carboxylic acid functionalised-tetracene dimer and PbS QDs have been determined.

Future Work

- Investigating different MAPbX3 perovskites using a selective mixture of Cl/Br and Br/I.
- Measuring the efficiency of DPP/ MAPbX3 perovskite to find the best performing binary film for PV.
- •Synthesising and characterising carboxylic acid functionalised-tetracene dimer and PbS QDs.

References

DEXTER, D. L. 1979. Two ideas on energy transfer phenomena: Ion-pair effects involving the OH stretching mode, and sensitization of photovoltaic cells. Journal of Luminescence, 18-19, 779-784.

FUTSCHER, M. H., RAO, A. & EHRLER, B. 2018. The Potential of Singlet Fission Photon Multipliers as an Alternative to Silicon-Based Tandem Solar Cells. ACS Energy Letters, 3, 2587-2592.

MAUCK, C. M., HARTNETT, P. E., MARGULIES, E. A., MA, L., MILLER, C. E., SCHATZ, G. C., MARKS, T. J. & WASIELEWSKI, M. R. 2016. Singlet Fission via an Excimer-Like Intermediate in 3,6-Bis(thiophen-2-yl) diketopyrrolopyrrole Derivatives. Journal of the American Chemical Society, 138, 11749-11761.

OU, Q., BAO, X., ZHANG, Y., SHAO, H., XING, G., LI, X., SHAO, L. & BAO, Q. 2019. Band structure engineering in metal halide perovskite nanostructures for optoelectronic applications. Nano Materials Science, 1, 268-287.

RAO, A. & FRIEND, R. H. 2017. Harnessing singlet exciton fission to break the Shockley–Queisser limit. Nature Reviews Materials, 2, 17063.

SMITH, M. B. & MICHL, J. 2010. Singlet Fission. Chemical Reviews, 110, 6891-6936.

F51 BEYOND THE THEORETICAL LIMIT: SILICON PHOTOVOLTAIC EFFICIENCIES THROUGH SINGLET FISSION AUGMENTATION

Lead Partner

University of Melbourne

University of Melbourne Team

Dr Calvin Lee

Funding Support

ACAP Fellowship

Aims

This Fellowship has the broad goal of designing new singlet fission (SF) materials energy-matched to the silicon bandgap in order to directly couple them with the best available silicon solar cells, with an overarching aim of advancing cell efficiencies beyond the theoretical single-junction efficiency limit.

It will achieve this energy-matching and the augmentation of silicon solar cell efficiency through two key routes, namely:

1. Raising the triplet-state energy levels of well-known organic dyes and SF chromophores to achieve thermodynamically favourable energy-transfer to silicon through alteration of molecular diradicaloid character via systematic structural perturbations,
2. Accessing non-traditional SF pathways via anti-Kasha photophysical behaviour for chromophores with energy levels already well-matched to silicon

This Fellowship has its primary focus on contributing towards ACAP's PP1 (Silicon Solar Cells) sector, and this report should be read in conjunction with the PP4 report.

Progress

1. Triplet energy matching via diradicaloid structural engineering

A recent review of reported SF materials found that the vast majority of chromophores with otherwise favourable properties for rapid development and practical applicability (i.e. photostable, large molar extinction coefficients) possess absolute T_1 triplet energies of <1 eV, well below the 1.1 eV bandgap of silicon and therefore unable to facilitate SF-mediated direct energy transfer to a silicon cell (Casillas et al., 2020). Therefore we aim to modify these poorly matched SF chromophores by raising their triplet energy levels to the 1.2–1.4 eV regime, while still adhering to the $E(S_1) \geq E(2T_1)$ requirement for exothermic singlet fission, and intend to do so via alteration to the chromophore's diradical character.

All SF-capable molecules possess some degree of diradical character (Minami et al., 2013) with a perfect diradical possessing virtually no separation between the degenerate S_0 singlet ground state and T_1. Structural perturbation of the molecule stabilises the S_0 state and destabilises the S_1/T_1 states, thereby raising the absolute energy levels of the latter as well as increasing the S_0-T_1 gap, with several theoretical papers discussing optimal uses of structural perturbation to fine-tune molecular energy levels for SF applications (Wen et al., 2015, Nakano, 2017). Despite this, few practical applications of this method have currently been reported (Conrad-Burton et al., 2019).

After a computational screening of the vertical excitation energies of various candidates by time-dependent density functional theory (TD-DFT), we initially selected three classes of chromophores theorised or known to possess SF behaviour to apply this diradical stabilisation technique, with the theoretical results suggesting that all target materials should be well-matched, energetically speaking, to silicon (Figure F51.1). Bulky moieties were strategically placed for their steric interferencewith the aryl planes of the chromophores, in order to introduce the structural perturbations necessary for diradical character alteration.

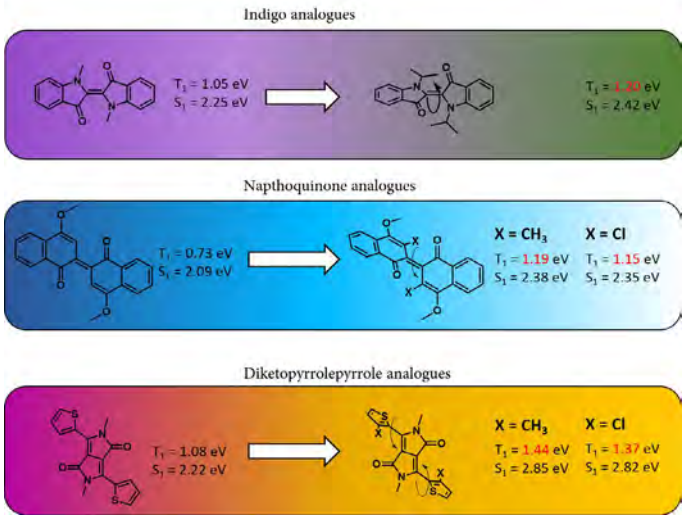

Figure F51.1: Candidates for structurally perturbed, high-T_1 singlet fission molecules identified through TD-DFT calculations (geometry optimisation for molecules in solution performed via B3LYP/6-311+G(2d,p), energy-level TD-DFT calculations performed via B3LYP/def2-TZVPP).

Due to various synthetic difficulties unfortunately both the target napthoquinone and indigo analogues were unable to be obtained, however we were successful in developing three new diketopyrrolopyrrole (DPP)-based chromophores that vary in both the nature of the sterically bulky moiety inducing the structural perturbation, as well as the alkyl sidechain to control crystal packing (Figure F51.2). Solid-state UV-Vis studies revealed that these analogues possessed significantly blue-shifted absorption regimes relative to the unstrained DPP chromophore, confirming that these structural alterations were successful in raising S_1 energy levels (Figure F51.3(a)). Triplet sensitisation studies are currently being performed in order to confirm a corresponding rise in triplet energy levels. Transient absorption studies (Figure F51.3(b)) on the other hand revealed only short-lived picosecond-scale photophysical processes

in the solid states for all three materials, suggesting that there is little evidence for the typically nanosecond-scale delayed singlet fission process.

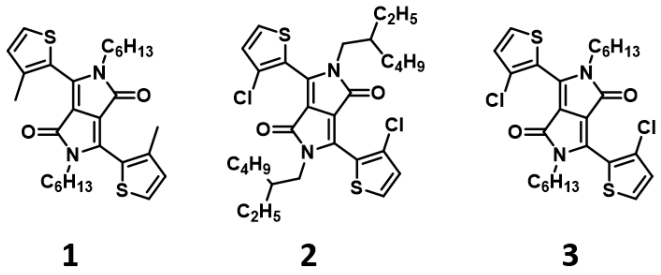

Figure F51.2: Molecular structures of high-T_1 singlet fission candidate DPP-based chromophores.

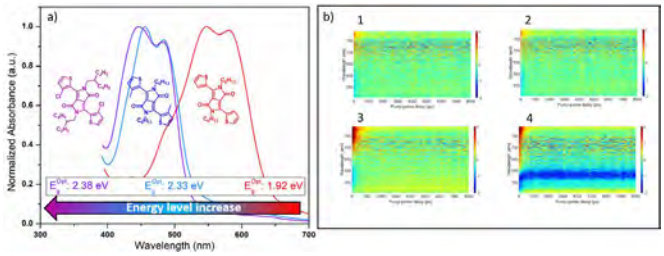

Figure F51.3: (a) Solid-state UV-Vis spectra of strained and non-strained DPP chromophores showing experimentally obtained optical energy gaps. (b) Solid-state transient absorption spectra of strained (1-3) and non-strained (4) DPP chromophores, with only four showing a long-lived depletion of ground-state carriers.

To understand this behaviour we examined both single crystal structures and performed GIWAXS analysis of the thin-film morphology. Crystal structures were obtained of compounds 1 and 2 (Figure F51.4(a), (b)) from which it can be observed that the dihedral twist induced by the sterically bulky moieties between the flanking thiophenes and the DPP core have adversely affected both π-stacking and core overlap, increasing both of these values relative to non-strained analogues (Hartnett et al., 2016). Here distances between the π-planes of the DPP cores of neighbouring chromophores are >0.5 nm with no π-overlap whatsoever, with the main π-stacking interaction between the flanking thiophene moieties. Analysis of the GIWAXS scattering patterns of these materials reveal weak-to-no π-stacking interactions (Figure F51.4(c), (d)) suggesting that the poor π-stacking interactions between these chromophores observed in the single crystal structures is carried over to the spin-coated, thin-film morphology. This therefore suggests that there is minimal interchromophore electronic coupling, and as such is a plausible explanation for why SF is not observed.

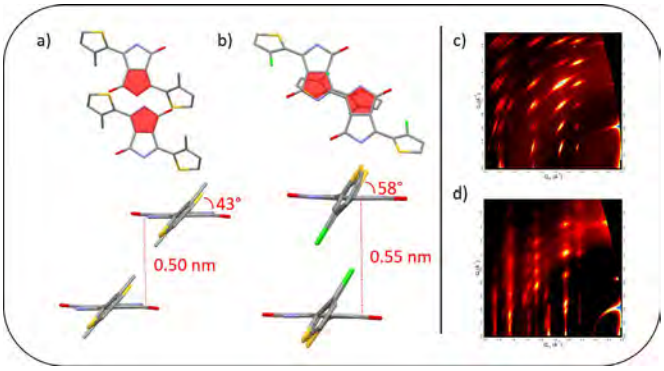

Figure F51.4: Single crystal structures of (a) 1 and (b) 2 labelled with π-stacking distances and core/flanking unit dihedral angles, and positions of DPP cores marked in red to illustrate the extent of π-overlap; GIWAXS scattering patterns of as-cast films of (c) 1 and (d) 2.

While their crystalline packing behaviours render these strained DPPs ill-suited for intermolecular SF applications, we believe that we are still able to harness their raised triplet energy level by turning to molecular architectures that can harness *intra*molecular SF. Our recently published article has demonstrated that coupling multiple chromophores to a self-assembling core can provide the necessary driving force to overcome the local order constraint hindering intermolecular SF (Masoomi-Godarzi et al., 2019) and we are currently harnessing both these approaches to develop high-T_1, intramolecular singlet fission molecules.

2. Anti-Kasha derived singlet fission processes

Chromophores exhibiting anti-Kasha type behaviour do not vibrationally relax to and subsequently radiatively emit from the lowest excited state of a given multiplicity, as mandated by the eponymous rule, but rather are capable of luminescence from higher states. Azulenes are one of the earliest known molecules exhibiting such behaviour, and are known to exhibit room-temperature fluorescence from the $S_2 \rightarrow S_0$ state, with several other factors contributing towards long S_2 lifetimes and limited $S_1 \rightarrow S_0$ fluorescence yields (Tétreault et al., 1999). Of interest to us is the decades-old prediction that S_2-derived SF was possible (Figure F51.5(a)) (Nickel and Klemp, 1993) and, indeed, several articles since then have confirmed that not only are the azulene energy levels on the threshold of facilitating exothermic singlet fission ($E(S_2) \geq E(2T_1)$), but that its relatively high T_1 energy of around 1.7 eV is more than sufficient for energy transfer to silicon (Steer, 2019, Vossköttter et al., 2015).

Our aim in this project was to design a series of azulene derivatives with (a) an expanded S_2-S_1 energy gap in order to hinder S_2-S_1 vibrational decay and increase the S_2 excited-state population, and (b) to increase the S_2-T_1 energy gap in order to ensure the exothermic nature of the SF process. This can be accomplished via functionalisation at specific sites in accordance with HOMO-LUMO overlap nodes, with resonant electron-donating substituents at odd-numbered positions and resonant electron-withdrawing substituents at even-numbered positions lowering both T_1/S_1 energy levels,(Xin and Gao, 2017) and increasing both our target energy gaps. After a computational screening of various combinations of functional

groups by TD-DFT calculations (Figure F51.5(b)), we selected three azulene analogues (4-6) to pursue. This project is being undertaken in collaboration with the Laser Chemistry Group at the University of Saskatchewan.

UV-Vis absorption studies on the three analogues find that our molecules exhibit significantly stronger S_2 absorbances (Figure F51.5(c)) in accordance with the weak oscillator strengths of the S_0S_1 transition – a favourable property for the absorption of high-energy photons as an SF material – and exhibit energy-level trends in accordance with our DFT calculations. As expected, detectable emission occurs exclusively from the S_2 band in the solution state, and we find that all analogues undergo efficient triplet-triplet energy transfer from a platinum *meso*-tetraphenyltetrabenzoporphyrin triplet sensitiser ($E(T_1)$ = 1.55 eV). We are currently conducting studies to determine exact triplet energy levels, fluorescence quantum yields and time-resolved solid-state photophysical behaviour in order to assess the degree to which singlet fission occurs. If observed, we will demonstrate a groundbreaking approach towards harnessing energy and redefine and broaden the requirements for a molecule to undergo singlet fission.

References

CASILLAS, R., PAPADOPOULOS, I., ULLRICH, T., THIEL, D., KUNZMANN, A. & GULDI, D. M. 2020. Molecular insights and concepts to engineer singlet fission energy conversion devices. *Energy & Environmental Science*, 13, 2741-2804.

CONRAD-BURTON, F. S., LIU, T., GEYER, F., COSTANTINI, R., SCHLAUS, A. P., SPENCER, M. S., WANG, J., SÁNCHEZ, R. H., ZHANG, B., XU, Q., STEIGERWALD, M. L., XIAO, S., LI, H., NUCKOLLS, C. P. & ZHU, X. 2019. Controlling Singlet Fission by Molecular Contortion. *Journal of the American Chemical Society*, 141, 13143-13147.

HARTNETT, P. E., MARGULIES, E. A., MAUCK, C. M., MILLER, S. A., WU, Y., WU, Y.-L., MARKS, T. J. & WASIELEWSKI, M. R. 2016. Effects of Crystal Morphology on Singlet Exciton Fission in Diketopyrrolopyrrole Thin Films. *The Journal of Physical Chemistry B,* 120, 1357-1366.

MASOOMI-GODARZI, S., LIU, M., TACHIBANA, Y., MITCHELL, V. D.,

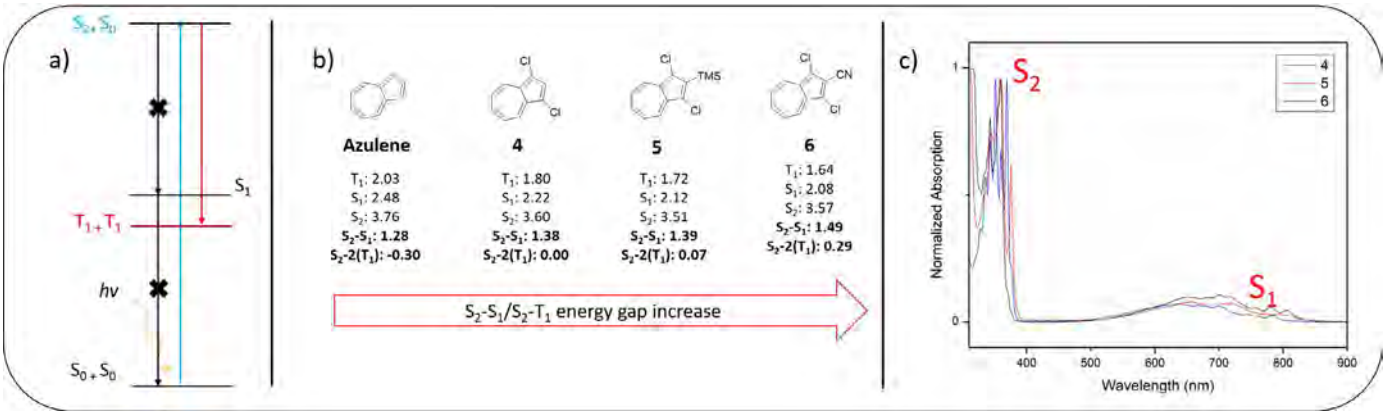

Figure F51.5: (a) A simplified diagram demonstrating the theorised S_2-derived singlet fission process; (b) candidates for a structure-property singlet fission study identified through TD-DFT calculations (geometry optimisation for molecules in solution performed via B3LYP/6-311+G(2d,p), energy-level TD-DFT calculations performed via B3LYP/def2-TZVPP); and (c) solution-state UV-Vis absorption spectra for the three azulene analogues.

Highlights

- A method for raising the triplet energy levels of well-known singlet fission materials to meet the requirements for energy transfer to silicon was investigated.
- A series of anti-Kasha molecules were designed to harness higher-state energy levels for currently unreported pathways towards singlet fission.

Future Work

- Probe the energy levels of the strained chromophores to confirm that systematic structural perturbation can be a reliable approach for raising triplet energy levels.
- Incorporate the strained chromophores with moieties capable of self-association to provide the solid-state order necessary for intramolecular singlet fission.
- Further characterise the azulene analogues to assess their capability for singlet fission.

GOERIGK, L., GHIGGINO, K. P., SMITH, T. A. & JONES, D. J. 2019. Liquid Crystallinity as a Self-Assembly Motif for High-Efficiency, Solution-Processed, Solid-State Singlet Fission Materials. *Advanced Energy Materials,* 9, 1901069.

MINAMI, T., ITO, S. & NAKANO, M. 2013. Fundamental of Diradical-Character-Based Molecular Design for Singlet Fission. *The Journal of Physical Chemistry Letters,* 4, 2133-2137.

NAKANO, M. 2017. Electronic Structure of Open-Shell Singlet Molecules: Diradical Character Viewpoint. *Topics in Current Chemistry,* 375, 47.

NICKEL, B. & KLEMP, D. 1993. The lowest triplet state of azulene-h8 and azulene-d8 in liquid solution. I. Survey, kinetic considerations, experimental technique, and temperature dependence of triplet decay. *Chemical Physics,* 174, 297-318.

STEER, R. P. 2019. Photophysics of molecules containing multiples of the azulene carbon framework. *Journal of Photochemistry and Photobiology C: Photochemistry Reviews*, 40, 68-80.

TÉTREAULT, N., MUTHYALA, R. S., LIU, R. S. H. & STEER, R. P. 1999. Control of the Photophysical Properties of Polyatomic Molecules by Substitution and Solvation: The Second Excited Singlet State of Azulene. *The Journal of Physical Chemistry A,* 103, 2524-2531.

VOSSKÖTTER, S., KONIECZNY, P., MARIAN, C. M. & WEINKAUF, R. 2015. Towards an understanding of the singlet–triplet splittings in conjugated hydrocarbons: azulene investigated by anion photoelectron spectroscopy and theoretical calculations. *Physical Chemistry Chemical Physics,* 17, 23573-23581.

WEN, J., HAVLAS, Z. & MICHL, J. 2015. Captodatively Stabilized Biradicaloids as Chromophores for Singlet Fission. *Journal of the American Chemical Society,* 137, 165-172.

XIN, H. & GAO, X. 2017. Application of Azulene in Constructing Organic Optoelectronic Materials: New Tricks for an Old Dog. *ChemPlusChem,* 82, 945-956.

AUSTRALIAN CENTRE FOR ADVANCED PHOTOVOLTAICS

UNSW SYDNEY NSW 2052 AUSTRALIA

Tel: +61 2 9385 4018
Email: acap@unsw.edu.au
Website: acap.org.au

Director: Scientia Professor Martin Green